

Black-Hole
Accretion Disk

Black-Hole Accretion Disk Towards a New Paradigm

Shoji Kato, Jun Fukue and Shin Mineshige



Shoji Kato, Jun Fukue



Kyoto University Press

ISBN978-4-87698-740-5
C3044 ¥6300E



9784876987405

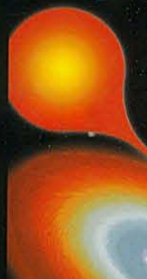
定価：本体6300円(税別)

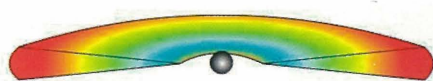


1923044063000

Accretion Disks Towards a New Paradigm

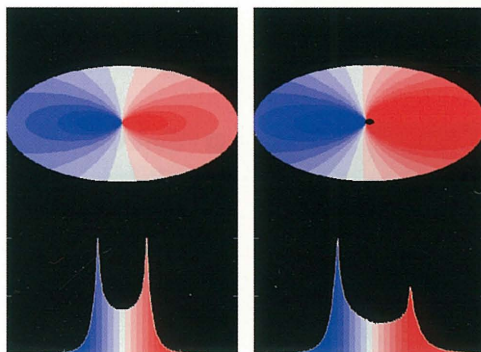
and Shin Mineshige





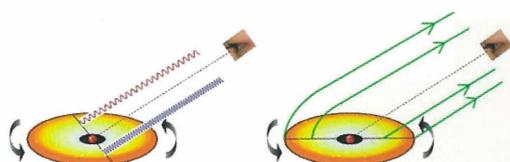
■ **Figure G.1**

Accretion disk around a black hole.



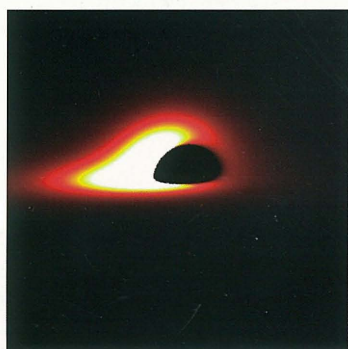
■ **Figure G.3**

Disk emission line (see figures 3.11 and 6.6).



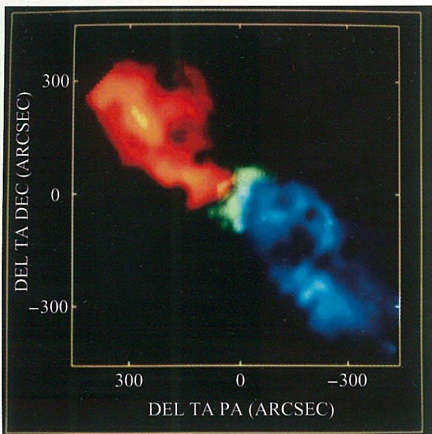
■ **Figure G.4**

Doppler effect and gravitational lensing
(see figure 6.4).



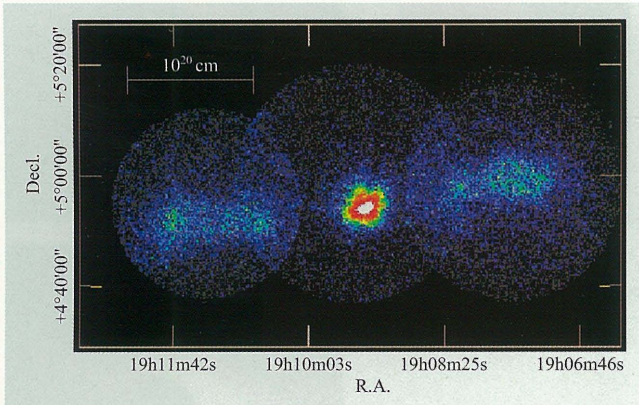
■ **Figure G.2**

Appearance of relativistic accretion disks. The spin parameter is 0, 0.8, and 1. (Courtesy of R. Takahashi)



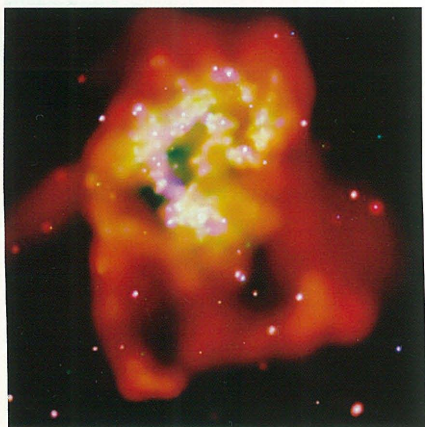
■ **Figure G.5**

L1551 bipolar jets (see figure 1.12).



■ **Figure G.6**

X-ray jets in SS433
(JAXA/ISAS).



■ **Figure G.7**

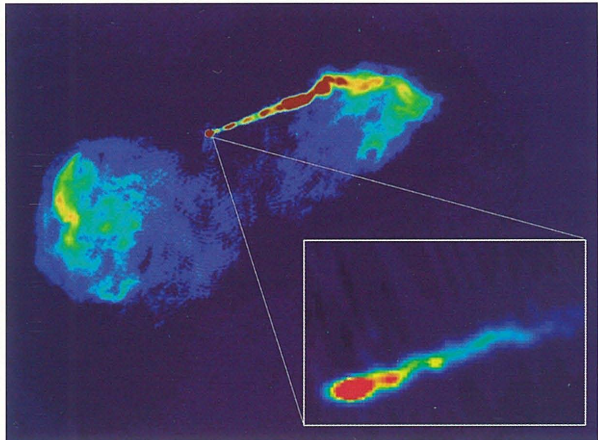
X-ray image of the Antennae Galaxy NGC 4038/9 (NASA/CXC/SAO/G. Fabbiano et al.).

Figure G.8

Optical image of M87
(NAOJ).

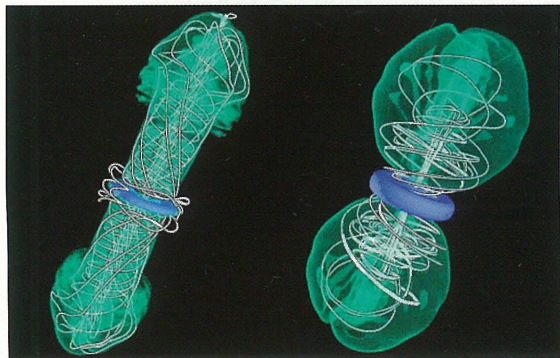
**Figure G.9**

Radio image of M87
(NRAO/JAXA).

**Figure G.10**

Magnetohydrodynamical
jets from an accretion
disk.

(Courtesy of Y. Kato)



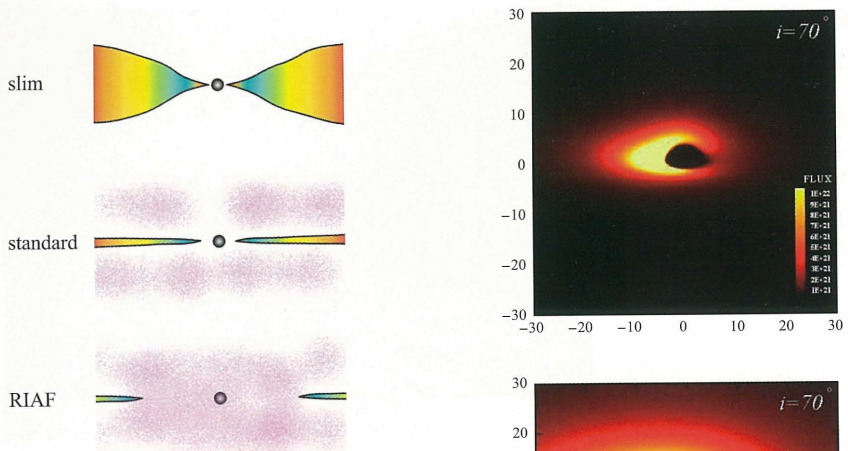


Figure G.11
New-type accretion disks (see figure 1.41).

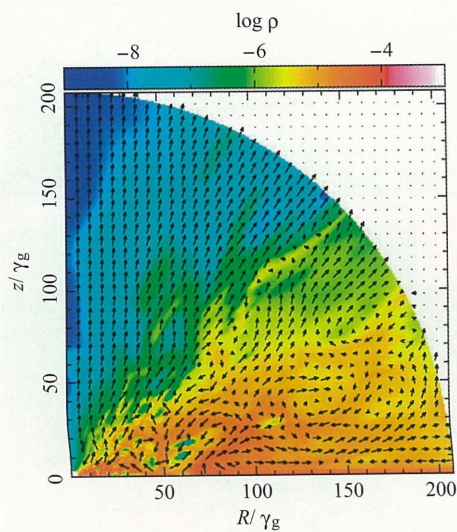


Figure G.13
Supercritical accretion flow
(see figure 10.19). (Courtesy of K. Ohsuga)

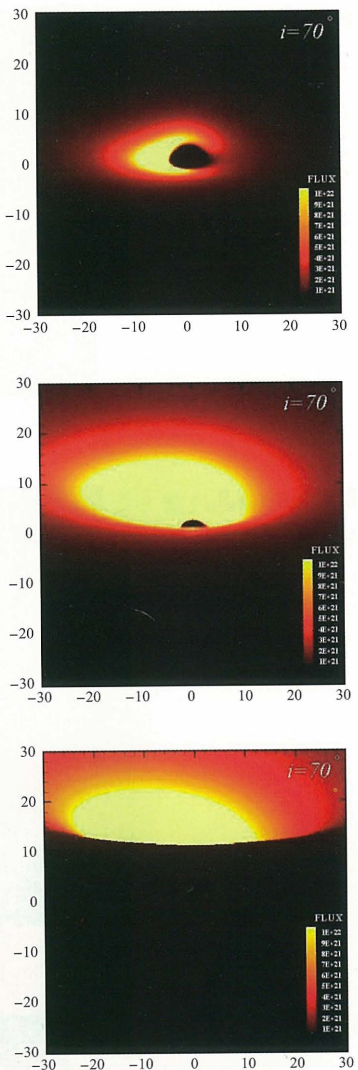


Figure G.12
Appearance of relativistic
slim disks.
(Courtesy of K. Watarai)

Black-Hole Accretion Disks

Towards a New Paradigm

by

Shoji Kato

Jun Fukue

Sin Mineshige



Kyoto University Press

The publication of this volume was partially funded by the Kyoto University Foundation.

First published in 2008 by:

Kyoto University Press
Kyodai Kaikan
15-9 Yoshida Kawara-cho
Sakyo-ku, Kyoto 606-8305, Japan Telephone: +81-75-761-6182
Fax: +81-75-761-6190
Email: sales@kyoto-up.or.jp
Web: <http://www.kyoto-up.or.jp>

Copyright © S. Kato, J. Fukue, and S. Mineshige 2008

All rights reserved. No production of any part of this book may take place without the written permission of Kyoto University Press.

ISBN 978-4-87698-740-5

Preface

Accretion onto black holes is one of the most fundamental concepts for understanding a variety of active phenomena in the Universe, including active galactic nuclei, stellar-mass black holes, ultra-luminous X-ray sources, γ -ray bursts, and stellar and galactic jets.

Theoretical studies on black-hole accretion flows were initiated in the 1960's and a classical picture of accretion disks was established by the early 1970's. A large body of observational data accumulated since then, however, required some another type of disk models distinct from the classical one. As a model to meet this requirement, advection-dominated accretion flows appeared before the footlights and were extensively studied in the 1990's. We published the first edition of this book in that epoch in order to present a systematic review of the accretion-disk theories at that stage, while emphasizing the contributions of our group in Kyoto.

Nearly a decade has passed since then, and much progress during that term makes the first edition already behind our current understanding of accretion flows. In particular, models of advection-dominated accretion flows and their comparison with observations, including cases of super-Eddington accretion, have been greatly developed and deepened. The launch of the Rossi X-ray Timing Explorer led to the discovery of high-frequency quasi-periodic oscillations, which seem to have originated in the innermost part of relativistic accretion disks. Furthermore, direct observations of black-hole accretion-disk systems are now drawing near owing to the development of observational techniques. Considering these situations, we think it is a good time to fully revise the first edition in order to meet the developments mentioned above, while again emphasizing contributions by our group in Kyoto.

Under our policy that the revised edition should not become thicker, some subjects in less developing fields are omitted in this revised edition, although this does not mean that they are less important.

The revised edition consists of four parts. We first outline in Part I the historical background and observational evidence for black-hole accretion disks and the basic physical processes necessary for understanding accretion. In Part II, the classical pictures of accretion disks are presented, including their stabilities and observabilities. Modern pictures of accretion disks are presented in Part III. After some prepara-

tions concerning basic equations and a discussion on the transonic nature of flows, current accretion-disk models are described in chapters 9 and 10. Chapter 9 is for low-luminosity accretion flows and chapter 10 for high-luminosity accretion flows. In Part IV, topics involving disk oscillations are described: introductory statements in chapter 11 and models of high-frequency quasi-periodic oscillations in chapter 12.

Many excellent books and proceedings on accretion disks have been published so far; e.g., *Accretion Power in Astrophysics* by Frank, King and Raine (Cambridge University Press, 1985, 1992, 2002) and *Accretion Disks in Compact Stellar Systems* edited by Wheeler (World Scientific, 1993). Compared with them, one of characteristics of the present book is that current accretion-disk models are carefully described from the basic processes concerning accretion. Furthermore, observational and dynamical features of the models are carefully presented. This book has also been designed so as to meet various requirements by readers. Students who are just starting to learn about black-hole accretion flows should first read Part I in order to obtain a basic understanding. If one wishes to study the basics of classical disk models from the fundamental levels, please read from Part II. Those who are already familiar with the classical models may start reading from Part III. All necessary ingredients, including the basic equations and important concepts for understanding, are repeated with some extension there.

We appreciate Fred Myers for his English editing. Ramesh Narayan is particularly appreciated for having encouraged us to publish this revised edition. Andrzej A. Zdziarski is particularly thanked for his pointing out some errors in the first edition. We are grateful to many colleagues and collaborators for their help in various stages of writing the first and second editions. In addition to those mentioned in the first edition, we would like to thank Ken Ohsuga, Rohta Takahashi and Ken-ya Watarai for discussion and the preparation of figures. Finally, many thanks are due to Tetsuya Suzuki of the Kyoto University Press for editorial arrangements. The publication of this book was supported in part by a Grant from the Kyoto University Foundation.

1 August, 2007 in Kyoto

Shoji Kato
Jun Fukue
Shin Mineshige

Outline of the Book

Part I. Concepts

1. Introduction
2. Basic physics

Part II. Classical Picture

3. Classical models
4. Stability
5. DN-type instability
6. Observability

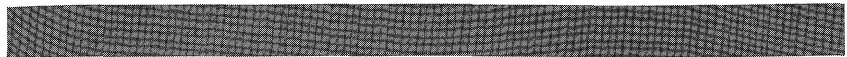
Part III. Modern Picture

7. Basic equations
8. Transonic flow
9. RIAF
10. Slim disk

Part IV. Oscillations

11. Disk oscillations
12. QPOs

Appendix



CONTENTS

Preface	iii
Contents	v

Part I Concepts of Accretion Disks

Chap. 1 Introduction	3
1.1 Accretion Energy – Historical Origin	3
1.2 Accretion-Disk Paradigm – Active Universe	11
1.3 Accretion-Powered Objects – Observational Reviews	18
1.4 X-Ray Binaries and Ultra-Luminous Sources	27
1.5 Active Galactic Nuclei	39
1.6 Present Paradigm	49

Chap. 2 Physical Processes Related to Accretion	57
2.1 Eddington Luminosity	57
2.2 Bondi Accretion	61
2.3 Viscous Process	66
2.4 Magnetic Instabilities	74
2.5 Relativistic Effects	82

Part II Classical Picture

Chap. 3 Classical Models	97
3.1 Viscous Accretion Disks	97
3.2 Standard Disks	103
3.3 Optically Thin Disks	133
3.4 Accretion Disk Coronae	138

3.5 Relativistic Standard Disks	143
3.6 Relativistic Tori	151
 Chap. 4 Secular and Thermal Instabilities	 161
4.1 Secular Instability	162
4.2 Thermal Instability	168
4.3 Stability Examination on $M\text{-}\Sigma$ and $T\text{-}\Sigma$ Planes	172
4.4 Mathematical Derivation of the Stability Criterion	175
 Chap. 5 Dwarf-Nova Type Instability	 183
5.1 Thermal-Ionization Instability	183
5.2 Time Evolution of Disks in X-Ray Novae	196
 Chap. 6 Observability of Relativistic Effects	 211
6.1 Ray Tracing	211
6.2 Imaging – Black Hole Silhouette	215
6.3 Spectroscopy – Continuum and Line	217
6.4 Photometry – Light Curve Diagnosis	222
6.5 Other Effects – Lensing and Jets	226

Part III Modern Picture

 Chap. 7 Equations to Construct Generalized Models	 237
7.1 Basic Equations and Importance of Advection	237
7.2 One-Temperature Disks	243
7.3 Two-Temperature Disks	251
7.4 Time-Dependent Equations	255
 Chap. 8 Transonic Nature of Accretion Flows	 259
8.1 Topology of Black-Hole Accretion	259
8.2 Regularity Condition at a Critical Radius	263
8.3 Topology around the Critical Radius in Isothermal Disks	265
8.4 Numerical Examples of Transonic Flows	272
8.5 Transonic Flows with Standing Shocks	276
 Chap. 9 Radiatively Inefficient Accretion Flows	 283
9.1 Advection-Dominated Accretion Flow	283
9.2 Radial Structure of Advection-Dominated Flow	293
9.3 Radiation Spectra of Advection-Dominated Flow	302
9.4 Stability of Advection-Dominated Flow	307

9.5 Multi-Dimensional Effects	320
Chap. 10 Slim Accretion Disks and Supercritical Flows	333
10.1 Photon Trapping and Slim Disk Model	333
10.2 Radial Structure of Slim Disks	344
10.3 Radiation Spectra of Slim Disks	350
10.4 Relaxation Oscillations in Hot Accretion Disks	353
10.5 Multi-Dimensional Effects of Supercritical Flow	361
10.6 Neutrino-Cooled Disks	369

Part IV Oscillations and Waves

Chap. 11 Fundamentals of Disk Oscillations	381
11.1 Classification of Disk Oscillations	381
11.2 Basic Equations	389
11.3 Dispersion Relation and Basic Properties	393
11.4 One-Armed Low-Frequency Global Oscillations	404
11.5 Amplification of Disk Oscillations by Viscosity	411
Chap. 12 Quasi-Periodic Oscillations	417
12.1 Observations of Quasi-Periodic Oscillations	417
12.2 Sonic-Point Instability and Trapped Oscillations	423
12.3 Resonant Oscillations in Warped Disks	433
12.4 Comparison of Warp Models with Observations	446
12.5 Other Disk-Oscillation Models of QPOs	454

Appendix

A Kerr Metric and its Basic Properties	465
A.1 Basic Properties	465
A.2 Circular Motion in Kerr Space-Time	469
B Navier-Stokes Equations	476
B.1 General Form	476
B.2 Cylindrical Coordinate Expression	481
C Equations for Relativistic Viscous Fluid	484
C.1 Metric and Energy-Momentum Tensor	484
C.2 General Form	486

D Radiative Transfer Equations	488
D.1 Radiation Fields	488
D.2 Equations of Radiative Transfer	489
D.3 Optically Thick to Thin Regimes	494
D.4 Matter Coupling	497
D.5 Plane-Parallel Expression	498
E Equations for Relativistic Radiation Hydrodynamics	500
E.1 Metric and Energy-Momentum Tensor	500
E.2 Equations of Radiative Transfer	504
E.3 Relativistic Regimes	508
E.4 Matter Coupling	510
E.5 Plane-Parallel Expression	513
F Magnetohydrodynamical Equations	516
F.1 Maxwell Equations and MHD Approximations	516
F.2 MHD Equations	517
F.3 Cylindrical Coordinate Expression	518
G Equations for Relativistic Magnetohydrodynamics	520
G.1 Metric and Energy-Momentum Tensor	520
G.2 Relativistic Maxwell Equations	521
G.3 Relativistic MHD Equations	523
H Relativistic Equation of State	524
H.1 Equation of State	524
H.2 Adiabatic Sound Speed and Effective Adiabatic Index	526
I Cooling of Relativistic Gas	528
I.1 Bremsstrahlung Cooling	528
I.2 Synchrotron Cooling	529
I.3 Comptonization	530
List of Symbols	532
Index	539
Credits	547

Part I Concepts of Accretion Disks

CHAPTER I

Introduction

It is traditionally believed that the basic unit of the constituents of the heavens is a star. In fact, visible objects are mostly made up of stars; star clusters and galaxies are assemblies of stars, and network distributions of galaxies form the large-scale structure of the universe. Since the main energy source of stars is nuclear reactions, which take place at their cores, one may even have the illusion that the most important energy-generation mechanism is nuclear. This is not the case, however. In many places, gravitational energy plays an important role, as we demonstrate throughout this book. In contrast to stars, which have been known from ancient eras, the presence of accretion disks has been recognized only quite recently, i.e., from the mid-20th century. In this sense, we may say that an accretion disk is a ‘new’ type of object in the heavens. It causes an energy revolution in the universe, once created; even the dead, a black hole, is brought to life. It causes or influences various active phenomena in the universe, such as the formation of a planetary system, the evolution of binary stars, the production of astrophysical jets, and even the formation of galaxies and gamma-ray bursts.

In this book we focus our attention on the accretion disk surrounding a black hole. Before going into the details of this specific subject, however, it might be useful to describe the general background. In this chapter, therefore, we briefly discuss the importance of accretion energies in the universe, explain the basic picture of an accretion disk, and overview the current observational evidence for accretion disks at various astronomical sites.

1.1 Accretion Energy – Historical Origin

On Earth, we usually harness chemical, gravitational, and atomic energy. That is, we use the heat energy from the burning of matter to produce

electricity in thermal power plants, gravitational energy from the infall of water in hydroelectric power plants, and atomic energy from nuclear fission in nuclear power plants.

When we look up to the heavens, on the other hand, there are stars. We now understand that nature uses nuclear fusion to shine stars. Namely, the principal energy source in the universe is atomic energy. This fact was made clear in the 1930's, after long discussions in the 19th century when astronomers believed that the Sun creates energy by making use of its gravitational binding energy through contraction. Over a period of a half century, nuclear-energy generation had become the central paradigm in astronomy.

During these decades, however, this "common sense" view seems to have shifted. This is because *accretion disks*, where gravitational energy plays the dominant role, have become widely recognized.

In this subsection we first review several energy sources in the universe, and discuss the significance of the accretion energy, referring to the discovery of quasars as an example.

1.1.1 Energy Sources in the Universe

As is well known, the main energy source of stars is nuclear fusion, which takes place in their central regions. Historically, however, other candidates, such as chemical reactions or gravitational energy, were considered to be the energy source. Here, we compare chemical, gravitational, and nuclear energies from the viewpoint of the energy-conversion *efficiency* from the rest-mass energy.

In the case of the Sun, for instance, the solar mass M_{\odot} , the solar luminosity L_{\odot} , and the solar age τ_{\odot} are, respectively,

$$M_{\odot} = 1.99 \times 10^{33} \text{ g}, \quad (1.1)$$

$$L_{\odot} = 3.85 \times 10^{33} \text{ erg s}^{-1}, \quad (1.2)$$

$$\tau_{\odot} = 4.60 \times 10^9 \text{ yr}. \quad (1.3)$$

The total radiant energy E_{\odot} of the Sun until today has thus been

$$E_{\odot} = L_{\odot} \times \tau_{\odot} = 5.60 \times 10^{50} \text{ erg}, \quad (1.4)$$

if the solar luminosity has not changed very much since its birth. However, the total rest-mass energy of the Sun is

$$M_{\odot}c^2 = 1.79 \times 10^{54} \text{ erg}, \quad (1.5)$$

where $c (= 3.00 \times 10^{10} \text{ cm s}^{-1})$ is the speed of light.

Hence, the ratio of the total radiant energy to the total rest-mass energy, the efficiency η_{\odot} of the energy conversion, becomes

$$\eta_{\odot} = \frac{L_{\odot}\tau_{\odot}}{M_{\odot}c^2} = 0.000313, \quad (1.6)$$

which is a dimensionless parameter of the system from the viewpoint of energetics. In the case of the Sun, the efficiency of the actual energy source must exceed this estimate.

(a) Chemical energy

In our daily life we use chemical energy, which is the binding energy of atoms and/or molecules. For example, 1 kg of coal is perfectly burned to produce 5000–8000 kcal of heat, while 1 kg of kerosene gives about 10000 kcal, which equals 4.2×10^{14} erg. The efficiency η_C of a chemical reaction is

$$\eta_C \sim 5 \times 10^{-10}. \quad (1.7)$$

This is too small to account for the solar and stellar energy sources.

(b) Gravitational energy

If an object of mass M gravitationally contracts from infinity to radius R , the gravitational energy released is approximately GM^2/R , while the material energy is Mc^2 . The efficiency η_G of gravitational energy is

$$\eta_G \sim \frac{GM}{Rc^2} \sim 2 \times 10^{-6} \quad (1.8)$$

for the Sun. This is also too small to be a solar energy source, although it may be quite important during the birth phase of protostars.

(c) Nuclear energy

Finally, in hydrogen nuclear fusion, where four hydrogen atoms convert into one helium atom, the mass deficit per particle is $(4 \times 1.0079 - 4.0026)/4 \sim 0.029/4 \sim 7 \times 10^{-3}$. The efficiency η_N of hydrogen nuclear fusion is

$$\eta_N \sim 0.007. \quad (1.9)$$

This is sufficient for solar energy. If we consider normal stellar cases, therefore, nuclear energy is the best energy source. However, this is no longer the case for astrophysical objects containing compact objects, such as neutron stars or black holes.

1.1.2 Discovery of Quasars

Several sky-survey projects, in which the sky is systematically scanned in the radio band and a radio-source catalogue is compiled, were started as radio astronomy was developed after World War II.

Among them, for example, the third Cambridge radio-source catalogue, the so-called 3C catalogue, was published in 1959 by Cambridge University. In this 3C catalogue, 471 objects are listed, which lie between -25° and 70° in declination, and which radiate greater than 8 Jy at a frequency of 159 MHz. Based upon this catalogue, the identification of their optical counterparts was started.

Using the 5 m reflector at the Palomar Observatory, Matthews and Sandage found in 1960 a 16-magnitude “star” (point-like) at the position of 3C 48, the 48th registered object in the 3C catalogue (Matthews and Sandage 1963). This “star” is extremely blue compared with a normal star, changes its brightness within one year or on a much shorter timescale, has some faint nebulosity around itself, and is *not* normal. This discovery of “radio stars” excited the astronomical community. Soon, Greenstein obtained the spectrum of 3C 48, which was revealed to be extraordinary in the sense that it exhibits broad emission features (Greenstein and Matthews 1963). He concluded that these features originated from metal, since he considered 3C 48 to be a peculiar star.



Figure 1.1
Luminous quasar 3C 273. (NOAO/AURA/NSF)

In 1962, using lunar occultation, Hazard and his colleagues identified another strong radio source, 3C 273, as a 13-mag “star” (Hazard et al. 1963)(figure 1.1). They determined accurate positions of two components, A and B; the latter coincided with a point-like source and the former showed a jet-like structure. At the end of the year, Schmidt observed its spectrum, where there exist six bizarre emission features. In February of 1963, Schmidt noticed that these emission features are

just the hydrogen Balmer lines, although they are shifted toward long wavelengths (i.e., redshifted) by 16 percent from their rest wavelengths (Schmidt 1963) (figure 1.2). This was the moment of the discovery of quasars.

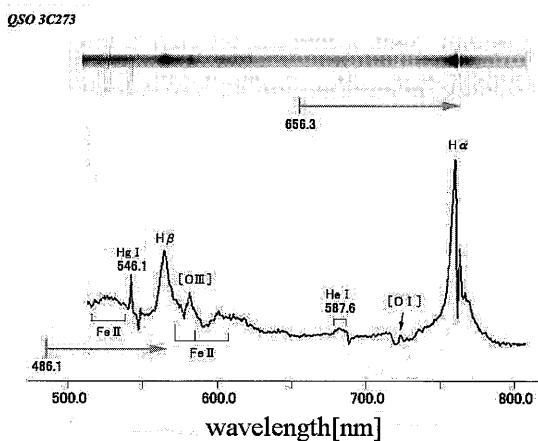


Figure 1.2

Optical spectra of 3C 273. (Courtesy of T. T. Takeuchi and T. T. Ishii /OAO/NAOJ)

It was immediately found that the redshift of 3C 48 is 0.367. They say that upon hearing about Schmidt's discovery Greenstein gazed up to the sky.

Like 3C 273 and 3C 48, those star-like objects, which exhibit strong emission lines and are remarkably redshifted, were coined *quasar* by H. Chiu in 1964 (Chiu 1965).

There was a long discussion as to whether quasars are extragalactic or Galactic objects. Since large gravitational redshifts can arise at a place where gravity is very strong, quasars could be members of our Galaxy if the optical lines originate from the vicinity of a relativistic object, such as a black hole. We now believe, however, that quasars are cosmological objects and that their large redshifts represent the cosmological expansion. The fact that the redshift z of 3C 273 is 0.158 means that its distance is about 1.9×10^9 light years ($H_0 = 71 \text{ km s}^{-1} \text{ Mpc}^{-1}$).¹

If so, quasars should release an enormous amount of energy, which

¹Using the redshift z and the Hubble constant H_0 , the distance r is estimated as $r = cz/H_0$ in the non-relativistic regime of $z \lesssim 0.1$. In the relativistic regime of $z \gtrsim 0.1$, on the other hand, $r = (c/H_0)2(1 - 1/\sqrt{1+z})$, when the universe is flat.

was a puzzle in those days. In the case of 3C 273, for example, the radiant energy, evaluated based on its apparent luminosity and distance (estimated from its redshift), is up to 10^{47} erg s $^{-1}$. Since the typical galaxy radiates about 10^{44} erg s $^{-1}$, 3C 273 is a thousand-times more luminous than a normal galaxy. In addition, this tremendous energy is radiated from the very center of quasars.

Since the discovery in 1963, the energy source of quasars has been a great enigma in astronomy. This was finally solved (at least energetically) by the concept of *supermassive black holes and surrounding accretion disks*.

1.1.3 Energetics of Quasars

Quasars are remarkably luminous and radiate in all electromagnetic wavelengths from radio to X-ray and gamma-ray. Furthermore, they temporally change their luminosities. These two characteristics impose severe conditions on the nature of the energy source sitting at the center of a quasar.

(a) Total amount of radiant energy

The total energy E radiated from quasars is $E \sim L\tau$, where L is the luminosity and τ the lifetime. Of these, the luminosity L is estimated from the observed apparent luminosity and the redshift (i.e., distance). Although the luminosity differs in individuals, it is typically 10^{45-46} erg s $^{-1}$.

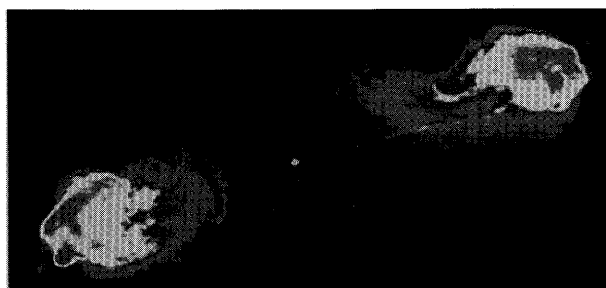


Figure 1.3

Double structure of Cyg A, the radio galaxy. (NRAO)

On the other hand, the lifetime τ is evaluated from an extension of the radio structure around quasars (figure 1.3). That is, there often exist extended radio structures around quasars, and it is believed that they

originate from the center of quasars. Therefore, if we divide the extension of the radio lobe by the speed of light, c , we obtain the lower limit of the lifetime. In the typical case we have $\tau \gtrsim 10^6$ yr.

From these values, the total radiant energy becomes

$$E \gtrsim 10^{60} \text{ erg.} \quad (1.10)$$

(b) Size of the energy source

If the size of the energy source is infinitesimally small, it can vary on an infinitesimally short timescale. In general, however, the energy source has a finite size and the timescale of the variations should also be finite. That is, the timescale t is related to the size R by $t \gtrsim R/c$. In other words, when the source varies on timescale t , the size R of the source must be

$$R \lesssim ct. \quad (1.11)$$

In some cases the quasar luminosity varies by more than 10 percent on timescales of a few days or less (figure 1.4). From these observational results, the size of the energy source in quasars would be smaller than

$$R \lesssim \text{one light day} \sim 10^{15} \text{ cm.} \quad (1.12)$$

(c) Candidates for the energy source

The energy source of quasars must typically radiate 10^{60} erg and has a size smaller than a few light days. We will compare the nuclear and gravitational energies as candidates for the energy source of quasars.

Let us first consider nuclear energy. Since the efficiency of hydrogen burning is 0.007, hydrogen of mass M , when perfectly converted to helium, would release energy E of

$$E = 0.007Mc^2. \quad (1.13)$$

Therefore, hydrogen gas of $10^8 M_\odot$ would burn to produce nuclear energy of 10^{60} erg needed for quasars. However, if such a large mass is concentrated in a small region of a few light days, the gravitational energy would be greater than the nuclear energy, as estimated below.

Let us next consider gravitational energy. As already stated, the gravitational energy E of an object of mass M and size R is approximately

$$E \sim \frac{GM^2}{R}. \quad (1.14)$$

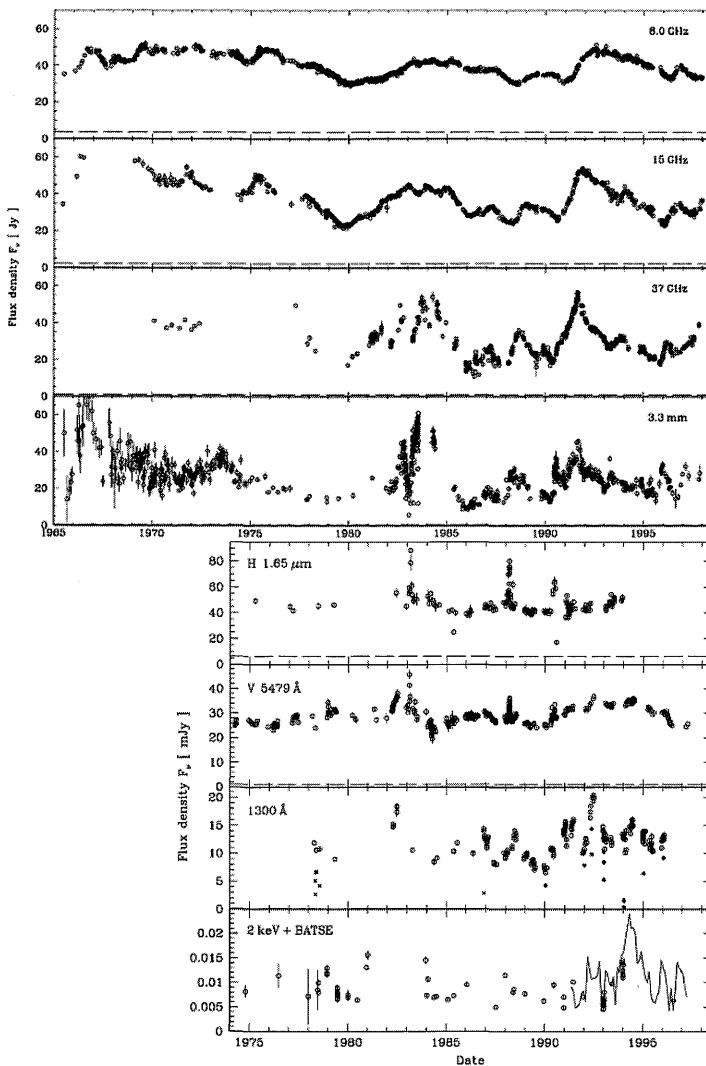


Figure 1.4
30 years of multi-wavelength observations of quasar 3C 273. (After Türler et al. 1999)

Therefore, if material of $10^8 M_\odot$ is confined in a small region of one light day ($\sim 10^{15}$ cm), the resultant gravitational energy could easily exceed 10^{60} erg.

Thus, in contrast to stars, where the main energy source is nuclear, *gravitational energy plays a dominant role in quasars*.

In the case of stars the gravitational potential at their surface (GM/R per unit mass) is relatively smaller than that in quasars and the energy-production efficiency (out of rest-mass energy) via gravitational energy is small. Its efficiency increases, however, as the potential becomes deeper. In the case of a black hole, the efficiency is from 0.057 for a Schwarzschild (non-rotating) black hole to 0.42 for an extreme Kerr (rotating) black hole (see section 2.5 and appendix A).

Then, how to release gravitational energy in quasars ?

1.2 Accretion-Disk Paradigm – Active Universe

Historically, since the discovery of quasars in 1960's, many researchers have proposed various models of quasars, including compact star clusters, superstars, and so on. In such a chaotic state, Lynden-Bell (1969) proposed a concept of black-hole disk accretion — *a supermassive black hole-accretion disk system*, which is now widely accepted and observationally supported. Furthermore, the accretion-disk system turns out to be a clue to understanding various astronomical activities. That is, the accretion disk is believed to operate as the *prime mover* for active phenomena in the universe (see section 1.3).

In this section, after we make several historical remarks, we overview the basic concept of an accretion-disk model and its implications to astronomy.

1.2.1 Theoreticians

In the previous section we estimated the gravitational energy of a contracting object, which is implicitly assumed to be isolated. When the gas infalls on a compact object, some of gravitational energy of the gas is released. This is a *mass-accretion* process in astronomy. Since the mass accretion liberates gravitational energy, the accretion process may be important in several situations in astronomy.

The importance of such an energy liberation associated with mass-accretion processes was first pointed out by Zel'dovich and Novikov (1964) and Salpeter (1964), independently. They considered, however, an isolated system. As an energy source of X-ray stars, Hayakawa and Matsuoka (1964) proposed accretion processes in a binary system, while Shklovsky (1967) explained Sco X-1 as accretion onto a neutron star.

Before long, in order to explain the energy source of quasars, Lynden-Bell at Cambridge University proposed the concept of a *viscous accretion disk* in 1969 (see, however, Lüst 1952).

In those days (around 1970), the importance of the accretion process and the concept of accretion disks began to be recognized in the field of interacting binary stars. Several attempts to construct a standard model had been made by a number of authors until Shakura and Sunyaev proposed a fundamental model for accretion disks in 1973. The Shakura-Sunyaev model is now referred to as the *standard accretion-disk model*, or, in short, as an alpha disk. (The relativistic version was given by Novikov and Thorne in 1973.) This was an epoch-making paper and this standard picture of their accretion-disk model has been a central dogma in the field of accretion disks for more than two decades (see chapter 3).

Since then, from the late 1970's to the early 1980's, the Shakura-Sunyaev theory has been applied to cool disks, in which hydrogens become recombined, and a distinct cool branch has been found (e.g., Hōshi 1979; Meyer and Meyer-Hofmeister 1981). This branch seems to be important when discussing the evolution of transient sources (chapter 5).

According to the Shakura-Sunyaev theory, gravitational energy is efficiently transformed into radiation, so that a bright disk can be observed. Distinct types of accretion disks, which have low emissivity, but high temperature, had also been considered from several different viewpoints. At around 1980, for example, geometrically thick astrophysical tori had been studied, where the gas radiates inefficiently, and purely rotating without accreting motion. A Warsaw group examined an optically thick torus, a so-called *Polish doughnut* (Abramowicz et al. 1978; Kozłowski et al. 1978; Paczyński and Wiita 1980; see also Fishbone and Moncrief 1976). Further, a Cambridge group considered hot ion tori, which are optically thin and have such a low density that they cannot radiate efficiently (Rees et al. 1982).

In the late 1980's, the presence of a new type of hot, optically thick disks was recognized by a Trieste group: i.e., *slim disks* (Abramowicz et al. 1988). In this model, *advective* energy transport plays a dominant role in the energy balance (see chapter 10). In the 1990's, furthermore, the importance of advective energy transport in the optically thin regime was recognized by a Harvard group (Narayan and Yi 1994) and a Polish group (Abramowicz et al. 1995; see also Ichimaru 1977).² This type of optically thin advection-dominated accretion flows (ADAFs) is now included in a wider notion of radiatively inefficient accretion flows (RIAFs) and has been intensively investigated by several groups, including a NORDIC group, a Harvard group, and a Kyoto group (see chapter 9).

²Ichimaru at the University of Tokyo was the first to recognize the importance of advection in the very early days of the late 1970's.

1.2.2 Concept of Accretion Disks

Accretion disks are rotating gaseous disks with accretion flow, which form around gravitating objects, such as protostars, main-sequence stars (MSs), white dwarfs (WDs), neutron stars (NSs), and *black holes* (BHs).

Accretion disks have been observed both directly and indirectly at various sites in the universe. It is now widely believed that accretion disks cause and/or activate various active phenomena in the universe: star formations, high-energy radiation, binary evolution, novae and type Ia supernovae, X-ray stars, quasars and active galaxies, astrophysical jets, and so on.

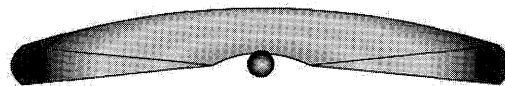


Figure 1.5

Schematic picture of a classical standard accretion disk around a black hole (see figure G.1). The disk is geometrically thin and optically thick. There is an inner edge, inside of which the disk gas freely falls into a black hole.

(a) Basic picture of standard accretion disks

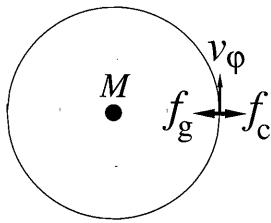
An accretion disk consists mainly of hydrogen gas (sometimes in highly ionized and sometimes in molecular forms), although helium and other elements are included in cosmical abundance.

In the classical standard picture, an accretion disk is flat (*geometrically thin*) and opaque (*optically thick*). One can imagine a *flat, but rotating, star* (see figure 1.5).

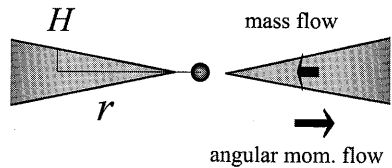
The gas in the disk is rotating around the central object with different velocities at different radii, like the planets in the solar system. That is, the gravitational force is just balanced by the centrifugal force as $GM/r^2 = r\Omega^2$, where G is the gravitational constant, M the mass of the central object, r the distance from the center, and Ω the angular speed of the gas. Therefore, the angular speed Ω is inner-faster and outer-slower according to

$$\Omega = \Omega_K \equiv \sqrt{\frac{GM}{r^3}}. \quad (1.15)$$

This differential rotation law of a geometrically thin disk is called *Keplerian rotation* (figure 1.6).

**Figure 1.6**

Rotation law in an accretion disk. The gravitational force f_g is balanced by the centrifugal force f_c ; the rotational velocity v_φ becomes Keplerian.

**Figure 1.7**

Mass and angular momentum transfer in a disk. The mass accretes inward through the disk, while the angular momentum is transferred outward.

Unlike the planets in the solar system, however, there is *friction* (*viscosity*) working between the adjacent gas layers in an accretion disk. As a result, the gas is heated up and begins to radiate electromagnetic radiation (see below). This radiation is believed to be the source of the quasar luminosity and X-ray radiation from X-ray binaries.

The friction/viscosity between the adjacent gas layers transfers angular momentum. That is, through the viscous interaction between the inner and outer layers, the faster inner layer loses angular momentum and infalls slightly, while the slower outer layer gains angular momentum slightly. Thus, the rotating disk gas gradually infalls (*accretes*) toward the center, whereas angular momentum is transferred toward the outer region (figure 1.7).

Finally, in the vicinity of a relativistic object, such as a black hole, the gravitational attraction force increases inward so strongly that there is no stable circular orbit of a particle for $r < r_{\text{ms}}$, where r_{ms} stands for the radius of the marginally stable circular orbit (section 2.5). As a result, the standard accretion disk has an *inner edge* (see figure 1.5). In the case of a Schwarzschild (non-rotating) black hole, for example, the radius r_{in} of the inner edge is

$$r_{\text{in}} \cong r_{\text{ms}} = 3r_g, \quad (1.16)$$

where r_g is the Schwarzschild radius ($= 2GM/c^2$). In the general case of a Kerr black hole, see section 2.5 and appendix A.

When gas is continually supplied from outside of the disk, the accretion disk maintains its steady form.

(b) Basic parameters

The basic parameters of an accretion disk are the mass M of the central object, the mass-accretion rate \dot{M} , and the viscous parameter α , where the mass-accretion rate means the amount of gas that infalls to the central object per unit time, and the viscous parameter represents the magnitude of the friction between the gas layers (which is explicitly defined in later sections). Of these parameters, the former two are external parameters, while the latter one is an internal parameter.

In addition, from a relativistic viewpoint, the spin parameter a_* , the amount of spin of the central black hole, is also one of basic parameters. Furthermore, from the observational viewpoint, the inclination angle i between the line-of-sight and disk normal is important, since the apparent luminosity and spectrum depend on the inclination angle, and self-occultation happens for a geometrically thick disk.

(c) Temperature, spectrum, and luminosity

It is worth noting some properties of the electromagnetic spectra and the luminosity of accretion disks in the non-relativistic limit (see chapter 3 for details).

Since the gravitational potential is deep at the center and the rotation speed is fast there, the heating rate is also larger in the inner region than in the outer region. Thus, the gas temperature of the disk is higher in the inner region (figure 1.8). This multi-temperature nature of the accretion disk is usually designated as *multi-color* from a spectrum point of view.

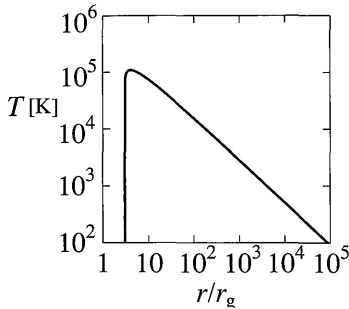
In the standard picture, the disk gas is assumed to radiate locally a blackbody spectrum with an effective temperature there. Since the disk has different temperatures at different radii (multi-temperature), the resultant disk spectrum is a superposition of the blackbody spectra with a wide range of effective temperatures (see figure 1.9 and chapter 3). Such a spectrum is called a *disk blackbody* (DBB).

Finally, let us roughly estimate the disk luminosity L_d and discuss the energy-conversion efficiency for disk accretion. A test particle of unit mass rotating circularly at radius r has kinetic energy

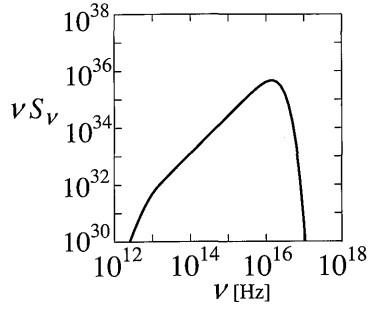
$$K = \frac{1}{2}v_\varphi^2 = \frac{GM}{2r}, \quad (1.17)$$

since $v_\varphi = r\Omega_K$ (equation 1.15), while the potential energy there is

$$U = -\frac{GM}{r} = -2K. \quad (1.18)$$

**Figure 1.8**

Temperature distribution in the standard disk for the non-relativistic case. The abscissa is the radius r , while the ordinate is the effective temperature T . The parameters are for a typical case of quasars; $M = 10^8 M_\odot$ and $\dot{M} = 1 M_\odot \text{ yr}^{-1}$. In this case, $r_{\text{in}} = 6 \text{ AU}$.

**Figure 1.9**

Spectrum of the standard disk for the non-relativistic case. The abscissa is the frequency ν , while the ordinate is the radiation intensity S_ν multiplied by the frequency, νS_ν . The parameters are for a typical case of quasars; $M = 10^8 M_\odot$ and $\dot{M} = 1 M_\odot \text{ yr}^{-1}$.

If the particle falls from infinity to radius r with zero total energy, the excess energy that can be radiated is

$$0 - (U + K) = K = \frac{GM}{2r}. \quad (1.19)$$

This implies that in the case of the (non-relativistic) standard disk the disk luminosity L_d (see also chapter 3) is given by

$$L_d = \frac{GM\dot{M}}{2r_{\text{in}}}. \quad (1.20)$$

This is *just* half of the gravitational energy (per unit mass) at the inner radius r_{in} times the mass-accretion rate. As expected, based on the nature of gravitational energy, this disk luminosity is proportional to the mass of the central object and the mass-accretion rate. In addition, it is inversely proportional to the inner radius of the disk.

For accretion disks around the Schwarzschild black holes, if we set $r_{\text{in}} = 3r_g = 6GM/c^2$, the disk luminosity becomes

$$L_d = \frac{1}{12}\dot{M}c^2, \quad (1.21)$$

which depends only on the mass-accretion rate. The radiation energy liberated associated with the mass accretion is generally written as

$$L = \eta\dot{M}c^2, \quad (1.22)$$

where η is the efficiency, at which gravitational energy is converted to radiation energy. Hence, in the above approximation the efficiency of the disk accretion onto black holes is

$$\eta_{\text{NR}} = \frac{1}{12} \quad (1.23)$$

(see section 2.5 and appendix A for details and correct values).

The disk luminosity for typical parameters becomes

$$L_d = 7.50 \times 10^{36} \left(\frac{\eta}{1/12} \right) \left(\frac{\dot{M}}{10^{17} \text{ g s}^{-1}} \right) \text{ erg s}^{-1} \quad (1.24)$$

in the case of black-hole binaries, and

$$L_d = 4.72 \times 10^{45} \left(\frac{\eta}{1/12} \right) \left(\frac{\dot{M}}{1 M_\odot \text{ yr}^{-1}} \right) \text{ erg s}^{-1} \quad (1.25)$$

in the case of active galactic nuclei.

For example, in the case of luminous active galactic nuclei with a luminosity of $L \sim 10^{46} \text{ erg s}^{-1}$, the mass-accretion rate should be $\dot{M} \sim 3 M_\odot \text{ yr}^{-1}$, if the efficiency is $\eta \sim 0.1$.

1.2.3 Gravitational Power House

Described above is the basic concept of an accretion disk around a central gravitating body. That is, the fundamental mechanism of the energy source in active astronomical objects, such as X-ray stars or quasars, is now believed to be the release of gravitational energy associated with mass accretion. Such a picture is a new paradigm in modern astronomy. By wearing the accretion disk, even a black hole is brought from the dead world to life and activates the universe. This is a new view of the cosmos. We summarize here the influences of black-hole accretion disks on our view of the universe:

1. In traditional astronomy, the central dogma was that the main energy source in the universe is nuclear reactions, and that gravitational energy only works as a secondary effect, or in rather special cases. It now turns out that gravitational energy works quite generally as the major energy source in shining various astronomical objects. Even a black hole can work as an energy source when it accretes environmental gas. Namely, the black-hole accretion-disk system is the *gravitational power house* in the universe.

2. As usually recognized, a luminous object in the sky is a star. However, an accretion disk is an even more luminous object. That is, the temperature of stars is at most a few tens of thousands of Kelvins, while that of accretion disks is up to 10^5 – 10^{12} K.
3. According to common sense, a black hole is unseen. However, we can “see” a *silhouette* of a black hole if it wears an accretion disk. In addition, we can obtain information about the central black hole as well as the surrounding disk by observing its spectra.
4. In the black-hole accretion-disk system, the black hole does not stand alone, but interacts with the external environment through the accretion disk and/or mass outflow as well as the electromagnetic interaction. For example, the galactic nuclei and the galaxy, itself, interact with each other and may co-evolve.
5. Finally, from ancient days, the dominant idea has been that the sky is calm and everlasting. The black-hole accretion disk broke this idea into pieces. Even in the case of a gigantic system of galaxies, near to a supermassive black hole, where information propagates within the timescale of a few days or shorter, the system varies within a very short time. *The violent living – the accretion disk – whirls around the nothingness – the black hole.*

1.3 Accretion-Powered Objects – Observational Reviews

In this book our main focus is on the theoretical side of accretion disks around a black hole. In this section, however, we briefly review the observational evidence of accretion disks at various astronomical sites for the convenience of our readers. There are several excellent monographs (e.g., Wheeler 1993; Blandford et al. 1995; Lewin et al 1995; Warner 1995; Frank et al. 2002) that can be referred to for other details.

Tables 1.1 and 1.2 summarize central objects and surrounding accretion disks in various astronomical objects.

Table 1.1 Central Objects in Various Objects.

Object	Central “star”	Mass	Size
YSO	PS/TTS	$\sim M_\odot$	$\sim R_\odot$
CV/SSXS	WD	$\sim M_\odot$	$\sim 10^{-2} R_\odot$
XB	NS	$\sim M_\odot$	~ 10 km
XB(BHB)	BH	$\gtrsim 3M_\odot$	($r_g \gtrsim 10$ km)
ULX	IMBH	$\sim 10^{2-4} M_\odot$	($r_g \sim 300$ – 30000 km)
AGN	SMBH	$\sim 10^{5-9} M_\odot$	($r_g \sim 0.002$ – 20 AU)

Table 1.2 Accretion Disks in Various Objects.

Object	Mass	Size	Temperature	Luminosity
YSO	$\sim M_{\odot}$	~ 100 AU	$\sim 10^{1-4}$ K	$\sim L_{\odot}$
CV/SSXS	$\ll M_{\odot}$	$\sim R_{\odot}$	$\sim 10^{4-6}$ K	$\sim 10^{0-2} L_{\odot}$
XB/BHB	$\ll M_{\odot}$	$\sim R_{\odot}$	$\sim 10^{4-9}$ K	$\sim 10^{0-5} L_{\odot}$
AGN	$\lesssim 10^6 M_{\odot}$	~ 1 pc	$\sim 10^{3-5}$ K	$\sim 10^{10-13} L_{\odot}$

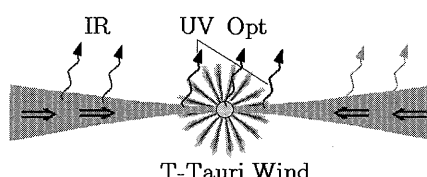
Note — YSO: young stellar object; PS: protostar; TTS: T Tauri star; CV: cataclysmic variable; SSXS: supersoft X-ray source; WD: white dwarf; XB: X-ray binary; NS: neutron star; BHB: black hole binary; BH: black hole; ULX: ultra-luminous X-ray sources; IMBH: intermediate-mass black hole; AGN: active galactic nucleus; SMBH: supermassive black hole

Let us consider in turn protoplanetary disks (young stellar objects), cataclysmic variables and supersoft X-ray sources, X-ray stars, black hole binaries, ultra-luminous X-ray sources, and active galactic nuclei.

1.3.1 Young Stellar Objects

When stars are born from interstellar molecular clouds, the central part shrinks to form a new star, called a *protostar*, while the envelope settles down as a gaseous disk around the newly born star. Since planets form in such a disk, it is often called a *protoplanetary disk* (figure 1.10).

Based upon the *spectral energy distribution* (SED) in IR and optical wavelengths, young stellar objects (YSOs) are classified into five categories: IR class 0, I, II, III, and IV (Adams et al. 1988). These classes are closely associated with the evolutionary stages of young stars: i.e., IR class 0 is a collapsing dense molecular cloud, IR class I contains a protostar, IR class II relates a classical T-Tauri star (CTTS), IR class III does a weak-line T-Tauri star (WTTS), and IR class IV is a zero-age main sequence star (ZAMS). Protoplanetary disks exist in the first three classes. Typically, disks around CTTS and WTTS have a radius and mass of ~ 100 AU and $0.001-0.5 M_{\odot}$, respectively.

**Figure 1.10**

Schematic picture of classical T Tauri stars.

(a) General properties

In class I objects, newly-born central protostars are surrounded by dense gaseous envelopes, which are rotating and dynamically infalling onto the central stars. Since the envelopes are so dense that the central protostars cannot be seen, instead, IR radiation from dust in the envelope dominates the radiation spectra (figure 1.11). Therefore, the peak of the spectrum lies in the far-infrared regions of $\sim 100 \mu\text{m}$. At this stage bipolar molecular flows are usually detected (see below).

In class II objects, the amount of the gas/dust envelope somewhat decreases and the central stars can be seen as a *classical T-Tauri star* (CTTS). Here, CTTS is defined so that the equivalent width (EW) of the H α emission lines is broader than 10 Å. However, since there exists a considerable amount of envelope, IR radiation from the envelope may be comparable to the star luminosity. As a result, the characteristic flat spectrum in the wavelength range of 1–100 μm is realized (figure 1.11).

In class III objects, the amount of the envelope decreases much more, and IR radiation from the envelope only modifies the spectrum of the central stars, which are now observed as a *weak-line T-Tauri star* (WTTS). Here, WTTS is defined as EW (H α) < 10 Å. The peak of the spectrum is now in the near-infrared. Finally, in class IV objects, the protoplanetary disks disappear and the spectrum is just of the central stars, the zero-age main-sequence stars (ZAMS).

In the past two decades, radio and infrared observations have revealed the birthplace of stars, and have detected protoplanetary disks. Among them is L 1551 in TMC1 (Taurus molecular cloud 1) (figure 1.12). In L 1551 bipolar molecular flows are ejected at a velocity of $\sim 15 \text{ km s}^{-1}$ from the vicinity of the central protostar IRS 5 (infrared source 5). This interesting feature was discovered by CO observations (Snell et al. 1980). A few years later CS observations revealed a gaseous molecular disk perpendicular to the bipolar jets (Kaifu et al. 1984). This disk was found to rotate as well as dynamically infall towards the center.

Many similar molecular disks have been detected with bipolar molecular flows (e.g., Lada 1985). These disks are believed to evolve to planetary systems within tens or hundreds of thousands of years.

In the Orion nebula M 42, direct images of protoplanetary disks were resolved by *HST* (the Hubble Space Telescope) as silhouettes in front of bright background light of the HII region (O'Dell et al. 1993) (figure 1.13). The sizes of the disks are typically on the order of $\sim 100 \text{ AU}$.

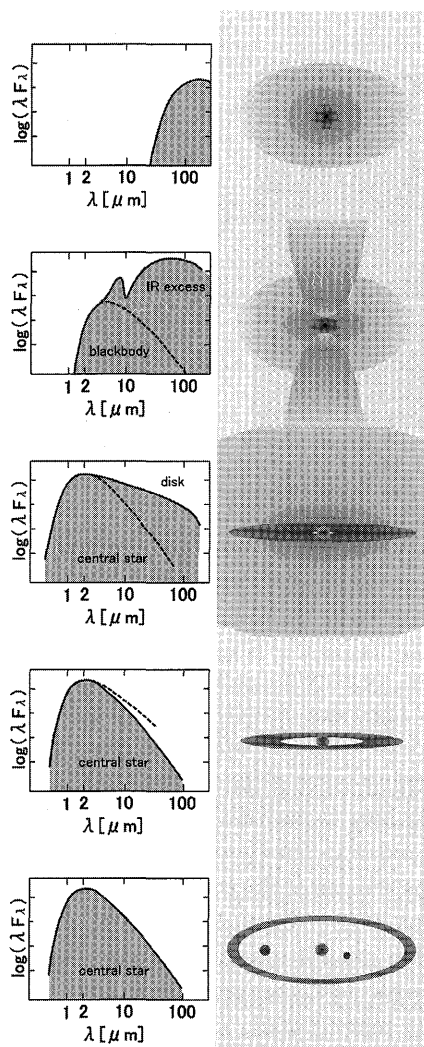


Figure 1.11

Five evolutionary stages of young stars with protoplanetary disks. From top to bottom, IR class 0, I, II, III, and IV. (Adapted from Lada 1987 and Shu and Adams 1987)

1.3.2 Cataclysmic Variables and Supersoft X-ray Sources

Some types of close binary systems comprising a white dwarf and a red companion from G type to M type (usually) show cataclysmic light variations. These are classified as *cataclysmic variables* (CVs), which include

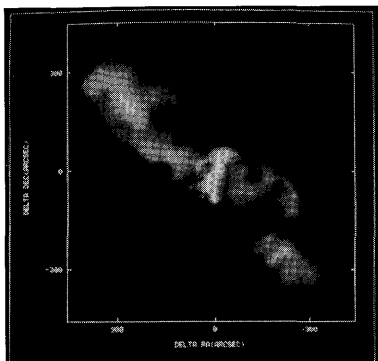
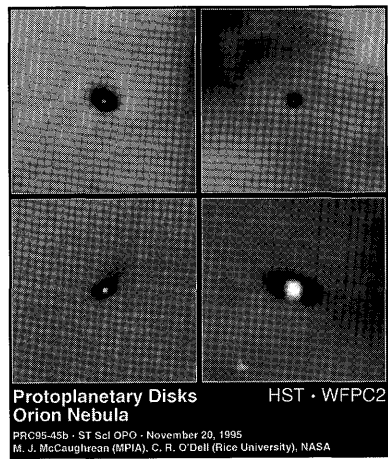


Figure 1.12
High-velocity CO bipolar flows and a rotating CS disk in L 1551 (see figure G.5). (Courtesy of N. Kaifu)



PRC95-45b - STScl OPO - November 20, 1995
M. J. McCaughrean (MPIA), C. R. O'Dell (Rice University), NASA

Figure 1.13

Protoplanetary disks discovered in the Orion nebula M 42. The images were taken by *HST*. (NASA/STScI)

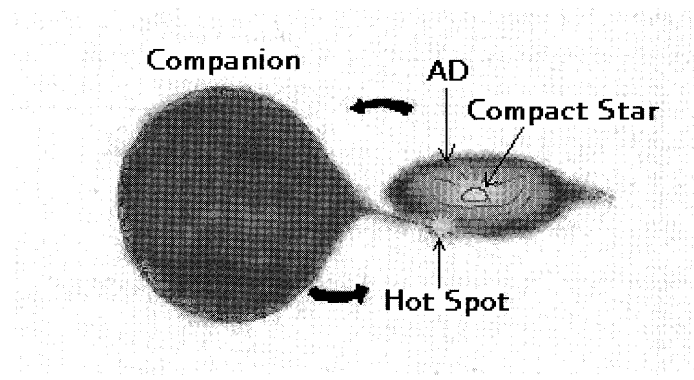
novae, dwarf novae, recurrent novae, nova-like variables, and polars as subclasses. When the mass-accretion rate is higher than that of CVs, they are supposed to be *supersoft X-ray sources* (SSXs), where the steady nuclear burning takes place on the surface of a white dwarf. Several excellent books have been written (e.g., Wheeler 1993; Warner 1995; see also Kahabka and van den Heuvel 1997).

In these systems the gas of the companion envelope overflows through the Lagrange point 1 (L_1) toward the white dwarf (*Roche overflow*). Since the overflowing gas possesses angular momentum due to the orbital motion, the gas forms an accretion disk around a compact star (unless the star is strongly magnetized), and the accreting disk causes various activities in cataclysmic variables and supersoft X-ray sources.

In *novae*, for example, hydrogen shell burning occasionally takes place on the surface of white dwarfs. This is a runaway process and releases an energy of 10^{43-44} erg. As a result, the luminosity of the system suddenly increases by ten magnitudes or so within a few days, and then declines on a timescale of some tens to hundreds of days. Nova explosions were usually detected only once.

Recurrent novae are similar to novae, but the explosions repeat with an interval of tens of years.

Nova-like variables show little variation, thus being suspected to be

**Figure 1.14**

Schematic picture of cataclysmic variables and supersoft X-ray sources.

in a steady-disk state.

In *dwarf novae* (DNe), on the other hand, small outbursts frequently take place. In the outburst phase the brightness increases by 2–5 magnitudes compared with the quiescent phase. The duration is a few days to a couple of weeks, while the interval is several months. The origin of dwarf-novae outbursts is believed to be an accretion-disk instability (see chapter 5). DNe are further classified into U Gem, Z Cam, SU UMa, and WZ Sge types.

In *polars*, white dwarfs have strong (dipole) magnetic fields and the accreting gas inflows to the polar caps guided by dipole fields.

In *supersoft X-ray sources* (SSXs), which are characterized by an extremely soft X-ray spectra with a blackbody temperature of $\sim 20\text{--}100$ eV and by their high X-ray luminosity of $10^{36}\text{--}38$ erg s $^{-1}$, steady nuclear burning on the surface of white dwarfs takes place due to the higher mass of the white dwarf ($\sim 1 M_\odot$) and a sufficiently high accretion rate ($\sim 1\text{--}4 \times 10^{-7} M_\odot \text{ yr}^{-1}$).

It is interesting to check the energy-generation efficiency for the case of CVs, as we did for the solar case (section 1.1). The energy-conversion efficiency by a nuclear reaction is the same as before, $\eta_N \sim 7 \times 10^{-3}$. As for gravitational energy release, on the other hand, the efficiency is larger in the present case than in the case for the Sun, since the potential is deeper, $GM_{\text{WD}}/R_{\text{WD}} \sim 10^2 GM_\odot/R_\odot$. Thus, the efficiency is

$$\eta_G \sim \frac{GM_{\text{WD}}}{R_{\text{WD}}c^2} \sim 2 \times 10^{-4}, \quad (1.26)$$

which is still smaller than η_N , but not by many orders. Hence, accretion

energy release becomes important in CVs. It is easy to imagine that accretion is even more important for a black-hole accretion.

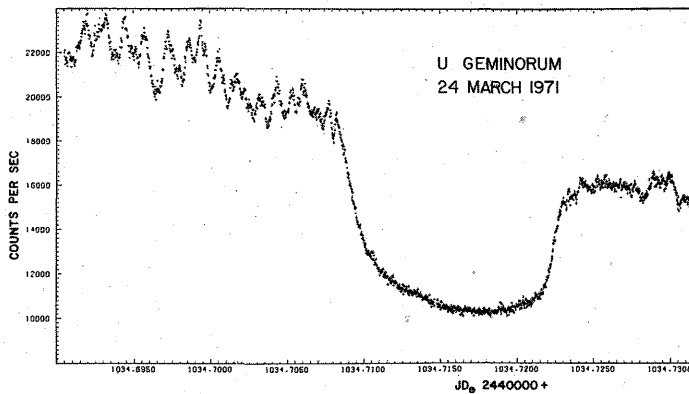


Figure 1.15

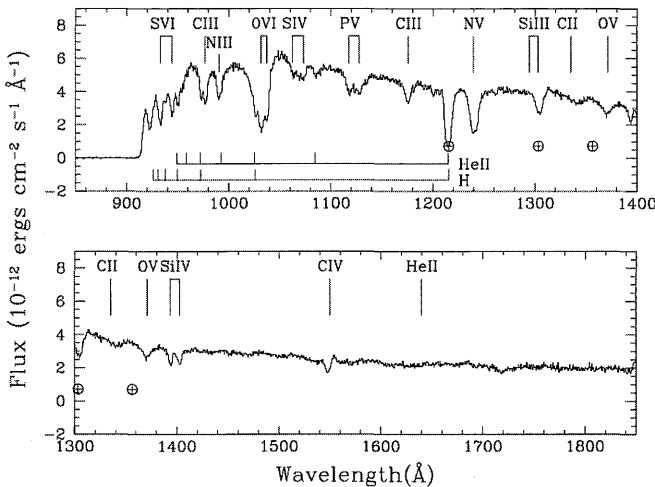
Light curves of the eclipse of accretion disks in U Gem. (After Warner 1976)

(a) General properties

Cataclysmic variables have been observed for many decades in detail without recognizing the presence of accretion disks there. Supersoft X-ray sources, on the other hand, were discovered and established with the Einstein observatory and the Röntgen Satellite (*ROSAT*). Various evidence of accretion disks has so far been accumulated by recent photometric and spectroscopic observations.

First of all, wide and deep primary minima in light curves mean the eclipse of luminous accretion disks and *hot spots* (the heated region where the Roche overflow stream bombards the disk) by companion stars.

For example, U Gem is a 14–15 magnitude object and a close binary system with a rotation period of 0.18 day. There exists an eclipse by a M-type companion in the light curve (figure 1.15). This eclipse, however, is very wide and deep, compared with the eclipses seen in usual eclipsing binaries. Moreover, out of the eclipse the light curve exhibits *flickering*: short-term, small-amplitude random fluctuations. These characteristics can be understood as follows. In the quiescence of U Gem, an accretion disk and a hot spot are the dominant sources of radiation. In particular, the hot spot is the most luminous and the primary eclipse is that of the hot spot. Furthermore, the flickering seen out of the eclipse is due to some fluctuation at the hot spot.

**Figure 1.16**

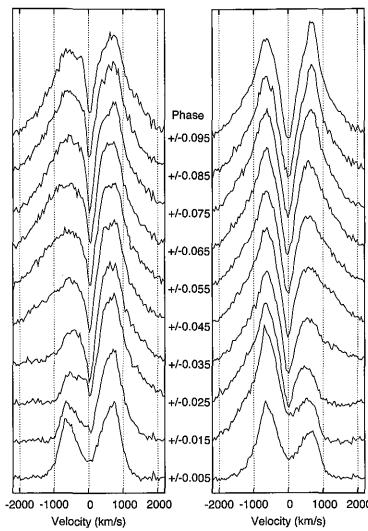
Spectrum of Z Cam in outburst. The positions and suggested identifications of absorption lines, as well as regions affected by airglow (\oplus), are indicated. (After Knigge et al. 1997)

The characteristic spectra, such as blue continua and double-peaked lines, also represent radiation originating from the disks. Indeed, accretion disks in CVs manifest themselves in their spectra.

Almost all CVs show blue continua (figure 1.16). If this is assumed to be a blackbody, the temperature would be up to 10^4 – 4×10^5 K. This is too high to radiate from the surface of a white dwarf or a red companion. Hence, in CVs the blue continua are believed to come from accretion disks. The model spectrum of the disk well reproduces the observed one.

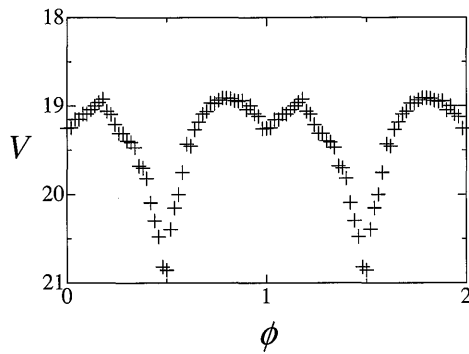
Many CVs show double-peaked emission lines during the quiescent phase (figure 1.17). The appearance of double peaks depends on the inclination of the system. That is, double peaks are generally seen in high-inclination systems, while the separation of peaks is not seen in low-inclination systems. The width of the lines becomes broader as the inclination angle becomes larger.

In recent years, furthermore, from analyses of light curves during an eclipse and the Doppler shifts of spectral lines, even the brightness distribution on the disk is examined using the technique of eclipse mapping and Doppler tomography (Horne 1985; Marsh and Horne 1988; see also Warner 1995; Boffin 2001). Hence, the existence of accretion disks in

**Figure 1.17**

Time variations of the double-peaked line spectrum of Z Cha during an eclipse. (Courtesy of M. Uemura)

cataclysmic variables is well established. See books by Wheeler (1993) and Warner (1995) for further details.

**Figure 1.18**

Light curves for a supersoft X-ray source CAL 87. (After Alcock et al. 1997; Kahabka and van den Heuvel 1997)

In supersoft X-ray sources, as already stated, the bolometric lumi-

nosities reach $\sim 10^{36-38}$ erg s $^{-1}$, and the radiation from the surface of white dwarfs dominates the total flux of the source (cf. figure 1.18).

It should be noted that in some cataclysmic variables and supersoft X-ray sources spectroscopic observations, such as P Cyg profiles, have revealed high-velocity mass outflows (winds). The wind velocity measured in these objects is about 3000–5000 km s $^{-1}$, which is on the order of the escape velocity of white dwarfs. In addition, the line profiles depend on the inclination angle; the P Cyg profiles are seen only in a system with an inclination angle of $i < 65^\circ$ in CVs. Furthermore, some SSXSSs exhibit evidence of jets. These facts indicate that the outflow is an accretion-disk wind and/or an aspherical white-dwarf wind.

1.4 X-Ray Binaries and Ultra-Luminous Sources

In this section we briefly show observational aspects of X-ray binaries and ultra-luminous X-ray sources.

1.4.1 X-Ray Binaries Containing Neutron Stars

In the case of a close binary system comprising a neutron star and a normal star, the activity can be observed not only in the optical ranges, but also in the X-ray and other wavelength regimes, since the gas temperature is higher due to the deep potential well of neutron stars, compared with the case of CVs. These systems are observed as *X-ray stars* (figure 1.19). X-ray stars are roughly classified into two categories: *low-mass X-ray binaries* (LMXBs) and *high-mass X-ray binaries* (HMXBs), according to the mass of a Roche-lobe filling star (and not of a compact component), while they are also classified into X-ray bursters, X-ray pulsars, and so on from the observational point of view. Some excellent books have been written (e.g., Wheeler 1993; Lewin et al. 1995; Lewin and van der Klis 2006).

Some X-ray stars exhibit *periodic* X-ray pulses, and are called *X-ray pulsars*. The period of X-ray pulses is typically a few seconds to several tens of seconds, although there are some that exhibit several tens of milliseconds or over ten minutes. Since companion stars of X-ray pulsars are usually blue supergiants, X-ray pulsars are usually HMXBs.

Since the lifetime of a massive star is short, the age of X-ray pulsars (and of neutron stars) should be young. A young neutron star has a remarkably strong magnetic field on the order of 10^{12} Gauss. Hence, the accreted material falls onto the polar caps of neutron stars, liberates the potential energy at the magnetic poles, and then brighten there. Since

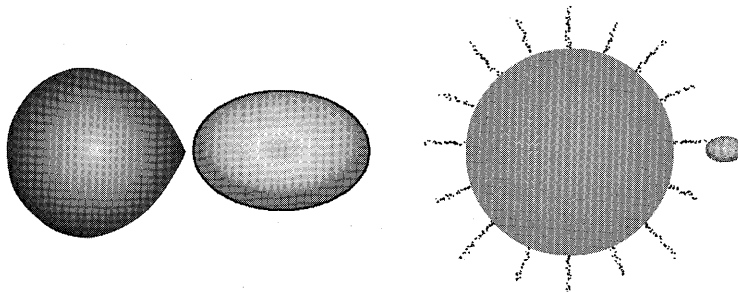


Figure 1.19

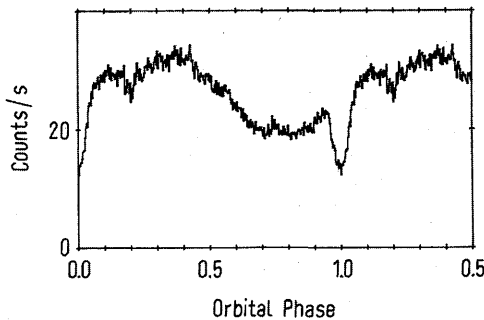
Schematic picture of X-ray stars: Low-mass X-ray binaries with red dwarfs (left) and high-mass X-ray binaries with blue giants (right).

the magnetic axis does not coincide with the rotation axis, in general, X-ray pulses are seen by a distant observer as the neutron star rotates (so-called light-house effect). X-ray pulsars are similar to polars in CVs.

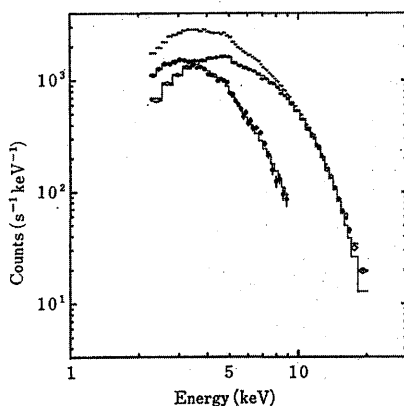
On the other hand, some X-ray stars that exhibit aperiodic transient X-ray brightening or X-ray bursts are called *X-ray bursters*. The interval of bursts is typically several hours to about a few days. In the burst phase, the X-ray luminosity quickly rises within a few seconds and declines with a timescale of a few tens of seconds. The maximum luminosity is on the order of 10^{38-39} erg s $^{-1}$. Since companion stars of X-ray bursters are usually red dwarfs, X-ray bursters are usually LMXBs.

The fact that the companion is a red dwarf means that the X-ray burster is an old system. Hence, the magnetic field of neutron stars disappears, and the accretion disks extend to the surface of neutron stars. The accreted material accumulates on the surface, and when the amount of gas is sufficient, a runaway nuclear burning (shell flash) takes place to cause X-ray bursts. X-ray bursters are similar to novae in CVs.

There also exist a group of LMXBs that show repetitive long-term light variations, outbursts (or X-ray novae), similar to dwarf-nova outbursts. They are called *X-ray transients* (or *X-ray novae*) and occasionally classified into hard X-ray transients, which are members of HMXBs, and soft X-ray transients, members of LMXBs, according to their spectra. The outbursts are characterized by a rapid rise within a few days, a large amplitude over several orders in X-rays, a slow decline over a month to a year, and a long quiescence of a year or so. The scales of outbursts are thus somewhat larger than those of dwarf-nova outbursts. The origin of outbursts is thought to be an accretion-disk instability of the sort invoked in dwarf novae (chapter 5).

**Figure 1.20**

X-ray light curve of X 1822–371 during an eclipse of an X-ray corona. (After Parmar et al. 1986)

**Figure 1.21**

X-ray continuum spectra of Sco X-1 obtained by *Tenma*. It is decomposed to a soft component (crossed circle) and a hard one (rhomb). (After Mitsuda et al. 1984)

(a) General properties

From a light-curve analysis and an X-ray spectral analysis, the existence of accretion disks in X-ray binaries has also been firmly established (cf. figure 1.20). Indeed, accretion disks play essential roles in many X-ray stars, including neutron stars.

In the quiescent phase LMXBs radiate persistent emissions in the X-

ray wavelength region. An example of the X-ray continuum spectra of LMXBs is shown in figure 1.21. From various analyses including time variabilities, it is found that such a continuum spectrum consists of *hard* and *soft* components (Mitsuda et al. 1984). The soft component was well fitted by the disk blackbody with a typical temperature of about 1 keV ($\sim 10^7$ K); we can see the X-ray emission from the inner disk. The hard component, on the other hand, was expressed by a single-temperature blackbody spectrum with a temperature of about 2 keV ($\sim 2 \times 10^7$ K); this is the X-ray radiation from the surface of the neutron star.

1.4.2 Black Hole Binaries and Microquasars

Some X-ray binaries consist of a normal star and a black hole; they are often called *black hole binaries* (BHs). Some (or almost) of BHs exhibit relativistic twin jets and called *microquasars* (MQs/ μ QSOs) because of an analogy of a miniature version of quasars (figure 1.22). Similar to X-ray transients comprising NSs (see the previous subsection), there are *soft X-ray transients* (*X-ray novae*) that show quasi-periodic outbursts characterized by a rapid rise over a period of a few days, exponential decays with *e*-fold times of one month to several months, and very long repetition periods of over several tens of years. In these systems the activity takes place in an X-ray region. Several excellent texts have been written (e.g., Wheeler 1993; Lewin et al. 1995; see also Mirabel and Rodríguez 1999; Fender et al. 2004).

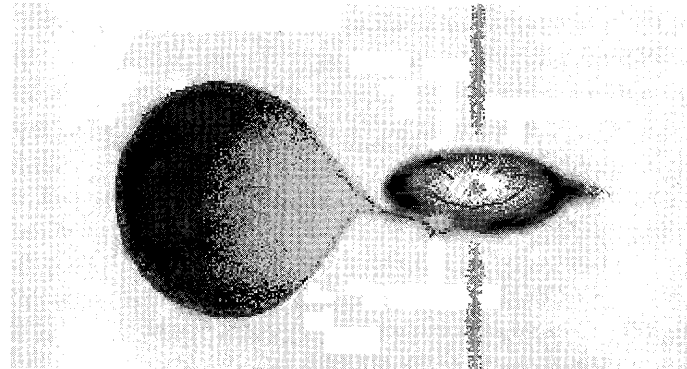


Figure 1.22

Schematic picture of black hole binaries and microquasars with relativistic jets.

Table 1.3 Black Hole Binaries.³

Source	$M_x [M_\odot]$	P [d]	$f(M)$ [M_\odot]	d [kpc]	Companion
HMXBs					
Cyg X-1	$\gtrsim 9.5$	5.6	0.244 ± 0.005	2.0 ± 0.1	O9.7Iab
SS 433	~ 9.0	13.1	3.0 ± 0.6	5.0 ± 0.5	A5/A7I
LMC X-3	5.9–9.2	1.70	2.3 ± 0.3	50 ± 2.3	B3V
LMC X-1	4.0–10.0	4.23	0.14 ± 0.05	50 ± 2.3	O7III
LMXBs					
GRO J0422+32	3.2–13.2	0.21	1.19 ± 0.02	2.6 ± 0.7	M2V
A 0620–003 [†]	8.7–12.9	0.325	2.72 ± 0.06	1.2 ± 0.1	K4V
1009–45	6.3–8.0	0.28	3.17 ± 0.12	5.0 ± 1.3	K7/M0V
1118+480	6.5–7.2	0.17	6.1 ± 0.3	1.8 ± 0.5	K5/M0V
GS 1124–684 [‡]	6.5–9.2	0.43	3.01 ± 0.15	5 ± 1.3	K3/K5V
1543+475	7.4–11.4	1.13	0.25 ± 0.01	7.5 ± 0.5	A2V
1550–564	8.4–10.8	1.54	6.86 ± 0.71	5.3 ± 2.3	G8/K8IV
GRO J1655–40	6.0–6.6	2.62	2.73 ± 0.09	3.2 ± 0.2	F3/F5IV
H1705–25	5.6–8.3	0.52	4.86 ± 0.13	8 ± 2	K3/7V
1819–25	6.8–7.4	2.82	3.13 ± 0.13	7.4 –12.3	B9III
GRS 1915+105	$\gtrsim 10.0$	33.5	9.5 ± 3.0	11–12	K/MIII
GS 2000+25	7.1–7.8	0.35	5.01 ± 0.12	2.7 ± 0.7	K3/K7V
GS 2023+338 ⁺	10.1–13.4	6.47	6.08 ± 0.06	2.2–3.7	K0III

Name — [†]: Nova Mon (V616 Mon); [‡]: Nova Muscae (GU Mus); +: V 404 Cyg.

Several black-hole candidates are listed in table 1.3. According to a conservative estimate, where only a few percent of supernovae leave black holes, there are $\sim 10^7$ black holes in our Galaxy. There may exist $\sim 10^8$ to 10^9 stellar-mass black holes in our Galaxy (e.g., Brown and Bethe 1994; Timmes et al. 1996).

(a) General properties

It is not easy to discriminate XB_s containing NS_s and those comprising BH_s at present. In principle, they should have different emission properties, since NS_s have a solid surface while BH_s do not. There are several observational (and somewhat empirical) properties to distinguish black-hole binaries from neutron-star binaries.

1. **Mass:** The most reliable method to establish black-hole candidacy is to calculate the mass function $f(M)$ from an analysis of the

³See chapter 1 of the first edition (Kato et al. 1998) and McClintock and Remillard 2003 and references therein.

binary motions. From the Kepler rotation periods, we find

$$\begin{aligned} f(M) \equiv \frac{(M_x \sin i)^3}{(M_x + M_2)^2} &= \frac{PK_2^3}{2\pi G} \\ &= 10^{-7} \left(\frac{P}{d}\right) \left(\frac{K_2}{\text{km s}^{-1}}\right)^3 M_\odot, \end{aligned} \quad (1.27)$$

where M_x and M_2 are the masses of the compact star and the normal component, respectively, i is the inclination angle between the line-of-sight and the normal to the orbital plane, P is the orbital period, and K_2 is the semi-amplitude of the radial-velocity variations of the normal component due to the orbital motion. By observations of P and K_2 one can derive $f(M)$, from which information about M_x can be derived. Obviously, the mass of the compact star should be larger than $f(M)$, since $M_2 > 0$ and $\sin i \leq 1$. If $f(M)$ exceeds the maximum mass of a neutron star, which is $2\text{--}3M_\odot$, depending on the assumed equation of state for NSs, we can safely conclude that the compact object is likely to be a black hole. Even when $f(M)$ is not very large, we can derive a reliable mass estimate, if we know i and/or M_2 . About a dozen black-hole candidates are known, some of which are listed in table 1.3.

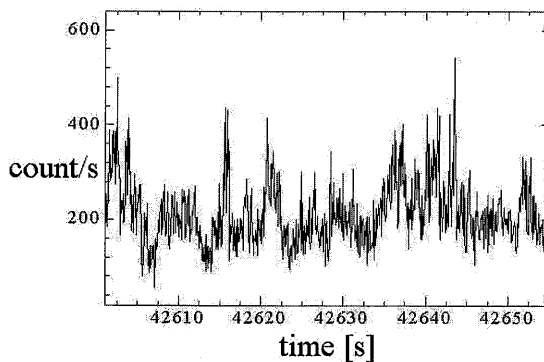


Figure 1.23

X-ray fluctuations in a black hole binary. (Courtesy of S. Kitamoto)

2. **Variability:** In black-hole binaries the time variations seem to be chaotic/fractal (figure 1.23). It had long been believed that these irregular variabilities are not seen in X-ray stars containing

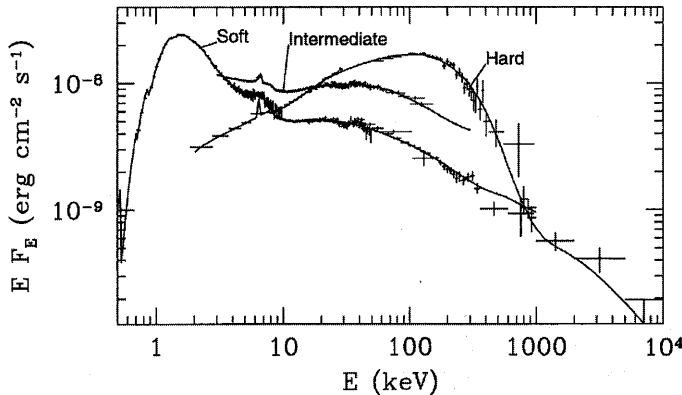


Figure 1.24

X-ray continuum spectra of Cyg X-1. The hard state was observed by *Ginga* and OSSE on 1991 June 6 and by COMPTEL 1991 May 30–June 8. The intermediate state was observed by *RXTE* on 1996 May 23. The soft state was observed by *ASCA* and *RXTE* on 1996 May 30 and by OSSE 1996 June 14–25. The curves correspond to the hybrid model. (After Gierlinski et al. 1999)

neutron stars. However, we now know several sources that show both aperiodic variability and X-ray bursts. If there are X-ray bursts or X-ray pulses observed, of course, the objects must include neutron stars. Therefore, we cannot simply conclude that XBs that show rapid fluctuations should contain black holes.

3. **Spectrum:** It is well known that black-hole candidates have two spectral states, a *high state* (soft state) and a *low state* (hard state) (figure 1.24). In the high/soft state the soft X-ray is strong and the X-ray spectrum is *disk blackbody* (DBB) with a temperature of $\sim 10^7$ K (1 keV), although there could be a small excess, called a hard tail, occasionally observed in the hard X-ray region (above a few keV). In the low/hard state, on the other hand, the soft blackbody spectrum is usually absent and the X-ray spectrum becomes a *power-law* (PL), which extends from the soft X-ray to the hard X-ray or gamma-ray region. In the low state the X-ray intensity varies irregularly on a timescale of a few seconds to tens of milliseconds. Several sources were observed to change the high and low states from time to time. Such on-off states also seem to be the empirical nature of black-hole binaries.

(b) Cyg X-1

The most famous, proto-type black hole candidate is a high-mass X-ray binary Cyg X-1 (1956+350), which was found in 1971. Cyg X-1 consists of an O9 supergiant, HD 226868, and a black hole (figure 1.25). The binary period is 5.6 days and the orbital semi-amplitude is 75 km s^{-1} (figure 1.26). Thus, the mass function becomes $0.241 M_{\odot}$. The mass of the supergiant is supposed to be $\sim 30 M_{\odot}$, while the mass of the black hole is estimated to be about $10 M_{\odot}$. Several (orbital) elements of Cyg X-1 are summarized in table 1.4.

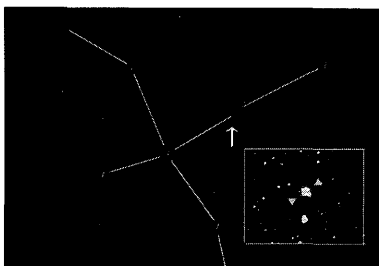


Figure 1.25

Cyg X-1 in CCD image inset in Cygnus. (Osaka Kyoiku University)

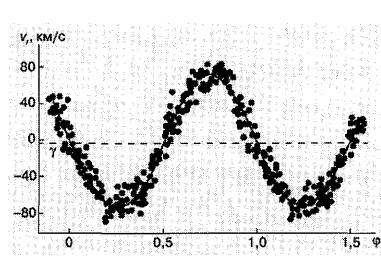


Figure 1.26

Radial velocity of Cyg X-1. (<http://images.nature.ru/nature/>)

Table 1.4 Elements of Cyg X-1.⁴

Elements	Values	Ref.
Optical counterpart	$V = 9 / \text{O9.7Iab}$	
Distance d	2 kpc	
Binary period P	5.6017 d	1
Ephemeris T_0 (2 440 000+)	1869.17 d	1
Semi-amplitude K	75.0 km s^{-1}	1
Mass function $f(M)$	$0.241 \pm 0.013 M_{\odot}$	
Inclination angle i	$27^{\circ}\text{--}35^{\circ}$	2
Ellipticity e	< 0.1	3

(c) Nova Muscae 1991

Like Cyg X-1, soft X-ray transients (SXTs) containing BHs exhibit soft-hard transitions, but in a complex way. Representative X-ray light curves of SXTs are displayed in figure 1.27.

There are roughly three distinct classes: The first class of SXTs, such as GS 2000+25 and Nova Musca 1991 (GS 1124–684), is in the

⁴References — (1) Ninkov et al. 1987, ApJ 321, 425; (2) Bolton 1975, ApJ 200, 269; (3) Gies and Bolton 1982, ApJ 260, 240

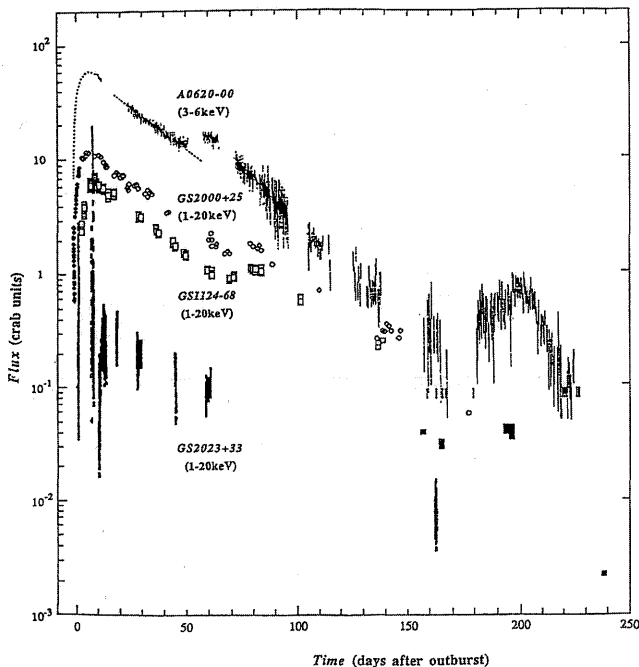


Figure 1.27

X-ray light curves of the representative black-hole X-ray novae or X-ray transients. Outbursts are characterized by rapid rises on timescales of a few days, exponential decays with e -fold times of ~ 30 days, and long quiescent times of several tens of years. There also exist distinct classes of X-ray novae that show quite irregular outburst light patterns, such as GS2023+338. (After Kaluzienski et al. 1977 and Tanaka 1992)

hard state during the early rise, shows both soft and hard components of spectra around the peak (sometimes called the very high state; VHS), and records a soft-to-hard transition about a few months after the peak. The second class, such as GS 2023+338, continues to stay in the hard state throughout the outburst. The third class, such as GRS 1915+105 and GRO J1655–40, (both are Galactic superluminal sources, micro-quasars), shows complex light curves and spectral transitions.

Among them, Nova Musca 1991 is probably the best source to study the time-dependent behavior of an SXT containing a black hole, since multi-wavelength observational data are available, and it recorded an interesting spectral transition, as mentioned above. Typical light curves

of SXTs are displayed in figure 1.27.

These behaviors of X-ray transients among a low/hard state (LS), a high/soft state (HS), and a very high state (VHS) are empirically interpreted by the disk-jet coupling (Fender et al. 2004; figure 1.28).

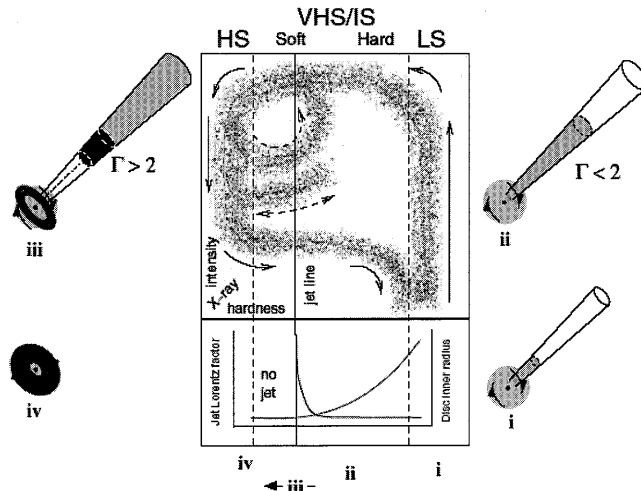


Figure 1.28

Schematic picture by Fender et al. (2004) for the disk-jet coupling in black hole binaries. The upper panel represents an X-ray hardness-intensity diagram in the high/soft state (HS), the very high/intermediate state (VHS/IS), and the low/hard state (LS). X-ray hardness increases to the right and intensity upwards. The lower panel represents the variation of the bulk Lorentz factor Γ of the outflow with hardness. In the LS and VHS/IS, the jet is steady with an almost constant Γ (< 2), progressing from state (i) to state (ii) as the luminosity increases. At some point, Γ increases rapidly, producing an internal shock in the outflow, state (iii), followed in general by cessation of jet production in a disk-dominated HS, state (iv). (After Fender et al. 2004)

(d) SS 433

A unique object, SS 433, known as a prototype of astrophysical jets, has attracted great attention because of its remarkable peculiarity (figures 1.29, 1.30; see figure G.6). That is, in SS 433 subluminal jets are ejected from a compact object surrounded by an accretion disk (excellent reviews are given by, e.g., Margon 1984; Cherepashchuk 1988; Fabrika 2004). There remain various mysterious puzzles concerning SS 433: the kind of compact object (a black hole or a neutron star), the nature of the accretion disk (e.g., fat or slim), the origin of its precession, and the

collimation and formation of relativistic jets.



Figure 1.29
SS 433 in CCD image. (Osaka Kyoiku University)

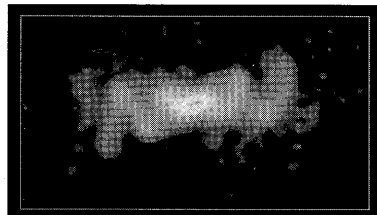


Figure 1.30
Corkscrew pattern of SS 433 jets.
(<http://www.nrao.edu/pr/2004/ss433corkscrew>)

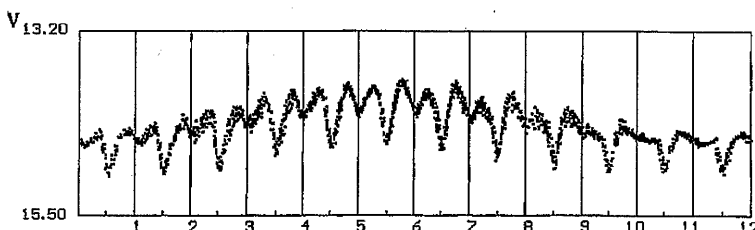


Figure 1.31
Folded light curves of SS 433 obtained by 19-year optical monitoring. (After Goranskij et al. 1998)

Since SS 433 is a relatively bright object ($V \sim 14$ mag and $A_V \sim 6\text{--}8$ mag), photometric observations have been extensively carried out by several groups (e.g., Kemp et al. 1986; Cherepashchuk et al. 1981; Gladyshev et al. 1987; Zwitter et al. 1991; Aslanov et al. 1993; Fukue et al. 1997; Goranskij et al. 1998; Cherepashchuk et al. 2005; see figure 1.31). Kemp et al. (1986), for instance, have collected 6-year V -band photoelectric photometric data, including over 800 observations on ~ 700 nights during 1979–1985. They show a mean light curve on the 13-day period as well as a synthesis of the average 162-day “precession” light curves broken down into four phase intervals on the 13-day cycle.

The wide and deep eclipses of the SS 433 light curves strongly suggest that the accretion disk (including disk wind) in SS 433 is not geometrically thin, but is somewhat *geometrically thick* with a height-to-radius

ratio of ~ 0.5 . From the analysis of the precession light curve, however, the configuration of the disk is not very thick, but should be mildly thick (Antokhina and Cherepashchuk 1987; Fukue et al. 1998). The favorite combination of parameters is that the mass ratio is around unity (a compact star is a black hole) and the surface temperature of the companion is around 17000 K.

Table 1.5 Elements of SS 433.⁵

Elements	Values	Ref.
Optical counterpart	$V \sim 14/\text{A5-A7I}$	1, 5
Distance d	$5.0 \pm 0.5 \text{ kpc}$	2
Binary period P	13.082 d	1
Binary ephemeris T_0 (2 440 000+)	6596.25 d	3
Semi-amplitude K_2	$112 \pm 5 \text{ km s}^{-1}$	4
	$132 \pm 9 \text{ km s}^{-1}$	5
Mass function $f(M)$	$2.0 \pm 0.3 M_{\odot}$	4
	$3.0 \pm 0.6 M_{\odot}$	5
Inclination angle i	78°8	1
Precession period	162.5 d	1
Precession ephemeris (2 440 000+)	4483 d	3
Precession angle ψ	19°8	1

(e) GRS 1915+105

A galactic superluminal motion was observed for the first time in the black-hole X-ray binary GRS 1915+105 (Mirabel and Rodríguez 1994). Because of the similarity to quasars with relativistic jets, the galactic objects with stellar-mass black holes and relativistic jets are called *microquasars* (Mirabel and Rodríguez 1999). Rather, at present, it is believed that all accreting black-hole X-ray binaries are jet sources (Mirabel 2004).

The luminosity of microquasar GRS 1915+105 exceeds the Eddington ones (L_E) during its outburst. In quiscent phase, its luminosity never drop below $\sim 0.3L_E$ (Done and Gierliński 2004).

1.4.3 Ultra-Luminous X-Ray Sources

In recent X-ray observations by *ASCA*, *ROSAT*, *Chandra*, and *XMM-Newton* satellites, revealed were a new class of X-ray sources, called *ultra-luminous X-ray sources* (ULXs). Ultra-luminous X-ray sources are

⁵References — (1) Margon B. 1984, *ARA&A* 22, 507; (2) Hjellming R.M. and Johnston K.J. 1981, *ApJ* 246, L141; (3) Gladyshev S.A., Goranskii V.P., Cherepashchuk A.M. 1987, *SvA* 31, 541; (4) D’Odorico S., Oosterloo T., Zwitter T., Calvani M. 1991, *Nature* 353, 329; (5) Cherepashchuk A.M. et al. 2005, *A&A* 437, 561

bright, compact, off-nuclear X-ray sources found in nearby galaxies (figure 1.32; see figure G.7).

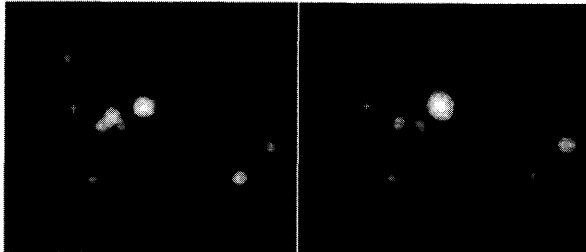


Figure 1.32

M82 X-1, located off-center in starburst galaxy M82, taken at a different epoch. The central bright X-ray source is ULX M82 X-1, while other sources are usual X-ray sources. Crosses mark the center of M82. (NASA/SAO/CXC)

The observed bolometric luminosity of ULXs exceeds the Eddington limit for a black hole with several tens of solar masses, if radiation is isotropic. If so, ULXs are supposed to harbor *intermediate-mass black holes* (IMBHs) with $20\text{--}50M_{\odot}$. For example, M82 X-1 ($\sim 10^{41}\text{erg s}^{-1}$) in the starburst galaxy M82 may host an IMBH of about $1000M_{\odot}$ (Matsumoto et al. 2001). While the discovery of a quasi-periodic oscillation (QPO) in the power spectrum of M82 X-1 suggests that a black hole mass is in the range of $\sim 50\text{--}260M_{\odot}$ (Dewangan et al. 2005).

However, there is a possibility that ULXs could be stellar-mass black-hole microquasars with non-isotropic emission, such as beaming jets or supercritical accretion disks (chapter 10), under a pole-on view. Hence, ULXs' true character is yet controversial.

1.5 Active Galactic Nuclei

Those galaxies whose nuclei are more or less active are called *active galaxies* or *active galactic nuclei* (AGNs). They include quasars, BL Lac objects, radio galaxies, Seyfert galaxies, low-ionization nuclear emission-line regions, starburst galaxies, and low-luminosity AGNs, although the classification is empirical and somewhat vague. Furthermore, in recent years almost all of galaxies may exhibit some type of activities during some stage in their life. Several excellent books have been written (Blandford et al. 1995; Robson 1996; Peterson 1997; Krolik 1999).

As already stated, *quasars* (QSOs)⁶ display star-like appearances, and show broad emission features with large redshifts. The typical luminosity is 10^{45-46} erg s⁻¹. The spectral features resemble Seyfert 1 galaxies below, except for their large redshifts. There are several subclasses: quasi-stellar radio sources (QSS) with strong radio emission, radio-quiet quasars or quasi-stellar sources (QSO), broad absorption line quasars (BAL), highly polarized quasars (HPQ), and optically violent variables (OVV). BL Lac objects⁷ resemble radio-loud quasars, but are characterized by absent (or weak) emission-line features. They are highly variable and highly polarized. These properties are believed to originate from the beaming of relativistic jets. BL Lacs and OVV are often grouped together into a single category, that is called *blazars*. The name, blazar, was proposed by E. A. Spiegel at the Pittsburgh Conference in 1977.

Radio galaxies (RGs)⁸ are those that radiate a tremendous amount of energy (up to 10^{60} erg) at radio wavelengths. The luminosity of radio galaxies is typically 10^{40-46} erg s⁻¹. From the radio luminosity, powerful radio galaxies (PRG) are defined so that the radio power at 1.4 GHz, $P_{1.4\text{GHz}}$, is greater than 10^{32} erg s⁻¹ Hz⁻¹, while for weak radio galaxies (WRG), $P_{1.4\text{GHz}} < 10^{32}$ erg s⁻¹ Hz⁻¹. Furthermore, from the radio spectrum, we can distinguish two types: steep-spectrum, extended radio structure and compact, flat-spectrum, core-dominated sources. Moreover, from the emission-line features they are classified into broad-line radio galaxies (BLRG) and narrow-line radio galaxies (NLRG); the former resemble Sy 1 and the latter Sy 2. The host galaxies are usually elliptical.

Seyfert galaxies (Sy),⁹ which were first classified by K. Seyfert (1943), have bright compact nuclei and exhibit broad emission features. The typical luminosity is 10^{43-45} erg s⁻¹. They are classified into two subclasses, type 1 and type 2. In the former Sy 1, the width of the recombination lines is very broad with the full width at half maximum (FWHM) corresponding to velocities up to 10^4 km s⁻¹, while the width of forbidden lines is about 500 km s⁻¹. In the latter Sy 2, the line width is on the order of 500 km s⁻¹ for both the permitted and forbidden lines. The host galaxies of Seyfert galaxies are known to be spirals.

It should be noted that these two subclasses have been unified in

⁶QSOs: 3C 273 ($z = 0.16$), 3C 48 ($z = 0.37$), 3C 279 ($z = 0.54$).

⁷BL Lacs: BL Lac ($z = 0.070$), OJ 287 ($z = 0.306$).

⁸RGs: NGC 5128/Cen A ($z = 0.0009$), M 87/Vir A ($z = 0.0043$), Cyg A ($z = 0.057$).

⁹Sys: NGC 4151 ($z = 0.0033$), NGC 1275/3C 84 ($z = 0.0176$), 3C 120 ($z = 0.0333$).

recent years. That is, the *apparent* difference between two subclasses is now supposed to be the *orientation* effect. Spectro-polarimetric observations (Antonucci and Miller 1985) and X-ray observations (Koyama et al. 1989) supported the picture that the majority of Seyfert nuclei are surrounded by an *obscuring molecular torus* of inner radius 1–10pc and similar thickness. Seyfert 2 galaxies are seen from edge on and the central broad-line region, which is seen in Sy 1, is obscured to an observer by this obscuring torus.

Low-ionization nuclear emission-line regions (LINERs)¹⁰ show relatively strong lines of low-ionization species, such as OI or SII, from their nuclei (Heckman 1980). In LINERs it is supposed that shock ionization may be important.

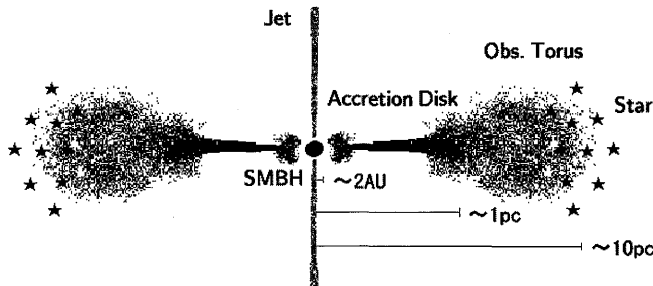


Figure 1.33
Schematic picture of active galactic nuclei.

Starburst galaxies (SBs)¹¹ are galaxies where star formation takes place at a remarkably high rate (Weedman et al. 1981). There is much observational evidence that suggests a positive link between nuclear starbursts and AGNs.

Low-luminosity AGNs (LLAGNs)¹² are AGNs whose luminosity is quite small, but clearly show some type of activities, e.g., in their nuclei.

(a) General properties

The properties of various types of active galaxies are typically summarized as follows (cf. figure 1.33):

¹⁰LINERs: M 81 ($d = 4.3 \times 10^6$ pc).

¹¹SBs: M 82 ($d = 4.3 \times 10^6$ pc).

¹²LLAGNs: Sgr A* ($d = 8.5 \times 10^3$ pc), M 32 ($d = 7.1 \times 10^5$ pc), M 81 ($d = 4.3 \times 10^6$ pc), M 82 ($d = 4.3 \times 10^6$ pc), NGC 4258/M106 ($d = 6.4 \times 10^6$ pc).

- Luminous:** AGNs are luminous compared with normal galaxies, as already stated. In the most luminous case, the luminosity is up to 10^{12} – $10^{13} L_\odot$, which is hundreds of times brighter than that of normal galaxies.

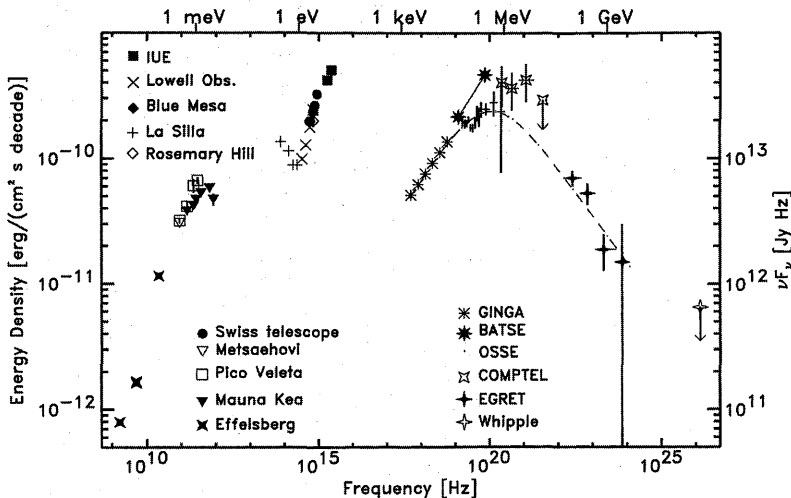


Figure 1.34

Multiwavelength continuum spectrum (SED) of quasar 3C 273. (After Lichti et al. 1995)

- Non-stellar spectra:** The luminosity of AGNs is believed to have non-stellar origins. Figure 1.34 shows a typical spectrum (SED: spectral energy distribution), which consists of a so-called UV bump and power-law spectrum. These properties can never be reproduced by the superpositions of any stellar spectra. The gas in the central region emits radio as well as X-rays, via thermal and non-thermal mechanisms like Synchrotron and/or Compton processes.
- Time variability:** AGNs vary their brightness on short timescales ranging from a few days or a few minutes to years, depending on the observational wavelengths (see figure 1.4). This means that some sort of activity takes place in a very compact central region (see section 1.1).
- Peculiar appearance:** AGNs frequently exhibit peculiar appearances, such as bursts of central regions, radio lobes, and jets. The

activity may locate in the very center, but can affect a parent galaxy and extragalactic space.

5. **Relativistic phenomena:** AGNs sometimes exhibit relativistic phenomena, such as superluminal motions of radio blobs and high-energy particle emission.

Many of (at least some of) these observational features of quasars and AGNs are successfully explained within the context of the grand unified theory (GUT) for AGNs (e.g., Lawrence 1987; Blandford et al. 1995 for reviews). All types of nuclear activity may be ‘unified’ by the orientation effect, such as the beaming of relativistic jets (Orr and Browne 1982; Barthel 1989) and/or the obscuring molecular torus. Under this GUT, Type 0 AGN (e.g., blazars) is explained by a pole-on view under the beaming effect of jets, Type 1 AGN (QSOs, BLRGs, Sy1s) is that whose central regions can be seen, and Type 2 AGN (NLRGs, Sy2s) is supposed to be an edge-on view where the central region is obscured by the obscuring equatorial ‘torus’ (see figure 1.33).

(b) Evidence of SMBHs and ADs

There is much evidence for *supermassive black holes* (SMBHs) and *accretion disks* (ADs) surrounding them in the heart of active galaxies; some comes from central star distributions, some from stellar and gas dynamics, and some from spectral profiles (see Kormendy and Richstone 1995; Kormendy and Gebhardt 2001; Ferrarese and Ford 2005 for reviews).

In some cases the mass of the central massive black hole is estimated by means of the stellar distribution, stellar rotation curve, and stellar velocity dispersion. A typical example is M 87, where the central luminosity cusp is explained by the SMBH with a mass of $\sim 3 \times 10^9$ (Young et al. 1978; Sargent et al. 1978). Their conclusions were confirmed using the refurbished *HST* (see below). Several tens of SMBHs were weighed based upon stellar dynamical technique (Ferrarese and Ford 2005).

In some cases, on the other hand, the gas motion in the central region, based on emission-line spectroscopy, provides a guess as to the mass of the black hole. A typical example is also the case of M 87 (see below). A dozen of SMBHs were weighed based upon gas dynamical and water-maser approaches (Ferrarese and Ford 2005).

Several examples for the masses of SMBHs estimated by stellar and gas dynamical search techniques are summarized in table 1.6. Several

tens of SMBHs were listed up (e.g., Kormendy and Gebhardt 2001; Ferrarese and Ford 2005).

Table 1.6 Supermassive Black Holes.¹³

Objects	Type	<i>d</i>	<i>M</i>
stellar dynamics			
Sgr A*/The Galaxy	Sbc	0.0085	3.7×10^6
M 31	Sb	0.7	3×10^7
M 32	dE	0.7	2×10^6
NGC 3115	S0	8.4	1×10^9
NGC 4594	Sa	9.2	5×10^8
NGC 3377	E	9.9	8×10^7
gas dynamics			
M 87	cD	15.3	3×10^9
NGC 4261	E	31.6	5×10^8
water maser			
NGC 4258/M 106	Sbc	7.5	4×10^7
NGC 1068	Sy	16	2×10^7
NGC 4258	Sy	7.2	4×10^7
IC 2560	Sy	38	3×10^6

Note — *d*: distance (Mpc); *M*: mass (solar mass).

In the UV region of the continuum spectra of AGNs there often exists a *big blue bump* (BBB), which is usually interpreted as spectra from optically thick standard accretion disks (see chapter 3), and therefore supposed to be evidence for accretion disks (Shields 1978). If this is the case, the profiles of continuum spectra give information about ADs and the central SMBHs; indeed, the mass of the central black hole can be estimated by model fitting (Malkan 1983; Shang et al. 2005). It is quite interesting that the UV bumps exist in the SED (spectral energy distribution) of luminous AGNs, where the bolometric luminosity is on the order of the Eddington luminosity. On the other hand, the UV bumps may not appear in the SED of low luminosity AGNs, which may be suffered from ADAF-like accretion.

Spectroscopic evidence of accretion disks was also found in several systems (figures 1.35 and 1.36). For example, the (asymmetric) double-peaked profiles for Balmer emission lines were found in Arp 102B and 3C 390.3 (Chen et al. 1989; Chen and Halpern 1989). Recent observations have revealed that nineteen AGNs have shown broad, double-peaked or twin shouldered, H α emission lines (Eracleous and Halpern 1994). A systematic survey of $z < 0.4$ BLRGs and radio-loud quasars

¹³see Kormendy and Richstone 1995; Ferrarese and Ford 2005 and references therein.

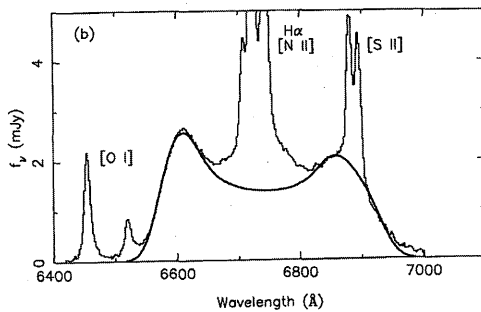


Figure 1.35

H α spectra of Arp 102B. (Adapted from Chen and Halpern 1989)

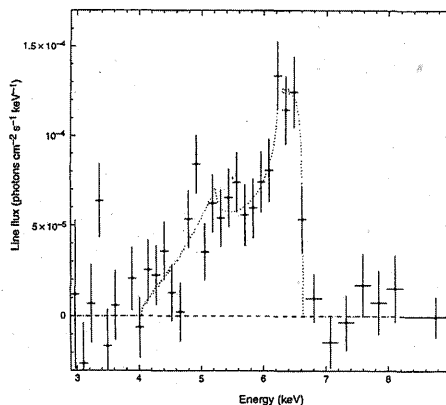


Figure 1.36

X-ray line spectra of MCG-6-30-15. (After Tanaka et al. 1995. Reprinted by permission from Nature Vol.375 No.6533 pp.659-661 22 June 1995 ©Macmillan Magazines Ltd.)

was undertaken later on, and it was found that ~ 20 percent of the observed objects exhibited double-peaked Balmer lines (Eracleous and Halpern 1994; 2003). These double-peaked Balmer lines originate in the outer regions of the accretion disk at distances from the black hole of hundreds to thousands of the Schwarzschild radii.

Furthermore, the X-ray line spectrum of the Seyfert 1 galaxy MCG-6-30-15 was observed by the ASCA satellite (Tanaka et al. 1995; Iwasawa et al. 1999). The spectrum was clearly seen as double-peaked, which is also

interpreted as being the redshifted iron K α line, evidence of relativistic effects (see chapter 3). The line originates from fluorescence in a cold, low-ionization gas; i.e., an accretion disk.

In the present day, the mass of supermassive black holes located at the center of AGNs and normal galaxies can be estimated in various ways. Accumulated data enables us a statistical discussion; demography of supermassive black holes (Kormendy and Richstone 1995; Magorrian et al. 1998; Ferrarese 2002; see also Merloni et al. 2005). The famous one is the Magorrian relation, which is a relation between the black-hole mass and the bulge luminosity and/or velocity dispersion. That is, the mass of SMBHs is large as the bulge luminosity and/or velocity dispersion are large.¹⁴

(c) M 87

In 1994 the second wide field planetary camera (WFPC2) on *HST* took an image of the center of the giant elliptical M 87, which lies at the center of the Virgo cluster, and revealed a whirling gaseous disk (Ford et al. 1994; figure 1.37; see figures G.8, G.9); further, the *HST* faint object spectrograph (FOS) obtained its spectra (Harms et al. 1994). The size of the disk is estimated to be about 20 pc based on the distance to M 87 (about 1.8×10^7 pc). From a spectral analysis of the gaseous disk, the rotational motion was found to be 500 km s^{-1} . If this gas is in circular motion and if the disk is inclined at 42° , as implied by the apparent axial ratio, then the true rotational speed is about 750 km s^{-1} , and the mass of the central supermassive black hole should be $\sim 2.4 \pm 0.7 \times 10^9 M_\odot$.

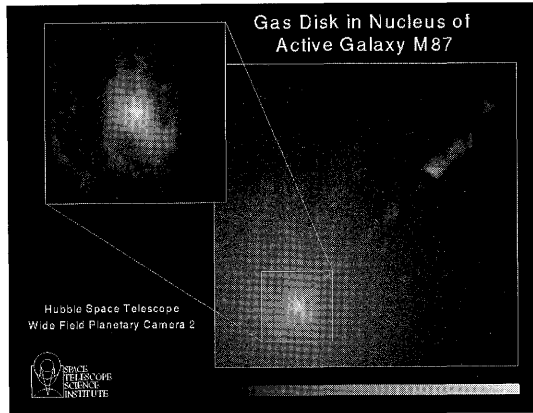
(d) NGC 4261

HST also resolved the gaseous disk at the center of the elliptical galaxy NGC 4261 (figure 1.38), which is in the Virgo cluster and whose distance is 1.4×10^7 pc (Jaffe et al. 1993; Ferrarese et al. 1996). The size of the disk is estimated to be some 60 pc. The outer region of the disk is supposed to be stars, while in the inner region there is a dusty envelope. At the very center, the high-energy radiation is observed. The mass of a SMBH is supposed to be $5 \times 10^8 M_\odot$.

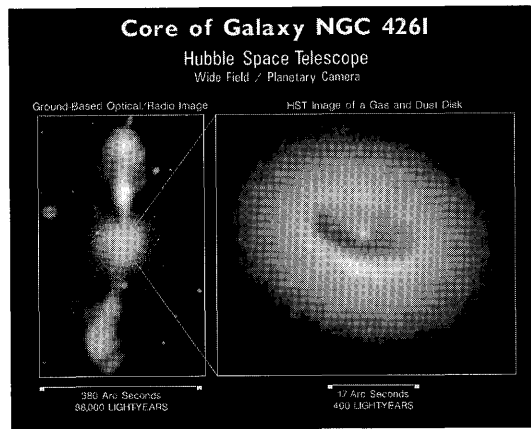
¹⁴In some case,

$$M_\bullet \sim 10^8 \left(\frac{\sigma}{200 \text{ km s}^{-1}} \right)^4 M_\odot,$$

where M_\bullet is the black-hole mass and σ the velocity dispersion of the bulge. In addition, the ratio of black-hole mass to bulge mass is supposed to be about 0.001.

**Figure 1.37**

Gaseous disk at the center of M 87. The image was taken by *HST*. (STScI, NASA; see also Ford et al. 1994)

**Figure 1.38**

Accretion disk in NGC 4261. This image was taken by *HST*. (STScI, NASA; see also Jaffe et al. 1993)

(e) NGC 4258 (M 106)

In NGC 4258 (M 106), which is a modest AGN and a type of LLAGN, a somewhat cold accretion disk was found by the observation of a water maser (Miyoshi et al. 1995). That is, they observed the Doppler shift of the water-maser emission line at 1.3 cm, and derived a rotation curve of

the disk, which is just on the Keplerian curve (figure 1.39). In the case of NGC 4258 a detailed analysis determined that the mass of the central black hole is $\sim 3.6 \times 10^7 M_{\odot}$.

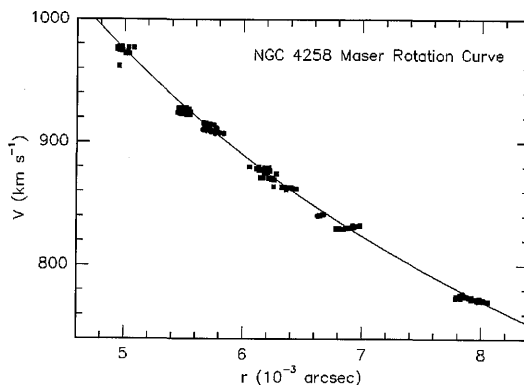


Figure 1.39

Rotational curve of the maser disk in NGC 4258. (After Miyoshi et al. 1995. Reprinted by permission from Nature Vol.373 No.6509 pp.127–129 5 Jan 2002 ©Macmillan Magazines Ltd.)

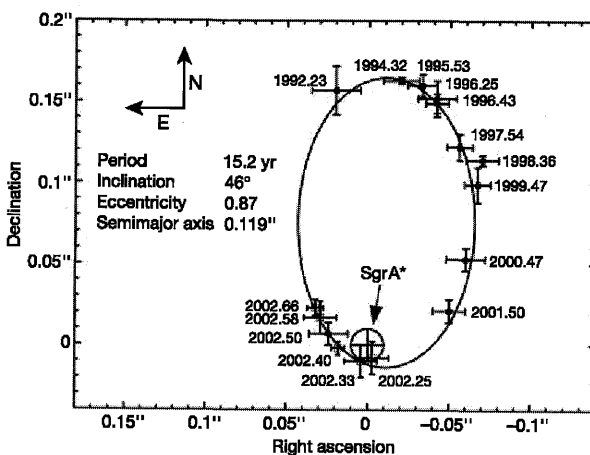


Figure 1.40

Orbit of star S2 rotating around Sgr A*. (After Schödel et al. 2002. Reprinted by permission from Nature Vol.419 No.6908 pp.694–646 17 Oct 2002 ©Macmillan Magazines Ltd.)

(f) Sgr A* (The Galactic Center)

The Galactic Center (GC), located in Sagittarius, is a strong compact radio source, called Sgr A*, whose distance is about 8.5 kpc. Sgr A* shows powerful flare activity both at X-ray and near-IR wavelengths. Our Galactic Center is the closest AGN, but a most ‘distant’ AGN for a long time, because of dust and gas in our Galaxy, which obscure GC. Radio and IR observations, and recent optical observation with large telescopes have revealed the nature of GC (see, e.g., Melia and Falcke 2001 for a review). That is, the Galactic Center also harbors a supermassive black hole.

Sgr A* is embedded in a central stellar cluster, whose core radius is on the order of 0.3–0.4 pc. This cluster has several tens of bright stars that are hot, blue, HeI emission line stars and asymptotic giant branch stars. Recently, proper motions of several stars rotating around Sgr A* have been traced by two groups, and stellar orbits as well as the mass of a SMBH were obtained (Ghez et al. 2000, 2005; Schödel et al. 2002; figure 1.40). The mass of the monster in GC is estimated as $3.7 \pm 1.5 \times 10^6 M_\odot$.

1.6 Present Paradigm

Now, the accretion-disk research has broken into a new era observationally as well as theoretically, since we know various modes of activity in X-ray binaries and active galactic nuclei, and since we know of multiple branches with different characters in the luminosity ranges of observational interest (see figure 1.41).

Roughly speaking, when the accretion rate is so low ($\dot{M} \lesssim 0.1 L_E/c^2$, where \dot{M} is the accretion rate and L_E the Eddington luminosity defined in chapter 2), the disk is supposed to be in the optically thin advection-dominated state (ADAF/RIAF) (see chapter 9), where the disk is optically thin with insufficient cooling and extends down to the surface of the central object. This dark branch may be related to the low/hard state of black-hole binaries and low-luminosity AGNs, such as Sgr A*.

When the accretion rate is mildly low ($\dot{M} \lesssim L_E/c^2$), the disk is in the Shakura-Sunyaev standard state (chapter 3), where the disk is geometrically thin and optically thick. This standard branch can be applied to the high/soft state of black-hole binaries and usual luminous AGNs.

When the accretion rate is very high ($\dot{M} \gtrsim L_E/c^2$), the disk is supposed to be in supercritical (slim disk) state (chapter 10), where the disk is optically thick with photon trapping, and extends down to the surface of the central object. This bright branch may be related to the very high

state of black-hole binaries and super-Eddington sources.

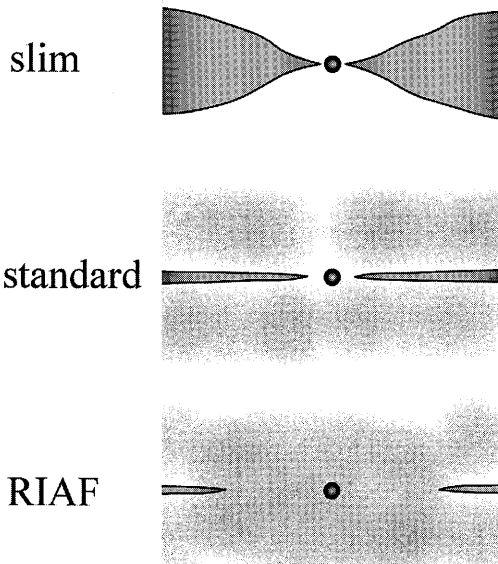


Figure 1.41

Schematic picture of several types of accretion disks. For a medium amount of the accretion rate, the disk is in the classical standard state (middle). There may exist a corona above and below an geometrically thin, and optically thick disk. For a very low accretion rate, the disk is supposed to be in the optically-thin advection-dominated state (bottom). For a supercritical accretion rate, the disk must be in the optically-thick advection-dominated state (top). There may exist an optically thick wind, blowing from the disk surface.

References

- Abramowicz M.A., Czerny B., Lasota J.-P., Szuszkiewicz E. 1988, ApJ 332, 646
 Abramowicz M., Jaroszyński M., and Sikora M. 1978, A&A 63, 221
 Adams F.C., Lada C.J., Shu F.H. 1988, ApJ 326, 865
 Alcock C. et al. 1997, MNRAS 287, 699
 Antokhina É.A., Cherepashchuk A.M. 1987, SvA 31, 295
 Antonucci R.R.J., Miller J.S. 1985, ApJ 297, 621
 Aslanov A.A., Cherepashchuk A.M., Goranskij V.P., Rakhimov V.Yu., Vermeulen R.C. 1993, A&A 270, 200
 Baldwin J.A. 1975, ApJ 201, 26
 Barthel P.D. 1989, ApJ 336, 606

- Blandford R.D., Begelman M.C. 1999, MNRAS 303, L1
- Blandford R., Netzer H., Woltjer L. 1995, *Active Galactic Nuclei* (Springer-Verlag, Berlin)
- Boffin H.M., Steeghs D., Cuypers J. (eds.) 2001, *Astrotomography* (Springer-Verlag, Berlin)
- Brown G.E., Bethe H.A. 1994, ApJ 423, 659
- Chen K., Halpern J.P., Filippenko A.V. 1989, ApJ 339, 742
- Chen K., Halpern J.P. 1989, ApJ 344, 115
- Cherepashchuk A.M. 1981, MNRAS 194, 761
- Cherepashchuk A.M. 1988, Soviet Sci. Rev. E (Astrophys. Space Phys.) 7, 183
- Cherepashchuk A. M. et al. 2005, A&A 437, 561
- Chiu H.-Y. 1965, in *Quasi-Stellar Sources and Gravitational Collapse*, eds. I. Robinson, A. Schild, E.L. Schucking (The University of Chicago Press, Chicago), p3
- Cowley A.P., Hutching J.B., Crampton D. 1981, ApJ 246, 489
- Dewangan G.C., Titarchuk L., Griffiths R.E. 2005, astro-ph/0509646
- Done C., Gierliński M. 2004, PTPS 155, 9
- Ebisawa K., Ueda Y., Inoue H., Tanaka Y., White N.E. 1996, ApJ 467, 419
- Eracleous M., Halpern J.P. 1994, ApJS 90, 1
- Eracleous M., Halpern J.P. 2003, Ap 599, 886
- Fabrika S.N. 2004, ApSpPhysRev 12, 1
- Fender R.P., Belloni T.M., Gallo E. 2004, MNRAS 355, 1105
- Ferrarese L. 2002, in *Current High-Energy Emission Around Black Holes*, eds. C.-H. Lee and H.-Y. Chang (World Scientific, Singapore), p3
- Ferrarese L., Ford H. 2005, SpSciRev 116, 523
- Ferrarese L., Ford H.C., Jaffe W. 1996, ApJ 470, 444
- Fishbone L.G., Moncrief V. 1976, ApJ 207, 962
- Ford H.C., Harms R.J., Tsvetanov Z.I., Harfig G.F., Dressel L.L., Kriss G.A., Bohlin R.C., Davidsen A.F., Margon B., Kochhar A.K. 1994, ApJ 435, L27
- Frank J., King A., Raine D. 2002, *Accretion Power in Astrophysics*, 3rd ed. (Cambridge University Press, Cambridge)
- Fukue J., Nakashima R., Arimoto J., Awano Y., Honda S., Ishikawa K., Kato T., Kawai N., Matsumoto K., Okugami M., Sakaguchi T., Tajima Y., Tanabe K., Tsuda K., Watanabe Y., Yamada Y., Yokoo T. 1997, PASJ 49, 93
- Fukue J., Obana Y., Okugami M. 1998, PASJ 50, 81
- Ghez A. M. et al. 2000, Nature 407, 349

- Ghez A. M. et al. 2005, ApJ 620, 744
- Gierliński M., Zdziarski A.A., Poutanen J., Coppi P.S., Ebisawa K., Johnson W.N. 1999, MNRAS 309, 496
- Gladyshev S.A., Goranskii V.P., Cherepashchuk A.M. 1987, SvA 31, 541
- Goranskij V.P., Esipov V.F., Cherepashchuk A.M. 1998, Astronomy Report 42, 209
- Greenstein J.L., Matthews T.A. 1963, AJ 68, 279
- Harms R.J., Ford H.C., Tsvetanov Z.I., Harfig G.F., Dressel L.L., Kriss G.A., Bohlin R.C., Davidsen A.F., Margon B., Kochhar A.K. 1994, ApJ 435, L35
- Hartman L., Kenyon S.J. 1996, ARA&A 34, 207
- Hayakawa S., Matsuoka M. 1964, PTPS 30, 204
- Hazard C., Mackey M.B., Shimmins A.J. 1963, Nature 197, 1037
- Heckman T. 1980, A&A 87, 152
- Horne K. 1985, MNRAS 213, 129
- Horne K., la Dous C.A., Shafter A.M. 1990, in *Accretion-Powered Compact Binaries*, ed. C.W. Mauche (Cambridge University Press, Cambridge), p109
- Hōshi R. 1979, PTP 61, 1307
- Ichimaru S. 1977, ApJ 214, 840
- Iwasawa K. et al. 1999, MNRAS 306, L191
- Jaffe W., Ford H.C., Ferrarese L., van den Bosch F., O'Connel R.W. 1993, Nature 364, 213
- Kahabka P., van den Heuvel E.P.J. 1997, ARA&A 35, 69
- Kaifu N., Suzuki S., Hasegawa T., Morimoto M., Inatani J., Nagane K., Miyazawa K., Chikada Y., Kanzawa T., Akabane K. 1984, A&Ap 134, 7
- Kaluzienski L.J., Holt S.S., Boldt E.A., Serlemitsos P.J. 1977, ApJ 212, 203
- Kawashima K., Kitamoto S. 1996, PASJ 48, L113
- Kemp J.C., Henson G.D., Kraus D.J., Carroll L.C., Beardsley I.S., Takagishi K., Jugaku J., Matsuoka M., Leibowitz E.M., Mazeh T., Mendelson H. 1986, ApJ 305, 805
- Knigge C., Long K.S., Blair W.P., Wade R.A. 1997, ApJ 476, 291
- Kormendy J., Richstone D. 1995, ARA&Ap 33, 581
- Kormendy J. and Gebhardt K. 2001, in *Relativistic Astrophysics*, eds. J. C. Wheeler and H. Martel, AIP
- Koyama K., Inoue H., Tanaka Y., Awaki H., Takano S., Ohashi T., Matsuoka M. 1989, PASJ 41, 731
- Kozłowski M., Jaroszyński M., Abramowicz M. 1978, A&A 63, 209

- Krolik I.H. 1999, *Active Galactic Nuclei* (Princeton University Press, Princeton)
- Lada C.J. 1985, ARA&Ap 23, 267
- Lada C.J. 1987, in *Star Forming Regions* IAU Symp No115, ed. M. Peimbert, J. Jugaku (D. Reidel Pub. Co., Dordrecht), p1
- Lawrence A. 1987, PASP 99, 309
- Lewin W.H.G., van Paradijs J., van den Heuvel E.P.J. 1995, *X-ray Binaries* (Cambridge University Press, Cambridge)
- Lewin W.H.G., van der Klis M. 2006, *Compact Stellar X-ray Sources* (Cambridge University Press, Cambridge)
- Lichti G.G., Balonek T., Courvoisier T.J.-L., Johnson N., McConnel M. McNamara B., von Montigny C., Paciesas W., Robson E.I., Sadun A., Schalinski C., Smith A.G., Staubert R., Steppe H., Swanenburg B.N., Turner M.J.L., Ulrich M.-H., Williams O.R. 1995, A&A 298, 711
- Lüst R. 1952, ZeitschrftNaturForschung 7a, 87
- Lynden-Bell D. 1969, Nature 223, 690
- Magorrian J. et al. 1998, AJ 115, 2285
- Makishima K., Maejima Y., Mitsuda K., Bradt H.V., Remillard R.A., Tuohy I.R., Hoshi R., Nakagawa M. 1986, ApJ 308, 635
- Malkan M.A. 1983, ApJ 268, 582
- Margon B. 1984, ARA&A 22, 507
- Marsh T.R., Horne K. 1988, MNRAS 225, 269
- Maththews T.A. and Sandage A.R. 1963, ApJ 138, 30
- Matsumoto H. et al. 2001, ApJ 547, L25
- McClintock J.E., Remillard R.A. 2003, in *Compact Stellar X-ray Sources*, eds. W.H.G. Lewin and M. van der Klis (Cambridge University Press, Cambridge) chap 4 (astro-ph/0306213)
- Melia F., Falcke H. 2001, AnnRevA&Ap 39, 309
- Merloni A., Nayakshin S., Sunyaev R.A. (eds.) 2005, *Growing Black Holes: Accretion in a Cosmological Context* (Springer-Verlag, Berlin)
- Meyer F. and Meyer-Hofmeister E. 1981, A&A 104, L10
- Mirabel I.F. 2004, PTPS 155, 71
- Mirabel I. F., Rodríguez L. F. 1994, Nature 371, 46
- Mirabel I. F., Rodríguez L. F. 1999, AnnRevA&Ap 37, 409
- Mitsuda K., Inoue H., Koyama K., Makishima K., Matsuoka M., Ogawara Y., Shibasaki N., Suzuki K., Tanaka Y., Hirano T. 1984, PASJ 36, 741
- Miyoshi M., Moran J., Herrnstein J., Greenhill L., Nakai N., Diamond P., Inoue M. 1995, Nature 373, 127

- Narayan R., Yi I. 1994, ApJ 428, L13
- Novikov I.D., Thorne K.S. 1973, in *Black Holes*, ed. C. DeWitt and B. DeWitt (Gordon and Breach, New York)
- O'Dell C.R., Wen Z., Hu X. 1993, ApJ 410, 696
- Orr M.J.L., Browne I.W.A. 1982, MNRAS 200, 1067
- Paczyński B. and Wiita P.J. 1980, A&A 88, 23
- Parmar A.N., White N.E., Giommi P., Gottwald M. 1986, ApJ 308, 199
- Perley P.A., Willis A.G., Scott J.S. 1979, Nature 281, 437
- Peterson B.M. 1997, *Active Galactic Nuclei* (Cambridge University Press, Cambridge)
- Quataert E., Gruzinov A. 2000, ApJ 539, 809
- Rees M.J., Begelman M.C., Blandford R.D., Phinney E.S. 1982, Nature 295, 17
- Robson I. 1996, *Active Galactic Nuclei* (John Wiley & Sons, Chichester)
- Salpeter E.E. 1964, ApJ 140, 796
- Sargent W.L.W., Young P.J., Boksenberg A., Shortridge K., Lynds C.R., Hartwick F.D.A. 1978, ApJ 221, 731
- Schmidt M. 1963, Nature 197, 1040
- Schödel R., Ott T., Genzel R. et al. 2002, Nature 419, 694
- Seyfert C.K. 1943, ApJ 97, 28
- Shakura N.I., Sunyaev R.A. 1973, A&A 24, 337
- Shang Z. et al. 2005, ApJ 619, 41
- Shields G.A. 1978, Nature 272, 706
- Shklovski I.S. 1967, SovAstron AJ 11, 749
- Shu F.H., Adams F.C. 1987, in *Circumstellar Matter*, IAU Symp No122, ed. I. Appenzeller, C. Jordan (D. Reidel Publishing Company, Dordrecht), p7
- Snell R. L., Loren R.B., Plambeck R.L. 1980, ApJ 239, L17
- Tanaka Y. 1992, in *Ginga Memorial Symp.*, ed. F. Makino, F. Nagase (ISAS, Sagamihara), p19
- Tanaka Y., Nandra K., Fabian A.C., Inoue H., Otani C., Dotani T., Hayashida K., Iwasawa K., Kii T., Kunieda H. Makino F., Matsuoka M. 1995, Nature 375, 659
- Timmes F.X., Woosley S.E., Weaver T.A. 1996, ApJ 457, 834
- Türler M., Paltani S., Courvoisier, T.J.-L. et al. 1999, A&Ap Supl. 134, 89
- Warner B. 1976, in *Structure and Evolution of Close Binary Systems*, IAU Symp. No. 73, eds. P. Eggleton, S. Mitton, J. Whelan (D. Reidel, Dordrecht), p85

- Warner B. 1995, *Cataclysmic Variables* (Cambridge University Press, Cambridge)
- Weedman D. et al. 1981, ApJ 248, 105
- Wheeler J.C. (ed) 1993, *Accretion Disks in Compact Stellar Systems* (World Scientific, Singapore)
- Young P.J., Westphan J.A., Kristian J., Wilson C.P. Landaurer F.P. 1978, ApJ 221, 721
- Zel'dovich Ya.B., Novikov I.D. 1964, Dokl.Acad.Nauk. 155, 1033
- Zwitter T., Calvani M., D'Odorico S. 1991, A&A 251, 92

CHAPTER 2

Physical Processes Related to Accretion

In chapter 1 we introduced several basic concepts related to accretion disks from an energetic viewpoint. As shown in chapter 1, the concept of accretion disks is remarkably important for modern astrophysics, and many researchers are involved in this field both directly and indirectly. Progress is very rapid, and there are many complexities and numerous new ideas. As a result, the majority of non-accretion-disk specialists among astrophysicists may not be familiar with accretion-disk physics. In this chapter we review several fundamental physical processes related to black-hole accretion disks, which include the Eddington luminosity, transonic properties, the nature of viscous processes, magnetic instabilities, and relativistic effects.

2.1 Eddington Luminosity

As we have seen previously, the disk luminosity L_d is a function of only \dot{M} and thus does not depend on M , as long as we take r_{in} in units of the Schwarzschild radius r_g .¹ So what role does M play in the nature of accretion disks? It is essential when considering the maximum accretion luminosity. Here, we briefly explain the *Eddington luminosity*, which is closely related to the energy-liberation rate associated with mass-accretion processes.

2.1.1 Derivation of the Eddington Luminosity

Let us consider a static gas particle (e.g., ionized hydrogen) near to a gravitating object of mass M and luminosity L . This particle is attracted inward by gravity, while it is pushed outward by radiation pressure (figure 2.1). When the luminosity of the object is not very large,

¹The situation may alter if the disk is advection-dominated; see chapter 9.

the radiation-pressure force is smaller than the gravitational force and the particle is confined in the gravitational field of the object. As the luminosity becomes larger for a fixed mass, the radiation-pressure force also increases and eventually overcomes the gravitational force; the gas particle is ultimately blown off. Hence, gas cannot accrete onto such an extremely luminous object. In other words, an infinitely luminous accretion-powered object cannot exist as an astronomical object in the usual sense. Thus, for a fixed mass of the object, there exists a maximum possible luminosity for it; this is the *Eddington luminosity*, L_E .

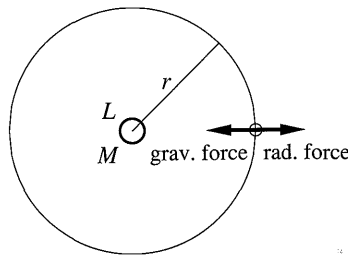


Figure 2.1

Eddington luminosity, defined as the luminosity at which the radiation-pressure force on ionized gas is exactly balanced by the gravitational force.

Let us derive the Eddington luminosity for spherical accretion flow comprising pure hydrogen. At distance r from a spherical object of luminosity L , the radiation flux (the amount of radiation energy flowing per unit time per unit area), f , is

$$f = \frac{L}{4\pi r^2}. \quad (2.1)$$

This energy flux carries a momentum flux of

$$\frac{1}{c} f = \frac{1}{c} \frac{L}{4\pi r^2}, \quad (2.2)$$

where c is the speed of light. Since the effective cross section of an electron is the Thompson scattering cross section σ_T , the force imposed on each electron by radiation is

$$\frac{\sigma_T}{c} f = \frac{\sigma_T}{c} \frac{L}{4\pi r^2}. \quad (2.3)$$

On the other hand, the gravitational force F_g asserted on each hydrogen atom is

$$F_g = \frac{GMm_H}{r^2}, \quad (2.4)$$

where m_H is the hydrogen mass.

We assume fully ionized hydrogen, in which the protons and electrons are coupled with each other by the electromagnetic force. Interestingly, both the gravitational force and the radiation force have the same radial dependence in the present situation; i.e., if they are balanced at some radius, they are exactly equal everywhere. By equating these forces, equations (2.3) and (2.4), we obtain the Eddington luminosity L_E ,

$$L_E = \frac{4\pi cGMm_H}{\sigma_T} = \frac{4\pi cGM}{\kappa_{es}}, \quad (2.5)$$

where κ_{es} ($= \sigma_T/m_H$) is the electron scattering opacity. Note that the Eddington luminosity does not depend on r . A spherical static object with mass M cannot shine with luminosity greater than the Eddington luminosity L_E .

The Eddington luminosity for typical parameters becomes

$$L_E = 1.25 \times 10^{39} \left(\frac{M}{10M_\odot} \right) \text{ erg s}^{-1} \quad (2.6)$$

in the case of black-hole binaries, and

$$L_E = 1.25 \times 10^{46} \left(\frac{M}{10^8 M_\odot} \right) \text{ erg s}^{-1} \quad (2.7)$$

in the case of active galactic nuclei. For example, in the case of luminous active galactic nuclei with luminosity $L \sim 10^{46} \text{ erg s}^{-1}$, the mass of the central supermassive black hole should be $M \sim 10^8 M_\odot$, if it shines with the Eddington luminosity. In the previous chapter we derived a similar value from the observational constraints based on the typical luminosity and variability timescale.

The critical mass-accretion rate \dot{M}_{crit} associated with the Eddington luminosity is defined as²

$$\dot{M}_{\text{crit}} \equiv \frac{L_E}{c^2} = 1.4 \times 10^{17} \frac{M}{M_\odot} \text{ g s}^{-1}. \quad (2.8)$$

If the energy conversion rate by accretion is η , the luminosity due to the mass-accretion rate \dot{M} is $\eta \dot{M} c^2$. Since this cannot overcome L_E , we have

$$\dot{M} \lesssim \frac{1}{\eta} \frac{L_E}{c^2}. \quad (2.9)$$

²In some literatures the critical mass accretion rate is defined as $\dot{M}_{\text{crit}} \equiv L_E / (\eta c^2)$ with η (~ 0.1) being the energy conversion efficiency. Throughout this book, we use the definition (2.8) unless specified otherwise.

In particular, \dot{M}_{crit} is the possible maximum mass-accretion rate when $\eta = 1$.

The Eddington timescale t_E , which is the e -folding (growth) time for the mass of a black hole accreting at the Eddington rate, is given by

$$t_E \equiv \frac{M}{\dot{M}_{\text{crit}}} = \frac{\sigma_T c}{4\pi G m_H} = 4.5 \times 10^8 \text{ yr.} \quad (2.10)$$

We see that this Eddington timescale is independent of the mass.

2.1.2 Super-Eddington Luminosity

One of the unique features of disk accretion is that it can result in super-Eddington luminosities. Only for spherical systems is the Eddington luminosity the maximally attainable luminosity. In disk configurations this is not always the case, as we will now demonstrate (M.A. Abramowicz, private communication).

A necessary condition for the presence of steady configurations in a cylindrically rotating luminous system is

$$-\nabla\psi + \Omega^2\mathbf{r} + \frac{\kappa_{\text{es}}}{c}\mathbf{F} \leq 0, \quad (2.11)$$

where ψ is the gravitational potential, $\Omega(\mathbf{r})$ the angular velocity of rotation, \mathbf{r} the radial vector from the rotating axis, κ_{es} ($= \sigma_T/m_H$) the opacity for electron scattering, and \mathbf{F} the radiation flux vector. Integrating equation (2.11) over the whole surface of the system in consideration, we have

$$\begin{aligned} L &\equiv \int \mathbf{F} \cdot d\mathbf{S} \\ &\leq \frac{c}{\kappa_{\text{es}}} \int \nabla\psi \cdot d\mathbf{S} - \frac{c}{\kappa_{\text{es}}} \int \Omega^2\mathbf{r} \cdot d\mathbf{S} \\ &= \frac{4\pi c G M}{\kappa_{\text{es}}} - \frac{c}{\kappa_{\text{es}}} \int \text{div}(\Omega^2\mathbf{r}) dV, \end{aligned} \quad (2.12)$$

where we have transformed the surface integration to a volume integral using the Gauss theorem and, further, we used the Poisson equation for the first integral. If there is no rotation, the maximum possible value of L is just the Eddington luminosity L_E .

Let us consider the case where the rotation is cylindrical. We then have

$$\text{div}(\Omega^2\mathbf{r}) = 2\Omega(\omega + S), \quad (2.13)$$

where ω and S are the *vorticity* and the rate of *strain (shear)*, defined respectively by

$$\omega = \frac{1}{2} \frac{d\ell}{rdr} \quad \text{and} \quad S = \frac{1}{2} r \frac{d\Omega}{dr}, \quad (2.14)$$

ℓ being the specific angular momentum; i.e., $\ell = r^2\Omega$. Then, equation (2.12) is reduced to

$$L \leq L_E - \frac{2c}{\kappa_{\text{es}}} \int \Omega(\omega + S) dV. \quad (2.15)$$

In the limit of uniform rotation ($S = 0$), we have $\omega > 0$, and the right-hand side of equation (2.15) is less than L_E . In the other limit of constant angular momentum ($\omega = 0$), we have $S < 0$ and the right-hand side of equation (2.15) exceeds L_E . Thus, the luminosity can exceed the Eddington luminosity if the shear is sufficiently large.

The reason why $L > L_E$ is possible is related to the appearance of funnels along the rotation axis. In the case of $\ell = \text{const.}$, the centrifugal force increases inward as $1/r^3$, which is faster than that of the gravitational force ($\propto 1/r^2$). Because of this, the accretion flow has a funnel (a vacuum region) along the rotation axis. This is one of characteristics of rotating tori. The force balance among the gravitational, centrifugal and pressure forces in the funnel results in the centrifugal force being directed inward towards the disk's (torus') surface. In other words, the component of the centrifugal force normal to the disk's (torus') surface is negative. Hence, a strong radiation pressure normal to the surface is allowed to maintain a steady state. How much super-Eddington luminosity is possible depends upon the configuration of the disks (tori). Geometrically thin disks cannot overcome the Eddington luminosity, but thick tori can have a moderate amount of super-Eddington luminosity (Sikora 1981; Madau 1988).

2.2 Bondi Accretion

In preparation for discussing the transonic properties of accretion flows, we consider here the simplest case: spherically-symmetric steady accretion and wind under the gravitational field around a point mass. Spherical accretion onto a gravitating body was first studied by Bondi (1952), and is often called *Bondi accretion*, which is now believed to be quite important, as stated in chapter 1. Spherical outflow was examined by Parker (1958) in relation to a *solar wind*, the existence of which is now well established. See, e.g., Holzer and Axford (1970) for the fundamentals of spherical transonic flows.

2.2.1 Basic Equations

Let us consider a spherically symmetric flow around an object of mass M . The flow is supposed to be steady and one-dimensional in the radial (r) direction. The flow is further assumed to be inviscid and adiabatic, and magnetic and radiation fields are ignored (an isothermal case is also examined in the footnotes).

Under the Newtonian approximation, the continuity equation and the equation of motion are, respectively,

$$\frac{1}{4\pi r^2} \frac{d}{dr} (4\pi r^2 \rho v) = 0, \quad (2.16)$$

$$v \frac{dv}{dr} = -\frac{1}{\rho} \frac{dp}{dr} - \frac{GM}{r^2}, \quad (2.17)$$

where v is the flow velocity (positive for wind and negative for accretion), ρ the density, and p the pressure. The polytropic relation is assumed,

$$p = K\rho^\gamma, \quad (2.18)$$

where K and γ are constants.

Integrating the above equations yields the mass conservation and the Bernoulli equation:

$$-4\pi r^2 \rho v = \dot{M}, \quad (2.19)$$

$$\frac{1}{2}v^2 + \frac{\gamma}{\gamma-1} \frac{p}{\rho} - \frac{GM}{r} = E, \quad (2.20)$$

where \dot{M} is the mass-accretion rate (which is constant in the present case) and E is the *Bernoulli constant*.³

2.2.2 Sound Speed and Critical Points

Let us introduce the *adiabatic sound speed* c_s , which is defined by $c_s^2 \equiv dp/d\rho$, and rewrite the basic equations as⁴

$$-4\pi r^2 c_s^{\frac{2}{\gamma-1}} v = (K\gamma)^{\frac{1}{\gamma-1}} \dot{M}, \quad (2.21)$$

³In the isothermal case ($\gamma = 1$), the Bernoulli equation becomes

$$\frac{1}{2}v^2 + \frac{p}{\rho} \ln \rho - \frac{GM}{r} = E.$$

⁴In the isothermal case, the Bernoulli equation is rewritten as

$$\frac{1}{2}v^2 + c_T^2 \ln \rho - \frac{GM}{r} = E,$$

where c_T^2 ($\equiv p/\rho$) is the *isothermal sound speed* and constant.

$$\frac{1}{2}v^2 + \frac{1}{\gamma - 1}c_s^2 - \frac{GM}{r} = E. \quad (2.22)$$

From the logarithmic differentiation of equation (2.19) we have $2/r + d\rho/(\rho dr) + dv/(v dr) = 0$, and by eliminating $d\rho/dr$ from equation (2.17) we finally obtain, after some manipulation, the *wind equation* as⁵

$$(v^2 - c_s^2)\frac{1}{v}\frac{dv}{dr} = \frac{2}{r}c_s^2 - \frac{GM}{r^2}. \quad (2.23)$$

Here, the sound speed is expressed as

$$c_s^2 = (\gamma - 1) \left(E + \frac{GM}{r} - \frac{1}{2}v^2 \right). \quad (2.24)$$

In the above equation (2.23), the term $(v^2 - c_s^2)$ on the left-hand side becomes zero at the *transonic point (critical point)*, where the flow velocity equals the sound speed. As long as the velocity gradient, dv/dr , is finite at the transonic point, the right-hand side of equation (2.23) must vanish simultaneously at the critical point. This condition (the *regularity condition*) gives the locations of critical points r_c as follows (the subscript “c” is for “critical”).

In the adiabatic case, inserting $r_c, v_c, c_{sc} [\equiv c_s(r_c)]$ into continuity and Bernoulli equations, (2.21) and (2.22), and considering the regularity condition, $v_c = -c_{sc}$ and $r_c = GM/2c_{sc}^2$, we have

$$(K\gamma)^{1/(\gamma-1)}\dot{M} = 4\pi r_c^2 |v_c|^{(\gamma+1)/(\gamma-1)}, \quad (2.25)$$

$$v_c^2 = \frac{2(\gamma - 1)}{5 - 3\gamma} E. \quad (2.26)$$

These give the relations between the quantities at the critical points and the flow parameters. Furthermore, the critical radius r_c is expressed as

$$r_c = \frac{GM}{2c_{sc}^2} = \frac{(5 - 3\gamma)GM}{4(\gamma - 1)E}. \quad (2.27)$$

Moreover, in order for the steady transonic solution to exist, E must be positive. Hence, the condition

$$1 < \gamma < 5/3 \quad (2.28)$$

should be satisfied in the case of spherically symmetric adiabatic flows.

Roughly speaking, outside the transonic (critical) point, the flow velocity is smaller than the sound speed and the flow resembles the hydrostatic equilibrium, whereas the flow velocity exceeds the sound speed and the flow becomes free-fall like inside the transonic point.

⁵In the isothermal case, c_s is simply replaced by constant c_T .

2.2.3 Mach Number and Singular Point Analysis

Let us next introduce the *Mach number* \mathcal{M} , which is defined by $\mathcal{M} \equiv v/c_s$, and derive the wind equation on \mathcal{M} .

In the adiabatic case, we easily derive

$$\frac{d\mathcal{M}}{dr} = \frac{\mathcal{N}}{\mathcal{D}}, \quad (2.29)$$

where the denominator \mathcal{D} and numerator \mathcal{N} are respectively

$$\mathcal{D} = \mathcal{M}^2 - 1, \quad (2.30)$$

$$\mathcal{N} = \mathcal{M} \left(\frac{\gamma - 1}{2} \mathcal{M}^2 + 1 \right) \left[\frac{2}{r} - \frac{\gamma + 1}{2(\gamma - 1)} \frac{1}{E + \frac{GM}{r^2}} \frac{GM}{r^2} \right], \quad (2.31)$$

after some manipulation.⁶

In order to examine the behavior of solutions near to the critical points, we linearize the wind equation in the vicinity of the critical points. That is, we expand the denominator and numerator as

$$\mathcal{D}(r, \mathcal{M}) \sim \mathcal{D}|_c + \frac{\partial \mathcal{D}}{\partial r} \Big|_c dr + \frac{\partial \mathcal{D}}{\partial \mathcal{M}} \Big|_c d\mathcal{M}, \quad (2.32)$$

$$\mathcal{N}(r, \mathcal{M}) \sim \mathcal{N}|_c + \frac{\partial \mathcal{N}}{\partial r} \Big|_c dr + \frac{\partial \mathcal{N}}{\partial \mathcal{M}} \Big|_c d\mathcal{M}. \quad (2.33)$$

Here, $|_c$ means the quantities evaluated at the critical points (i.e., $\mathcal{D}|_c = 0 = \mathcal{N}|_c$ trivially). Other coefficients are

$$\lambda_{11} \equiv \frac{\partial \mathcal{D}}{\partial r} \Big|_c = 0, \quad (2.34)$$

$$\lambda_{12} \equiv \frac{\partial \mathcal{D}}{\partial \mathcal{M}} \Big|_c = 2, \quad (2.35)$$

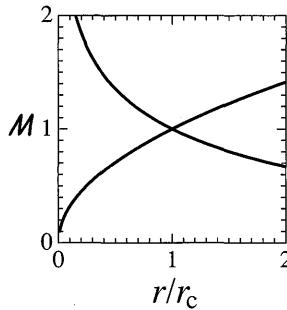
$$\lambda_{21} \equiv \frac{\partial \mathcal{N}}{\partial r} \Big|_c = \frac{5 - 3\gamma}{r_c^2}, \quad (2.36)$$

$$\lambda_{22} \equiv \frac{\partial \mathcal{N}}{\partial \mathcal{M}} \Big|_c = 0 \quad (2.37)$$

for the present adiabatic case.

⁶In the isothermal case, the numerator is expressed as

$$\mathcal{N} = \mathcal{M} \left(\frac{2}{r} - \frac{GM}{c_T^2 r^2} \right).$$

**Figure 2.2**

Transonic solutions in the vicinity of critical points. One corresponds to Bondi spherical accretion, and the other to the Parker solar wind.

Using these coefficients, λ_{ij} , the wind equation (2.29) can be expressed near to the critical point in a general form as

$$\frac{d\mathcal{M}}{dr} = \frac{\lambda_{21}dr + \lambda_{22}d\mathcal{M}}{\lambda_{11}dr + \lambda_{12}d\mathcal{M}} = \frac{\lambda_{21} + \lambda_{22}\frac{d\mathcal{M}}{dr}}{\lambda_{11} + \lambda_{12}\frac{d\mathcal{M}}{dr}}. \quad (2.38)$$

Hence, we have a quadratic equation on $d\mathcal{M}/dr$,

$$\lambda_{12}\left(\frac{d\mathcal{M}}{dr}\right)^2 + (\lambda_{11} - \lambda_{22})\frac{d\mathcal{M}}{dr} - \lambda_{21} = 0, \quad (2.39)$$

which has two roots:

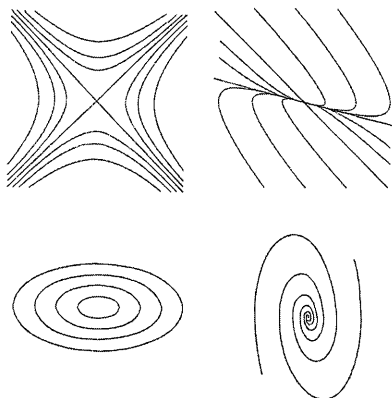
$$\frac{d\mathcal{M}}{dr} = \frac{-\lambda_{11} + \lambda_{22} \pm \sqrt{(\lambda_{11} - \lambda_{22})^2 + 4\lambda_{12}\lambda_{21}}}{2\lambda_{12}}. \quad (2.40)$$

In the present case of adiabatic flows⁷ with neither viscosity nor other dissipative processes, equation (2.40) simply reduces to

$$\frac{d\mathcal{M}}{dr} = \pm \sqrt{\frac{5 - 3\gamma}{2r_c^2}}. \quad (2.41)$$

Since $d\mathcal{M}/dr$ is just the slope of solutions on the (r, \mathcal{M}) -diagram, there are two slopes near to the critical points if transonic solutions exist (figure 2.2). One corresponds to Bondi spherical accretion, and the other to the Parker solar wind.

⁷In the isothermal case, $d\mathcal{M}/dr = \pm 1/r_c$.

**Figure 2.3**

Types (topologies) of critical points. From top-left to bottom-right, types are saddle, node, center, and spiral.

Table 2.1 Roots and Types of Critical Points.

Roots	Type
Two real roots with opposite sign	saddle
Two real roots with same sign	node
Pure imaginary roots	center
Complex roots	spiral

In general there are four types of critical points (*topologies*): *saddle*, *center*, *node*, and *spiral* (figure 2.3). The relation between the types and properties of the roots is summarized in table 2.1 (see also section 8.3). In the case of inviscid and adiabatic flows, as shown above, the transonic point is a saddle.

2.3 Viscous Process

In this book, we discuss the structure and time-dependent properties of viscous accretion disks. Viscosity plays two key roles in accretion disks: angular momentum transfer and viscous heating of disks. In this section we mainly describe how a Keplerian disk evolves under the effect of viscosity. The basic behavior is that most of the disk mass accretes inward, whereas most of the angular momentum is carried outward (cf. Lynden-Bell and Pringle 1974). In addition we describe the basic properties of viscosity in rotating disks.

2.3.1 Minimum Energy States of Rotating Disks

Suppose that we put a test particle in a potential ψ , which, in the case of a point-mass, is equal to $-GM/r$, where M is the mass of the central object and r is the distance from the center. If the particle has no angular momentum with respect to the central mass, it will fall into the center unless it has a large outward radial velocity, $v_r^2 \geq 2GM/r$. If it does have non-zero angular momentum, it will start to rotate around the center (generally) in an eccentric orbit. It is well known that for a given specific angular momentum, $\ell = rv_\varphi$, the specific energy of the test particle is minimum when the orbit is circular. We thus naively expect that the orbit will eventually become circular, if energy dissipation occurs somehow (say, by collisions with an incoming stream of particles or with other rotating particles).

Since the gravitational force due to the central object balances the centrifugal force,

$$-\frac{d\psi}{dr} = \frac{GM}{r^2} = \frac{v_\varphi^2}{r} = \frac{\ell^2}{r^3}, \quad (2.42)$$

the radius of the circular orbit is

$$r_{\text{circ}} = \frac{\ell^2}{GM}. \quad (2.43)$$

That is, as long as angular momentum is conserved, the test particle can never reach the center nor release its potential energy after circularization of the orbit. There is no mass accretion and, hence, no energy liberation to cause luminous disks. Viscosity is thus required as a mechanism to transfer angular momentum and dissipate gravitational energy, thereby explaining the observed, luminous accretion disks.

However, how does a rotating disk evolve under the effect of viscosity? That is, what is the final state of a viscous disk? Before going into the details of the viscous diffusion process, let us first discuss the evolution of rotating disks in general from the viewpoint of energy minimization. This discussion mainly follows Lynden-Bell and Pringle (1974).

Let us consider the minimum energy state of two particles of masses m_1 and m_2 in a fixed point-mass potential. First, we examine the one-particle case. For a specific angular momentum ℓ , the specific energy is

$$\epsilon(\ell) = \frac{1}{2}(v_r^2 + v_z^2) + \frac{1}{2}\frac{\ell^2}{r^2} - \frac{GM}{\sqrt{r^2 + z^2}}, \quad (2.44)$$

which achieves a minimum for a given ℓ when $z = 0$ and $v_r = v_z = 0$; i.e., when the particle is in a circular orbit of radius r_{circ} , as described

above. We then have

$$\epsilon(\ell) = -\frac{GM}{2r_{\text{circ}}} = -\frac{(GM)^2}{2\ell^2}. \quad (2.45)$$

We next consider how to minimize the energy of two circularly rotating particles,

$$E = m_1\epsilon(\ell_1) + m_2\epsilon(\ell_2), \quad (2.46)$$

by adjusting the angular momentum of each particle, $d\ell_1$ and $d\ell_2$, but keeping the total angular momentum constant,

$$J = m_1\ell_1 + m_2\ell_2 = \text{const.} \quad (2.47)$$

Hence, we impose the condition

$$dJ = m_1d\ell_1 + m_2d\ell_2 = 0. \quad (2.48)$$

The total energy change is expressed as

$$dE = m_1\epsilon'(\ell_1)d\ell_1 + m_2\epsilon'(\ell_2)d\ell_2, \quad (2.49)$$

where upon using equation (2.45) we obtain

$$\epsilon'(\ell) \equiv \frac{d\epsilon}{d\ell} = \frac{(GM)^2}{\ell^3} = \frac{\ell}{r_{\text{circ}}^2} = \Omega. \quad (2.50)$$

Here, Ω is the angular velocity of circular motion. With the help of equations (2.48) and (2.50), equation (2.49) becomes

$$dE = m_1d\ell_1 [\epsilon'(\ell_1) - \epsilon'(\ell_2)] = m_1d\ell_1 (\Omega_1 - \Omega_2). \quad (2.51)$$

For $dE < 0$, we require that $d\ell_1 < 0$ if $\Omega_1 > \Omega_2$, or $d\ell_1 > 0$ if $\Omega_1 < \Omega_2$. Thus, *energy can be reduced by exchanging angular momentum in such a way that the particle at the orbit with smaller Ω gains angular momentum*. Since Ω decreases outward in usual astrophysical situations, this means that the angular momentum should be transported outward as the system evolves.

As the next step, we consider the case in which mass exchange, together with the associated angular momentum exchange, is allowed between the two particles, while the total mass and total angular momentum are kept constant; i.e.,

$$dm_1 = -dm_2 \quad \text{and} \quad d(m_1\ell_1) = -d(m_2\ell_2). \quad (2.52)$$

Since the total energy change is

$$dE = d[m_1\epsilon(\ell_1) + m_2\epsilon(\ell_2)], \quad (2.53)$$

we obtain the following by using equations (2.52):

$$\begin{aligned} dE &= dm_1 [\epsilon(\ell_1) - \ell_1\epsilon'(\ell_1)] + d(m_1\ell_1)\epsilon'(\ell_1) \\ &\quad + dm_2 [\epsilon(\ell_2) - \ell_2\epsilon'(\ell_2)] + d(m_2\ell_2)\epsilon'(\ell_2) \\ &= dm_1 [(\epsilon(\ell_1) - \ell_1\Omega_1) - (\epsilon(\ell_2) - \ell_2\Omega_2)] \\ &\quad + d(m_1\ell_1)(\Omega_1 - \Omega_2). \end{aligned} \quad (2.54)$$

We see here that $\epsilon(\ell) - \ell\Omega$ increases outward, since from equation (2.45) we find

$$\epsilon - \ell\Omega = -\frac{3}{2}\frac{GM}{r_{\text{circ}}}, \quad (2.55)$$

for circular motions. This means that the total energy can be decreased not only by transferring the angular momentum outwards (towards smaller Ω), but also by moving mass inwards (towards smaller $\epsilon - \ell\Omega$). Thus, *the minimum energy configuration is the limit in which one particle of infinitesimal mass carries all of the angular momentum in a circular orbit at infinity, while all of the remaining mass aggregates at the center.*

2.3.2 Viscosity in Disks

Let us next consider how viscosity works in general. Suppose we have two parallel shear flows (see the left panel of figure 2.4). In such a case, momentum transfer occurs from flow 1 (with greater velocity) to flow 2 (with smaller velocity). As a result, flow 1 will be decelerated and flow 2 will be accelerated. Viscosity thus tends to reduce the shear ($|v_2 - v_1|$), and tends to produce uniform flows.

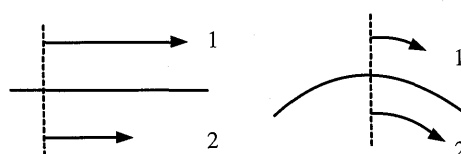


Figure 2.4

Parallel shear flows (left) and differentially rotating flows (right).

Mathematically, if the flow velocity (in the x -direction) has a gradient in the y -direction (perpendicular to the x -direction), the viscous force exerted in the x -direction on the unit surface of the interface plane of flow 2 at y (with normal being in the y -direction) is

$$t_{yx} = \eta \left(\frac{\partial v_x}{\partial y} \right), \quad (2.56)$$

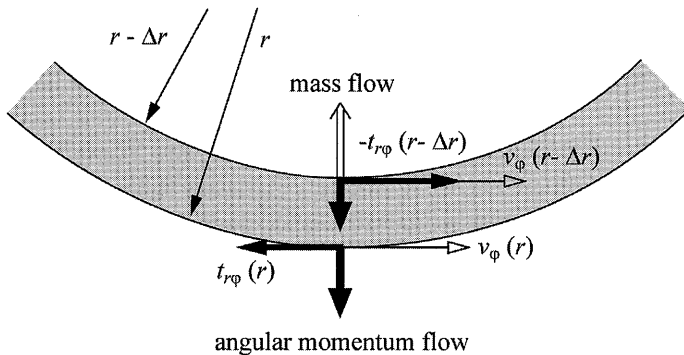
where η ($= \rho\nu$) is a dynamical viscosity with ρ and ν the density and kinematic viscosity, respectively, while the viscous force on flow 1 is $-t_{yx}$. This means that the x -component of momentum is transferred in the y -direction at a rate of $-t_{yx}$; i.e., the momentum flux in the y -direction is $-t_{yx}$.

The flow between $y = y$ and $y = y - \Delta y$ thus feels the force $t_{yx}(y)$ on the unit surface at $y = y$, while exerts the force $t_{yx}(y - \Delta y)$ on the unit surface at $y = y - \Delta y$. The net volume force, which the flow receives in the x -direction, is then

$$f_x = \frac{\partial t_{yx}}{\partial y} = \frac{\partial}{\partial y} \left(\eta \frac{\partial v_x}{\partial y} \right). \quad (2.57)$$

A unit volume of gas at y receives an x -component of momentum at the rate given by equation (2.57).

For two differentially rotating annuli with rotational velocity increasing inward (see the right panel of figure 2.4), angular-momentum transfer occurs from annulus 2 (with greater velocity) to annulus 1 (with smaller velocity). As a result, annulus 1 acquires angular momentum, and thus moves outward; its angular velocity becomes smaller than that at the original radius. Annulus 1 will thus be decelerated, while annulus 2 will be accelerated. The viscosity, in this case, tends to enhance the velocity difference between two annuli ($|v_2 - v_1|$). In other words, the two flows will be separated further. The outer annulus, however, can also lose angular momentum by transferring a greater amount than that it receives from inside to more distant annulus. If the disk has an infinite radius, therefore, all of the disk material can eventually lose its angular momentum and start to move inward. If the disk is cut off at a certain outer radius (i.e., the disk has a finite radius), the outermost region (with infinitesimal mass) will receive most of the disk's angular momentum and proceed outward to infinity, while the majority of the disk material will accrete on the central object (Lynden-Bell and Pringle 1974; see section 2.3.1). *Mass accretes inward, while angular momentum is transferred outward;* this is the key to understanding viscous disk evolution.

**Figure 2.5**

Angular-momentum flow within a viscous disk. The annulus between $r - \Delta r$ and r receives a force $t_{r\varphi}(r)$ per unit surface at r and thus a torque $G(r) (< 0)$ [equation (2.59)] through the entire surface at r . This is the rate of angular momentum gain of the annulus through the surface of r . Likewise, the annulus gains angular momentum at a rate of $-G(r - \Delta r) (> 0)$ through the surface at $r - \Delta r$. The net rate of angular momentum gain is thus $\Delta r \cdot dG/dr$ [equation (2.60)].

The torque asserted on a differentially rotating annulus is obtained as follows. We use cylindrical coordinates (r, φ, z) , with the origin at the central star and the z -axis perpendicular to the plane of the disk (see figure 2.5). Since the rotational velocity differs in the radial direction, the viscous force per unit area exerted in the φ -direction of the interface plane of the inner annulus (with normal being in the r -direction) is

$$t_{r\varphi} = \eta \left(\frac{\partial v_\varphi}{\partial r} - \frac{v_\varphi}{r} \right) = \eta r \frac{d\Omega}{dr}. \quad (2.58)$$

Then, the total torque exerted on the entire surface of the inner annulus from the outer annulus at r is

$$G(r) = 2\pi r \int r t_{r\varphi} dz \approx 4\pi r^3 \eta H \frac{d\Omega}{dr}, \quad (2.59)$$

where H is a half-thickness of the annulus in the direction parallel to the rotation axis (z -axis). The torque on the outer annulus is $-G(r)$. This means that the outward angular momentum flow through the surface at r is $-G(r)$.

Since the annulus between r and $r - \Delta r$ receives a torque $G(r)$ from the outer annulus, and exerts a torque $G(r - \Delta r)$ to the inner annulus, the net torque received by the gas in the annulus at r with unit length

in the radial direction is dG/dr . We thus have

$$2\pi r \cdot r F_\varphi = \frac{dG(r)}{dr}, \quad (2.60)$$

where F_φ is the net surface force (in the φ -direction) exerted on the gas in the annulus at r . That is, the gas at r receives the force F_φ per unit surface (integrated in the z -direction) in the φ -direction.

What, then, is the typical timescale for angular-momentum transfer? From a dimensional argument, the viscous timescale, over which angular-momentum transfer takes place, is $t_{\text{vis}} \sim r^2/\nu$, where r denotes a typical dimension of the disk.⁸ For molecular viscosity, we find

$$\nu_{\text{mol}} \sim v_{\text{mol}} \ell_{\text{mfp}} \sim 10^3 \text{ cm}^2 \text{ s}^{-1} \quad \text{and} \quad t_{\text{vis}} \equiv \frac{r^2}{\nu} \sim 3 \times 10^{11} \text{ yr}, \quad (2.61)$$

where v_{mol} is the random velocity of molecules (of the order of the sound speed), ℓ_{mfp} is the mean-free-path of the molecules, and we have used parameters for binary sources ($r \sim 10^{11}$ cm, $\rho \sim 10^{-8}$ g cm⁻³, and $T \sim 10^4$ K). The viscous timescale far exceeds the age of the universe, even in the case of binaries!! (For AGN the viscous timescale is much longer.) Anomalous viscosity is thus invoked, such as turbulence and/or magnetic fields.

For turbulent viscosity, we estimate

$$\nu_{\text{turb}} \sim v_{\text{turb}} \ell_{\text{turb}} \sim 10^{15} \text{ cm}^2 \text{ s}^{-1} \quad \text{and} \quad t_{\text{vis}} \sim 10^7 \text{ s}, \quad (2.62)$$

where we assigned $v_{\text{turb}} \sim c_s$ and $\ell_{\text{turb}} \sim H$ (half-thickness), and the parameters are again for binary sources ($H \sim 10^9$ cm at $r \sim 10^{11}$ cm and $T \sim 10^4$ K). This gives a reasonably short viscous timescale of t_{vis} .

2.3.3 Origin of Turbulence

One of the puzzles in understanding accretion phenomena was what is the viscous processes required to explain the high accretion rate in accretion disks. The molecular viscosity is obviously inadequate, since it is too small to drive accretion in Keplerian disks, as demonstrated in the above subsection. A natural idea is that turbulence is an origin of the viscous transfer of angular momentum and heat generation, since flows in systems with high Reynolds number are usually turbulent. Astrophysical

⁸The rate of angular-momentum gain in the annulus at r is $\sim G(r)/r \sim 4\pi r \eta H \Omega$ [see equations (2.59) and (2.60)], while the angular momentum contained in the annulus is $\sim 2\pi r \Sigma r^2 \Omega$. The viscous timescale is thus $r^3 \Sigma \Omega / (r \eta H \Omega) = r^2 \rho / \eta = r^2 / \nu$.

systems have very large Reynolds number because of their huge linear dimension. In spite of this, in the context of Keplerian disks, no instability could be identified, i.e., no linear instability in the Keplerian disks was found. This is because the Coriolis force associated with rotation in Keplerian disks acts so as to stabilize the growth of perturbations.

A breakthrough concerning this situation came by Balbus and Hawley (1991) through a rediscovery of the magnetorotational instability (MRI) (see the next subsection). A seed magnetic field grows exponentially in a few rotation times of disks, independent of the strength of the magnetic fields (Balbus and Hawley 1991). Numerical simulations further showed that the instability grows to a highly nonlinear state, which leads to turbulence. In this context, the origin of viscosity in accretion disks consisting of ionized gases is now believed to be hydromagnetic turbulence induced by the MRI.

In spite of this great success, the origin of viscosity in low-temperature disks is not still well understood. In disks such as protoplanetary disks, white dwarf disks in the low state, and outer regions of AGN disks, the ionization degree of the disk gases is so small that the MHD approximations do not hold there (Gammie 1996; Gammie, Menou 1998, Fromang et al. 2002). That is, the route of turbulence in these objects remains a puzzle.⁹ Recently, however, this outstanding puzzle has begun to be solved. Klahr and Bodenheimer (2003) have claimed to find a local hydrodynamical instability in global simulations. Klahr (2004) has performed a local linear analysis of a radially stratified accretion disk in an effort to explain the numerical results obtained by Klahr and Bodenheimer (2003). Subsequently, Johnson and Gammie (2005a, b), Mukhopadhyay et al. (2005) and Afshordi et al. (2005) made linear stability analyses, and clarified the instability mechanism. The instability mechanism invoked is a phenomenon of transient amplification as a shearing wave goes from leading to trailing.¹⁰

We should notice that even if all linear modes of definite frequencies are damping, this does not always imply stability in a shear flow. This is because the definite frequency linear modes are not orthogonal in a shear flow. A suitably tuned linear combination of damping modes can still show an arbitrary transient energy growth. The transient energy

⁹Observations require that even in these objects the viscous timescale must be much shorter than that of molecular viscosity.

¹⁰There might be a phenomenological similarity with the swing amplification of spiral density waves, which is known in the field of density wave theory in galactic dynamics, although the cause of the instability is different.

growth, supplemented by a nonlinear feedback process to repopulate the growing disturbances, could plausibly sustain turbulence for large enough Reynolds numbers. The idea that the transient growth may allow perturbations to grow to a nonlinear state and a subcritical transition to turbulence may take place is called the "bypass mechanism" to turbulence (see Afshordi et al. 2005; Mukhopadhyay et al. 2005).

2.4 Magnetic Instabilities

The presence of global magnetic fields in black-hole accretion disks is generally expected, since seed fields are stretched by differential rotation, and the resulting fields will be sustained by dynamo processes. The importance of global magnetic fields in accretion disks is widely recognized in issues of angular-momentum transport, the formation of jets, and the interactions between holes and disks, etc. Global magnetic fields are also important, since they lead to various kinds of instabilities, and these instabilities could be the origins of various kinds of active phenomena in disks [see Tajima and Shibata (1997) for general arguments on hydromagnetic phenomena in astrophysical objects, including the subjects which are discussed in this section]. In accretion disks, magnetic instabilities are particularly important as a possible origin of the strong turbulence required to transport angular momentum and to generate heat in disks. Among various magnetic instabilities, we briefly review here the magneto-rotational instability (MRI) (see, e.g., Balbus 2003 for a recent review) and the Parker instability in disks.

2.4.1 Magneto-Rotational Instability

Magneto-rotational instability (MRI) was originally found by Velikhov (1959) and Chandrasekhar (1960), and examined further by Fricke (1969). Recently, Balbus and Hawley (1991) and Hawley and Balbus (1991) re-discovered it and recognized its significance in relation to the origin of turbulence in accretion disks. Importantly, this is an instability in differentially rotating systems with specific angular momentum increasing outward (stable systems in the sense of the Rayleigh criterion). Even an extremely weak magnetic field can lead to a rapidly growing dynamical instability. Furthermore, three-dimensional numerical simulations (Hawley et al. 1995; Matsumoto and Tajima 1995; Brandenburg et al. 1995) show that the instability grows to a highly non-linear regime, providing the mechanism required for creating turbulence in accretion disks.

The Maxwell stress tensor can be decomposed into an isotropic pressure and a tension along the line of force. The force resulting from the latter resists against a deformation of the line of force, and acts so as to return a perturbed fluid element to its original position. In a differentially rotating system, this tensional force can lead the system to an instability. As a demonstration of the instability, we consider an axially-symmetric, cylindrically rotating, steady system with vertical magnetic fields (see figure 2.6).

If a fluid element is displaced outward in the radial direction under conservation of specific angular momentum ($\propto r^2\Omega$), the displaced particle rotates slowly because of $\Omega^*(r + \Delta r) < \Omega(r)$, the asterisk being attached to $\Omega(r + \Delta r)$ to emphasize that it is a quantity associated with the perturbed fluid element. Hence, it will lag behind to reach point P', while a particle at r reaches point P (see figure 2.6). The fluid element displaced outward is, however, elastically tethered by the magnetic-field lines, which tend to cause rigid rotation. Hence, angular momentum is transported along the distorted magnetic line of force so that the displaced part tries to co-rotate¹¹ with the unperturbed part of the same line of force (this trend is shown in figure 2.6 by \Rightarrow). If this is realized, the angular velocity of rotation at the perturbed part becomes larger than that of the surrounding gas.¹² Then, the fluid element has a tendency to go further outward by excess centrifugal force. This excess centrifugal force is, however, weaker than the force against it (i.e., the restoring force of magnetic tension), when the vertical size of perturbations is small. If the size of perturbations is moderately large, conversely, the former force can dominate over the latter one and an instability sets in. This is the main process of the *magneto-rotational instability*.

Let us briefly estimate the condition of the instability. We consider the radial force acting on fluid element at point P'. By a displacement of Δr under conserving *angular velocity* of rotation, Ω , the outward centrifugal force increases by ΔF_{cent} ($\sim \Omega^2 \Delta r$) per unit mass. The decrease of the gravitational force by the outward displacement is

$$\Delta F_{\text{grav}} = \frac{GM}{r^2} - \frac{GM}{(r + \Delta r)^2} \sim \frac{2GM\Delta r}{r^3} = 2\Omega^2\Delta r. \quad (2.63)$$

The net increase of the outward force (except for the force of magnetic

¹¹Recall Ferraro's isorotation law (Ferraro 1937); in magnetized axially-symmetric steady rotating systems, the gas along a magnetic field line must rotate with the same angular velocity.

¹²It is assumed that the angular velocity of rotation in the unperturbed disk is distributed so that it decreases outward.

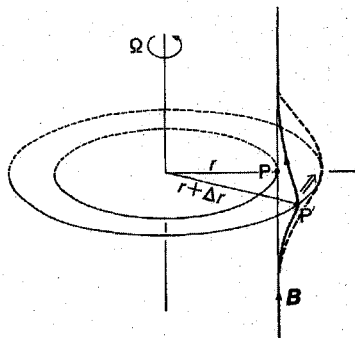


Figure 2.6

Schematic picture showing a magneto-rotational instability for the case of axisymmetric perturbations in differentially rotating disks with a vertical magnetic field.

tension) is thus $3\Omega^2\Delta r$, when the unperturbed state is a Keplerian disk (i.e., $\Omega^2 = GM/r^3$). Against this outward force, a magnetic tension acts in the opposite direction. The force is roughly $(B^2/4\pi\rho)/R$, where R is the radius of curvature of the magnetic field B and is roughly $\lambda^2/\Delta r$ when the wavelength of perturbations in the vertical direction is λ .¹³ If the outward force, i.e., $3\Omega^2\Delta r$, is larger than the inward force, i.e., $(B^2/4\pi\rho)/R$, which is $\sim (c_A^2/\lambda^2)\Delta r$, the fluid element moves further outward and instability sets in, where c_A ($\equiv \sqrt{B^2/4\pi\rho}$) is the Alfvén speed. This instability condition is roughly

$$\lambda > \frac{c_A}{\Omega} \sim \frac{c_A}{c_s} H \sim \sqrt{\frac{p_{\text{mag}}}{p_{\text{gas}}}} H, \quad (2.64)$$

where H is the half-thickness of the disk, and c_s is the speed of sound, i.e., $c_s \sim \Omega H$. It is noted that the instability sets in for perturbations with shorter wavelength when the magnetic fields are weaker.

The growth rate is roughly estimated by considering the timescale of realization of isorotation. As mentioned in the above paragraph, the cause of the instability is the angular-momentum transport along the line of force, which occurs with the Alfvén speed. Hence, the timescale is on the order of λ/c_A ($> 1/\Omega$). This shows that the growth rate is on the order of Ω [see inequality (2.64)]. In order to quantify the growth rate, however, we need a dispersion relation for a small-amplitude perturbation.

¹³Geometrically we can show that $R : \lambda \sim \lambda : \Delta r$.

Here, we consider an axisymmetric accretion disk threaded by uniform, vertical magnetic fields (the case shown in figure 2.6). To describe perturbations, a cylindrical coordinate system (r, φ, z) is introduced, where r is the perpendicular distance from the rotation axis (z -axis) of the disk. Hence, the unperturbed magnetic field \mathbf{B}_0 is $\mathbf{B}_0 = (0, 0, B_0)$, and the unperturbed gas flow in the disk is $(0, r\Omega(r), 0)$. Wavenumber of axisymmetric perturbations is denoted by $(k_r, 0, k_z)$. Then, we can easily derive the dispersion relation for the perturbations, using the Boussinesq approximation (Balbus and Hawley 1991; see also the first edition of this book 1998).¹⁴

An example of the growth rate obtained by the above approximations is shown in figure 2.7 as a function of k_z in the case of $k_r = 0$, $\kappa^2 = \Omega^2$, and $N_r^2 = 0.008\Omega^2$, where N_r is the Brunt-Väisälä frequency in the radial direction (see sections 11.1 and 11.2 for details of the Brunt-Väisälä frequency). The instability occurs for small k_z . Figure 2.7 shows that the growth rate is as large as $\sim 1/\Omega$. The critical k_z , say $k_{z,\text{crit}}$, below which the instability sets in, is

$$k_{z,\text{crit}} H \sim \frac{c_s}{c_A}. \quad (2.65)$$

It is noted that $k_{z,\text{crit}}$ is much larger than $1/H$ when the magnetic field is weak.

The magneto-rotational instability is not restricted to the case of the magnetic-field configuration considered above. It occurs in a general configuration. Let us consider the case where magnetic fields are toroidal and non-axisymmetric perturbations are imposed there (see figure 2.8). A fluid element perturbed from a point P outward under the conservation of angular momentum delays in its rotation and is displaced to a point P' (figure 2.8). The magnetic-field line in the forward part of P' is stretched, while that of the following part is compressed. Hence, a tension force in the forward direction acts on fluid at P', as shown by the arrow in figure 2.8. This makes the angular velocity of rotation at a point P' faster than that of the surrounding medium. Then, for the same reason as discussed before, excess centrifugal force pushes the fluid element at point P' outward, leading to an instability.

¹⁴For details of the Boussinesq approximation, see, for example, Spiegel and Veronis (1960). In the Boussinesq approximation, in order to filter out the acoustic perturbations, the gas motion (velocity \mathbf{u}) is taken to be incompressible. That is, $\text{div } \mathbf{u} = 0$, and the Eulerian pressure variation is neglected in the energy equation. The terms of a pressure variation in the momentum equation are, however, retained in order to correctly take into account the effects of buoyancy. Although $\text{div } \mathbf{u} = 0$ is adopted, this does not mean that the Eulerian density variation ρ_1 is neglected.

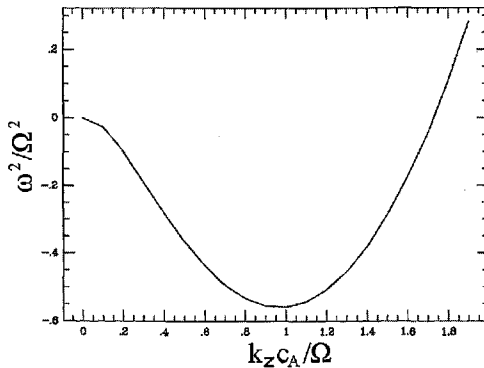


Figure 2.7

Dimensionless growth rate as a function of the dimensionless vertical wavelength for $k_r = 0$, $\kappa = \Omega$, and $N_r^2 = 0.008\Omega^2$. We set that the perturbation is proportional to $e^{i\omega t}$. Notice that $\omega^2 < 0$ corresponds to an instability. (After Balbus and Hawley 1991)

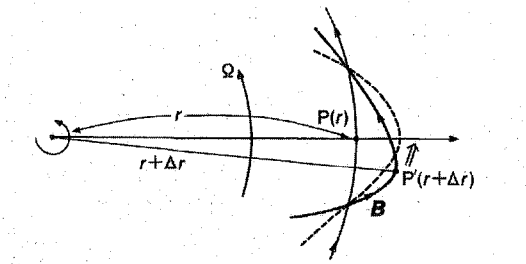


Figure 2.8

Schematic picture showing a magneto-rotational instability for the case of non-axisymmetric perturbations in disks with a toroidal magnetic field.

2.4.2 Parker Instability

Another important magnetic instability in disks is the *Parker instability* (Parker 1966). In order to demonstrate the essence of the Parker instability, we consider an isothermal *atmosphere* stratified in the z -direction under a *constant* gravitational acceleration, g , acting in the negative direction of z . In this medium there are magnetic fields, $B(z)$, which are directed in a given horizontal direction. The fields are stratified in the vertical direction so that the ratio of the Alfvén speed c_A to the acoustic speed c_s is constant in the vertical direction, implying that both of c_s and c_A are constant vertically in the isothermal atmosphere. Then, the

density $\rho(z)$ is stratified in the vertical direction as

$$\rho(z) \propto \exp\left(-\frac{z}{H}\right), \quad (2.66)$$

where H is the scaleheight, given by¹⁵

$$H = \frac{c_s^2 + c_A^2/2}{g}. \quad (2.67)$$

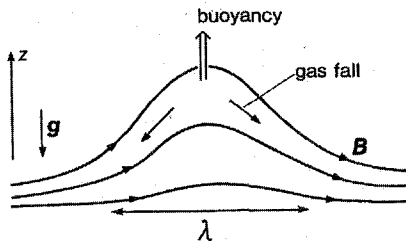


Figure 2.9

Schematic picture showing the mechanism of the Parker instability.

A part of the magnetic fields is raised up over a small distance Δz with horizontal scale λ , as is shown schematically in figure 2.9. (This perturbation is taken to be two-dimensional.) The magnetic tension, of course, resists this deformation. This resisting force is roughly $B^2/(4\pi R)$ per unit volume, where R is the radius of curvature of the magnetic field. In the present problem, however, a gas lifted up by the magnetic field falls along the line of force. This gives rise to buoyancy in the lifted region. The buoyancy can be estimated in the following way. Along the deformed flux sheet no magnetic force works. Hence, after a fall of gas along the line of force, the density in the sheet, ρ^* , is stratified in the vertical direction with a smaller scale height than that in the unperturbed atmosphere, i.e.,

$$\rho^* \propto \exp\left(-\frac{z}{H^*}\right), \quad (2.68)$$

¹⁵The hydrostatic balance in the vertical direction is

$$-\frac{1}{\rho} \frac{\partial}{\partial z} \left(\rho c_s^2 + \frac{B^2}{8\pi} \right) = \rho g.$$

Integration of this equation with $c_s = \text{const.}$ and $c_A/c_s = \text{const.}$ gives relations (2.66) and (2.67).

where $H^* = c_s^2/g$. This implies that the density at the top of the raised part of the sheet is smaller than the surrounding one by $\Delta\rho$, which is roughly estimated by

$$\frac{\Delta\rho}{\rho} \sim \exp\left(-\frac{\Delta z}{H}\right) - \exp\left(-\frac{\Delta z}{H^*}\right) \sim \frac{c_A^2/g}{2HH^*} \Delta z. \quad (2.69)$$

If the buoyancy force, $g\Delta\rho$, is larger than the restoring force, $B^2/(4\pi R)$, instability sets in. Since $R \sim \lambda^2/\Delta z$, the instability condition, $g\Delta\rho > B^2/(4\pi R)$, becomes

$$\lambda > \left(2 + \frac{c_A^2}{c_s^2}\right)^{1/2} H^*. \quad (2.70)$$

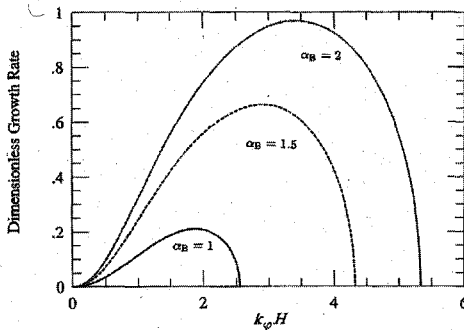
This shows that perturbations with a long horizontal scale can grow.

In summary, when the wavelength of a perturbation in the horizontal direction, λ , is short, the buoyancy force per unit volume cannot overcome the magnetic tension. When it is long, however, the situation is changed, since the magnetic restoring force decreases. The growth rate becomes the maximum at a certain finite wavelength, since for too long-scale perturbations, much time is required for gas to fall along the sheet. Parker (1966) showed that this kind of instability really exists. This instability is called the *Parker instability*. It is also called a magnetic Rayleigh-Taylor instability, since the cause of the instability is due to the fall of dense gas along the line of force.

The Parker instability is important in the sense that the growth rate can become as large as the order of $1/\Omega$, as in MRI, and it grows to a highly non-linear stage (e.g., Matsumoto et al. 1988). Because of this, the instability becomes the origin of various active phenomena in disks, as in solar surface phenomena.

Different from MRI, (differential) rotation of the system is not essential in the Parker instability. The disk rotation and its non-uniformity (i.e., differential rotation), however, have important effects in determining the characteristics of the Parker instability in the disks (e.g., Shibata et al. 1990). Another important factor that makes the Parker instability in the disk distinct from that in stellar atmospheres is non-uniform gravitational acceleration in the vertical direction. Even the direction of the gravitational acceleration changes at the equator.

An analysis of the Parker instability in rotating disks is complex, since the differential rotation tends to stretch perturbations in the azimuthal direction. Hence, in general a normal-mode analysis can no longer be applied. Here, we present an example of the growth rate in the case where

**Figure 2.10**

Dimensionless growth rate, $\Re(n/\Omega_K)$, as a function of the dimensionless wavenumber for some values of α_B ($\equiv p_{\text{mag}}/p_{\text{gas}}$). We set that the perturbation is proportional to e^{nt} . The parameters are $\kappa/\Omega_K = 1.0$, $\gamma = 5/3$, and $\epsilon = 10$.

the perturbation patterns are not stretched. That is, the unperturbed magnetic fields in the disks are assumed to be toroidal with no other components:

$$\mathbf{B}_0(r, z) = (0, B_0(r, z), 0). \quad (2.71)$$

We further assume that the gas is isothermal throughout the disks and that the magnetic fields \mathbf{B}_0 are distributed in such a way that the Alfvén speed is constant throughout the disk: $(B_0^2/4\pi\rho_0)^{1/2} = \text{constant}$. The equilibrium disk models are then characterized by three dimensionless parameters. Two of them are $\alpha_B \equiv c_A^2/c_s^2$, which is constant in the present model, and γ (the ratio of specific heats). The remaining one is a parameter characterizing the vertical thickness of the disk. Since we are interested in the region around a radius, say r_0 , a convenient dimensionless parameter is $r_0/H(\equiv \epsilon)$.

On such disks, we impose local perturbations, whose wavenumbers on the horizontal plane are (k_r, k_φ) . Concerning the vertical direction we consider the fundamental mode of perturbations under some approximation [see the first edition (Kato et al. 1998)]. As a typical example, the growth rate in the case of $\kappa/\Omega_K = 1.0$ (Keplerian disk), $\gamma = 5/3$, and $\epsilon = 10$ is shown in figure 2.10 as a function of $k_\varphi H$ for some values of α_B with $k_r = 0$. This figure shows that perturbations grow for a moderate size in the azimuthal direction. The growth rate can become as large as $1/\Omega$ when $\alpha_B \sim 1$. Detailed discussions on the Parker instability are given by Tajima and Shibata (1997), and in the first edition of this book (Kato et al. 1998).

2.5 Relativistic Effects

In the vicinity of black holes, sometimes general-relativistic effects are essential; e.g., the existence of marginally stable circular orbits, gravitational redshifts, and the bending of light. These relativistic effects often modify the models both quantitatively and qualitatively. Relativistic treatments, however, are usually complicated and tiresome. In order to make our work easier, in this section we derive several important (general) relativistic quantities in the framework of the Newtonian analogue, introduce a useful tool, called a pseudo-Newtonian potential, and show useful expressions for relativistic dynamics. A full general-relativistic treatment for a Kerr space-time is presented in appendix A.

2.5.1 Newtonian Analogue

Besides the radius of the event horizon, there is a characteristic radius near to a black hole: the radius of a *marginally stable circular orbit*, r_{ms} . This radius is important in the sense that it determines the inner edge of the standard disk, and thus the efficiency of energy release, η , which depends on this radius. To derive r_{ms} and η , general-relativistic considerations are necessary, which are given in appendix A. In the case of the Schwarzschild metric, however, they can be easily derived by using a Newtonian analogue.

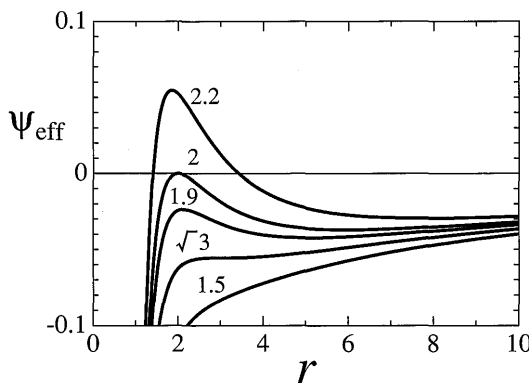


Figure 2.11

Effective potential, ψ_{eff} , as a function of r for several values of ℓ . The units of r , ψ_{eff} , and ℓ are r_g , c^2 , and $r_g c$, respectively, where $r_g (= 2GM/c^2)$ is the Schwarzschild radius. The value of ℓ is attached on each curve.

(a) Effective potential

Let us consider a test particle of unit mass rotating around a non-rotating black hole. In the Newtonian analogue, the motion of a particle is governed by the energy integral; i.e., $K + U = E_{\text{NR}}$, where K and U are the kinetic and potential energies and their sum, E_{NR} , is constant (subscript “NR” denotes the non-relativistic case). Of these, the kinetic energy is given by

$$K = \frac{1}{2}v_r^2 + \frac{\ell^2}{2r^2}, \quad (2.72)$$

where v_r is the radial velocity and ℓ the (constant) specific angular momentum of the particle. The potential energy is

$$U = -\frac{GM}{r} \left(1 + \frac{\ell^2}{c^2 r^2}\right). \quad (2.73)$$

The appearance of the term $\ell^2/c^2 r^2 (= v_\varphi^2/c^2)$ can be interpreted as the effect of a mass increase of a test particle by rotational motion. Since we are treating a non-relativistic analogue, the energy E_{NR} must be related to the total energy of the test particle, E (the relativistic energy including the rest mass energy), by $E_{\text{NR}} = (1/2)(E^2/c^2 - c^2)$. We note that far from the central object the particle becomes free, and for a free particle $(E^2 - c^4)/c^2$ is the square of the momentum.

The energy integral is therefore

$$\frac{1}{2} \left(\frac{dr}{d\tau}\right)^2 + \psi_{\text{eff}} = \frac{E^2 - c^4}{2c^2}, \quad (2.74)$$

where τ is the proper time and ψ_{eff} is the effective potential, defined by

$$\psi_{\text{eff}}(r) \equiv -\frac{GM}{r} \left(1 + \frac{\ell^2}{c^2 r^2}\right) + \frac{\ell^2}{2r^2}. \quad (2.75)$$

The r -dependence of ψ_{eff} is shown in figure 2.11 for several values of ℓ . As can be seen in figure 2.11, the effective potential, ψ_{eff} , has an extremum for large values of ℓ , while it does not have for small ℓ .

(b) Marginally stable circular orbit

The radius of a steady circular orbit of a particle with angular momentum ℓ is the one where the effective potential $\psi_{\text{eff}}(r)$ is an extremum; i.e., $d\psi_{\text{eff}}/dr = 0$ under a fixed ℓ . This condition gives the relation between radius (r) and angular momentum (ℓ) for the Keplerian circular motions:

$$\ell^2(r) = \frac{GMr^2}{r - 3r_g/2} \equiv \ell_K^2(r), \quad (2.76)$$

where the subscript "K" denotes the Keplerian motion. The Keplerian angular momentum ℓ_K has a minimum value, $\sqrt{3}r_g c (\equiv \ell_{\text{ms}})$, at $r = 3r_g$, and increases both inwards and outwards. This result implies that for a particle with $\ell > \ell_{\text{ms}}$, we always have two different radii where circular motions are possible. (See that the curves in figure 2.11 have $d\psi_{\text{eff}}/dr = 0$ at two different radii when $\ell > \ell_{\text{ms}}$.) One is inside $3r_g$ and the other is outside $3r_g$. The inner circular orbit is unstable, since ψ_{eff} is the maximum there, while the outer circular one is stable, since it is the minimum there (see figure 2.11). For a particle with $\ell < \ell_{\text{ms}}$, however, there is no steady circular orbit, since there is no extremum in $\psi_{\text{eff}}(r)$ for such a particle (see figure 2.11). This is different from the case of Newtonian mechanics. In the latter case we have always a stable circular orbit for a particle with any value of angular momentum ℓ . This difference between relativistic and non-relativistic mechanics is very important, since it is related to the presence of an inner edge of black-hole accretion disks. The physical reason of this difference is accounted for in the following paragraph in a way slightly different from the above.

In Newtonian mechanics, ψ_{eff} always has a minimum, since the centrifugal potential $\ell^2/2r^2$ increases inward as $1/r^2$ and overcomes, in the region of small r , the gravitational potential, which is proportional to $1/r$. In the present case of equation (2.75), however, the gravitational potential varies as $1/r^3$ for small r . This means that if ℓ is small enough that the radius of the circular orbit becomes smaller than a certain value, the centrifugal force can no longer compete against the gravitational force. Namely, there is no circular orbit. This critical radius, say r_{ms} , is called the *marginally stable radius*. This radius can be roughly estimated by equating $(GM/r)(\ell^2/c^2 r^2)$ and $\ell^2/2r^2$ in equation (2.75); they become equal at $r = r_g$. This implies that the radius of a marginally stable circular orbit, r_{ms} , occurs near to the Schwarzschild radius. The condition of $d\psi_{\text{eff}}/dr = d^2\psi_{\text{eff}}/dr^2 = 0$ gives a rigorous value of r_{ms} ; that is,

$$r_{\text{ms}} = 3r_g \quad (2.77)$$

(see also figure 2.11). The corresponding angular momentum at r_{ms} is $\ell_{\text{ms}} = \sqrt{3}r_g c$.

In the case of the Kerr metric, r_{ms} for a particle in a prograde orbit becomes smaller than $3r_g$ (see the next subsection and appendix A). This can be interpreted as an effect of the outward-directed Coriolis force due to frame dragging.

(c) Binding energy

The value of $\psi_{\text{eff}}(r)$ at $r = 3r_g$ is $\psi_{\text{eff}} = -c^2/18$. Hence, the total energy E of a particle in a circular orbit at $r = 3r_g$ is $E = (8/9)^{1/2}c^2$ [see equation (2.74)]. This means that the binding energy E_b at r_{ms} is given by

$$E_b = c^2 - \left(\frac{8}{9}\right)^{1/2} c^2 = 0.0572c^2, \quad (2.78)$$

implying that the efficiency η is 0.0572. This gives the correct value for the Schwarzschild metric in spite of the fact that we use the Newtonian analogue here.

In the case of the Kerr metric, a full general-relativistic treatment is necessary, which is presented in appendix A.

(d) Epicyclic frequency

Consider a particle that is rotating around an axisymmetric central object in a circular orbit. If the particle motion is perturbed infinitesimally in the orbital plane from its stable circular orbit with its angular momentum being unchanged, the particle oscillates around the initial circular orbit. Its radial motion is periodic around the radius of the circular orbit. This periodic motion in the radial direction is called *epicyclic oscillation*, and its frequency is the (radial) *epicyclic frequency* κ .

This frequency is very important for understanding disk oscillations (section 11). Its radial distribution in relativistic disks is quite different from that in Newtonian disks. This difference introduces some properties of oscillations in black-hole accretion disks that are quite different from that in Newtonian disks.

The equation describing this radial oscillation is obtained from equation (2.74) by taking its time-derivative under a fixed ℓ :

$$\frac{d^2r}{d\tau^2} = -\frac{d\psi_{\text{eff}}}{dr}. \quad (2.79)$$

This equation shows that a circular orbit exists when $d\psi_{\text{eff}}/dr = 0$, as mentioned before. Equation (2.79) further shows that if a particle is perturbed from a circular orbit (at radius r_0), the deviation of the radial coordinate from the equilibrium radius, say Δr ($\equiv r - r_0$), is governed by

$$\frac{d^2\Delta r}{d\tau^2} = -\left(\frac{d^2\psi_{\text{eff}}}{dr^2}\right)_0 \Delta r, \quad (2.80)$$

where the derivative with respect to r is taken under a fixed ℓ , and the subscript 0 denotes the value at the radius of the circular orbit.

This equation shows that Δr oscillates harmonically with frequency $(d^2\psi_{\text{eff}}/dr^2)_0^{1/2}$, which is just the epicyclic frequency. With the help of equation (2.75), we have

$$\left(\frac{d^2\psi_{\text{eff}}}{dr^2} \right)_0 = \left(1 - \frac{3r_g}{r} \right) \frac{GM/r^2}{r - 3r_g/2}. \quad (2.81)$$

This quantity $(d^2\psi_{\text{eff}}/dr^2)_0$ is the square of the epicyclic frequency observed in proper time. Since the redshift factor for the circular motion is

$$\left(1 - \frac{3r_g}{2r} \right)^{-1/2}, \quad (2.82)$$

we divide $(d^2\psi_{\text{eff}}/dr^2)_0$ by the square of this redshift factor to obtain the epicyclic frequency¹⁶ observed at infinity:

$$\kappa_{\text{GR}}^2 = \frac{GM}{r^3} \left(1 - \frac{3r_g}{r} \right). \quad (2.83)$$

In the limit of the Newtonian regime, we have $\kappa_N = \Omega_K$, as is well known.¹⁷

An important consequence of equation (2.83) is that κ has the maximum at $r = 4r_g$ and vanishes at $r = 3r_g$. The latter corresponds to the well-known fact that a circular orbit at $r = 3r_g$ is marginally stable. The radial distribution of κ in the Schwarzschild metric is shown in figure 2.14.

In the case of the Kerr metric, a full general-relativistic treatment is necessary, which will be given in appendix A (see also figure 2.15).

2.5.2 Pseudo-Newtonian Potential

In order to mimic general-relativistic effects, various modifications to the Newtonian potential (force) have been proposed, since Paczyński and Wiita (1980). These are often referred as *pseudo-Newtonian potentials*.

(a) Pseudo-Newtonian potential for a Schwarzschild black hole

For the case of a non-rotating black hole of mass M , instead of the Newtonian potential ψ_N ($= -GM/R$), Paczyński and Wiita (1980) pro-

¹⁶Here, the subscript “GR” means the general-relativistic case for the non-rotating black hole (see the next section and appendix A for a case of a rotating black hole).

¹⁷Here, the subscript “N” indicates Newtonian.

posed a pseudo-Newtonian potential¹⁸ of the form

$$\psi_{\text{PN}} = -\frac{GM}{R - r_g}, \quad (2.84)$$

where r_g ($= 2GM/c^2$) is the Schwarzschild radius and R ($= \sqrt{r^2 + z^2}$) is the distance from the origin. Although several alternatives have been proposed, the best is this Paczyński-Wiita potential, which gives a very reasonable approximation with an accuracy of 10%–20% in the region of $r \geq r_{\text{ms}}$.

Figure 2.12 shows this pseudo-Newtonian potential in the equatorial plane as well as the usual Newtonian potential.

(b) Pseudo-Newtonian force for a Kerr black hole

For the case of a rotating black hole of mass M and spin parameter a_* ($0 \leq a_* < 1$), Artemova et al. (1996) proposed a pseudo-Newtonian force (per unit mass)¹⁹ of the form

$$F_{\text{PK}} = -\frac{GM}{r^{2-\beta}(r - r_H)^\beta}, \quad (2.85)$$

where where a_* ($0 \leq a_* < 1$) is a dimensionless parameter specifying the amount of angular momentum of the central black hole; $a_* = 0$ is the case of the Schwarzschild metric, and $a_* = 1$ is the case where the central object has the maximum rotation (the case of the extreme Kerr).²⁰ In addition, the radius r_H of the event horizon, the radius r_{ms} of the marginally stable orbit, and the index β [2 (Schwarzschild) $\geq \beta > 0$ (extreme Kerr)] are given, respectively, as follows:

$$r_H = \frac{r_g}{2} \left(1 + \sqrt{1 - a_*^2} \right), \quad (2.86)$$

$$r_{\text{ms}} = \frac{r_g}{2} \left[3 + Z_2 - \sqrt{(3 - Z_1)(3 + Z_1 + 2Z_2)} \right], \quad (2.87)$$

$$\beta = \frac{r_{\text{ms}}}{r_H} - 1, \quad (2.88)$$

where

$$Z_1 \equiv 1 + (1 - a_*^2)^{1/3} \left[(1 + a_*)^{1/3} + (1 - a_*)^{1/3} \right], \quad (2.89)$$

$$Z_2 \equiv \sqrt{3a_*^2 + Z_1^2}. \quad (2.90)$$

¹⁸Here, the subscript “PN” refers pseudo-Newtonian for a static black hole.

¹⁹Here, the subscript “PK” refers pseudo-Newtonian for a rotating black hole.

²⁰This force is only applicable near the equatorial plane since the Kerr hole is asymmetric in the polar direction.

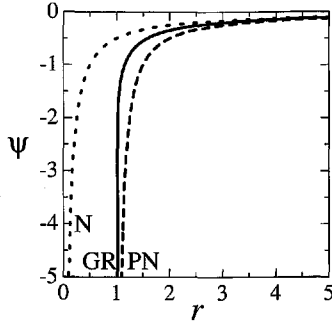


Figure 2.12

Pseudo-Newtonian potential ψ (in units of c^2) as a function of radius r (in units of r_g). The Paczyński-Wiita potential is plotted by a dashed curve, while the usual Newtonian potential is shown by a dotted curve. The general relativistic case ($a_* = 0$) is shown by a solid curve.

This pseudo-Newtonian force is constructed so that r_{ms} coincides with the correct expression obtained under the full Kerr metric, and also gives a good approximation with the accuracy of 10%–20% in the region of $r \geq r_{\text{ms}}$. In the limit of $a_* = 0$ (i.e., $\beta = 2$) this pseudo-Newtonian force reduces to that derived from the Paczyński-Wiita potential.

2.5.3 Relativistic Dynamics for a Circular Motion

We here summarize several important expressions for relativistic dynamics under a circular motion in the equatorial plane. The subscripts “GR” and “Kerr” refer the Schwarzschild and Kerr cases, respectively, while the subscripts “PN” and “PK” refer the pseudo-Newtonian cases for non-rotating and rotating black holes, respectively, which are often used as an approximation.

(a) Angular velocity

The angular velocity Ω_K of the circular motion is $\Omega_N = \sqrt{GM/r^3}$ in the Newtonian case. The angular velocity measured at infinity is

$$\Omega_{\text{GR}} = \sqrt{\frac{GM}{r^3}}. \quad (2.91)$$

in the Schwarzschild metric,²¹ whereas it is expressed as

$$\Omega_{\text{PN}} = \sqrt{\frac{GM}{(r - r_g)^2 r}} \quad (2.92)$$

in the Paczyński-Wiita potential.

For the case of a rotating black hole, we have

$$\Omega_{\text{Kerr}} = \sqrt{\frac{GM}{r^3}} \left[1 + \frac{a_*}{(8\hat{r}^3)^{1/2}} \right]^{-1}, \quad (2.93)$$

where $\hat{r} = r/r_g$ (see appendix A for details), whereas

$$\Omega_{\text{PK}} = \sqrt{\frac{GM}{r^{3-\beta}(r - r_H)^\beta}} \quad (2.94)$$

in the Artemova et al. (1996) force.

(b) Rotational velocity

Similarly, the rotational velocity V ($= r\Omega$), which is $V_N = \sqrt{GM/r}$ in the Newtonian case, is expressed for a non-rotating black hole as

$$V_{\text{GR}} = \sqrt{\frac{GM}{r}}, \quad (2.95)$$

$$V_{\text{PN}} = \sqrt{\frac{GMr}{(r - r_g)^2}}. \quad (2.96)$$

For a rotating black hole,

$$V_{\text{Kerr}} = \sqrt{\frac{GM}{r}} \left[1 + \frac{a_*}{(8\hat{r}^3)^{1/2}} \right]^{-1}, \quad (2.97)$$

$$V_{\text{PK}} = \sqrt{\frac{GM}{r^{1-\beta}(r - r_H)^\beta}} \quad (2.98)$$

in the Artemova et al. (1996) force.

²¹The angular velocity measured at disk is

$$\Omega_{\text{GR}} = \sqrt{\frac{GM}{(r - 3r_g/2)r^2}}.$$

(c) Specific angular momentum

The specific angular momentum ℓ , which is $\ell_N = \sqrt{GMr}$ in the Newtonian case, is expressed for a non-rotating black hole as

$$\ell_{\text{GR}} = \sqrt{\frac{GMr^2}{r - 3r_g/2}}, \quad (2.99)$$

$$\ell_{\text{PN}} = \sqrt{\frac{GMr^3}{(r - r_g)^2}}. \quad (2.100)$$

For a rotating black hole,

$$\ell_{\text{Kerr}} = \sqrt{GMr} \frac{1 - 2a_*/(8\hat{r}^3)^{1/2} + a_*^2/(4\hat{r}^2)}{\sqrt{1 - 3/(2\hat{r}) + 2a_*/(8\hat{r}^3)^{1/2}}}, \quad (2.101)$$

$$\ell_{\text{PK}} = \sqrt{\frac{GMr^{1+\beta}}{(r - r_H)^\beta}}. \quad (2.102)$$

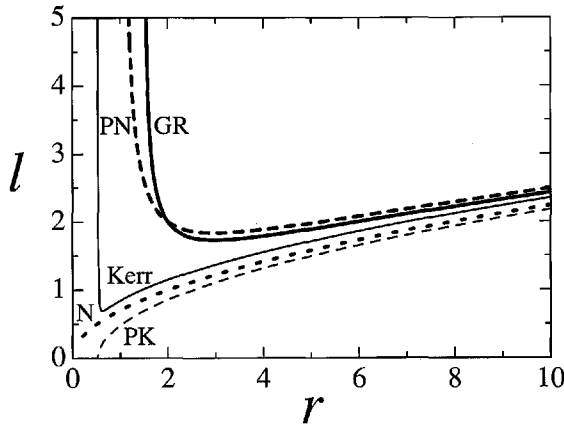


Figure 2.13

Specific angular momenta ℓ for various cases. The abscissa is a radius r in units of r_g , whereas the ordinate is ℓ in units of $r_g c$. The Paczyński-Wiita case for a nonrotating black hole ($a_* = 0$) and the Artemova et al. case for a rotating black hole ($a_* = 0.998$) are shown by thick and thin dashed curves, respectively, the usual Newtonian case by a thick dotted one, and the Schwarzschild ($a_* = 0$) and Kerr ($a_* = 0.998$) cases are shown by thick and thin solid curves, respectively.

These specific angular momenta are shown in figure 2.13.

As can be seen in figure 2.13, the specific angular momentum has a minimum at some radius. This radius corresponds to a marginally stable circular orbit, as mentioned before.

(d) Epicyclic frequency

The epicyclic frequency κ , which is $\kappa_N = \Omega_N$ in the Newtonian case, becomes

$$\kappa_{\text{GR}} = \sqrt{\frac{GM}{r^3} \left(1 - \frac{3r_g}{r}\right)}, \quad (2.103)$$

$$\kappa_{\text{PN}} = \sqrt{\frac{GM(r - 3r_g)}{r(r - r_g)^3}}, \quad (2.104)$$

for a non-rotating black hole. Note that κ_{PN} becomes zero at $r = 3r_g$, as is required. Also, it has a maximum of $[(\sqrt{3} - 1)/(2 + \sqrt{3})/(1 + \sqrt{3})^3]^{1/2} (GM/r_g^3)^{1/2}$ [$\sim 0.098(GM/r_g^3)^{1/2}$] at $r = (2 + \sqrt{3})r_g$. This result qualitatively agrees with, but is somewhat different from, that derived rigorously with general relativity. For example, κ_{GR} has a maximum of $(1/16)(GM/r_g^3)^{1/2}$ [$\sim 0.0625(GM/r_g^3)^{1/2}$] at $r = 4r_g$.

For a rotating black hole,

$$\kappa_{\text{Kerr}}^2 = \frac{GM}{r^3} \frac{1 - 3r_g/r + 8a_*(r_g/2r)^{3/2} - 3a_*^2(r_g/2r)^2}{[1 + a_*(r_g/2r)^{3/2}]^2}, \quad (2.105)$$

which is the rigorous form for κ_{Kerr} derived by Okazaki et al. (1987) (see also Fukue 1980; Aliev and Galtsov²² 1981).

These epicyclic frequencies are also shown in figure 2.14.

As shown above, the pseudo-Newtonian potentials/forces, particularly the Paczyński-Wiita potential, well reproduce the dynamical properties around a nonrotating black hole. In this book we use them in many chapters. We point out, however, that the pseudo-Newtonian potentials *cannot* reproduce light propagation in curved space-time, nor frame-dragging around rotating black holes.

(e) Vertical epicyclic frequency

Finally, the radial distribution of the vertical epicyclic frequency, Ω_\perp , is noted. If a particle on the equator is displaced in the vertical direction, it receives a restoring force toward the equator. The restoring force is proportional to the displacement. Hence, the particle makes harmonic oscillations up and down around the equatorial plane with a certain frequency, which is called the *vertical epicyclic frequency*. In the case of the Schwarzschild metric, the frequency is equal to the Keplerian one, $\Omega_\perp = \Omega_K$. When the metric is a Kerr, however, the vertical epicyclic

²²They derived a more general expression, considering the case of a charged particle in the metric of a charged Kerr black hole.

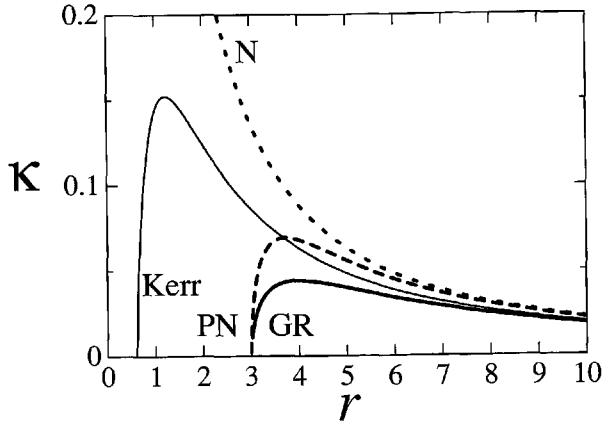


Figure 2.14

Epicyclic frequency κ for various cases. The abscissa is radius r in units of r_g , whereas the ordinate is κ in units of c/r_g . The Paczyński-Wiita case for a nonrotating black hole ($a_* = 0$) is shown by a thick dashed curve and the usual Newtonian case by a thick dotted one; the Schwarzschild ($a_* = 0$) and Kerr ($a_* = 0.998$) cases are shown by thick and thin solid curves, respectively.

frequency differs from the Keplerian one, and is given as (Aliev and Galtsov²³ 1981; Kato 1990)

$$\Omega_\perp^2(r) = \Omega_K^2 \left[1 \mp 4 \left(\frac{r_g}{2r} \right)^{3/2} a_* + 3 \left(\frac{r_g}{2r} \right)^2 a_*^2 \right], \quad (2.106)$$

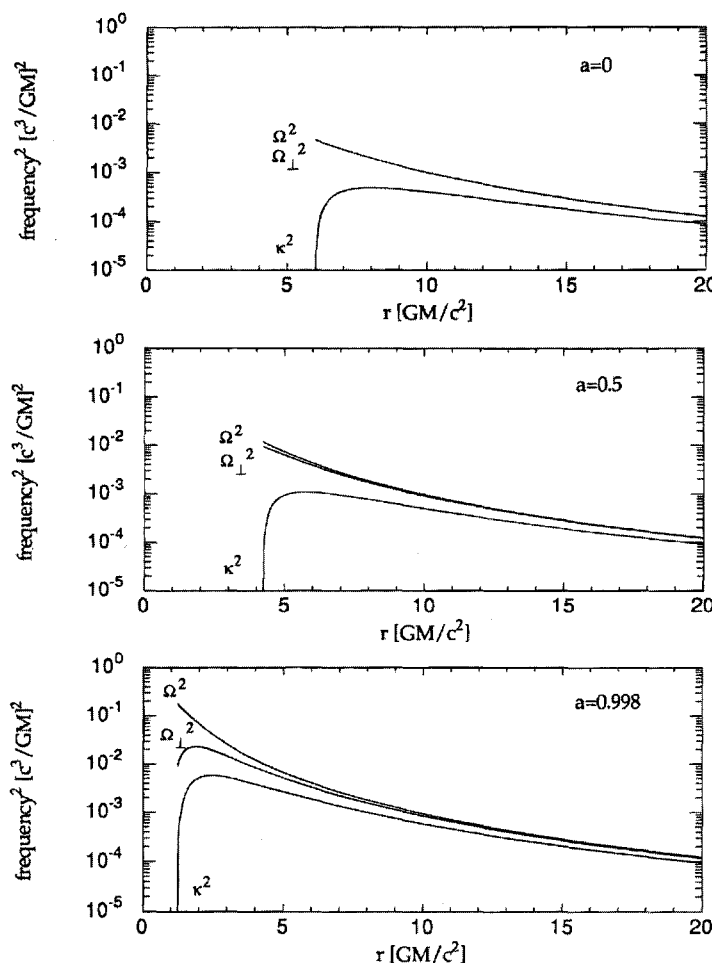
where a minus/plus sign corresponds to a direct/retrograde orbit.

The radial dependences of three basic frequencies (the Kepler frequency Ω , the (radial) epicyclic frequency κ , and the vertical epicyclic frequency Ω_\perp) are shown in figure 2.15 for some values of the spin parameter, a_* .

References

- Afshordi N., Mukhopadhyay B., Narayan R. 2005, ApJ, 629, 373
 Aliev A.N., Galtsov D.V. 1981, General Relativity and Gravitation 13, 899
 Artemova I.V., Björnsson G., Novikov I.D. 1996, ApJ 565, 571
 Balbus S.A. 2003, ARA&A, 41, 555

²³They derived a more general expression, considering the case of a charged particle in the metric of a charged Kerr black hole.

**Figure 2.15**

Dependences of the fundamental free-particle frequencies on the radius for $a_* = 0, 0.5, 0.998$ of the black-hole angular-momentum parameter. (After Perez et al. 1997)

Balbus S.A., Hawley J.F. 1991, ApJ 376, 214

Balbus S.A., Hawley J.F. 1992a, ApJ 392, 662

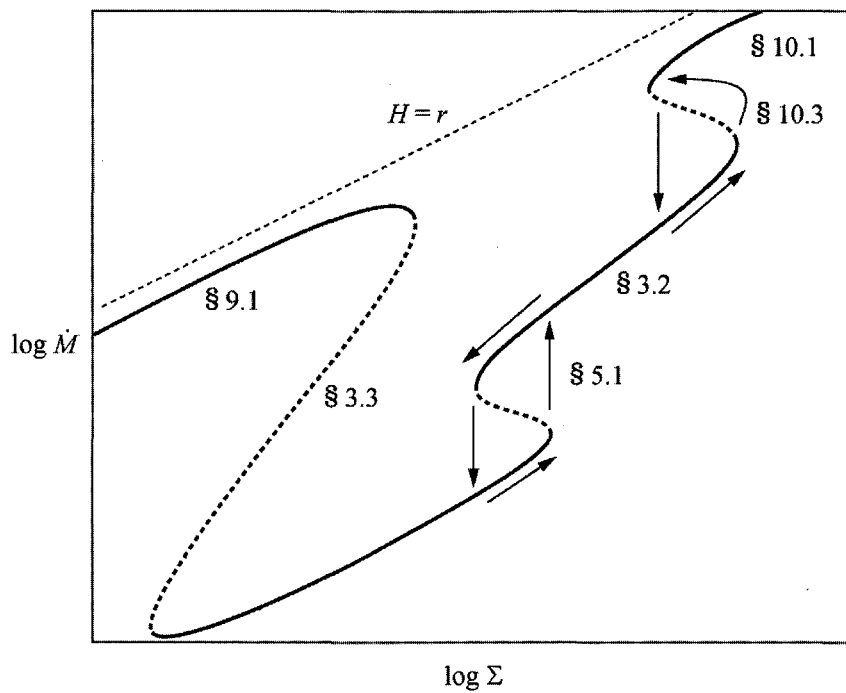
Balbus S.A., Hawley J.F. 1992b, ApJ 400, 610

Bondi H. 1952, MNRAS 112, 195

- Brandenburg A., Nordlund A., Stein R.F., Torkelsson U. 1995, ApJ 446, 741
- Chandrasekhar S. 1960, Proc.Nat.Acad.Sci. 46, 253
- Ferraro V.C.A. 1937, MNRAS 97, 458
- Fricke K. 1969, A&A 1, 388
- Fukue J. 1980, Master Thesis of Kyoto University (in Japanese)
- Gammie C. 1966, ApJ, 457, 355
- Goldreich P., Lynden-Bell D. 1965, MNRAS 130, 125
- Hawley J.F., Balbus S.A. 1991, ApJ 376, 223
- Hawley J.F., Gammie C.F., Balbus S.A. 1995, 440, 742
- Holzer T.E., Axford W.I. 1970, ARA&Ap 8, 31
- Klahr H., Bodenheimer P. 2003, ApJ, 582, 869
- Klahr H. 2004, ApJ 606, 1070
- Lynden-Bell D., Pringle J.E. 1974, MNRAS 168, 603
- Madau P. 1988, ApJ 327, 116
- Matsumoto R., Horiuchi T., Hanawa T., Shibata K. 1988, PASJ 40, 171
- Matsumoto R., Tajima T. 1995, ApJ 445, 767
- Mukhopadhyay B., Afshordi, N., Narayan, R., 2005, ApJ 629, 383
- Ogilvie G.I., Pringle J.E. 1996, MNRAS 279,15
- Okazaki A.T., Kato S., Fukue J. 1987, PASJ 39, 473
- Paczynski B., Wiita P.J. 1980, A&A 88, 23
- Papaloizou J.C.B., Trequem C. 1997, MNRAS 287, 771
- Parker E.N. 1958, ApJ 132, 175
- Parker E.N. 1955, ApJ 121, 491
- Parker E.N. 1966, ApJ 145, 811
- Perez C.A., Silbertgleit A.S., Wagoner R.V., Lehr D.E. 1997, ApJ 476, 589
- Sikora M. 1981, MNRAS, 196, 257
- Shibata K., Tajima T., Matsumoto R. 1990, ApJ 350, 295
- Spiegel E.A., Veronis G. 1960, ApJ 131, 442
- Tajima T., Shibata K. 1997, *Plasma Astrophysics* (Addison Wesley, Reading)
- Trequem C., Papaloizou J.C.B. 1996, MNRAS 279, 767
- Velikhov E. 1959, Sov.Phys.JETP 36, 1398

Part II Classical Picture

Thermal Equilibrium Curves



Thermal equilibrium curves.

CHAPTER 3

Classical Models

More than three decades have passed since the standard α disk model was established in the early 1970's owing to theoretical efforts by Lynden-Bell, Pringle, Rees, Shakura, Sunyaev, Novikov, Thorne, and others. Theoretical research of accretion disks has developed mainly based on this α -model. In this chapter we describe the basic properties and limitations of the classical picture.

3.1 Viscous Accretion Disks

As shown in section 2.3, a disk evolves towards the minimum energy state under the effects of viscosity. In this section, we construct time-dependent basic equations for a simple case, and demonstrate how a viscous disk actually evolves.

3.1.1 Basic Equations for Viscous Diffusion

We make the following assumptions in this section:

1. Gas in the disk is rotating around a central star in a nearly circular orbit with the local Keplerian velocity,

$$v_\varphi(r) = r\Omega_K(r) \equiv \sqrt{r \frac{d\psi(r)}{dr}}, \quad (3.1)$$

where $\psi(r)$ is the gravitational potential ($\psi = -GM/r$ in the case of a Newtonian, point-mass potential). In other words, the centrifugal force is balanced by the central gravitational force, with the pressure being negligible. We regard that the disk is axisymmetric.

2. On a longer timescale (than Ω_K^{-1}), the disk mass gradually drifts inward with a radial velocity, v_r (negative for inflow), of

$$|v_r| \ll v_\varphi \quad (3.2)$$

by transferring its angular momentum outwards by viscosity. Under such circumstances (rapid rotation with slow inflow in an axisymmetric disk), the $r\varphi$ -component of the shear-stress tensor plays a predominant role on mass accretion.

3. The disk is geometrically thin in the sense that

$$H \ll r, \quad (3.3)$$

where H is the half thickness of the disk. Typically, $H/r \sim 0.01$ or less for disk temperatures of $T \sim 10^4$ K (as shown later). The disk is thus not like a pancake, but like a compact disc.

To sum up the relation between the timescales, the viscous timescale (or drift timescale) t_{vis} , over which the radial disk structure changes, is much longer than the dynamical timescale, t_{dyn} :

$$t_{\text{vis}} \equiv \left| \frac{r}{v_r} \right| \gg t_{\text{dyn}} \equiv \frac{r}{v_\varphi} = \frac{1}{\Omega_K}. \quad (3.4)$$

It is also assumed that the viscous timescale is much longer than the hydrostatic timescale, t_{hyd} , over which the vertical disk structure varies, and the thermal timescale, t_{th} , over which the disk temperature changes as

$$t_{\text{vis}} \gg t_{\text{hyd}} \equiv \frac{H}{c_s} \quad \text{and} \quad t_{\text{vis}} \gg t_{\text{th}}, \quad (3.5)$$

where c_s is the speed of sound. (We will check these relations later after constructing a model.) It is then reasonable to use a one-zone approximation for the vertical structure of the disk.

We can then safely decouple the two-dimensional equations (in the r and z directions) into a set of two, separate, one-dimensional equations: those describing the radial (r) structure and those for the vertical (z) structure. We first consider the global (radial) disk evolution in this subsection and discuss the vertical disk structure later. Since we are concerned with the long-term disk evolution on a viscous timescale, and since by assumption (3.5) we can regard the disk to be in hydrostatic

equilibrium in the vertical direction and in energy balance, it is convenient to use vertically integrated variables, such as the surface density,

$$\Sigma = \int_{-\infty}^{\infty} \rho dz, \quad (3.6)$$

and the vertically integrated viscous stress [cf. equation (2.58)],

$$T_{r\varphi} \equiv \int_{-\infty}^{\infty} t_{r\varphi} dz = \nu \Sigma r \frac{d\Omega}{dr}, \quad (3.7)$$

where Ω is the angular speed of disk rotation and ν is the kinematic viscosity.

With the above assumptions and simplifications in mind, let us formulate the basic equations for viscous disk evolution. To begin with, we consider the time evolution of a part of the disk (or an annulus) at $r' \equiv r - \Delta r$ to r with $\Delta r \ll r$ (cf. figure 2.5).

Mass conservation of this annulus leads to

$$\begin{aligned} \frac{\partial}{\partial t} (2\pi r \Delta r \Sigma) &= (-v_r \cdot 2\pi r \Sigma)_r - (-v_r \cdot 2\pi r \Sigma)_{r'} \\ &\simeq -2\pi \Delta r \frac{\partial}{\partial r} (r \Sigma v_r), \end{aligned} \quad (3.8)$$

(note $v_r < 0$ for accretion). In the limit of $\Delta r \rightarrow 0$, we obtain the continuity equation,

$$r \frac{\partial \Sigma}{\partial t} + \frac{\partial}{\partial r} (r \Sigma v_r) = 0. \quad (3.9)$$

If we denote the mass-flow rate by

$$\dot{M} \equiv -2\pi r v_r \Sigma, \quad (3.10)$$

(which is positive for inflow), we obtain

$$\frac{\partial \Sigma}{\partial t} = \frac{1}{2\pi r} \frac{\partial \dot{M}}{\partial r}. \quad (3.11)$$

The angular-momentum transfer at this annulus is described by

$$\begin{aligned} \frac{\partial}{\partial t} (2\pi r \Delta r \Sigma r^2 \Omega) &= (-v_r \cdot 2\pi r \Sigma \cdot r^2 \Omega)_r \\ &\quad - (-v_r \cdot 2\pi r \Sigma \cdot r^2 \Omega)_{r'} + \frac{\partial G}{\partial r} \Delta r \\ &\simeq -2\pi \Delta r \frac{\partial}{\partial r} (r \Sigma v_r r^2 \Omega) + \frac{\partial G}{\partial r} \Delta r, \end{aligned} \quad (3.12)$$

where the total torque $G(r)$ is, from equations (2.59) and (3.7),

$$G(r, t) = 2\pi r^2 T_{r\varphi} = 2\pi r^3 \nu \Sigma \frac{d\Omega}{dr}. \quad (3.13)$$

In the limit of $\Delta r \rightarrow 0$, we find

$$r \frac{\partial(\Sigma r^2 \Omega)}{\partial t} + \frac{\partial}{\partial r} (r \Sigma v_r r^2 \Omega) = \frac{1}{2\pi} \frac{\partial G}{\partial r}. \quad (3.14)$$

With the help of the continuity equation (3.9), and replacing v_r by \dot{M} , we have

$$\dot{M} \left[\frac{d}{dr} (r^2 \Omega) \right] = -2\pi \frac{\partial}{\partial r} (r^2 T_{r\varphi}) = -2\pi \frac{\partial}{\partial r} \left(r^3 \nu \Sigma \frac{d\Omega}{dr} \right), \quad (3.15)$$

where Ω is a function of r . Substituting equation (3.15) into equation (3.11), we finally obtain the following differential equations for Σ :

$$\frac{\partial \Sigma}{\partial t} = -\frac{1}{r} \frac{\partial}{\partial r} \left[\frac{\frac{\partial}{\partial r} (r^2 T_{r\varphi})}{\frac{d}{dr} (r^2 \Omega)} \right] = -\frac{1}{r} \frac{\partial}{\partial r} \left[\frac{\frac{\partial}{\partial r} \left(r^3 \nu \Sigma \frac{d\Omega}{dr} \right)}{\frac{d}{dr} (r^2 \Omega)} \right]. \quad (3.16)$$

In the case of a point-mass potential, especially, we find

$$\frac{\partial \Sigma}{\partial t} = -\frac{2}{r} \frac{\partial}{\partial r} \left[\left(\frac{r}{GM} \right)^{1/2} \frac{\partial}{\partial r} (r^2 T_{r\varphi}) \right] \quad (3.17)$$

or

$$\frac{\partial \Sigma}{\partial t} = \frac{3}{r} \frac{\partial}{\partial r} \left[r^{1/2} \frac{\partial}{\partial r} (\nu \Sigma r^{1/2}) \right], \quad (3.18)$$

where we used $\Omega = \sqrt{GM/r^3}$. Here, $T_{r\varphi}$ (or $\nu \Sigma$) is generally a function of Σ , T , and r , although temperature T will be uniquely determined by r and Σ when the energy equation is solved (demonstrated later).

3.1.2 Examples of Viscous Diffusion

The basic equation (3.18) describes the mass-accretion process under viscous diffusion. In fact, equation (3.18) consists of two main terms. For constant ν , for simplicity, we derive

$$\frac{\partial(r^{1/2}\Sigma)}{\partial t} = 3\nu \frac{\partial(r^{1/2}\Sigma)}{\partial(r^2)} + 3\nu \frac{\partial^2(r^{1/2}\Sigma)}{\partial(r^2)^2}. \quad (3.19)$$

The first term on the right-hand side represents the mass accretion. In fact, the solution of the equation

$$\frac{\partial(r^{1/2}\Sigma)}{\partial t} = 3\nu \frac{\partial(r^{1/2}\Sigma)}{\partial(r^2)} \quad (3.20)$$

is

$$r^{1/2}\Sigma(r, t) = f(x); \quad x \equiv r^2 + 3\nu t, \quad (3.21)$$

with $f(x)$ being an arbitrary function of x . That is, the initial distribution of the angular momentum ($\Sigma\sqrt{GMr}$) plotted against r^2 simply shifts towards the origin at later times on the viscous timescale $t_{\text{vis}} = r^2/(3\nu)$. The second term on the right-hand side, on the other hand, represents mass diffusion on the same timescale.

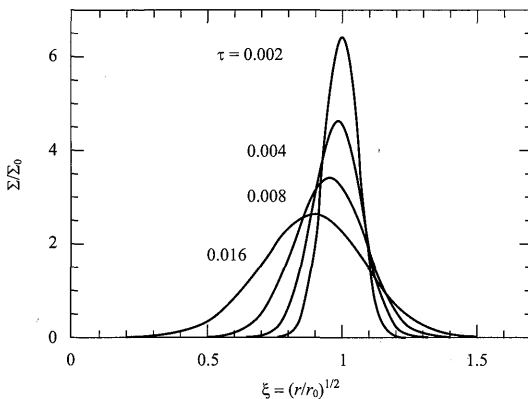


Figure 3.1

Viscous diffusion for the case of $\nu \propto r$. The abscissa is $\xi \equiv (r/r_0)^{1/2}$, while the ordinate is the normalized surface density. The unit of time τ is the viscous timescale at $r = r_0$ ($\xi = 1$).

In some special cases, we can solve the diffusion equation (3.18) analytically. When the kinematic viscosity, ν ($\propto -r^{3/2}T_{r\varphi}/\Sigma$) [see equation (3.7)], is a power-law function of radius r , the solutions can be expressed by using the Green's function [Lynden-Bell and Pringle 1974; see appendix I of the first edition (Kato et al. 1998) for derivation]. For the case with $\nu \propto r$ ($T_{r\varphi} \propto -r^{-1/2}\Sigma$), for example, the analytic solution with the δ -function type initial condition, $\Sigma(r, 0) \propto \delta(r - r_0)$, and the torque-free inner boundary condition, $T_{r\varphi}(0, t) = 0$, is

$$\Sigma(\xi, \tau) = \frac{\Sigma_0}{2\xi^3\sqrt{\pi\tau}} \left\{ \exp \left[-\frac{(\xi - 1)^2}{4\tau} \right] - \exp \left[-\frac{(\xi + 1)^2}{4\tau} \right] \right\}. \quad (3.22)$$

Here, $\xi \equiv \sqrt{r/r_0}$ and $\tau \equiv t/t_0$, where r_0 , t_0 , and Σ_0 are numerical constants (t_0 corresponds to the viscous timescale at r_0). Typical viscous diffusion displayed in figure 3.1 nicely demonstrates how the mass-accretion process proceeds in a viscous disk.

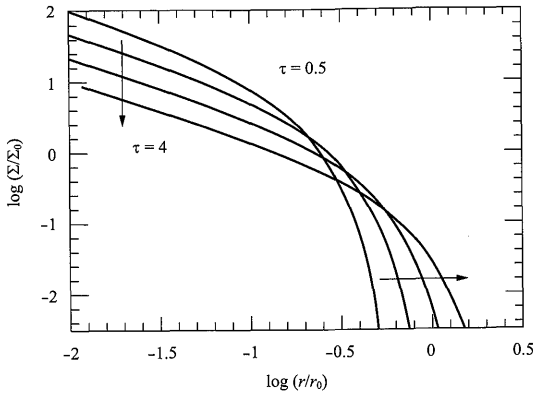


Figure 3.2

Example of self-similar viscous diffusion. We prescribed the shear-stress tensor to be $T_{r\varphi} \propto -\Sigma^{6/5} r^{-1/2}$.

When $T_{r\varphi}$ (and so ν) is a power-law function of Σ and r , there exists a self-similar solution for which the total angular momentum is conserved [cf. Pringle 1974; Filipov et al. 1988; see appendix I of the first edition (Kato et al. 1998)]. For $T_{r\varphi} \propto -\Sigma^{6/5} r^{-1/2}$, for instance, the explicit form of the solution is

$$\Sigma(r, t) = \Sigma_0 \left(\frac{t}{t_0} \right)^{-5/3} \left(\frac{r}{r_d} \right)^{-5/6} \left[1 - \left(\frac{r}{r_d} \right)^{7/6} \right]^5, \quad (3.23)$$

where r_d is the dimension of the disk,

$$r_d = r_0 \left(\frac{t}{t_0} \right)^{2/3}, \quad (3.24)$$

and r_0 , t_0 , and Σ_0 are numerical constants. Again, t_0 corresponds to the viscous timescale at the reference radius, r_0 . For this solution, a disk expands with time, while the surface density at a fixed radius decreases (see figure 3.2). As a result, the disk mass and the disk luminosity are both monotonically decreasing with time.¹

¹In more general cases, for which $T_{r\varphi} \propto -r^\delta \Sigma^\gamma$, the disk radius r_d , the disk mass M_d , and the disk luminosity $L_d (\propto dM_d/dt)$ are expressed as

$$r_d \propto t^{2a}, \quad M_d \propto t^{-a}, \quad L_d \propto t^{-(a+1)},$$

with $a = 1/(5\gamma - 4 - 2\delta)$. In some special cases, such as on the radiation-pressure dominated branch, a could be negative. Then, the disk will shrink, rather than expand.

3.2 Standard Disks

In this section we review the basic properties of geometrically thin, optically thick, standard disks, known as α disks, with emphasis on their structure and emergent spectra. Most of the other disk models that we discuss later are constructed as extensions and/or modifications of this standard-type disk.

3.2.1 Shakura-Sunyaev Model

We describe in this section the radial disk structure, following the standard accretion-disk model of Shakura and Sunyaev (1973). To begin with, we make the following assumptions:

1. The gravitational field is determined by a black hole, and the self-gravity of the disk is ignored.
2. The disk lies in the equatorial plane of the hole.
3. The disk is steady.
4. The disk is axisymmetric.
5. The disk is geometrically thin in the sense that $H/r \ll 1$.
6. Rotational motion is dominant (Keplerian rotation); $|v_r| \ll v_\varphi$.
7. Hydrostatic balance holds in the vertical direction.
8. The disk is optically thick in the vertical direction.
9. A specialized viscous law is adopted; *the $r\varphi$ -component of the viscous stress tensor is proportional to the pressure*. Other components are neglected.
10. Global magnetic fields are ignored.

On the basis of these assumptions and simplifications, we can construct a basic set of equations describing the Shakura-Sunyaev disks.

(a) Mass conservation

The disk is in a steady state in the sense that the mass inflow rate,

$$\dot{M} = -2\pi r v_r \Sigma, \quad (3.25)$$

is constant in space and time [cf. equation (3.10)]. Here, the surface density under a (vertically) one-zone approximation is

$$\Sigma = 2\rho H. \quad (3.26)$$

(b) Momentum conservation

The central black hole is non-rotating and the gravitational potential is given by a Newtonian, point-mass potential. Therefore, the angular velocity and rotation velocity of the axisymmetric disk are, respectively,

$$\Omega = \Omega_K \equiv \sqrt{\frac{GM}{r^3}} \quad \text{and} \quad v_\varphi = v_K \equiv \sqrt{\frac{GM}{r}}, \quad (3.27)$$

from linear (radial) momentum conservation.

(c) Angular-momentum conservation

Since \dot{M} is constant, we can easily integrate equation (3.15),

$$\frac{\dot{M}}{2\pi} r^2 \Omega = -r^2 T_{r\varphi} + \text{const.} = -r^3 \nu \Sigma \frac{d\Omega}{dr} + \text{const.} \quad (3.28)$$

The numerical constants are determined by the inner boundary conditions. If we adopt a torque-free boundary condition, $T_{r\varphi} = 0$, and set $\ell \equiv r^2 \Omega = \ell_{\text{in}} = \text{constant}$ at the inner edge of the disk, r_{in} , we have

$$\frac{\dot{M}}{2\pi} (\ell - \ell_{\text{in}}) = -r^2 T_{r\varphi} = -r^3 \nu \Sigma \frac{d\Omega}{dr}. \quad (3.29)$$

In the case of a point-mass potential, $\psi = -GM/r$, we have $\ell = \sqrt{GMr}$ and $\ell_{\text{in}} = \sqrt{GMr_{\text{in}}}$, and hence

$$T_{r\varphi} = -\frac{1}{2\pi} \sqrt{\frac{GM}{r^3}} \dot{M} \left(1 - \sqrt{\frac{r_{\text{in}}}{r}} \right) \quad \text{or} \quad \nu \Sigma = \frac{\dot{M}}{3\pi} \left(1 - \sqrt{\frac{r_{\text{in}}}{r}} \right). \quad (3.30)$$

(d) Hydrostatic balance

Hydrostatic balance in the vertical direction is expressed as

$$-\frac{\partial p}{\partial z} = -\rho g_z, \quad (3.31)$$

where p is the total pressure and

$$g_z = -\frac{GMz}{(r^2 + z^2)^{3/2}} \sim -\frac{GMz}{r^3}. \quad (3.32)$$

Under the one-zone approximation this condition is written as

$$\frac{p}{H} = -\rho g_z(H), \quad (3.33)$$

where ρ is the mean density of the disk, and $g_z(H)$ is the vertical component of the gravitational acceleration at the surface of the disk ($z = H$) due to the central star,

$$g_z(H) \simeq -\frac{GM}{r^2} \frac{H}{r} = -\Omega_K^2 H, \quad (3.34)$$

if we neglect the self-gravity of the low-mass disk. Sometimes it is useful to rewrite equation (3.33) as

$$\Omega_K^2 H^2 = \frac{p}{\rho} = c_s^2 \quad \text{or} \quad H = \frac{c_s}{\Omega_K}, \quad (3.35)$$

where c_s denotes the speed of sound.²

(e) Energy balance

The potential energy of accreting gas is first converted to thermal energy via viscous processes, and is then released as radiation. Since the viscous heating rate per unit volume is $\rho\nu(r d\Omega/dr)^2$ (see appendix B), the vertically integrated heating rate per unit surface area is

$$Q_{\text{vis}}^+ = \int_{-\infty}^{\infty} \nu \rho \left(r \frac{d\Omega}{dr} \right)^2 dz = \frac{9}{4} \nu \Sigma \Omega^2 = -\frac{3}{2} T_{r\varphi} \Omega, \quad (3.36)$$

where $\Omega = \Omega_K \propto r^{-3/2}$.

Cooling is due to radiation from the disk surface. Since the disk is effectively optically thick in the vertical direction,

$$\tau = \bar{\kappa} \rho H = \frac{\bar{\kappa} \Sigma}{2} \gg 1, \quad (3.37)$$

²Precisely, this is the isothermal sound speed, although we do not distinguish adiabatic sound speed and isothermal one in order-of-magnitude arguments here.

where τ ($= \bar{\kappa}\Sigma/2$) is the optical depth and $\bar{\kappa}$ is the Rosseland-mean opacity (see below). In addition, it is assumed that the disk gas emits a blackbody spectrum with an effective temperature of T_{eff} .

Further, we assume that the main energy transfer inside the disk is due to radiation. The radiative flux in the z -direction is

$$F(z) = -\frac{4ac[T(z)]^3}{3\kappa(z)\rho(z)} \frac{\partial T}{\partial z} \quad (3.38)$$

at each height z , where a is the radiation constant ($\sigma = ac/4$) and T is the temperature inside the disk. Under the one-zone approximation, we can then express the cooling rate in terms of the temperature T_c at $z = 0$ as

$$Q_{\text{rad}}^- = 2F(H) = 2\frac{4acT_c^4}{3\tau} = \frac{32\sigma T_c^4}{3\tau}. \quad (3.39)$$

Finally, the local energy balance at each radius is given by

$$Q_{\text{vis}}^+ = Q_{\text{rad}}^-, \quad (3.40)$$

where heating is due to the viscosity [equation (3.36)] and cooling is via the spatial diffusion of the blackbody radiation [equation (3.39)]. For this to be efficient, the thermal timescale needs to be much shorter than the matter diffusion timescale; $t_{\text{th}} \ll t_{\text{vis}}$.

(f) Equation of state

The disk plasmas are assumed to consist of pure, ionized hydrogen. In other words, the disk temperature is assumed to exceed $\sim 10^4$ K, since otherwise hydrogen (and helium) may become recombined. Thus, the local pressure p given by the sum of gas and radiation pressures is written as

$$p = p_{\text{gas}} + p_{\text{rad}} = \frac{2k_B}{m_H} \rho T_c + \frac{aT_c^4}{3}, \quad (3.41)$$

where m_H is the mass of a hydrogen atom and k_B is the Boltzmann constant. Here and hereafter, the disk temperature $T(z)$ is often approximated by T_c . The vertical integration of equation (3.41) becomes

$$\Pi = \Pi_{\text{gas}} + \Pi_{\text{rad}} = \frac{2k_B}{m_H} \Sigma T_c + \frac{aT_c^4}{3} \cdot 2H, \quad (3.42)$$

where $\Pi = \int pdz$, $\Pi_{\text{gas}} = \int p_{\text{gas}}dz$, and $\Pi_{\text{rad}} = \int p_{\text{rad}}dz$.

(g) Opacity

In high-temperature disks with $T \geq 10^4$ K, the main opacity sources are electron scattering and free-free absorption,³

$$\bar{\kappa} = \kappa_{\text{es}} + \kappa_{\text{ff}} = \kappa_{\text{es}} + \kappa_0 \rho T_{\text{c}}^{-3.5}, \quad (3.43)$$

where $\kappa_{\text{es}} = 0.40 \text{ cm}^2 \text{ g}^{-1}$ and $\kappa_0 = 0.64 \times 10^{23}$ in cgs units for pure hydrogen plasmas. When the former dominates over the latter, we may use the effective optical depth, defined by

$$\tau_* \equiv \sqrt{(\kappa_{\text{es}} + \kappa_{\text{ff}})\kappa_{\text{ff}}} \rho H \sim \sqrt{\kappa_{\text{es}}\kappa_{\text{ff}}} \rho H, \quad (3.44)$$

which is smaller than the optical depth, τ ($= \bar{\kappa}\rho H$).

(h) Viscosity prescription

The viscosity in the accretion disks plays two important roles: transport of angular momentum and heating of the disk plasma. The dominant sources of viscosity are assumed to be chaotic magnetic fields and turbulence in the gas flow (section 2.3). We prescribe the $r\varphi$ -component of the shear stress tensor to be

$$t_{r\varphi} = \rho \nu r \frac{d\Omega}{dr} = -\alpha p \quad \text{or} \quad T_{r\varphi} = \nu \Sigma r \frac{d\Omega}{dr} = -\alpha \Pi, \quad (3.45)$$

where α is the viscosity parameter ($\alpha \leq 1$), and p is the total pressure [see equations (2.58) and (3.7)]. The α prescription is sometimes expressed in terms of ν . Using equation (3.35), we may rewrite equation (3.45) as

$$\nu = A_\nu \alpha \frac{c_s^2}{\Omega} = A_\nu \alpha c_s H; \quad A_\nu \equiv \left(-\frac{d \ln \Omega}{d \ln r} \right)^{-1}. \quad (3.46)$$

For a point-mass potential, in particular, we find $\Omega = \Omega_K \propto r^{-3/2}$ and so $A_\nu = 2/3$, leading to

$$\nu = \frac{2}{3} \alpha c_s H. \quad (3.47)$$

In the dimension argument given in section 2.3, we estimate ν to be

$$\nu_{\text{turb}} \sim v_{\text{turb}} \ell_{\text{turb}} \quad (3.48)$$

for turbulent viscosity. That is, α corresponds to

$$\alpha \sim \frac{v_{\text{turb}}}{c_s} \frac{\ell_{\text{turb}}}{H}. \quad (3.49)$$

³In the case of standard metal abundance, the bound-free opacity dominates the free-free opacity (see appendix D). In this chapter, however, we construct the standard disk model under the condition of low metal abundance.

For subsonic turbulence with turbulent eddies confined within a disk, we expect $\alpha \leq 1$.

We need to remark on an alternative prescription for the viscosity. It is also possible to assume

$$t_{r\varphi} = -\alpha p^{1-\mu} p_{\text{gas}}^\mu \quad \text{or} \quad T_{r\varphi} = -\alpha \Pi^{1-\mu} \Pi_{\text{gas}}^\mu \quad (3.50)$$

with μ being a parameter ($0 \leq \mu \leq 1$). For $\mu = 0$, we recover equation (3.45). These different prescriptions give different results when the disk is supported by radiation pressure.

3.2.2 Disk Energetics

Before presenting the detailed structure, we first pick up the basic energetics of the Shakura-Sunyaev disks (cf. chapter 1).

Since the cooling rate is the amount of emergent energy flux from a unit area of the surface, it is also expressed as

$$Q_{\text{rad}}^- = 2F = 2\sigma T_{\text{eff}}^4, \quad (3.51)$$

where σ is the Stefan-Boltzmann constant, and the factor 2 represents radiation from the two sides of the disk. Using relations (3.30), (3.36), (3.40), and (3.51), we find

$$F = \sigma T_{\text{eff}}^4 = \frac{3GMM}{8\pi r^3} \left(1 - \sqrt{\frac{r_{\text{in}}}{r}} \right). \quad (3.52)$$

The emergent local flux from the surface of the disk is thus independent of the magnitude of the viscosity parameter, α , and is proportional to r^{-3} at $r \gg r_{\text{in}}$.

The result that F does not depend on α may sound strange, but it can be understood as follows. When we increase α (and thus ν), the viscous heating rate [equation (3.36)] should increase for a fixed Σ . At the same time, the efficiency of the angular-momentum transport should also increase, thereby increasing the radial velocity v_r , and thus reducing Σ [cf. equation (3.30)]. These two effects (increasing the heating rate per unit mass and reducing the surface density) totally compensate each other, yielding the same total heating rate Q_{vis}^+ . Since $Q_{\text{vis}}^+ = Q_{\text{rad}}^- = 2F$, the emergent flux is also unchanged by changes in α . This reflects the fact that an accretion disk releases gravitational energy via viscosity and that viscosity itself does not produce energy, but works as a “catalyst”.

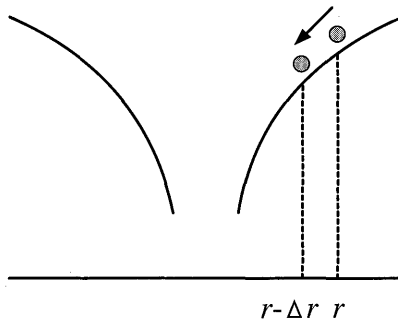


Figure 3.3

Simple picture of mass accretion. The abscissa is the distance from the center, while the ordinate is the depth of the gravitational potential.

Here, we note an interesting nature of viscous disks. The local potential energy release by accreting material falling in the potential well from r to $r - \Delta r$ is (cf. figure 3.3)

$$\Delta L_{\text{pot}} = \left(-\frac{GM}{r} + \frac{GM}{r - \Delta r} \right) \dot{M} \simeq \frac{GMM}{r^2} \Delta r. \quad (3.53)$$

Half of this goes to kinetic energy (rotation energy), while the rest should be radiated away. The local radiation loss should be

$$\Delta L_{\text{local}} \simeq \frac{1}{2} \frac{GMM}{r^2} \Delta r. \quad (3.54)$$

The actual radiation energy loss per unit time from a ring at $r - \Delta r \sim r$ is, from equation (3.52),

$$\Delta L_{\text{rad}} = 2\pi r \Delta r \cdot 2F \simeq \frac{3}{2} \frac{GMM}{r^2} \Delta r, \quad (3.55)$$

at $r \gg r_{\text{in}}$, which is three-times larger than L_{local} [equation (3.54)].

The total energy balance holds, however, since the radially integrated disk luminosity is

$$L_d = \int_{r_{\text{in}}}^{\infty} 2F 2\pi r dr = \int_{r_{\text{in}}}^{\infty} \frac{3GMM}{2r^2} \left(1 - \sqrt{\frac{r_{\text{in}}}{r}} \right) dr = \frac{GMM}{2r_{\text{in}}}, \quad (3.56)$$

which equals to half of the total potential-energy difference (between infinity to the inner disk radius) multiplied by the mass-accretion rate.

That is, the accretion disk shines at an enhanced rate in the outer portions by extracting energy from the inner portions. This is due to the viscous work done by the inner ring to the outer ring [see the term of $v^\varphi t_{r\varphi}$ in the viscous heat flux in equation (B.9)].

It should be stressed here again that, unlike in the stellar case, the effective temperature of the disk has radial dependence in accretion disks (see figure 1.8). From equation (3.52), we have

$$T_{\text{eff}} = \left[\frac{3GM\dot{M}}{8\pi\sigma r^3} \left(1 - \sqrt{\frac{r_{\text{in}}}{r}} \right) \right]^{1/4}. \quad (3.57)$$

At a radius far from the inner edge, especially, we approximate

$$T_{\text{eff}} \propto r^{-3/4}. \quad (3.58)$$

Thus, the surface of the disk is hotter in the inner region than in the outer one. It is then straightforward that the total disk spectra are composed of multi-color blackbody spectra; high-energy photons mainly come from the inner portion of the disk, whereas low-energy photons originate from the outer portions (see figure 1.10). This multi-temperature nature of the accretion disk is usually designated as a *multi-color* from the viewpoint of spectra (see subsection 3.2.5).

3.2.3 Steady Disk Structure

To sum up, we have the following 11 basic equations:

$$\begin{aligned} \dot{M} &= -2\pi r v_r \Sigma, \\ \Omega &= \Omega_K \equiv \sqrt{\frac{GM}{r^3}}, \\ \nu\Sigma &= \frac{1}{3\pi} \dot{M} \left(1 - \sqrt{\frac{r_{\text{in}}}{r}} \right), \\ H &= \frac{c_s}{\Omega_K}, \\ \frac{9}{4}\nu\Sigma\Omega_K^2 &= \frac{8acT_c^4}{3\tau}, \\ \Sigma &= 2\rho H, \\ c_s &= \left(\frac{p}{\rho} \right)^{1/2}, \\ \tau &= \frac{1}{2}\bar{\kappa}\Sigma, \end{aligned}$$

$$\begin{aligned}
p &= \frac{2\rho k_B T_c}{m_H} + \frac{\alpha T_c^4}{3}, \\
\bar{\kappa} &= \kappa_{\text{es}} + \kappa_0 \rho T_c^{-3.5}, \\
\frac{3}{2} \rho \nu \Omega_K &= \alpha p \quad (= -t_{r\varphi}). \tag{3.59}
\end{aligned}$$

We can now obtain expressions for 11 physical quantities (v_r , Σ , Ω , H , ρ , ν , c_s , p , T_c , $\bar{\kappa}$, and τ) as functions of radius r for given parameters (M , \dot{M} , and α).

We are now ready to write explicit solutions for basic equations (Shakura and Sunyaev 1973) (see figure 3.4). We introduce the following dimensionless quantities:

$$m = \frac{M}{M_\odot}, \quad \dot{m} = \frac{\dot{M}}{\dot{M}_{\text{crit}}}, \quad \hat{r} = \frac{r}{r_g}. \tag{3.60}$$

Here, r_g is the Schwarzschild radius,

$$r_g \equiv \frac{2GM}{c^2} = 2.95 \times 10^5 m \text{ cm}, \tag{3.61}$$

and the critical mass-flow rate is defined as

$$\dot{M}_{\text{crit}} \equiv \frac{L_E}{c^2} = 1.40 \times 10^{17} m \text{ g s}^{-1} = 2.22 \times 10^{-9} m M_\odot \text{ yr}^{-1}, \tag{3.62}$$

where L_E ($= 4\pi c GM m_H / \sigma_T$) is the Eddington luminosity and σ_T is the Thomson cross section. Note that different definitions are adopted in various literature: namely, $\dot{M}_{\text{Edd}} \equiv \dot{M}_{\text{crit}}/\eta$ with η being the energy conversion factor; $\eta \sim 0.1$ for disk accretion onto a non-rotating black hole.

The entire disk is generally divided into three distinct regions, depending on the sources of opacity and pressure.

(a) The inner region

Because the density and temperature are high, $p \sim p_{\text{rad}}$ and $\bar{\kappa} \sim \kappa_{\text{es}}$. We then have:

$$\begin{aligned}
H &= 5.5 \times 10^4 m \dot{m} f \text{ cm}, \\
\Sigma &= 1.0 \times 10^2 \alpha^{-1} \dot{m}^{-1} \hat{r}^{3/2} f^{-1} \text{ g cm}^{-2}, \\
\rho &= 9.0 \times 10^{-4} \alpha^{-1} m^{-1} \dot{m}^{-2} \hat{r}^{3/2} f^{-2} \text{ g cm}^{-3}, \\
|v_r| &= 7.6 \times 10^8 \alpha \dot{m}^2 \hat{r}^{-5/2} f \text{ cm s}^{-1}, \\
T_c &= 4.9 \times 10^7 (\alpha m)^{-1/4} \hat{r}^{-3/8} \text{ K}, \\
\tau_* &= 8.4 \times 10^{-3} \alpha^{-17/16} m^{-1/16} \dot{m}^{-2} \hat{r}^{93/32} f^{-2}, \tag{3.63}
\end{aligned}$$

where we have abbreviated

$$f \equiv 1 - \sqrt{\frac{3r_g}{r}}. \quad (3.64)$$

Note that region (a) only exists when

$$\dot{m} \geq 0.097(\alpha m)^{-1/8}. \quad (3.65)$$

(b) The middle region

Since the density and temperature are modest, we may set $p \sim p_{\text{gas}}$ and $\bar{\kappa} \sim \kappa_{\text{es}}$, leading to:

$$\begin{aligned} H &= 2.7 \times 10^3 \alpha^{-1/10} m^{9/10} \dot{m}^{1/5} \hat{r}^{21/20} f^{1/5} \text{ cm}, \\ \Sigma &= 4.3 \times 10^4 \alpha^{-4/5} m^{1/5} \dot{m}^{3/5} \hat{r}^{-3/5} f^{3/5} \text{ g cm}^{-2}, \\ \rho &= 8.0 \alpha^{-7/10} m^{-7/10} \dot{m}^{2/5} \hat{r}^{-33/20} f^{2/5} \text{ g cm}^{-3}, \\ |v_r| &= 1.7 \times 10^6 \alpha^{4/5} m^{-1/5} \dot{m}^{2/5} \hat{r}^{-2/5} f^{-3/5} \text{ cm s}^{-1}, \\ T_c &= 2.2 \times 10^8 \alpha^{-1/5} m^{-1/5} \dot{m}^{2/5} \hat{r}^{-9/10} f^{2/5} \text{ K}, \\ \tau_* &= 2.4 \times 10^1 \alpha^{-4/5} m^{1/5} \dot{m}^{1/10} \hat{r}^{3/20} f^{1/10}. \end{aligned} \quad (3.66)$$

The boundary between regions (a) and (b) resides at

$$\hat{r}_{ab} \approx 18(\alpha m)^{2/21} \dot{m}^{16/21}, \quad (3.67)$$

where we approximated $f(r_{ab}) \approx 1$, since usually $r_{ab} \gg 3r_g$.

(c) The outer region

Here, the density and temperature are low, and thus $p \sim p_{\text{gas}}$ and $\bar{\kappa} \sim \kappa_{\text{ff}}$. We thus have:

$$\begin{aligned} H &= 1.5 \times 10^3 \alpha^{-1/10} m^{9/10} \dot{m}^{3/20} \hat{r}^{9/8} f^{3/20} \text{ cm}, \\ \Sigma &= 1.4 \times 10^5 \alpha^{-4/5} m^{1/5} \dot{m}^{7/10} \hat{r}^{-3/4} f^{7/10} \text{ g cm}^{-2}, \\ \rho &= 4.7 \times 10^1 \alpha^{-7/10} m^{-7/10} \dot{m}^{11/20} \hat{r}^{-15/8} f^{11/20} \text{ g cm}^{-3}, \\ |v_r| &= 5.4 \times 10^5 \alpha^{4/5} m^{-1/5} \dot{m}^{3/10} \hat{r}^{-1/4} f^{-7/10} \text{ cm s}^{-1}, \\ T_c &= 6.9 \times 10^7 \alpha^{-1/5} m^{-1/5} \dot{m}^{3/10} \hat{r}^{-3/4} f^{3/10} \text{ K}, \\ \tau &= 7.9 \times 10^1 \alpha^{-4/5} m^{1/5} \dot{m}^{1/5} f^{1/5}. \end{aligned} \quad (3.68)$$

The boundary between regions (b) and (c) reside at

$$\hat{r}_{bc} \approx 2.5 \times 10^3 \dot{m}^{2/3}, \quad (3.69)$$

where we have again approximated $f(r_{bc}) \approx 1$.

Note the α -dependence of each quantity. Roughly, the temperature is insensitive to α ($T_{\text{eff}} \propto \alpha^0$), whereas the gas density (ρ, Σ) is proportional to α^{-1} and $v_r \propto \alpha$, since \dot{M} ($\propto v_r \Sigma$) is kept constant in a steady disk.

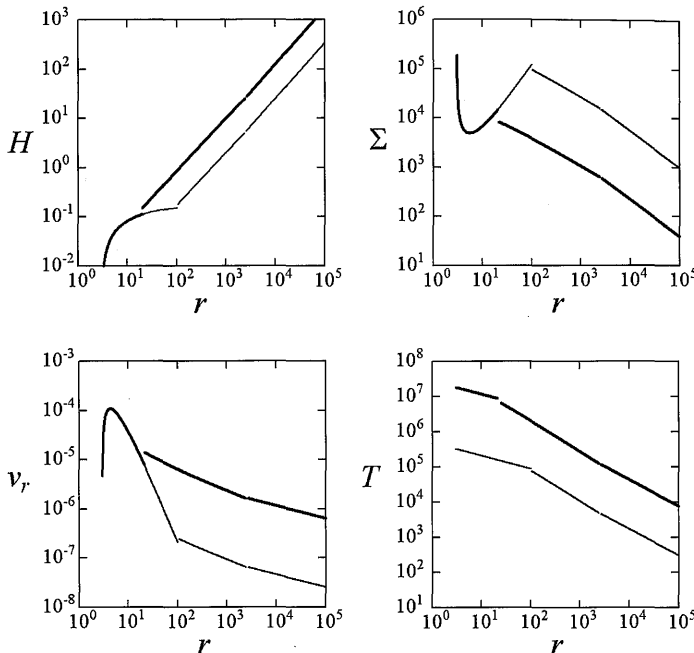


Figure 3.4

Typical solutions of standard accretion disks. The abscissae are the radius in units of the Schwarzschild radius. The ordinates are the disk half-thickness in units of the Schwarzschild radius (top-left panel), the surface density in units of g cm^{-2} (top-right panel), the radial velocity in units of the speed of light (bottom-left panel), and the disk temperature in units of K (bottom-right panel). The parameters are (a) $m = 10$, $\dot{m} = 1$, and $\alpha = 1$ for thick solid curves, and (b) $m = 10^8$, $\dot{m} = 1$, and $\alpha = 1$ for solid curves.

Solutions for typical cases are shown in figure 3.4; the half-thickness H in units of the Schwarzschild radius (top-left panel), the surface density Σ in units of g cm^{-2} (top-right panel), the radial velocity v_r in units of the speed of light (bottom-left panel), and the disk temperature T in units of K (bottom-right panel) as a function of radius r in units of the Schwarzschild radius. The parameters are (a) $m = 10$, $\dot{m} = 1$, and $\alpha = 1$ for thick solid curves, and (b) $m = 10^8$, $\dot{m} = 1$, and $\alpha = 1$ for thin solid

curves. As can be seen in these figures, in the case of stellar-mass black holes ($m = 10$), the inner region exists for the critical accretion rate of $\dot{m} = 1$. On the other hand, in the case of supermassive black holes ($m = 10^8$), the inner region rather extends toward the outer region.

Finally, we check if the assumptions made at the beginning of the model construction are self-consistent. From hydrostatic balance (3.35), we have

$$\frac{H}{r} \sim \frac{c_s}{r\Omega_K} \sim \left(\frac{T_c}{T_{\text{vir}}} \right)^{1/2} \simeq 10^{-3} \left(\frac{T_c}{10^7 \text{K}} \right)^{1/2} \left(\frac{r}{r_g} \right)^{1/2}, \quad (3.70)$$

where $T_{\text{vir}} \equiv 2GMm_p/(3k_B r) \simeq 4 \times 10^{12}(r/r_g)^{-1}$ K. Condition (3.3) is thus quite generally fulfilled (except for very hot disks, see section 3.3). Furthermore, we find the following relations for various timescales:

$$\begin{aligned} t_{\text{hyd}} &= \frac{H}{c_s} \sim \frac{1}{\Omega_K} = t_{\text{dyn}}, \\ t_{\text{th}} &= \left| \frac{\Sigma C_p T_c}{T_{r\varphi} \Omega_K} \right| \sim \frac{1}{\alpha \Omega_K}, \\ t_{\text{vis}} &= \frac{\pi 4 r^2 \Sigma}{\dot{M}} \sim \frac{1}{\alpha \Omega_K} \left(\frac{r}{H} \right)^2, \end{aligned} \quad (3.71)$$

where C_p is the specific heat at constant pressure and is on the order of the gas constant ($\sim p/\rho T$). It is obvious that conditions (3.5) hold when $r \gg H$ (i.e., when cooling is efficient). Likewise, we have

$$|v_r| \sim \alpha c_s \frac{H}{r} \ll c_s, \quad v_\varphi \sim c_s \frac{r}{H} \gg c_s, \quad v_z \sim 0. \quad (3.72)$$

These inequalities do not always hold in hot accretion flow (chapter 9).

3.2.4 Thermal-Equilibrium Curves

To classify disk models and to discuss the stability, thermal-equilibrium diagrams are very useful. These are the sequence of thermal-equilibrium solutions (for which the viscous heating rate is equal to the radiative cooling rate) in the $\dot{M}-\Sigma$ plane.

The relation between the surface density Σ and the mass-accretion rate \dot{M} is depicted in figure 3.5. Here, we employ two different viscosity prescriptions: the standard α viscosity (3.45) and the modified viscosity (3.50) with $\mu = 1$.

We first discuss the case with the standard α prescription. There are two solutions for an ionized hydrogen plasma at a fixed value of Σ :

The upper solution lies in the radiation-pressure dominated regime (p_{rad} -branch) and the lower one is in the gas-pressure dominated regime (p_{gas} -branch). The transition from the p_{gas} -dominated regime to the p_{rad} -dominated regime occurs at a mass-accretion rate of about the critical one (at a disk luminosity about 10% of the Eddington luminosity). As we demonstrate in the next chapter, the stability properties are distinct above and below this transition.

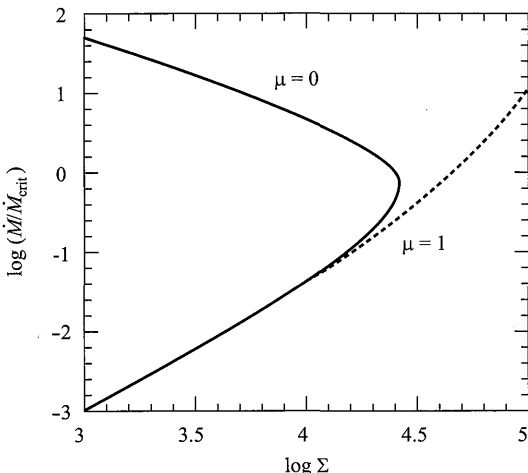


Figure 3.5

Thermal-equilibrium curves in the \dot{M} - Σ plane of the α disk for $\mu = 0$ (by the solid curve), and for $\mu = 1$ (by the dotted curve), respectively. The parameters are $M = 10M_\odot$, $r/r_g = 5.0$, and $\alpha = 0.1$.

To understand the reason for the double-valued solutions for fixed Σ and r , we plot in figure 3.6 the heating rate and the cooling rate as functions of temperature for a fixed value of Σ . The functional dependences of Q_{vis}^+ and Q_{rad}^- are easily found from the basic equations. In the low-temperature regime, where $p = p_{\text{gas}}$ and the opacity is due to free-free absorption, $\bar{\kappa} = \kappa_{\text{ff}}$ ($\propto \rho T^{-3.5}$), we find,⁴ from equations (3.35), (3.36), (3.39), (3.43) and (3.45), that $H \propto \sqrt{p_{\text{gas}}/\rho} \propto T^{1/2}$ and $\rho \sim \Sigma/H \propto \Sigma/T^{1/2}$, and therefore,

$$Q_{\text{vis}}^+ \sim \alpha \frac{p_{\text{gas}}}{\rho} \Omega \Sigma \propto T \Sigma \quad \text{and} \quad Q_{\text{rad}}^- \sim \frac{\sigma T^4}{\kappa_{\text{ff}} \Sigma} \propto \frac{T^8}{\Sigma^2}. \quad (3.73)$$

Since $Q_{\text{vis}}^+ \propto T$ and $Q_{\text{rad}}^- \propto T^8$, the energy balance is realized at a certain T when Σ is fixed, as is shown in the left-lower corner of figure 3.6.

⁴Hereafter we drop the subscript ‘c’ of T_c for simplicity.

The energy balance, $Q_{\text{vis}}^+ = Q_{\text{rad}}^-$, leads to $T \propto \Sigma^{3/7}$. Substituting this relation into $\dot{M} \propto Q_{\text{vis}}^+ \propto \Sigma T$, we find that the slope of the equilibrium sequence in the \dot{M} - Σ diagram is

$$\left(\frac{\partial \ln \dot{M}}{\partial \ln \Sigma} \right)_{Q_{\text{vis}}^+ = Q_{\text{rad}}^-} = \frac{10}{7}. \quad (3.74)$$

In the high-temperature regime, where $p = p_{\text{rad}}$ and the opacity is due to electron scattering, $\bar{\kappa} = \kappa_{\text{es}}$ ($= \text{constant}$), we find that $H \sim p_{\text{rad}}/\rho H \propto T^4/\Sigma$ and $\rho \sim \Sigma/H \propto \Sigma^2/T^4$. We thus have

$$Q_{\text{vis}}^+ \sim 2\alpha p_{\text{rad}} H \propto \frac{T^8}{\Sigma} \quad \text{and} \quad Q_{\text{rad}}^- \sim \frac{\sigma T^4}{\kappa_{\text{es}} \Sigma} \propto \frac{T^4}{\Sigma}. \quad (3.75)$$

Unlike the case of $p = p_{\text{gas}}$, Q_{vis}^+ increases sharply with an increase of T (i.e., $Q_{\text{vis}}^+ \propto T^8$), while the temperature dependence of Q_{rad}^- becomes weaker than that in the case of $p = p_{\text{gas}}$. Hence, as shown in figure 3.6, another point of energy balance is realized in the Q - T plane. Two thermal-equilibrium solutions, $Q_{\text{vis}}^+ = Q_{\text{rad}}^-$, are thus possible for a fixed Σ .⁵

The energy balance thus leads to $T \sim \text{constant}$; hence, from $\dot{M} \propto Q_{\text{vis}}^+ \propto \Sigma^{-1}$, the slope of the equilibrium sequence in the \dot{M} - Σ diagram is found to be

$$\left(\frac{\partial \ln \dot{M}}{\partial \ln \Sigma} \right)_{Q_{\text{vis}}^+ = Q_{\text{rad}}^-} = -1. \quad (3.76)$$

If the alternative viscosity prescription (3.50) is adopted, on the other hand, we find for $\mu = 1$

$$Q_{\text{vis}}^+ \sim 2\alpha p_{\text{gas}} H \propto \Sigma T, \quad (3.77)$$

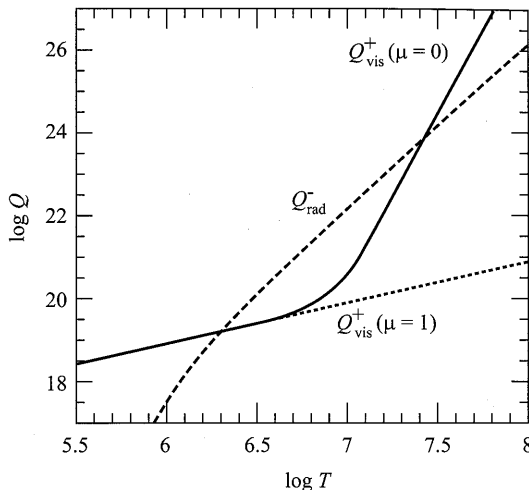
while the expression for Q_{rad}^- is unchanged [equation (3.75)]. In this case there is no additional solution of $Q_{\text{vis}}^+ = Q_{\text{rad}}^-$, as is shown in figure 3.6.

The energy balance requires $T \propto \Sigma^{2/3}$. The slope of the equilibrium sequence in the \dot{M} - Σ diagram is thus

$$\left(\frac{\partial \ln \dot{M}}{\partial \ln \Sigma} \right)_{Q_{\text{vis}}^+ = Q_{\text{rad}}^-} = \frac{5}{3}. \quad (3.78)$$

Only one solution is possible in this case for a fixed Σ (figure 3.5).

⁵We will show that the radiation pressure-dominated branch is unstable if $\mu = 0$ (see chapter 4).

**Figure 3.6**

Heating function Q_{vis}^+ and cooling function Q_{rad}^- of the α disk for different viscosity prescriptions ($\mu = 0$ and 1) at a fixed value of $\Sigma = 10^3 \text{ g cm}^{-2}$. Other parameters are $M = 10M_\odot$, $r/r_g = 5.0$, and $\alpha = 0.1$.

Table 3.1 Accretion Disk Branches.

Branch	$Q^+(\Sigma, T)$	$Q^-(\Sigma, T)$	$Q^+(\Sigma, \dot{M})$	$Q^-(\Sigma, \dot{M})$	$\dot{M}(\Sigma)$
Hot ($\mu = 0$)	$\Sigma^{-1}T^8$	$\Sigma^{-1}T^4$	\dot{M}	$\Sigma^{-1/2}\dot{M}^{1/2}$	Σ^{-1}
Hot ($\mu = 1$)	ΣT	$\Sigma^{-1}T^4$	\dot{M}	$\Sigma^{-5}\dot{M}^4$	$\Sigma^{5/3}$
Cool	ΣT	$\Sigma^{-2}T^8$	\dot{M}	$\Sigma^{-10}\dot{M}^8$	$\Sigma^{10/7}$

Finally, the dependences of Q 's on T and Σ and those on \dot{M} and Σ are summarized in table 3.1.

3.2.5 Disk Continuum Spectra

In the following subsections we examine the electromagnetic spectra emitted from geometrically thin accretion disks and observed by a distant observer, based on the standard models.

Let us first consider the continuum spectra. When the disk is optically thick in the vertical direction, the heat generated in the disk, Q_{vis}^+ , is radiated from the surface of the disk as roughly blackbody radiation. Independent of the nature of the disk viscosity, the surface temperature $T_{\text{eff}}(r)$ can be uniquely given by equation (3.57) as a function of M , \dot{M} , and r in a nonrelativistic disk.

As already stated, it is assumed that the surface of the disk radiates

locally the blackbody radiation:

$$B_\nu(r) = \frac{2h}{c^2} \frac{\nu^3}{\exp[h\nu/k_B T_{\text{eff}}(r)] - 1}, \quad (3.79)$$

which has a different temperature at different radii (*multi-color*). The observed flux S_ν of the disk is calculated by integrating the specific intensity, I_ν ($= B_\nu$), of the disk over the surface of the disk. That is, S_ν is given by

$$S_\nu = \int I_\nu d\Omega = \frac{\cos i}{D^2} \int_{r_{\text{in}}}^{r_{\text{out}}} B_\nu(r) 2\pi r dr, \quad (3.80)$$

where i is the inclination angle of the disk, Ω the solid angle subtended by the disk in the observer's sky, and D the distance to the disk.

Exactly speaking, in order to calculate the spectra S_ν by performing the integration in equation (3.80), we should use equation (3.57) for the effective temperature distribution. However, since the variation near to the inner edge has little influence on the overall structure of the spectra, we can safely drop the boundary effects and approximate the surface temperature as a power-law form, as long as we are interested in the overall spectra. Therefore, we approximate here the surface (effective) temperature of the disk as

$$T_{\text{eff}} = T_{\text{in}} \left(\frac{r}{r_{\text{in}}} \right)^{-p}, \quad (3.81)$$

where T_{in} is the temperature at $r = r_{\text{in}}$ and the exponent p is $3/4$ for the standard disk.⁶ Then, from equations (3.79) and (3.81) the observed flux (3.80) is expressed as

$$\begin{aligned} S_\nu &= \frac{\cos i}{D^2} 2\pi \left(-\frac{r_{\text{in}}^2}{p} \right) T_{\text{in}}^{2/p} \int B_\nu T^{-(2/p)-1} dT \\ &= \frac{\cos i}{D^2} \frac{4\pi h}{c^2} \frac{r_{\text{in}}^2}{p} \left(\frac{k_B T_{\text{in}}}{h\nu} \right)^{2/p} \nu^3 \int_{x_{\text{in}}}^{x_{\text{out}}} \frac{x^{(2/p)-1}}{e^x - 1} dx, \end{aligned} \quad (3.82)$$

where

$$x_{\text{in}} = \frac{h\nu}{k_B T_{\text{in}}} \quad \text{and} \quad x_{\text{out}} = \frac{h\nu}{k_B T_{\text{in}}} \left(\frac{r_{\text{out}}}{r_{\text{in}}} \right)^p. \quad (3.83)$$

As a result, the observed flux of the disk becomes

$$S_\nu \propto \nu^{3-(2/p)} \quad \text{for} \quad \frac{k_B T_{\text{in}}}{h} \left(\frac{r_{\text{in}}}{r_{\text{out}}} \right)^p \ll \nu \ll \frac{k_B T_{\text{in}}}{h}. \quad (3.84)$$

⁶A different value of exponent is used for, e.g., irradiated disks discussed in section 3.7 of the first edition (Kato et al. 1998) and in slim disks in chapter 10.

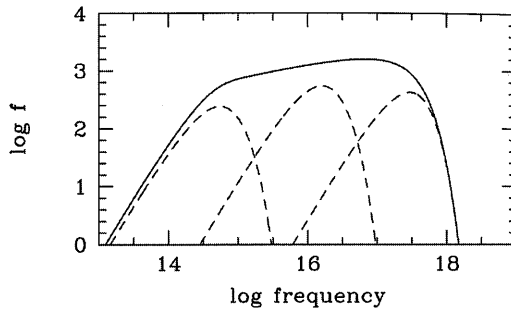


Figure 3.7

Typical spectrum of the standard accretion disk. The abscissa is the frequency ν and the ordinate is S_ν in arbitrary units. The exponent p is set to be $p = 3/4$. The parameters are $M = 10M_\odot$, $\dot{M} = 10^{18}\text{g s}^{-1}$, $r_{\text{in}} = 3r_g = 9 \times 10^6\text{cm}$, and $r_{\text{out}} = 10^{11}\text{cm}$, corresponding to the disks in soft X-ray transients (see figure 1.9 for the AGN case).

Hence, for the viscous standard disk, where $p = 3/4$, the spectrum becomes $S_\nu \propto \nu^{1/3}$. For the irradiated disk, where $p = 3/7$, on the other hand, we find $S_\nu \propto \nu^{-5/3}$ (cf. section 3.7 of Kato et al. 1998). A numerical example of the continuum spectra is shown in figure 3.7.

As easily seen in figure 3.7, the middle part of the continuum spectra from the standard disks are approximately expressed by

$$S_\nu \propto \nu^{1/3}, \quad (3.85)$$

although there exist a Wien cut-off in the high-frequency region (due to the presence of an inner edge of the disk) and a Rayleigh-Jeans slope in the low-frequency region (due to radiation from the outermost region). This characteristic spectrum is the *disk-blackbody spectrum* (or *multi-color spectrum*), as already stated (see also the next subsection).

3.2.6 Disk Blackbody Model

Since the disk spectra depend on both the black-hole mass M and the mass-accretion rate \dot{M} , it is, in principle, possible to derive these quantities from the observed X-ray spectra of black-hole binaries (BHs) during their high/soft state, when a thermal spectral component is dominant. Such a disk spectral model is often referred to as the multi-color disk (MCD) blackbody model, or simply as the disk blackbody (DBB)

model, which was proposed by Mitsuda et al. (1984). This MCD formalism has been frequently utilized, since it gives a reasonable fit to the observed spectra during the high/soft state (e.g., Ebisawa 1991; Dotani et al. 1997; Kubota et al. 1998).

We first explain the original MCD model, according to Makishima et al. (2000). Since this model is based on the standard Shakura-Sunyaev model, we set $p = 0.75$ in the temperature profile [equation (3.81)]. There are two fitting parameters: r_{in} and T_{in} . Then, the emergent spectra can be calculated according to equation (3.80) for given M and \dot{M} , and can be fitted to the observational data. Making a transformation of the independent variable from r to $T(r)$ in equation (3.80), we have

$$S_{\nu} = \frac{8\pi r_{\text{in}}^2 \cos i}{3D^2} \int_{T_{\text{out}}}^{T_{\text{in}}} \left(\frac{T}{T_{\text{in}}} \right)^{-8/3} B_{\nu}(T) d\ln T. \quad (3.86)$$

Cautions should be needed concerning the physical meanings of r_{in} and T_{in} . First of all, the value of r_{in} does literally mean the radius of the inner edge of the disk. However, this is not the maximum-flux radius r_{max} , where the radiation flux per unit surface reaches the maximum, because of a boundary term. Rather, the emergent flux (and, hence, the effective temperature) reaches its maximum at $r = (3/7)^{1/2}(6/7)^3 r_g \simeq 2.4r_{\text{in}}$ and then decreases inward [see equation (3.57)]. To relate with the emission spectra, therefore, we need a correction,

$$r_{\text{max}} = \frac{1}{\xi_1} r_{\text{in}} \quad (> r_{\text{in}}) \quad (3.87)$$

with $\xi_1 \sim 0.41$.

Second, T_{in} does not mean the surface temperature at r_{max} , but means the color temperature. To obtain the real effective temperature at r_{max} , we need another correction,

$$T_{\text{eff}}(r_{\text{max}}) = \frac{1}{\xi_2} T_{\text{in}} \quad (< T_{\text{in}}) \quad (3.88)$$

with $\xi_2 \sim 1.7$ being a spectral hardening factor due mainly to Compton scattering (Ross et al. 1993; Shimura and Takahara 1995). As a result, the bolometric luminosity should be (Kubota et al. 1998),

$$L_{\text{bol}} = 4\pi \left(\frac{r_{\text{in}}}{\xi_1} \right)^2 \sigma \left(\frac{T_{\text{in}}}{\xi_2} \right)^4. \quad (3.89)$$

Then, the inner-edge radius is given by

$$r_{\text{in}} = \xi_1 \xi_2^2 \left(\frac{L_{\text{bol}}}{4\pi \sigma T_{\text{in}}^4} \right)^{1/2}. \quad (3.90)$$

The observational quantities are the bolometric luminosity, which can be calculated from the observed flux, f_{bol} , through the relations

$$L_{\text{bol}} = \frac{2\pi D^2 f_{\text{bol}}}{\cos i}, \quad (3.91)$$

and T_{in} obtained through the fitting.

To see how the MCD model works, we fit observational data by extending the original DBB model to the non-standard temperature profile, $T \propto r^{-p}$ [see equation (3.81)]. We now have three fitting parameters: r_{in} , T_{in} , and p . If the standard picture is correct, we should have $p = 0.75$. To have a good fitting result, especially in p , wider spectral ranges are certainly preferable. In this fitting model, T_{in} and r_{in} are basically determined by the photon energy and the intensity at exponential roll-over, while p depends on the slope in the lower energy bands (i.e., soft X-rays).

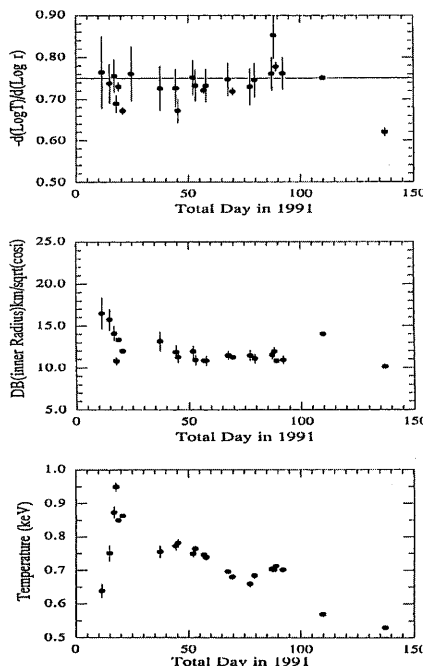


Figure 3.8

Results of the spectral fitting of Nova Muscae 1991 with the extended disk blackbody model: from the top to the bottom, the temperature exponent p , the innermost disk radius r_{in} , and the innermost disk temperature T_{in} . (After Mineshige et al. 1994)

The results of fitting to the sequence of the X-ray spectra of Nova

Muscae 1991⁷ are presented in figure 3.8. There are several noteworthy features seen in this figure. First, the temperature slopes are consistent with the canonical value of $p = 0.75$. This is, in a sense, surprising, since the disk in Nova Muscae is not completely in a steady state. This means that time variations are sufficiently slow, so that they do not greatly affect the emergent spectra. This result justifies the standard-disk description. Second, the disk inner edge is constant, except at the rising phase, when power-law spectral components are dominant, even when the luminosity decreases by more than an order of magnitude. Finally, the innermost temperature monotonically decreases in the decay phase, as is expected from the relation, $L_{\text{disk}} \propto r_{\text{in}}^2 T_{\text{eff}}^4$ with constant r_{in} .

3.2.7 Electron Scattering Effects and Comptonization

In the previous subsections we assumed that radiation emitted from the surface of the disk is locally blackbody. Here, we briefly describe the opacity effects which modify the local blackbody spectra.

For fully ionized hydrogen, the electron-scattering opacity and free-free absorption opacity are, respectively,

$$\kappa_{\text{es}} = \frac{\sigma_{\text{T}}}{m_{\text{p}}} = 0.40 \text{ cm}^2 \text{ g}^{-1}, \quad (3.92)$$

$$\kappa_{\text{ff}}(\nu) = 1.5 \times 10^{25} \rho T^{-7/2} \frac{1 - e^{-h\nu/k_{\text{B}}T}}{(h\nu/k_{\text{B}}T)^3} \text{ cm}^2 \text{ g}^{-1}, \quad (3.93)$$

where ρ is the disk density, T the disk temperature, and ν the frequency (Rybicki and Lightman 1979). Here, the quantum correction is neglected. The Rosseland mean of the free-free opacity κ_{ff} is⁸

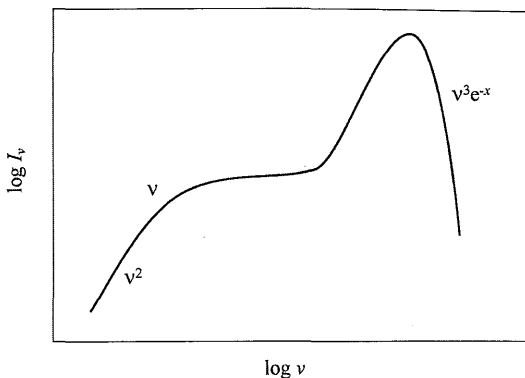
$$\kappa_{\text{ff}} = 0.64 \times 10^{23} \rho T^{-7/2} \text{ cm}^2 \text{ g}^{-1}. \quad (3.94)$$

In the spectral range where the absorption opacity dominates the electron-scattering opacity, the emitted spectrum is described as a blackbody. In the inner part of accretion disks around a relativistic object, however, the density is so low and the temperature is so high that the effect of (elastic) electron scattering (*coherent scattering* or Thomson scattering) becomes important.⁹ When free-free and bound-free opacities

⁷Nova Muscae 1991 is a representative black-hole binaries; see subsection 1.4.2 for the detailed description.

⁸In the case of standard metal abundance, the bound-free opacity usually dominates the free-free opacity (see appendix D).

⁹In a coherent (elastic) scattering the energy is conserved.

**Figure 3.9**

Spectrum from a thermal plasma characterized by a free-free and Compton processes. At low frequencies the spectrum is a blackbody, at intermediate ones it becomes a modified blackbody, and at high frequencies it is a Wien spectrum. Here, $x = h\nu/k_B T$. (Adapted from Rybicki and Lightman 1979)

are low compared with the electron-scattering opacity, photons diffuse out from large optical depth where thermal equilibrium exists. In such a case, where (elastic) electron scattering dominates, one has a *modified blackbody spectrum* (Rybicki and Lightman 1979),

$$I_\nu = \frac{2B_\nu}{1 + \sqrt{[\kappa_{\text{ff}}(\nu) + \kappa_{\text{es}}]/\kappa_{\text{ff}}(\nu)}} \sim 2B_\nu \sqrt{\frac{\kappa_{\text{ff}}(\nu)}{\kappa_{\text{ff}}(\nu) + \kappa_{\text{es}}}}, \quad (3.95)$$

where I_ν is the emitted intensity and B_ν is the Planck function. This modified blackbody spectrum is lower than that of a blackbody with the same effective temperature (however, the color temperature corresponding to the mean energy of photons is higher than the effective temperature), which causes a flattening of the spectrum. An example is shown in figure 3.9 (see also figure 3.14).

The frequency ν_{es} , above which the electron scattering dominates the absorption, can be calculated from the condition $\kappa_{\text{es}} = \kappa_{\text{ff}}(\nu_{\text{es}})$:

$$\frac{h\nu_{\text{es}}}{k_B T} \sim 6 \times 10^{12} \rho^{1/2} T^{-7/4}, \quad (3.96)$$

when $h\nu_{\text{es}}/k_B T \ll 1$ (Rybicki and Lightman 1979). The modification due to electron scattering becomes important for a temperature of

$$T_{\text{es}} = 3.0 \times 10^4 (\alpha m_8 \dot{m})^{-4/15} \text{ K}, \quad (3.97)$$

where $m_8 = M/(10^8 M_\odot)$. This temperature depends only weakly on the disk parameters (Czerny and Elvis 1987; Wandel and Petrosian 1988).

The frequency ν_{thin} , above which the medium becomes effectively thin, is also given by the condition $\kappa_{\text{es}} = \kappa_{\text{ff}}(\nu_{\text{thin}})\tau_{\text{es}}^2$,

$$\frac{h\nu_{\text{thin}}}{k_B T} \sim 6 \times 10^{12} \rho^{1/2} T^{-7/4} \tau_{\text{es}}, \quad (3.98)$$

when $h\nu_{\text{thin}}/k_B T \ll 1$. Here and hereafter, τ_{es} and τ_{ff} are the optical depths to electron scattering and free-free absorption, respectively. The disk becomes optically thin ($\tau_* < 1$) at

$$T_{\text{thin}} = 1.4 \times 10^5 (\alpha^{3/2} m_8 \dot{m})^{-8/31} \text{ K}, \quad (3.99)$$

where the effective optical depth τ_* is defined as $\tau_* \equiv \sqrt{(\tau_{\text{ff}} + \tau_{\text{es}})\tau_{\text{ff}}}$ (Wandel and Petrosian 1988).

When the electron temperature is sufficiently high, the (incoherent) Compton scattering (here called *Comptonization*) becomes important.¹⁰ The realm of Comptonization is represented by the Compton y parameter,

$$y = \frac{4k_B T}{mc^2} \text{ Max}(\tau_{\text{es}}, \tau_{\text{es}}^2), \quad (3.100)$$

in the non-relativistic case (see, e.g., Rybicki and Lightman 1979). On the right-hand side of equation (3.100), the first factor approximates the energy increases per scattering (for $h\nu < 4k_B T$) and the second factor represents the mean number of scatterings.

For $y \ll 1$, coherent scattering is important and a modified blackbody spectrum (3.95) will be realized. When $y \gg 1$, on the other hand, Comptonization becomes important, and the Wien spectrum will be produced (see subsection 3.3.3):

$$I_\nu \propto \frac{2h\nu^3}{c^2} \exp\left(-\frac{h\nu}{k_B T}\right). \quad (3.101)$$

The frequency ν_{Com} , above which Comptonization becomes important, is obtained from $y(\nu_{\text{Com}}) = 1$:

$$\frac{h\nu_{\text{Com}}}{k_B T} \sim 2.4 \times 10^{17} \rho^{1/2} T^{-9/4} \quad (3.102)$$

(Rybicki and Lightman 1979). Comptonization significantly influences the emerging spectrum for $k_B T \geq h\nu_{\text{Com}}$. For standard accretion disks we have

$$T_{\text{Com}} = 1.3 \times 10^5 (\alpha m_8 \dot{m})^{-4/17} \text{ K}, \quad (3.103)$$

¹⁰An incoherent (inelastic) scattering involves energy changes.

above which Comptonization is important (Czerny and Elvis 1987; Wandel and Petrosian 1988).

The effect of electron scattering (Comptonization) on the continuum spectrum of accretion disks was discussed by Shakura and Sunyaev (1973) in their original model. Recently, in relation to the soft X-ray excess in active galactic nuclei, several researchers have stressed the importance of scattering effects (e.g., Czerny and Elvis 1987; Wandel and Petrosian 1988; Ross et al. 1992; Shimura, Takahara 1993; Yamada et al. 1994; see chapter 6).

3.2.8 Disk Line Spectra

Next, let us consider the line spectra emitted from geometrically thin accretion disks. Spectral lines, particularly emission lines, have been found in various systems, including accretion disks. For example, strong hydrogen and helium emission lines are observed in soft X-ray transients during quiescence, cataclysmic variables, and supersoft X-ray sources. Hydrogen lines are also detected in X-ray stars, such as SS433 (section 1.4). In active galaxies (section 1.5), hydrogen lines as well as Fe fluorescence lines have been detected. In X-ray binaries, further, 511 keV electron-positron annihilation lines have been detected. We thus focus our attention on the emission lines in this subsection.

In accretion disks, the global emission-line profile is obtained by summing the local line profiles emitted from each part of disks, which are Doppler-shifted with different magnitudes. A significant nature of spectral lines from accretion disks is, observationally and theoretically, that they often have *double peaks*. In addition, they become *asymmetric double* if the relativistic effects operate, although we shall examine here only the nonrelativistic case (see subsection 6.3.2 for the relativistic case).

Due to the (Keplerian) rotation of the disk, spectral lines emitted from each segment on the disk are Doppler-shifted when they are observed by a distant observer. The redshift z , which arises from the usual Doppler effect, then becomes

$$1 + z = 1 - \mathbf{n} \cdot \frac{\mathbf{v}}{c}, \quad (3.104)$$

where \mathbf{v} is the velocity vector of the emitting gas, \mathbf{n} the normal vector to the observer, and c the speed of light. In the Cartesian coordinates (x, y, z) shown in figure 3.10, the components of vectors are expressed as

$$\mathbf{v} = (-v_\varphi \sin \varphi, v_\varphi \cos \varphi, 0) \quad \text{and} \quad \mathbf{n} = (\sin i, 0, \cos i), \quad (3.105)$$

where $v_\varphi(r)$ is the rotational speed of the disk, φ the azimuthal angle, and i the inclination angle. Hence, the redshift z at a position on the disk with radius r and azimuthal angle φ becomes

$$1 + z = \frac{\lambda}{\lambda_e} = \frac{\nu_e}{\nu} = 1 + \frac{v}{c} \sin i \sin \varphi, \quad (3.106)$$

where $\lambda_e(\nu_e)$ is the emitted wavelength (frequency), $\lambda(\nu)$ the observed wavelength (frequency), and $v(r) = v_\varphi(r)$.

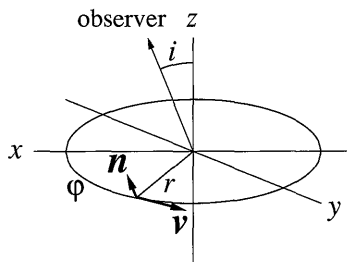


Figure 3.10

Geometry for disk line spectra.

Unlike the relativistic case, the redshifts of photons are the same when they originate from regions where the line-of-sight velocities,

$$V = v \sin i \sin \varphi, \quad (3.107)$$

are the same. In other words, the *iso-redshift* contours are coincident with the *iso-velocity* contours, the loci of constant line-of-sight velocity on the disk plane. Such iso-velocity contours are familiar in the field of galactic astronomy, where the rotation of galaxies is observed by HI 21cm lines. In accretion disks, however, the situation is simpler, since the rotation of the disk is Keplerian. That is, the iso-redshift/iso-velocity contours have a dipole pattern, as shown in figure 3.11. The upper panel of figure 3.11 shows the iso-velocity contours, while the lower panel illustrates the global line profile calculated by the procedure discussed below (Horne and Marsh 1986; Fukue and Sanbuichi 1993).

In the calculation of the global emission line profile, the observed intensity in equation (3.80), discussed for the continuum spectra, should be read as the local line profiles, I_ν , which are Doppler-shifted from the rest frequency to the observed frequency via equation (3.106). This local profile I_ν is divided into the local line emissivity $j(r, \varphi)$ and the normalized local line profile $\phi_\nu(z)$, which satisfies the normalized conditions

$\int \phi_\nu d\nu = 1$. [Note that redshift z is also a function of r and φ ; see equation (3.106).] That is, the observed line profile is expressed as

$$F_\nu = \int I_\nu d\Omega = \frac{\cos i}{D^2} \int j(r, \varphi) \phi_\nu r dr d\varphi, \quad (3.108)$$

where i is the inclination angle of the disk, Ω the solid angle subtended by the disk in the observer's sky, and D the distance to the disk.

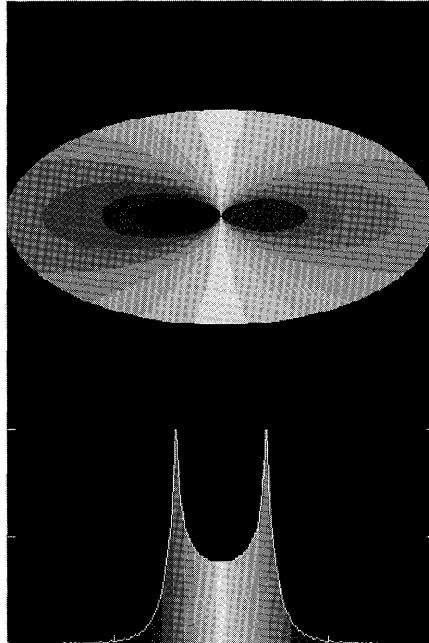


Figure 3.11

Iso-velocity contours and typical emission-line profiles from nonrelativistic accretion disks (see figure G.3). The shaded regions come from the corresponding regions. In this example, the parameters are the emissivity $j = \text{const.}$ for $2000r_g < r < 200000r_g$ and the inclination angle $i = 60^\circ$. The velocity ranges in the lower panel are $-2000 \text{ km s}^{-1} \leq v \leq 2000 \text{ km s}^{-1}$.

Here, the local line emissivity $j(r, \varphi)$ is independent of the redshift. Furthermore, it is usually assumed to be independent of the azimuthal angle, and is often assumed to be a power-law form,

$$j(r) \propto r^{-b}, \quad (3.109)$$

where b is a constant (however, see Fukue and Sanbuichi 1993; Okazaki 1996). In some cataclysmic variables, observations of the emission lines require that $b = 3/2$; $j(r) \propto r^{-3/2}$ (e.g., Young et al. 1981).

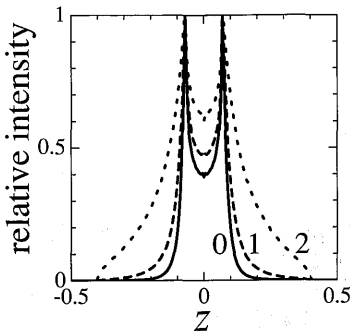


Figure 3.12

Emission-line profiles of nonrelativistic disks. The emissivity index b is 0 (thick solid curve), 1 (thick dashed one), and 2 (thick dotted one) for $3r_g < r < 100r_g$, while the inclination angle i is 80° . See figure 1.17 for observations.

The normalized local line profile ϕ_ν is often assumed to be a Gaussian profile function, such as

$$\phi_\nu = \frac{1}{\sqrt{2\pi}\sigma} e^{-(\nu_e - \nu_0)^2 / 2\sigma^2}, \quad (3.110)$$

where σ is the line width, ν_e the emitted frequency [cf. equation (3.106)], and ν_0 the rest frequency of that line (e.g., Chen and Helpert 1989). The shape of the normalized local line profile, however, has little effect on the global line profile, provided that its line width is sufficiently smaller than the line shift due to the Doppler effect caused by rotation. Physically, the local turbulent or thermal speed is small compared with the rotational speed [see equation (3.70)]. Therefore, in such a case as shown in figure 3.11, the normalized local line profile is assumed to be rectangular of the delta-function type,

$$\phi_\nu = \delta(\nu_e - \nu_0), \quad (3.111)$$

which is Doppler-shifted according to equation (3.106). At last, in the simplest case the observed line profile is calculated by

$$F_\nu \propto \cos i \int r^{-b} \delta(\nu_e - \nu_0) r dr d\varphi. \quad (3.112)$$

A sequence of synthetic emission line profiles for several values of a power-law exponent b are shown in figure 3.12.

As is shown in figures 3.11 and 3.12, the prominent feature of the spectral emission lines from accretion disks is that they often show *double-peaked spectra*. Although the global profile of such a double-peaked spectrum depends on the power-law exponent or other parameters, such as an inclination angle, it gives much information about accretion disks; e.g., the separation between the peaks gives the physical size of the disk, and the extension of the wing gives the power-law exponent.

In relation to cataclysmic variables, double-peaked spectra have been investigated by many researchers (e.g., Smak 1981; Horne and Marsh 1986). In particular, the Doppler tomography technique, which reproduces the image of accretion disks using the variation of emission-line profiles in various phases, was developed by Marsh and Horne (1988).

3.2.9 Disk Radiative Transfer

In this subsection we briefly discuss radiative transfer in the accretion-disk atmosphere, and show the emergent intensity from the disk surface within the framework of the α viscosity. The disk atmosphere differs from the stellar atmosphere in several aspects: (i) Viscous heating in the atmosphere may exist as an energy source for radiation. (ii) The gravitational acceleration is quite different from that of a star. That is, it increases with z for $z \ll r$, while it is almost constant in the stellar atmosphere. (iii) The optical depth of the disk is finite in some cases. In the usual state of the standard disk, the optical depth is sufficiently large. It, however, would not be so large in the innermost region, in the outer region in low-temperature disks, or in the corona. Thus, we cannot apply the usual stellar plane-parallel case to the disk case, and should consider more general situations with a finite optical depth.

Application of the theory of radiative transfer to the accretion-disk atmosphere has been done by several authors. The first item employed was the diffusion approximation for radiative transfer (Meyer and Meyer-Hofmeister 1982; Cannizzo and Wheeler 1984). Although a diffusion approximation provides a satisfactory description at large optical depths, the emergent radiation field originates at optical depths on the order of unity. Gray and non-gray models of accretion disks were then constructed under numerical treatments (Kříž and Hubeny 1986; Shaviv and Wehrse 1986; Adam et al. 1988; Mineshige and Wood 1990; Ross et al. 1992; Shimura and Takahara 1993; Hubeny, Hubeny 1997, 1998; Hubeny et al. 2000, 2001; Davis et al. 2005; Hui et al. 2005) and under analytical ones (Hubeny 1990; Artemova et al. 1996; Fukue and Akizuki 2006; cf.

Fukue 2007 for a disk wind).

The main assumptions adopted here are as follows: (i) The disk is steady and axisymmetric. (ii) It is also geometrically thin and plane parallel. (iii) As a closure relation, we use the Eddington approximation. (iv) The gray approximation, where the opacity does not depend on frequency, is adopted. (v) The viscous heating rate is uniform in the vertical direction.

The radiative transfer equations for the plane-parallel geometry (z) are given in appendix D. That is, the frequency-integrated transfer equation, the zeroth moment equation, and the first moment equation become, respectively,

$$\cos \theta \frac{dI}{dz} = \rho \left[\frac{j}{4\pi} - (\kappa_{\text{abs}} + \kappa_{\text{sca}}) I + \kappa_{\text{sca}} \frac{c}{4\pi} E \right], \quad (3.113)$$

$$\frac{dF}{dz} = \rho (j - c\kappa_{\text{abs}} E), \quad (3.114)$$

$$\frac{dP}{dz} = -\frac{\rho(\kappa_{\text{abs}} + \kappa_{\text{sca}})}{c} F, \quad (3.115)$$

where I is the frequency-integrated specific intensity, E the radiation energy density, F the vertical (z) component of the radiative flux, P the zz -component of the radiation stress tensor, and θ the polar angle. The mass emissivity j and opacity κ_{abs} and κ_{sca} are assumed to be independent of the frequency (gray approximation).

For matter, the vertical momentum balance and energy equation are, respectively,

$$0 = -\frac{d\psi}{dz} - \frac{1}{\rho} \frac{dp}{dz} + \frac{\kappa_{\text{abs}} + \kappa_{\text{sca}}}{c} F, \quad (3.116)$$

$$0 = q_{\text{vis}}^+ - \rho (j - c\kappa_{\text{abs}} E), \quad (3.117)$$

where ψ is the gravitational potential, p the gas pressure, and q_{vis}^+ the viscous-heating rate. Here, we do not solve the hydrostatic equilibrium (3.116), although we suppose that the density distribution in the vertical direction would be adjusted so as to maintain hydrostatic equilibrium throughout the main part of the disk atmosphere, under the radiative flux obtained below.

Using this energy equation (3.117) and introducing the optical depth, defined by

$$d\tau \equiv -\rho (\kappa_{\text{abs}} + \kappa_{\text{sca}}) dz, \quad (3.118)$$

we rewrite the radiative transfer equations:

$$\mu \frac{dI}{d\tau} = I - \frac{c}{4\pi} E - \frac{1}{4\pi} \frac{1}{\kappa_{\text{abs}} + \kappa_{\text{sca}}} \frac{q_{\text{vis}}^+}{\rho}, \quad (3.119)$$

$$\frac{dF}{d\tau} = - \frac{1}{\kappa_{\text{abs}} + \kappa_{\text{sca}}} \frac{q_{\text{vis}}^+}{\rho}, \quad (3.120)$$

$$c \frac{dP}{d\tau} = F, \quad (3.121)$$

$$cP = \frac{1}{3} cE, \quad (3.122)$$

where $\mu \equiv \cos \theta$. The final equation (3.122) is the usual Eddington approximation.

We assume that the heating rate is vertically uniform in the sense that $q_{\text{vis}}^+ / [(\kappa_{\text{abs}} + \kappa_{\text{sca}})\rho] = \text{constant}$. This means that the kinetic viscosity ν is constant in the vertical direction, since $q_{\text{vis}}^+ / \rho = \nu (rd\Omega/dr)^2$, as long as the opacities are constant.

Finally, the disk total optical depth becomes

$$\tau_0 = - \int_H^0 \rho (\kappa_{\text{abs}} + \kappa_{\text{sca}}) dz, \quad (3.123)$$

where H is the disk half-thickness.

Now, integrating moment equations (3.120) and (3.121) under the boundary conditions:

$$F = 0 \quad \text{at} \quad \tau = \tau_0, \quad (3.124)$$

$$F = F_s \quad \text{at} \quad \tau = 0, \quad (3.124)$$

$$cP = \frac{1}{3} cE = \frac{2}{3} F_s \quad \text{at} \quad \tau = 0, \quad (3.125)$$

we obtain analytical expressions for E , F , and P (Laor and Netzer 1989; Hubeny 1990; Fukue and Akizuki 2006). Since we obtain the radiation energy density E in the explicit form, we can now integrate the radiative transfer equation (3.119), and explicitly obtain both an outward intensity, $I(\tau, \mu)$ ($\mu > 0$), and an inward intensity, $I(\tau, -\mu)$, under the appropriate boundary conditions (see Fukue and Akizuki 2006 for more details).

We finally obtain the outward intensity as

$$\begin{aligned} I(\tau, \mu) = & \frac{3F_s}{4\pi} \left[\frac{2}{3} + \tau + \mu + \frac{1}{\tau_0} \left(\frac{1}{3} - \frac{\tau^2}{2} - \mu\tau - \mu^2 \right) \right. \\ & \left. - \left(\frac{2}{3} - \mu + \frac{1}{3\tau_0} - \frac{\mu^2}{\tau_0} \right) e^{(\tau-2\tau_0)/\mu} \right]. \end{aligned} \quad (3.126)$$

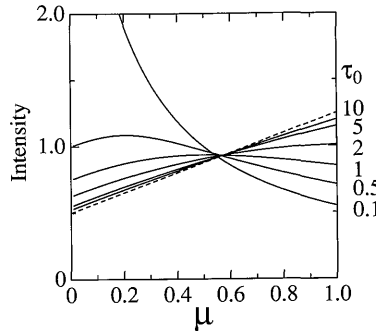


Figure 3.13

Normalized emergent intensity as a function of μ for the case with uniform heating. The numbers attached on each curve are values of τ_0 at the disk midplane. The dashed straight line is for the usual plane-parallel case with infinite optical depth. (After Fukue and Akizuki 2006)

For a sufficiently large optical depth τ_0 , this equation (3.126) reduces to the usual Milne-Eddington solution,

$$I = \frac{3F_s}{4\pi} \left(\frac{2}{3} + \tau + \mu \right). \quad (3.127)$$

On the other hand, the emergent intensity $I(0, \mu)$ emitted from the disk surface for the finite optical depth becomes

$$\begin{aligned} I(0, \mu) &= \frac{3F_s}{4\pi} \left[\frac{2}{3} + \mu + \frac{1}{\tau_0} \left(\frac{1}{3} - \mu^2 \right) \right. \\ &\quad \left. - \left(\frac{2}{3} - \mu + \frac{1}{3\tau_0} - \frac{\mu^2}{\tau_0} \right) e^{-2\tau_0/\mu} \right]. \end{aligned} \quad (3.128)$$

In figure 3.13, the emergent intensity $I(0, \mu)$, normalized by the isotropic value, \bar{I} ($= F_s/\pi$), is shown for several values of τ_0 as a function of μ .

As for the angle-dependence of the emergent intensity (3.128), for a large optical depth ($\tau_0 > 10$) the usual limb-darkening effect in the case with infinite optical depth is seen. For a small optical depth, however, the angle-dependence is drastically changed. In the vertical direction of $\mu \sim 1$, the emergent intensity decreases as the optical depth decreases. This is due to the finiteness of the optical depth. That is, we cannot see the ‘deeper’ position in the atmosphere, compared with the case of a semi-infinite disk. In the inclined direction of small μ , on the other hand, the emergent intensity becomes larger than that in the case of

the infinite optical depth. Moreover, when the optical depth is less than unity, the emergent intensity for small μ is greater than that for $\mu = 1$: the *limb brightening* takes place. Indeed, in the limiting case of $\tau_0 \sim 0$, $I(0, \mu) \sim (F_s/\pi)(2\mu)$. This is because that a path length is longer for such a case of small μ . That is, in the case for a low optical depth, the source function is very uniform. This is why the geometric effect (longer path length) is dominant and one finds limb ‘brightening’ or an *anti-peaking* effect (see Fukue and Akizuki 2006 for more discussions).

3.3 Optically Thin Disks

As we have described in the previous section, optically thick disks have difficulty to produce very hard radiation, such as hard X-rays and gamma-rays (up to ~ 100 keV), since the surface temperature is at most $\sim 10^7$ K (corresponding to 1 keV) for typical binary parameters (the temperature is much less for active galactic nuclei). Therefore, it is clear that we need a modification of the optically thick model, or an alternative disk model. One such attempt was made by Shapiro et al. (1976), who modified energy equations in optically thick disks. This is a subject of this section. Note that distinct approaches are adopted in the disk-corona model (section 3.4) and the advection-dominated disk model (chapter 9).

3.3.1 Shapiro-Lightman-Eardley Disks

Thorne and Price (1975) were the first to demonstrate that if the inner portion of an accretion disk consists of an optically thin, high (electron) temperature gas ($\sim 10^9$ K), the observed hard radiation could be explained. In fact, we have two alternatives of how to relate gravitational energy release and the disk temperature. If a disk is optically thick, we obtain (cf. section 3.2)

$$T_{\text{eff}} \sim 4 \times 10^6 \left(\frac{M}{10M_\odot} \right)^{-1/2} \left(\frac{\dot{M}}{10^{18} \text{ g s}^{-1}} \right)^{1/4} \left(\frac{r}{10r_g} \right)^{-3/4} \text{ K} \quad (3.129)$$

at $r \gg r_{\text{in}}$. If a disk is optically thin, in contrast, radiation is less efficient and the possible maximum temperature is virial,

$$T_{\text{vir}} \sim \frac{2GMm_p}{3k_B r} = \frac{1}{3} \frac{m_p c^2}{k_B} \left(\frac{r}{r_g} \right)^{-1} \sim 4 \times 10^{11} \left(\frac{r}{10r_g} \right)^{-1} \text{ K}. \quad (3.130)$$

Following this idea, Shapiro et al. (1976) found a hot, self-consistent optically thin accretion disk around a black hole. The disk is quite

different from the standard one, which is optically thick and cool. The basic assumptions and equations are as follows:

1. Since the disk is steady, \dot{M} is kept constant in space and time.
2. The disk is axisymmetric.
3. Gas in the disk is rotating around a central black hole on a circular orbit with the local Keplerian velocity (3.1). That is, the black hole is assumed to be non-rotating and Newtonian gravity is used.
4. Mass gradually moves inward via viscosity. Again, the α viscosity prescription (4.62) is adopted.
5. The disk is geometrically thick, but the aspect ratio is barely below unity,

$$H \lesssim r, \quad (3.131)$$

so that the height-averaged basic equations can still be employed. The basic equations describing the global viscous diffusion are thus unchanged [see equation (3.30)].

6. Hydrostatic balance holds in the vertical direction.
7. The gas is optically thin to absorption ($\tau \ll 1$). Hence, the dominant pressure source is the gas pressure ($p_{\text{rad}} \ll p_{\text{gas}}$). If a copious supply of soft photons is available, radiation cooling is mainly by inverse (unsaturated) Compton scattering.
8. Due to inefficient coupling between ions and electrons, the ion and electron temperatures may differ from each other; $T_i \neq T_e$.

Note that only items (7) and (8) differ from the optically thick cases. Thus, all of the basic equations, except for the energy equation, are the same as those of the optically thick cases.

(a) Energy equation

We assume that the ions and electrons are coupled by the collisional energy exchange (Coulomb encounter), and further coupling (due to plasma turbulence, for example) is ignored. The energy-exchange rate per unit surface is (see also section 7.3)

$$\Lambda_{ie} = \frac{3}{2} \nu_E \frac{\Sigma k_B (T_i - T_e)}{m_p} \quad (3.132)$$

with the electron-ion coupling being (Spitzer 1962)

$$\nu_E = 2.4 \times 10^{21} (\ln \Lambda) \rho T_e^{-3/2} \text{ s}^{-1}, \quad (3.133)$$

where the Coulomb logarithm is $\ln \Lambda \approx 15$. Thus, we need two energy-balance equations:

$$Q_{\text{vis}}^+ = \Lambda_{ie} \quad (3.134)$$

for ions [see equation (3.36) for expression of Q_{vis}^+] and

$$\Lambda_{ie} = Q_{\text{rad}}^- \quad (3.135)$$

for electrons.

The radiative cooling rate by the inverse Compton process is (see also section 7.3)

$$Q_{\text{rad}}^- = \left(\frac{4k_B T_e}{m_e c^2} \right) \Sigma \kappa_{es} E c, \quad (3.136)$$

where E is the radiation energy density. In other words, the Compton y -parameter,

$$y \equiv \left(\frac{4k_B T_e}{m_e c^2} \right) \text{Max}(\tau_{es}, \tau_{es}^2), \quad (3.137)$$

is taken to be unity.

Now, the equation sets are completed and we can calculate the physical quantities, such as Σ , T_i , T_e , p , and ρ , as functions of M , \dot{M} , α , and r . Interestingly, the computed electron temperature is nearly flat, $T_e \sim 10^9 \text{ K}$, and is nearly independent of M , \dot{M} , and α throughout the two-temperature domain.

We need to maintain caution concerning the employment of height-averaged equations. Indeed, we find

$$\frac{H}{r} \sim \frac{c_s}{r \Omega} \simeq 0.4 \left(\frac{T_i}{10^{12} \text{ K}} \right)^{1/2} \left(\frac{r}{r_g} \right)^{1/2}. \quad (3.138)$$

Therefore, the disk is only marginally geometrically thin when the ion temperatures are about virial [equation (3.130)].

3.3.2 Equilibrium Structure

Let us briefly discuss the functional dependence of the present solution. Since the disk is gas-pressure dominated by assumption, and since the ion temperature is higher than the electron temperature, we obtain $H \propto \sqrt{p_{\text{gas}}/\rho} \propto T_i^{1/2}$ and $\rho \sim \Sigma/H \propto \Sigma/T_i^{1/2}$, leading to

$$Q_i^+ = Q_{\text{vis}}^+ \sim \alpha \frac{p_{\text{gas}}}{\rho} \Sigma \Omega \propto T_i \Sigma, \quad Q_i^- = \Lambda_{ie} \propto \Sigma^2 T_i^{1/2} T_e^{-3/2}, \quad (3.139)$$

$$Q_e^+ = \Lambda_{ie} \propto \Sigma^2 T_i^{1/2} T_e^{-3/2}, \quad Q_e^- = Q_{rad}^- \propto \Sigma T_e \quad (3.140)$$

for ions and electrons, respectively, where we assumed that the radiation energy density E remains constant.¹¹

Further, from the energy balance of ions and electrons, we find $T_i \propto \Sigma^{1/2}$ and $T_e \propto \Sigma^{1/2}$. The slope in the \dot{M} - Σ diagram is¹²

$$\left(\frac{\partial \ln \dot{M}}{\partial \ln \Sigma} \right)_{Q^+ = Q^-} = \frac{3}{2}. \quad (3.141)$$

3.3.3 High-Energy Spectra

The emission spectra can be calculated by using the modified steady-state Kompaneets equation, which describes the evolution of the photon distribution function, n , due to repeated, nonrelativistic, inverse Compton scattering [see Rybicki and Lightman (1979) for derivation]:

$$0 = \left(\frac{k_B T_e}{m_e c^2} \right) \frac{1}{x^2} \frac{d}{dx} \left[x^4 \left(\frac{dn}{dx} + n + n^2 \right) \right] + Q(x) - \frac{n}{\text{Max}(\tau_{es}, \tau_{es}^2)}, \quad (3.142)$$

where x is the normalized photon energy, $x = h\nu/k_B T_e$, $Q(x)$ represents the photon supply rate, and the last term on the right-hand side describes photon escape via a spatial diffusion process. The photon occupation number $n(\nu)$ is related to the intensity I_ν as

$$n = \frac{c^2}{2h\nu^3} I_\nu. \quad (3.143)$$

In optically thin disks, $n \ll 1$, so that the nonlinear term ($\propto n^2$) is in equation (3.142) usually neglected.

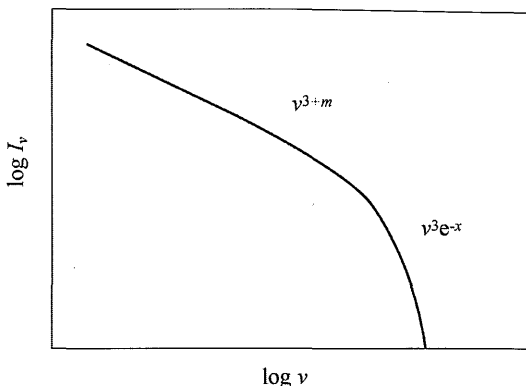
¹¹Since we find

$$\left(\frac{\partial \ln Q_i^+}{\partial \ln T_i} \right)_\Sigma > \left(\frac{\partial \ln Q_i^-}{\partial \ln T_i} \right)_\Sigma,$$

the disks are *thermally unstable* for ion temperature modulations (see chapter 4), unless the electron temperature significantly increases (decreases) when the ion temperature decreases (increases). Likewise, the disks are stable for electron-temperature perturbations, since

$$\left(\frac{\partial \ln Q_e^+}{\partial \ln T_e} \right)_\Sigma < \left(\frac{\partial \ln Q_e^-}{\partial \ln T_e} \right)_\Sigma.$$

¹²The relation between Σ and \dot{M} implies secular stability (chapter 4), although the significance of the secular stability is questionable, since the disk in any case suffers a thermal instability which grows on a much shorter timescale than the viscous timescale.

**Figure 3.14**

Spectrum produced by unsaturated Comptonization of low-energy photons by thermal electrons. Here, $x = h\nu/k_B T$. (Adapted from Rybicki and Lightman 1979)

How does the emergent spectrum look when we supply soft photons with energy $x \leq x_{\text{soft}}$? Then, $Q(x)$ has a nonzero contribution only below $x \leq x_{\text{soft}}$. At energy ranges of $x_{\text{soft}} \ll x \ll 1$, where the n and n^2 terms may be neglected compared with the (dn/dx) term, the emergent spectrum will be a power-law:

$$n \propto x^m, \quad I_\nu \propto \nu^{3+m}, \quad m = -\frac{3}{2} \pm \left(\frac{9}{4} + \frac{4}{y} \right)^{1/2}, \quad (3.144)$$

for a given y value [cf. equation (3.137)]. For $y = 1$, for example, we obtain $m = 1$ and -4 , giving rise to $I_\nu \propto \nu^4$ and $\propto \nu^{-1}$. The latter agrees with the observed spectrum. At a higher energy band, $x \gg 1$, we find $(dn/dx) + n \sim 0$. An approximate solution is

$$n \propto e^{-x} \quad \text{and} \quad I_\nu \propto \nu^3 \exp \left(-\frac{h\nu}{k_B T_e} \right). \quad (3.145)$$

We thus expect an exponential roll-over at ~ 100 keV, which is actually observed in some X-ray binaries and AGN. A typical X- γ ray spectrum is illustrated in figure 3.14.¹³

¹³This case corresponds to the case where the Compton y parameter is approximately unity. For the case of $y \gg 1$, see figure 3.9.

3.4 Accretion Disk Coronae

There is a common belief that hard X-ray radiation of black-hole binaries (BHBs) and active galactic nuclei (AGNs) arises from hot gas around black holes. In the preceding section we introduced the classical high-temperature disk model, which was expected to account for high-energy emission from accretion disks (see chapter 9 for more contemporary hot disk models). However, co-existing soft and hard X-ray components observed in Seyfert 1 type AGNs and BHBs during their very high state cannot be described by simple one-zone models. Rather, they require a two-component structure either with horizontal separation (a combination of inner hot and outer cool regions) or with vertical separation (disk-corona structure; see figure 3.15, see also, e.g., Liang and Nolan 1984; Haardt and Maraschi 1991; Mushotzky et al. 1993; Narayan et al. 1998). In this section we overview the basic physical processes that seem to operate in disk coronae.

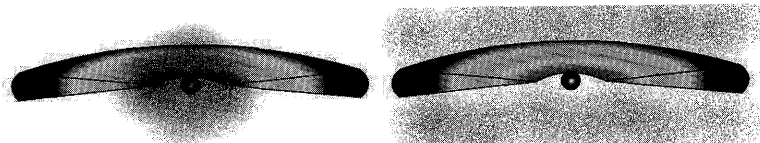


Figure 3.15

Two possible sites where high-energy emission is produced: hot inner torus (left) or accretion disk corona (right).

3.4.1 Historical Background

There is a long research history regarding accretion-disk coronae. Yet, we do not have a standard way of modeling disk coronae despite many attractive attempts (e.g., Haardt and Maraschi 1991; Meyer et al. 2000; Różańska and Czerny 2000; Kawaguchi et al. 2001). One of the reasons is complex interactions between the disk main body and corona through the exchange of radiation, matter, and energy. Further, magnetic fields that seem to play essential roles in disk coronae tend to produce rapid time variations and spatial inhomogeneity (Kawaguchi et al. 2000), which makes the situation even more complex.

Nevertheless, one thing has recently been made clear. As was demonstrated by Haardt and Maraschi (1991), we cannot account for the typical Seyfert 1 type SED, unless substantial fraction of energy is dissipated within a corona, whereas most of accreting material is retained within a

main body of the flow. More specifically, they introduced a parameter f , which represents a fraction of the gravitational energy dissipated in a corona via buoyancy and reconnection of magnetic fields out of the disk main body. To account for the spectral slope of $\alpha \sim 1$, where flux is proportional to $\nu^{-\alpha}$, they find that f should be close to unity. Otherwise, we can never account for both of the thermal bump and the high-energy emission component as are observed in Seyfert 1 type AGNs. Note that about a half of the radiation emitted within a corona goes downward to the disk main body to be absorbed and re-emitted as thermal emission with a lower temperature than the coronal temperature. Accordingly, we have two spectral components with approximately equal strength: a thermal component from the disk body with a disk temperature of $\sim 10^5$ K, and a power-law component arising from the disk corona with a higher temperature of $\sim 10^9$ K. Their model can successfully reproduce not only such composite spectra, but also the presence of the reflection of hard radiation by “cold matter”, as envisaged by Guilbert and Rees (1988) and Lightman and White (1988).

Thus, the introduction of a parameter f has made it possible to make a simple disk-corona modeling, although the physics underlying the parameter f needs to be investigated.

3.4.2 The Case of Solar Coronae

It is useful to comment about our knowledge on the solar corona, since there are good reasons to believe that the accretion-disk corona may share some common features with the solar corona (e.g., Galeev et al. 1979; Zhang et al. 2000). For example, violent fluctuations are observed in both coronae (Takahara 1979), and the fluctuation properties are remarkably similar in the power-spectral density plot (Ueno et al. 1997). Interesting theoretical investigations have also been presented in the frame of magnetized disk corona (e.g., Di Matteo 1998; Di Matteo et al. 1999; Merloni and Fabian 2001; Liu et al. 2002).

There has been a long research history of the solar corona and flares, and our knowledge regarding the structure and time variations has been enormously enriched thanks to intensive X-ray observations from space by the *GOES* and *Yohkoh* satellites (Uchida et al. 1996 and references therein). For example, a tight relation between the emission measure (EM) and temperature (EM- T relation) has been obtained.

Shibata and Yokoyama (1999) could successfully account for this EM- T relation based on a magnetic reconnection model. First, they

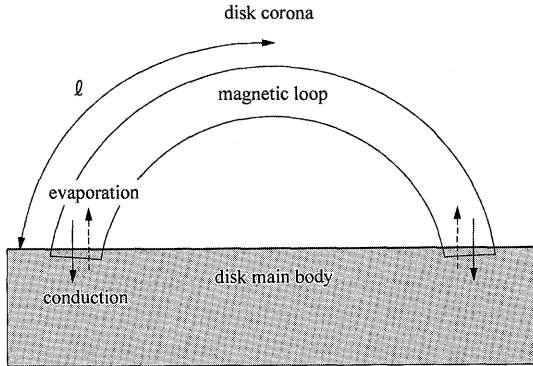


Figure 3.16

Schematic view of a magnetic loop and mass evaporation.

performed MHD simulations and found a relationship between the flare temperature T and magnetic field strength B of $T \propto B^{6/7}$ (Yokoyama and Shibata 1998). Second, they realized that this relation can be nicely understood in terms of the energy balance between reconnection heating of magnetic fields and conductive cooling,

$$\frac{B^2}{4\pi} \frac{c_A}{\ell} \approx k_0 \frac{T^{7/2}}{\ell^2}, \quad (3.146)$$

where c_A ($= B/\sqrt{4\pi\rho_0}$) is the Alfvén speed with ρ_0 being the constant pre-flare electron density, k_0 ($\sim 10^{-6}$) is the coefficient of the Spitzer-type thermal conduction, and ℓ is a characteristic length of the magnetic loops in the corona (see figure 3.16). Next, they assume energy equipartition between the gas and the magnetic fields in the corona,

$$\frac{B^2}{4\pi} \approx 2nk_B T, \quad (3.147)$$

where n is the post-flare electron number density and k_B is the Boltzmann constant. Then, the emission measure is related to the temperature by

$$EM \approx n^2 \ell^3 \propto \rho_0^{3/2} B^{-5} T^{17/2}. \quad (3.148)$$

This theoretical EM- T relation is in good agreement with the observation of solar, stellar, and proto-star flares over more than 10 orders of magnitudes in EM (see also Yokoyama and Shibata 2001).

Then, what determines the coronal density? They conjecture that it basically depends on how much photospheric gas can evaporate as a

result of thermal conductive heating by the corona. They estimated the coronal density based on the energy balance between conductive heating and evaporation cooling of the chromospheric plasma,

$$\frac{k_0 T^{7/2}}{\ell} \approx \frac{\gamma}{\gamma - 1} n k_B T \left(\frac{k_B T}{m_H} \right)^{1/2}, \quad (3.149)$$

finding values again consistent with the observations.

3.4.3 Simple Model for Disk Coronae

How can we apply our knowledge about the solar corona to the case of disk coronae? Here, we introduce one attempt by Liu et al. (2002, 2003).

First, they consider what relations determine the thermal structure of magnetic-reconnection-heated-corona. From X-ray observations of BHs and AGNs, we know that the emitting temperature of hot plasma is $\sim 10^9$ K, and the power-law spectrum requires a Compton y parameter of $y \sim 1$ [equation (3.137)], leading to the constraint on the density of the hot plasma to be $n \lesssim 5 \times 10^9 \text{ cm}^{-3}$ in a hot region of size $\ell \sim 10r_g$ (r_g is Schwarzschild radius). A successful model should account for these observational data.

Next, they consider the energy balance in the magnetic flux tube. In good analogy with the solar case we can safely assume a heating source to be magnetic reconnection. How about cooling? It is provided by thermal conduction, Comptonization, and cyclo-synchrotron radiation. For a typical AGN system with a black-hole mass of $M \sim 10^8 M_\odot$ and mass-accretion rate of $\dot{M} \sim \dot{M}_E (\equiv L_E/c^2)$, the radiation energy density in the disk is $U_{\text{rad}} \sim 1.1 \times 10^5 \text{ erg cm}^{-3}$. For the magnetic field, energy equi-partition with the gas is assumed in the disk, $B^2/4\pi = n_{\text{disk}} k_B T_{\text{disk}}$, which gives a magnetic field of $B \sim 10^3$ Gauss. We find that the Compton scattering is the most efficient cooling mechanism in the range of the above-mentioned parameters. We thus have

$$\frac{B^2}{4\pi} c_A \approx \frac{4k_B T}{m_e c^2} n \sigma_T c U_{\text{rad}} \ell, \quad (3.150)$$

where $U_{\text{rad}} = U_{\text{rad}}^{\text{in}} + U_{\text{rad}}^{\text{re}}$ is the soft photon field to be Compton up-scattered from both the intrinsic disk and reprocessed radiation, and the other constants have their standard meanings. Therefore, the temperature in the magnetic flux tube is estimated as

$$T \approx 1.2 \times 10^9 n_9^{-3/2} U_5^{-1} B_3^3 \ell_{14}^{-1} \text{ K}, \quad (3.151)$$

which is around the observed value of $\sim 10^9$ K for typical parameters of n_9 , U_5 , B_3 , and ℓ_{14} in units of 10^9 cm^{-3} , 10^5 erg cm^{-3} , 10^3 Gauss , $3 \times 10^{14} \text{ cm} (= 10 r_g)$, respectively.

Then, how to determine the density? As in the solar atmosphere, it is expected that the formation of a very thin, but dense, transition layer occurs between the corona and the chromosphere, where the temperature changes very steeply. The thermal conductive flux from the magnetic tube to the transition layer cannot be overwhelmingly cooled by the Compton radiation flux any more because of the thinness and the low temperature there. In a similar way to the solar corona, the thermal conduction from the magnetic tube heats up some of the chromospheric plasma into the magnetic tube (this process is called chromospheric evaporation). Since the pressure gradient at the interface is rather large, the mass evaporates to the magnetic tube at a speed around the sound speed, $c_s = \sqrt{k_B T / m_H}$. The evaporated mass density can then be estimated from the balance between conductive heating and evaporation cooling at the interface [see equation (3.149)]. In this equation the heat flux going to the chromosphere is assumed to be the continuous flux from the magnetic tube, and is thus approximated as $k_0 T^{7/2} / \ell$, and the evaporated mass is heated to the same temperature of the tube. We find $n \approx 1.6 \times 10^9 \text{ cm}^{-3}$ for $T = 1.2 \times 10^9 \text{ K}$, which is just what is required.

Therefore, we expect two processes: in the flux tube the magnetic reconnection continuously takes place and the heat is radiated away by Compton scattering [equation (3.150)]; however at the bottom of the flux tube, thermal conduction flows from the tube to the chromosphere and slowly evaporates the chromospheric plasma to the corona [equation (3.149)]. Mass evaporation plays an essential role to understand the density in the corona. To be more precise, we need to consider a back reaction; that is, the energy transferred from the disk to the corona by magnetic reconnection essentially affects the disk structure.

We can then calculate f , the fraction of accretion energy released in the reconnected magnetic corona, by

$$f \equiv \frac{F_{\text{cor}}}{F_{\text{tot}}} = \left(\frac{B^2}{4\pi} c_A \right) \left(\frac{3GM\dot{M}}{8\pi r^3} \right)^{-1}. \quad (3.152)$$

To do so, we replace \dot{M} in the expression of disk quantities, such as the pressure (and hence B) and U_{rad} , by $(1-f)\dot{M}$. Then, the coronal temperature and density should be modified appropriately, which, in turn, affects the amount of reprocessed radiation. We can thus iteratively

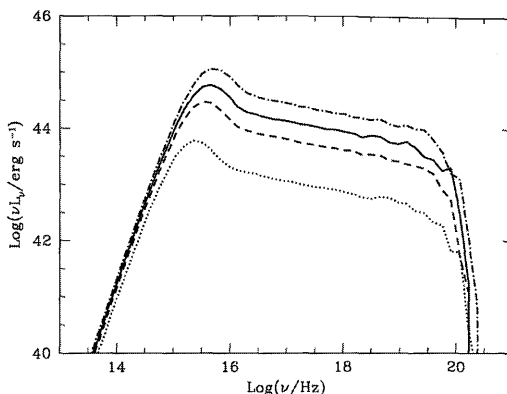


Figure 3.17

Typical SED of the simple disk-corona model for a black-hole mass of $10^8 M_\odot$ and accretion rates of $\dot{m} \equiv \dot{M}/\dot{M}_E = 1.0, 5.0, 10.0$, and 20.0 from the bottom to the top, respectively, each corresponding to the luminosity of $L/L_E \sim 0.07, 0.35, 0.7$, and 1.4 , respectively. (After Liu et al. 2003)

calculate f for a given black-hole mass and accretion rate. Through calculations, we find that f is indeed close to unity, regardless of the black-hole mass and mass-accretion rate (Liu et al. 2002).

On the basis of this model, it is straightforward to calculate the emergent spectra by means of Monte-Carlo simulations (Liu et al. 2003). Figure 3.17 displays typical SEDs of the disk-corona system in AGN for several mass-accretion rates. As expected, the SEDs are composed of the thermal component, which is dominant at around UV to soft X-rays, and a hard, power-law component extending to hard X-ray ranges. The spectral indices are $\alpha \sim 1.1$, a little steeper than that observed in Seyfert galaxies, regardless of the disk luminosity.

3.5 Relativistic Standard Disks

In this section we summarize the basic properties of the relativistic version of standard disks. The relativistic accretion-disk model under the alpha description was constructed by Novikov and Thorne (1973) (see also Page and Thorne 1974).

3.5.1 Basic Equations of Relativistic Disks

According to Novikov and Thorne (1973), we now describe the basic equations for relativistic accretion disks and their analytical solutions.

The main assumptions are essentially the same as those in the non-relativistic case given in section 3.2: (i) The gravitational field is determined by a black hole, and the self-gravity of the disk gas is ignored. (ii) The disk lies in the equatorial plane of the hole. (iii) The disk is steady. (iv) The disk is axisymmetric. (v) The disk is geometrically thin in the sense that $H/r \ll 1$. Hence, we integrate the physical quantities in the vertical direction. (vi) Rotational motion is dominant. That is, the gas of the disk moves very nearly in direct, circular, geodesic orbits – *relativistic Keplerian*; $|v_r| \ll v_\varphi$. (vii) Hydrostatic balance holds in the vertical direction. (viii) The disk is optically thick in the vertical direction. (ix) For viscosity, the alpha prescription is adopted. (x) The global magnetic fields are ignored. (xi) Finally, energy and angular momentum exchanges between (distant) different parts of the disk are not considered, although returning radiation from the inner disk to the outer disk would be significant [for irradiation see section 3.7 of the first edition (Kato et al. 1998); for returning radiation see Cunningham 1975].

Under these assumptions, the basic equations governing the relativistic accretion disks are given below [see Novikov and Thorne (1973) and Page and Thorne (1974) for derivations; see Kato (1993) and Riffert and Herold (1995) for correction on the hydrostatic balance; see also appendix A], using the following relativistic correction factors (Novikov and Thorne 1973; appendix A):

$$\mathcal{A} = 1 + \frac{a_*^2}{4\hat{r}^2} + \frac{a_*^2}{4\hat{r}^3}, \quad (3.153)$$

$$\mathcal{B} = 1 + a_* \sqrt{\frac{1}{8\hat{r}^3}}, \quad (3.154)$$

$$\mathcal{C} = 1 - \frac{3}{2\hat{r}} + 2a_* \sqrt{\frac{1}{8\hat{r}^3}}, \quad (3.155)$$

$$\mathcal{D} = 1 - \frac{1}{\hat{r}} + \frac{a_*^2}{4\hat{r}^2}, \quad (3.156)$$

$$\mathcal{E} = 1 + \frac{a_*^2}{\hat{r}^2} - \frac{a_*^2}{2\hat{r}^3} + \frac{3a_*^4}{16\hat{r}^4}, \quad (3.157)$$

$$\mathcal{F} = 1 - 2a_* \sqrt{\frac{1}{8\hat{r}^3}} + \frac{a_*^2}{4\hat{r}^2}, \quad (3.158)$$

$$\mathcal{G} = 1 - \frac{1}{\hat{r}} + a_* \sqrt{\frac{1}{8\hat{r}^3}}, \quad (3.159)$$

$$\mathcal{H} = 1 - 4a_* \sqrt{\frac{1}{8\hat{r}^3}} + \frac{3a_*^2}{4\hat{r}^2}, \quad (3.160)$$

$$\mathcal{J} = \exp \left[+\frac{3}{4} \int_{\hat{r}}^{\infty} \frac{\mathcal{F}}{\mathcal{BC}} \frac{d\hat{r}}{\hat{r}^2} \right], \quad (3.161)$$

$$\mathcal{L} = \frac{\ell - \ell_{\text{ms}}}{\sqrt{GMr}} = \frac{\mathcal{F}}{\mathcal{C}^{1/2}} - \frac{\ell_{\text{ms}}}{\sqrt{GMr}}, \quad (3.162)$$

$$\mathcal{Q} = \mathcal{L} - \frac{3}{4\hat{r}^{1/2}} \mathcal{J} \int_{\hat{r}_{\text{ms}}}^{\hat{r}} \frac{\mathcal{F}^2}{\mathcal{BC}^{3/2} \mathcal{J}} \frac{d\hat{r}}{\hat{r}^{3/2}}, \quad (3.163)$$

where

$$\hat{r} \equiv \frac{r}{r_g} \quad (3.164)$$

is the dimensionless radius, $\hat{r}_{\text{rm}} \equiv r_{\text{ms}}/r_g$ (r_{ms} being the marginally stable radius), ℓ is the specific angular-momentum with relativistic corrections, ℓ_{ms} is the specific angular-momentum at r_{ms} , and $a_* = a/(r_g/2)$ is the spin parameter of the hole ($0 \leq a_* < 1$). Analytical expressions for r_{ms} and \mathcal{Q} are given in appendix A.

(a) Continuity equation

The equation of mass conservation is written as

$$2\pi r \Sigma u^r = 2\pi r \Sigma v^r \mathcal{D}^{1/2} = -\dot{M} = \text{const.}, \quad (3.165)$$

where $\Sigma (= \int \rho dz)$ is the surface density, ρ being the density of the rest mass, as measured in the local rest frame of the gas, u^r is the radial component of the four velocity, v^r is the radial velocity of the gas, \dot{M} is the constant *mass-accretion rate*, and \mathcal{D} is a relativistic correction factor.

(b) Momentum equation

Similar to the non-relativistic case, in the radial direction, we assume that the gravitational force is balanced by the centrifugal force; in the momentum equation in the radial direction the pressure-gradient force and the inertial term are negligible. That is, the angular-velocity distribution is relativistic Keplerian:

$$\begin{aligned} \Omega &= \Omega_K = \sqrt{\frac{GM}{r^3}} \frac{1}{\mathcal{B}}, \\ \ell &= \ell_K = \sqrt{GMr} \frac{\mathcal{F}}{\mathcal{C}^{1/2}}, \end{aligned} \quad (3.166)$$

where ℓ is the specific angular momentum, and \mathcal{B} , \mathcal{C} , and \mathcal{F} are relativistic correction factors.

(c) Angular-momentum conservation

The rate of change of angular-momentum in the radial direction is written as

$$\mathcal{D}^{1/2} \Sigma v^r \frac{d\ell}{dr} - \frac{1}{r} \frac{d}{dr} \left(r^2 \mathcal{B} \mathcal{C}^{-1/2} \mathcal{D} T_{r\varphi} \right) + 2\ell \frac{F}{c^2} = 0, \quad (3.167)$$

where $T_{r\varphi}$ ($= \int t_{r\varphi} dz$) is the vertically integrated shear stress, $t_{r\varphi}$ being the $r\varphi$ -component of the stress tensor, and F is the radiative flux from the surface of the disk [cf. equation (3.15) for a Newtonian case].

The first term on the left-hand side is the rate of angular-momentum change in the gas, the second is the rate at which angular momentum is transferred by the shear stress, and the third is the rate at which angular momentum is carried off by photons.

Combining this equation (3.167) with the continuity equation (3.165), we obtain the equation of angular momentum conservation [cf. equation (3.28) for a Newtonian case]:

$$\frac{d}{dr} \left(\frac{\dot{M}}{2\pi} \ell + r^2 \mathcal{B} \mathcal{C}^{-1/2} \mathcal{D} T_{r\varphi} \right) - 2r\ell \frac{F}{c^2} = 0. \quad (3.168)$$

(d) Hydrostatic balance

The hydrostatic balance in the vertical direction is written as (cf. Kato 1993; Riffert and Herold 1995)

$$-\frac{1}{\rho} \frac{dp}{dz} = \frac{GMz}{r^3} \frac{\mathcal{H}}{\mathcal{C}}, \quad (3.169)$$

where p is the pressure measured in the comoving frame, and \mathcal{H} is a relativistic correction factor. Integration of this equation in the vertical direction yields

$$\frac{GM}{r^3} H^2 \frac{\mathcal{H}}{\mathcal{C}} = \frac{p}{\rho} \equiv c_s^2, \quad (3.170)$$

where H is the half-thickness of the disk and c_s the isothermal sound speed.

(e) Energy equation

The equation of energy conservation is written as

$$\frac{d}{dr} \left(\frac{\dot{M}}{2\pi} E + r^2 \mathcal{B} \mathcal{C}^{-1/2} \mathcal{D} T_{r\varphi} \Omega \right) - 2rE \frac{F}{c^2} = 0, \quad (3.171)$$

where E is the specific energy. Using the relation $dE/dr - \Omega d\ell/dr = 0$ (see appendix A) and the angular-momentum conservation (3.168), this equation becomes

$$Q_{\text{vis}}^+ = Q_{\text{rad}}^-, \quad (3.172)$$

where

$$Q_{\text{vis}}^+ = -\frac{3}{2} \sqrt{\frac{GM}{r^3}} \frac{\mathcal{D}}{\mathcal{C}} T_{r\varphi}, \quad (3.173)$$

$$Q_{\text{rad}}^- = 2F = 2\sigma T_{\text{eff}}^4. \quad (3.174)$$

That is, the heating due to viscosity is balanced by the radiative cooling from a unit surface area of the disk.

Eliminating F from the angular-momentum conservation (3.168) and energy conservation (3.172), we obtain a differential equation for the integrated stress $T_{r\varphi}$:

$$\frac{d}{dr} \left(\frac{\dot{M}}{2\pi} \ell + r^2 \mathcal{B} \mathcal{C}^{-1/2} \mathcal{D} T_{r\varphi} \right) + \frac{3}{2c^2} \sqrt{\frac{GM}{r}} \ell \frac{\mathcal{D}}{\mathcal{C}} T_{r\varphi} = 0. \quad (3.175)$$

As already explained, in the standard picture of accretion disks the gas density is supposed to drop quickly inside the marginally stable radius. Hence, in the zeroth approximation the viscous stress vanishes at a marginally stable radius; $T_{r\varphi} = 0$ at $r = r_{\text{ms}}$ (see, however, chapter 8 for the transonic nature).

We can integrate equation (3.175) and find a solution that satisfies the above boundary condition:

$$T_{r\varphi} = -\frac{\dot{M}}{2\pi} \sqrt{\frac{GM}{r^3}} \frac{\mathcal{C}^{1/2} \mathcal{Q}}{\mathcal{B} \mathcal{D}}, \quad (3.176)$$

$$Q_{\text{vis}}^+ = 2F = \frac{3GM\dot{M}}{4\pi r^3} \frac{\mathcal{Q}}{\mathcal{B} \mathcal{C}^{1/2}}, \quad (3.177)$$

where the latter is derived from the energy equation (3.172) [cf. equation (3.50) for a Newtonian case].

If the disk is optically thick in the vertical direction and the energy transfer in the vertical direction is due to radiation, the radiative flux is written as

$$F = -\frac{4acT^3}{3\kappa\rho} \frac{\partial T}{\partial z}, \quad (3.178)$$

which is the same as that of the non-relativistic case. We integrate this equation in the vertical direction to obtain

$$Q_{\text{rad}}^- = 2F = \frac{16acT_c^4}{3\bar{\kappa}\Sigma} = \frac{32\sigma T_c^4}{3\tau}, \quad (3.179)$$

where T_c is the temperature on the equator ($z = 0$) and $\tau = \bar{\kappa}\Sigma/2$.

(f) Equation of state

The equation of state is

$$p = p_{\text{gas}} + p_{\text{rad}} = \frac{k_B}{\bar{\mu}m_p} \rho T_c + \frac{aT_c^4}{3}, \quad (3.180)$$

where $\bar{\mu}$ is the mean molecular weight.

(g) Opacity

The opacity is written as

$$\bar{\kappa} = \kappa_{\text{es}} + \kappa_{\text{ff}} = 0.40 + 0.64 \times 10^{23} \rho T_c^{-7/2} \text{ cm}^2 \text{ g}^{-1}, \quad (3.181)$$

where κ_{es} is the electron scattering opacity and κ_{ff} the free-free opacity.¹⁴

(h) Viscosity

Finally, the viscous law is the alpha prescription:

$$t_{r\varphi} = -\alpha p \quad \text{or} \quad T_{r\varphi} = -2\alpha p H, \quad (3.182)$$

where α is the viscosity parameter ($0 < \alpha \lesssim 1$).

3.5.2 Structure of Relativistic Disks

Now let us write down explicit solutions for relativistic standard disks. The basic equations for the physical quantities Σ , v^r , Ω , H , p , T ,... are similar to those for the non-relativistic case (section 3.2) without relativistic correction factors. These equations can be solved algebraically (Novikov and Thorne 1973; Page and Thorne 1974).

In order to express the solutions, we introduce the following nondimensional variables:

$$m \equiv \frac{M}{M_\odot}, \quad \dot{m} \equiv \frac{\dot{M}}{M_{\text{crit}}}, \quad \hat{r} \equiv \frac{r}{r_g}, \quad (3.183)$$

where $M_{\text{crit}} = L_E/c^2$ and $r_g = 2GM/c^2$.

As in the non-relativistic case, the disk is divided into three regions according to the dominant pressure and opacity.

¹⁴In the case of standard metal abundance, the bound-free opacity dominates the free-free opacity (see appendix D). In this chapter, however, we construct the standard disk model under the condition of low metal abundance.

(a) **The inner region where $p = p_{\text{rad}}$ and $\bar{\kappa} = \kappa_{\text{es}}$:**

$$\begin{aligned}
 H &= 5.5 \times 10^4 m \dot{m} \\
 &\quad \times \mathcal{B}^{-1} \mathcal{C}^{1/2} \mathcal{H}^{-1} \mathcal{Q} \text{ cm}, \\
 \Sigma &= 1.0 \times 10^2 \alpha^{-1} \dot{m}^{-1} \hat{r}^{3/2} \\
 &\quad \times \mathcal{B} \mathcal{C}^{1/2} \mathcal{D}^{-1} \mathcal{H} \mathcal{Q}^{-1} \text{ g cm}^{-2}, \\
 \rho &= 9.0 \times 10^{-4} \alpha^{-1} m^{-1} \dot{m}^{-2} \hat{r}^{3/2} \\
 &\quad \times \mathcal{B}^2 \mathcal{D}^{-1} \mathcal{H}^2 \mathcal{Q}^{-2} \text{ g cm}^{-3}, \\
 v^r &= -7.6 \times 10^8 \alpha \dot{m}^2 \hat{r}^{-5/2} \\
 &\quad \times \mathcal{B}^{-1} \mathcal{C}^{-1/2} \mathcal{D}^{1/2} \mathcal{H}^{-1} \mathcal{Q} \text{ cm s}^{-1}, \\
 T_c &= 4.9 \times 10^7 \alpha^{-1/4} m^{-1/4} \hat{r}^{-3/8} \\
 &\quad \times \mathcal{D}^{-1/4} \mathcal{H}^{1/4} \text{ K}, \\
 \tau_* &= 8.4 \times 10^{-3} \alpha^{-17/16} m^{-1/16} \dot{m}^{-2} \hat{r}^{93/32} \\
 &\quad \times \mathcal{B}^2 \mathcal{C}^{1/2} \mathcal{D}^{-17/16} \mathcal{H}^{25/16} \mathcal{Q}^{-2}. \tag{3.184}
 \end{aligned}$$

(b) **The middle region where $p = p_{\text{gas}}$ and $\bar{\kappa} = \kappa_{\text{es}}$:**

$$\begin{aligned}
 H &= 2.7 \times 10^3 \alpha^{-1/10} m^{9/10} \dot{m}^{1/5} \hat{r}^{21/20} \\
 &\quad \times \mathcal{B}^{-1/5} \mathcal{C}^{1/2} \mathcal{D}^{-1/10} \mathcal{H}^{-1/2} \mathcal{Q}^{1/5} \text{ cm}, \\
 \Sigma &= 4.3 \times 10^4 \alpha^{-4/5} m^{1/5} \dot{m}^{3/5} \hat{r}^{-3/5} \\
 &\quad \times \mathcal{B}^{-3/5} \mathcal{C}^{1/2} \mathcal{D}^{-4/5} \mathcal{Q}^{3/5} \text{ g cm}^{-2}, \\
 \rho &= 8.0 \alpha^{-7/10} m^{-7/10} \dot{m}^{2/5} \hat{r}^{-33/20} \\
 &\quad \times \mathcal{B}^{-2/5} \mathcal{D}^{-7/10} \mathcal{H}^{1/2} \mathcal{Q}^{2/5} \text{ g cm}^{-3}, \\
 v^r &= -1.7 \times 10^6 \alpha^{4/5} m^{-1/5} \dot{m}^{2/5} \hat{r}^{-2/5} \\
 &\quad \times \mathcal{B}^{3/5} \mathcal{C}^{-1/2} \mathcal{D}^{-1/5} \mathcal{Q}^{-3/5} \text{ cm s}^{-1}, \\
 T_c &= 2.2 \times 10^8 \alpha^{-1/5} m^{-1/5} \dot{m}^{2/5} \hat{r}^{-9/10} \\
 &\quad \times \mathcal{B}^{-2/5} \mathcal{D}^{-1/5} \mathcal{Q}^{2/5} \text{ K}, \\
 \tau_* &= 2.4 \times 10^1 \alpha^{-4/5} m^{1/5} \dot{m}^{1/10} \hat{r}^{3/20} \\
 &\quad \times \mathcal{B}^{-1/10} \mathcal{C}^{1/2} \mathcal{D}^{-4/5} \mathcal{H}^{1/4} \mathcal{Q}^{1/10}. \tag{3.185}
 \end{aligned}$$

The boundary between the middle and inner regions lies at

$$\hat{r}_{ab} = 18 \alpha^{2/21} m^{2/21} \dot{m}^{16/21} \mathcal{B}^{-16/21} \mathcal{D}^{2/21} \mathcal{H}^{-10/21} \mathcal{Q}^{16/21}. \tag{3.186}$$

(c) The outer region where $p = p_{\text{gas}}$ and $\bar{\kappa} = \kappa_{\text{ff}}$:

$$\begin{aligned}
 H &= 1.5 \times 10^3 \alpha^{-1/10} m^{9/10} \dot{m}^{3/20} \hat{r}^{9/8} \\
 &\quad \times \mathcal{B}^{-3/20} \mathcal{C}^{1/2} \mathcal{D}^{-1/10} \mathcal{H}^{-19/40} \mathcal{Q}^{3/20} \text{ cm}, \\
 \Sigma &= 1.4 \times 10^5 \alpha^{-4/5} m^{1/5} \dot{m}^{7/10} \hat{r}^{-3/4} \\
 &\quad \times \mathcal{B}^{-7/10} \mathcal{C}^{1/2} \mathcal{D}^{-4/5} \mathcal{H}^{-1/20} \mathcal{Q}^{7/10} \text{ g cm}^{-2}, \\
 \rho &= 4.7 \times 10^1 \alpha^{-7/10} m^{-7/10} \dot{m}^{11/20} \hat{r}^{-15/8} \\
 &\quad \times \mathcal{B}^{-11/20} \mathcal{D}^{-7/10} \mathcal{H}^{17/40} \mathcal{Q}^{11/20} \text{ g cm}^{-3}, \\
 v^r &= -5.4 \times 10^5 \alpha^{4/5} m^{-1/5} \dot{m}^{3/10} \hat{r}^{-1/4} \\
 &\quad \times \mathcal{B}^{7/10} \mathcal{C}^{-1/2} \mathcal{D}^{-1/5} \mathcal{H}^{1/20} \mathcal{Q}^{-7/10} \text{ cm s}^{-1}, \\
 T_c &= 6.9 \times 10^7 \alpha^{-1/5} m^{-1/5} \dot{m}^{3/10} \hat{r}^{-3/4} \\
 &\quad \times \mathcal{B}^{-3/10} \mathcal{D}^{-1/5} \mathcal{H}^{1/20} \mathcal{Q}^{3/10} \text{ K}, \\
 \tau &= 7.9 \times 10^1 \alpha^{-4/5} m^{1/5} \dot{m}^{1/5} \\
 &\quad \times \mathcal{B}^{-1/5} \mathcal{C}^{1/2} \mathcal{D}^{-4/5} \mathcal{H}^{1/5} \mathcal{Q}^{1/5}.
 \end{aligned} \tag{3.187}$$

The boundary between the outer and middle regions lies at

$$\hat{r}_{bc} = 2.5 \times 10^3 \dot{m}^{2/3} \mathcal{B}^{-2/3} \mathcal{H}^{-1/3} \mathcal{Q}^{2/3}. \tag{3.188}$$

3.5.3 Effective Temperature and Relativistic Effect

Using equations (3.174) and (3.177), we have an explicit expression for the disk flux (and for the effective temperature) as

$$F = \frac{3GM\dot{M}}{8\pi r^3} f_R, \tag{3.189}$$

where the correction factor

$$f_R \equiv \frac{\mathcal{Q}}{\mathcal{B}\mathcal{C}^{1/2}} \tag{3.190}$$

includes both the boundary and relativistic corrections.

Using the explicit expressions for \mathcal{B} , \mathcal{C} , and \mathcal{Q} (see appendix A), we

obtain this correction factor as an explicit form:

$$f_R = \frac{1}{C\sqrt{\hat{r}}} \left[\sqrt{\hat{r}} - \sqrt{\hat{r}_{ms}} - \frac{3}{2\sqrt{2}} a_* \ln \frac{\sqrt{\hat{r}}}{\sqrt{\hat{r}_{ms}}} \right. \\ \left. - \frac{3}{2} \frac{(\sqrt{\hat{r}_1} - a_*)^2}{\sqrt{\hat{r}_1}(\sqrt{\hat{r}_1} - \sqrt{\hat{r}_2})(\sqrt{\hat{r}_1} - \sqrt{\hat{r}_3})} \ln \frac{\sqrt{\hat{r}} - \sqrt{\hat{r}_1}}{\sqrt{\hat{r}_{ms}} - \sqrt{\hat{r}_1}} \right. \\ \left. - \frac{3}{2} \frac{(\sqrt{\hat{r}_2} - a_*)^2}{\sqrt{\hat{r}_2}(\sqrt{\hat{r}_2} - \sqrt{\hat{r}_1})(\sqrt{\hat{r}_2} - \sqrt{\hat{r}_3})} \ln \frac{\sqrt{\hat{r}} - \sqrt{\hat{r}_2}}{\sqrt{\hat{r}_{ms}} - \sqrt{\hat{r}_2}} \right. \\ \left. - \frac{3}{2} \frac{(\sqrt{\hat{r}_3} - a_*)^2}{\sqrt{\hat{r}_3}(\sqrt{\hat{r}_3} - \sqrt{\hat{r}_1})(\sqrt{\hat{r}_3} - \sqrt{\hat{r}_2})} \ln \frac{\sqrt{\hat{r}} - \sqrt{\hat{r}_3}}{\sqrt{\hat{r}_{ms}} - \sqrt{\hat{r}_3}} \right], \quad (3.191)$$

where

$$\sqrt{\hat{r}_1} = \sqrt{2} \cos \left(\frac{1}{3} \cos^{-1} a_* - \frac{\pi}{3} \right), \quad (3.192)$$

$$\sqrt{\hat{r}_2} = \sqrt{2} \cos \left(\frac{1}{3} \cos^{-1} a_* + \frac{\pi}{3} \right), \quad (3.193)$$

$$\sqrt{\hat{r}_3} = -\sqrt{2} \cos \left(\frac{1}{3} \cos^{-1} a_* \right). \quad (3.194)$$

It should be noted that in the non-relativistic limit this boundary correction is reduced to the boundary correction factor:

$$f_{NR} = 1 - \sqrt{\frac{\hat{r}_{in}}{\hat{r}}}. \quad (3.195)$$

Correction factors f_R in the relativistic disk as well as f_{NR} in the non-relativistic disk are shown in figure 3.18.

In the case of the Schwarzschild black hole ($a_* = 0$), the relativistic correction factor is smaller than the non-relativistic one, and the relativistic correction is significant. In the case of $a_* \sim 0.2$, the relativistic correction factor resembles the non-relativistic one, except for a somewhat smaller inner edge. For $a_* \gtrsim 0.2$, due to the relativistic correction of the hole spin, the correction factor increases with decreasing the inner edge. When $a_* \sim 0.9$, the relativistic correction factor is almost unity, and therefore the effective temperature becomes almost Newtonian without the boundary correction.

3.6 Relativistic Tori

So far, we have considered geometrically thin disks with accretion flows. Their generalization toward geometrically thick systems are of importance, but not straightforward due to our poor understanding on detailed

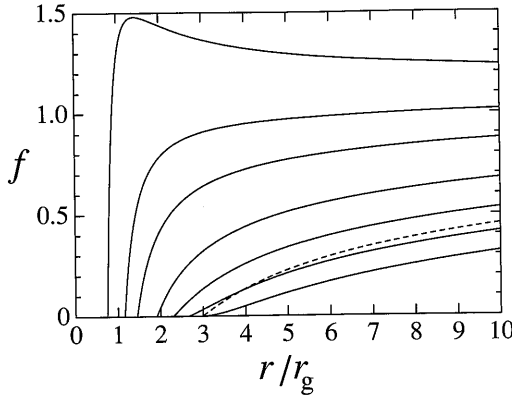


Figure 3.18

Boundary corrections f_R in the relativistic disk (solid curves) and f_{NR} in the non-relativistic disk (dashed one). The spin parameter a_* for f_R is 0, 0.2, 0.4, 0.6, 0.8, 0.9, 0.998 from bottom to top.

processes concerning angular-momentum transport and heat generation in disks. However, some important characteristics of geometrically thick disks might be perspective without considering the angular-momentum and heat-transport processes. In this context, we present here classical studies on relativistic tori – Polish doughnuts – with no accretion flow, constructed by Abramowicz et al. (1978) and Kozłowski et al. (1978).¹⁵

We consider the case where the gravitational field by a central black hole is steady and axially symmetric (see appendix A). The metric is then given in terms of spherical coordinates as

$$ds^2 = g_{tt}dt^2 + 2g_{t\varphi}dtd\varphi + g_{\varphi\varphi}d\varphi^2 + g_{rr}dr^2 + g_{\theta\theta}d\theta^2, \quad (3.196)$$

where $\partial g_{ik}/\partial t = \partial g_{ik}/\partial\varphi = 0$ with $g_{tt} > 0$. The gas in a torus is assumed to be a perfect fluid. The energy-momentum tensor, T_i^k , is then written as

$$T_i^k = (\varepsilon + p)u_i u^k - \delta_i^k p, \quad (3.197)$$

where ε is the internal energy per unit proper volume, p the gas pressure measured in the comoving frame, and u^i the four velocity of the fluid.

Now, let us define the angular velocity of the fluid, Ω , and its angular

¹⁵The structure of relativistic tori under the pseudo-Newtonian potential (Madau 1988) as well as their continuum and line spectra are explained in section 3.4 of the first edition (Kato et al. 1998).

momentum per unit mass, ℓ , by

$$\Omega \equiv \frac{u^\varphi}{u^t} = \frac{d\varphi}{dt}, \quad (3.198)$$

$$\ell \equiv -\frac{c^2 u_\varphi}{u_t}. \quad (3.199)$$

The angular velocity defined above is that observed at infinity.¹⁶

Concerning definition of angular momentum, there is some ambiguity.¹⁷ The above definition of ℓ is natural and reasonable in the sense that it is a constant of motion not only in the vacuum, but also in an axi-symmetric perfect fluid (Kozłowski et al 1978).¹⁸

Then, from the above definitions it follows that

$$(u_t)^{-2} = -\frac{g_{\varphi\varphi} + 2\ell g_{t\varphi} + \ell^2 g_{tt}}{g_{t\varphi}^2 - g_{tt}g_{\varphi\varphi}}, \quad (3.200)$$

$$\Omega = \frac{g_{t\varphi} + \ell g_{tt}}{g_{\varphi\varphi} + \ell g_{t\varphi}}, \quad \ell = -\frac{g_{t\varphi} + \Omega g_{\varphi\varphi}}{g_{tt} + \Omega g_{t\varphi}}. \quad (3.201)$$

The relativistic Euler equation is then written as (Abramowicz et al. 1978)

$$\frac{1}{\varepsilon + p} \nabla_i p = -\nabla_i \ln(u_t) + \frac{\Omega}{1 - \Omega \ell} \nabla_i \ell, \quad (3.202)$$

where ∇_i is $\partial/\partial r$ or $\partial/\partial\theta$. Now we consider a barotropic gas where p is a function of ε , i.e.,

$$p = p(\varepsilon). \quad (3.203)$$

Then, the left-hand side of equation (3.202) can be expressed as a gradient of a term, which means that the second term on the right-hand side must also be so, i.e., $\Omega = \Omega(\ell)$. That is, the surfaces of constant p , ε , ℓ , and Ω all coincide with each other.

Integration of equation (3.202) gives

$$\int_{p_{\text{in}}}^p \frac{dp}{\varepsilon + p} \equiv W_{\text{in}} - W = -\ln \frac{u_t}{(u_t)_{\text{in}}} + F(\ell), \quad (3.204)$$

¹⁶The angular velocity measured by an observer at disk is $\Omega_0 = cu^\varphi = d\varphi/d\tau$.

¹⁷Alternative definitions are, e.g., $\ell_0 \equiv -cu_\varphi$, or $\ell_* \equiv -c^2 u_\varphi u^t$.

¹⁸In section 2.5, we have defined angular momentum by $-cu_\varphi$. In this definition, the angular momentum ℓ is given by $\ell = [GMr^2/(r - 3r_g/2)]^{1/2}$ in the case of the Schwarzschild metric. The radius of the marginally stable circular orbit, r_{ms} , is $3r_g$ and the angular momentum of the circular orbit at the radius, ℓ_{ms} , is $\sqrt{3}cr_g$ (see section 2.5). In the present definition of angular momentum, it is $\ell = [GMr^3/(r - r_g)^2]^{1/2}$ in the case of the Schwarzschild metric and $\ell_{\text{ms}} = (3\sqrt{6}/4)cr_g$, although $r_{\text{ms}} = 3r_g$ is unchanged.

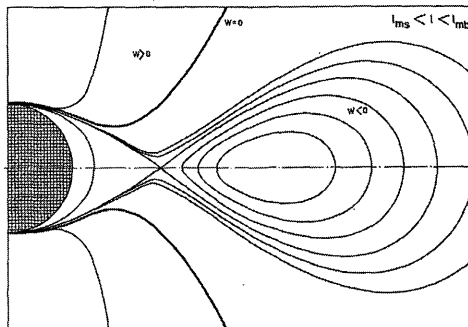


Figure 3.19

Schematical picture showing equatorial surfaces of tori with $\ell_{\text{ms}} < \ell < \ell_{\text{mb}}$. The interior of the hole is dashed. This is the meridional section of the torus. (After Abramowicz et al. 1978)

where

$$F(\ell) = \int_{\ell_{\text{in}}}^{\ell} \frac{\Omega d\ell}{1 - \Omega\ell}. \quad (3.205)$$

Here, the subscript “in” refers to the inner edge of the tori. The quantity W is taken so that it becomes negative inside the tori where $p > 0$.

If we specify $\Omega = \Omega(\ell)$, we can construct a torus model by solving the above set of equations. That is, by solving equation (3.201) with respect to Ω or ℓ we obtain $\ell(r, \theta)$ and $\Omega(r, \theta)$. Then, from equation (3.204), we have $W(r, \theta)$ and $p(r, \theta)$.

As an important example, a torus model with a constant ℓ is shown in figure 3.19 to a case in which $\ell_{\text{ms}} < \ell < \ell_{\text{mb}}$. The equipotential surfaces with $W < 0$ are closed and detached from the central hole. The matter can fill each of these closed equipotential surface [i.e., surfaces $W(r, \theta) = \text{const.} < 0$]. One of equipotential surfaces has a sharp cusp on the equatorial plane, which is located between r_{mb} and r_{ms} . Figure 3.20 schematically shows locations of the cusp and the center of the torus in relation to the radial distribution of the Keplerian angular momentum. At the center of the torus, the pressure is maximum, since the rotation is super-Keplerian inside while sub-Keplerian outside. Between the cusp and the center, the pressure gradient force is directed inward, but at the cusp it vanishes. Inside the cusp the gas freely falls toward the central hole.

Topological differences of equipotential surfaces by differences of (constant) ℓ are shown in figure 3.21. As shown in panel (a), there is no steady

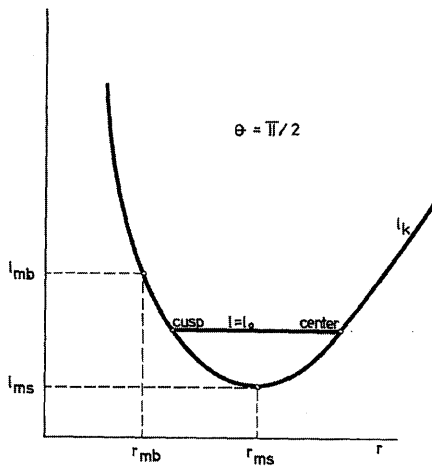


Figure 3.20

Schematic picture showing locations of the center and cusp of torus in the case of $\ell_{ms} < \ell < \ell_{mb}$. (After Abramowicz et al. 1978)

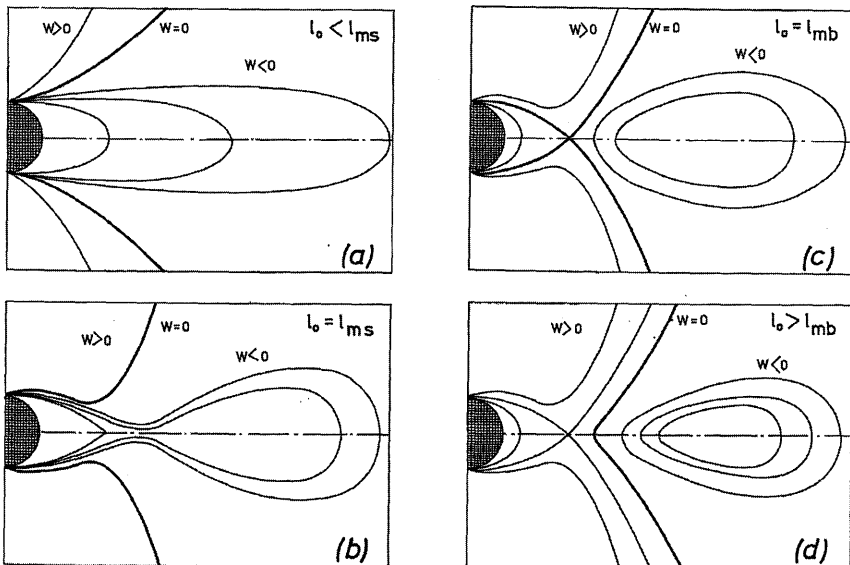


Figure 3.21

Topological differences of equipotential surfaces by difference of (constant) angular momentum ℓ . (After Abramowicz et al. 1978)

torus when $\ell < \ell_{\text{ms}}$, since all equipotential surfaces touch the hole. In the case in which $\ell > \ell_{\text{mb}}$, the disks have no cusp, since the curve of $W = 0$ is detached from a hole.

As will be discussed in section 8.3, the innermost region of steady accretion disks is classified by their direct origin of accretion into two types, i.e., *pressure-driven* and *viscosity-driven* accretion flows. The torus models presented here suggest some important characteristics of accretion disks in the vertical direction, which distinguish the pressure-driven and viscosity-driven accretion flows. The torus with $\ell_{\text{ms}} < \ell < \ell_{\text{mb}}$ suggests that the pressure-driven flows will have a relatively sharp inner edge and a clear funnel along the rotation axis. The torus with $\ell < \ell_{\text{ms}}$ suggests that the viscosity-driven accretion flows will have no sharp inner edge and the matter will fall toward the center, while keeping a relatively wide vertical thickness. It is further supposed that a funnel along the rotation axis will develop less, compared with the case of pressure-driven accretion flows.

References

- Abramowicz M., Jaroszyński M., Sikora M. 1978, A&A 63, 221
 Adams F.C., Shu F.H. 1986, ApJ 308, 836
 Adams F.C., Lada C.J., Shu F.H. 1987, ApJ 312, 788
 Adam J., Störzer H., Shaviv G., Wehrse R. 1988, A&A 193, L1
 Adams J. 1990, A&A 240, 541
 Artemova I.V., Bisnovatyi-Kogan G.S., Björnsson G., Novikov I.D. 1996,
 ApJ 456, 119
 Asaoka I. 1989, PASJ 41, 763
 Bardeen J.M., Press W.H., Teukolsky S.A. 1972, ApJ 178, 347
 Beall J.H. 1987, ApJ 316, 227
 Begelman M.C., McKee C.F. 1983, ApJ 271, 89
 Begelman M.C., McKee C.F., Shields G.A. 1983, ApJ 271, 70
 Blandford R.D., Znajek R.I. 1977, MNRAS 179, 433
 Calvani M., Nobili L. 1983, in *Astrophysical Jets*, ed. A. Ferrari and A.G.
 Pacholczyk (Reidel, Dordrecht), p189
 Cannizzo J.K., Wheeler J.C. 1984, ApJS 55, 367
 Chandrasekhar S. 1960, *Radiative Transfer* (Dover Publishing Inc., New
 York)
 Chen K., Halpern J.P., Filippenko A.V. 1989, ApJ 339, 742
 Chen K., Halpern J.P. 1989, ApJ 344, 115
 Cunningham C. 1975, ApJ 202, 788
 Cunningham C. 1976, ApJ 208, 534

- Czerny B., Czerny M., Grindlay J.E. 1986, ApJ 311, 241
Czerny B., Elvis M. 1987, ApJ 321, 305
Davis S. W., Blaes O. M., Hubeny I., Turner N. J. 2005, ApJ 621, 372
Di Matteo T. 1998, MNRAS 299, L15
Di Matteo T., Celotti A., Fabian A. C. 1999, MNRAS 304, 809
Dotani T. et al. 1997, ApJ 485, L87
Ebisawa K., Mitsuda K., Hanawa T. 1991, ApJ 367, 213
Eracleous M., Halpern J.P. 1994, ApJS 90, 1
Fabian A.C., Rees M.J., Stella L., White N.E. 1989, MNRAS 238, 729
Fanton C., Calvani M., de Felice F., Čadež A. 1997, PASJ 49, 159
Filipov L., Shakura N.I., Ljubarskii Yu. 1988, Adv. Space Res. 8, 163
Fishbone L.G., Moncrief V. 1976, ApJ 207, 962
Friedjung M. 1985, A&Ap 146, 366
Fu A., Taam R.E. 1990, ApJ 349, 553
Fukue J. 1982, PASJ 34, 163
Fukue J. 1992, PASJ 44, 669
Fukue J. 2007, PASJ 59, 687
Fukue J., Akizuki C. 2006, PASJ 58, 1039
Fukue J., Sanbuichi K. 1993, PASJ 45, 831
Fukue J., Yokoyama T. 1988, PASJ 40, 15
Galeev A. A., Rosner R., Vaiana G. S. 1979, ApJ 229, 318
Gebal D., Pelat D. 1981, A&A 95, 18
Guilbert P. W., Rees M.J. 1998, MNRAS 233, 475
Haardt F., Maraschi L. 1991, ApJ 380, L51
Hanawa T. 1989, ApJ 341, 948
Hayakawa S. 1981, PASJ 33, 365
Horne K., Marsh T.R. 1986, MNRAS 218, 761
Hōshi R. 1984, PASJ 36, 785
Hōshi R., Inoue H. 1988, PASJ 40, 421
Hubeny I. 1990, ApJ 351, 632
Hubeny I., Agol E., Blaes O., Krolik J. H. 2000, ApJ 533, 710
Hubeny I., Blaes O., Krolik J. H., Agol E. 2001, ApJ 559, 680
Hubeny I., Hubeny V. 1997, ApJ 484, L37
Hubeny I., Hubeny V. 1998, ApJ 505, 558
Hui Y., Krolik J. H., Hubeny I. 2005, ApJ 625, 913
Karas V., Kraus P. 1996, PASJ 48, 771
Karas V., Vokrouhlický D., Polnarev A.G. 1992, MNRAS 259, 569
Kato S. 1993, PASJ 45, 219
Kawaguchi T., Mineshige S., Machida M., Matsumoto R., Shibata K. 2000, PASJ 52, L1

- Kenyon S.J., Hartmann L. 1987, ApJ 323, 714
Ko Y.-K., Kallman T.R. 1991, ApJ 374, 721
Kojima Y. 1991, MNRAS 250, 629
Kozłowski M., Jaroszyński M., Abramowicz M. 1978, A&A 63, 209
Křiž S., Hubeny I. 1986, BAIC 37, 129
Kubota A., Tanaka Y., Makishima K., Ueda Y., Dotani T., Inoue H., Yamaoka K. 1998, PASJ 50, 667
Kusaka T., Nakano T., Hayashi C. 1970, PTP 44, 1580
Laor A. 1991, ApJ 376, 90
Laor A., Netzer H. 1989, MNRAS 238, 897
Liang E.P., Nolan P.L. 1984, SSRv 38, 353
Lightman A. P., White T. R. 1988, ApJ 335, 57
Lindquist R.W. 1966, AnnPhys 37, 487
Liu B.F., Mineshige S., Shibata K. 2002, ApJ 572, L173
Liu B.F., Mineshige S., Ohsuga K. 2003, ApJ 587, 571
Lu Y.J., Zhou Y.Y., Yu K.N., Young E.C.M. 1996, ApJ 472, 564
Luminet J.-P. 1979, A&A 75, 228
Lynden-Bell D., Pringle J.E. 1974, MNRAS 168, 603
Lynden-Bell D. 1978, Physica Scripta 17, 185
Lyutyi V.M., Syunyaev R.A. 1976, SovAstron 20, 290
Madau P. 1988, ApJ 327, 116
Makishima K. et al. 2000, ApJ 535, 632
Malbet F., Bertout C. 1991, ApJ 383, 814
Marsh T.R., Horne K. 1988, MNRAS 235, 269
Matt G., Perola G.C., Stella L. 1993, A&A 267, 643
Merloni A., Fabian A.C. 2001, MNRAS 321, 549
Meyer F., Meyer-Hofmeister E. 1982, A&A 106, 34
Meyer F., Liu B. F., Meyer-Hofmeister E. 2000, A&A 361, 175
Mihalas D., Mihalas B.W. 1984, *Foundations of Radiation Hydrodynamics* (Oxford University Press, New York)
Mineshige S., Tuchman Y., Wheeler J.C. 1990, ApJ 359, 176
Mineshige S., Wood J.H. 1990, MNRAS 247, 43
Mineshige S., Hirano A., Kitamoto S., Yamada T.T., Fukue J. 1994, ApJ 426, 308
Mitsuda K., Inoue H., Koyama K., Makishima K., Matsuoka M., Ogawara Y., Shibasaki M., Suzuki K., Tanaka Y., Hirano T. 1984, PASJ 36, 741
Moderski R., Sikora M. 1996, MNRAS 283, 854

- Mushotzky R. F., Done, C., Pounds K. A. 1993, ARA&A 31, 717 Narayan R., Mahadevan R., Grindlay J. E., Popham R. G., Gammie C. 1998, ApJ 492, 554
- Novikov I.D. and Thorne K.S. 1973, in *Black Holes*, ed. C. DeWitt and B. DeWitt (Gordon and Breach, New York)
- Okazaki A.T. 1996, PASJ 48, 305
- Okazaki A.T., Kato S., Fukue J. 1987, PASJ 39, 473
- Paczyński B. and Wiita P.J. 1980, A&A 88, 23
- Page D.N., Thorne K.S. 1974, ApJ 191, 499
- Pringle J.E. 1974, PhD Thesis, Cambridge University
- Rees M.J., Begelman M.C., Blandford R.D., Phinney E.S. 1982, Nature 295, 17
- Riffert H., Herold H. 1995, ApJ 450, 508
- Ross R.R., Fabian A.C., Mineshige S. 1992, MNRAS 258, 189
- Rozanska A., Czerny B. 2000, arxxt conf, E120
- Rybicki G.B., Lightman A.P. 1979, *Radiative Processes in Astrophysics* (John Wiley & Sons, New York)
- Saito N. 1989, PASJ 41, 1174
- Sanbuichi K., Yamada T., Fukue J. 1993, PASJ 45, 443
- Shakura N.I., Sunyaev R.A. 1973, A&A 24, 337
- Shapiro S.L., Lightman A.P., Eardley D.H. 1976, ApJ 204, 187
- Shaviv G., Wehrse R. 1986, A&A 159, L5
- Shimura T., Takahara F. 1993, ApJ 440, 610
- Shu F.H. 1991, *The Physics of Astrophysics Vol.1: Radiation* (University Science Books, California)
- Shibata K., Yokoyama T. 1999, ApJ 526, L49
- Sikora M., Wilson D.B. 1981, MNRAS 197, 529
- Smak J. 1981, Acta Astron 31, 395
- Smak J. 1989, Acta Astron 39, 201
- Takahara F. 1979, PTP 62, 629
- Tanaka Y., Nandra K., Fabian A.C., Inoue H., Otani C., Dotani T., Hayashida K., Iwasawa K. et al. 1995, Nature 375, 659
- Thorne K.S., Price R.H. 1975, ApJ 195, L101
- Tuchman Y., Mineshige S., Wheeler J.C. 1990, ApJ 359, 164
- Ueno S., Mineshige S., Negoro H., Shibata K., Hudson H. S. 1997, ApJ 484, 920
- Wade R.A. 1984, MNRAS 208, 381
- Wandel A., Petrosian V. 1988, ApJ 329, L11
- Yamada T., Fukue J. 1993, PASJ 45, 97
- Yamada T., Mineshige S., Ross R.R., Fukue J. 1994, PASJ 46, 553

- Yokoyama T., Shibata K. 1998, ApJ 494, L113
Yokoyama T., Shibata K. 2001, ApJ 549, 1160
Young P., Schneider D.P., Shectman S.A. 1981, ApJ 245, 1035
Zhang S. N., Cui W., Chen W., Yao Y., Zhang X., Sun X., Wu X., Xu H. 2000, Science 287, 1239

Secular and Thermal Instabilities

Various kinds of time variabilities have been observed in black-hole binaries and AGNs. Some of these time variations could be due to the instabilities of accretion disks surrounding black holes. Viscous and non-adiabatic processes are really known to introduce many kinds of instabilities in accretion disks. These instabilities may be classified into three types: secular instability, thermal one, and overstabilities of waves and oscillations. Among them, the secular and thermal instabilities of the classical types of disks (introduced in chapter 3) are discussed in this chapter. Overstabilities of waves and oscillations are briefly discussed in chapter 11.

An examination of the instability processes under general circumstances is not always useful for understanding the mechanism or essence of each instability process. An appropriate way to do this is to examine each instability separately by filtering out other instabilities and oscillation modes by introducing some approximations. This filtering can be done by considering timescales. The secular instability is due to a viscous process, which occurs on the viscous timescale. The thermal instability is due to a thermal process, which occurs on the thermal timescale. In standard disks the viscous timescale is much longer than the thermal one, as discussed in the previous chapter. Hence, when we consider the secular instability, we filter out the thermal mode by assuming that thermal balance is achieved instantly. When we consider the thermal instability, on the other hand, we assume that the instability occurs without any viscous adjustment of the structure of the disks to the perturbations.

In any study of both the secular and thermal instabilities, we always filter out acoustic oscillations, which occur on a shorter timescale than those of the above-mentioned two instabilities. The filtering of acoustic

oscillations is made by neglecting the terms of the time derivatives in the momentum equations.

Generally, phenomena of longer timescale can be examined with fewer modifications of steady equilibrium models, or of equations describing steady equilibrium states. In this sense, we start from the secular instability.

4.1 Secular Instability

The *secular instability*¹ is a phenomenon that results from a spatial modulation of the accretion rate, and leads to a coaxial density variation pattern. Since this density variation is the result of a spatial change in the accretion rate, it is obvious that the timescale associated with this instability is the viscous timescale, which is longer than the thermal and dynamical ones in geometrically thin accretion disks (see section 3.2). Hence, the essence of this instability mechanism can be understood well by introducing approximations in which the dynamical and thermal equilibria are maintained during development of the perturbations. That is, we use the same equations as those used to derive the steady standard disk models, as far as the momentum and thermal balances are concerned. By introducing these approximations, the thermal and oscillatory modes are filtered out. The secular instability of accretion disks was found by Lightman and Eardley (1974).

4.1.1 Basic Equations

The hydrostatic balance in the vertical direction is written as [see equation (3.35)]

$$p = \frac{1}{2} \Omega^2 \Sigma H, \quad (4.1)$$

where p is the pressure and H the disk half-thickness. The radial-force balance is the balance between the gravitational and centrifugal forces [equation (3.27)],

$$\Omega = \Omega_K = \sqrt{\frac{GM}{r^3}}. \quad (4.2)$$

The steady-force balance in the φ -direction can be written in the form of angular-momentum balance, which is [see equation (3.15)]

$$\dot{M} \frac{d}{dr} (r^2 \Omega) = - \frac{\partial}{\partial r} (2\pi r^2 T_{r\varphi}). \quad (4.3)$$

¹The name of this instability comes from the fact that it occurs due to a long time scale. This instability is sometimes called the viscous instability.

Here, $T_{r\varphi}(r, t)$ is the $r\varphi$ -component of the viscous stress tensor and \dot{M} is the mass-accretion rate at radius r ; i.e.,

$$\dot{M}(r, t) = -2\pi r \Sigma v_r, \quad (4.4)$$

which is now not constant, but depends on time as well as radius.

In addition to the dynamical equilibria in the z -, r -, φ -directions, we adopt thermal balance; i.e., $Q_{\text{vis}}^+ = Q_{\text{rad}}^-$. Since we consider here optically thick disks, the heat balance between viscous heating, Q_{vis}^+ , and radiative cooling, Q_{rad}^- , is written as [equations (3.36), (3.39), and (3.40)]

$$\frac{16cp_{\text{rad}}}{\bar{\kappa}\Sigma} = -\frac{3}{2}\Omega T_{r\varphi}, \quad (4.5)$$

where $\bar{\kappa}$ is the opacity.

The remaining equation is the equation of mass conservation. The equation should be in a time-dependent form, since we are now interested in the viscous evolution of disks. Since we consider axisymmetric perturbations, we adopt [see equation (3.11)]

$$2\pi r \frac{\partial \Sigma}{\partial t} = \frac{\partial \dot{M}}{\partial r}. \quad (4.6)$$

Elimination of \dot{M} from equations (4.6) and (4.3) gives [see equation (3.16)]

$$\frac{\partial \Sigma}{\partial t} = \frac{\partial}{r\partial r} \left\{ \left[\frac{d}{dr} (r^2 \Omega) \right]^{-1} \frac{\partial}{\partial r} \left(-r^2 T_{r\varphi} \right) \right\}. \quad (4.7)$$

If $T_{r\varphi}$ is expressed in terms of Σ and r (this is made below), equation (4.7) becomes a kind of diffusion equation governing the viscous (secular) time evolution of Σ . An examination of this equation is made in section 3.1. We show there for some typical cases of the form $T_{r\varphi}$ how angular momentum is transported outward and how the disk expands in the radial direction by viscous processes. In the case of radiation-pressure-dominated disks, however, the diffusion process can have a negative diffusion coefficient, and thus can lead to instability. This instability is known as a secular instability (Lightman and Eardley 1974).

4.1.2 Negative Diffusion and Instability

Here, we adopt the conventional Shakura-Sunyaev type α -model,

$$T_{r\varphi} = -2\alpha p H. \quad (4.8)$$

Furthermore, we consider the innermost region of the standard Shakura-Sunyaev disk, where the radiation pressure dominates over the gas pressure,

$$p = p_{\text{rad}} = \frac{1}{3}aT^4, \quad (4.9)$$

and $\bar{\kappa}$ comes from electron scattering; i.e., $\bar{\kappa} = \kappa_{\text{es}}$.

Since $\kappa_{\text{es}} \sim \text{const.}$, combining equations (4.1) and (4.5) gives $-T_{r\varphi} \propto \Omega H$, which, if combined with equation (4.8), leads to $p \propto \Omega \propto r^{-3/2}$. That is, p is a spatially given function, independent of time and the distributions of other physical quantities. The relations $p \propto \Omega$ and $p \propto \Omega^2 \Sigma H$ [equation (4.1)] give $H \propto 1/(\Omega \Sigma)$. Equation (4.8) then leads to

$$-T_{r\varphi} \propto \frac{1}{\Sigma}. \quad (4.10)$$

This relation can be derived more directly. In a radiation-pressure-dominated disk, a perturbation of the surface density may occur without any pressure (and temperature) variation, since the pressure is not directly related to the density. If we assume $p = \text{const.}$, the energy balance [equation (4.5)] gives $-T_{r\varphi} \propto 1/\Sigma$, and the vertical hydrostatic balance [equation (4.1)] leads to $H \propto 1/\Sigma$. Furthermore, the definition of $T_{r\varphi}$ [equation (4.8)] gives $-T_{r\varphi} \propto H \propto 1/\Sigma$, which is consistent with the results derived from equation (4.5) under the assumption of $p = \text{const.}$ That is, $-T_{r\varphi} \propto 1/\Sigma$, and $p = \text{const.}$ are really solutions in the present problem.

If relation (4.10) is substituted into equation (4.7), we obtain an equation describing how the surface density Σ evolves with space and time by a viscous process. To clarify the presence of instability, we consider a small-amplitude perturbation superposed on the equilibrium disk. The relation $-T_{r\varphi} \propto \Sigma^{-1}$ shows that the perturbed quantities $T_{r\varphi,1}$ and Σ_1 are related by

$$-T_{r\varphi,1} = \frac{T_{r\varphi,0}}{\Sigma_0} \Sigma_1, \quad (4.11)$$

where subscripts 0 and 1 denote the unperturbed and perturbed quantities, respectively. Since equation (4.7) gives

$$\frac{\partial \Sigma_1}{\partial t} = \frac{\partial}{\partial r} \left\{ \left[\frac{d}{dr} (r^2 \Omega) \right]^{-1} \frac{\partial}{\partial r} \left(-r^2 T_{r\varphi,1} \right) \right\}, \quad (4.12)$$

for small-amplitude perturbations, substitution of equation (4.11) into this equation yields

$$\frac{\partial \Sigma_1}{\partial t} = r \frac{T_{r\varphi,0}}{\Sigma_0} \left[\frac{d}{dr} (r^2 \Omega) \right]^{-1} \frac{\partial^2 \Sigma_1}{\partial r^2} \quad (4.13)$$

for local perturbations, where the derivatives of the unperturbed quantities, say $d\ln\Sigma_0/dr$, are ignored compared with that of the perturbed quantities, say $(1/\Sigma_1)\partial\Sigma_1/\partial r$.

An important point is that equation (4.13) is a kind of a diffusion equation describing the evolution of Σ_1 . The diffusion coefficient, the coefficient of $\partial^2\Sigma_1/\partial r^2$ on the right-hand side of equation (4.13), is negative, since $T_{r\varphi,0} < 0$ and $d(r^2\Omega)/dr > 0$. Negative diffusion means an instability; an annulus region with $\Sigma_1 > 0$ increases Σ_1 further, and the region with $\Sigma_1 < 0$ behaves oppositely.

The diffusion coefficient is on the order of $-\alpha c_s^2/\Omega$. Hence, if the radial wavelength of perturbations is denoted by λ , the growth rate of the instability is $\sim \alpha c_s^2/(\Omega\lambda^2)$. In other words, the timescale, τ , of the instability is

$$\tau \sim \tau_{\text{vis}} \left(\frac{\lambda}{r} \right)^2, \quad (4.14)$$

where τ_{vis} is the viscous timescale, defined by $\tau_{\text{vis}} = (\alpha\Omega)^{-1}(r^2\Omega^2/c_s^2)$. Since we are considering local perturbations ($\lambda < r$), the growth time is shorter than the viscous time, τ_{vis} , by the factor $(\lambda/r)^2$.

The above argument is, however, sufficient to show a general criterion concerning the secular instability. That is, the instability occurs if the changes (at a given radius) of $T_{r\varphi}$ and Σ occur with the same signs [see equation (4.10) or (4.11)], namely

$$\left(\frac{\partial T_{r\varphi}}{\partial \Sigma} \right)_{Q_{\text{vis}}^+ = Q_{\text{rad}}^-} > 0. \quad (4.15)$$

The reason why inequality (4.15) is the criterion of the secular instability can be understood from following considerations. Let us consider a local and sinusoidal perturbation of the surface density in the radial direction, say $\Sigma_1(r) \propto \sin[k(r - r_0)]$, where k is the radial wavenumber of the perturbation and $r = r_0 + \pi/(2k)$ is the place where the amplitude of the surface-density perturbation is the maximum. If inequality (4.15) is satisfied, a spatial variation of the stress tensor, $T_{r\varphi,1}(r)$, resulting from $\Sigma_1(r)$ is in phase with $\Sigma_1(r)$. Then, $T_{r\varphi,1}(r)$ gives rise to a spatial variation of the angular-momentum transport, leading to a spatial variation of the mass-accretion rate, $\dot{M}_1(r)$. Equation (4.3) shows that $\dot{M}_1 \propto -\partial T_{r\varphi,1}/\partial r \propto -\cos[k(r - r_0)]$. This spatial variation of the mass-accretion rate, $\dot{M}_1(r)$, leads to a spatial surface-density variation proportional to $\sin[k(r - r_0)]$, since they are related by continuity [see equation of continuity (4.6)]. This surface-density variation is in phase with the

initial perturbation imposed. This means that the initial perturbation of the surface density is amplified by gas being further accumulated there.

In the middle region of the standard disks, where the opacity still comes from electron scattering, but the gas pressure dominates over the radiation pressure, a secular instability does not occur. In the case of $p \sim p_{\text{gas}}$, equations (4.5) and (4.8) give, respectively,

$$-T_{r\varphi} \propto \frac{T^4}{\Omega\Sigma} \quad \text{and} \quad -T_{r\varphi} \propto \Sigma T. \quad (4.16)$$

Then, combining them leads to $-T_{r\varphi} \propto \Omega^{1/3}\Sigma^{5/3}$. Unlike the case of $p_{\text{rad}} \gg p_{\text{gas}}$, an increase in $-T_{r\varphi}$ brings about an increase in Σ [i.e., inequality (4.15) does not hold]. Hence, in the diffusion equation of Σ_1 , which is obtained from equation (4.12), the diffusion coefficient is positive, different from the case of $p_{\text{rad}} \gg p_{\text{gas}}$. This means that the middle region of the disk is secularly stable.

Similar arguments easily show that the outer region of the disk, where the gas pressure dominates over the radiation pressure and the opacity comes from the free-free processes, is also secularly stable.

4.1.3 Instability Criterion

The marginal state of stability lies between the two extreme cases of $p_{\text{rad}} \gg p_{\text{gas}}$ and $p_{\text{gas}} \gg p_{\text{rad}}$. To obtain the criterion of stability, we consider the case where the equation of state is the sum of the gas and radiation pressures, as

$$p = p_{\text{gas}} + p_{\text{rad}} = \frac{k_B}{\bar{\mu}m_H} \rho T + \frac{1}{3}aT^4, \quad (4.17)$$

where $\bar{\mu}$ is the mean molecular weight. We introduce a dimensionless parameter, β , defined by

$$\beta \equiv \frac{p_{\text{gas}}}{p}. \quad (4.18)$$

Therefore, $p_{\text{rad}}/p = (1 - \beta)$. The $r\varphi$ -component of stress tensor, $T_{r\varphi}$, is assumed to have a general form [see equation (3.50)]:

$$T_{r\varphi} = -2\alpha(p_{\text{gas}}^\mu p^{1-\mu})H. \quad (4.19)$$

The case of $\mu = 0$ corresponds to the conventional Shakura-Sunyaev case considered above, and $\mu = 1$ to the case where $T_{r\varphi}$ is proportional to the gas pressure, p_{gas} , instead of total pressure, p . The opacity is, however, still taken to be constant.

For small-amplitude perturbations over the equilibrium state, equations (4.1) and (4.17) give, respectively,

$$\frac{p_1}{p_0} = \frac{\Sigma_1}{\Sigma_0} + \frac{H_1}{H_0}, \quad (4.20)$$

$$\frac{p_1}{p_0} = \beta \frac{\Sigma_1}{\Sigma_0} - \beta \frac{H_1}{H_0} + (4 - 3\beta) \frac{T_1}{T_0}. \quad (4.21)$$

Furthermore, by eliminating $T_{r\varphi}$ from equations (4.5) and (4.19), we obtain

$$(1 + \mu) \frac{\Sigma_1}{\Sigma_0} + (-4 + \mu) \frac{T_1}{T_0} + (1 - \mu) \frac{H_1}{H_0} + (1 - \mu) \frac{p_1}{p_0} = 0. \quad (4.22)$$

Combining the above three equations, we can express p_1/p_0 , H_1/H_0 , and T_1/T_0 in terms of Σ_1/Σ_0 . The results are

$$\frac{p_1}{p_0} = -\frac{8\beta + 8\mu - 8\beta\mu}{4 - 10\beta - 7\mu + 7\beta\mu} \frac{\Sigma_1}{\Sigma_0}, \quad (4.23)$$

$$\frac{H_1}{H_0} = -\frac{4 - 2\beta + \mu - \beta\mu}{4 - 10\beta - 7\mu + 7\beta\mu} \frac{\Sigma_1}{\Sigma_0}, \quad (4.24)$$

$$\frac{T_1}{T_0} = -\frac{4\beta + 2\mu - 2\beta\mu}{4 - 10\beta - 7\mu + 7\beta\mu} \frac{\Sigma_1}{\Sigma_0}. \quad (4.25)$$

The use of these relations and equation (4.19) finally gives

$$\frac{T_{r\varphi,1}}{T_{r\varphi,0}} = -\frac{4 + 6\beta + \mu - \beta\mu}{4 - 10\beta - 7\mu + 7\beta\mu} \frac{\Sigma_1}{\Sigma_0}, \quad (4.26)$$

where we have used $\rho_1/\rho_0 = \Sigma_1/\Sigma_0 - H_1/H_0$. In the limit of $\beta = 0$ and $\mu = 0$, this equation certainly reduces to equation (4.11).

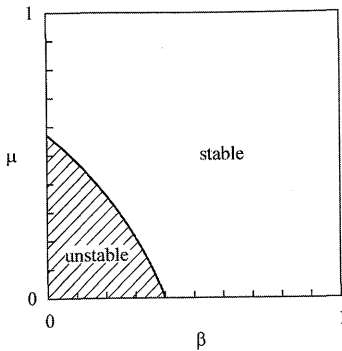
The numerator of equation (4.26) is always positive. Hence, a condition of a secular instability, inequality (4.15), is

$$4 - 10\beta - 7\mu + 7\beta\mu > 0. \quad (4.27)$$

The unstable domain on the $\mu-\beta$ plane is shown in figure 4.1.

In the case of the conventional Shakura-Sunyaev type stress tensor, i.e., $\mu = 0$, the condition of instability is

$$\beta < \frac{2}{5}. \quad (4.28)$$

**Figure 4.1**

Secularly unstable domain on the parameter plane (the μ - β plane). The dimensionless parameters are β ($\equiv p_{\text{gas}}/p$) and μ , specifying $t_{r\varphi}$; i.e., $t_{r\varphi} = -\alpha p_{\text{gas}}^{\mu} p^{1-\mu}$.

That is, if the fraction of the radiation pressure increases to over 3/5 of the total pressure, the disk becomes secularly unstable. Even in disks with $p = p_{\text{rad}}$ (i.e., $\beta = 0$), however, they are stable if

$$\mu > \frac{4}{7}. \quad (4.29)$$

In the limit of gas pressure-dominated disks ($\beta = 1$), the left-hand side of equation (4.27) is -6 , and thus the disks are always secularly stable.

4.2 Thermal Instability

A *thermal instability* is a process where a temperature perturbation over the equilibrium one is amplified by thermal processes. This implies that the energy equation should be taken into account in a time-dependent form. This suggests that the characteristic timescale associated with this instability is the thermal one. The detailed examinations given below really shows that the instability occurs on the thermal timescale. The thermal instability has been studied since the middle of the 1970's (Shibazaki and Hōshi 1975; Shakura and Sunyaev 1976; Pringle et al. 1976; Pringle 1976; Piran 1978, and others).

4.2.1 Basic Equations

In a study of the thermal instability, perturbations can be approximated to occur while maintaining dynamical equilibrium, since the dynamical

timescale is shorter than the thermal one. That is, as in the case of a secular instability, we take equations (4.1) and (4.2); that is,

$$p = \frac{1}{2} \Omega^2 \Sigma H, \quad (4.30)$$

$$\Omega = \Omega_K = \sqrt{\frac{GM}{r^3}}. \quad (4.31)$$

Unlike the case of a secular instability, we do not adopt here the equation (4.3), the equation of angular momentum balance, although it approximately holds during the development of thermal perturbations. The adoption of equation (4.3) makes analyses of thermal instability complicated, since an additional variable, v_r , is then introduced, and we need one more equation to describe v_r . Without performing such complicated procedures, we can study thermal instability by introducing a simple approximation.

Since the force balance between two major forces, the centrifugal force and the gravitational one, holds in the radial direction to a good approximation [see equation (4.31)], mass motion resulting from a temperature change can occur only in the vertical direction. That is, the surface density, Σ , is approximately unchanged during the development of thermal perturbations; i.e.,

$$\Sigma = \text{const.} \quad (4.32)$$

Although a vertical expansion or contraction occurs, the vertical hydrostatic balance is maintained during the development of perturbations, because, as mentioned before, the dynamical timescale is shorter than the thermal one by a factor of $\sim 1/\alpha (> 1)$ (see subsection 3.2.3). That is, a constant Σ means [see equation (4.30)]

$$p \propto H. \quad (4.33)$$

Another difference from the case of the secular instability is that we do not adopt $Q_{\text{vis}}^+ = Q_{\text{rad}}^-$, since a thermal imbalance between Q_{vis}^+ and Q_{rad}^- is the source of the present instability.

4.2.2 Thermal Behaviors

Let us first consider the innermost region of disks, where $p \simeq p_{\text{rad}}$, $\bar{\kappa} \sim \kappa_{\text{es}}$, and $-T_{r\varphi}$ is given by equation (4.8). The heating per unit

surface, $Q_{\text{vis}}^+ (= -3\Omega T_{r\varphi}/2)$, is proportional to $-T_{r\varphi}$, which is proportional further to pH , and thus [see equation (4.33) and subsection 3.2.4]

$$Q_{\text{vis}}^+ \propto H^2 \propto T^8. \quad (4.34)$$

On the other hand, the cooling rate per unit surface, $Q_{\text{rad}}^- (= 16cp_{\text{rad}}/\bar{\kappa}\Sigma)$, is proportional to H (see also subsection 3.2.4),

$$Q_{\text{rad}}^- \propto H \propto T^4. \quad (4.35)$$

In the unperturbed state, Q_{vis}^+ and Q_{rad}^- are balanced. However, if, for example, the temperature increases slightly over that of the equilibrium state, the disk expands in the vertical direction, since $H \propto p \propto T^4$. Then, both Q_{vis}^+ and Q_{rad}^- increase, but the increase of heating overcomes that of cooling [compare equations (4.34) and (4.35)]. This means that the specific entropy of the gas increases, which leads to an increase in T , since the specific entropy, s , is $4aT^3/3\rho$, which increases with T , as $s \propto T^7$. In this way, the increase of T is fed back positively to the increase of T , and the disk becomes unstable.

The above examination was made in the special case of $p \sim p_{\text{rad}}$ and $\bar{\kappa} \sim \kappa_{\text{es}}$. The above process of argument, however, is sufficient to show that a general criterion concerning the thermal instability of disks can be expressed as (Pringle 1976)

$$\left[\frac{\partial}{\partial T} (Q_{\text{vis}}^+ - Q_{\text{rad}}^-) \right]_{\Sigma} > 0. \quad (4.36)$$

Next, we consider the middle region where the opacity still comes from electron scattering, but the gas pressure dominates over the radiation pressure; i.e., $\bar{\kappa} \sim \kappa_{\text{es}}$ and $p \sim p_{\text{gas}}$. The $r\varphi$ -component of the stress tensor is still given by equation (4.8). In this case, as the rate of viscous heating, we have

$$Q_{\text{vis}}^+ \propto H^2 \propto T. \quad (4.37)$$

The last relation comes from $\Omega H \sim c_s$ [see equation (4.30)]. The temperature dependence of the rate of radiative cooling is, on the other hand, unchanged; i.e., we have

$$Q_{\text{rad}}^- \propto T^4. \quad (4.38)$$

A comparison of the T -dependences of Q_{vis}^+ and Q_{rad}^- shows that in the gas pressure-dominated case the disk is thermally stable.

4.2.3 Instability Criterion

The above argument is now generalized to disks where the equation of state is given by equation (4.17) and the $r\varphi$ -component of the integrated stress tensor by equation (4.19). The opacity is taken again to be constant. For the thermal mode of perturbations, where $\Sigma_1/\Sigma_0 = 0$, we easily obtain from equations (4.20) and (4.21) that

$$\frac{p_1}{p_0} = \frac{H_1}{H_0}, \quad (4.39)$$

$$\frac{T_1}{T_0} = \frac{1 + \beta}{4 - 3\beta} \frac{H_1}{H_0}. \quad (4.40)$$

Since the heating rate per unit surface, $Q_{\text{vis}}^+ (= -3\Omega T_{r\varphi}/2)$, is proportional to $-T_{r\varphi}$, and thus to $p_{\text{gas}}^\mu p^{1-\mu} H$, the use of equations (4.39), (4.40) and $\rho_1/\rho_0 + H_1/H_0 = 0$ gives

$$\frac{Q_{\text{vis},1}^+}{Q_{\text{vis},0}^+} = \frac{8 - 6\beta - 7\mu + 7\beta\mu}{1 + \beta} \frac{T_1}{T_0}. \quad (4.41)$$

On the other hand, $Q_{\text{rad}}^- \propto p_{\text{rad}}$ and we have

$$\frac{Q_{\text{rad},1}^-}{Q_{\text{rad},0}^-} = 4 \frac{T_1}{T_0}. \quad (4.42)$$

Since the condition of instability is given by equation (4.36), a comparison of equations (4.41) and (4.42) shows that the disk is thermally unstable when

$$4 - 10\beta - 7\mu + 7\beta\mu > 0. \quad (4.43)$$

This criterion is the same as that given for the secular instability [i.e., inequality (4.27)].²

In the above argument the opacity, $\bar{\kappa}$, was taken to be constant, since the case of electron scattering was considered. A generalization to the case where $\bar{\kappa}$ is a function of ρ and T is straightforward. More generally, a generalization to the case where both the cooling rate Q_{rad}^- and the heating rate Q_{vis}^+ are arbitrary function of ρ and T , is also straightforward (Piran 1978).

We notice here some characteristics of the disk thermal instability, which is different from the thermal instability in spherical self-gravitating

²When both thermal and secular instabilities occur, the time development of the disks is governed by the thermal instability, since the timescale of thermal instability is shorter than that of the secular one.

systems (stars). We may simply argue that a system is thermally unstable if an increase in the temperature leads to an increase in the net heating (i.e., heating – cooling). This argument is, however, not always correct. A direct result of an increase in the net heating is not an increase in the temperature, but an increase in the entropy.

A problem is whether a dynamical adjustment of the system to an increase in the entropy results in an increase in the temperature. In self-gravitating stars, if a temperature increase occurs on a global scale, the star expands. This expansion brings about, in many cases, a decrease in the temperature, because the expansion decreases the pressure more than the density,³ leading to a temperature decrease and to thermal stability. In our present problem, however, an increase of temperature brings about an increase in the pressure [see equation (4.1)], rather than a decrease. In other words, the temperature increase leads to an expansion of the disk in the vertical direction, and this expansion does not act so as to decrease the temperature, but rather acts so as to increase the temperature. This is the reason why we can determine the condition of the thermal instability in disks simply only by the sign of $[\partial(Q_{\text{vis}}^+ - Q_{\text{rad}}^-)/\partial T]_{\Sigma} > 0$.

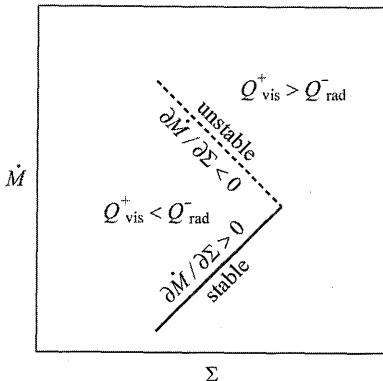
4.3 Stability Examination on \dot{M} - Σ and T - Σ Planes

It is well known in various fields of physics that there are cases where the stability of equilibrium systems can be examined by studying the turning points of equilibrium sequences in some parameter space. Secular and thermal stabilities of disks also belong to such cases. By drawing a sequence of equilibrium disk models on the T - Σ plane (or \dot{M} - Σ plane), we can study the stabilities simply and powerfully.

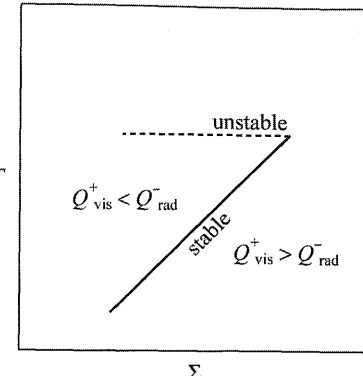
Let us first consider the secular instability. As discussed in chapter 3, the standard disk model at a given radius is a one-parameter sequence on the \dot{M} - Σ plane (figure 4.2, see also figure 3.8). The turning point of the curve is the critical point of the secular stability as long as the effects of accretion motions in the unperturbed disks are neglected. That is, the disks on the lower branch are secularly stable, while the disks on

³Let us consider the case where the dynamical adjustment is made by a homologous expansion of a spherical system. In a homologous expansion, the radial displacement, Δr , of a fluid element, whose initial radial coordinate being r , is proportional to r , i.e., $\Delta r/r = \text{const}$. In such an expansion, the density decreases as $\Delta\rho/\rho = -3\Delta r/r$. The hydrostatic balance, $-dp/dr = \rho GM_r/r^2$, then gives $\Delta p/p = -4\Delta r/r$. (Notice that the mass M_r within the radius r is unchanged.) The equation of state then gives $\Delta T/T = (1/4)(\Delta p/p) = -\Delta r/r$ for gas pressure-dominated stars.

the upper branch are secularly unstable. It is easy to understand that the turning point of the equilibrium sequence on the $\dot{M}-\Sigma$ plane is the marginal state of the secular stability. This is shown below.

**Figure 4.2**

Schematic picture showing a secular instability on the $\dot{M}-\Sigma$ plane.

**Figure 4.3**

Schematic picture showing a thermal instability on the $T-\Sigma$ plane.

As we have shown before, the instability condition is [equation (4.15)]

$$\left(\frac{\partial T_{r\varphi}}{\partial \Sigma} \right)_{Q_{\text{vis}}^+ = Q_{\text{rad}}^-} > 0. \quad (4.44)$$

That is, a secular instability at a given radius occurs when the changes (at the radius) of $T_{r\varphi}$ and Σ occur with the same signs. The next problem is to rewrite this instability condition in terms of other convenient physical quantities. This should be made under the assumption of momentum and thermal equilibria, i.e., on the equilibrium sequence. Along the equilibrium sequence, the angular-momentum balance, $\dot{M}(\ell - \ell_{\text{in}}) = -2\pi r^2 T_{r\varphi}$, holds.⁴ Hence, an increase of $-T_{r\varphi}$ leads to an increase in \dot{M} as long as the boundary condition is unchanged during the time evolution of the perturbations, since ℓ is fixed to be the Keplerian, as $\ell = \Omega_K r^2$. The instability condition is then that changes of Σ and \dot{M} occur with opposite signs along the equilibrium sequence. That is, the instability condition is

$$\left(\frac{\partial \dot{M}}{\partial \Sigma} \right)_{Q_{\text{vis}}^+ = Q_{\text{rad}}^-} < 0. \quad (4.45)$$

⁴This is the integration of equation (4.3), and ℓ_{in} is the specific angular momentum swallowed to the central black hole (also see section 3.2).

On the lower branch of the equilibrium curve, the changes of \dot{M} and Σ occur with the same trend, but after passing the turning point they have an opposite trend. This implies that the turning point represents just the marginally stable disk for the secular stability. As the process of the above derivation shows, this criterion is rather general, and free from the form of the stress tensor and the details of the heating and cooling processes. That is, the condition of a secular instability can be generally written as

$$\left(\frac{\partial \dot{M}}{\partial \Sigma} \right)_{Q^+ = Q^-} < 0, \quad (4.46)$$

independent of the detailed processes of heating and cooling.

We next consider the thermal instability. In this case the turning point on the equilibrium sequence on the T - Σ plane is the marginal point of stability. This can be easily understood, since we have already shown that the instability condition is [equation (4.36)]

$$\left(\frac{\partial Q_{\text{vis}}^+}{\partial T} \right)_{\Sigma} > \left(\frac{\partial Q_{\text{rad}}^-}{\partial T} \right)_{\Sigma}. \quad (4.47)$$

The processes of deriving this relation suggest that this condition of a thermal instability is free from any details of the heating and cooling processes. That is, the condition of thermal instability can be generalized as

$$\left(\frac{\partial Q^+}{\partial T} \right)_{\Sigma} > \left(\frac{\partial Q^-}{\partial T} \right)_{\Sigma}, \quad (4.48)$$

independent of the detailed processes of heating and cooling.

An examination of the shape of the equilibrium sequence on the T - Σ plane (or on the \dot{M} - Σ plane) is a very powerful method to study disk stabilities. Indeed, this method has been extensively applied to studying the accretion-disk thermal-instability in dwarf novae and soft X-ray transients, which is discussed in chapter 5.

It is noted here that the turning points of the equilibrium disk sequence in figures 4.2 and 4.3 are the same. That is, the condition of marginal stability against a secular instability and that against a thermal instability are the same in the case of the standard disks (see previous subsections and also the next subsection). This comes from the following situations. Some examination shows that the equilibrium sequence in figure 4.3 is the sequence of \dot{M} . That is, on the lower-left corner of the curve, \dot{M} is low, and as \dot{M} increases the disk model moves upwards along the curve, and finally reaches the upper-left corner of the curve.

This means that the sign of $(\partial \dot{M} / \partial \Sigma)_{Q+ = Q-}$ is changed at the turning point in figure 4.3, as well as at the turning point in figure 4.2.

4.4 Mathematical Derivation of the Stability Criterion

In previous sections we individually considered the thermal and secular instabilities of standard disks under simplified situations in order to understand the essences of instabilities. Here, mathematical derivations of the stability criteria and of the growth rates are presented in a form that is convenient to generalize, e.g., to studies of those in advection-dominated disks (see section 9.4).

4.4.1 Basic Equations

We now consider geometrically thin axisymmetric disks. We adopt cylindrical coordinates (r, φ, z) whose origin is at the center of the central object and the vertical axis is in the direction of disk rotation. In geometrically thin disks, the thermal and secular timescales are longer than the dynamical one. Because of this, the disks are taken to be in a steady state in the force balances in the r -, φ -, and z -directions, even when the disks are perturbed from an equilibrium state.

(a) Mass conservation

The vertical integration of the equation of continuity is written as

$$\frac{\partial \Sigma}{\partial t} + \frac{\partial}{r \partial r} (r \Sigma v_r) = 0. \quad (4.49)$$

(b) Keplerian rotation

As the force balance in the radial direction, we take simply

$$\Omega = \Omega_K. \quad (4.50)$$

(c) Angular-momentum balance

As already mentioned in sections 4.1 and 4.2, we can adopt

$$\Sigma v_r \frac{d}{r dr} (r^2 \Omega) = \frac{\partial}{r^2 \partial r} (r^2 T_{r\varphi}), \quad (4.51)$$

where $T_{r\varphi}$ is the vertical integration of the $r\varphi$ -component of the viscous stress tensor.

(d) Hydrostatic balance

The vertical integration of the equation of vertical hydrostatic balance gives that the vertically integrated pressure, Π , and the surface density, Σ , are related to the half-thickness of the disk, H , through the angular velocity of Keplerian rotation, Ω_K , as

$$\Omega_K^2 H^2 = \frac{\Pi}{\Sigma}. \quad (4.52)$$

(e) Thermal-energy conservation

We need to carefully consider the vertical integration of the energy equation. The energy equation is now written here in the form (see appendix B)

$$\frac{\partial}{\partial t}(\rho e) + \text{div}[\mathbf{v}(\rho e + p)] - (\mathbf{v} \cdot \nabla)p = q_{\text{vis}}^+ - q_{\text{rad}}^-, \quad (4.53)$$

where ρe is the thermal energy density per unit volume and is

$$\rho e = \frac{1}{\gamma - 1} p_{\text{gas}} + aT^4 = \left[\frac{\beta}{\gamma - 1} + 3(1 - \beta) \right] p, \quad (4.54)$$

since the disk consists of gas and radiation, γ being the ratio of specific heat. The quantity β is the fraction of gas pressure, p_{gas} , to the total pressure, p ($= p_{\text{gas}} + p_{\text{rad}}$); i.e., $\beta = p_{\text{gas}}/(p_{\text{gas}} + p_{\text{rad}})$, \mathbf{v} is the velocity, and q_{vis}^+ and q_{rad}^- are the heating and cooling rates per unit volume, respectively. Other notations have their usual meanings.

We now integrate equation (4.53) in the vertical direction. The vertical integration of $v_z \partial p / \partial z$ is expressed in terms of Π (the vertical integration of pressure) and H in section 7.2 when the disk is steady [see equation (7.37)]. Generalizing the calculations to the time-dependent case, we have

$$-\int v_z \frac{\partial p}{\partial z} dz = \Pi \left(\frac{\partial}{\partial t} + v_r \frac{\partial}{\partial r} \right) \ln H. \quad (4.55)$$

Then, the vertical integration of equation (4.53) gives

$$\frac{\partial E}{\partial t} + \Pi \frac{\partial \ln H}{\partial t} + \frac{1}{r} \frac{\partial}{\partial r} [rv_r(E + \Pi)] - v_r \frac{\partial \Pi}{\partial r} + v_r \Pi \frac{\partial \ln H}{\partial r} = Q_{\text{vis}}^+ - Q_{\text{rad}}^-, \quad (4.56)$$

where E is the vertical integration of ρe , and is⁵

$$E = \left[3(1 - \beta) + \frac{\beta}{\gamma - 1} \right] \Pi, \quad (4.57)$$

⁵In polytropic gases (i.e., $p \propto \rho^{1+1/N}$) with polytropic index of $N = 3$, the value of β is constant in the vertical direction.

and Q_{vis}^+ and Q_{rad}^- are, respectively, the vertical integration of q_{vis}^+ and q_{rad}^- . By using the equation of continuity [equation (4.49)], we can reduce the above energy equation (4.56) to

$$\frac{\partial E}{\partial t} - (E + \Pi) \frac{\partial \ln \Sigma}{\partial t} + \Pi \frac{\partial \ln H}{\partial t} + Q_{\text{adv}}^- = Q_{\text{vis}}^+ - Q_{\text{rad}}^-, \quad (4.58)$$

where Q_{adv}^- is the advective cooling, defined by

$$Q_{\text{adv}}^- = v_r \left[- (E + \Pi) \frac{\partial \ln \Sigma}{\partial r} + \frac{\partial E}{\partial r} + \Pi \frac{\partial \ln H}{\partial r} \right]. \quad (4.59)$$

In equation (4.58) Q_{vis}^+ is written as

$$Q_{\text{vis}}^+ = r T_{r\varphi} \frac{d\Omega}{dr} \quad (4.60)$$

(see also chapter 3), while a detailed expression for Q_{rad}^- is given later when it becomes necessary.

(f) Equation of state

The equation of state is

$$\Pi = \frac{k_B}{\bar{\mu} m_H} \Sigma T + \frac{2}{3} a T^4 H. \quad (4.61)$$

(g) Viscosity description

We adopt the so-called α -model and $T_{r\varphi}$ is taken as

$$T_{r\varphi} = -\alpha \Pi. \quad (4.62)$$

Equations (4.49)–(4.52), (4.58), and (4.61) are basic equations in our present problem with subsidiary relations (4.60) and (4.62).

4.4.2 Perturbations

A small-amplitude, axisymmetric perturbation is superposed on unperturbed steady disks. The perturbation is assumed to have a short wavelength, $2\pi/k$, in the radial direction in the sense that $H \ll 1/k \ll r$, where k is the radial wavenumber. Since we are considering accretion disks, there is, of course, accretion flow in the unperturbed disks. The effects of accretion flows in the unperturbed disks are, however, negligible in standard disks, since the flow is slow. Hence, the radial velocity

in the unperturbed state, v_{r0} , is taken to be zero in the analyses of perturbations, where the subscript 0 denotes the unperturbed quantities. One of the implications involved in this approximation is that advective cooling in an unperturbed disk is neglected (i.e., standard disks).

The Eulerian perturbations superposed over the unperturbed quantities Σ_0 , $v_{r0}(= 0)$, Π_0 , and H_0 are denoted by Σ_1 , v_{r1} , Π_1 , and H_1 , respectively, and we hereafter adopt the following dimensionless variables:

$$\sigma = \frac{\Sigma_1}{\Sigma_0}, \quad \varpi = \frac{\Pi_1}{\Pi_0}, \quad u = \frac{v_{r1}}{r\Omega}, \quad h = \frac{H_1}{H_0}. \quad (4.63)$$

The subscript 0 to Σ , Π and H is often omitted hereafter for simplicity. All of the perturbed quantities are taken to be proportional to $\exp(n\Omega t - ikr)$, where n (generally complex) is the dimensionless growth rate.

(a) Perturbed equations

From equation (4.49) we have

$$n\sigma - ikru = 0, \quad (4.64)$$

which is the mass conservation. The φ -component of the equation of motion, equation (4.51), gives

$$\frac{\kappa^2}{2\Omega^2}u - i\alpha kr\left(\frac{c_s}{r\Omega}\right)^2\varpi = 0, \quad (4.65)$$

where equation (4.62) has been used and c_s is the speed of sound, defined by $c_s^2 = \Pi/\Sigma$; κ is the epicyclic frequency, defined by $\kappa^2 = 2\Omega(2\Omega + rd\Omega/dr)$. Equation (4.65) implies that a change of the viscous force in the φ -direction is balanced by a change of the Coriolis force resulting from the radial motion associated with the perturbations.

The hydrostatic balance in the vertical direction, equation (4.52), gives

$$2h = \varpi - \sigma. \quad (4.66)$$

Finally, we consider a perturbation of the energy equation (4.58). First, we comment on the term Q_{adv}^- , since in the standard disk models the cooling (or heating) by advective heat transport is neglected compared with those due to viscosity and radiation, i.e., $v_r = 0$. Hence, in local approximations the variation of Q_{adv}^- can be neglected. Equation (4.58) then leads to

$$n\left[3(1-\beta) + \frac{\beta}{\gamma-1}\right]\varpi + n\frac{4-3\gamma}{\gamma-1}\beta_1 - n\left(4-3\beta + \frac{\beta}{\gamma-1}\right)\sigma + nh$$

$$= G_{\varpi} \varpi + G_{\sigma} \sigma, \quad (4.67)$$

where β_1 is the perturbed part of β . Since β is defined by $\beta = p_{\text{gas}}/(p_{\text{rad}} + p_{\text{gas}})$, its logarithmic change gives

$$\frac{\beta_1}{\beta} = (1 - \beta) \left(\frac{\rho_1}{\rho_0} - 3 \frac{T_1}{T_0} \right). \quad (4.68)$$

The unperturbed part of β has been written simply by β without subscript 0. This abbreviation is used hereafter. The relation $2\rho H \sim \Sigma$ gives

$$\frac{\rho_1}{\rho_0} = \sigma - h. \quad (4.69)$$

Furthermore, the relation $2(p_{\text{gas}} + p_{\text{rad}})H \sim \Pi$ gives

$$(4 - 3\beta) \frac{T_1}{T_0} = \varpi - \beta\sigma - (1 - \beta)h. \quad (4.70)$$

Substituting equations (4.69) and (4.70) into equation (4.68), we finally know that β_1/β is expressed in terms of σ , ϖ , and h by

$$\frac{\beta_1}{\beta} = \frac{1 - \beta}{4 - 3\beta} (-3\varpi + 4\sigma - h). \quad (4.71)$$

Furthermore, we have

$$G_{\varpi} = \frac{1}{\Omega} \left[\left(\frac{\partial Q_{\text{vis}}^+}{\partial \Pi} \right)_{\Sigma} - \left(\frac{\partial Q_{\text{rad}}^-}{\partial \Pi} \right)_{\Sigma} \right], \quad (4.72)$$

$$G_{\sigma} = -\frac{1}{\Omega c_s^2} \left(\frac{\partial Q_{\text{rad}}^-}{\partial \Sigma} \right)_{\Pi}. \quad (4.73)$$

In deriving the right-hand side of equations (4.72) and (4.73), we have considered that Q_{rad}^- is a function of Π and Σ , but Q_{vis}^+ is a function of Π alone.

(b) Dispersion relation and growth rate

The elimination of h from equation (4.67) by using equations (4.64) and (4.66) gives

$$n(C_1 \varpi - C_2 \sigma) = G_{\varpi} \varpi + G_{\sigma} \sigma, \quad (4.74)$$

where

$$\begin{aligned} C_1 &= \frac{7 - 6\beta}{2} + \frac{\beta}{\gamma - 1} - \frac{7}{2}\beta \frac{4 - 3\gamma}{\gamma - 1} \frac{1 - \beta}{4 - 3\beta}, \\ C_2 &= \frac{9 - 6\beta}{2} + \frac{\beta}{\gamma - 1} - \frac{9}{2}\beta \frac{4 - 3\gamma}{\gamma - 1} \frac{1 - \beta}{4 - 3\beta}. \end{aligned} \quad (4.75)$$

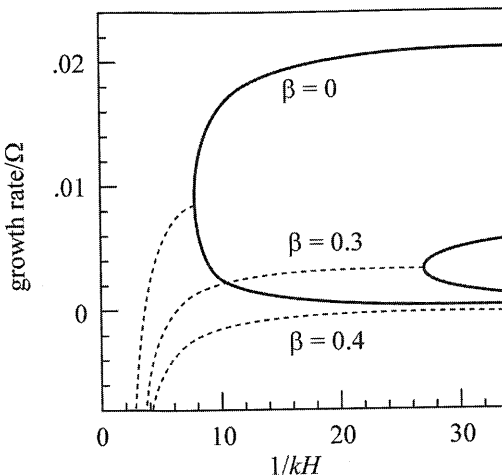


Figure 4.4

Growth rate, $\Re(n/\Omega)$, as functions of the radial wavelength of perturbations for some values of β . The ordinate is $\Re(n/\Omega)$ and the abscissa is $(kH)^{-1}$. The disk models adopted are the standard α -model with $\alpha = 0.1$ and $\gamma = 5/3$. The upper branch of the curves denotes the thermal mode, while the lower one represents the secular one. On the dotted curves the growth rates of both modes become complex conjugates, the real parts being the same.

Another relation between ϖ and σ is obtained by eliminating u from equations (4.64) and (4.65). Combining this relation and equation (4.74), as the condition of having a non-trivial solution, we obtain a dispersion relation,

$$C_1 n^2 + \left[2\alpha(kr)^2 C_2 \left(\frac{c_s}{\kappa r} \right)^2 - G_\varpi \right] n + 2\alpha(kr)^2 \left(\frac{c_s}{\kappa r} \right)^2 G_\sigma = 0. \quad (4.76)$$

The wavenumber dependence of the growth rates obtained by solving the dispersion relation, equation (4.76), is shown in figure 4.4.

Equation (4.76) is a second-order equation with respect to n ; i.e., there are two modes of perturbations. One is the thermal mode and the other is the secular one, as will become clear later. In the limit of long-wavelength perturbations ($kr \ll 1$), the growth rates (say n_1 and n_2 with $|n_1| > |n_2|$) of these two modes of perturbations are given by

$$n_1 \sim \frac{G_\varpi}{C_1} \quad \text{and} \quad n_2 \sim 2\alpha(kr)^2 \left(\frac{c_s}{\kappa r} \right)^2 \frac{G_\sigma}{G_\varpi}. \quad (4.77)$$

The former is the growth rate of the thermal mode, while the latter is that of the secular mode. In general, $C_1 > 0$ and $G_\sigma > 0$ (see below);

thus, both modes grow when $G_\varpi > 0$. More generally, the condition that n governed by equation (4.76) has a positive real part (i.e., $\Re n > 0$) is

$$2\alpha(kr)^2 C_2 \left(\frac{c_s}{\kappa r} \right)^2 - G_\varpi < 0. \quad (4.78)$$

This means that the disks are unstable for long-wavelength perturbations when

$$G_\varpi > 0. \quad (4.79)$$

It is sometimes convenient to express the instability condition, $G_\varpi > 0$, in terms of Σ and T , instead of Σ and Π . Changing the independent variables from Σ and Π to Σ and T , we have

$$\left(\frac{\partial Q_{\text{rad}}^-}{\partial \Pi} \right)_\Sigma = \left(\frac{\partial Q_{\text{rad}}^-}{\partial T} \right)_\Sigma \left(\frac{\partial T}{\partial \Pi} \right)_\Sigma, \quad (4.80)$$

$$\left(\frac{\partial Q_{\text{rad}}^-}{\partial \Sigma} \right)_\Pi = \left(\frac{\partial Q_{\text{rad}}^-}{\partial \Sigma} \right)_T + \left(\frac{\partial Q_{\text{rad}}^-}{\partial T} \right)_\Sigma \left(\frac{\partial T}{\partial \Sigma} \right)_\Pi. \quad (4.81)$$

Similar expressions are obtained for derivatives of Q_{vis}^+ . Hence, we obtain from equation (4.72)

$$G_\varpi = \frac{1}{\Omega} \left[\left(\frac{\partial Q_{\text{vis}}^+}{\partial T} \right)_\Sigma - \left(\frac{\partial Q_{\text{rad}}^-}{\partial T} \right)_\Sigma \right] \left(\frac{\partial T}{\partial \Pi} \right)_\Sigma. \quad (4.82)$$

This shows that the instability condition, $G_\varpi > 0$, is equivalent to inequality (4.47), since $(\partial T / \partial \Pi)_\Sigma$ is generally positive.

We now consider detailed expressions for G_ϖ and G_σ . Taking the derivative with respect to Π of the equation of state, given by

$$\Pi = \frac{k_B}{\mu m_H} \Sigma T + \frac{2}{3} a T^4 \frac{1}{\Omega} \left(\frac{\Pi}{\Sigma} \right)^{1/2}, \quad (4.83)$$

we have

$$\left(\frac{\partial \ln T}{\partial \ln \Pi} \right)_\Sigma = \frac{1 + \beta}{2(4 - 3\beta)}. \quad (4.84)$$

Similarly, the derivative of equation (4.83) with respect to Σ leads to

$$\left(\frac{\partial \ln T}{\partial \ln \Sigma} \right)_\Pi = \frac{1 - 3\beta}{2(4 - 3\beta)}. \quad (4.85)$$

Hence, we obtain

$$\left(\frac{\partial Q_{\text{rad}}^-}{\partial \Pi} \right)_\Sigma = \frac{1 + \beta}{2(4 - 3\beta)} \frac{T}{\Pi} \left(\frac{\partial Q_{\text{rad}}^-}{\partial T} \right)_\Sigma, \quad (4.86)$$

$$\left(\frac{\partial Q_{\text{rad}}^-}{\partial \Sigma} \right)_{\Pi} = \left(\frac{\partial Q_{\text{rad}}^-}{\partial \Sigma} \right)_T + \frac{1 - 3\beta}{2(4 - 3\beta)} \frac{T}{\Sigma} \left(\frac{\partial Q_{\text{rad}}^-}{\partial T} \right)_{\Sigma}. \quad (4.87)$$

We now consider the case when the disk is optically thick and the opacity comes from electron scattering; i.e., $Q_{\text{rad}}^- = Q_{\text{rad}} \propto T^4/\Sigma$. Then, $(\partial Q_{\text{rad}}^-/\partial \Pi)_{\Sigma}$ and $(\partial Q_{\text{rad}}^-/\partial \Sigma)_{\Pi}$ can be easily obtained by using the relations in the above paragraph, and we have

$$G_{\varpi} = \frac{2 - 5\beta}{4 - 3\beta} \frac{Q}{\Omega \Pi}, \quad (4.88)$$

$$G_{\sigma} = \frac{2 + 3\beta}{4 - 3\beta} \frac{Q}{\Omega \Pi}, \quad (4.89)$$

where $Q = Q_{\text{vis}}^+ = Q_{\text{rad}}^-$. Hence, the condition for the growth of both modes, $G_{\varpi} > 0$, is

$$\beta < \frac{2}{5} \quad (4.90)$$

(Shibazaki and Hōshi 1975; Shakura and Sunyaev 1976; Pringle 1976), which is, of course, the same with the limit of $\mu = 0$ in inequality (4.43).

References

- Lightman A.P. Eardley D.M. 1974, ApJ 187, L1
- Piran T. 1978, ApJ 221, 652
- Pringle J.E. 1976, MNRAS 177, 65
- Pringle J.E. Rees M.J. Pacholczyk A.G., 1976, A&A 29, 179
- Shakura N.I. Sunyaev R.A. 1976, MNRAS 175, 613
- Shibazaki N. Hōshi R. 1975, PTP 54, 706

Dwarf-Nova Type Instability

We are now in a position to discuss an extension of the standard disk model into low-temperature regimes. In the standard model, the disk temperature is assumed to be moderately high (with $T > 10^4$ K) so that the accreting gas (hydrogen and helium) should be fully ionized. This is not always the case, e.g., in X-ray novae (XNe) during quiescence. It is thus of great importance to investigate how the disk properties change when hydrogens and heliums are recombined. Interestingly enough, an S-shaped equilibrium curve appears in the \dot{M} - Σ plane, and relaxation oscillations between the upper, hot, ionized (HII) branch and the lower, cool, neutral (HI) branch are inevitable. Quasi-periodic outburst behavior can be produced in this way. This is the (*dwarf-nova type*) *disk-instability model*, which was originally proposed for outbursts of dwarf novae (DNe); we now believe that the same mechanism operates in X-ray novae as well. This model has most successfully linked the time-dependent theory of viscous accretion disks and observations.

5.1 Thermal-Ionization Instability

In low-mass X-ray binaries, the gas on the surface of the companion star is transferred to the compact component via Roche-lobe overflow, thereby forming an accretion disk around the compact star. As long as this accreting process onto the compact star proceeds steadily, we cannot expect any time-dependent behavior. In order to trigger outbursts of X-ray novae (see figure 1.27 in section 1.4), some mechanisms are needed to modulate the accretion flow from a companion star to a compact star. This situation is quite analogous to that of the outbursts of dwarf novae, semi-detached binaries containing white dwarfs (see section 1.3), and led

to the discovery of the *thermal-ionization instability*.¹

5.1.1 Two Competing Models for X-Ray Novae

Two competing models have been discussed concerning the outbursts of X-ray novae, which are similar to the case of DNe: one seeks to locate the origin of \dot{M} modulation outside of the disk; the other does this within the disk. The mass-overflow instability model asserts that the secondary star regulates the accretion flow. According to Hameury et al. (1986), the layer below the photosphere of a companion star is heated by efficient X-ray irradiation during quiescence. When the surface of the companion star expands to a certain limit, a mass-overflow instability sets in, leading to mass-transfer bursts. An enhancement in the mass-transfer rate into the disk causes a rapid brightening of the disk luminosity in both the optical and X-ray energy range.

In the disk-instability model, on the other hand, it is the accretion disk that is responsible for modulation in the mass-accretion rate onto the compact star (Cannizzo et al. 1982, 1985). This model states that an accretion disk is thermally unstable when the temperature of the disk is too cool for hydrogen and helium to be ionized. This situation is exactly the same as that in DNe. Unstable disks unavoidably alternate between a hot state and a cool state, producing sporadic light variations (Lin and Taam 1984; Huang and Wheeler 1989; Mineshige and Wheeler 1989; Cannizzo et al. 1995).

One of the key observations for discriminating these models is to measure the X-ray intensities during quiescence. It has now been shown to be mostly very weak, $L_X \sim 10^{31-33} \text{ erg s}^{-1}$ (Mineshige et al. 1992; Narayan et al. 1997); the irradiation effects on the secondary surface are unimportant during quiescence.² From this fact, we may conclude that the disk-instability model is more favorable. In what follows, we first discuss an extension of the standard-type disk into low-temperature regimes, and then explain the basic theory of the dwarf-nova-type limit-cycle instability in the context of X-ray novae.

¹There had been a long debate between the mass-transfer instability model by Bath (1973) and the disk-instability model by Osaki (1974). It is now widely believed that thermal-ionization instability takes place in accretion disks in dwarf novae, and yields dwarf-nova outbursts (see Cannizzo 1993, Osaki 1996 for reviews).

²A simple evaluation shows that an X-ray luminosities of $L_X \gtrsim 10^{34} \text{ erg s}^{-1}$ is needed in the energy range above $\sim 7 \text{ keV}$ to have significant influence on the secondary surface (Mineshige et al. 1992).

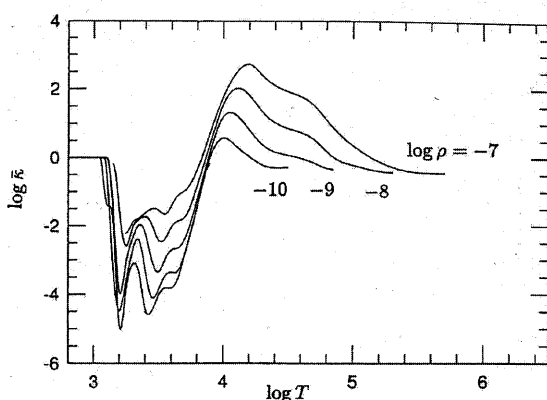


Figure 5.1

Temperature dependence of the Rosseland-mean opacities calculated based on the opacity tables by Cox and Stewart (1970) and Alexander et al. (1983).

5.1.2 Partial Ionization of Hydrogen

The key to understanding the dwarf-nova-type instability (sometimes called a limit-cycle instability or a thermal-ionization instability) is the complex temperature dependence of the Rosseland-mean opacity, $\bar{\kappa}$. We depict in figure 5.1 a spline fit of the Rosseland-mean opacities, taken from the opacity tables of Cox and Stewart (1970) and of Alexander et al. (1983), as a function of the temperature for some values of the density; $\log \rho [\text{g cm}^{-3}] = -7, -8, \dots, \text{and } -11$.

At high temperatures with $T \gtrsim 10^4$ K, the power-law index a ($\bar{\kappa} \propto \rho T^a$) is about -3.5 . When the plasma temperature is sufficiently low for hydrogen to recombine and to be in *partially ionized* state (at a temperature around 10^4 K), the opacity $\bar{\kappa}$ steeply changes along with a decrease in the temperature, $a = 5 - 10$. At even lower temperatures with $T \sim 1000$ K, since the grain opacity dominates, the value of $\bar{\kappa}$ drastically increases, with $a \lesssim -5$, as T drops.

In the case of stars, such dramatic opacity changes cause interesting phenomena, e.g., radial pulsations in Cepheid stars and convective envelopes of cool stars. In the case of accretion disks, the opacity changes are even more important, since they crucially affect the cooling rate in the disk, and since the energy balance is the most important factor that determines the equilibrium structure of the accretion disk. Under a (vertically) one-zone approximation, we find $H \sim c_s/\Omega \propto T^{0.5}$, since the gas

pressure, p_{gas} , is dominant and $c_s^2 \approx p_{\text{gas}}/\rho \propto T$. Thus,

$$Q_{\text{rad}}^- = 2F \propto \frac{T^4}{\bar{\kappa}\Sigma} \propto \frac{T^{4.5}}{(\bar{\kappa}/\rho)\Sigma^2} \propto \frac{T^{4.5-a}}{\Sigma^2} \quad (5.1)$$

for optically thick disks, where we assume $\bar{\kappa} \propto \rho T^a$. Since Q_{vis}^+ is a monotonically increasing function of T , $Q_{\text{vis}}^+ \propto T\Sigma$ (cf. section 3.2), and Q_{rad}^- has a rather complex temperature dependence, we expect multiple thermal-equilibrium solutions for a fixed value of the surface density, even under a one-zone approximation (Hōshi 1979).

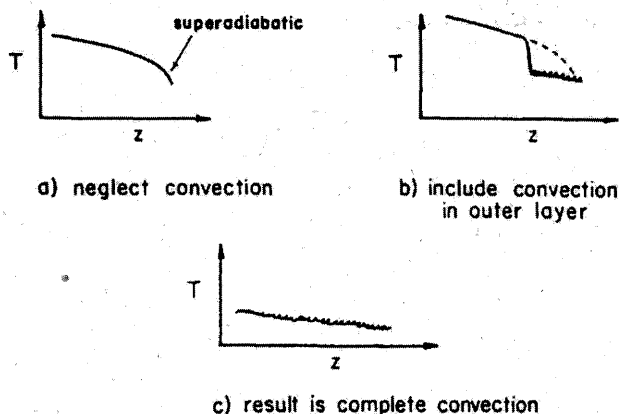
The one-zone treatment is, however, unable to produce the S-shaped equilibrium curves necessary for limit-cycle oscillations. This is a part of the reason why the important paper of Hōshi (1979) had not attracted much attention of researchers until independent research was conducted by Meyer and Meyer-Hofmeister (1981). Then, what was missing in Hōshi's work?

Note that the one-zone approximation is valid only for radiative disks. From an analogy with low-mass stars, rather, it is natural to expect the onset of convection in cool disks where hydrogens are partially ionized. When the contribution by convective energy transport becomes non-negligible, substantial changes occur in the vertical distribution of physical quantities (see below for more details). This concept filled out a gap between the theory and the observations of dwarf-nova outbursts.

The primary cause of convection is a drastic increase of the opacities in the partial-ionization zone of hydrogen (at $T \sim 10^4$ K, see figure 5.1). This is due to the formation of negative hydrogen (H^-) ions, which results in a large reduction in the efficiency of radiative energy transport. To convey energy produced in the disk to its surface, convective motions should compensate for the reduced radiative energy transport. Furthermore, a significant reduction in the adiabatic temperature gradient in the partial-ionization regimes of hydrogen and helium also helps to excite convection, since this allows superadiabatic temperature gradient to more easily appear.³ It is thus not surprising that considerable structural changes also occur in the accretion disk due to the presence of vertical convection (figure 5.2).

³The condition for a convective instability is written as $\nabla > \nabla_{\text{ad}}$, where $\nabla \equiv d \ln T / d \ln p$ is temperature gradient and $\nabla_{\text{ad}} = (\gamma - 1)/\gamma$ with γ being the ratio of specific heats. Note that $\gamma \sim 1$ in the ionization zone.

**Accretion Disk: Effective temperature fixed
by accretion rate**



Star: Fixed central temperature

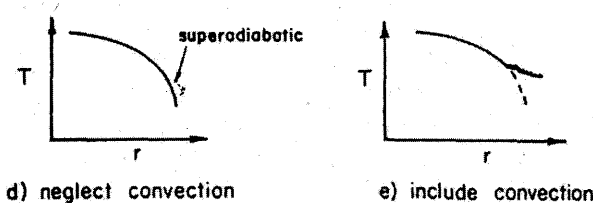


Figure 5.2

Role of vertical convection in accretion disks and stars. (After Cannizzo and Wheeler 1984)

5.1.3 Vertical Integration of Convective Disks

Let us solve the vertical structure of convective disks. The calculation methods are similar to those for the stellar interior structure (Kippenhahn et al. 1967). We consider concentric, plane-parallel annuli with radius r . Instead of the mass coordinate, $M_r = \int_0^r 4\pi r^2 \rho dr$, which is generally used to solve the stellar structure, we define here the surface-density coordinate, $\Sigma_z^* = 2 \int_0^z \rho dz$. Since, however, we integrate the vertical disk structure from its surface downward, it is more convenient to define the surface-density coordinate as

$$\Sigma_z(z) = 2 \int_z^\infty \rho dz. \quad (5.2)$$

Likewise, we define the optical depth and vertically integrated shear stress as

$$\tau_z(z) = \int_z^\infty \bar{\kappa} \rho dz, \quad (5.3)$$

$$T_{r\varphi,z}(z) = 2 \int_z^\infty t_{r\varphi} dz = -2\alpha \int_z^\infty p dz, \quad (5.4)$$

where we adopt the α prescription,⁴ i.e., $t_{r\varphi} = -\alpha p$.

The basic differential equations are the equations of continuity,

$$\frac{d\Sigma_z}{dz} = -2\rho, \quad (5.5)$$

hydrostatic balance,

$$\frac{dp}{dz} = \rho g_z(z), \quad (5.6)$$

energy balance,

$$\frac{dF_z}{dz} = \frac{3}{2}\alpha p \Omega, \quad (5.7)$$

and energy transport,

$$\frac{d \ln T}{d \ln p} = \nabla_{\text{rad}} \quad \text{or} \quad \nabla_{\text{conv}}, \quad (5.8)$$

with the following supplementary equations:

$$\frac{d\tau_z}{dz} = -\bar{\kappa} \rho, \quad (5.9)$$

$$\frac{dT_{r\varphi,z}}{dz} = 2\alpha p, \quad (5.10)$$

$$p = p(\rho, T) \quad \text{and} \quad \bar{\kappa} = \bar{\kappa}(\rho, T). \quad (5.11)$$

Here,

$$g_z(z) = -\frac{GM}{r^3} z \quad (5.12)$$

is the vertical component of the gravitational force due to the central object, F_z is the energy flux at z , and ∇_{rad} and ∇_{conv} are the temperature gradients for radiative energy transport and convective energy transport, respectively. The convective gradient can be calculated using the mixing-length theory (Cox and Giuli 1968; Paczyński 1969).

We integrate these equations from the surface, where $\tau_z = 2/3$ and $T = T_{\text{eff}}$, towards the equator ($z = 0$) for a given effective temperature

⁴Radiation pressure never becomes important in such low-temperature disks as those discussed in this chapter. Hence we set $p = p_{\text{gas}}$.

T_{eff} at some r . The other physical quantities at the surface are derived as follows. Since we do not know the height of the surface, H , above the equatorial plane, we first guess a value of H and set

$$\tau_z(H) = 2/3 \quad \text{and} \quad T(H) = T_{\text{eff}}. \quad (5.13)$$

We can then fix the density at surface, ρ_s , and so pressure at H by solving

$$\bar{\kappa}(\rho_s, T_{\text{eff}}) p(\rho_s, T_{\text{eff}}) = \frac{2}{3} \Omega^2 H, \quad (5.14)$$

which was derived by combining equations (5.6) and (5.9). The other quantities at the surface are

$$\begin{aligned} \Sigma_z(H) &= \frac{2\tau_z(H)}{\bar{\kappa}(\rho_s, T_{\text{eff}})}, & F_z(H) &= \sigma T_{\text{eff}}^4, \\ T_{r\varphi,z}(H) &= -\alpha p(\rho_s, T_{\text{eff}}) \frac{\Sigma_z(H)}{\rho_s}. \end{aligned} \quad (5.15)$$

Using those surface values, we start vertical integration of equations (5.5) – (5.10) towards $z = 0$. Since we assign H quite arbitrarily, the numerical integration does not always give a solution that satisfies the boundary condition on the equatorial plane, which is

$$F_z = 0 \quad \text{at} \quad z = 0. \quad (5.16)$$

We repeat these procedures by improving our guess for H until the boundary condition (5.16) is met. For given values of T_{eff} and r , therefore, we can finally uniquely determine H , and therefore, obtain

$$\begin{aligned} \Sigma &= \Sigma_z(0), & \rho_c &= \rho(0), & T_c &= T(0), \\ p_c &= p(\rho_c, T_c), & \tau &= \tau_z(0), & T_{r\varphi} &= T_{r\varphi,z}(0), \dots \end{aligned} \quad (5.17)$$

The corresponding mass-flow rate is calculated by

$$\dot{M} = \frac{8\pi r^3 F}{3 GM} \left(1 - \sqrt{\frac{r_{\text{in}}}{r}} \right)^{-1}, \quad (5.18)$$

with $F \equiv F_z(H) = \sigma T_{\text{eff}}^4$, assuming that the disk is optically thick, and r_{in} is the radius of the inner edge of the disk.

There are both similarities and differences between the radial structure of stars and the vertical structure of disks. Similarly to the stellar structure, the surface gravity (or H) and the effective temperature are the main parameters, which characterize the vertical structure of the

disk. By fixing the energy-production rate, one can even fix the gravity for a given effective temperature (or vice versa) in both cases. One of the major differences between them is the functional forms of the heating rate; heating occurs at the core in main-sequence stars, whereas it is available everywhere (since $p \neq 0$) in the disk. Like the stellar interior structure which is uniquely determined, if its mass and chemical composition (distribution) are given, the vertical disk structure is uniquely determined *at each radius* for a given mass-flow rate, \dot{M} , viscosity parameter, α , and chemical composition.⁵

For sufficiently low temperatures the disk becomes optically thin. Then, we may simply assume isothermality in the vertical direction, and calculate the disk structure by equating the viscous heating rate to the optically thin, radiative cooling one. It will be shown, however, that the optically thin solutions are generally unimportant except at small radii, $r \ll 10^9 \text{ cm}$ (for $\alpha \lesssim 0.1$, as required from a fitting to the observations).

5.1.4 Local Limit-Cycle Behavior

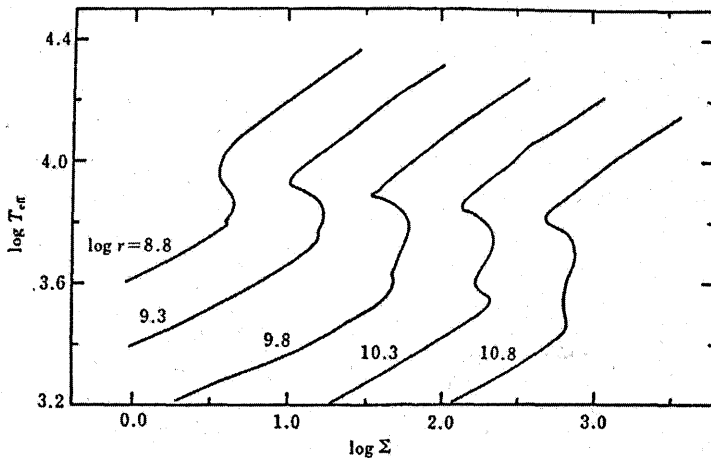
From now on we develop the theory of a dwarf-nova (DN) type disk instability based on the low-temperature disk structure calculated by the methods mentioned above. As is the case for the standard disks, we may reasonably assume that the thermal timescale, which controls the thermal behavior of the disk, is much shorter than the accretion timescale. We thus first discuss the local behavior of low-temperature disks, and then consider the global effects in section 5.2.

(a) S-shaped thermal-equilibrium curves

By changing \dot{M} (or T_{eff}), we successively obtain a family of solutions for fixed values of r , α , and M . Figure 5.3 displays the equilibrium relation among the effective temperature T_{eff} and Σ . Each equilibrium curve has roughly an S-shape.⁶ The essence of the thermal instability lies in this S-shaped equilibrium curve. There exist three solutions for a certain range of Σ . Hydrogen is fully ionized in the upper (hot) branch (HII branch), partially ionized in the middle branch (H^{*} branch) and is neutral in the lower (cool) branch (HI branch).

⁵If we ultimately succeed in constructing a theory of disk viscosity, in which the magnitude of viscosity is self-consistently determined, we no longer need to assign α .

⁶More exactly, each equilibrium curve has two kinks (“double S-shaped”); the upper kink is due to partial ionization of hydrogens, whereas the lower one is due to H_2O , TiO , and an optically thick-thin transition (Cannizzo and Wheeler 1984). We, however, do not go into the details of the curve in this book.

**Figure 5.3**

Thermal equilibrium curves of cool disks. The ordinate represents the effective temperatures, whereas the abscissa is the surface density. The parameters are $\alpha = 0.1$ and $M = 1M_\odot$. This diagram was originally made for the DN disk, but is also relevant to the disks in XBs. (After Mineshige and Osaki 1983)

Crudely speaking, the shape of the equilibrium curve is self-similar; if we change M , r , and α , we find that the equilibrium curve simply shifts mainly in the horizontal (Σ) direction, basically retaining its S-shape, as is clear from figure 5.3. In other words, there exist scaling laws for each physical quantity with respect to α , r , and M .⁷ Roughly speaking, the effective temperature as a function of the surface density Σ is

$$T_{\text{eff}} \sim 10^{3.3} \left(\frac{\alpha}{0.1} \right)^{0.29} \left(\frac{\Sigma}{\text{g cm}^{-2}} \right)^{0.36} \left(\frac{r}{10^{10} \text{cm}} \right)^{-0.46} \left(\frac{M}{M_\odot} \right)^{0.15} \text{K} \quad (5.19)$$

on the upper branch,

$$T_{\text{eff}} \sim 10^{4.2} \left(\frac{\alpha}{0.1} \right)^{-0.18} \left(\frac{\Sigma}{\text{g cm}^{-2}} \right)^{-0.22} \left(\frac{r}{10^{10} \text{cm}} \right)^{0.15} \left(\frac{M}{M_\odot} \right)^{-0.05} \text{K} \quad (5.20)$$

⁷Note that M only enters the basic equations [(5.5) – (5.12)] through the combination of GM/r^3 ($= \Omega^2$). The M -dependence is thus always one-third power of the r -dependence.

on the middle branch, and

$$T_{\text{eff}} \sim 10^{2.8} \left(\frac{\alpha}{0.1} \right)^{0.40} \left(\frac{\Sigma}{\text{g cm}^{-2}} \right)^{0.50} \left(\frac{r}{10^{10} \text{cm}} \right)^{-0.60} \left(\frac{M}{M_{\odot}} \right)^{0.20} \text{K} \quad (5.21)$$

on the lower branch. At the upper turning point, B, the effective temperatures, surface densities, and mass-flow rates are, respectively,

$$T_B \simeq 10^{3.9} \left(\frac{r}{10^{10} \text{cm}} \right)^{-0.10} \left(\frac{M}{M_{\odot}} \right)^{0.03} \text{K}, \quad (5.22)$$

$$\Sigma_B \simeq 10^{1.7} \left(\frac{\alpha}{0.1} \right)^{-0.80} \left(\frac{r}{10^{10} \text{cm}} \right)^{1.05} \left(\frac{M}{M_{\odot}} \right)^{-0.35} \text{g cm}^{-2}, \quad (5.23)$$

$$\dot{M}_B \simeq 10^{16.2} \left(\frac{r}{10^{10} \text{cm}} \right)^{2.6} \left(\frac{M}{M_{\odot}} \right)^{-0.87} \text{g s}^{-1}, \quad (5.24)$$

while at the lower turning point, A, we have

$$T_A \simeq 10^{-0.1} T_B, \quad (5.25)$$

$$\Sigma_A \simeq 10^{0.3} \Sigma_B, \quad (5.26)$$

$$\dot{M}_A \simeq 10^{-0.8} \dot{M}_B. \quad (5.27)$$

(b) Thermal stability of cool disks

To examine the thermal stability of these three branches, we must know the temperature dependences of Q_{vis}^+ and Q_{rad}^- for a fixed Σ (see section 4.3). For this purpose, we need to obtain non-thermal-equilibrium solutions; i.e., the solutions in which $Q_{\text{vis}}^+ \neq Q_{\text{rad}}^-$. A simple way to assess non-equilibrium structure is to prescribe the functional form of $F_z(z)$ as

$$F_z = \sigma T_{\text{eff}}^4 \left(\frac{z}{H} \right) \left[2 - \left(\frac{z}{H} \right) \right], \quad (5.28)$$

instead of solving the energy-balance equation (5.7) at each height.⁸ With this formula one can obtain a unique solution for each combination of T_{eff} and H [or $g_z(H)$] at a given r :

$$\begin{aligned} T_c &= T_c(T_{\text{eff}}, H, r), \\ \Sigma &= \Sigma(T_{\text{eff}}, H, r), \\ T_{r\varphi} &= T_{r\varphi}(T_{\text{eff}}, H, r), \\ &\dots \end{aligned} \quad (5.29)$$

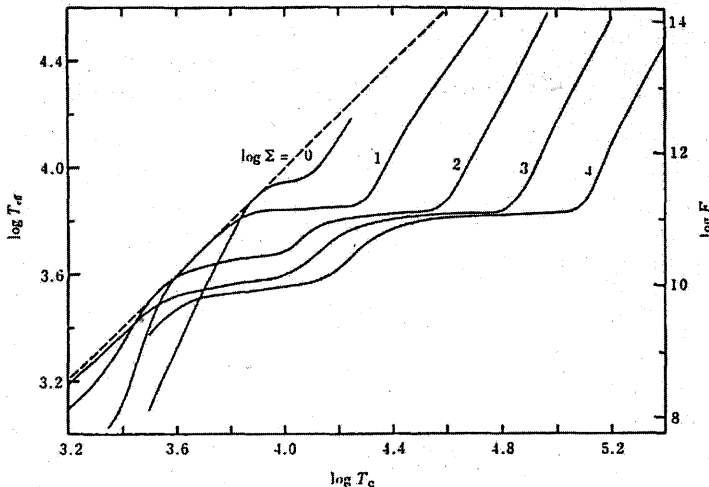


Figure 5.4

Cooling rate ($F = Q_{\text{rad}}^-/2$) of cool accretion disks for $\log \Sigma = 0, 1, \dots, 4$. Again, this figure was originally made for the DN disk. Parameters are $\alpha = 0.1$ and $M = 1M_\odot$. (After Mineshige and Osaki 1983)

We then find expressions

$$T_{\text{eff}} = T_{\text{eff}}(\Sigma, T_c, r) \quad \text{and} \quad H = H(\Sigma, T_c, r) \quad (5.30)$$

using an inverse transformation. Substituting equation (5.30) into equation (5.29), we finally summarize the results in the forms of

$$Q_{\text{vis}}^+ = -\frac{3}{2} T_{r\varphi}(\Sigma, T_c, r) \Omega(r) \quad \text{and} \quad Q_{\text{rad}}^- = 2F(\Sigma, T_c, r). \quad (5.31)$$

Similar expressions are also obtained for optically thin regimes; we combine these data together in forms of (5.31). Figure 5.4 depicts how F depends on the temperature for a given Σ and r . As expected, $F (= Q_{\text{rad}}^-/2)$ shows a complex behavior, reflecting the large temperature dependence of the opacity (see figure 5.1) and the onset of convection.

Since $Q_{\text{vis}}^+ \sim \Sigma T \Omega \propto T$ for fixed Σ and r , the thermal-instability criterion (section 4.3) becomes

$$\left(\frac{\partial \ln Q_{\text{rad}}^-}{\partial \ln T} \right)_\Sigma < 1. \quad (5.32)$$

⁸This expression is obtained from the thermal-equilibrium models (Meyer and Meyer-Hofmeister 1982), but is shown to be a good approximation for the non-thermal equilibrium structure (Mineshige et al. 1990). Note that the boundary condition on the equatorial plane, $F_z(0) = 0$, is automatically satisfied in this expression.

We find that two parts of each curve that have small gradients are thermally unstable. These parts correspond to those having negative slopes in the \dot{M} - Σ diagram (figure 5.3). It is easy to show that these parts are also unstable for secular instability according to the secular-instability criterion (section 4.3).

The thermal timescale is much shorter than the viscous timescale. This implies that the disk initially on these thermally unstable branches cannot stay there for a long time (\sim viscous timescale); it will make a transition to either the upper or lower branches, where the corresponding mass accretion rates are greater or smaller than that of the middle branch. The imbalance between the mass input and output rates leads to a limit-cycle behavior (see below).

We summarize the representative three branches in table 5.1. Note that the power-law indices in this table are rough typical values (estimated from figure 5.4) and may not be very accurate.

Table 5.1 Cool Accretion Disk Branches.

Branch	$Q^+(\Sigma, T)$	$Q^-(\Sigma, T)$	$Q^+(\Sigma, \dot{M})$	$Q^-(\Sigma, \dot{M})$	$\dot{M}(\Sigma)$
H _I (cool)	ΣT	$\Sigma^{-2}T^4$	\dot{M}	$\Sigma^{-6}\dot{M}^4$	Σ^2
H _I *	ΣT	$\Sigma^{-0.1}T^{0.4}$	\dot{M}	$\Sigma^{-0.5}\dot{M}^{0.4}$	$\Sigma^{-0.8}$
H _{II} (hot)	ΣT	$\Sigma^{-2}T^8$	\dot{M}	$\Sigma^{-10}\dot{M}^8$	$\Sigma^{10/7}$

(c) Limit cycles

First consider the evolution of an annulus at radius r . We now demonstrate that when the mass-input rate into the annulus, \dot{M}_{in} , falls within a range $\dot{M}_A < \dot{M} < \dot{M}_B$ (see figure 5.5), a limit-cycle behavior of the annulus unavoidably appears. The basic evolutionary equations are written as

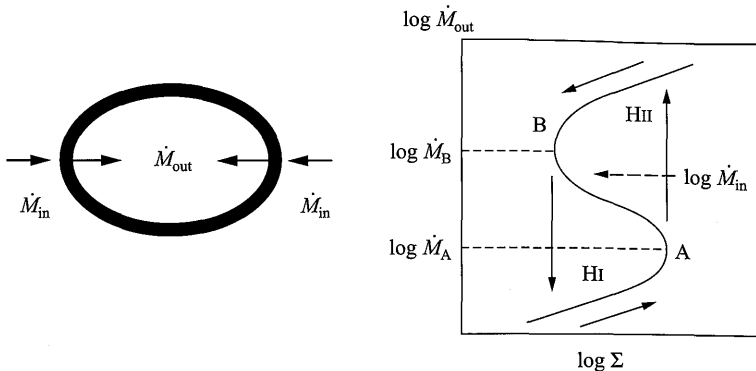
$$\frac{\partial \Sigma}{\partial t} \propto \dot{M}_{\text{in}} - \dot{M}_{\text{out}} \quad (5.33)$$

from mass conservation [equation (3.11)], and

$$\frac{\partial T}{\partial t} \propto Q_{\text{vis}}^+ - Q_{\text{rad}}^- \quad (5.34)$$

from the energy equation [see equation (4.58)]. Here, the mass-input rate \dot{M}_{in} is assumed to be constant in time, while the mass-output rate from the annulus to a black hole, \dot{M}_{out} , is proportional to the temperature T of the annulus for fixed r and Σ , since from equation (3.15) we obtain

$$\dot{M}_{\text{out}} \propto (-T_{r\varphi}) \sim \alpha c_s^2 \Sigma \propto T. \quad (5.35)$$

**Figure 5.5**

Schematic view of an annulus (left) and the calculated S-shaped equilibrium curves (right). When \dot{M}_{in} falls onto the range between \dot{M}_A and \dot{M}_B , the limit cycle behavior is initiated.

Suppose the annulus lies in the cool state (HI state). Since $\dot{M}_{\text{in}} > \dot{M}_{\text{out}}$ in this state (see figure 5.5), Σ (and the annulus mass) should increase according to equation (5.33). The evolutionary track of such an unstable annulus follows the low equilibrium line up to point A, as indicated by the arrow in figure 5.5. Since there is no cool state at $\Sigma > \Sigma_A$, and since $Q_{\text{vis}}^+ > Q_{\text{rad}}^-$ on the right side of the S-shape, the temperature will increase [see equation (5.34)]. Accordingly, \dot{M}_{out} also increases. Hydrogen in the annulus starts to become ionized and eventually the annulus jumps to the upper HII hot state, where $\dot{M}_{\text{out}} > \dot{M}_{\text{in}}$ holds. Surface density (and disk mass) should decrease there, as the gas falls onto the central star [see equation (5.33)]. At point B, a thermal instability again takes place and the annulus falls into the HI cool state because $Q_{\text{vis}}^+ < Q_{\text{rad}}^-$. All of the hydrogen in the annulus again becomes neutral there. One limit cycle is completed.

To sum up, when the mass-input rates fall within the range

$$\dot{M}_A < \dot{M}_{\text{in}} < \dot{M}_B, \quad (5.36)$$

the annulus undergoes thermal limit cycles.

In global simulations we can see that the disk undergoes relaxation oscillations if criterion (5.36) is satisfied, at least at the outer rim of the disk. For practical use, therefore, it suffices to check whether the value of \dot{M}_{in} is less than that of point B at the outer rim of the disk, $r = r_d$.

From the expression for \dot{M}_B [equation (5.24)], we have

$$\dot{M}_{\text{in}} < 10^{16.2} \left(\frac{r_d}{10^{10} \text{cm}} \right)^{2.6} \left(\frac{M}{M_\odot} \right)^{-0.9} \text{g s}^{-1}. \quad (5.37)$$

When criterion (5.37) is satisfied, since there should be some region inside r_d , where the condition (5.36) is satisfied, we expect variations in the disk luminosity (shown later).⁹

Cannizzo et al. (1985) plotted several XNe in a (\dot{M}, r_d) diagram, as Smak (1982) did for cataclysmic variables, and concluded that the disks in XNe are thermally unstable, and thus, are very likely to produce light variations. Actually, the criterion is easily satisfied for the typical parameters of transient BHBs known at present: $r_d \gtrsim 10^{11} \text{cm}$, $M \lesssim 10 M_\odot$, and $\dot{M}_{\text{in}} \sim 10^{15-16} \text{g s}^{-1}$.

To summarize, accretion disks which are too cool for hydrogens and helium to be ionized are unstable against a thermal instability and undergo limit-cycle oscillations. Sporadic burst behavior spontaneously arises as a result of the instability; that is, even though mass supply rate into the disk is kept constant in time, mass accretion rate onto a black hole should be variable.

5.2 Time Evolution of Disks in X-Ray Novae

As we pointed out in the previous section, the local behavior of a cool disk is characterized by thermal limit cycles. A cool disk is like numerous limit-cycle oscillators lying in one direction, being strongly coupled with each other. When one of them is activated somehow, it influences its neighbors, thus producing a coherent behavior of the entire system.

5.2.1 Global Evolution of Unstable Disks

As a next step, we simulate such a global response of the local instability. The basic time-dependent equations for the radial disk structure are the conservation of mass, angular momentum, and energy. Since we are concerned with the outer cool portions of the disk far from the black hole, $r \gg r_g$, a Newtonian potential can be used; i.e., $\psi(r) = -GM/r$. We thus have

$$\frac{\partial \Sigma}{\partial t} = \frac{1}{2\pi r} \frac{\partial \dot{M}}{\partial r}, \quad (5.38)$$

⁹Rigorously speaking, this is only true when irradiation is negligible (see subsection 5.2.4).

$$\dot{M} \sqrt{\frac{GM}{r}} = -4\pi \frac{\partial(r^2 T_{r\varphi})}{\partial r}, \quad (5.39)$$

and the vertically integrated energy equation,¹⁰

$$\Sigma T \left(\frac{\partial s}{\partial t} + v_r \frac{\partial s}{\partial r} \right) = Q_{\text{vis}}^+ - Q_{\text{rad}}^- - \frac{2H}{r} \frac{\partial(rF_r)}{\partial r}, \quad (5.40)$$

where s is the specific entropy¹¹ and F_r is the radial heat flux, for which we consider two processes. One is radiative heat transport,

$$F_{\text{rad}} = -\frac{4acT^3}{3\bar{\kappa}\rho} \frac{\partial T}{\partial r}, \quad (5.41)$$

and the other is turbulent heat transport,

$$F_{\text{turb}} = -K\rho T \frac{\partial s}{\partial r}, \quad (5.42)$$

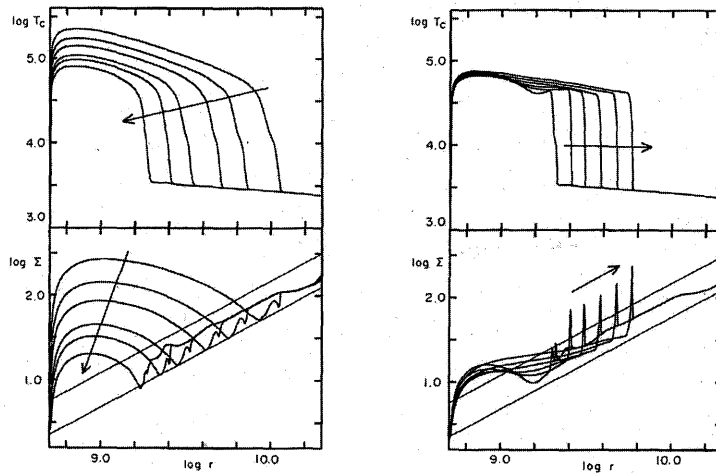
where K is the thermometric conductivity due to turbulence and is usually of the order of the turbulent kinematic viscosity ν .

By means of numerical simulations, we can see how the local instability is spatially propagated and how the disk luminosity is modulated (Mineshige and Wheeler 1989; Cannizzo et al. 1996). The results of transition wave propagation are displayed in figure 5.6.

The local limit cycle in each concentric annulus is linked with its adjacent annuli via an exchange of gas [see equations (5.38) and (5.39)]. When an upward transition is excited in one annulus in a cool disk, rapid mass flow occurs from that annulus to the outer and inner adjacent annuli, and so the surface density there is abruptly increased, leading to the onset of an upward transition in these annuli. The upward-transition waves are generated in this way and propagate toward both the outer and inner directions. The propagation of transition waves, transforming the region of the HI (neutral) state into the HII (ionized) state or vice versa, gives a typical example of a dissipative structure (Nicolis and Prigogine 1977).

¹⁰In the standard disk the second term on the left-hand side and the last term on the right-hand side are both neglected, however, since the width of an instability front (a transition layer) could be of the order of $\sim H$ (over which temperature and density change), and since $v_r \sim \alpha c_s$ near to the front (Meyer 1984), these terms turn out to be non-negligible in the present case.

¹¹We may simply rewrite $Tds = C_p dT$ with C_p being the specific heat at constant pressure. Strictly speaking, however, the specific heat used here is neither C_p nor one at constant volume, C_v , since the surface density Σ is a conserved value during a thermal transition. For an exact expression, see section 7.4.

**Figure 5.6**

Time-dependent properties of unstable disks. The left and right panels illustrate the propagation of the cooling and heating waves, respectively. Parameters are $\alpha = 0.03 - 0.1$ and $M = 1M_\odot$. (After Mineshige 1987)

5.2.2 Light Curves

The light curves of X-ray novae are characterized by rapid rises, slow exponential declines interrupted by reflares (see figure 1.27), and long recurrence times of several tens of years.¹² In the following, we discuss the physics underlying such light variations within the framework of the DN-type disk instability model.

(a) Overall behavior

Figure 5.7 illustrates a typical example of the light variations calculated based on the disk-instability model. The model parameters are the mass-input rate, $\dot{M}_{\text{in}} = 10^{15.0} \text{ g s}^{-1}$ ($= 10^{-10.8} M_\odot \text{ yr}^{-1}$), the mass of the central object, $M = 10 M_\odot$, and the outer and inner radii of the disk, $\log r_d = 10.5$ and $\log r_{\text{in}} = 6.5$. It is easy to check that the condition to have outbursts (5.37) is satisfied for these parameters. The viscosity parameter is prescribed so as to give typical amplitudes and duration of the outbursts of X-ray novae:

$$\alpha = 10^{2.0} \left(\frac{H}{r} \right)^{1.5} \approx 0.02 \left(\frac{T_c}{10^4 \text{ K}} \right)^{0.75} \left(\frac{r}{10^{10} \text{ cm}} \right)^{0.75}. \quad (5.43)$$

¹²For example, the X-ray nova eruptions of A0620–003 were recorded in 1917 and 1975, and those of GS2023+338 occurred in 1938, 1956, and 1989.

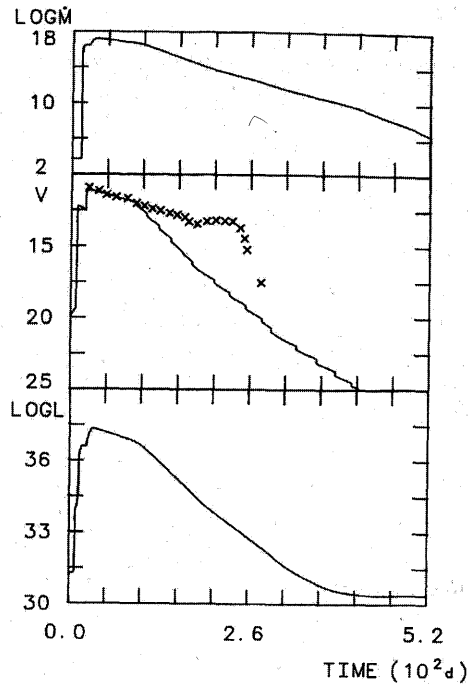


Figure 5.7

Theoretical model for A0620-00; from top, the mass-accretion rate at $r = r_{\text{in}}$, the V -magnitude ($d = 840$ pc is assumed), and the total disk luminosity. The crosses are the observed V -magnitude by Whelan et al. (1977). Parameters are $\alpha = 10^{2.0}(H/r)^{1.5}$ and $M = 1M_{\odot}$. (After Mineshige and Wheeler 1989)

Note that it is essential to take larger α in the hot state than that in the cool state by a factor of at least ~ 3 , since otherwise small-amplitude rapid fluctuations, instead of clear-cut large-amplitude variations, result (e.g., Smak 1984; Mineshige and Osaki 1985).

Once the time development of the effective temperature distribution is calculated, it is then easy to derive the total disk luminosity,

$$L_d = 2 \int_{r_{\text{in}}}^{r_d} F(r) 2\pi r dr, \quad (5.44)$$

and the V -magnitude,

$$m_v = -2.5 \log \left[\frac{1}{4\pi D^2} \int \int B_{\lambda} [T_{\text{eff}}(r)] V_{\lambda} 4\pi r dr d\lambda \right] - 13.74, \quad (5.45)$$

where $B_\lambda(T)$ is the Planck function,¹³ V_λ is the response function for the V -band (Allen 1973), and D [pc] is the distance to the object.

Figure 5.7 depicts the mass-accretion rate at $r = r_{\text{in}}$ (which approximately gives the X-ray luminosity variation), the V -magnitude, and the total disk luminosity calculated by Mineshige and Wheeler (1989). The crosses in the middle panel indicate the observed V -magnitude variation of A0620–00 by Whelan et al. (1977). We find a relatively good agreement with the theoretical and observed light curves, especially in the early decline phase. The observed exponential decay of X-rays was also basically reproduced by the disk-instability model.

Typical timescales predicted by the DN-type disk-instability model are the following: the rise timescale corresponds to the time for a thermal transition wave (with a speed of αc_s)¹⁴ to travel over the entire disk,

$$\tau_{\text{rise}} \sim \frac{r_d}{\alpha c_s} \simeq 10 \left(\frac{\alpha}{0.1} \right)^{-1} \left(\frac{r_d}{10^{11} \text{cm}} \right)^{1/2} \left(\frac{T_{\text{front}}}{10^4 \text{K}} \right)^{-1} \text{d}, \quad (5.46)$$

where T_{front} is the disk temperature at the front on the equatorial plane. Likewise, the decay timescale is the viscous diffusion timescale in the hot state,

$$\tau_{\text{decay}} \simeq 100 \left(\frac{\alpha}{0.1} \right)^{-1} \left(\frac{M}{5M_\odot} \right)^{1/2} \left(\frac{r_d}{10^{11} \text{cm}} \right)^{1/2} \left(\frac{T_{\text{hot}}}{10^5 \text{K}} \right)^{-1} \text{d}, \quad (5.47)$$

while the quiescent timescale is the viscous diffusion timescale in the cool state,

$$\tau_Q \simeq 80 \left(\frac{\alpha}{0.01} \right)^{-1} \left(\frac{M}{5M_\odot} \right)^{1/2} \left(\frac{r_d}{10^{11} \text{cm}} \right)^{1/2} \left(\frac{T_{\text{cool}}}{10^{3.5} \text{K}} \right)^{-1} \text{yr}, \quad (5.48)$$

where T_{hot} and T_{cool} are, respectively, a typical equatorial temperature of the disk at $z = 0$ in hot and cool states. Black-hole X-ray novae, in which the mass of the central object and the disk dimension are both larger than those in CVs, should systematically give longer decay and quiescent timescales, compared with the case of dwarf novae. This is qualitatively consistent with the observations.

The original disk-instability model (Mineshige and Wheeler 1989) failed to produce a plateau in the V -magnitude observed during 100–200

¹³Note $B_\lambda d\lambda = |B_\nu d\nu| = B_\nu (c/\lambda^2) d\lambda$

¹⁴This speed is larger than the accretion velocity of the standard disk; $v_r \sim \alpha(H/r)c_s$ [equation (3.72)]. This is because temperature (and thus $T_{r\varphi}$) changes abruptly in the transition front, $|dT/dr| \sim T/H$ (Meyer 1984).

days after the peak. This was probably due to irradiation of the outer portions of the disk, which was not taken into account there (see subsection 5.2.4). Long recurrence timescales of ~ 60 yr for A0620–00 are essentially the consequence of the low temperature and smaller α values. Evaporation of inner-disk material may also be important to lengthen the repetition periods (Meyer and Meyer-Hofmeister 1994; Mineshige et al. 1998).

(b) Exponential decays

The Nova-Musca type BH novae exhibit beautiful exponential decays over several orders of magnitudes. How can we understand this?

The basic theory of the viscous diffusion process in disks says that the disk luminosity usually decays in a power-law fashion. This is related to the fact that as disk material diffuses away, the disk temperature usually decreases, so does the kinematic viscosity $\nu (\sim \alpha c_s^2 / \Omega \propto T)$, which results in increasing the viscous timescale, $t_{\text{vis}} \sim r^2 / \nu$. (An exponential decay implies a temporally constant viscous timescale.) As shown in the footnote in section 3.1, in fact, the self-similar solution yields power-law decays, $L \propto t^{-(1+a)}$, with a being a constant ($0 < a < 1$ in general), as long as the total angular momentum is conserved.

It is easy, however, to demonstrate that exponential decays are reproduced if the angular momentum is somehow removed from the inner hot portions of the disk (Mineshige et al. 1993). Suppose that the disk has disposed of mass and angular momentum at a constant rate at each radius.¹⁵ The basic equations are as follows:

$$\frac{\partial \Sigma}{\partial t} = \frac{1}{2\pi r} \frac{\partial \dot{M}}{\partial r} - \frac{\Sigma}{t_{\text{ex}}}, \quad (5.49)$$

$$\frac{\partial(\Sigma\ell)}{\partial t} = \frac{1}{2\pi r} \frac{\partial(\dot{M}\ell)}{\partial r} - \frac{3}{2r} \frac{\partial}{\partial r} (\nu\Sigma\ell) - \frac{\Sigma\ell}{t_{\text{ex}}}, \quad (5.50)$$

where the last terms on the right-hand side represent the removal of mass and angular momentum at each radius at a constant rate of $1/t_{\text{ex}}$, and $\ell = \sqrt{GMr}$ is specific angular momentum for a point-mass potential, $\psi = -GM/r$ (see section 3.2). From combining equations (5.49) and (5.50), we recover equation (5.39).

¹⁵We first construct a simple model producing exponential decays and do not specify how this occurs; it could be due to outgoing wind in the vertical direction or something else. It can also be shown numerically that exponential decays are produced even in the case that mass and angular momentum are removed only from the outermost region (Mineshige et al. 1993). The physical relevance is discussed at the end.

We now seek a solution to this set of equations. If we let $\Sigma_1(r, t)$ be the solution in the case without mass removal [equation (3.18)];

$$\frac{\partial \Sigma_1}{\partial t} = \frac{3}{r} \frac{\partial}{\partial r} \left\{ \sqrt{r} \frac{\partial}{\partial r} \left[\nu_0 \left(\frac{\Sigma_1}{\Sigma_0} \right)^b \left(\frac{r}{r_0} \right)^a \sqrt{r} \Sigma_1 \right] \right\}, \quad (5.51)$$

where we assume $\nu \propto r^a \Sigma^b$ and r_0 , ν_0 , and Σ_0 are numerical constants. Also, let $\Sigma_2(r, t)$ be the solution in the case with mass removal. From equations (5.49) and (5.39), we have

$$\frac{\partial \Sigma_2}{\partial t} + \frac{\Sigma_2}{t_{\text{ex}}} = \frac{3}{r} \frac{\partial}{\partial r} \left\{ \sqrt{r} \frac{\partial}{\partial r} \left[\nu_0 \left(\frac{\Sigma_2}{\Sigma_0} \right)^b \left(\frac{r}{r_0} \right)^a \sqrt{r} \Sigma_2 \right] \right\}. \quad (5.52)$$

Here, we look for Σ_2 solution having the form

$$\Sigma_2(r, t) = \exp \left(-\frac{t}{t_{\text{ex}}} \right) \cdot \Sigma_1(r, t') \quad (5.53)$$

(with t' being a function of t), provided that the solution $\Sigma_1(r, t)$ is already known [e.g., self-similar solutions; see appendix I of the first edition (Kato et al. 1998)]. By substituting equation (5.53) into (5.52), we find after some algebra that

$$t' = \frac{t_{\text{ex}}}{b} \left[1 - \exp \left(-b \frac{t}{t_{\text{ex}}} \right) \right]. \quad (5.54)$$

For short $t (\ll t_{\text{ex}})$, we find $t' \approx t$, whereas for long $t (\gg t_{\text{ex}})$, we find $t' \rightarrow t_{\text{ex}}/b = \text{constant}$. If $t_{\text{ex}} \lesssim t_{\text{vis}}$, therefore, the surface-density distribution everywhere decreases exponentially, no matter how $\Sigma_1(r, t)$ itself decreases, causing an exponential decay in the disk luminosity.

According to the DN-type disk instability model, a rapid *outward* mass flow occurs from the inner hot (HII) to the outer cool (HI) zones during the decay. This is because of a steep negative gradient in $\nu (\propto T)$ and, hence, in $T_{r\varphi}$ [see equation (5.39)]. Such a rapid mass outflow also carries angular momentum outwards. Since the decay process depends on how quickly angular momentum can be removed from the inner parts of the disk, such an angular-momentum outflow promotes rapid accretion. This will maintain a rapid decline, even at the late decline phase, a condition to produce exponential decays.

There are two lines of thoughts. One might argue that the occurrence of exponential decays may depend on the precise viscosity prescription; for instance, Cannizzo et al. (1995) claimed that beautiful exponential

decays can be produced by the disk instability only if $\alpha \propto (H/r)^{3/2}$. However, why should such a (rather peculiar) viscosity prescription be chosen? Alternatively, one might think (or believe) that the nature of exponential decays could be related to fundamental physics and should not critically depend on any detailed modeling. The answer is still unknown.

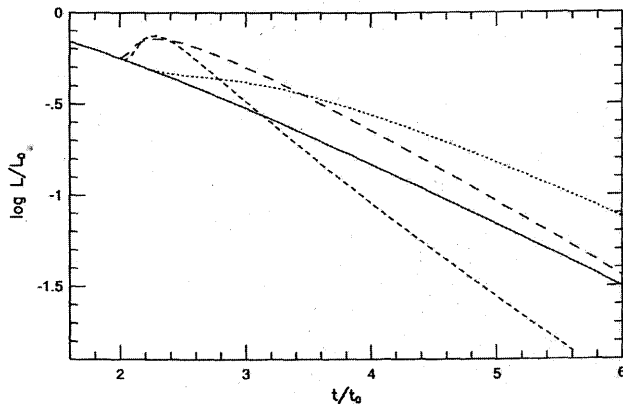
(c) Reflares

Reflares (or secondary maxima, secondary peaks) are commonly observed in Nova-Musca type transient black-hole candidates at 50–70 days after the main peaks (see figure 1.27). From a theoretical point of view, there are basically two ways to produce light enhancement: by either increasing \dot{M} or increasing ν (and thus temperature). We now show how such effects modify the light curve of a disk by numerically solving the equation of viscous accretion disks.

Here, we simply assume an exponentially damping mass-input rate to the disk in order to produce exponential decays, $\dot{M}_0 \propto \exp(-t/t_0)$, with t_0 being a constant corresponding to the viscous timescale. The X-ray luminosity of the disk can be approximated by $L \approx \eta \dot{M}(r_{\text{in}}) c^2$ with η (~ 0.1) being an energy-conversion factor. The dimensionless luminosity, L/L_0 , is plotted against time in figure 5.8 by the solid curve. This model forms the basis on which we introduce some perturbations to produce the reflares. Possible perturbations are a mass-transfer burst (Chen et al. 1993; Augusteijn et al. 1993), abrupt heating of the disk (Shakura, private communication; Mineshige 1994), or both.

We first examine the case in which the mass-input rate is suddenly increased by a factor of 4 at $t/t_0 \geq 2.0$. The resultant variation in the disk luminosity is displayed in figure 5.8 by the dotted curve. An enhanced mass input first causes an increase in Σ , which then increases $\dot{M}(r)$. The mass-accretion rate at r_{in} thus increases only on the diffusion timescale t_0 since an enhanced mass flow takes $\sim t_0$ to produce a substantial change in L via viscous diffusion. This feature contradicts with reflares, which show a rapid rise on a timescale of less than t_0 .

Next, we abruptly increase ν ($\propto T$) by a factor of 5 at $t/t_0 \geq 2.0$ at $r > 0.1 r_d$. The viscosity inside this radius remains unchanged. The resultant disk luminosity is illustrated in figure 5.8 by the short dashed curve. In contrast with the previous case, the disk luminosity can quickly grow, since ν -perturbations directly induce an overall enhancement in $\dot{M}(r)$. At later times, however, L becomes lower than that of the unperturbed model (indicated by the solid curve). This is because the enhanced mass inflow, the rate of which much exceeds the mass-supply

**Figure 5.8**

Several models for reflares: the basic model (solid curve), the mass-transfer burst model (dotted curve), the abrupt heating model (short dashed curve), and the composite model (long dashed curve). (After Mineshige 1994)

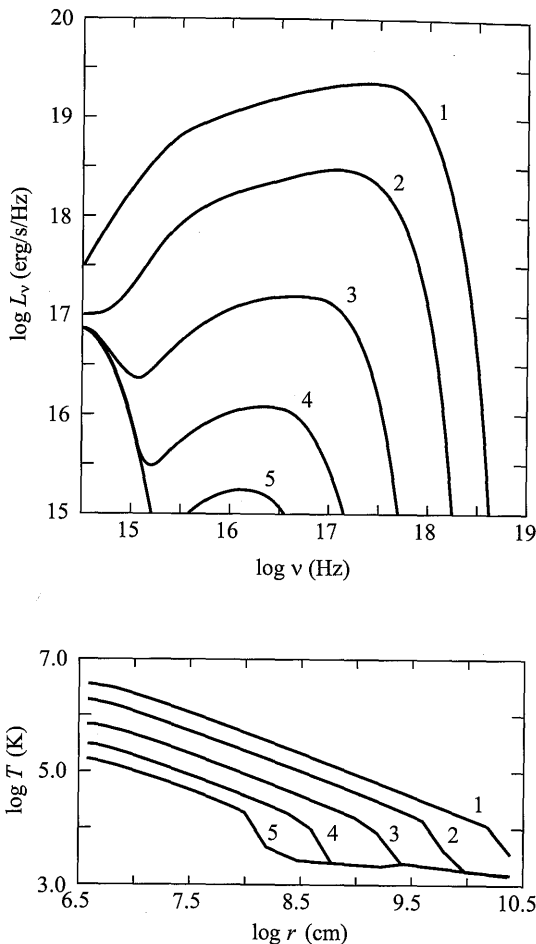
rate, causes mass depletion at the outer portions.

To reproduce the observations, therefore, we need to increase both ν and \dot{M} . Finally, we abruptly increase both ν (at $r/r_d \geq 0.9$) and $\dot{M}(r_d)$ by factors of 2 and 4, respectively. The light curve, depicted in figure 5.8 by the long dashed curve, yields a rapid rise and slow exponential-like decay. This is the most favorable case compared with the observed light curve. How is this possible?

One possibility is that when the disk is exposed to strong X-ray irradiation the outer cool region, which has just undergone a downward transition to the cool state, returns to the hot state; in other words, the cooling front recedes transiently. Another possibility is that a mass flow in the optically thin, (probably) coronal region now joins in the optically thick, disk flow, thus increasing the mass-flow rate within the disk (instead of the mass input rate to the disk). Although the basic behavior has been revealed, the origin of reflares still remains a puzzle at present.

5.2.3 Basic Spectral Variation

Soft X-rays are thought to arise from the inner portions of optically thick accretion disks. We can thus calculate the soft X-ray spectra by assuming black-body spectra. The resultant evolution of the spectra and the effective temperature distribution in the decay phase of the outburst

**Figure 5.9**

Time evolution of the theoretical disk spectra (upper panel) and the effective temperature profiles (lower panel) calculated based on the model depicted in figure 5.7. (After Mineshige et al. 1990)

are displayed in figure 5.9.

The disk in the decline phase comprises two regions: a hot, inner, approximately steady-state region ($T_{\text{eff}} \propto r^{-3/4}$) and a cool outer region of nearly constant effective temperatures,¹⁶ say, $\log T_{\text{eff}} \sim 3.2$. At

¹⁶The original DN-type disk-instability model predicts a very low effective temperature in the cool state, which does not always agree with the observations, even in dwarf-nova cases, since a much hotter (color) temperature ($\sim 5000\text{K}$) was estimated (Wood et al. 1986, 1989). A similar disagreement seems to also appear in black-hole

maximum light, the entire disk resides in the steady-state regime. As time goes on, the cool, constant- T_{eff} regime expands from the outer edge to inner radii, thus reducing the mass-flow rate into the inner steady state region. The resultant spectra depicted in figure 5.9 are essentially the sum of a sequence of steady state disk spectra (with the same central mass and inner radius, but with decreasing mass-flow rates), and the single-temperature black-body spectra. As the mass-accretion rate onto a central black hole decreases with time, the size of the soft X-ray emitting region shrinks, thereby reducing the soft X-ray luminosity.

A spectral analysis of the X-ray Nova Muscae 1991 shows that the soft X-ray spectra at different times are well fitted by the disk blackbody spectra and that the inner radius of the emitting region is nearly constant, while the effective temperature at the inner edge decreases with time (figure 3.8; see also Tanaka 1989). This is exactly what is predicted by the DN-type disk instability model. The origin of hard X-rays and the place where hard X-rays are generated will be discussed later (see chapter 9).

5.2.4 Effects of Irradiation

Accretion disks have two major heating sources: i) viscous heating generated in the body of the disk and ii) surface heating by irradiation from the central compact object, by the inner part of the disk, and perhaps by the companion star in binaries with high-mass companion stars [see section 3.7 of the first edition (Kato et al. 1998)]. Neglecting any external heating may be justified in CVs. Since in low-mass X-ray binaries, however, the inner regions of the disk releases about 10^3 times more radiation than in CVs, the heating by irradiation cannot be neglected. The thermal structure of the disk would be significantly altered by the presence of the strong X-ray flux (Shakura and Sunyaev 1973; Hayakawa 1981). The heated surface might expand, form an optically thin corona, and may escape from the disk as wind (Begelman et al. 1983). As a result, the thermal instability of a sort invoked in dwarf novae might be at least partly suppressed (Meyer and Meyer-Hofmeister 1984; Saito 1989). We should therefore calculate how an irradiating flux penetrates into the disk, thereby modifying the properties of the disk instabilities.

We follow Tuchman et al. (1990) to determine how an S-shape is affected by irradiation. The basic equations, based on the α model, are essentially the same as those presented in section 5.1.3, except that the

systems (Mineshige and Wood 1990).

internal flux (flux from the interior to the surface), F_{ex} , is calculated by

$$F_{\text{ex}} = \frac{4\sigma T_{\text{ex}}^4}{3f_2(\tau_{\text{ex}})} - F_{\text{irr}}, \quad (5.55)$$

where the first term on the right-hand side represents the outgoing flux from the surface, F_{irr} denotes the incident flux into the surface layer by external heat sources, T_{ex} is a parameter representing the disk temperature at $\tau = \tau_{\text{ex}}$, and $f_2(\tau)$ is a correction factor of order of unity.¹⁷ For convenience, we define the irradiation temperature as

$$T_{\text{irr}} = \left(\frac{F_{\text{irr}}}{\sigma} \right)^{1/4}. \quad (5.56)$$

We assume the surface optical depth τ_{ex} to be ~ 0.01 . This procedure is based on the assumption that the X-ray radiation, caused by mass accretion upon a compact star, is thermalized *above* the disk surface (at $\tau_{\text{ex}} = 0.01$ for Rosseland-mean opacity). This assumption may be justified if the spectrum of the incident X-ray flux is relatively soft (less than a few keV), because the absorption coefficients are larger for soft X-rays compared with those for optical light.

The resultant thermal-equilibrium curve depicted in figure 5.10 shows that at a given radius the kinks in the thermal equilibrium curves, which are responsible for the thermal instability, are weakened as T_{irr} rises, until finally they disappear for the irradiation temperatures,

$$T_{\text{irr}} > 10^4 \text{ K.} \quad (5.57)$$

For higher T_{irr} , the thermal limit-cycle instability is suppressed.

We can roughly evaluate the critical X-ray luminosity, below which the disk instability is viable. The irradiation flux F_{irr} is related to the X-ray luminosity L_x by

$$F_{\text{irr}} \simeq C \frac{L_x}{2\pi r^2}. \quad (5.58)$$

Here, C represents the fraction of the X-ray energy which is caught by the outer portions of the disk at radius r . For direct irradiation from the inner portions of the disk (i.e., neglecting scattering or irradiation from any corona), $C \lesssim A(H/r) \sim 10^{-2}$, where A is the X-ray albedo and H is the half-thickness of the disk. From combining equations (5.57) and

¹⁷Roughly speaking, this is equivalent to setting $F_z(H) = \sigma T_{\text{eff}}^4 - F_{\text{irr}}$ at the upper layer of $\tau = 2/3$ instead of $F_z(H) = \sigma T_{\text{eff}}^4$ [equation (5.15)].

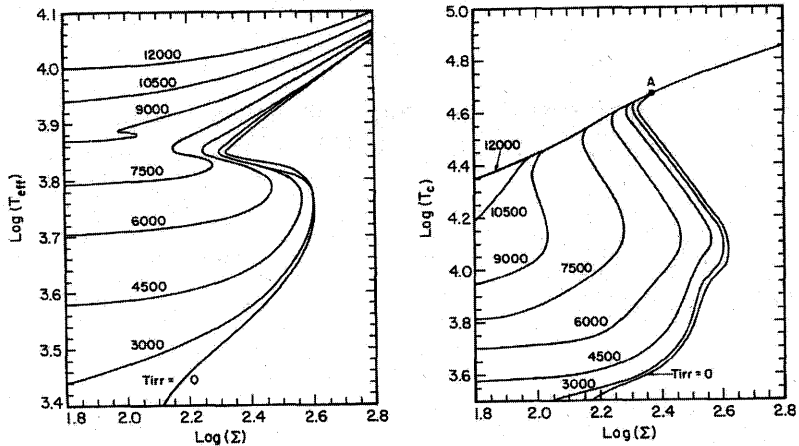


Figure 5.10

Influence of the irradiation to the S -shaped thermal equilibrium curves in the (T_{eff}, Σ) -plane (left panel) and in the (T_c, Σ) -plane (right panel), respectively. The parameters are $\log r(\text{cm}) = 10.5$, and $\alpha = 0.1$. The number attached to each line represents the irradiation temperatures. (After Tuchman et al. 1990)

(5.58), we find the condition for the X-ray luminosity, below which the disk is thermally unstable;

$$L_x < 10^{35.5} \left(\frac{C}{10^{-2}} \right)^{-1} \left(\frac{r}{10^{10.5} \text{ cm}} \right)^2 \text{ erg s}^{-1}. \quad (5.59)$$

This condition is easily satisfied, at least during quiescence (see section 5.1).¹⁸ The irradiating flux in outburst is, in contrast, never negligible and is expected to cause a plateau in the V -magnitude light curve (see figure 5.7). Further investigation is needed in this area.

References

- Alexander D.R., Johnson H.R., Rypma R.L. 1983, ApJ 272, 773
 Allen C.W. 1973, *Astrophysical Quantities* (Athlone Press, London)
 Augusteijn T., Kuulkers E., Shaham J. 1993, A&A 279, L13
 Bath G.T. 1973, Nature Phys. Sci. 246, 84
 Begelman M.C., McKee C.F., Shields G.A. 1983, ApJ 271, 70
 Cannizzo J.K. 1993, in *Accretion Disks in Compact Stellar Systems*, ed. J.C. Wheeler (World Scientific, Singapore), p6

¹⁸In neutron-star binaries strong radiation from the neutron-star surface tends to suppress a disk instability. This would explain why not so many neutron-star binaries show XN eruptions (van Paradijs 1996).

- Cannizzo J.K., Chen W., Livio M. 1995, ApJ 454, 880
Cannizzo J.K., Wheeler J.C. 1984, ApJS 55, 367
Cannizzo J.K., Wheeler J.C., Ghosh P. 1982, in *Pulsations in Classical and Cataclysmic Variables*, ed. J.P. Cox, C.J. Hansen (Univ. Colorado Press, Boulder), p13
Cannizzo J.K., Wheeler J.C., Ghosh P. 1985, in *Cataclysmic Variables and Low-Mass X-ray Binaries*, ed. D. Q. Lamb, J. Patterson (Reidel Publishing Company, Dordrecht), p307
Chen W., Livio M., Gehrels N. 1993, ApJL 408, L5
Cox A.N., Stewart J.N. 1970, ApJS 19, 243
Cox J.P., Giuli R.T. 1968, *Principle of Stellar Structure* (Gordon and Breach, New York)
Hameury J.M., King A.R., Lasota J.-P. 1986, A&A 162, 71
Hayakawa S. 1981, PASJ 33, 365
Hōshi R. 1979, PTP 61, 1307
Huang M., Wheeler J.C. 1989, ApJ 343, 229
Kippenhahn R., Weigert A., Hofmeister E. 1967, in *Methods in Computational Physics*, Vol. 7, ed. B. Adler, S. Fernbach, M. Rotenberg (Academic Press, New York), p129
Lin D.N.C., Taam R.E. 1984, in *High-Energy Transients in Astrophysics (AIP Conf. Proc. 115)*, ed. S. E. Woosely (AIP, New York), p83
Meyer F. 1984, A&A 131, 303
Meyer F., Meyer-Hofmeister E. 1981, A&A 104, L10
Meyer F., Meyer-Hofmeister E. 1982, A&A 106, 34
Meyer F., Meyer-Hofmeister E. 1984, A&A 140, L35
Meyer F., Meyer-Hofmeister E. 1994, A&A 288, 175
Mineshige S. 1987, ApSS 130, 331
Mineshige S. 1994, ApJL 431, L99
Mineshige S. et al. 1992, PASJ 44, 115
Mineshige S., Kim S.-W., Wheeler J.C. 1990, ApJL 358, L5
Mineshige, S., Liu, B., Meyer, F., and Meyer-Hofmeister, E. 1998, PASJ 50, L5.
Mineshige S., Osaki Y. 1983, PASJ 35, 377
Mineshige S., Osaki Y. 1985, PASJ 37, 1
Mineshige S., Tuchman Y., Wheeler J.C. 1990, ApJ 359, 176
Mineshige S., Wheeler J.C. 1989, ApJ 343, 241
Mineshige S., Wood J.H. 1990, MNRAS 247, 43
Mineshige S., Yamasaki T., Ishizaka C. 1993, PASJ 45, 707
Narayan R., Garcia M., McClintock J. 1997, ApJL 478, L79
Narayan R., McClintock J., Yi I. 1996, ApJ 457, 821

- Nicolis G., Prigogine I. 1977, *Self-Organization in Nonequilibrium Systems* (John Wiley and Sons, New York)
- Osaki Y. 1974, PASJ 26, 429
- Osaki Y. 1996, PASP 108, 39
- Paczyński B. 1969, Acta Astron. 19, 1
- Saito N. 1989, PASJ 41, 1173
- Shakura N.I., Sunyaev R.A. 1973, A&A 24, 337
- Smak J. 1982, Acta Astron. 32, 213
- Smak J. 1984, Acta Astron. 34, 161
- Tanaka Y. 1989, in *Proc. 23rd ESLAB Symp. on Two Topics in X-Ray Astronomy*, ed. J. Hunt, B. Battrick (ESA SP-296, Dordrecht), p3
- Tuchman Y., Mineshige S., Wheeler J.C. 1990, ApJ 359, 164
- Whelan J.A.J. et al. 1977, MNRAS 180, 657
- Wood J.H., Horne K., Berriman G., Wade R.A., O'Donoghue D., Warner B. 1986, MNRAS 219, 629
- Wood J.H., Horne K., Wade R.A., Berriman G. 1989, ApJ 341, 974
- van Paradijs, J. 1996, ApJ 464, L139

CHAPTER 6

Observability of Relativistic Effects

Black-hole accretion disks manifest their relativistic nature in various ways: their appearances are metamorphosed in a curved space, photometric light curves of the disk are also influenced, both continuum and line spectra are different from those expected for non-relativistic disks, and so on. Turning our attention to observation, we can confirm the existence of a relativistic disk and a central black hole through these relativistic manifestations of the disk. In this chapter we discuss in turn the observability of relativistic effects around a black hole.

6.1 Ray Tracing

The emergent spectra from relativistic accretion disks around a neutron star or a black hole are influenced by various relativistic effects. There are three major relativistic effects: (i) the gravitational bending of light rays, (ii) the gravitational redshift, and (iii) the relativistic Doppler effect. In this section we briefly describe the procedure to calculate the emergent spectrum of relativistic accretion disks, using the ray-tracing method (Luminet 1979; Fukue and Yokoyama 1988; Karas et al. 1992; Jaroszyński et al. 1992; Fanton et al. 1997; Takahashi 2004).

(a) Photon trajectory

Let us consider an accretion disk surrounding a Schwarzschild black hole of mass M . The situation is schematically shown in figure 6.1. The accretion disk is a geometrically thin standard one (chapter 3), which has an inner edge at a marginally stable radius of $3r_g$. The observer is located at (ϱ_0, θ_0) , where ϱ_0 is the observer's distance from the center of the disk and θ_0 is the observer's polar angle measured from the symmetry axis of the disk. Actually, ϱ_0 is taken to be sufficiently large, and therefore we

can consider that the observer is located at infinity. Finally, the accretion disk rotates counterclockwise against the line-of-sight of the observer.

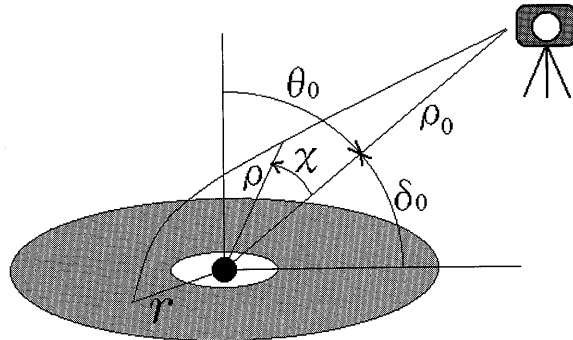


Figure 6.1

Schematic view of an accretion disk around a Schwarzschild black hole and a distant observer. In the central region of the disk there is a ‘hole’ inside the inner edge of the disk around the black hole. The light rays travel from the disk to the observer along the null geodesics and vice versa.

A photon emitted from some point on the disk travels along the null geodesics to be received by the observer. In the ray-tracing method, however, the light ray is traced from the observer to the point where it originates, based on Fermat’s Principle.¹ In the Schwarzschild space-time (figure 6.1), the trajectory of light rays is determined by

$$\frac{d^2}{d\chi^2} \left(\frac{1}{\varrho} \right) + \frac{1}{\varrho} = \frac{3r_g}{2\varrho^2}, \quad (6.1)$$

where (ϱ, χ) are the spherical coordinates and r_g ($= 2GM/c^2$) is the Schwarzschild radius (Landau and Lifshitz 1971). The “energy” integral of this equation is

$$\left[\frac{d}{d\chi} \left(\frac{1}{\varrho} \right) \right]^2 + \frac{1}{\varrho^2} \left(1 - \frac{r_g}{\varrho} \right) = \frac{1}{b^2}, \quad (6.2)$$

¹This principle states in its simplest form that light travels the path between two points that takes the least time. As a result, light can travel both directions on the same path, and therefore we can trace back the light ray *from* the observer *to* the emitting point.

where b is the impact parameter (see figure 6.2 below). The second term on the left-hand side of this equation can be interpreted as an effective potential in analogy with Newtonian mechanics. For further discussions concerning the trajectories of light rays, consult Luminet (1979).

(b) Redshift

The redshift z of light emitted from a point on the surface of the disk consists of three parts:

$$1 + z = \frac{\nu_{\text{em}}}{\nu_{\text{obs}}} = L^{-1} \gamma D^{-1}, \quad (6.3)$$

where ν_{em} and ν_{obs} are the emitted and observed frequencies, respectively, L the lapse function representing the gravitational redshift, γ the Lorentz factor denoting the transverse Doppler effect, and D the Doppler factor expressing the longitudinal Doppler effect.

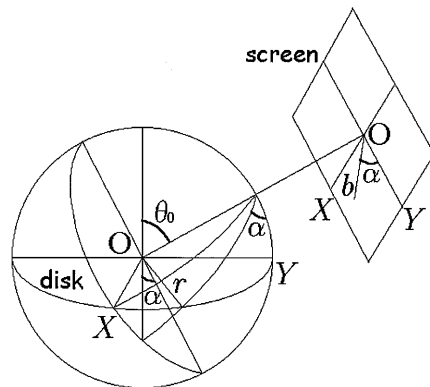


Figure 6.2

Coordinate system for the ray-tracing method (based upon figure 3 of Luminet 1979). The black hole lies at the center of both the Cartesian coordinates (x, y, z) and the cylindrical coordinates (r, φ, z) . The observer lies in the xz -plane in the direction of the polar angle θ_0 . On the observer's screen, the black hole lies at the center of the Cartesian coordinates (X, Y) and the polar coordinate (b, α) .

Of these, the lapse function for the Schwarzschild case is

$$L = \sqrt{1 - \frac{r_g}{r}}, \quad (6.4)$$

where r is the radial distance of the emitting point on the disk. The Lorentz factor γ of a circularly rotating gas is $\gamma = \sqrt{1 + r^2 \Omega^2 / c^2}$, where

Ω is the angular velocity of the gas measured at the disk. For a Keplerian rotating disk, $\Omega = \sqrt{r_g c^2 / [r^2(2r - 3r_g)]}$ (see a footnote of subsection 2.5.3); therefore, the Lorentz factor becomes

$$\gamma = \sqrt{\frac{1 - r_g/r}{1 - 3r_g/2r}}, \quad (6.5)$$

where we assume that the observer is at rest. The longitudinal Doppler factor ($D = 1 - \mathbf{v} \cdot \mathbf{n}/c$) is expressed as (Luminet 1979)

$$D^{-1} = 1 + \sqrt{\frac{r_g}{2r^3}} b \sin \theta_0 \sin \alpha, \quad (6.6)$$

where b is the impact parameter, α the angle on the screen, and θ_0 the polar angle (figure 6.2). Hence, the redshift z finally becomes

$$1 + z = \left(1 - \frac{3r_g}{2r}\right)^{-1/2} \left(1 + \sqrt{\frac{r_g}{2r^3}} b \sin \theta_0 \sin \alpha\right). \quad (6.7)$$

(c) Observed flux

In the case of a Schwarzschild black hole ($a_* = 0$), we have an explicit form on \mathcal{Q} in equation (3.163) [see equation (A.34)] (Page and Thorne 1974). Then, from equation (3.189), the bolometric flux of radiation from the disk, F , is explicitly given by

$$F(\hat{r}) = \frac{3GM\dot{M}}{8\pi r_g^3} \frac{1}{(\hat{r} - 1.5)\hat{r}^{5/2}} \times \left(\sqrt{\hat{r}} - \sqrt{\hat{r}_{\text{ms}}} + \frac{\sqrt{1.5}}{2} \ln \frac{\sqrt{\hat{r}} + \sqrt{1.5}}{\sqrt{\hat{r}} - \sqrt{1.5}} \frac{\sqrt{\hat{r}_{\text{ms}}} - \sqrt{1.5}}{\sqrt{\hat{r}_{\text{ms}}} + \sqrt{1.5}} \right), \quad (6.8)$$

where $\hat{r} \equiv r/r_g$ and $\hat{r}_{\text{ms}} \equiv r_{\text{ms}}/r_g = 3$. The effective temperature of the disk is then obtained by $T(\hat{r}) = (F/\sigma)^{1/4}$.

Once the emitting point on the disk is traced back from the observer by equation (6.2), and the redshift is given by equation (6.7), the observed flux F_{obs} and the observed blackbody temperature T_{obs} are transformed from the emitted flux F and the effective temperature T by

$$F_{\text{obs}} = \frac{1}{(1+z)^4} F, \quad (6.9)$$

$$T_{\text{obs}} = \frac{1}{(1+z)} T, \quad (6.10)$$

since $F_{\text{obs}}/\nu_{\text{obs}}^4 = F/\nu_{\text{em}}^4$ and $T_{\text{obs}}/\nu_{\text{obs}} = T/\nu_{\text{em}}$ are Lorentz invariants (cf. appendix E).

6.2 Imaging – Black Hole Silhouette

Although a black hole without gas or background light cannot be seen, this is not true for a black hole in a luminous robe. When a black hole wears a luminous accretion disk, the appearance of the disk is remarkably distorted by the strong gravitational field of the black hole, and can be seen by a distant observer as a space-time silhouette of the black hole. Direct imaging of the black-hole accretion disk gives information on the luminous disk as well as the space-time structure.

Let us first demonstrate the unique properties of relativistic accretion disks with the help of figure 6.3 (see also figure 6.4). Figure 6.3 displays a (color) photograph of standard accretion disks around a Schwarzschild black hole, which was obtained numerically using a ray-tracing method (Fukue and Yokoyama 1988) (for a Kerr case, see, e.g., Fanton et al. 1997; Takahashi 2004).

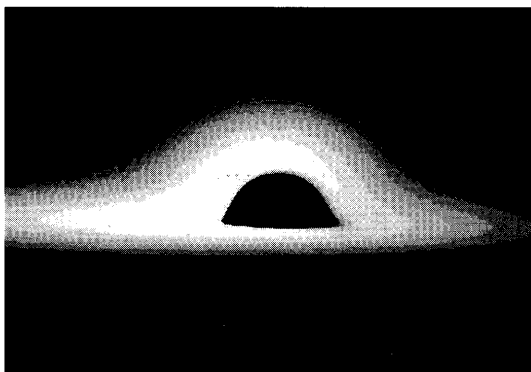


Figure 6.3

“Photograph” of a relativistic accretion disk (see figure G.2). The inclination angle is 80° and the horizontal size is $30r_g$ across. The central black region corresponds to that inside the inner edge of the disk. (After Fukue and Yokoyama 1988)

As already stated, around a neutron star or a black hole, the relativistic effects, such as *gravitational focusing* (gravitational bending of light), *gravitational redshift*, and *Doppler effects*, significantly modify the appearance and spectra. This situation can be seen visually in figure 6.3 (and figure 6.4). In the relativistic case, the apparent image of the disk is significantly distorted by the Doppler effect associated with the disk rotation and by gravitational bending of light rays near to the black hole (Luminet 1979). That is, the emergent radiation from the left part of the photograph, which is approaching the photographer at relativistic

speed, is remarkably enhanced by the Doppler shift, while that from the right part is reduced. This is the reason why the photograph image is asymmetric with respect to the rotation axis. In addition, the light ray originating from the opposite side of the disk (opposite to the photographer with respect to the hole) is strongly bent in the gravitational field of the black hole before it reaches the photographer, while that from this side (between the photographer and the hole) is almost coming straight. This is the reason why the photograph is asymmetric with respect to the horizontal line passing the central hole.

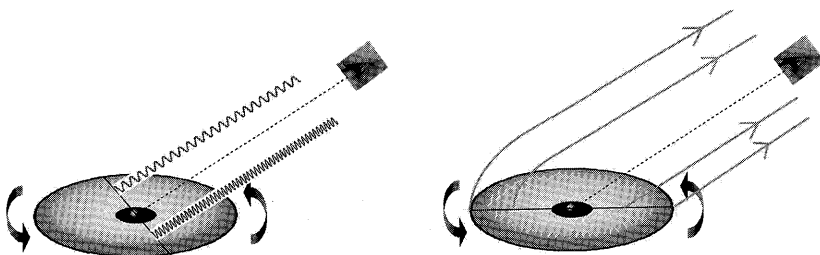


Figure 6.4

Explanation of the distorted image of the relativistic disk around a black hole (see figure G.4). Left: Due to the Doppler effect associated with disk rotation, the photograph image becomes asymmetric with respect to the rotation axis. Right: Due to bending of the light ray around the black hole, the photograph image becomes asymmetric with respect to the horizontal line.

Up to now, as robes surrounding a black hole, traditional standard disks were usually considered (Luminet 1979; Fukue and Yokoyama 1988; Karas et al. 1992; Jaroszyński et al. 1992; Fanton et al. 1997; Takahashi 2004, 2005), or spherically-distributed optically-thin gas was examined (Falcke et al. 2000). There are supposed, however, to exist other types of robes with different velocity fields, different temperature distributions, and different sizes of the inner radius (e.g., slim disk in chapter 10; Fukue 2003a; Watarai et al. 2005a). In the case of geometrically thick disks, such as slim disks, the self-occultation of the innermost disk by the outer disk becomes important (Fukue 2000b; Watarai et al. 2005a; Kawata et al. 2006).

In the case of the traditional standard disk with an inner radius of $3r_g$ around a Schwarzschild black hole, there appears to be a dark central shadow with a radius of about $3r_g$. In the case of a disk extending down to $1r_g$, on the other hand, we found that the radius of the dark

shadow is about $2r_g$ (Fukue 2003a). These shadow sizes are different from that obtained by Falcke et al. (2000), who considered an optically thin spherical envelope, and where the shadow radius is about $2.6r_g$ (the apparent size of the hole seen at infinity is $3\sqrt{3}/2r_g$). This difference is just because of the existence of the disk; in the former case with the disk, a light ray with an impact parameter somewhat smaller than $2.6r_g$ can be intercepted by the disk (*projection effect*). As a result, the “black hole shadow” becomes smaller than that without the disk. Furthermore, in an edge-on view the central shadow becomes a semicircle due to the projection effect. Such a silhouette of a dressed black hole throws light on the space-time structure of the hole as well as the type of surrounding disk.

In the case of the supermassive black hole at our galactic center, Sgr A*, the measured mass (Melia and Falcke 2001, and section 1.5) is $M \sim 3 \times 10^6 M_\odot$. Hence, its Schwarzschild radius is $r_g = 2GM/c^2 = 9 \times 10^{11}$ cm, which corresponds to about 7 micro-arcsec. In Falcke et al. (2000), for an optically-thin spherical envelope, the diameter of the shadow is on the order of $5r_g = 35$ micro-arcsec. In the standard disk, on the other hand, the apparent diameter of the inner edge is $6r_g = 42$ micro-arcsec. In optically-thick luminous disks with extended inner regions down to $1r_g$, the diameter of the shadow is $4r_g = 28$ micro-arcsec. Moreover, the shape of the shadow may be a semicircle for the case of Sgr A*, since the inclination angle is supposed to be large.

In the near future, maybe in the radio wavelength band first, real photographs of supermassive black holes in luminous robes, the *black hole face*, will be taken (cf. Miyoshi et al. 2004). The appearance of robes depends on the types of dresses and inclination angles as well as the space-time structure. However, the size and shape of the shadow, the *silhouettes*, only depend on the black-hole type and the innermost radius of the luminous part of the robes. When we can take real photographs, while bearing the properties of luminous robes in mind, we must examine the size and shape of the central shadow, the tone of a pseudo color and the extension of luminous robes to determine the mass of the black holes and types of accretion disks.

6.3 Spectroscopy – Continuum and Line

As already stated, around a neutron star or a black hole, the appearance of accretion disks significantly suffers from relativistic effects, such as gravitational focusing (gravitational bending of light), gravitational

redshift, and Doppler effects. These properties of relativistic accretion disks are also reflected in both the continuum and line spectra.

6.3.1 Continuum Spectra

First of all, accretion disks emit *multi-color* spectra. Like stars, gas in the accretion disk (atmosphere) radiates mainly thermal radiation. In standard disks, which are geometrically thin and optically thick in the vertical direction, radiation from the disk surface is treated locally as blackbody radiation in the zeroth-order approximation. Unlike stars, however, in accretion disks the surface temperature is not uniform, but varies as a function of the distance from the center (see section 3.2). As a result, the overall spectrum from accretion disks is not a blackbody spectrum of single temperature, but a modified one of multi-temperatures — the *disk-blackbody spectrum* or the *multi-color spectrum* (Mitsuda et al. 1984) (see section 3.2).

In addition, the emergent spectra from relativistic accretion disks around a neutron star or a black hole are influenced by relativistic effects. In particular, the high-frequency part of the observed spectra coming from the inner disk is remarkably modified. As already stated, there are three major relativistic effects: (i) the gravitational bending of light rays, (ii) the gravitational redshift, and (iii) the Doppler effect. Due to the gravitational bending of light, the effective area of the inner disk becomes large (figure 6.3), and therefore the spectra become somewhat harder. Due to the gravitational redshift, the spectra from the inner disk become somewhat softer (redder). Unless we see the disk from pole-on, this gravitational redshift has a minor effect. The most prominent is the Doppler effect. That is, radiation emitted from the approaching side of the disk is Doppler-boosted and becomes harder (bluer). As a result, the observed spectra from accretion disks around a relativistic object in general becomes hard in the high-frequency part, although it depends on the inclination angle.

The emergent spectra from relativistic accretion disks are calculated by summing up the *observed* local blackbody spectra over the *observed* disk. A numerical example of the continuum spectra calculated by full relativistic simulations using the procedure described above is shown in figure 6.5 (Yamada et al. 1994). In this example, the effect of Compton scattering is also taken into consideration. In figure 6.5 the abscissa is the frequency ν in units of Hz and the ordinate is the observed flux F_ν in cgs units. The thick solid curve represents the spectrum of a rel-

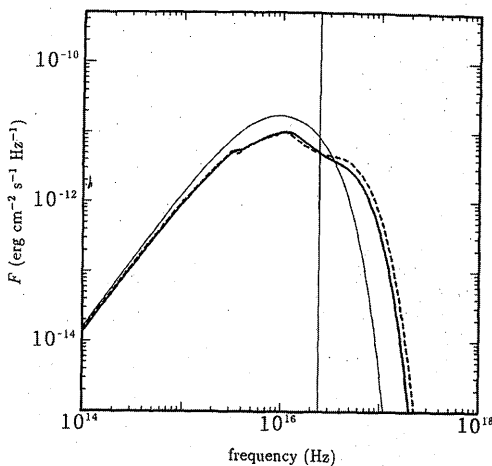


Figure 6.5

Entire relativistic disk spectra seen from a distant observer for an inclination angle of $i = 80^\circ$ (nearly edge-on). The parameters are $M = 10^6 M_\odot$ and $\dot{M} = 0.01 M_\odot \text{ yr}^{-1}$. The thick solid and dashed curves, respectively, denote the spectra of a relativistic disk and a Newtonian one. The thin solid curve is a blackbody spectrum that has the same energy loss. The vertical thin line indicates the energy of 0.1 keV. (After Yamada et al. 1994)

ativistic disk, while the thick dashed one is that of a Newtonian disk. (In the latter case, all of the photon trajectories are straight.) To our surprise, these spectra look quite similar in both cases. Although the disk spectra become substantially softer when the relativistic disk model is employed, the gravitational Doppler and lensing effects both tend to harden the spectra. These two opposite effects are counteracted, producing an apparently similar spectra.

The continuum spectra from relativistic standard accretion disks have been pioneeringly investigated by Cunningham (1975, 1976). Since then, many researchers have investigated the observed spectra from the relativistic disk around a black hole [see chapter 3 of the first edition (Kato et al. 1998) for more details].

6.3.2 Line Spectra

The spectral lines emitted in the inner region of accretion disks around a relativistic object are greatly modified by such relativistic effects as a gravitational redshift, gravitational lensing, and a relativistic Doppler

effect (figure 6.6).

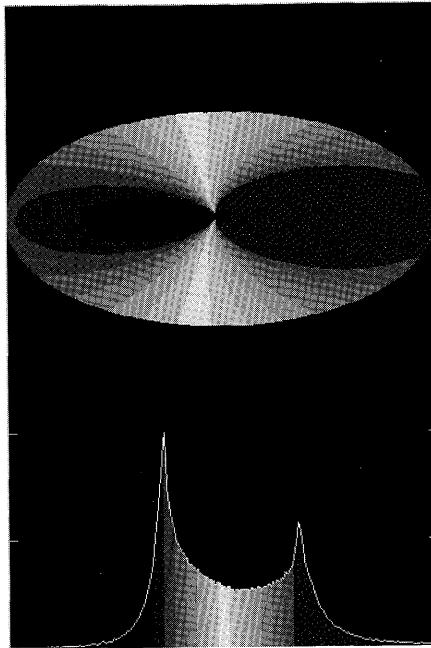


Figure 6.6

Iso-redshift contours and typical emission-line profiles from relativistic accretion disks (see figure G.3). The shaded regions come from the corresponding regions. In this example, the parameters are the emissivity, which is constant for $3r_g < r < 100r_g$, and the inclination angle, $i = 60^\circ$. The redshift ranges in the lower panel are $-0.2 \leq z \leq 0.2$.

The treatment is essentially the same as that for the continuum spectra. That is, the trajectory of light rays is first calculated by, e.g., a ray-tracing method, and the physical disk plane is mapped to the observer's sky. Then, the redshift of each part on the disk is calculated by equation (6.7). Similar to the isovelocity contours, iso-redshift contours can be obtained (figure 6.6). Finally, instead of summing up the local blackbody spectra, we collect the local line profiles I_ν over the entire disk.

It should be stressed that in addition to the redshift of the frequency the intensity of local lines is modified. That is, the Lorentz invariant is not the intensity I_ν but I_ν/ν^3 :

$$I_\nu = \left(\frac{\nu}{\nu_e} \right)^3 I_{\nu_e} = \frac{1}{(1+z)^3} I_{\nu_e}, \quad (6.11)$$

where I_ν is the observed intensity and I_{ν_e} the emitted intensity. Due to this Doppler enhancement, the characteristic double-peaked spectrum generally becomes *asymmetric* with respect to the line center, unless we see the disk from face-on; the blueshifted peak is remarkably enhanced due to the relativistic Doppler effect, while the redshifted peak is weakened. A numerical example is shown in figure 6.7.

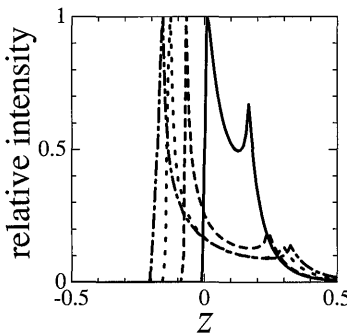


Figure 6.7

Emission-line profiles of relativistic disks. The inclination angle i is 20° (thick solid curve), 40° (thick dashed one), 60° (thick dotted one), and 80° (thick chain-dotted one), while the emissivity is constant for $3r_g < r < 10r_g$.

An asymmetric, double-peaked profile of spectral lines emitted from relativistic accretion disks was first noticed by Gerbal and Pelat (1981). In relation to the Balmer lines observed in active galactic nuclei, Chen et al. (1989) and Chen and Halpern (1989) calculated the asymmetric double-peaked lines under the weak-field approximations. In relation to iron fluorescent lines detected in Galactic X-ray sources and active galactic nuclei, line profiles have also been calculated for the Schwarzschild case (Fabian et al. 1989; see also Matt et al. 1993). Rigorous relativistic calculations of the line profiles from geometrically thin accretion disks around a Kerr black hole have been carried out by Laor (1991) and Kojima (1991). They showed that the line profile is not a double-peaked structure, but a broad single-peaked one if most of the flux originates from the inner regions of the disk. If the emitting region is extended farther from the black hole, this is not the case. Even in such a case, the line is significantly asymmetric, having a steep blue wing and an extended red wing. See also Bromley et al. (1997); Pariev and Bromley (1998).

The diagnostics of asymmetric double-peaked emission lines expected from the relativistic accretion disks is now applied to various active objects (Eracleous and Halpern 1994; Karas and Kraus 1996). Eracleous and Halpern (1994) surveyed the H α emission of 94 radio galaxies and radio-loud quasars, and identified 12 objects whose line profiles were well fitted by an accretion disk. The ASCA satellite observed a skewed iron K α line in the spectrum of the Seyfert galaxy MCG-6-30-15, which may have originated from relativistic accretion disks (Tanaka et al. 1995; see section 1.3). See also Beckwith and Done (2004).

Finally, line transfer was examined by Fuerst and Wu (2004).

6.4 Photometry – Light Curve Diagnosis

In the usual cases for distant faint sources, before imaging, we try photometry and spectroscopy. The observed luminosity (and spectrum) of accretion disks changes with time due to many reasons. One possible case is a disk instability (chapters 4 and 5 and later chapters). The disk instability, however, strongly depends on the disk properties, and does not very much reflect the central relativistic effect. Another plausible case is disk oscillation. *Discoseismology* would be one of the strong tools to investigate the relativistic properties of the central object, which is discussed in chapters 11 and 12.

Among other causes to give rise to variations of observed disk luminosities, the following would reflect the relativistic effects: precession of the inner disk, eclipse of the innermost relativistic region, orbital and/or infall motions of bright spots in the inner disk, flares and mass ejections from the innermost disk, and so on.

6.4.1 Light Curves during Inner-Disk Eclipse

When the innermost region of the accretion disk is occulted by another object, such as a companion, the X-ray luminosity would vary during an eclipse. Such eclipsing light curves contain information about the space-time structure as well as the disk surface brightness. Hence, light-curve analysis can be a strong tool for studying black-hole accretion disks.

Because of the asymmetric appearance of the relativistic disk (figures 6.3 and 6.4), the eclipsing light curves are expected to become *asymmetric* with respect to the ingress and egress phases (Fukue 1987). By using X-ray facilities with sufficient sensitivity and time resolution, this asymmetric feature can be observed.

A rough estimate of the timescales is follows (Fukue 1987). First, the eclipsing timescale of ingress and egress is $t_{\text{ingress}} \sim 2r/v_{\text{orb}}$, where r is the inner-disk radius and v_{orb} is the orbital velocity. This orbital velocity is expressed as $v_{\text{orb}} = \sqrt{G(M+m)/a}$, where G is the gravitational constant, M and m are a black hole and a companion mass, respectively, and a represents the binary separation. Hence, a rough estimate gives

$$\begin{aligned} t_{\text{ingress}} &\sim \frac{2r}{v_{\text{orb}}} \\ &= 0.85 \frac{r}{20r_g} \frac{M}{10M_\odot} \left(\frac{a}{R_\odot} \right)^{1/2} \left(\frac{M+m}{10M_\odot} \right)^{-1/2} \text{s} \\ &= 4.24 \frac{r}{20r_g} \frac{M}{10M_\odot} \left(\frac{M+m}{10M_\odot} \right)^{-1/3} \left(\frac{P}{2.62\text{d}} \right)^{1/3} \text{s}. \quad (6.12) \end{aligned}$$

Here, we have adopted $P = 2.62$ day for the period of GRO J1655-40 as an observational value (Watarai et al. 2005b). Clearly, a larger black-hole mass or longer orbital period would increase t_{ingress} .

On the other hand, the duration time of the total eclipse of the disk is roughly given as

$$\begin{aligned} t_{\text{duration}} &\sim \frac{2R_*}{v_{\text{orb}}} \\ &= 10^3 \frac{R_*}{R_\odot} \left(\frac{a}{R_\odot} \right)^{1/2} \left(\frac{M+m}{10M_\odot} \right)^{-1/2} \text{s} \\ &= 4.15 \times 10^3 \frac{R_*}{R_\odot} \left(\frac{M+m}{10M_\odot} \right)^{-1/3} \left(\frac{P}{2.62\text{d}} \right)^{1/3} \text{s}. \quad (6.13) \end{aligned}$$

Here, R_* is the radius of the companion.

To detect this timescale t_{ingress} , a high time resolution of at least ~ 0.01 –1 seconds is required. In the X-ray band, the current instrument already has a sufficiently high time resolution (for example, the *RXTE* Proportional Counter Array has a time resolution of milliseconds). Observations of eclipsing black-hole X-ray binaries therefore provide an opportunity to study the physics around black holes.

Figure 6.8 shows the light curve during ingress and egress phases of an eclipse (Watarai et al. 2005b). The orbital velocity is assumed to be 200 km s^{-1} . The total eclipse phase ($\sim 10^3$ s) has been removed, and the ingress phase (~ 1 s) is directly joined to the egress phase. The calculated size is $60r_g \times 60r_g$, which is very small relative to the radius of the companion star. We therefore ignored the curvature of the edge of the companion star in calculating the light curves.

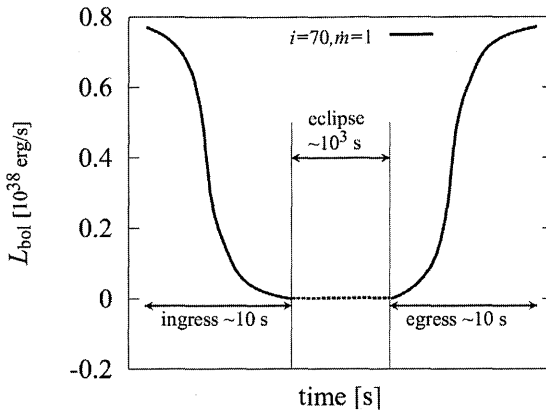


Figure 6.8

Asymmetric light curves during ingress and egress of eclipse by a companion star. The total eclipsing phase is expressed by a dashed line. (Adapted Watarai et al. 2005b)

As already stated and shown in figure 6.8, the eclipsing light curve exhibits an asymmetric profile. These light-curve features are explained as follows. At the ingress phase, the light curve will quickly drop because the left blueshifted part of the disk is first occulted by the companion. This area is then covered, and we receive only radiation originating from the receding part of the disk. Accordingly, the light curve gradually drops. At the egress phase, on the other hand, the situation is reversed; the approaching part appears first and the receding part next. Hence, the light curve rapidly increases, and then gradually increases. See Watarai et al. (2005b) for general cases including geometrical effects for slim disks, and how to analyze the asymmetric light curve.

6.4.2 Light Curves of Orbiting Spots

Besides the global structure, the emergent spectra, and the time variation of accretion disks, the light curves of emitting hot spots comoving with disks have been investigated by several researchers. Such a hot spot can be easily created by flares, internal instabilities, asteroid or stellar impacts, initial irregularities, and so on. Observationally, there exist many types of time variabilities. Hence, it is very interesting and important to examine the light variation produced by irregularities in accretion disks.

Light curves of a hot spot rotating in a relativistic Keplerian disk are periodic with typically two peaks, originating from a gravitational

focusing effect and a Doppler boost (Asaoka 1989).

In figure 6.9 light curves of a hot spot on a relativistic Keplerian disk are shown for several radii and inclination angles (Fukue 2003c). The radial distance r_s of a hot spot is $10 r_g$ and $5 r_g$, while the inclination angle i is $20^\circ, 40^\circ, 60^\circ, 70^\circ, 80^\circ$, and 85° . The abscissa is the non-dimensional time in units of r_g/c , while the ordinate is the flux. The mean flux is higher for a small inclination angle, mainly due to the projection effect of the disk.

As can be seen from figure 6.9, the light curve of a hot spot for a Keplerian case is *periodic* with the rotation period. Furthermore, as Asaoka (1989) pointed out, there exist two types of peaks. One is a broad sinusoidal variation, which originates from a Doppler effect (*a Doppler variation*). The other is a narrow higher peak, which originates from a gravitational focusing effect (*a lensing peak*). When the inclination angle is small ($0^\circ \leq i \leq 60^\circ$), the former Doppler variation dominates. On the other hand, when the inclination angle is large ($i \geq 80^\circ$), the latter lensing peak is prominent.

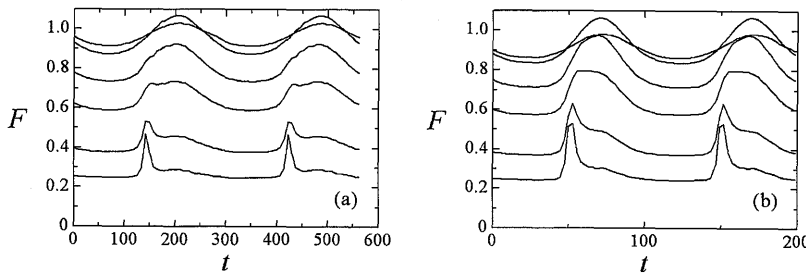


Figure 6.9

Light curves of a hot spot on a relativistic Keplerian disk for several radii and inclination angles. The rotation radius r_s of a hot spot is $10 r_g$ in (a) and $5 r_g$ in (b), whereas the inclination angle i is $20^\circ, 40^\circ, 60^\circ, 70^\circ, 80^\circ$, and 85° from top to bottom. (After Fukue 2003c)

Asaoka (1989) first calculated light curves observed at infinity from an emitting bright spot comoving with a Keplerian disk. She showed only limited cases, but found the essential properties of apparent light curves of a hot spot orbiting around a black hole. Karas and Bao (1992) examined the influence of a self-eclipse due to the thickness of the disk on the light curve of an X-ray emitting hot spot located on the disk surface. They showed that the eclipsed light curve has a narrow cusp. Light curves of corotating hot spots in disks were investigated more generally

by others (e.g., Bao 1992; Karas et al. 1992; Karas 1996).

In these studies, the background disk is usually assumed to be a relativistic Keplerian disk with circular motion. However, there exists another type of disk with advective motion, where the radial infall speed is on the order of the rotational speed (see chapters 9 and 10). Light curves of a hot spot in such disks with infalling motion were examined by Fukue (2003b). He found that light curves of a hot spot spirally infalling in a sub-Keplerian advective disk are aperiodic with typically a single peak, originating from a gravitational focusing effect or a Doppler boost. Such a difference in the light curves of a hot spot can discriminate background disk models.

It should be noted that even for a circularly rotating hot spot, differential rotation would destroy it. If so, the light curves of a hot spot in a Keplerian disk may gradually decay. However, the peak interval maintains its periodicity with the rotation period. Such a decaying light curve was shown in Karas et al. (1992).

In addition, instead of a single hot spot, there can appear multiple hot spots on the disk at each given moment of time, and light curves may be a superposition of individual curves. In such a case, light curves become complicated, and a periodicity analysis is required. For a Keplerian disk, such a case of multiple hot spots and superposition of light curves was discussed by Karas et al. (1992) (cf. Martocchia et al. 2000).

Instead of a hot spot, a wave pattern on the disk is expected in some cases (chapters 11 and 12). In the case of a Keplerian disk, Karas et al. (2001) discussed variable line profiles and light curves due to non-axisymmetric wave patterns (cf. Sanbuichi et al. 1994). Light curves of such a wave pattern under the relativistic effect are also of interest, and would be used to search for an oscillating disk.

6.5 Other Effects – Lensing and Jets

There are several other effects used to detect the relativistic nature of black-hole accretion disks. Among them are microlensing of the innermost region of accretion disks around a supermassive black hole, and relativistic jets and winds from the innermost region of relativistic accretion disks.

6.5.1 Microlensing Test

Gravitational microlensing can be used as a ‘gravitational-lens telescope’ prepared by the universe to resolve the fine structure of cosmological

objects (Chang and Refsdal 1984).

There are two important length scales in microlensing phenomena. One is the Einstein-ring radius r_E on the source plane,

$$\begin{aligned} r_E &\equiv \theta_E D_{\text{os}} \equiv \left(\frac{4GM_{\text{lens}}}{c^2} \frac{D_{\text{ls}} D_{\text{os}}}{D_{\text{ol}}} \right)^{1/2} \\ &\sim 1.5 \times 10^{17} \left(\frac{M_{\text{lens}}}{M_\odot} \right)^{1/2} \text{ cm}, \end{aligned} \quad (6.14)$$

where θ_E is the apparent Einstein-ring radius, and M_{lens} the typical mass of a lens star; D_{ls} , D_{os} , and D_{ol} are the angular diameter distances from the lens to the source, from the observer to the source, and from the observer to the lens, respectively (Schneider et al. 1992; Yonehara et al. 1998; Takahashi et al. 2001). Here, the numerical values are chosen for the Einstein Cross Q 2237+0305, where the redshifts are $z_{\text{os}} = 1.675$ and $z_{\text{ol}} = 0.039$ (Takahashi et al. 2001).

In quasars located at a cosmological distance, the angular diameter distance is on the order of 1 Gpc $\sim 3 \times 10^{27}$ cm. If the mass of the central black hole is about $10^8 M_\odot$, the disk size of $1000 r_g$ will be 3×10^{16} cm. Hence, the apparent disk size is only $\sim 10^{-11}$ radian, or $\sim 1 \mu\text{arc}$ s. On the other hand, a typical Einstein-ring radius of a stellar mass lens is $\theta_E \sim 10^{-11}$ radian for cosmological objects; or the typical Einstein-ring radius on the source plane is $r_E \sim 10^{17}$ cm. Hence, with such a gravitational telescope we may be able to obtain information about the disk structure by observing the disk emergent spectra as a function of the distance from the central black hole.

Another important length scale is the caustic crossing length over the quasar image plane per unit time (Yonehara et al. 1998),

$$\begin{aligned} r_{\text{cross}} &= v_t t \frac{D_{\text{os}}}{D_{\text{ol}}} \\ &\sim 6.9 \times 10^{13} \left(\frac{v_t}{1000 \text{ km s}^{-1}} \right) \left(\frac{t}{1 \text{ d}} \right) \text{ cm}, \end{aligned} \quad (6.15)$$

where t is a certain time during which the caustic moves on the quasar disk plane and v_t is the transverse velocity of the lens object on the lens plane, including the transverse velocity of the peculiar motion of the foreground galaxy relative to the source and the observer.

Fortunately, this crossing length is comparable to the Schwarzschild radius for a supermassive black hole [$r_g \sim 3 \times 10^{13} M/(10^8 M_\odot)$ cm], and is much smaller than r_E . Namely, due to a finite source-size effect, we are

able to resolve the source structure on scales much less than the Einstein-ring radius. By daily observations we can resolve the disk structure with a good spatial resolution.

The observational possibility of the (innermost) disk structure using the microlensing technique was examined and discussed in several articles (e.g., Wambsganss and Paczyński 1991; Jaroszyński et al. 1992; Yonehara et al. 1998; Yonehara et al. 1999; Mineshige and Yonehara 1999; Takahashi et al. 2001). One example for caustic crossing light curves is shown in figure 6.10.

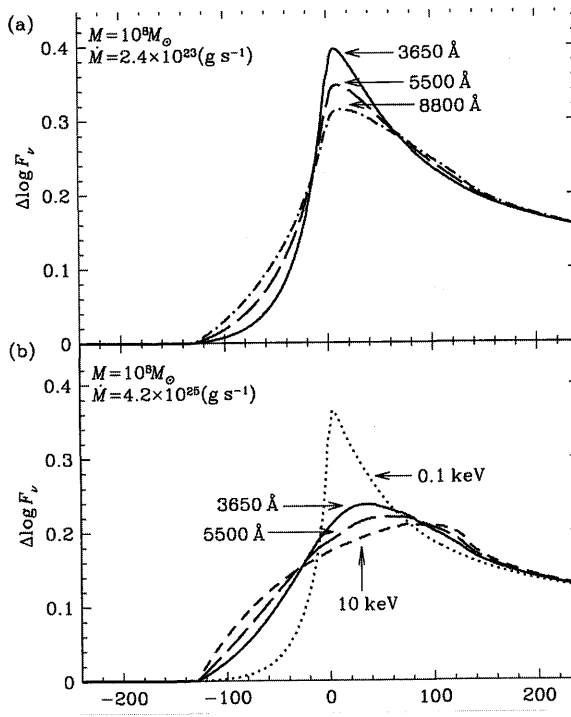


Figure 6.10

Caustic crossing light curves of (a) the standard disk, and (b) the disk-corona model, at several energy bands. (Adapted Takahashi et al. 2001)

6.5.2 Relativistic Jets

Astrophysical jets, (highly collimated) bipolar outflows with or without relativistic speeds, are ubiquitous features in accreting and collapsing gravitating objects. When the speed of jets is on the order of the speed

of light, the central object must be relativistic; e.g., neutron stars or *black holes*. It is believed that the central engine of jets is a gravitating object surrounded by a gaseous disk (chapter 1).

From an observational view point and in relation to the relativistic manifestation, the terminal (final) speed of jets is of great interest. It seems that there are several categories for the relativistic jet speed: (i) mildly relativistic ($v \sim 0.26 c$, $\gamma \sim 1.04$), (ii) highly relativistic ($v \sim 0.92 c$, $\gamma \sim 2.55$), (iii) extremely relativistic ($v \sim 0.99 c$, $\gamma \sim 10$), and (iv) ultra-relativistic ($v \sim 0.9999 c$, $\gamma \sim 100$). The first examples are SS 433, Cyg X-3, and maybe 1E 1740.7 2942. The second types are galactic superluminal microquasars, such as GRS 1915+105 and GRO J1655–40 (Mirabel and Rodríguez 1994; Tingay et al. 1995). In AGN jets, furthermore, the jet speed is supposed to be extremely relativistic, while jets in the gamma-ray bursts may be ultra-relativistic.

Astrophysical jets and winds emanating from accretion disks have been extensively investigated by many researchers (see Fukue 2004, 2005 for references). Various driving forces have been proposed so far, including thermal, magnetic, and radiative. In the current works, mildly to highly relativistic jets can successfully form by several driving forces. However, no one can theoretically produce extremely to ultra-relativistic jets, which are most prominent manifestations of relativistic effects.

(a) Radiation drag

There has been a long-standing problem on radiatively driven jets and winds: the *radiation drag limit*. For jet flows immersed in an intense radiation field of a luminous accretion disk, the effect of radiation drag becomes important when the jet speed v is on the order of c . Hence, the jet speed reaches a ceiling in a mildly relativistic regime.

In the optically thin regions above and below the optically thick luminous accretion disk, the jet gas suffers from the radiation field of the disk. In the zeroth order of (v/c) , the radiative flux \mathbf{F} accelerates the jet gas outward. In the first order of (v/c) , however, the radiation energy density E and pressure stress tensor P^{ij} terms become important [see chapter 16 of the first edition (Kato et al. 1998)], and these terms act as radiation drag forces, which are roughly proportional to the flow velocity (cf. appendices D and E). When the radiative flux force is balanced by the radiation drag force, the jet gas has a *terminal speed*.² In the fully special relativistic regime, the situation is essentially the same, although

²For example, Icke (1989) found that the terminal speed of flows from a flat uniform

the radiative terms are very complicated (appendix E).

Ever since Phinney (1987) first pointed out, the problem of radiation drag has been examined in relation to jets on the axis with no angular momentum (Icke 1989; Sikora et al. 1996; Fukue 2005), and to relativistic winds emanating from the innermost disk with angular momentum (e.g., Tajima and Fukue 1998; Hirai and Fukue 2001).

According to previous studies, in jets emanating from a luminous disk, the terminal speed of jets can easily reach a mildly relativistic regime, such as $0.26 c$, where the jet gas consists of electron–proton normal plasmas. It can approach a highly relativistic regime, such as $0.9 c$, when the jet gas consists of electron–positron pair plasmas. Because of the effect of radiation drag, however, it seems to be very difficult for the jet speed to reach an extremely relativistic regime, such as $0.99 c$, as long as the jet flow is steady, continuous, homogeneous, and optically thin.

(b) Relativistic radiative flow

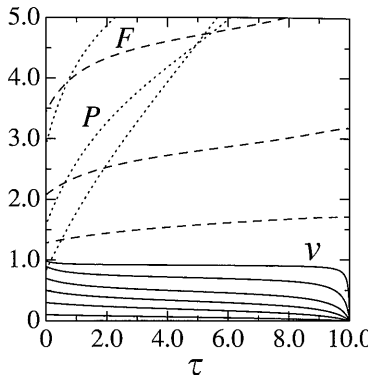
In order to break down this situation, we should abandon some of the current assumptions. For example, Fukue (2000) proposed a multi-stage drive, where the jets are accelerated by radiation fields of successive radiators, while taking account of the spatial *inhomogeneity* (see also Fukue 2003b for wavy stratus under photon surfing over luminous disks).

Another possibility is an *optically thick* relativistic radiative flow, where the radiative energy is efficiently converted to the energy of bulk motion to accelerate the gas up to the relativistic regime. In the highly relativistic regime of $\gtrsim 0.3 c$, however, radiation moment equations show a pathological behavior (appendix E). When the gaseous flow is radiatively accelerated up to the relativistic regime, the velocity gradient becomes large in the direction of the flow. As a result, even in the comoving frame of the gas, the radiation field becomes *anisotropic*, since the mean-free path becomes longer in the downstream direction than in the upstream direction.

Hence, in such a flow accelerated from subrelativistic to relativistic regimes, the Eddington factor should be different from $1/3$ in the diffusion limit, even if the gas is optically thick, similar to the flow from optically thick to thin regimes. We should modify the usual closure re-

source without gravity becomes

$$v_{\text{term}} = \frac{4 - \sqrt{7}}{3} c \sim 0.45 c.$$

**Figure 6.11**

Vertical radiative flow in a luminous disk. The flow three velocity v (solid curves), radiative flux F (dashed curves), and radiation pressure P (dotted curves) are shown as a function of the optical depth τ for several values of v_s at the flow top in the case of the initial optical depth $\tau_0 = 10$. The values of v_s are 0.1, 0.3, 0.5, 0.7, 0.9, and 0.99 from bottom to top of v and 0.1, 0.3, and 0.5 from bottom to top of F and P . The quantities are normalized in units of c and πI_s (the emergent flux at the flow top). That is, the unit of F and cP is πI_s . (After Fukue 2006)

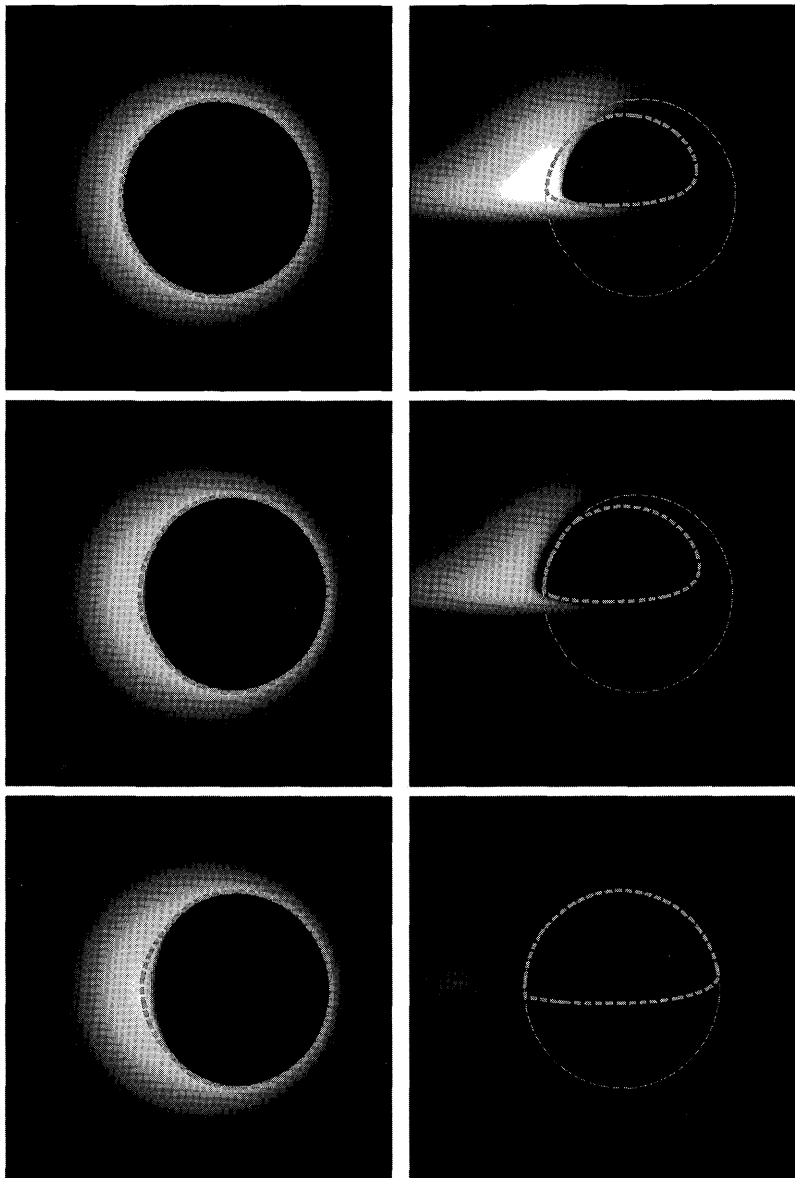
lation under the Eddington approximation. One possibility is a *velocity-dependent* variable Eddington factor (appendix E; Fukue 2006; Akizuki and Fukue 2007). Using the velocity-dependent Eddington factor, we can solve the rigorous equations of the relativistic radiative flow accelerated up to the order of the speed of light (figure 6.11). The Eddington factor depending on the velocity as well as the optical depth should be used in various relativistic radiatively-driven flows, such as black-hole accretion flows, relativistic astrophysical jets and outflows, and relativistic explosions like gamma-ray bursts.

References

- Akizuki C., Fukue J. 2007, submitted to PASJ
- Bao G. 1992, A&A 257, 594
- Beckwith K., Done C. 2004, PTPS 155, 259
- Bromley B.C., Chen K., Miller W.A. 1997, ApJ 475, 57
- Chang K., Refsdal S. 1984, A&A 132, 168
- Chen K., Halpern J.P., Filippenko A.V. 1989, ApJ 339, 742
- Chen K., Halpern J.P. 1989, ApJ 344, 115
- Cunningham C. 1975, ApJ 202, 788

- Cunningham C. 1976, ApJ 208, 534
- Eracleous M., Halpern J.P. 1994, ApJS 90, 1
- Fabian A.C., Rees M.J., Stella L., White N.E. 1989, MNRAS 238, 729
- Falcke, H., Melia, F., Agol, E. 2000, ApJ, 528, L13
- Fanton C., Calvani M., de Felice F., Čadež A. 1997, PASJ 49, 159
- Fuerst S.V., Wu K. 2004, A&A 424, 733
- Fukue J. 1987, Nature 327, 600
- Fukue J. 2000, PASJ 52, 613
- Fukue J. 2003a, PASJ 55, 155
- Fukue J. 2003b, PASJ 55, 451
- Fukue J. 2003c, PASJ 55, 1121
- Fukue J. 2004, PASJ 56, 181
- Fukue J. 2005, PASJ 57, 691
- Fukue J. 2006, PASJ 58, 461
- Fukue J., Yokoyama T. 1988, PASJ 40, 15
- Gebal D., Pelat D. 1981, A&A 95, 18
- Hirai Y., Fukue J. 2001, PASJ 53, 285
- Icke V. 1989, A&A 216, 294
- Jaroszyński M., Wambsganss J., Paczyński B. 1992, ApJ 396, L65
- Karas V. 1996, ApJ 470, 743
- Karas V., Bao G. 1992, A&A 257, 531
- Karas V., Kraus P. 1996, PASJ 48, 771
- Karas V., Martocchia A., Šubr L. 2001, PASJ 53, 189
- Karas V., Vokrouhlický D., Polnarev A.G. 1992, MNRAS 259, 569
- Kawata A., Watarai K., Fukue J. 2006, PASJ 58, 477
- Kojima Y. 1991, MNRAS 250, 629
- Landau L.D., Lifshitz E.M. 1971, *The Classical Theory of Fields* (Pergamon Press, Oxford)
- Laor A. 1991, ApJ 376, 90
- Luminet J.-P. 1979, A&A 75, 228
- Martocchia A., Karas V., Matt G. 2000, MNRAS 312, 817
- Matt G., Perola G.C., Stella L. 1993, A&A 267, 643
- Melia F., Falcke H. 2001, ARA&A 39, 309
- Mineshige S., Yonehara A. 1999, PASJ 51 497
- Mirabel I.F., Rodríguez L.F. 1994, Nature 371, 46
- Mitsuda K., Inoue H., Koyama K., Makishima K., Matsuoka M., Ogawara Y., Shibasaki M., Suzuki K., Tanaka Y., Hirano T. 1984, PASJ 36, 741
- Miyoshi M., Ishitsuka J.K., Kameno S., Shen Z., Horiuchi S. 2004, PTPS 155, 186

- Pariev V.I., Bromley B.C. 1998, ApJ 508, 590
Page D.N., Thorne K.S. 1974, ApJ 191, 499
Phinney E.S. 1987, in *Superluminal Radio Sources*, ed J.A. Zensus and T.J. Pearson (Cambridge University Press, Cambridge), p301
Sanbuichi K., Fukue J., Kojima Y. 1994, PASJ 46, 605
Schneider P., Ehler J., Falco E.E. 1992, *Gravitational Lenses* (Springer-Verlag, Berlin)
Sikora M., Sol H., Begelman M.C., Madejski G.M. 1996, MNRAS 280, 781
Tajima Y., Fukue J. 1998, PASJ 50, 483
Takahashi R. 2004, ApJ 611, 996
Takahashi R. 2005, PASJ 57, 273
Takahashi R., Yonehara A., Mineshige S. 2001, PASJ 53, 387
Tanaka Y., Nandra K., Fabian A.C., Inoue H., Otani C., Dotani T., Hayashida K., Iwasawa K. et al. 1995, Nature 375, 659
Tingay S.J., Jauncey D.L., Preston R.A., Reynolds J.E., Meier D.L., Murphy D.W., Tzioumis A.K., McKay D.J., 1998, Nature 374, 141
Wambsganss J., Paczyński B. 1991, AJ 102, 864
Watarai K., Ohsuga K., Takahashi R., Fukue J. 2005a, PASJ 57, 513
Watarai K., Takahashi R., Fukue J. 2005b, PASJ 57, 827
Yamada T., Mineshige S., Ross R.R., Fukue J. 1994, PASJ 46, 553
Yonehara A., Mineshige S., Manmoto T., Fukue J., Umemura M., Turner E.L. 1998, ApJ 501, L41
Yonehara A., Mineshige S., Fukue J., Umemura M., Turner E.L. 1999, A&A 343, 41



Black hole shadows in optically thin emitting plasmas (left panels) and optically thick and geometrically thin disks (right panels). The black hole spins are $a^* = 0.5$, 0.9 and 0.99999 from top to bottom. The inclination angles are set to be $i = 80^\circ$ for all images. The dashed curves represent the apparent regions of the ergosphere. (Courtesy of R. Takahashi)

Part III Modern Picture

Equations to Construct Generalized Models

As described in part II, the Shakura-Sunyaev-type standard model has been successful in many respects. At the same time, however, its limitations have become clear: e.g., the disk is too cool to emit hard X- and gamma-rays observed in black-hole objects. Mathematically speaking, the limitations are related to simplified treatments made in deriving the basic equations. We thus need to relax some of these approximations so as to incorporate the important processes that are neglected in the Shakura-Sunyaev model. We consider here two such important processes: the *transonic nature* of accretion flows and *heat transport by advective motions*. The former is essential in the innermost disk structure, especially in black-hole accretion, providing a relevant inner boundary condition. A detailed examination of the inner region of the disks is indispensable, since most radiation originates from there. The latter (advective heat transport) is even more important, since it gives rise to disk models that are distinct from the standard one (see chapters 9 and 10). In this chapter we derive and summarize full basic equations in preparation to construct generalized disk models.

7.1 Basic Equations and Importance of Advection

In this section, basic hydrodynamical equations to be used for constructing disk models beyond the Shakura-Sunyaev model are described.

7.1.1 Basic Assumptions

The basic assumptions that we adopt to construct disk models are as follows:

1. The disk gas is subject to the gravitational field of a central point mass. The self-gravity of the disk gas can be neglected.

2. The disk is steady and axisymmetric; i.e., $\partial/\partial t = \partial/\partial\varphi = 0$. Non-steady disks are, however, briefly discussed in section 7.4.
3. All components of the viscous stress tensor are neglected, except for the $r\varphi$ -component, $t_{r\varphi}$.
4. Global magnetic fields are assumed to have no essential effect on the disk structure, but turbulent magnetic fields are assumed to be the main contributor to a large value of the $r\varphi$ -component of the viscous stress tensor, $t_{r\varphi}$.
5. The disk is in hydrostatic balance in the vertical direction, and we decouple the disk structures in the vertical direction and those in the radial direction.

The third assumption involves the idea that the radial component of the viscous force can be neglected in the force-balance equation. Although this term is not always negligible for small-scale motions in disks, we can safely neglect it as long as we are concerned with the global disk structure. Hydrostatic balance holds in the vertical direction, since the dynamical timescale is shorter than the viscous timescale over which accretion proceeds.

Since we are interested in general disk models where the standard disks are involved as a limit, Keplerian rotation is not assumed; i.e., the pressure force could become substantial in the radial force balance. Likewise, neither slow accretion, $v_r \ll v_\varphi$, nor a local heat balance, $Q_{\text{vis}}^+ = Q_{\text{rad}}^-$, is assumed; the accretion velocity could become comparable to the rotation velocity, and advective heat flow could play a key role in the thermal heat balance. Although the disk may become moderately thick, $H/r \lesssim 1$, we still use vertically integrated quantities and equations.

7.1.2 Basic Equations

The basic hydrodynamical equations to be used are summarized here, using the cylindrical coordinates (r, φ, z) . (see appendix B for general forms of the hydrodynamical equations).

(a) Equation of continuity

Since the disks are steady and axisymmetric, we have

$$\frac{\partial}{r\partial r}(\rho rv_r) + \frac{\partial}{\partial z}(\rho v_z) = 0, \quad (7.1)$$

where ρ is the density, and v_r and v_z are the radial and vertical components of the velocity, respectively.

(b) The r -component of the momentum equation

Neglecting the viscous terms, we have

$$\frac{\partial}{\partial r}(r\rho v_r^2) + \frac{\partial}{\partial z}(\rho v_r v_z) - \frac{\rho v_\varphi^2}{r} = -\frac{\partial p}{\partial r} - \rho \frac{\partial \psi}{\partial r}, \quad (7.2)$$

where v_φ is the azimuthal component of the velocity, p is the pressure, and ψ is the gravitational potential due to the central object; its explicit form will be specified later (see subsection 7.2.1).

(c) The φ -component of momentum equation

The $r\varphi$ -component of the stress tensor, $t_{r\varphi}$, is taken into account. We then have

$$\frac{\partial}{\partial r}(r\rho v_r v_\varphi) + \frac{\partial}{\partial z}(\rho v_\varphi v_z) + \frac{\rho v_r v_\varphi}{r} = \frac{\partial}{\partial r}(r^2 t_{r\varphi}). \quad (7.3)$$

(d) Hydrostatic balance in the z -direction

Neglecting the viscous and inertial terms, we have

$$0 = -\frac{\partial p}{\partial z} - \rho \frac{\partial \psi}{\partial z}. \quad (7.4)$$

(e) Energy equation

We write the energy equation in the form

$$\rho T(\mathbf{v} \cdot \nabla)s = \rho(\mathbf{v} \cdot \nabla)e + p \operatorname{div} \mathbf{v} = q^+ - q^-, \quad (7.5)$$

or

$$\operatorname{div} \left[\rho \left(e + \frac{p}{\rho} \right) \mathbf{v} \right] - (\mathbf{v} \cdot \nabla)p = q^+ - q^-, \quad (7.6)$$

where T is the temperature, s is the specific entropy, e is the internal energy per unit mass (see appendix B), and q^+ and q^- are the heating and cooling rates per unit volume, respectively.

The heating comes mainly from the viscosity term, q_{vis}^+ . Its general expression in the case of molecular-type viscosity is given in appendix B. According to the assumptions introduced at the beginning of this section, we adopt here the following form for the viscous heating rate:

$$q_{\text{vis}}^+ = t_{r\varphi} r \frac{\partial}{\partial r} \left(\frac{v_\varphi}{r} \right). \quad (7.7)$$

The heating (sometimes cooling) resulting from heat transport by turbulent conduction, q_{cond}^+ , is non-negligible in advection-dominated disks (see sections 9.1 and 9.4 for details). In such a case we write q^+ as

$$q^+ = q_{\text{vis}}^+ + q_{\text{cond}}^+, \quad (7.8)$$

where

$$q_{\text{cond}}^+ = \text{div} (K \rho T \text{grad } s). \quad (7.9)$$

Here, K is the thermometric conductivity due to turbulence, and is generally on the order of the turbulent kinematic viscosity. A detailed discussion on turbulent heat transport is presented later when it becomes necessary.

The explicit form of the cooling rate q^- depends on the cooling processes in question. Its detailed expression is thus discussed later when the cooling processes are specified (see also appendix I). In general, the cooling process in the optically thick case is radiative diffusion, while that in the optically thin case is bremsstrahlung and synchrotron radiation.

(f) Equation of state

In optically thick disks, the pressure p is the sum of the gas pressure p_{gas} and radiation pressure p_{rad} as

$$p = p_{\text{gas}} + p_{\text{rad}} = \frac{k_{\text{B}}}{\bar{\mu} m_{\text{H}}} \rho T + \frac{1}{3} a T^4, \quad (7.10)$$

where $\bar{\mu}$ is the mean molecular weight, m_{H} is the mass of a hydrogen atom, and a is the radiation constant. If the disks are optically thin, the radiation-pressure term should be omitted. If the disks have magnetic fields, magnetic pressure should be added.

(g) Opacity

The opacity, $\bar{\kappa}$, is expressed in terms of a function of the mean density and temperature, e.g.,

$$\bar{\kappa} = \kappa_{\text{es}} + \kappa_{\text{ff}} = 0.40 + 0.64 \times 10^{23} \rho T^{-7/2} \text{ g}^{-1} \text{ cm}^2 \quad (7.11)$$

for pure hydrogen gas, where κ_{es} is the electron scattering and κ_{ff} the free-free opacity.¹

¹In the case of standard metalicity, the bound-free opacity dominates the free-free opacity (see appendix D). Furthermore, in a cold regime, dust opacity, which depends only on temperature, becomes important (see chapter 5).

(h) Viscosity

To close the above equations we must specify $t_{r\varphi}$. Although it will come from (hydromagnetic) turbulence,² it is very hard to derive a reliable expression. According to the conventional theory of accretion disks, we adopt

$$t_{r\varphi} = -\alpha p \quad (7.12)$$

or

$$t_{r\varphi} = \frac{2}{3} \alpha \rho c_s^2 \frac{d \ln \Omega}{d \ln r}, \quad (7.13)$$

where α ($0 < \alpha \leq 1$) is a free parameter and $\Omega(r)$ is the angular velocity of disk rotation. Although prescriptions (7.12) and (7.13) bring about no essential difference in the disk structures when the disk rotation is proportional to the Keplerian one ($\Omega \propto r^{-3/2}$), this is not generally the case. This will be seen later (section 8.3), when the topology around the sonic radius is discussed.

As a generalization of equation (7.12), we sometimes adopt

$$t_{r\varphi} = -\alpha p_{\text{gas}}^\mu p^{1-\mu}, \quad (7.14)$$

where μ ($0 \leq \mu \leq 1$) is another free parameter. In radiation-pressure-dominated disks, $t_{r\varphi}$ may depend not only on the total pressure p , but also on gas pressure p_{gas} . To take into account such a situation phenomenologically, one more free parameter, μ , has been introduced in equation (7.14).

An attempt to derive a form of $t_{r\varphi}$ from a consideration of the elementary processes of turbulence is presented in chapter 18 of the first edition of this book (Kato et al. 1998).

7.1.3 Importance of Advection

In the remaining part of this section, we explain the importance of the advection terms in the momentum and energy equations in two different contexts.

The first is the *transonic nature* of the flow. In the standard models, the centrifugal force by rotation is assumed to be balanced by the gravitational force (Keplerian rotation). That is, the pressure-gradient force and the inertial force in equation (7.2) have been neglected. The magnitude of these terms in the equation of the radial-force balance is generally small in geometrically thin disks. These forces are on the order

²Molecular and radiative viscosities are generally negligible.

of $(H/r)^2$, compared with the gravitational and centrifugal forces.³ Although they are small overall, they could be essential near to the inner boundary, since the structure of transonic flows cannot be determined without carefully considering these terms. This is because the sonic radius is a critical radius, and the flow cannot pass this radius unless a fine tuning of the flow structure is made there. *The black-hole accretions are essentially transonic*, since the matter must fall onto the black hole at the speed of light, while the sound speed cannot exceed $c/\sqrt{3}$. In this sense, consideration of the pressure and inertial terms in the radial force balance is very important to determine an appropriate inner boundary condition imposed on transonic accretion flows. The unphysical divergences of some physical quantities at the inner boundary in the Shakura-Sunyaev standard disks⁴ stem from the fact that this *regularity condition* at the sonic radius was not considered.

In addition, when we consider hot disks with a moderate vertical thickness ($H/r \leq 1$), the pressure force is obviously non-negligible, even at radii far from the inner edge, since (H/r) is the ratio of pressure force to centrifugal force (or gravitational force).

Another important effect of advection on disk structures is *advective heat transport*, which is neglected in the standard models. In the standard disks it is assumed that the heat generated by viscous processes is radiated out at the same place where it is generated. That is, advective heat transport [the left-hand side of equation (7.6)] has been neglected. It is by a factor of $v_r/v_\varphi \sim \alpha(H/r)^2$ smaller than the heating rate. There are, however, cases where the approximation of local heat balance is violated. The heat generated by viscosity is transported inwards without being radiated there. This is *advective heating/cooling*, and such disks (flows) are called *advection-dominated accretion flows* (ADAFs). Such advection-dominated flows are actually possible both in optically thin disks with a low accretion rate (chapter 9) and in optically thick disks with a high density (chapter 10).

In optically thin disks with low density and high temperature, temperature separation between the ion gas and electron gas may take place, if the coupling between the ions and electrons occurs only through the Coulomb coupling. This situation is similar to that of a model by Shapiro

³In gas-pressure-dominated disks, the ratio $(H/r)^2$ is roughly equal to the ratio of temperature T to the virial temperature T_{vir} , i.e., $(H/r)^2 \sim T/T_{\text{vir}}$ (see subsection 3.2.3).

⁴For example, the surface density becomes infinite in the radiation-pressure dominated case [see equation (3.63)], while in the gas-pressure dominated case the radial velocity becomes infinite [see equations (3.66) and (3.68)].

et al. (1976, see section 3.3). In this case, the energy equations should be considered separately for the ion gas and for the electron gas. Such equations are discussed in section 7.3.

In subsequent sections, the basic equations mentioned above are integrated in the vertical direction, and we treat the vertically integrated, or averaged, quantities in constructing disk models. This geometrically thin-disk approximation is one of the major approximations adopted throughout this textbook. Except for some particular cases, the central black holes are assumed to have no rotation, and the general relativistic effects by the central holes are mimicked by introducing a pseudo-Newtonian potential (see also chapters 2 and 3).

In the last section, the set of time-dependent, vertically integrated equations are briefly summarized in the case where motions are axisymmetric.

7.2 One-Temperature Disks

We derive and summarize here a basic set of equations that we can use to study disk structures by using vertically integrated quantities. The use of vertically integrated equations is practically valid even for moderately thick disks ($H \simeq r$) as long as $d\ln H/d\ln r$ does not change abruptly, where H is the half thickness of the disks.

7.2.1 Vertically Integrated Equations

(a) Gravitational potential

A central black hole with mass M is assumed to be non-rotating.

The general relativistic effects of the gravity of the central black hole are simulated by a pseudo-Newtonian potential (see chapter 2),

$$\psi(R) = -\frac{GM}{R - r_g}, \quad (7.15)$$

introduced by Paczyński and Wiita (1980), where r_g is the Schwarzschild radius, defined by $r_g = 2GM/c^2$, and $R [= (r^2 + z^2)^{1/2}]$ is the distance from the origin. This potential is known to mimic well the general relativistic effects as long as $r \geq 2r_g$ (Paczyński and Wiita 1980; Abramowicz et al. 1980). Actually, the marginally stable and marginally bound circular radii calculated by this potential are, respectively, $3r_g$ and $2r_g$, and coincide, respectively, with those calculated by general relativity (see chapter 2 and appendix A).

(b) **Equations of mass and momentum conservation**

The disks are assumed to be hydrostatic in the vertical direction; i.e., equation (7.4) holds. In order to avoid ambiguity in relations among vertically integrated quantities, following Höshi (1977), we assume a polytropic relation, $p = K\rho^{1+1/N}$, in the vertical direction, where p is the pressure, ρ is the density and N is the polytropic index. The vertical integration of equation (7.4) then gives⁵

$$T(r, z) = T_0(r) \left(1 - \frac{z^2}{H^2}\right), \quad (7.16)$$

$$\rho(r, z) = \rho_0(r) \left(1 - \frac{z^2}{H^2}\right)^N, \quad (7.17)$$

$$p(r, z) = p_0(r) \left(1 - \frac{z^2}{H^2}\right)^{N+1}, \quad (7.18)$$

where subscript 0 represents the quantities on the equatorial plane.⁶ The half-thickness of the disk, H , is given by

$$\Omega_K^2 H^2 = 2(N + 1) \frac{p_0}{\rho_0}. \quad (7.19)$$

Here, Ω_K is the Keplerian angular velocity of rotation, defined by

$$\Omega_K = \left. \left(\frac{\partial \psi}{r \partial r} \right)^{1/2} \right|_{z=0} = \frac{r}{r - r_g} \left(\frac{GM}{r^3} \right)^{1/2}. \quad (7.20)$$

The vertically integrated density Σ and pressure Π are then

$$\Sigma \equiv \int_{-H}^H \rho dz = \int_{-H}^H \rho_0 \left(1 - \frac{z^2}{H^2}\right)^N dz = 2\rho_0 I_N H, \quad (7.21)$$

$$\Pi \equiv \int_{-H}^H p dz = \int_{-H}^H p_0 \left(1 - \frac{z^2}{H^2}\right)^{N+1} dz = 2p_0 I_{N+1} H, \quad (7.22)$$

⁵The vertical integration of equation (7.4) gives only equations (7.17) and (7.18). There is no restriction on the vertical distribution of temperature. In disks where radiation pressure can be neglected compared with gas pressure, however, the equation of state forces the temperature distribution to be equation (7.16). Even in radiation-pressure-dominated disks, equation (7.16) holds if $N = 3$. Based on these situations, we adopt, as an approximation, equation (7.16) in order to derive vertically integrated equations. As is shown later, the form of temperature distribution in the vertical direction has effects only on vertical integrations of energy equation and of the equation of state.

⁶Although in many other chapters subscript 0 is used to represent quantities in the unperturbed state, here we use it for quantities on the equatorial plane.

where⁷

$$I_N = \frac{(2^N N!)^2}{(2N+1)!}. \quad (7.23)$$

We now integrate the other basic equations given in section 7.1 in the vertical direction under the assumption that the radial velocity, v_r , and the specific angular momentum, ℓ ($= rv_\varphi = r^2\Omega$), do not depend on the vertical coordinate. Since the density vanishes at the disk surface, vertical integration of the continuity equation (7.1) gives

$$-2\pi r \Sigma v_r = \dot{M} = \text{const.}, \quad (7.24)$$

where \dot{M} is the mass-accretion rate [cf. equation (3.25)].

Integration of equation (7.2) gives the radial component of the momentum equation [cf. equation (3.27)],

$$v_r \frac{dv_r}{dr} + \frac{1}{\Sigma} \frac{d\Pi}{dr} = \frac{\ell^2 - \ell_K^2}{r^3} - \frac{\Pi}{\Sigma} \frac{d\ln\Omega_K}{dr}, \quad (7.25)$$

where ℓ_K is the Keplerian angular momentum defined by

$$\ell_K = r^2\Omega_K = \frac{r}{r - r_g}(GMr)^{1/2}. \quad (7.26)$$

The last term on the right-hand side of equation (7.25) is a correction resulting from the fact that the radial component of the gravitational force changes with height (Matsumoto et al. 1984). That is, using $\psi(r, z) \simeq \psi(r, 0) + \Omega_K^2 z^2/2$ and the hydrostatic balance, $\partial p/\partial z = -\rho\Omega_K^2 z$, we have

$$\begin{aligned} \int_{-H}^H \rho \frac{\partial \psi}{\partial r} dz &\simeq \Sigma \left(\frac{\partial \psi}{\partial r} \right)_{z=0} + \frac{1}{2} \frac{d\Omega_K^2}{dr} \int_{-H}^H \rho z^2 dz \\ &= \Sigma \frac{\ell_K^2}{r^3} - \frac{d\ln\Omega_K}{dr} \int_{-H}^H z \frac{\partial p}{\partial z} dz \\ &= \Sigma \frac{\ell_K^2}{r^3} + \frac{d\ln\Omega_K}{dr} \Pi. \end{aligned} \quad (7.27)$$

We integrate equation (7.3) in the vertical direction, finding that the result can easily be integrated in the radial direction, as well. The angular-momentum balance is thus written as [cf. equation (3.29)]

$$\dot{M}(\ell - \ell_{in}) = -2\pi r^2 T_{r\varphi}, \quad (7.28)$$

⁷

$I_1 = 2/3 = 0.667$, $I_2 = 8/15 = 0.633$,
 $I_3 = 16/35 = 0.457$, $I_4 = 128/315 = 0.406$.

where ℓ_{in} is an integration constant, which represents the specific angular momentum finally swallowed by the black hole, and $T_{r\varphi}$ is the vertical integration of $t_{r\varphi}$,

$$T_{r\varphi} \equiv \int_{-H}^H t_{r\varphi} dz. \quad (7.29)$$

It is noted that by using Π and Σ equation (7.19) can be written as

$$\Omega_K^2 H^2 = (2N + 3) \frac{\Pi}{\Sigma}. \quad (7.30)$$

This is an equation expressing H in terms of Π and Σ .

(c) Energy equation

The vertical integration of equation (7.6) gives the energy equation:

$$Q_{\text{adv}}^- = Q_{\text{vis}}^+ - Q_{\text{rad}}^-, \quad (7.31)$$

where Q_{adv}^- is the advective cooling, defined by

$$Q_{\text{adv}}^- = \frac{1}{r} \frac{d}{dr} [rv_r(E + \Pi)] - v_r \frac{d\Pi}{dr} - \int_{-H}^H v_z \frac{\partial p}{\partial z} dz, \quad (7.32)$$

E being the vertical integration of the volume energy density ρe . The viscous energy generation rate, Q_{vis}^+ , and the radiative loss rate, Q_{rad}^- , in unit area integrated in the vertical direction are given, respectively, by

$$Q_{\text{vis}}^+ = \int_{-H}^H q_{\text{vis}}^+ dz \quad \text{and} \quad Q_{\text{rad}}^- = \int_{-H}^H q_{\text{rad}}^- dz. \quad (7.33)$$

We now derive an explicit expression for Q_{adv}^- in terms of vertically integrated quantities. If the hydrostatic balance in the vertical direction, integration by part, and equation of continuity are used, we have

$$-\int_{-H}^H v_z \frac{\partial p}{\partial z} dz = \frac{1}{2} \Omega_K^2 \int_{-H}^H \frac{z^2}{r} \frac{\partial}{\partial r} (r \rho v_r) dz. \quad (7.34)$$

The performance of the vertical integration makes the right-hand side of the above equation become

$$\frac{1}{2} \Omega_K^2 \frac{I_{N+1}}{N+1} \frac{1}{r} \frac{d}{dr} (\rho_0 v_r H^3), \quad (7.35)$$

which is

$$\Omega_K^2 \frac{I_{N+1}}{N+1} \rho_0 H^2 v_r \frac{dH}{dr}. \quad (7.36)$$

It can be further reduced to $\Pi v_r d\ln H/dr$. That is, we have

$$-\int_{-H}^H v_z \frac{\partial p}{\partial z} dz = \Pi v_r \frac{d\ln H}{dr}. \quad (7.37)$$

In a polytropic gas of $N = 3$, the ratio of the radiation pressure p_{rad} to the gas pressure p_{gas} is independent of z . Hence, E is approximated as

$$E \equiv \int_{-H}^H \rho e dz = \int_{-H}^H \left(\frac{p_{\text{gas}}}{\gamma - 1} + 3p_{\text{rad}} \right) dz = A\Pi, \quad (7.38)$$

where

$$A = 3(1 - \beta) + \frac{\beta}{\gamma - 1}, \quad (7.39)$$

with γ being the ratio of the specific heats and β is defined by $\beta \equiv p_{\text{gas}}/p = p_{\text{gas}}/(p_{\text{rad}} + p_{\text{gas}})$. Hereafter, we neglect the radial variation of A . Then, using equations (7.24), (7.30), and (7.37) – (7.39), from equation (7.32) we have

$$Q_{\text{adv}}^- = \frac{\Pi}{\Sigma} \frac{\dot{M}}{2\pi r^2} \xi, \quad (7.40)$$

where

$$\xi = - \left[\left(A + \frac{1}{2} \right) \frac{d\ln \Pi}{d\ln r} - \left(A + \frac{3}{2} \right) \frac{d\ln \Sigma}{d\ln r} - \frac{d\ln \Omega_K}{d\ln r} \right] \quad (7.41)$$

and is a quantity of the order of unity (see also section 7.4). In advective cooling-dominated disks, ξ is positive.⁸

The next issue is to explicitly write Q_{vis}^+ . Integrating equation (7.7) over the vertical direction, we obtain the rate of viscous heat generation,

$$Q_{\text{vis}}^+ = r T_{r\varphi} \frac{d\Omega}{dr}. \quad (7.42)$$

Expressions for Q_{rad}^- are not given here. They are discussed for optically thick and thin cases separately in the following subsections.

⁸It is easy to generalize expression (7.41) so that the radial variation of A is taken into account [see the first edition of this book (Kato et al. 1998)], which is

$$Q_{\text{adv}}^- = - \frac{1}{\Gamma_3 - 1} \frac{\Pi}{\Sigma} \frac{\dot{M}}{2\pi r^2} \left[\frac{\Gamma_1 + 1}{2} \frac{d\ln \Pi}{d\ln r} - \frac{3\Gamma_1 - 1}{2} \frac{d\ln \Sigma}{d\ln r} - (\Gamma_1 - 1) \frac{d\ln \Omega_K}{d\ln r} \right].$$

Here, Γ_1 and Γ_2 are generalized adiabatic exponents (see appendix B).

(d) **Equation of state**

The vertical integration of equation (7.10) gives

$$\Pi = \Pi_{\text{gas}} + \Pi_{\text{rad}}, \quad (7.43)$$

where Π_{gas} and Π_{rad} are the vertical integrations of the gas pressure p_{gas} and the radiation pressure p_{rad} , respectively, and are given by

$$\Pi_{\text{gas}} \equiv \frac{k_B}{\bar{\mu}m_H} \frac{I_4}{I_3} \Sigma T_0 \quad (7.44)$$

and

$$\Pi_{\text{rad}} \equiv \int_{-H}^H \frac{1}{3} a T_0^4 \left(1 - \frac{z^2}{H^2}\right)^4 dz = \frac{2}{3} I_4 a T_0^4 H. \quad (7.45)$$

Here, $I_4/I_3 = 8/9$ and $I_4 \sim 0.406$.

(e) **Viscous stress tensor**

A remaining problem is to specify $T_{r\varphi}$ in terms of physical quantities to close the set of equations. According to the expressions for $t_{r\varphi}$ given before [equations (7.12), (7.13), and (7.14)], we adopt here

$$T_{r\varphi} = -\alpha \Pi \quad (7.46)$$

or

$$T_{r\varphi} = \alpha \frac{2}{3} \Sigma c_s^2 \frac{d \ln \Omega}{d \ln r} \quad (7.47)$$

or

$$T_{r\varphi} = -\alpha \Pi_{\text{gas}}^\mu \Pi^{1-\mu}, \quad (7.48)$$

where α ($0 < \alpha < 1$) and μ ($0 \leq \mu \leq 1$) are free parameters.

In summary, the basic equations to construct steady disk models are equations (7.24), (7.25), (7.28), (7.30), (7.31), and (7.43). Among three Q 's in equation (7.31), Q_{adv}^+ and Q_{vis}^- are given by equations (7.40) and (7.42), respectively. The remaining one, Q_{rad}^- , is discussed later. The $r\varphi$ -component of viscous stress tensor, $T_{r\varphi}$, is given by one of equations (7.46)–(7.48).

7.2.2 Vertically Isothermal Disks

It is useful to see how the above-mentioned basic relations are modified if the disks are vertically isothermal instead of polytropic. For simplicity,

the disks are assumed to be gas-pressure-dominated, i.e., $\beta = 1$.⁹ Then, the vertical integration of equation (7.4) gives

$$T = T_0(r), \quad (7.49)$$

$$\rho = \rho_0(r) \exp\left[-\frac{z^2}{2H^2(r)}\right], \quad (7.50)$$

$$p = p_0(r) \exp\left[-\frac{z^2}{2H^2(r)}\right]. \quad (7.51)$$

The half-thickness H of the disk is defined by

$$H(r) \equiv \frac{c_T(r)}{\Omega_K(r)}. \quad (7.52)$$

Here, $c_T(r)$ is the isothermal sound speed.

$$c_T(r) = \left(\frac{p_0}{\rho_0}\right)^{1/2} \propto T_0^{1/2}(r). \quad (7.53)$$

The surface density Σ and the vertically integrated pressure Π are then related to the quantities on the equatorial plane by

$$\Sigma = (2\pi)^{1/2} \rho_0 H \quad \text{and} \quad \Pi = (2\pi)^{1/2} p_0 H. \quad (7.54)$$

The basic equations [(7.24), (7.25), and (7.28)] are unchanged even in the case of isothermal disks. The relation between Ω_K , Π , and Σ is, however, changed and becomes simpler. That is, equation (7.30) is now changed to [equation (7.52)]

$$\Omega_K^2 H^2 = \frac{\Pi}{\Sigma}. \quad (7.55)$$

Since radiation pressure is neglected, the equation of state is

$$\Pi = \frac{k_B}{\bar{\mu} m_H} \Sigma T_0. \quad (7.56)$$

Finally, we should discuss the energy equation. Even in isothermal disks, relation (7.37) holds. Hence, from equation (7.32), using equations (7.24), $E = \Pi/(\gamma - 1)$, and (7.55), we have

$$Q_{\text{adv}}^- = -\frac{\Pi}{\Sigma} \frac{\dot{M}}{2\pi r^2} \left[\frac{\gamma + 1}{2(\gamma - 1)} \frac{d\ln\Pi}{d\ln r} - \frac{3\gamma - 1}{2(\gamma - 1)} \frac{d\ln\Sigma}{d\ln r} - \frac{d\ln\Omega_K}{d\ln r} \right]. \quad (7.57)$$

⁹Optically thin advection-dominated disks which are discussed in chapter 9 belong to this case.

This is the counter equation corresponding to equations (7.40) and (7.41). In the limit of $\beta = 1$, equations (7.40) and (7.41) really become to the above equation.

In summary, among the basic equations [(7.24), (7.25), (7.28), (7.30), (7.31), and (7.43)] in polytropic disks, equations (7.24), (7.25), (7.28) and (7.31) still hold even in isothermal disks, but (7.30) and (7.43) are now changed to equations (7.55) and (7.56). Furthermore, the expression for Q_{adv}^- is now equation (7.57).

7.2.3 Optically Thick Disks

The heat exchange in the radial direction is generally small compared with the heat loss in the vertical direction. Hence, when the disk is optically thick in the vertical direction, we have $Q_{\text{rad}}^- = -[2\chi \partial T / \partial z]_{\text{surface}}$, where χ is the radiative diffusivity. In a polytropic gas of $N = 3$, the value of β is independent of z , as mentioned before. Hence, if the opacity, $\bar{\kappa}$, is approximated to be constant in the vertical direction, we obtain [see equation (3.38)]

$$Q_{\text{rad}}^- = -2\chi \frac{\partial T}{\partial z} \Big|_{\text{surface}} = \frac{8acT_0^4}{3\bar{\kappa}\rho_0 H}. \quad (7.58)$$

Adopting this form of Q_{rad}^- , the opacity is expressed as a function of the mean density $\bar{\rho}$ and temperature \bar{T} as

$$\bar{\kappa} = \kappa_{\text{es}} + \kappa_{\text{ff}} = 0.40 + 0.64 \times 10^{23} \bar{\rho} \bar{T}^{-7/2} \text{ g}^{-1} \text{ cm}^2 \quad (7.59)$$

for pure hydrogen gas. In this equation $\bar{\rho}$ and \bar{T} are the vertically averaged density and temperature, respectively; i.e., $\bar{\rho} = (16/35)\rho_0$ and $\bar{T} = (2/3)T_0$ for the $N = 3$ polytropic case, and $\bar{T} = T_0$ and $\bar{\rho} = (\pi/4)^{1/2}\rho_0$ for the isothermal case.

7.2.4 Optically Thin Disks

The main difference from the case of optically thick disks is the cooling processes. The main cooling processes are the thermal bremsstrahlung and synchrotron cooling, enhanced by Compton processes; i.e.,

$$Q_{\text{rad}}^- = Q_{\text{brems}}^- + Q_{\text{syn}}^-. \quad (7.60)$$

Detailed expressions for Q_{brems}^- and Q_{syn}^- including relativistic effects are summarized in the next section and appendix I, in relation to two-

temperature disks. We mention here only that the non-relativistic thermal bremsstrahlung per unit area, Q_{brems}^- , is given by

$$Q_{\text{brems}}^- = 1.24 \times 10^{21} H \bar{\rho}^2 \bar{T}^{1/2} \text{ erg s}^{-1} \text{ cm}^{-2}, \quad (7.61)$$

when relativistic corrections are not considered.

7.3 Two-Temperature Disks

As discussed in the previous section, high-temperature and low-density states are realized in optically thin disks. In the standard picture, the viscous heating process mainly gives energy to the ions gas, while cooling occurs on the electron gas. Hence, if the thermal coupling between ions and electrons is weak, a temperature separation between ions and electrons can be expected.

7.3.1 Equations for Ions and Electrons

In spite of temperature separation, there can be no velocity separation between ions and electrons, since the Coulomb coupling between them is strong enough to force the electron gas to move with the ion gas. This suggests that the continuity and momentum equations are unchanged from those of one-temperature disks. That is, equations (7.24), (7.25), (7.28), and (7.30) [or (7.55)] can be applied as they are. The energy equations, however, should be modified; they need to be considered separately for ions and electrons.

In this section, for simplicity, the disks are assumed to be isothermal in the vertical direction. Furthermore, the gas is assumed to consist of electrons and protons; there are no helium nor heavy ions. The number densities of electrons and protons, n_e and n_i , are then equal by charge neutrality,¹⁰ i.e., $n = n_e = n_i$. The density ρ is given by

$$\rho = m_i n_i + m_e n_e = (m_i + m_e) n, \quad (7.62)$$

where m_i and m_e are the ion and electron masses, respectively. The surface densities of the electrons and ions, Σ_e and Σ_i , are related to the

¹⁰If there exist a considerable amount of electron-positron pairs, the charge neutrality should be written as

$$n_i + n_+ = n_e,$$

where n_+ is the positron number density. The equation of state is then

$$\Pi_{\text{gas}} = \Pi_i + \Pi_e + \Pi_+.$$

total surface density of the gas, Σ , by

$$\Sigma_e = \frac{m_e}{m_i + m_e} \Sigma \quad \text{and} \quad \Sigma_i = \frac{m_i}{m_i + m_e} \Sigma, \quad (7.63)$$

respectively, where $\Sigma = \int \rho dz$. Similarly, the vertically-integrated pressures of electrons, Π_e , and of ions, Π_i , are, respectively, given by

$$\Pi_e = \frac{T_e}{T_i + T_e} \Pi \quad \text{and} \quad \Pi_i = \frac{T_i}{T_i + T_e} \Pi, \quad (7.64)$$

where T_i and T_e are the ion and electron temperatures, respectively.

The equation of state is

$$\Pi = \Pi_{\text{gas}} = \Pi_i + \Pi_e = \Sigma \frac{k_B}{m_i + m_e} (T_i + T_e), \quad (7.65)$$

where k_B is the Boltzmann constant.

The energy equations for the electrons and ions are, respectively, [see equation (7.5)]

$$\Sigma_e v_r \frac{d\epsilon_e}{dr} + \Pi_e \frac{d}{r dr} (rv_r) + \Pi_e v_r \frac{d \ln H}{dr} = \Lambda_{ie} - Q_{\text{rad}}^-, \quad (7.66)$$

$$\Sigma_i v_r \frac{d\epsilon_i}{dr} + \Pi_i \frac{d}{r dr} (rv_r) + \Pi_i v_r \frac{d \ln H}{dr} = Q_{\text{vis}}^+ - \Lambda_{ie}, \quad (7.67)$$

where ϵ_e and ϵ_i are the internal energies of electron and ion gases per unit mass, respectively. It is noted that the last term on the left-hand sides of equations (7.66) and (7.67) comes from the vertical integrations of $p_e dv_z/dz$ and $p_i dv_z/dz$, respectively [cf. equation (7.37)].¹¹

¹¹Since the disks are assumed to be isothermal in the vertical direction, the procedure for deriving the last terms on the right-hand side of equations (7.66) and (7.67) are slightly different from those used to derive equation (7.37). Since $p_e = n_e k_B T_e$, and the density distribution in the vertical direction is given by equation (7.50), integration by parts gives

$$\int_{-\infty}^{\infty} p_e \frac{\partial u_z}{\partial z} dz = \frac{k_B T_e}{H^2} \int_{-\infty}^{\infty} z n_e u_z dz = -\frac{k_B T_e}{2H^2} \int_{-\infty}^{\infty} z^2 \frac{\partial}{\partial z} (n_e u_z) dz.$$

After rewriting the integrand by using the equation of continuity, we perform a vertical integration to obtain

$$\int_{-\infty}^{\infty} p_e \frac{\partial u_z}{\partial z} dz = \frac{k_B T_e}{2H^2} \frac{d}{r dr} \left(r u_r \frac{\Sigma_e}{m_e} H^2 \right).$$

Using mass conservation, we have

$$\int_{-\infty}^{\infty} p_e \frac{\partial u_z}{\partial z} dz = \Pi_e u_r \frac{d \ln H}{dr}.$$

In the inner region of advection-dominated disks, the electron temperature becomes comparable to, or higher than, that of the electron rest mass energy. Hence, the special relativistic effects should be taken into account in evaluating the internal energy of an electron gas, and we adopt (Chandrasekhar 1967; Cox and Giuli 1968)

$$\epsilon_e = c^2 \left[\frac{K_1(m_e c^2 / k_B T_e)}{K_2(m_e c^2 / k_B T_e)} + 3 \frac{k_B T_e}{m_e c^2} - 1 \right]. \quad (7.68)$$

Here, $K_1(z)$ and $K_2(z)$ are modified Bessel functions of the second kind of order 1 and 2 with argument z , respectively. In the non-relativistic limit of $k_B T_e / m_e c^2 \ll 1$, K_1/K_2 tends to $1 - (3/2)(k_B T_e / m_e c^2)$, and we have $\epsilon_e \sim (3/2)k_B T_e / m_e$. In the extreme relativistic limit of $k_B T_e / m_e c^2 \gg 1$, we have $K_1/K_2 \sim 1$, and thus $\epsilon_e \sim 3k_B T_e / m_e$. For an ion gas, a relativistic correction is unimportant, and we simply adopt

$$\epsilon_i = \frac{3}{2} \frac{k_B}{m_i} T_i. \quad (7.69)$$

In energy equations (7.66) and (7.67), Λ_{ie} is the energy transfer rate from the ion gas to the electron gas per unit area due to Coulomb collisions, Q_{vis}^+ is the viscous heating rate of the ion gas per unit area [equation(7.42)], and Q_{rad}^- is the cooling rate of the electron gas per unit area. As shown before in equation (7.60), Q_{rad}^- consists of cooling by bremsstrahlung, Q_{brems}^- , and that by synchrotron, Q_{syn}^- , enhanced by Compton processes. In the following, Λ_{ie} , Q_{brems}^- , and Q_{syn}^- are discussed separately.

7.3.2 Coulomb Coupling

The energy transfer rate, \dot{E}_{ie} , from ions to electrons per unit volume by Coulomb collisions is given by Stepney and Guilbert (1983) as

$$\begin{aligned} \dot{E}_{ie} = & -\frac{3}{2} \frac{m_e}{m_i} n_e n_i \sigma_T c \frac{k_B T_e - k_B T_i}{K_2(1/\Theta_e) K_2(1/\Theta_i)} \ln \Lambda \\ & \times \left[\frac{2(\Theta_e + \Theta_i)^2 + 1}{\Theta_e + \Theta_i} K_1 \left(\frac{\Theta_e + \Theta_i}{\Theta_e \Theta_i} \right) + 2K_0 \left(\frac{\Theta_e + \Theta_i}{\Theta_e \Theta_i} \right) \right], \end{aligned} \quad (7.70)$$

It is noted that this relation can be easily extended to the time-dependent case as

$$\int_{-\infty}^{\infty} p_e \frac{\partial u_z}{\partial z} dz = \Pi_e \frac{d \ln H}{dt},$$

where d/dt is the Lagrangian time derivative.

where σ_T is the Thomson cross section, K_0 , K_1 , and K_2 are modified Bessel functions of the second kind of order 0, 1, and 2, respectively, and $\ln\Lambda$ is the Coulomb logarithm, which is about 20. The quantities Θ_i and Θ_e are the dimensionless ion and electron temperatures, defined, respectively, as

$$\Theta_i = \frac{k_B T_i}{m_i c^2} \quad \text{and} \quad \Theta_e = \frac{k_B T_e}{m_e c^2}. \quad (7.71)$$

In vertically isothermal disks, the energy-transfer rate, \dot{E}_{ie} , changes with height as $\exp(-z^2/H^2)$. The energy-transfer rate per unit area, Λ_{ie} , is thus given by¹²

$$\Lambda_{ie} = \sqrt{\pi}(\dot{E}_{ie})_0 H, \quad (7.72)$$

where $(\dot{E}_{ie})_0$ is the value of \dot{E}_{ie} at the equator. To evaluate $(\dot{E}_{ie})_0$ we need $(n_i)_0$ and $(n_e)_0$, the values of n_i and n_e at the equator. In our present model they are related to Σ_i by $(n_i)_0 = (n_e)_0 = (2\pi)^{-1/2}(\Sigma_i/m_i H)$.

The next issue is to give detailed expressions for Q_{rad}^- , which consists of cooling by bremsstrahlung, Q_{brems}^- , and that by synchrotron emission, Q_{syn}^- , enhanced by the Compton process [see equation (7.60)].

7.3.3 Bremsstrahlung Cooling

The bremsstrahlung radiation is amplified by Compton scattering. Let us write the amplification factor as A_{brems}^C . Then, the cooling rate (per unit surface) by bremsstrahlung, Q_{brems}^- , is given by

$$Q_{brems}^- = \sqrt{\pi}(\dot{E}_{brems})_0 A_{brems}^C H, \quad (7.73)$$

where $(\dot{E}_{brems})_0$ is the bremsstrahlung cooling per unit volume, \dot{E}_{brems} , at the equator. A detailed expressions for \dot{E}_{brems} and the amplification factor A_{brems}^C are given in appendix I.

7.3.4 Synchrotron Cooling

The spectrum of synchrotron emission by relativistic Maxwellian electrons with density n_e was calculated by Pacholczyk (1970) under an optically thin condition. Mahadevan et al. (1996) fitted it by a simple functional form. Below some critical frequency, ν_c , however, the emission becomes self-absorbed and the spectra obtained under optically thin conditions is no longer valid there. In such a low-frequency region, the volume emissivity is approximated by the blackbody emission from the

¹²See equation (3.132) for the non-relativistic expression.

disk surface divided by the disk volume. Under these considerations, the cooling rate per unit volume by synchrotron emission integrated over frequency, q_{syn}^- , has been obtained. An approximate analytical form of q_{syn}^- (e.g., Esin et al. 1996) is given in appendix I.

By taking into account the amplification factor, A_{syn}^C , by Compton processes, we can write the cooling rate (per unit surface) due to the synchrotron emission, Q_{syn}^- , in the form

$$Q_{\text{syn}}^- = \sqrt{\pi} (q_{\text{syn}}^-)_0 A_{\text{syn}}^C(\nu_c) H, \quad (7.74)$$

where $(q_{\text{syn}}^-)_0$ represents the value of q_{syn}^- at the equator. A detailed expression for the amplification factor, $A_{\text{syn}}^C(\nu_c)$, is also given in appendix I.

7.4 Time-Dependent Equations

So far, we focused our attention only on steady time-independent disks. Here, we present the time-dependent, vertically integrated forms of the basic equations. The disks are assumed to be axisymmetric. Furthermore, the radial and azimuthal components of the velocity, v_r and v_φ , are assumed to be independent of z , even in the time-dependent state. The equations that describe the time evolution of v_r , v_φ , Σ , and Π (the vertical integration of the pressure) are the conservation equations of mass, momentum (radial and azimuthal components), and energy. We write these equations in slightly different forms from those in previous sections.

(a) Equation of mass conservation

Since axisymmetric perturbations are considered, we have

$$\frac{\partial}{\partial t}(r\Sigma) + \frac{\partial}{\partial r}(r\Sigma v_r) = 0. \quad (7.75)$$

(b) Radial component of momentum equation

With the help of equation (7.75), we can easily see that equation (7.25) is generalized to the time-dependent case as

$$\frac{\partial}{\partial t}(r\Sigma v_r) + \frac{\partial}{\partial r}(r\Sigma v_r^2 + r\Pi) = \left(1 - \frac{d\ln\Omega_K}{d\ln r}\right)\Pi + \Sigma[v_\varphi^2 - (r\Omega_K)^2]. \quad (7.76)$$

(c) **Azimuthal component of momentum equation**

The φ -component of momentum equation is

$$\frac{\partial}{\partial t}(r^2\Sigma v_\varphi) + \frac{\partial}{\partial r}(r^2\Sigma v_r v_\varphi - r^2 T_{r\varphi}) = 0, \quad (7.77)$$

where $T_{r\varphi}$ is the vertical integration of the $r\varphi$ -component of the stress tensor.

(d) **Energy equation**

First, we consider the equation of the total energy conservation, which is given by equation (B9) in appendix B. Performing vertical integration of the equation, we have

$$\frac{\partial}{\partial t}(rE_{\text{tot}}) + \frac{\partial}{\partial r}\left[r(E_{\text{tot}} + \Pi)v_r - rT_{r\varphi}v_\varphi\right] = -rQ_{\text{rad}}^-, \quad (7.78)$$

where Q_{rad}^- is the cooling rate per unit surface area on both the upper and lower planes. The quantity E_{tot} is the total energy per unit surface, defined by

$$E_{\text{tot}} = \left(A + \frac{1}{2}\right)\Pi + \frac{1}{2}\Sigma(v_r^2 + v_\varphi^2) + \Sigma\psi_0(r), \quad (7.79)$$

where $A\Pi$ on the right-hand side comes from the vertical integration of thermal energy density ρe [see equations (7.38) and (7.39)], $\psi_0(r)$ is the gravitational potential at the equator due to the central object and is simulated by using the pseudo-Newtonian one $\psi_0 = -GM/(r - r_g)$, introduced by Paczyński and Wiita (1980). The term $(1/2)\Pi$ in E_{tot} comes from the vertical integration of $\rho\psi(r, z)$. As discussed in deriving the last term on the right-hand side of equation (7.25), we have $\psi(r, z) \simeq \psi_0(r) + \Omega_K^2 z^2/2 = \psi_0(r) - (z/2)\partial p/\rho\partial z$. Hence, this leads to

$$\int \rho\psi(r, z)dz \simeq \Sigma\psi_0(r) + \frac{\Pi}{2}. \quad (7.80)$$

Next, we consider the conservation of thermal energy. Instead of starting from the equation of thermal energy conservation per unit volume, say equation (B13), we here start from equation (4.58),

$$\frac{\partial E}{\partial t} - (E + \Pi)\frac{\partial \ln \Sigma}{\partial t} + \Pi\frac{\partial \ln H}{\partial t} + Q_{\text{adv}}^- = Q_{\text{vis}}^+ - Q_{\text{rad}}^-, \quad (7.81)$$

where $E (= A\Pi)$ is the vertical integration of thermal energy [equation (4.57) or (7.38)] and Q_{adv}^- is the advective cooling given by equation (4.59).

In the case where A is approximated to be constant, the thermal energy conservation, equation (7.81), is written, by using equation (7.30), as

$$\left(A + \frac{1}{2} \right) \frac{\partial \Pi}{\partial t} - \left(A + \frac{3}{2} \right) \frac{\Pi}{\Sigma} \frac{\partial \Sigma}{\partial t} + Q_{\text{adv}}^- = Q_{\text{vis}}^+ - Q_{\text{rad}}^-, \quad (7.82)$$

and Q_{adv}^- , which is given by equation (4.59), is

$$Q_{\text{adv}}^- = v_r \Pi \left[\left(A + \frac{1}{2} \right) \frac{\partial \ln \Pi}{\partial r} - \left(A + \frac{3}{2} \right) \frac{\Pi}{\Sigma} \frac{\partial \ln \Sigma}{\partial r} - \frac{d \ln \Omega_K}{dr} \right], \quad (7.83)$$

which is the same as equation (7.40).

In addition to the above basic equations for time-dependent hydrodynamic flows, some subsidiary relations are necessary to solve these basic equations. They are the same as those used to construct steady disk models in the previous sections.

References

- Abramowicz M.A., Calvani M., Nobili L. 1980, ApJ 242, 772
 Chandrasekhar S. 1967, *Stellar Structure* (The Univ. of Chicago Press, Chicago)
 Cox J.P., Giuli R.T. 1968, *Principle of Stellar Structure* Vol. 2 (Gordon and Breach, New York)
 Esin A.A., Narayan R., Ostriker E., Yi I. 1996, ApJ 465, 312
 Hōshi R. 1977, PTP 58, 1191
 Mahadevan R., Narayan R., Yi I. 1996, ApJ 465, 327
 Matsumoto R., Kato S., Fukue J., Okazaki A.T. 1984, PASJ 36, 71
 Pacholczyk A.G. 1970, *Radio Astrophysics* (Freeman, San Francisco)
 Paczyński B., Wiita P.J. 1980, A&A 88, 23
 Shapiro S.L., Lightman A.P., Eardley D.M. 1976, ApJ 204, 187
 Stepney S., Guilbert P.W. 1983, MNRAS 204, 1269

CHAPTER 8

Transonic Nature of Accretion Flows

In black-hole accretion, the gas finally falls to the central hole at the speed of light. The flow is thus transonic, provided that it is initially subsonic far from the hole. That is, the flow must pass a *critical point (sonic radius)*.¹ Furthermore, different from Newtonian accretion, the gas can be swallowed to the hole, even if it has finite angular momentum relative to the hole. Because of this, in addition to the fact that the critical radius requires a regularity condition that the flow must satisfy there, the topology around the radius is different from that in the Newtonian case. In this chapter, emphasizing these topological characteristics of black-hole accretion, we discuss the regularity condition and possible flow structures in the innermost region of black-hole accretion.

8.1 Topology of Black-Hole Accretion

In Newtonian disks, gas cannot fall to a sufficiently small central object, unless it has sufficiently small angular momentum with respect to the central source. This is because repulsion due to the centrifugal force becomes strong as the gas falls toward the source. In the case of black-hole accretion, however, the gas can fall to the central source at the speed of light even if it has angular momentum. This is a general-relativistic effect and is related to the presence of a marginally stable circular orbit. Because of this, the topology around the critical point of accretion flow in relativistic disks is distinct from that in the case of Newtonian flows.

¹Exactly speaking, the critical radius is the radius where the flow speed is equal to the characteristic speed of acoustic perturbations, which is not always equal to the radius where the flow speed is the sound speed. In fact, viscosity and non-adiabatic processes cause a discrepancy between them.

8.1.1 Cases of Inviscid and Adiabatic Flows

We compare the topology around a critical point in both the non-relativistic and relativistic cases, assuming that the flow is adiabatic and inviscid. The flow is assumed to be steady and axisymmetric. The specific angular momentum, ℓ , is thus conserved along the flow.

(a) Newtonian accretion with angular momentum

Let us first consider the case where the gravitational potential of the central object (mass M) is Newtonian.

In the case of Bondi accretion flow with no angular momentum (section 2.2), the accreting gas can reach the surface of the central object after passing a sonic radius. If the gas has angular momentum and the size of the central object is sufficiently small, however, the accreting gas cannot reach the central object because of an *angular-momentum barrier*. That is, the centrifugal force increases inward as $1/r^3$ along with a decrease of radius r , while the gravitational force increases as $1/r^2$ (recall discussion in section 2.3). As a result, the outward centrifugal force eventually overcomes the inward gravitational one, and accretion is stopped. This angular-momentum barrier is located at around

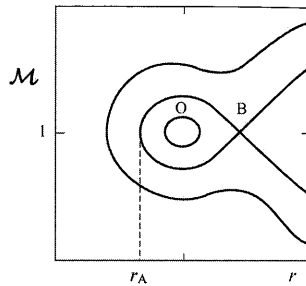
$$r_{\text{barrier}} = \frac{\ell^2}{GM}, \quad (8.1)$$

which is derived by equating the gravitational force, GM/r^2 , and the centrifugal one, ℓ^2/r^3 (cf. section 2.3).

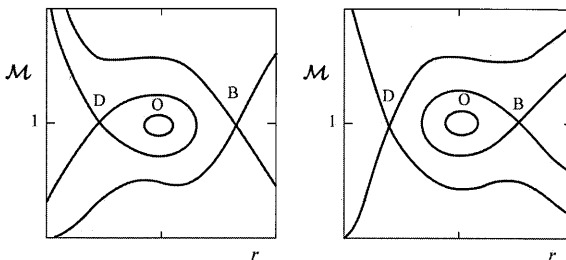
Around the radius of this angular-momentum barrier, the topological structure of transonic accretion flows with constant angular momentum (see figure 2.2 for the case of $\ell = 0$) is schematically expressed in figure 8.1. Here, the abscissa is the radius r , while the ordinate is the Mach number \mathcal{M} .

In contrast to spherical Bondi accretion, which has only one critical point, two critical points exist in accretion flow with angular momentum in the Newtonian regime. The outer one (say B, in figure 8.1), which is just the same critical point as in Bondi flows, is a saddle type, while the inner one (say O, in figure 8.1), which appears due to the effect of rotation, is a center type (see section 2.2 for explanations of the topological types).

The flow passing through the outer critical radius (point B) cannot fall onto the central object due to the angular-momentum barrier (as long as the radius of the central object is less than r_A).

**Figure 8.1**

Schematic picture of gas accretion with constant specific angular momentum in the Newtonian regime. This figure is drawn for some values of mass accretion rate, other integration constants (parameters) being fixed. There exist two critical points: the outer one is a *saddle* (Bondi type, B) and the inner one is a *center* (center type, O). The gas cannot transonically accrete inside some radius ($\sim r_A$) due to the angular-momentum barrier.

**Figure 8.2**

Schematic picture of gas accretion with constant specific angular momentum in the relativistic regime for a few values of mass accretion rate. The left panel is a case of small ℓ , while the right panel is a case of large ℓ . There exist three critical points: the outermost one is a *saddle* (Bondi type, B), the intermediate one is a *center* (center type, O), and the innermost one is a *saddle* (disk type, D). The gas can infall to the center, after passing either the outermost critical point (Bondi-type critical point)(left) or innermost one (disk-like critical point)(right).

(b) Black-hole accretion with angular momentum

In the case of accretion onto a relativistic object, such as a black hole or a neutron star, however, the situation is drastically changed due to a relativistic effect. That is, near to the black hole, an attractive force ($\propto 1/r^4$) appears to predominate over the centrifugal force ($\propto 1/r^3$, see section 2.5). This implies that, if the gas is pushed inward beyond a certain radius, the gas can fall further to the black hole against the centrifugal force.

The topological structure of transonic accretion flows with angular

momentum in the relativistic regime is schematically expressed in figure 8.2, where the abscissa is the radius r and the ordinate is the Mach number \mathcal{M} .

In accretion flow with angular momentum under relativistic flow, there exist three critical points: the outermost one (say B, in figure 8.2) is a saddle type, the intermediate one (say O, in figure 8.2) is a center type, and the innermost one (say D, in figure 8.2), which appears due to the relativistic effect, is a saddle type.

The flow passing through the outermost critical point B is decelerated by the effect of rotation, but can eventually fall onto the central object (left panel of figure 8.2). In the case of the right panel of figure 8.2, the flow passing through point B cannot fall onto the hole, as in the Newtonian case. However, another flow, which has a different parameter value (e.g., mass accretion rate) from that of the flow passing point B, can fall onto the hole by passing the innermost critical point D.

An important consequence of the above considerations is the appearance of the innermost critical (sonic) radius D. The appearance of this critical radius (which is a saddle) is due to the effect of general relativity, as stated. Accretion flows passing this critical radius are hereafter called *disk-like accretion flows*.

The presence of two types of accretion flows (disk-like accretion and Bondi-type accretion) is one of the important characteristics of black-hole accretion. Depending on the parameter values (e.g., specific angular momentum and specific energy of flows), the topological structure of the flow and the number of critical radii change (for details, see Fukue 1987).

Another important feature of transonic accretion is a possible presence of *shocks*. In the relativistic regime of accretion, the disk-type accretion flows appear in addition to the Bondi-type accretion ones. Hence, a transition from a Bondi-type flow to a disk-type one through shock may be possible to finally fall to a central object. This issue is discussed in section 8.5, after the general natures of viscous and non-adiabatic transonic flows are discussed in sections 8.2 – 8.4.

Finally, we briefly summarize here references of inviscid and adiabatic flows of rotating gas. Such transonic flows of rotating gas with constant angular momentum have been investigated for the Newtonian case (Limber 1967; Henriksen and Heaton 1975) and for the relativistic cases for non-rotating black holes (Liang and Thompson 1980; Abramowicz and Zurek 1981; Fukue 1987) and for the rotating holes (Lu 1985, 1986; Nakayama and Fukue 1989; Lu et al. 1997). In the case where global magnetic fields are present, additional critical points appear, cor-

responding to the fact that hydromagnetic perturbations propagate with three types of modes (slow mode, Alfvén mode, and fast mode). That is, the accretion flow must pass three critical radii (those of the slow wave, Alfvén wave, and fast wave) in turn, before falling to a central black hole. The structures of inviscid and adiabatic black-hole accretion flows passing these three critical radii have been investigated by Takahashi (2002).

8.2 Regularity Condition at a Critical Radius

Realistic accretion flows are viscous and non-adiabatic. Hence, the regularity condition at the critical radius is changed from that in the case of inviscid and adiabatic flows. In some cases this change brings about a qualitative change of the local topological structure around the point. Here, we examine this issue in the cases where the α viscosity or a diffusion-type viscosity are adopted. The local topological change around a critical radius is of interest in relation to the instability of the innermost region of disks (see section 12.2).

8.2.1 Basic Equations and Types of Transonic Flows

Transonic numerical models of viscous accretion flows in relativistic disks were first obtained by Paczyński and Bisnovatyi-Kogan (1981) and Muchotrzeb and Paczyński (1982), based on the α -model. After these studies, many researchers examined the structure and stability of transonic accretion flows (e.g., Muchotrzeb 1983; Matsumoto et al. 1984, 1985; Muchotrzeb-Czerny 1986; Abramowicz and Kato 1989; Kato et al. 1988a, b; Chen and Taam 1993).

Here, we first consider, for simplicity, the case where the disk temperature is constant throughout the disk; namely, we adopt $\Pi/\Sigma = c_T^2 = \text{constant}$, instead of using the energy equation (7.31). Then, the elimination of Σ from equations (7.24) and (7.25) gives an equation describing the radial variation of v_r :

$$\frac{dv_r}{dr} = \frac{N}{D}. \quad (8.2)$$

Here, the denominator D and the numerator N are, respectively,

$$D = v_r - \frac{c_T^2}{v_r}, \quad (8.3)$$

$$N = \frac{\ell^2 - \ell_K^2}{r^3} + c_T^2 \frac{d\ln(r/\Omega_K)}{dr}. \quad (8.4)$$

The effects of the gravitational force appear in N through the form of $\ell_K(r) = [r/(r - r_g)]\sqrt{GMr}$ and $\Omega_K(r) = [r/(r - r_g)]\sqrt{GM/r^3}$.

The numerator N involves $\ell(r)$. The radial distribution of ℓ is determined by the equation of angular-momentum balance [equation (7.28)], which is

$$\dot{M}(\ell - \ell_{in}) = -2\pi r^2 T_{r\varphi}. \quad (8.5)$$

Concerning the expression for $T_{r\varphi}$, we consider the following two cases: $T_{r\varphi} = -\alpha\Pi$ and $T_{r\varphi} = \alpha\Sigma c_T^2 d\ln\Omega/d\ln r$ [see equations (7.46) and (7.47)]. As shown later, the resulting topology of the critical point differs in these two cases.

Equation (8.2) shows that a transonic flow must satisfy a regularity condition, $N = 0$, at the critical radius, r_c , where $D = 0$ (i.e., $v_r = -c_T$). Before discussing the topology in detail, it is useful to see some direct consequences of the regularity condition, $N = 0$. This actually gives a relation between r_c and the specific angular momentum at that radius, ℓ_c , for a given parameter, c_T , as illustrated in figure 8.3.²

To understand the implication of this figure, let us first recall the case of inviscid flow (cf. section 8.1). In this case, the specific angular momentum is constant. Hence, the path of accretion flow in the ℓ_c - r_c diagram is a straight horizontal line. Figure 8.3 shows that for an accretion flow with a given ℓ that is much smaller than ℓ_{ms} , a horizontal straight line crosses the curve with a constant c_T at $r \gg r_{ms}$ (unless $c_T = 0$); that is, the sonic radius appears far outside the radius of the marginally stable circular orbit, r_{ms} . This is *Bondi-type* accretion flow, since Bondi flow corresponds to flow with vanishing ℓ . If ℓ is much larger than ℓ_{ms} , on the other hand, the sonic radius is smaller than r_{ms} . This is *disk-type* accretion flow, which is realized by the relativistic effects. For flows with intermediate values of ℓ , there appear three sonic radii for a given ℓ . Two critical points specifying two different types of flows (Bondi-type and disk-type flows) are separated by the middle critical point (cf., figure 8.2). No flow can pass the middle critical point, since the topology around that point is center-type. Our concern in this chapter is transonic flow belonging to disk-type accretion flow.

In general, flow passing a disk-type critical point can always fall to the central hole; however, flow passing a Bondi-type critical point does not always, since the inward flow may finally be stopped due to a strong outward centrifugal force (unless ℓ is very small), even if it passes once

²The ℓ_c - r_c relation in the case of inviscid and adiabatic flows is given by Fukue (1987) and figure 7.3 in chapter 7 of the first edition (Kato et al. 1998).

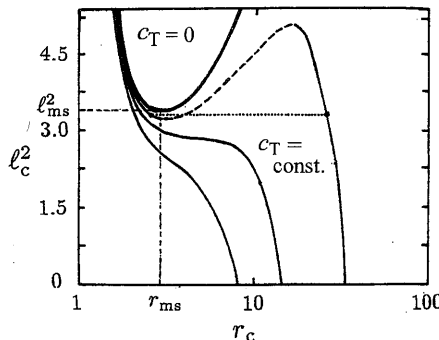
**Figure 8.3**

Diagram showing the position of the critical points in the (ℓ_c, r_c) -plane for some given values of parameter c_T , where ℓ_c is the specific angular momentum at the critical radius, r_c . The thick solid curve shows the case of $c_T = 0$, nothing but the relativistic Keplerian curve. The parts of broken curves are center-type critical point and any transonic flow cannot pass there. Other parts of the curves are saddle-type critical points. Any isothermal transonic flow with a given specific angular momentum (see the dotted horizontal line) must pass a point on the $\ell_c^2 - r_c$ curve with the same c_T as that of the flow. In the case of viscous flows, situations are changed (see figures 8.5 and 8.6). (Adapted from Abramowicz and Kato 1989)

a critical point (see figure 8.2). This problem is discussed in section 8.5 in relation to shock formation in relativistic accretion flow.

In the case of viscous flow, the specific angular momentum is not constant, but decreases inward, since the gas loses angular momentum as it falls. Hence, unlike the case of inviscid flow, we cannot illustrate transonic flow in figure 8.3, until we obtain numerically a global distribution of $\ell(r)$. Numerical models of accretion flow are explained in section 8.4. Before such a discussion, in the subsequent section we examine the flow topology around the critical radius, since the viscosity and form of the stress component, $T_{r\varphi}$, have important effects on the topology of flow around the critical radius.³

8.3 Topology around the Critical Radius in Isothermal Disks

For viscosity we separately consider two cases: $T_{r\varphi} = -\alpha\Pi$ and $T_{r\varphi} = \alpha\Sigma c_T^2 d\ln\Omega/d\ln r$.

³Unlike the case of inviscid flow, a nodal-type critical radius may appear in viscous flow.

8.3.1 The Case of $T_{r\varphi} = -\alpha\Pi$

When $T_{r\varphi}$ is algebraically expressed as $T_{r\varphi} = -\alpha\Pi$, equation (8.5) gives

$$\ell = \ell_{\text{in}} - \alpha r \frac{c_T^2}{v_r}. \quad (8.6)$$

Here, we have used the equation of continuity ($\dot{M} = -2\pi r \Sigma v_r = \text{constant}$) and $c_T^2 = \Pi/\Sigma$. If this expression for ℓ is substituted into equation (8.4), N becomes an explicit function of v_r and r . Equation (8.2) is then a differential equation of v_r with respect to r .

Solutions of equation (8.2) on the (v_r, r) -plane exhibit an interesting behavior around the critical radius, since D tends to zero there. To examine the behavior, we introduce a variable, s , defined by

$$\left(v_r - \frac{c_T^2}{v_r} \right) ds = d(\Delta r), \quad (8.7)$$

where Δr is the radial distance from the critical radius r_c ; i.e.,

$$|\Delta r| = |r - r_c| \ll r_c. \quad (8.8)$$

All of the variables of steady disks at $r = r_c + \Delta r$ are now expanded around those at the critical radius, say

$$v_r(r_c + \Delta r) = -c_T + \Delta v_r, \quad \ell(r_c + \Delta r) = \ell_c + \Delta \ell. \quad (8.9)$$

Here, subscript c denotes the values at the critical radius, r_c . We examine how variables Δv_r and $\Delta \ell$ behave near to the critical radius.

Retaining only the linear terms with respect to Δv_r and $\Delta \ell$, from equations (8.7) and (8.2) we obtain

$$\frac{d\Delta r}{ds} = 2\Delta v_r, \quad (8.10)$$

$$\frac{d\Delta v_r}{ds} = 2\alpha\Omega_c\Delta v_r - 2X\Delta r, \quad (8.11)$$

where

$$X = \left[\frac{3}{2}(\Omega^2 - \Omega_K^2) + \frac{\ell_K}{r^3} \frac{d\ell_K}{dr} - \frac{1}{2} c_T^2 \frac{d^2 \ln(r/\Omega_K)}{dr^2} - \alpha\Omega \frac{c_T}{r} \right]_c. \quad (8.12)$$

In deriving equation (8.11) from equation (8.2), $\Delta \ell$ was expressed in terms of Δr and Δv_r by using equation (8.6) as

$$\Delta \ell = \alpha c_T \Delta r + \alpha r_c \Delta v_r. \quad (8.13)$$

Equations (8.10) and (8.11) are simultaneous differential equations for Δr and Δv_r with respect to s . Assuming that Δr and Δv_r depend on s in the form of $\exp(\lambda s)$, we obtain the following characteristic equation which determines the eigenvalue λ :

$$\lambda^2 - 4\alpha\Omega_c\lambda + 4X = 0. \quad (8.14)$$

The solutions of this characteristic equation depend on the sign of the determinant, $D \equiv \alpha^2\Omega_c^2 - X$, and that of X . The topology of the critical points is classified into three types by the set of eigenvalues λ (e.g., Bogoliubov and Mitropolsky 1961).

(1) Spiral type

If $D < 0$, and thus two solutions of λ of equation (8.14) are complex conjugate, the critical point is a *spiral*.⁴ A spiral-type critical point is not interesting in our present problem, since the flow velocities should be double-valued around the spiral-type critical point, while the fluid velocities cannot be. Therefore, it is only a mathematical solution, and no realistic transonic flow can pass this point. We thus proceed to the cases where the two solutions of λ are both real.

(2) Saddle type

If $D > 0$ and $X < 0$, the two solutions should be real and have different signs,

$$\lambda_1\lambda_2 < 0. \quad (8.15)$$

We now demonstrate that the critical point is then a *saddle*. If we denote, say, $\lambda_1 > 0$ and $\lambda_2 < 0$, we obtain

$$\Delta r = c_1 \exp(\lambda_1 s) + c_2 \exp(-|\lambda_2|s), \quad (8.16)$$

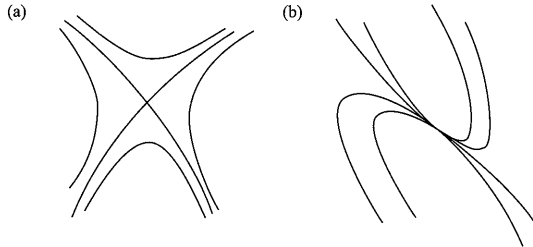
$$\Delta v_r = \frac{\lambda_1}{2} c_1 \exp(\lambda_1 s) - \frac{|\lambda_2|}{2} c_2 \exp(-|\lambda_2|s), \quad (8.17)$$

where c_1 and c_2 are arbitrary constants. The elimination of s from the above two equations gives

$$\left(\Delta v_r - \frac{\lambda_1}{2} \Delta r \right)^{\lambda_1} \left(\Delta v_r - \frac{\lambda_2}{2} \Delta r \right)^{|\lambda_2|} = C, \quad (8.18)$$

where C is a constant specifying each curve. For $C = 0$, this equation gives two asymptotic curves, $\Delta v_r = (\lambda_1/2)\Delta r$ and $\Delta v_r = (\lambda_2/2)\Delta r$.

⁴If the eigenvalues are pure imaginary, the critical point is a center-type. This type appears when $\alpha = 0$ (i.e., when the flow is inviscid, see section 8.1).

**Figure 8.4**

Schematic pictures showing types of critical points: (a) a saddle-type critical point, and (b) a nodal-type critical point. See figure 2.3 for more details.

Except for these curves, no other curves pass the critical point. This is a saddle-type critical point, and is the same as that which appears in the Bondi-flow problem (see sections 2.1 and 8.1). The topology around this type of a critical point is schematically illustrated in figure 8.4a.

(3) Nodal type

If $D > 0$ and $X > 0$, we obtain

$$\lambda_1 \lambda_2 > 0. \quad (8.19)$$

The point is then a *node*, as shown in the following. The solutions of equations (8.10) and (8.11) are

$$\Delta r = c_1 \exp(\lambda_1 s) + c_2 \exp(\lambda_2 s), \quad (8.20)$$

$$\Delta v_r = \frac{\lambda_1}{2} c_1 \exp(\lambda_1 s) + \frac{\lambda_2}{2} c_2 \exp(\lambda_2 s), \quad (8.21)$$

where c_1 and c_2 are arbitrary constants. The elimination of s from the above two equations leads to

$$\Delta v_r - \frac{\lambda_1}{2} \Delta r = C \left(\Delta v_r - \frac{\lambda_2}{2} \Delta r \right)^{\lambda_2/\lambda_1}, \quad (8.22)$$

where C is a constant specifying each curve, and is determined by c_1 , c_2 , λ_1 , and λ_2 . This equation shows that when $\lambda_2/\lambda_1 > 1$, all curves around the critical point tend to the line of $\Delta v_r = (\lambda_1/2)\Delta r$, except when $C = \infty$. In this case $\Delta v_r = (\lambda_2/2)\Delta r$. This is schematically shown in figure 8.4b. This is a nodal-type critical point. That is, all curves tend to the curve of $\Delta v_r = (\lambda_1/2)\Delta r$, except for a singular curve, which tends to $\Delta v_r = (\lambda_2/2)\Delta r$.

In summary, three types of critical radius appear in isothermal disks with α -viscosity. The type depends on the value of X [see equation (8.14)] and notice that the characteristics of λ are determined by X . This is summarized in table 8.1.

Table 8.1 Type of critical points ($T_{r\varphi} = -\alpha\Pi$).

Type	Condition	Eigenvalues
spiral	$\alpha^2\Omega_c^2 < X$	complex conjugate
nodal	$0 < X < \alpha^2\Omega_c^2$	real; $\lambda_1\lambda_2 > 0$
saddle	$X < 0$	real; $\lambda_1\lambda_2 < 0$

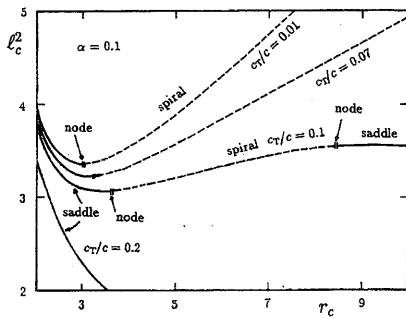


Figure 8.5

Diagram showing the type of critical point on the $N = 0$ curve in the case of $\alpha = 0.1$. Nodal-type critical points appear in narrow transition regions between the regions of a saddle-type critical point (solid curve) and of a spiral-type one (broken curve). (Adapted from Abramowicz and Kato 1989)

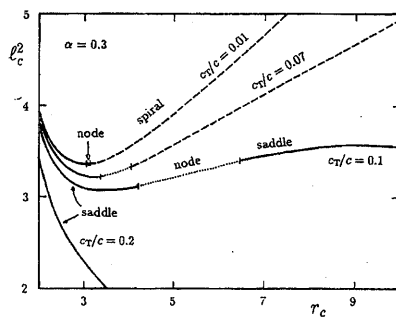


Figure 8.6

Same as figure 8.5, except for $\alpha = 0.3$. The region of the nodal-type critical point (dotted curve) is more extended on the curve of $N = 0$, compared with the case of $\alpha = 0.1$. When c_T is large, the region of spiral-type critical point disappears. (Adapted from Abramowicz and Kato 1989)

Figures 8.5 and 8.6 show where on the curve of $N = 0$ these three types of critical points appear in the (ℓ_c, r_c) -plane. Figure 8.5 is for $\alpha = 0.1$ and figure 8.6 for $\alpha = 0.3$. As the value of α increases, the part of the nodal-type critical points extends over a wide range on the curves of $N = 0$.

The appearance of a nodal-type critical point is due to the presence of viscosity ($\alpha \neq 0$). That is, if the flow is inviscid and isothermal, the transonic point is always a saddle (or center). Note again, however, that this conclusion depends on the form of the viscosity. Even when the viscosity is taken into account, nodal-type critical points do not appear, if a diffusion form ($T_{r\varphi} \propto d\Omega/dr$) is adopted, as is shown below.

8.3.2 The Case of $T_{r\varphi} = \alpha \Sigma c_T^2 d \ln \Omega / d \ln r$

In this case, equation (8.5) gives

$$\frac{d\ell}{dr} = 2\frac{\ell}{r} + \frac{\ell v_r}{\alpha c_T^2 r^2} (\ell - \ell_{in}). \quad (8.23)$$

The radial distribution of ℓ is now given by a differential equation, unlike the previous case where $\ell(r)$ is given by an algebraic equation (8.6).

To examine the type of critical point, we again introduce a variable, s , defined by equation (8.7). We then find that the radial distributions of Δv_r and $\Delta \ell$ are determined by

$$\frac{d\Delta r}{ds} = 2\Delta v_r, \quad (8.24)$$

$$\frac{d\Delta v_r}{ds} = 2\frac{\ell_c}{r_c^3} \Delta \ell - 2\left(X + \alpha \frac{\ell_c}{r_c^3} c_T\right) \Delta r, \quad (8.25)$$

$$\frac{d\Delta \ell}{ds} = 2Y \Delta v_r, \quad (8.26)$$

where

$$Y = \frac{\ell_c}{r_c} \left(2 - \frac{\ell - \ell_{in}}{\alpha r c_T}\right)_c, \quad (8.27)$$

and X is given by equation (8.12). Equations (8.24)–(8.26) are simultaneous differential equations of Δr , Δv_r , and $\Delta \ell$ with respect to s . Taking again Δr , Δv_r , and $\Delta \ell$ to depend on s , as $\exp(\lambda s)$, we obtain an equation that determines the eigen-value λ ,

$$\lambda \left[\lambda^2 - 4\frac{\ell_c}{r_c^3} (Y - c_T) + 4X \right] = 0. \quad (8.28)$$

We have $\lambda = 0$ and

$$\lambda^2 = 4\frac{\ell_c}{r_c^3} (Y - c_T) - 4X. \quad (8.29)$$

In the present case, there is no term proportional to λ in equation (8.29). That is, we always have $\lambda_1 = -\lambda_2$ when the λ 's are real (see table 8.2). This implies that the critical radius at which the accretion flow passes is always a saddle, and there is no case of a nodal-type critical radius (Abramowicz and Kato 1989).

Table 8.2 Type of critical points ($T_{r\varphi} \propto d\Omega/dr$).

Type	Condition	Eigenvalues
center	$\ell_c(Y - c_T)/r_c^3 < X$	pure imaginary
saddle	$X < \ell_c(Y - c_T)/r_c^3$	real; $\lambda_1 \lambda_2 < 0$

8.3.3 Comments on general cases

So far, we have concentrated our attention only on isothermal accretion flows. It is, however, straightforward to generalize the above analyses to non-isothermal flows. If the energy equation is taken into account instead of isothermality being assumed, the set of differential equations describing the accretion flows become

$$\frac{dv_r}{dr} = \frac{N_1}{D} \quad \text{and} \quad \frac{d\ell}{dr} = \frac{N_2}{D}, \quad (8.30)$$

where D , N_1 , and N_2 are some functions of r , v_r , and ℓ [see, e.g., Matsumoto et al. (1984) for flows with $T_{r\varphi} = -\alpha\Pi$, and Narayan et al. (1997) and Chen et al. (1997) for advection-dominated flows with $T_{r\varphi} = \alpha\Sigma c_s^2 d\ln\Omega/d\ln r$]. In this case, the regularity conditions at the critical radius of $D = 0$ are $N_1 = N_2 = 0$. At first glance, the number of conditions increases. It turns out, however, that this is not the case; the conditions $D = 0$ and $N_2 = 0$ are identical to those of $D = 0$ and $N_1 = 0$. That is, there appears to be no additional regularity condition, even if the number of differential equations describing transonic flows increases. In other words, in (r, v_r, ℓ) -space, three surfaces ($D = 0$, $N_1 = 0$, and $N_2 = 0$) intersect each other along some common curves. These curves are called *critical curves*, and all of the points on them are critical points (Flammang 1982).

If two-temperature disks are considered, for example, we have two energy equations. One is for ions and the other is for electrons. Accordingly, the number of differential equations increases even when $T_{r\varphi} = -\alpha\Pi$ is adopted, and we have (Nakamura et al. 1996, 1997)

$$\frac{dv_r}{dr} = \frac{N_1}{D}, \quad \frac{dT_i}{dr} = \frac{N_2}{D}, \quad \frac{dT_e}{dr} = \frac{N_3}{D}, \quad (8.31)$$

where D , N_1 , N_2 , and N_3 are some functions of r , v_r , T_i , and T_e . Here, as dependent variables, we have used temperatures instead of ℓ . The number of regularity conditions at $D = 0$ is still just one, i.e., $N_i = 0$ ($i = 1$, or 2, or 3), since if $D = 0$ and one of N_1 , N_2 , and N_3 vanishes there, two others automatically vanish. This result, that the number of regularity conditions is always one, seems to be reasonable, because the singular behavior of the flow at the critical point originates from a coincidence of the characteristic speed of the acoustic wave to the flow speed, and this occurs only from the r -component of the momentum equation.⁵

⁵It seems that the number of regularity conditions is always one and does not

If global magnetic fields exist in disks, three types of critical points appear at different radii (see, e.g., Takahashi 2002), corresponding to the presence of three types of characteristics, resulting from the slow, Alfvén and fast modes. (The sonic-type critical point discussed here corresponds to the critical point of the fast mode.) Even in such a case, the number of regularity conditions is still one at each critical point.

8.3.4 Comments on the usage of the l'Hospital theorem

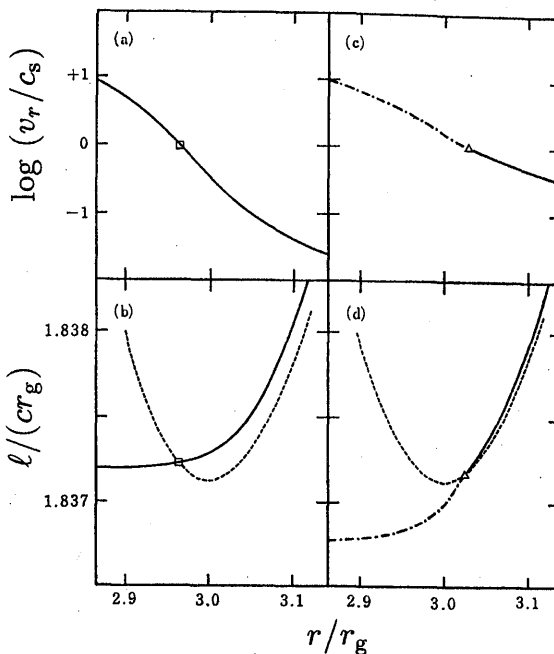
Occasionally, the l'Hospital theorem is used to classify the topology around a critical point. The theorem gives the gradients of curves passing the critical point (i.e., eigen-functions). Although these gradients are related to the eigenvalue λ 's, they are not generally equal. Hence, we must be careful when using the l'Hospital theorem to judge the type of critical point. If we adopt relevant variables, however, the gradients are identical to the eigenvalues. This issue has been discussed in detail in subsection 9.1.5 in the first edition (Kato et al. 1998).

8.4 Numerical Examples of Transonic Flows

Geometrically thin transonic disk solutions that tend to the standard α -disks at large radii $r \gg r_g$ were first obtained numerically by Paczyński and Bisnovatyi-Kogan (1981) and Muchotrzeb and Paczyński (1982), using the pseudo-Newtonian potential and the α -form of viscosity. Muchotrzeb (1983) reported that there is no smooth transonic solution in the case of a large viscosity ($\alpha \geq \alpha^*$). The critical value, α^* , was between 0.015 and 0.05, depending on the mass of the black hole and the accretion rate. Subsequently, Matsumoto et al. (1984) pointed out that the difficulty in finding steady solutions for $\alpha > \alpha^*$ is related to the types of topology around the sonic point. That is, they found that for any value of α there *exist* transonic solutions satisfying the outer boundary conditions of the Keplerian disk. When α is larger than a value close to α^* , however, the type of sonic point changes from a saddle type to a nodal one, for which it is generally difficult to find transonic solutions numerically, since fine-tuning is necessary around the critical point.

The equations that Matsumoto et al. (1984) adopted are equations (7.24), (7.25), (7.28), (7.30), (7.31), and (7.43) with advective cooling

increase, even when more sophisticated equations are adopted, although it has not yet been proven.

**Figure 8.7**

Examples of numerical solutions: (a) and (b) are for $(\alpha, \dot{M}/\dot{M}_{\text{crit}}, \ell_{\text{in}}/cr_g) = (0.01, 1.6, 1.8372125)$, while (c) and (d) are for $(\alpha, \dot{M}/\dot{M}_{\text{crit}}, \ell_{\text{in}}/cr_g) = (0.2, 1.6, 1.83674)$. The position and the type of critical point are indicated by symbols squares (saddle) and triangles (node). The dashed curves show the Keplerian angular-momentum distribution. (After Matsumoto et al. 1984)

given by footnote 8 in section 7.2, optically-thick cooling formula [equations (7.58) and (7.59)] and the Shakura-Sunyaev type α -viscosity [equation (7.46)]. An important result obtained is that the disk structure differs qualitatively in the two cases of small α and large α . Typical examples are shown in figure 8.7; the main differences in these two cases are summarized in table 8.3.⁶ In the case of small α (figure 8.7a and 8.7b), a transonic solution passes through a saddle-type critical point, which is located inside r_{ms} , where r_{ms} is the radius of the marginally stable circular orbit ($= 3r_g$ in the present case of a non-rotating black hole). The value of ℓ_{in} is uniquely determined by the transonic condition. If

⁶The last column of this table gives the relation between topology and stability, which is discussed later in section 12.2.

α is large (figure 8.7c and 8.7d), on the other hand, the solution passes through a nodal-type critical point, which is located outside r_{ms} , as long as the parameter ℓ_{in} lies in a certain range.

Table 8.3 Different natures of transonic flows ($T_{r\varphi} = -\alpha\Pi$).

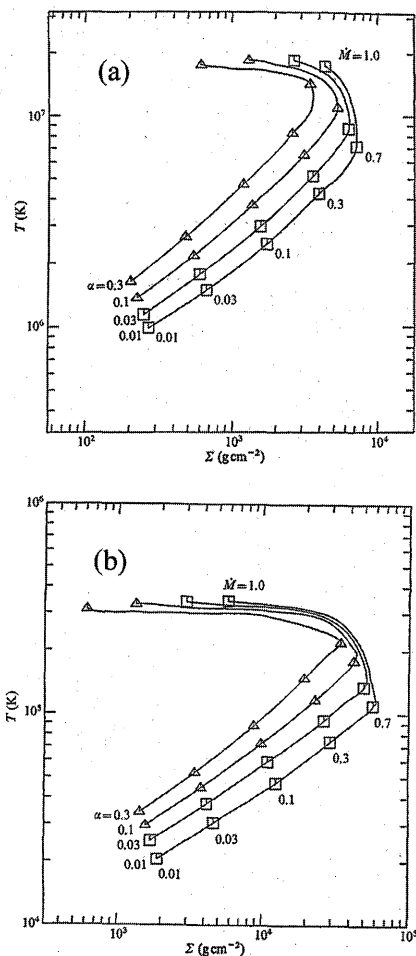
α	ℓ_{in}	r_c	Infall process	Topology	Stability
small	$> \ell_{\text{ms}}$	$< r_{\text{ms}}$	pressure-driven	saddle	stable
large	$< \ell_{\text{ms}}$	$> r_{\text{ms}}$	viscosity-driven	node	unstable

The different behaviors of transonic solutions for small and large α 's come from the different processes to promote gas infall toward the black hole. In the case of a small α , the direct cause of the infall is the pressure-gradient force. Due to this force, a gas with large angular momentum is pushed inside r_{ms} , so that it falls dynamically toward the hole. Hence, ℓ_{in} is larger than ℓ_{ms} (specific angular momentum of a particle orbiting circularly at $r = r_{\text{ms}}$) and the sonic radius is inside r_{ms} . The critical point is the saddle type, as in the case of a pressure-driven solar wind or Bondi flow.

In the case of a large α , on the other hand, the primary cause of the infall toward the hole is a decrease of ℓ due to viscous effects. Hence, ℓ decreases below ℓ_K in a region outside $r = r_{\text{ms}}$, so that the gas can fall toward the hole. Hence, the sonic radius is larger than r_{ms} and ℓ_{in} is smaller than ℓ_{ms} . The critical point is the nodal type in the case of $T_{r\varphi} = -\alpha\Pi$.

The above-mentioned distinction of disk structures by small and large α -values is a universal feature of transonic accretion flows, independent of the precise forms of $T_{r\varphi}$ and of the energy equations. For example, similar changes in the disk structures by α are realized even in advection-dominated disks [e.g., Chen and Taam (1993) for optically thick disks (slim disks) and Narayan et al. (1997) and Chen et al. (1997) for optically thin disks (ADAFs)].

Finally, we mention how the type of critical points changes as the disk parameters are varied in the case of $T_{r\varphi} = -\alpha\Pi$. Here, we restrict our attention to disks that tend to the Shakura-Sunyaev-type standard disks in the outer region. Figure 8.8 shows the loci of the critical point on the T - Σ plane when $M = 10M_\odot$ (panel a) and $M = 10^8M_\odot$ (panel b) for some values of α . (In this figure the advection-dominated branches with large M , i.e., the slim-disk branches, are not considered.) The type of critical point that the steady flow passes is indicated by square (saddle) and triangle (node). It is shown that the type of the critical point depends little on M , but changes from a saddle to a node as the

**Figure 8.8**

Position of the critical radius of the steady accretion-disk models, shown in the temperature-surface density plane with some values of parameters α and \dot{M} . (a) for $M = 10M_{\odot}$ and (b) for $M = 10^8M_{\odot}$. The square indicates that the sonic point is a saddle-type critical point and is stable, while the triangle indicates that the sonic point is a nodal-type critical point, and thus unstable. (After Kato et al. 1988b)

value of α increases. The critical value of α , say α_c , of this transition is $\alpha_c \sim 0.08$ when $M = 10M_{\odot}$. In the case when $M = 10^8M_{\odot}$, α_c is slightly smaller and we have⁷ $\alpha_c \sim 0.05$.

⁷Numerically, the critical value, α_c , differs slightly from α^* at which Muchotrzeb

It is noted again that the results shown in figure 8.8 are only for the case of $T_{r\varphi} = -\alpha\Pi$. If a diffusion-type stress tensor is adopted, the results are changed, as mentioned before, i.e., in the isothermal disks the critical point is always a saddle. In general cases, however, there seems to still be no careful analyses.

8.5 Transonic Flows with Standing Shocks

In the previous sections, we examined the characteristics of disk-type critical points that steady transonic accretion flow must pass to fall to black holes. Almost all numerical simulations show that whatever accretion flows in the outer region are, they finally pass a disk-type critical point to fall to a black hole, adjusting their flow structure, without having any discontinuity. This, however, may not always be the case. For example, there may be a possibility that before passing a disk-like critical point, a flow becomes transonic by passing an outer Bondi-type critical point. This supersonic flow may make a transition to a subsonic flow through a shock to finally pass a disk-like critical point. Another example is a transonic flow falling on a rigid surface of a neutron star. A transonic flow will have a shock to fall on the surface. In order to have a rough image on disk accretions with shocks, we study here standing shock solutions in the limit of inviscid and adiabatic flows, according to Fukue (1987).⁸

Since inviscid and adiabatic flows are considered here, we have two free parameters specifying the flows. They are the specific energy, E , of the flow measured at infinity in units of c^2 , and the specific angular momentum, ℓ , of the gas measured at infinity in units of cr_g . In order to derive the jump conditions at a shock, we must use the relativistic Rankine-Hugoniot relations (Thorne 1973). Considered here are shocks standing stationary in accreting flows, so that the shock frame (a local Lorentz frame) coincides with the rest one. Moreover, it is unnecessary to consider the tangential component of the flow under the jump conditions. It is assumed that the thickness of the flow does not change at the shock.

supposed steady solutions to disappear. We think, however, that α^* and α_c have the same physical origin and should have an identical number, if numerical computations with good resolutions are performed.

⁸In the context of the spherical geometry adopted in this paper, we cannot properly deal with standing shocks in disk-accreting flows. This is because the hydrostatic equilibrium in the vertical direction of the disk is not considered, and hence the vertical expansion just behind the shock will not be taken into account (see Fukue 1983). Qualitative features, however, can be found under the limited treatment (cf. Chakrabarti 1989 for the hydrostatic case).

Hence, the jump conditions become:

$$n_1 u_1 = n_2 u_2, \quad (8.32)$$

$$(\varepsilon_1 + p_1)u_1^2 + p_1 = (\varepsilon_2 + p_2)u_2^2 + p_2, \quad (8.33)$$

$$(\varepsilon_1 + p_1)\gamma_1 u_1 = (\varepsilon_2 + p_2)\gamma_2 u_2, \quad (8.34)$$

where subscript 1 denotes the front side of the shock and 2 the back side. Furthermore, n and u are the number density of gas and the radial component of the four velocity, ε and p are the total internal energy density and the total pressure, respectively. The Lorentz factor is written as γ .

By adopting temperature T and u , equations (8.32)–(8.34) are reduced to

$$(f_p + f_e + 2kT)\gamma|_1 = (f_p + f_e + 2kT)\gamma|_2, \quad (8.35)$$

$$\frac{2kT + (f_p + f_e + 2kT)u^2}{u} \Big|_1 = \frac{2kT + (f_p + f_e + 2kT)u^2}{u} \Big|_2, \quad (8.36)$$

where $f = \varepsilon/n$ and subscripts p and e represent the proton and the electron. Detailed expressions for f_p and f_e are given in appendix H [see also Fukue (1987)]. From these equations (8.35) and (8.36), we can calculate the postshock quantities from the given preshock quantities.

8.5.1 Neutron Stars

Before describing the black-hole case, let us first consider standing shocks in disk accretion onto a neutron star that has a rigid surface. In this case, the subsonic flow inside the standing shock must connect smoothly to the boundary conditions at the star surface.

A typical example is shown in figure 8.9, where the parameters are fixed as $E = 1.005$ and $\ell = 1.500$. In this case, the outer critical point is located at $r_c = 27.67$ (in units of the Schwarzschild radius r_g) and the effective adiabatic index⁹, Γ_c , there is 1.445. The radius r_* of the neutron star is assumed to be $2r_g$ and the temperature there is set as $kT/m_p c^2 = 0.03$ in this example.

In figure 8.9, the Mach number, \mathcal{M} , is plotted as a function of r . The dotted curve denotes the locus of \mathcal{M} at the postshock position. The supersonic solution jumps on this curve at the shock. The relevant parts of the solutions are denoted by thick curves. It is found that, *for the*

⁹The effective adiabatic index, Γ , is defined by $\Gamma = [1 + p / \sum T n_a f'_a(T_a)]$, where the prime denotes differentiation with respect to T_a (see appendix H).

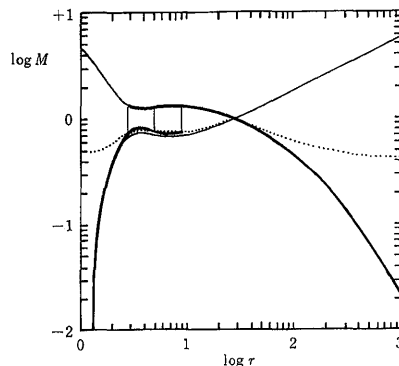


Figure 8.9

Mach number M of an example of solutions with standing shocks in the case of accretion onto a neutron star. Parameters are $(\ell, E) = (1.500, 1.005)$. The dotted curve denotes the locus of the Mach number just behind the shock. Thin vertical lines represent the positions of standing shocks for the conditions specified. The shocks can stand at three distinct locations for the same parameters and the same boundary conditions. (After Fukue 1987)

same parameters of the flow and for the same boundary conditions at the star surface, shocks can stand at three distinct positions. In figure 8.9, the possible locations of standing shocks are $r \sim 9$, ~ 5 , and ~ 2.6 .

This phenomenon may be associated with the multiplicity of the critical points (Fukue 1987). Of these three locations of standing shocks, the outermost position is that of the usual type formed in spherical flow. The intermediate one appears due to the effect of rotation. Finally, the innermost one is related to the relativistic effect.

8.5.2 Black Holes

In usual situations, it seems to be difficult to imagine standing shocks in a transonic accretion onto a black hole, since it has *no rigid* surface. The multiplicity of critical points (Fukue 1987), however, enables standing shocks in a transonic flow onto a black hole.

An example is displayed in figure 8.10, where the parameters are $E = 1.005$ and $\ell = 1.513$, and therefore $r_c = 27.3$ and $\Gamma_c = 1.445$.

In figure 8.10, the dotted curve denotes the locus of the Mach number just behind the shock. The supersonically accreting flow that has passed through the *outer* critical point of the saddle type becomes subsonic at the standing shock. Then, it is again accelerated to be supersonic at

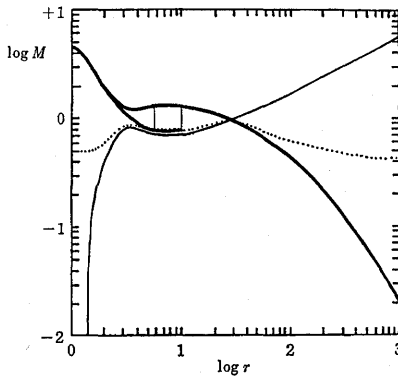


Figure 8.10

Same as figure 8.9, but for a black hole. The parameters are $(\ell, E) = (1.513, 1.005)$. In addition to the transonic solution without shock, there exist two solutions with standing shocks at different radii. (After Fukue 1987)

the *inner* critical point, and eventually falls into the hole. In the case of figure 8.10, it is possible for standing shocks to exist at two different places, $r = 5.6$ and 10 . This is also due to reasons similar to those discussed before. In addition, it is of course possible to have a transonic solution without shock.

8.5.3 Stability of Shocks

As shown in the previous subsections, due to the effects of rotation and general relativity, there appear *multiple sonic points* and associated *multiple shocks* (multiple positions for shock transitions). Which location of these shock positions does nature favor?

Nakayama examined the stability of (isothermal and adiabatic) accretion flow with standing shocks in the non-relativistic regime (Nakayama 1992, 1993, 1994) and in the general relativistic regime (Nakayama 1995).

For an isothermal, inviscid and axisymmetric accretion (and wind), Nakayama (1992, 1993) found that the stability properties are determined by the quantity ν_{iso} , defined by

$$\begin{aligned} \nu_{\text{iso}} &\equiv -\frac{1}{v_2} \left(\frac{d\psi}{dr} - \frac{\ell^2}{r^3} - \frac{c_T^2}{r} \right) \Big|_{r=R} \\ &= \frac{v_2^2 - c_T^2}{2v_2^3} \frac{dv^2}{dr} \Big|_2 = \frac{v_1^2 - c_T^2}{2c_T^2 v_1} \frac{dv^2}{dr} \Big|_1, \end{aligned} \quad (8.37)$$

where ψ is the gravitational potential, ℓ the specific angular momentum, and c_T the isothermal sound speed. Subscript 2 denotes the value at the post-shock side of the unperturbed shock wave, which is located at $r = R$, and 1 denotes the pre-shock side value. The other quantities are evaluated at the position of the shock ($r = R$).

He proved that $\nu_{\text{iso}} < 0$ is a necessary and sufficient condition for instability. That is, if $\nu_{\text{iso}} \geq 0$ no unstable mode exists, while we can always find a linearly unstable mode whose growth rate is real, if $\nu_{\text{iso}} < 0$. This criterion means that *the flow is unstable if the post-shock flow is accelerated*. These properties are essentially the same in the adiabatic case, if c_T is replaced by $c_T \equiv \sqrt{(p_2 - p_1)/(\rho_2 - \rho_1)}$ (Nakayama 1994), and also in the relativistic case (Nakayama 1995).

Moreover, Nobuta and Hanawa (1994) studied the detailed properties of the isothermal instability by numerical experiments, including simulations of non-linear evolution. They considered the instability mechanism from the viewpoint of dynamics, and showed that the flow is destabilized by a pressure imbalance between pre- and post-shock flows.

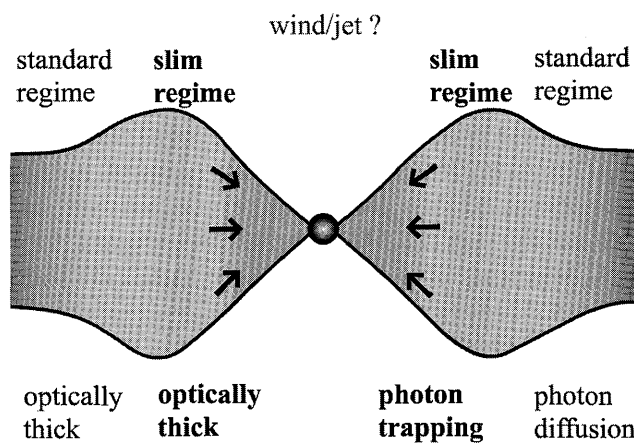
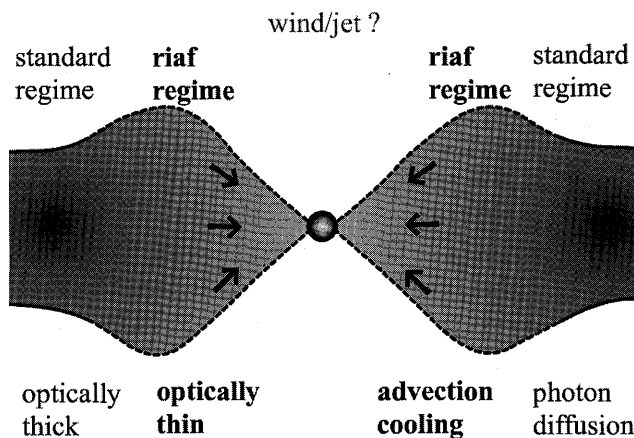
According to Nakayama's criterion, *the inner shock is unstable* in the present case. More generally, in the case of accretion flows the *inner* shock wave standing in close to the black hole is always unstable and the *outer* one is stable, while the relation is reversed for wind flows. Therefore, the possible location of the standing shock is uniquely determined by the instability.

So far, we discussed accretion flows with no magnetic fields. In general, however, the presence of global magnetic fields near black holes is expected. Shock formation for accreting MHD plasmas in a rotating black hole magnetosphere has been examined (Takahashi et al. 2002). Furthermore, the results presented above are for the cases of inviscid and adiabatic flows, but similar situations (presence of shocks and their instability) will be expected even in realistic viscous and non-adiabatic accretion flows. Further studies on these directions are astrophysically interesting because they can be one of the possible origins of activity in the highly energetic inner region of black-hole accretion.

References

- Abramowicz M.A., Kato S. 1989, ApJ 336, 304
- Abramowicz M.A., Zurek W.H. 1981, ApJ 246, 314
- Bogoliubov N.N., Mitropolsky E.A. 1961, *Asymptotic Methods in the Theory of Non-linear Oscillations* (Gordon and Breach, New York)
- Chakrabarti S.K. 1989, ApJ 347, 365

- Chen X., Taam R.E. 1993, ApJ 412, 254
Chen X., Abramowicz M.A., Lasota J.-P. 1997, ApJ 476, 61
Flammang R.A. 1982, MNRAS 199, 833
Fukue J. 1983, PASJ 35, 355
Fukue J. 1987, PASJ 39, 309
Henriksen R.N., Heaton K.C. 1975, MNRAS 171, 27
Kato S., Honma F., Matsumoto R. 1988a, MNRAS 231, 37
Kato S., Honma F., Matsumoto R. 1988b, PASJ 40, 709
Liang E.P.T., Thompson K.A. 1980, ApJ 240, 271
Limber D.N. 1967, ApJ 148, 141
Lu J.F. 1985, A&A 148, 176
Lu J.F. 1986, Gen. Relativ. Gravitation 18, 45
Lu J.F., Yu K.N., Yuan F., Young E.C.M. 1997, A&A 321, 665
Matsumoto R., Kato S., Fukue J., Okazaki A.T. 1984, PASJ 36, 71
Matsumoto R., Kato S., Fukue J. 1985, in *Theoretical Aspects on Structure, Activity, and Evolution of Galaxies III*, eds. S.Aoki, M.Iye, Y.Yoshii (Tokyo Astr. Obs. Publ., Tokyo), p102
Muchotrzeb B. 1983, Acta Astron 33, 79
Muchotrzeb-Czerny B. 1986, Acta Astron 36, 1
Muchotrzeb B., Paczyński B. 1982, Acta Astron 32, 1
Nakamura K., Matsumoto R., Kusunose M., Kato S. 1996, PASJ 48, 761
Nakamura K., Kusunose M., Matsumoto R., Kato S. 1997, PASJ 49, 503
Narayan R., Kato S., Honma F. 1997, ApJ 476, 49
Nakayama K. 1992, MNRAS 259, 259
Nakayama K. 1993, PASJ 45, 167
Nakayama K. 1994, MNRAS 270, 871
Nakayama K. 1995, MNRAS 281, 226
Nakayama K., Fukue J. 1989, PASJ 41, 271
Nobuta K., Hanawa T. 1994, PASJ 46, 257
Paczyński B., Bisnovatyi-Kogan G. 1981, Acta Astron 31, 283
Thorne K.S. 1973, ApJ 179, 897
Takahashi M. 2002, ApJ 570, 264
Takahashi M., Rilett D., Fukumura K., Tsuruta S. 2002, ApJ 572, 950



Optically thick slim disks (above) and optically thin ADAFs (below).

CHAPTER 9

Radiatively Inefficient Accretion Flows

Standard-type disks (chapter 3) cannot produce high-energy emission, such as gamma-rays. What then is lacking there? One of the most important processes that are not considered in the standard accretion-disk models is *advectional cooling*. In the standard models, the accreting material cools so efficiently that all of the energy released through viscosity can be radiated locally. There exist, however, distinct branches of steady disk solutions, in which this assumption is violated. In a *radiatively inefficient accretion flow* (RIAF), for example, the energy released via viscosity is stored as entropy and transported inward with accretion. The flow then becomes very hot, being able to produce high-energy emission.

The proto-type model of the RIAF is an optically thin *advection-dominated accretion flow* (abbreviated as an ADAF). Great attention has been paid to this model and rapid progress has been made in this field due mainly to the theoretical efforts by Abramowicz, Lasota, Narayan, Yi, and others. The recent development stems from the recognition that the ADAFs are globally stable and can well explain observations. In this chapter, we overview the theoretical attempts towards constructing a new paradigm for hot accretion flows. We first overview the essence of the ADAF in section 9.1, discuss its structure and spectral properties in sections 9.2 and 9.3, respectively, and then proceed to a discussion of its stability in section 9.4. The recent developments are outlined in section 9.5.

9.1 Advection-Dominated Accretion Flow

We first explain what differs between ADAFs and standard disks and why the notion of the ADAF is so important. Although our discussion here is based on the ADAF formulation, the results are mostly relevant to the RIAFs, in general.

9.1.1 What is Advective Cooling and Why So Important?

Optically thin, radiative-cooling-dominated disks have been known since Shapiro et al. (1976, see section 3.3). The disks are, however, thermally unstable (e.g., Pringle 1976; Piran 1978), and their applicability to realistic objects is rather restricted. A construction of alternative, more realistic hot accretion flow models had been awaited.

A distinct type of optically thin, high-temperature disks was considered in relation to the bimodal spectral transition of Cygnus X-1 (Ichimaru 1977), in which advective cooling dominates over radiative cooling. Rees et al. (1982) proposed the idea of starved black holes in low-luminosity galactic nuclei. Matsumoto et al. (1985) found that advection domination forms an independent branch of models in the \dot{M} - Σ diagram. It is only recently, however, that a great development has been made on optically thin ADAFs. An extensive discussion on optically thin advection-dominated disks was begun by Narayan and Yi (1994, 1995a, b) and Abramowicz et al. (1995). It was recognized that they are thermally stable (see, however, section 9.4), and can well reproduce spectra of our Galactic Center, Sgr A* (Narayan et al. 1995), as well as black-hole binaries (Narayan et al. 1996).

We, here, make a remark about the meaning of “advective cooling”, since this terminology is sometimes misleading. We need to distinguish two different views: the comoving frame and the rest frame. In the former, we keep our eyes on accreting material. Then, we will see that the matter does not cool at all because of inefficient radiative cooling, but rather heats up due to viscous heat dissipation. The matter temperature becomes high, nearly the virial temperature.

Then, why did we say ‘advective cooling’ before? To answer this question, we need to consider the rest frame; i.e., we keep our eyes on a fixed region at some radius. Then, we will see that low-entropy material enters this region from an adjacent outer zone. That inflow material will eventually go out to an adjacent inner zone, after acquiring entropy as a result of viscous heat dissipation. Hence, low-entropy material comes in and high-entropy material goes out, giving rise to net cooling at some fixed radius. We call this process “advective cooling.”

9.1.2 Low Density Disks and Advection

First, in preparing for subsequent discussions, we show how the temperature depends on r , Σ , and \dot{M} in optically thin disks. We adopt the approximation of the angular-momentum balance, $(\ell - \ell_{\text{in}})\dot{M} = 2\pi r^2 \alpha \Pi$

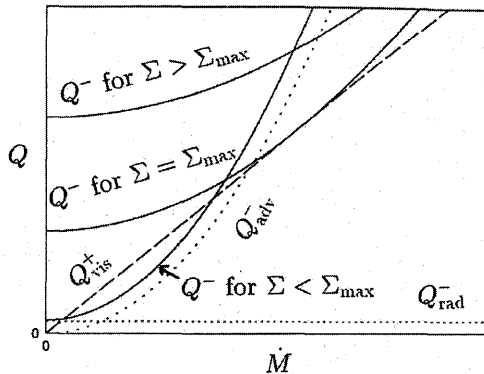


Figure 9.1

Schematic picture showing how Q_{vis}^+ , Q_{adv}^- , Q_{rad}^- , and Q^- ($\equiv Q_{\text{adv}}^- + Q_{\text{rad}}^-$) depend on \dot{M} when Σ and r are fixed. In the cases of $\Sigma = \Sigma_{\text{max}}$ and $\Sigma > \Sigma_{\text{max}}$, only the total cooling rates, Q^- , are plotted, while the values of the individual cooling rates, Q_{adv}^- and Q_{rad}^- , are shown solely for a case of $\Sigma < \Sigma_{\text{max}}$. In the case of $\Sigma < \Sigma_{\text{max}}$, the curve of Q^- , which is a solid curve, crosses the curve of Q_{vis}^+ at two points. When $\Sigma = \Sigma_{\text{max}}$, the curve of Q^- touches that of Q_{vis}^+ only at one point, while it does not contact with the curve of Q_{vis}^+ when $\Sigma > \Sigma_{\text{max}}$.

[see equation (7.28)], as

$$\Pi \sim \frac{\Omega_K \dot{M}}{2\pi\alpha}. \quad (9.1)$$

Here, we neglect ℓ_{in} compared with ℓ ($\ell \gg \ell_{\text{in}}$) and the disk rotation is approximated by the Keplerian one, $\Omega = \Omega_K = (GM/r^3)^{1/2}$. Since the equation of state is $\Pi \propto \Sigma T$ in optically thin disks, we have

$$T \propto \Omega_K \frac{\dot{M}}{\alpha \Sigma}. \quad (9.2)$$

To demonstrate the importance of advective cooling in optically-thin, low-density disks, let us next examine how the heating and cooling rates depend on r , Σ , and \dot{M} . Radiative cooling generally has very complicated parameter dependences, as discussed later. Here, we consider only bremsstrahlung cooling by non-relativistic electrons, neglecting relativistic bremsstrahlung as well as synchrotron and Compton cooling.

Using equation (9.1) as well as equations (7.42) and (7.46), we have

$$Q_{\text{vis}}^+ = r T_{r\varphi} \frac{d\Omega}{dr} = -\alpha r \frac{d\Omega}{dr} \Pi \sim \frac{3}{4\pi} \Omega_K^2 \dot{M}, \quad (9.3)$$

$$Q_{\text{rad}}^- = \epsilon_{\text{br}} \rho^2 T^{1/2} H \sim \frac{\epsilon_{\text{br}}}{4} \left(\frac{k_B}{\mu m_H} \right)^{-1/2} \Omega_K \Sigma^2, \quad (9.4)$$

$$Q_{\text{adv}}^- = \frac{\dot{M}}{2\pi r^2} \frac{\Pi}{\Sigma} \xi \sim \frac{\xi}{4\pi^2} \frac{\Omega_K}{r^2} \frac{\dot{M}^2}{\alpha \Sigma}, \quad (9.5)$$

where $\epsilon_{\text{br}} = 1.24 \times 10^{21} \text{ erg s}^{-1} \text{ cm}^{-2}$ and ξ is a dimensionless quantity on the order of unity [see equation (7.41)].

We next fix Σ and consider the \dot{M} -dependence of Q_{vis}^+ , Q_{adv}^- , and Q_{rad}^- at some radius r . As shown schematically in figure 9.1, Q_{vis}^+ increases linearly along with an increase in \dot{M} , while Q_{adv}^- increases with the square of \dot{M} . On the other hand, Q_{rad}^- is independent of \dot{M} . This implies that the curve of $Q_{\text{adv}}^- + Q_{\text{rad}}^-$ crosses that of Q_{vis}^+ at two points, if Σ is below some critical value Σ_{max} , as sketched in figure 9.1. That is, there are two thermal equilibrium states for a given surface density. One is for a small \dot{M} , and the other is for a large \dot{M} . In the former solution of a small \dot{M} , Q_{vis}^+ is roughly balanced by Q_{rad}^- . This is the *radiative cooling-dominated disk* found by Shapiro et al. (1976). On the other hand, the other solution has a large \dot{M} , and Q_{vis}^+ is balanced by Q_{adv}^- . This is an *advectional cooling-dominated disk*.

9.1.3 Model Sequence on the \dot{M} - Σ Plane

If we increase Σ slightly in figure 9.1, Q_{rad}^- increases and Q_{adv}^- decreases, while Q_{vis}^+ neither increases nor decreases. Still two solutions of $Q_{\text{vis}}^+ = Q_{\text{adv}}^- + Q_{\text{rad}}^-$ exist. Since Σ continuously increases, the trajectories of the two solutions give rise to two model sequences in the optically thin domain of the \dot{M} - Σ plane: the lower is radiative cooling-dominated and the upper is advective cooling-dominated (or advection-dominated).

Note that the two crossing points approach together in figure 9.1 as Σ increases. When Σ increases further beyond a certain value (say, Σ_{max}), the curve of $Q_{\text{adv}}^- + Q_{\text{rad}}^-$ no longer crosses that of Q_{vis}^+ in the Q - M diagram; that is, no equilibrium solution exists at $\Sigma > \Sigma_{\text{max}}$. Thus, two model sequences merge at Σ_{max} on the \dot{M} - Σ plane (see figure 9.2).

The above-mentioned behavior of the model sequence can be described in the \dot{M} - Σ plane as follows. The radiative cooling-dominated sequence is characterized by $Q_{\text{vis}}^+ \sim Q_{\text{rad}}^-$; for the sequence we have

$$\dot{M} \propto r_g \left(\frac{r}{r_g} \right)^{3/2} \Sigma^2. \quad (9.6)$$

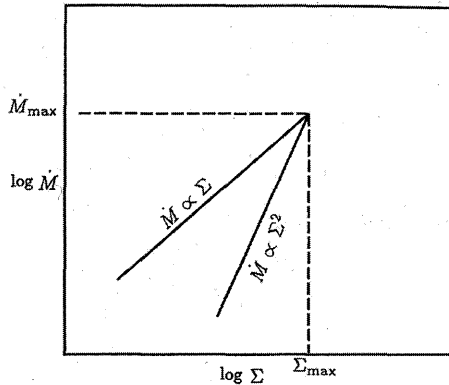


Figure 9.2

Schematic picture showing the $\dot{M}-\Sigma$ relation of an optically thin model sequence. The upper-left branch of a hook-shaped equilibrium sequence is an advection-dominated one, while the lower-right branch is a cooling-dominated one.

On the other hand, by equating Q_{vis}^+ and Q_{adv}^- for advection-dominated disks, we have

$$\dot{M} \propto r_g \left(\frac{r}{r_g} \right)^{1/2} \alpha \Sigma. \quad (9.7)$$

These results are schematically shown in figure 9.2.

The above two curves merge at Σ_{max} . The value of Σ_{max} can be obtained by equating the above two equations at radius r as

$$\Sigma_{\text{max}}(r) \propto \alpha \left(\frac{r}{r_g} \right)^{-1}. \quad (9.8)$$

Substituting this into one of the above equations [(9.6) or (9.7)], we obtain the mass-accretion rate, $\dot{M}_{\text{max}}(r)$, corresponding to $\Sigma_{\text{max}}(r)$, as

$$\dot{M}_{\text{max}}(r) \propto \alpha^2 r_g \left(\frac{r}{r_g} \right)^{-1/2} \quad \text{or} \quad \dot{m}_{\text{max}}(r) \equiv \frac{\dot{M}_{\text{max}}(r)c^2}{L_E} \propto \alpha^2 \left(\frac{r}{r_g} \right)^{-1/2}. \quad (9.9)$$

It is noted that if we take the derivative of $Q_{\text{vis}}^+ = Q_{\text{adv}}^- + Q_{\text{rad}}^-$ with respect to Σ under the condition $d\dot{M}/d\Sigma = 0$, we easily obtain (Abramowicz et al. 1995)

$$\dot{m}_{\text{max}}(r) = 2.0 \times 10^3 \xi^{-2} \alpha^2 \left(\frac{r}{r_g} \right)^{-1/2}. \quad (9.10)$$

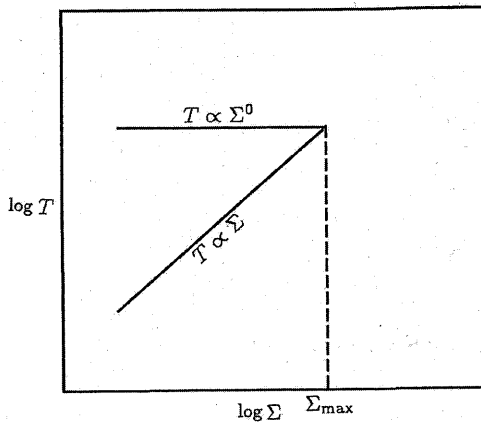


Figure 9.3

Schematic picture showing the equilibrium sequence of optically thin disks on the T - Σ plane.

Equation (9.10) shows that the value of $\dot{m}_{\max}(r)$ increases inward as $r^{-1/2}$. In realistic situations, however, this expression is not very accurate inside a certain critical radius. This is because in the inner region of disks, synchrotron and Compton cooling, which is neglected here, far dominate over bremsstrahlung cooling. Enhanced cooling results in an upward shift of the curve of $Q_{\text{rad}}^- + Q_{\text{adv}}^-$ in figure 9.1, so that the two equilibrium solutions approach together and merge at a smaller $\Sigma(r)$ than $\Sigma_{\max}(r)$ for the case without additional cooling. This implies that $\dot{m}_{\max}(r)$ no longer increases inward as $r^{-1/2}$. Detailed numerical calculations made by Narayan and Yi (1995b) show that after reaching a maximum value at a certain radius, the value of $\dot{m}_{\max}(r)$ is kept roughly constant for decreasing radius (see also Nakamura et al. 1997). Approximately, the maximum value of $\dot{m}_{\max}(r)$ is

$$\dot{m}_{\max} \sim 3\alpha^2. \quad (9.11)$$

For $\dot{m} > \dot{m}_{\max}$ there is no place where ADAF solution exists. The presence of \dot{m}_{\max} is one of the important characteristics of ADAFs.¹

¹This conclusion seems to be valid for other types of RIAFs, as well, although there is no strict proof.

9.1.4 Model Sequence on the T - Σ Plane

So far, we have discussed the equilibrium sequence on the \dot{M} - Σ plane. Considerations of the equilibrium sequence on the T - Σ plane are also useful, and many discussions using this plane have been made. A transformation of the equilibrium sequence on the \dot{M} - Σ plane to that on the T - Σ plane is simple. Since T , Σ , and \dot{M} are related by equation (9.2), from equations (9.3)–(9.5), we have

$$Q_{\text{vis}}^+ \propto \alpha \Omega_K \Sigma T, \quad (9.12)$$

$$Q_{\text{rad}}^- \propto \Omega_K \Sigma^2, \quad (9.13)$$

$$Q_{\text{adv}}^- \propto \frac{\alpha}{r^2 \Omega_K} \Sigma T^2. \quad (9.14)$$

Equating Q_{vis}^+ and Q_{adv}^- , we obtain the advection-dominated branch as

$$T \propto r^2 \Omega_K^2 \propto \left(\frac{r}{r_g} \right)^{-1}. \quad (9.15)$$

Equation (9.15) shows that the equilibrium sequence is horizontal on the T - Σ plane, independent of α and Σ , and that the temperature increases inward as $1/r$. This is easy to understand, since the gas falls inward by converting the potential energy into internal energy; i.e., $GMm_p/r \sim k_B T$, where m_p is the proton mass. In other words, T is roughly equal to the virial temperature, $T_{\text{vir}} \equiv 3GMm_p/2k_B r$.

On the other hand, the radiative-cooling-dominated branch can be obtained by equating Q_{vis}^+ and Q_{rad}^- :

$$T \propto \alpha^{-1} \Sigma. \quad (9.16)$$

A schematic picture showing the equilibrium sequence on the T - Σ plane is sketched in figure 9.3.

An optically thin, advection-dominated disk is marginally geometrically thick because of the very high temperature, since

$$\frac{H}{r} \sim \frac{c_s}{\Omega r} \sim \left(\frac{k_B T r}{G M m_p} \right)^{1/2} \sim \left(\frac{T}{T_{\text{vir}}} \right)^{1/2} \sim 1. \quad (9.17)$$

This is an interesting feature; even when $\dot{M} \ll \dot{M}_{\text{crit}} \equiv L_E/c^2$ (or disk luminosity $L \ll L_E$), the disk temperature is very high and the disk is marginally thick. Again, the advection-dominated flow is roughly a conical flow with $H/r \sim 1$, independent of \dot{M} .

9.1.5 Disk Luminosity

The term of “inefficient radiation” is sometimes misunderstood as “no radiation.” But this is totally wrong. Rather, the greater is the mass-accretion rate, the larger becomes the luminosity. This can be derived from $Q_{\text{rad}}^- \propto \Omega_K \Sigma^2$ [equation (9.4)]. Since $\dot{M} \propto r_g(r/r_g)^{1/2}\alpha\Sigma$ in advection-dominated disks [equation (9.7)], we have $Q_{\text{rad}}^- \propto \dot{M}^2$ or, more precisely,

$$Q_{\text{rad}}^- \propto \frac{1}{\alpha^2 r_g} \left(\frac{r}{r_g} \right)^{-5/2} \dot{m}^2, \quad (9.18)$$

where $\dot{m} \equiv \dot{M}c^2/L_E$. The total luminosity, L , becomes

$$L = \int_{r_{\text{in}}}^{\infty} Q_{\text{rad}}^- 2\pi r dr \propto \frac{\dot{m}^2}{\alpha^2} r_g \left(\frac{r_{\text{in}}}{r_g} \right)^{-1/2} \sim \frac{\dot{m}^2}{\alpha^2} r_g, \quad (9.19)$$

where the inner radius of the disk is set to be on the order of the Schwarzschild radius. Hence, the total luminosity L (from the advection-dominated region) is found to be proportional to

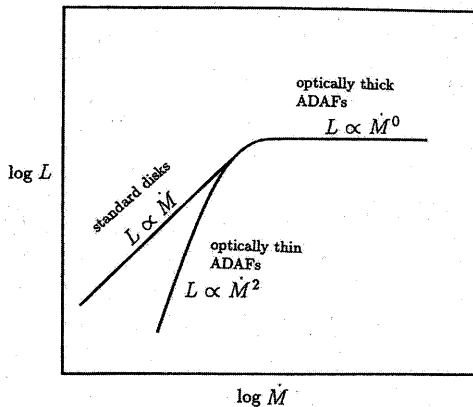
$$\frac{L}{L_E} \propto \frac{\dot{m}^2}{\alpha^2}, \quad (9.20)$$

since $L_E \propto r_g \propto M$. Note that the energy-conversion efficiency, which is expressed by $L/(\dot{M}c^2)$, is proportional to \dot{M} , and thus increases as \dot{M} increases, until \dot{M}_{max} , where the efficiency is roughly equal to that of the standard (i.e., radiative cooling-dominated) disk, ~ 0.1 for the case of a non-rotating black hole. To sum up,

$$L \approx 0.1 \left(\frac{\dot{M}}{\dot{M}_{\text{max}}} \right) \dot{M}c^2 \quad \text{for } \dot{M} \leq \dot{M}_{\text{max}}, \quad (9.21)$$

where again $\dot{M}_{\text{max}} = \dot{m}_{\text{max}}(L_E/c^2)$, \dot{m}_{max} being given by equation (9.11). See Mahadevan (1997) for more detailed discussion on parameter dependences of L .

Finally, let us plot the bolometric disk luminosity, L , as functions of \dot{M} schematically in figure 9.4 for all of the branches. The standard disk (cooling-dominated disk) has a line of $L \propto \dot{M}$, regardless of whether the disk is optically thick or thin. Indeed, although the spectral shapes are distinct, the total disk luminosity should be the same, since $Q_{\text{rad}}^- = Q_{\text{vis}}^+ \propto \dot{M}$ for both [equation (9.3), see also chapter 3]. The two lines thus coincide with each other.

**Figure 9.4**

Schematic picture showing the relations between the bolometric luminosity, L , and the mass-accretion rate, \dot{M} . As for the discussion in the high- \dot{M} regimes, see section 10.1.

The advection-dominated branches, in contrast, have different slopes. The optically thin, ADAF branch shows the relation $L \propto \dot{M}^2$, and thus its slope is steeper. The optically thick branch (i.e., the slim disk branch), on the other hand, has a roughly constant L , since an increase in the disk temperature due to an increase in \dot{M} is compensated by an increase in the surface density, $Q_{\text{rad}}^- \propto T_c^4 \Sigma^{-1}$ (see section 10.1).

9.1.6 Effects of Turbulent Conduction

We have so far neglected the (non-advective) heat transport in the radial direction. We emphasize here, however, the importance of turbulent heat diffusion in the radial direction in constructing global models of advection-dominated disks. Since advection-dominated disks have high temperature, the internal energy per particle is high. This is one of the reasons why advective cooling overcomes radiative cooling. For the same reason, turbulent heat transport in the radial direction is non-negligible in the heat balance in disks.

An explicit expression for the heating rate by turbulent conduction, Q_{cond}^+ , is (see section 7.1)

$$Q_{\text{cond}}^+ = -\frac{1}{r} \frac{d}{dr} (r F_{\text{turb}}) \quad \text{with} \quad F_{\text{turb}} = -K \Sigma T \frac{ds}{dr}, \quad (9.22)$$

where K is the turbulent thermometric conductivity. The order of K is

$v_{\text{turb}} \ell_{\text{turb}}$, where v_{turb} and ℓ_{turb} are the turbulent velocity and the mean free path of the turbulent elements, respectively. Since measures of v_{turb} and ℓ_{turb} are c_s and H , respectively, we write K in the form

$$K = \alpha_{\text{turb}} \frac{c_s^2}{\Omega}, \quad (9.23)$$

where α_{turb} is a dimensionless constant specifying the magnitude of turbulence. The quantity α_{turb} is generally of the same order of α -value in the standard α -models.

The vertically integrated heat flux by turbulent conduction, F_{turb} , is thus

$$F_{\text{turb}} \sim \alpha_{\text{turb}} \frac{1}{\Omega_K R} \frac{\Pi^2}{\Sigma} \xi, \quad (9.24)$$

where ξ is a dimensionless quantity representing the entropy gradient [see equation (7.41) in section 7.2]. Here, R is the characteristic radial length of the disk structure. This implies that the heating (or cooling) by turbulent heat transport per unit surface, Q_{cond}^+ , is given by

$$Q_{\text{cond}}^+ \sim \alpha_{\text{turb}} \frac{1}{\Omega_K R^2} \frac{\Pi^2}{\Sigma} \xi. \quad (9.25)$$

Since Π has been approximated by equation (9.1), the above equation is reduced to

$$Q_{\text{cond}}^+ \sim \frac{\xi}{4\pi^2} \frac{\alpha_{\text{turb}}}{\alpha} \frac{\Omega_K}{R^2} \frac{\dot{M}^2}{\alpha \Sigma}. \quad (9.26)$$

The comparison of Q_{cond}^+ given above and Q_{adv}^- , given by equation (9.5), shows that both of them have the same parameter dependences and are comparable in magnitude if $R \sim r$ and $\alpha_{\text{turb}} \sim \alpha$. That is, the heating due to turbulent heat diffusion could be substantial in the heat balance in advection-dominated optically thin disks.

In summary, the turbulent heat transport is negligible in the standard disks, since $Q_{\text{cond}}^+ \sim Q_{\text{adv}}^- \ll Q_{\text{rad}}^-$. Conversely, it is important in advection-dominated flows, because $Q_{\text{cond}}^+ \sim Q_{\text{adv}}^- \gg Q_{\text{rad}}^-$.

A similar argument has been made by Narayan and Yi (1994, 1995a). A disk model with turbulent heat conduction has been constructed by Honma (1996), focusing attention on the transition zone from a geometrically thin standard disk to an advection-dominated one (see subsection 9.2.3). The effects of turbulent heat diffusion on the global structure of advection-dominated disks is, however, not yet fully understood.

9.2 Radial Structure of Advection-Dominated Flow

The basic equations of ADAF are differential equations (see chapter 7) and thus require numerical integration for solving its radial structure. However, there is a powerful technique to give an approximate solution, the self-similar solution.

9.2.1 Self-Similar Model

The unique characteristics of optically thin ADAFs manifest themselves not only in the energy balance, but also in the dynamical behavior due to a strong pressure force; substantially, sub-Keplerian rotation is one such example. We thus need to solve the full basic equations. This is not an easy task, and we usually require numerical calculations. Fortunately, however, there exist self-similar solutions with

$$Q_{\text{adv}}^- = f Q_{\text{vis}}^+ \quad (9.27)$$

under the non-relativistic Newtonian potential and under neglect of ℓ_{in} in comparison with ℓ . Here, f represents the fraction of advective cooling to the total cooling, and is taken to be radially constant (Narayan and Yi 1994, 1995a).²

An inspection of the basic equations (section 7.1),

$$\begin{aligned} \dot{M} &= -4\pi r v_r \rho H = \text{const.}, \\ v_r \frac{dv_r}{dr} &= r(\Omega^2 - \Omega_K^2) - \frac{1}{\rho} \frac{dp}{dr}, \\ \rho r H v_r \frac{d(r^2 \Omega)}{dr} &= \frac{d}{dr} \left(\nu \rho H r^3 \frac{d\Omega}{dr} \right), \\ \frac{1}{\gamma - 1} \rho H v_r \frac{dc_s^2}{dr} - c_s^2 H v_r \frac{d\rho}{dr} &= f Q_{\text{vis}}^+ = f \nu \rho H \left(r \frac{d\Omega}{dr} \right)^2, \\ \nu &= \alpha c_s H, \quad H = c_s / \Omega_K, \quad \text{and} \quad c_s = (p/\rho)^{1/2} \end{aligned} \quad (9.28)$$

shows that there are solutions where all of the physical quantities can be taken to be power-law functions of the radius. The existence of self-similar solutions is thus suspected.

²Starting from the self-similar solution, Narayan and Yi (1995b) constructed two-temperature disk models, taking into account detailed cooling processes of electrons. We, however, introduce their solutions in this section of one-temperature disk model so that readers can at first understand the basic disk structure. The application of the self-similar solutions to two-temperature plasma and its spectral properties will be discussed in section 9.3.

It is known that one self-similar solution is usually associated with some physical constants.³ The constants characterizing self-similar solutions in the present case are \dot{M} and GM (the product of the gravitational constant and a black-hole mass).⁴ The dimensions of these constants are

$$[GM] = L^3 T^{-2} \quad \text{and} \quad [\dot{M}] = M T^{-1}, \quad (9.29)$$

where L , M , and T , respectively, represent the dimensions of length, mass, and time. For the self-similar solutions to exist, we require that time, velocity, and density are scaled as [see equations (9.29)]

$$T \propto L^{3/2}, \quad [V] = LT^{-1} \propto L^{-1/2}, \quad [\Sigma] = \frac{[\dot{M}]}{L[V]} \propto L^{-1/2}. \quad (9.30)$$

We thus assume⁵

$$\begin{aligned} v_r &\propto r^{-1/2}, & v_\varphi &\propto r^{-1/2}, & T &\propto c_s^2 \propto r^{-1}, & \Omega &= v_\varphi/r \propto r^{-3/2}, \\ \Sigma &\propto r^{-1/2}, & H &\sim c_s/\Omega \propto r, & \rho &\sim \Sigma/H \propto r^{-3/2}. \end{aligned} \quad (9.31)$$

If we adopt the above scaling, in fact, the radial dependences of all physical quantities are canceled out, and all of the differential equations are transformed to algebraic equations for proportionality constants in the above scaling laws.⁶

Detailed discussions by Narayan and Yi (1994) gave

$$v_r(r) = -\frac{(5+2\epsilon')}{3\alpha} g(\alpha, \epsilon') v_{\text{ff}}, \quad (9.32)$$

$$\Omega(r) = \left[\frac{2\epsilon'(5+2\epsilon')}{9\alpha^2} g(\alpha, \epsilon') \right]^{1/2} \frac{v_{\text{ff}}}{r}, \quad (9.33)$$

$$c_s^2(r) = \frac{2(5+2\epsilon')}{9\alpha^2} g(\alpha, \epsilon') v_{\text{ff}}^2, \quad (9.34)$$

³A good example is found in Sedov's self-similar solution for an expanding shell after a supernova; in this case the constants are the explosion energy and the density of the ambient material.

⁴In the case of self-gravitating disks, G instead of GM should be used to derive the self-similar variables. It then follows that $v_r \sim \text{constant}$, $T \sim \text{constant}$, and $\Sigma \propto r^{-1}$ (cf. Mineshige and Umemura 1996).

⁵The toroidal magnetic fields are easily included in this scaling (Akizuki and Fukue 2006). For more general expression that take into account the poloidal components, see Meier (2005) and Shadmehri and Khajenabi (2005).

⁶This scaling is excellent for advection-dominated disks, since then heating and cooling have the same radial dependence, $Q_{\text{vis}}^+ \sim \alpha \Sigma c_s^2 \Omega \propto r^{-3}$ and $Q_{\text{adv}} \sim \Sigma T v_r (ds/dr) \propto r^{-3}$. The radiative cooling rate, on the other hand, depends on the detailed cooling process, and does not necessarily have the same radial dependence as Q_{vis}^+ .

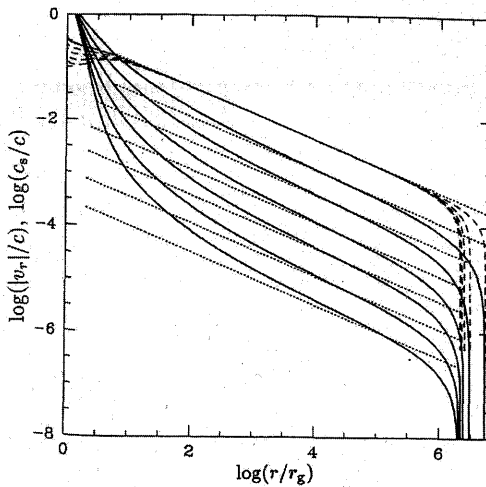


Figure 9.5

Radial distributions of the physical quantities of advection-dominated accretion flows. The solid curves show the variation of the radial velocity, v_r , as a function of the radius for six advection-dominated solutions. From below, the models correspond to $\alpha = 0.001, 0.003, 0.01, 0.03, 0.1$, and 0.3 , respectively. All of the models have $\gamma = 1.5$ and $f = 1$ (fully advection-dominated). The dashed curves show the variation in the sound speed, c_s , for the same six models with the lowest curve corresponding to the lowest value of α . The lower six dotted curves show the variation of $v_r(r)$ expected according to the self-similar solution [equations (9.32)]. The upper dotted line is the self-similar solution [equation (9.34)] for c_s in the limit $\alpha \ll 1$. (Adapted from Narayan et al. 1997a)

where $v_{\text{ff}}(r)$ is the free-fall speed, defined by

$$v_{\text{ff}}(r) = \left(\frac{GM}{r} \right)^{1/2}, \quad (9.35)$$

and ϵ' and $g(\alpha, \epsilon')$ are constants, defined by

$$\epsilon' = \frac{1}{f} \left(\frac{5/3 - \gamma}{\gamma - 1} \right), \quad (9.36)$$

$$g(\alpha, \epsilon') = \left[1 + \frac{18\alpha^2}{(5 + 2\epsilon')^2} \right]^{1/2} - 1, \quad (9.37)$$

and γ is the ratio of the specific heats. The parameters specifying the flows are γ , α , and f .

The self-similar models show that the accretion speed, $v_r(r)$, the sound speed, $c_s(r)$, and the rotational speed, $r\Omega(r)$, are all constant

fractions of the free-fall speed, $v_{\text{ff}}(r)$, given by equation (9.35). Each ratio, however, depends on the parameters γ , α , and f . Since the sound speed c_s is a constant fraction of v_{ff} , the temperature is rather high, and is proportional to the virial one. In some cases, the rotational speed becomes subsonic and vanishes when $\gamma = 5/3$. Since the ratio of $v_r(r)$ to $c_s(r)$ is taken to be constant from the requirement for the existence of similarity solutions, this similarity solution cannot be extended near to the sonic radius, where $v_r(r)$ must be equal to $c_s(r)$.

There is an interesting characteristic found by this solution. In steady inviscid adiabatic flows, the quantity

$$\frac{1}{2}v_r^2 + \frac{1}{2}\Omega^2 r^2 - \Omega_K^2 r^2 + \frac{\gamma}{\gamma - 1}c_s^2 \quad (9.38)$$

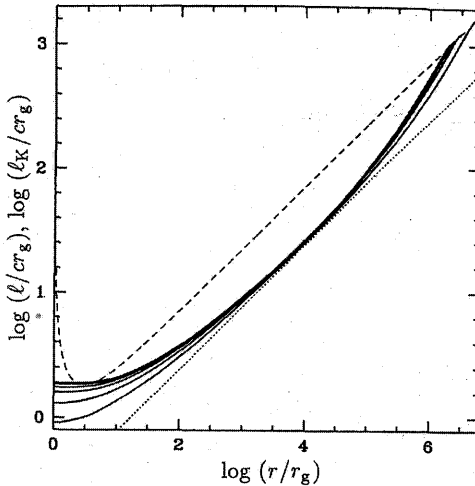
is constant along a stream line (the Bernoulli theorem). In the present similarity solutions, this quantity is found to be positive so long as $f > 1/3$ (Narayan and Yi 1994). From this, Narayan and Yi speculate that winds, jets, and other outflows may easily originate in ADAFs.⁷

This result seems to be odd at first glance from the viewpoint of energetics, but can be understood as being the result of the work done by the adjacent inner ring via viscosity (i.e., viscous energy transport). In the standard disk we have already noted that the local radiation-cooling rate at $r \gg r_{\text{in}}$ is three-times as much as that expected by the local argument (see section 3.2.2). In the present case, since radiation is suppressed, excess energy production is stored as internal energy, making the Bernoulli constant positive.

9.2.2 Transonic Numerical Models

In all of the models mentioned above, the transonic nature of accretion flows is not treated properly. Seminal work concerning the construction of numerical ADAF models, in which the transonic nature of the flows is taken fully into account, was done by Matsumoto et al. (1985), and only recently more extensive studies follow by Chen et al. (1997) and Narayan et al. (1997a). In the latter two calculations a diffusion-type stress tensor was adopted, except for some cases. Here, we present the results by Narayan et al. (1997a). In their calculations the radiative cooling was neglected; i.e., $Q_{\text{vis}}^+ = Q_{\text{adv}}^-$. They adopted outer boundary conditions at

⁷It should be kept in mind, however, that a positive Bernoulli parameter may not necessarily mean the occurrence of strong outflow (see section 9.5). Note also that if the boundary conditions are properly set, the Bernoulli parameter is mostly negative (Nakamura 1998).

**Figure 9.6**

Radial variation of the specific angular momentum, $\ell (= r^2\Omega)$, in the six solutions shown in figure 9.5. The lowest curve corresponds to $\alpha = 0.3$ and the uppermost curve to $\alpha = 0.001$. The dashed line shows the Keplerian-specific angular momentum and the dotted line corresponds to the self-similar solution. (Adapted from Narayan et al. 1997a)

a maximum radius, r_{out} , of $10^6 r_g$. At $r = r_{\text{out}}$, two boundary conditions are imposed:

$$\Omega = \Omega_K \quad \text{and} \quad c_s = 10^{-3} r \Omega_K. \quad (9.39)$$

As the inner boundary condition, they adopted a no-torque condition at $r = r_g$, in addition to the regularity condition at the critical radius. The outer boundary condition (9.39) implies that we impose geometrically thin disk conditions in the outer region.

Figure 9.5 shows the radial distributions of advection flow velocity and of the sound speed for some parameter values. For a comparison, the similarity solutions by Narayan and Yi (1994) are shown by dotted curves. Near to the sonic radius, the flow must approach the sound speed, and therefore it deviates from the similarity solutions (v_r should be a constant fraction of the sound speed in the similarity solution). Otherwise, the similarity solution is a good approximation of the global numerical solution of the flow.

Figure 9.6 shows the radial distribution of the specific angular momentum, ℓ . It is notable that at intermediate radii the rotation is strongly sub-Keplerian. Near to the inner edge of the disks, furthermore, the char-

Table 9.1 Standard and Advection-Dominated Disks.

Model	Standard disk	Optically thin ADAF
Energy balance	$Q_{\text{vis}}^+ = Q_{\text{rad}}^-$	$Q_{\text{vis}}^+ = Q_{\text{adv}}^- (\text{gas})^\dagger$
Temperature*	$T \sim 10^5 x^{-3/4} \text{K}$ (AGN) $T \sim 10^7 x^{-3/4} \text{K}$ (XBs)	$T(\text{ion}) \sim 10^{12} x^{-1} \text{K}$ $T(\text{electron}) \sim 10^9 \text{K}$
Luminosity	$L \propto \dot{M}$	$L \propto \dot{M}^2$
Accretion timescale	$t_{\text{acc}} \gg t_{\text{ff}}^*$	$t_{\text{acc}} \gtrsim t_{\text{ff}}$
Scale-height	$H \ll r$	$H \lesssim r$
Flow shape	disk shape	(nearly) spherical shape
Spectra	big blue bump (AGN) soft X bump (XBs)	hard power-law + Compton bump

[†] Advection of gas entropy; ^{*} free-fall timescale.

* We set $x \equiv r/r_g$, $M \sim 10^8 M_\odot$ (AGNs), and $M \sim 1 M_\odot$ (XBs).

acteristic of the flows is different for large α and for lower α .

For low α , the inner edge is close to the marginally bound orbit, and the rotation is super-Keplerian close to the sonic radius. That is, a steady accretion flow is realized by the gas being pushed inwards across the sonic radius by the pressure-gradient force. In other words, the flow is a *pressure-driven* one, and the pressure maximum exists outside the sonic radius (cf. section 8.4).

For high α , in contrast, the viscosity is so efficient that the gas loses much angular momentum before arriving at $3r_g$. Hence, the sonic radius is outside $3r_g$, and the rotation is sub-Keplerian (cf. section 8.4). That is, the flow is a *viscosity-driven* one. This change in the character of the flow between small and large α was already recognized by Matsumoto et al. (1984).

Fully relativistic models with the Kerr metric have been investigated by Abramowicz et al. (1996), Peitz and Appl (1997), Gammie and Popham (1998), Popham and Gammie (1998), Oka and Manmoto (2003), and others, with some simplifications being introduced.

To complete this topic, we summarize in table 9.1 the distinctive characters of the standard, Shakura-Sunyaev disks and the optically thin advection-dominated disks. We wish to stress that advection-dominated disks are not minor modifications made to the standard disks, but are independent, co-existing solutions with distinctive natures.

9.2.3 Transition to ADAFs from Outer Standard Disks

We have seen in section 9.1 that there should be no ADAF (RIAF) solutions at large radii for moderately high \dot{M} , since $\dot{m}_{\text{max}} \propto r^{-1/2}$. In actual situations, therefore, the flows will start as Shakura-Sunyaev-type

standard disks (SSDs) in a far outer region and transfer to ADAFs at a certain radius by being heated up. Where and how does the transition from a SSD to an ADAF occur? This is the subject of this subsection.

Two possible ways of the transition from a SSD to an ADAF are conceivable. One is evaporation of disk gas due to heating by a hot corona surrounding the disk (see section 3.4). The other one is that cool standard-disk gas is heated up by turbulent or radiative heat transports from the inner hot region, and the disk becomes a bimodal system of SSD–ADAF with a radial transition at a certain radius. The second possibility is considered here, which was first considered by Honma (1996).

Without detailed calculations, we can derive some important characteristics regarding the transition from the SSD to the ADAF. The first is that a super-Keplerian region must exist inside the transition region, if the transition occurs in a narrow region (Abramowicz et al. 1998). Let us consider pressure distributions in the radial direction in ADAF and SSD. Their analytical expressions are known both in the self-similar solution of ADAF and in the conventional model of SSD. A comparison of them at the same radius shows quite generally that $p_{\text{SSD}} \gg p_{\text{ADAF}}$.⁸ This means that when the transition is narrow, the pressure force in the transition zone should be inward. That is, the angular velocity of disk rotation must be locally super-Keplerian, although it is sub-Keplerian in the conventional self-similar ADAFs (see Figure 9.6).

The second one, which is more important, is a constraint concerning the total-energy flux within the flow.⁹ In standard disks, the thermal energy generated inside the disks by viscosity is radiated away from the disk surface (i.e., radiative cooling). Hence, the energy conservation requires that the (outward) total-energy flux in the disk is positive; $W_S > 0$.¹⁰ In ADAFs, on the other hand, there is practically no radiative cooling, and thus infinitely extended ADAFs, such as self-similar ADAFs,

⁸From equation (3.72) and $H \sim c_s/\Omega$, we find $v_r \sim \alpha c_s(H/r) \propto c_s^2$. We thus have $p \propto \rho T \sim \dot{M}T/(4\pi r H v_r) \propto T/c_s^3 \propto T^{-1/2}$ for a fixed \dot{M} , meaning higher p for lower T .

⁹The total-energy flux consists of enthalpy flux, potential-energy flux, kinetic-energy flux, and viscous-energy flux [see equation (B.9) in appendix B]. If there are radiative and conductive heat fluxes within the disk, they should also be included in the total-energy flux.

¹⁰The outward energy flux at r_0 is given by (Honma 1996; Kato and Nakamura 1998)

$$W_S = \frac{3}{4} M c^2 \left(\frac{r_g}{r_0} \right).$$

This is due to the viscous energy transport (see section 3.2.2).

have zero total-energy flux, i.e. $W_A = 0$.

Now, we assume that a transition occurs from an outer SSD to an inner ADAF in a narrow region at r_0 and consider a fitting condition concerning energy at r_0 . In this transition zone, thermal energy is transported from ADAF to SSD because of a large temperature difference between them. If this thermal energy transported toward the outer SSD is not radiated away in the transition zone, the fitting condition concerning the total-energy flux at r_0 is $W_A = W_S$. In real situations, however, the thermal energy will partially be radiated away from the system in the transition zone, since the thermal energy is transported from an optically thin region to a thick region. Hence, the total-energy flux conservation requires

$$W_A > W_S (> 0), \quad (9.40)$$

at radius r_0 . The amount of the difference between W_A and W_S depends on the structure of the transition region. Obviously, the self-similar ADAF (in which $W_A = 0$) cannot satisfy the fitting condition (9.40).

The connection of an inner ADAF with an outer SSD with relevant fitting conditions was examined semi-analytically by Honma (1996) and numerically by Manmoto and Kato (2000). Roughly speaking, the position (and the width) of the transition zone is determined so that turbulent conductive heating and radiative cooling are just balanced in the transition region. Let us tentatively assume the position of this transition zone. Then, heating and cooling are generally not balanced in the zone. If the heat from the ADAF toward the SSD is more than what can be radiated away in the transition zone, the SSD region is heated up and the transition zone retreats outward. If the heat cannot supply the transition zone with a sufficient amount of thermal energy, conversely, the SSD penetrates inward so that the transition radius decreases. It should be emphasized that the transition zone is a luminous region.

According to Manmoto and Kato (2000), the location of the transition radius is not unique for a given set of parameters, but a finite region is allowed as the transition radius.¹¹ An example of parameter dependences of the transition radius is shown in figure 9.7. The possible transition radius is divided into two regions, i.e., around $10r_g$ and 10^4r_g , when the mean accretion rate, \dot{m} , is small.

Gracia et al. (2003) performed time-dependent simulations, using almost the same equations as those of Manmoto and Kato (2000), except

¹¹The reason for non-uniqueness of the solutions is not clear. A delicate structural change of the transition zone would make non-uniqueness of the solution possible.

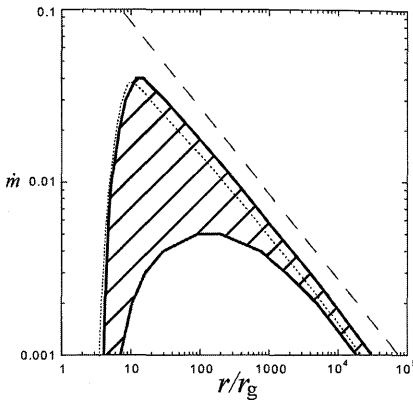


Figure 9.7

Location of the transition region in the case where $\alpha = 0.4$ and $\alpha_{\text{turb}} = 0.4$. The shaded area represents the possible location of the transition radius within which we can find the ADAF-SSD solutions. The dotted line represents the location of the transition radius found by Honma for the same value of α . The dashed line corresponds to the semi-analytical estimate of the location of the transition radius given by Honma (1996). (After Manmoto and Kato 2000)

for the time-dependent terms. In their cases, the radial profiles of the physical quantities are never stationary. The time-averaged profiles are, however, similar to the stationary solutions obtained by Manmoto and Kato (2000).

The transition region obtained by Gracia et al. (2003) is highly variable. In particular, rapid oscillations of the transition radius are present on a timescale comparable with the local Keplerian rotation time. The time variability of the transition region is interesting in relation to the time variability of the hard state of BHs (see subsection 9.4.6), since the transition zone is a luminous region, as mentioned above, and also since high-density blobs might be supplied toward the ADAF region.

Arguments concerning the transition radius are highly controversial. Recently, Lu et al. (2004) insist that any extra heat transport is unnecessary around the transition zone and the transition occurs at a radius rather close to the central black hole in the case of high viscosity. They argue that the smallness of the transition radius is related to the thermal instability-triggered transition of SSD to ADAF, suggested by Takeuchi and Mineshige (1998) and Gu and Lu (2000).

All of the models presented here assume that the transition is cylindrical and also treat vertically integrated or averaged quantities. The heat-transport processes in the transition region is essentially two-dimensional,

since the disk thickness changes abruptly. To obtain reliable models of the transition, two-dimensional analyses and simulations are essential, in addition to more reliable formula concerning turbulent heat transport in a narrow region.

9.3 Radiation Spectra of Advection-Dominated Flow

So far, we have discussed one-temperature disk models. Although these models give a good representation of the structure of ADAFs, such as the surface density and ion-temperature distribution, they cannot adequately account for the observed emission spectra. This is because the emission spectra more sensitively depend on the electron temperatures, and because in optically thin, advection-dominated disks, a temperature separation between the ions and electrons is likely to occur, unless a strong thermal coupling exists between the ions and electrons through some plasma instabilities. Further, two-temperature models are favored to reproduce the observed spectra. The underlying physics causing a temperature separation is that the ion gas is heated due to the dissipation of turbulence,¹² while the electron gas is cooled by various radiation processes. In this section we consider disk models that have such a two-temperature nature, and calculate the resulting disk spectra.

9.3.1 Optically-Thin Two-Temperature Disk Models

In the previous section, only bremsstrahlung was considered to be a cooling process of the electron gas. As we have already seen, however, the electron temperature is so high that the inverse Compton processes cannot be neglected. If (turbulent) magnetic fields exist in the disks, more importantly, synchrotron cooling and its enhancement by Compton processes also become efficient. For these reasons, a large temperature separation between ions and electrons may occur. Equations to describe such two-temperature disks have already been given in section 7.3 (see also appendix I).

Two-temperature, advection-dominated disk models were first constructed by Narayan and Yi (1995b), on the basis of the self-similar solutions for ions. As far as the ion gas is concerned, $Q_{\text{vis}}^+ = Q_{\text{adv},i}^-$ (the subscript i means ion gas), i.e., $f = 1$, is a good approximation. The heat transfer from ions to electrons by a Coulomb interaction is negligible in

¹²This assumption is usually adopted, but its relevance is not always clear. Some part of dissipation of magnetic turbulence may go directly to electron gas (e.g., Bisnovatyi-Kogan and Lovelace 1997).

the thermal energy balance for ions. Hence, the structure of ion gas can be obtained, to a good approximation, without considering the details of the thermal properties of the electron gas. Only after the surface density and ion temperature distributions are obtained, one can determine the electron-temperature distribution by solving the energy equation for electrons; $Q_{\text{adv},e}^- + Q_{\text{rad}}^- = \Lambda_{ie}$, where Λ_{ie} is the heating rate (per unit surface) of electron gas by Coulomb coupling with ion gas. Synchrotron and Compton cooling, as well as bremsstrahlung, are taken into account in Q_{rad}^- . If necessary, the cooling rate of the ion gas obtained by these procedures is fed back so as to modify the original approximation, $f = 1$, and iterative procedures are performed.

As we have seen in the previous section, the self-similar solutions cannot well represent the disk structure in the transonic region. To improve this situation, Narayan et al. (1998) calculated transonic, fully general relativistic models numerically for the ions, and obtained the electron-temperature distributions by solving the energy equation for an electron gas with cooling.

The Kyoto group has independently constructed two-temperature disk models by simultaneously solving both energy equations for ions and electrons (Nakamura et al 1996, 1997; Manmoto et al. 1997a). Here, we present the results by Nakamura et al. (1997).

We assume that the pressure of a turbulent magnetic field is a constant fraction of the total pressure throughout the disk; i.e., $1 - \beta \equiv \Pi_{\text{mag}}/\Pi = \text{constant}$, as did Narayan and Yi (1995b). As for the cooling, we consider bremsstrahlung and synchrotron, enhanced by Compton processes (see formulae in section 7.3 and appendix I). The outer boundary is set to be at $r_{\text{out}} = 10^3 r_g$. The boundary conditions imposed at $r = r_{\text{out}}$ are $\ell = 0.5\ell_K$, $T_i = 0.2T_{\text{vir}}$, and $\Lambda_{ie} = Q_{\text{rad}}^-$, where T_{vir} is the virial temperature, given by $T_{\text{vir}} = 2GMm_i/3k_B r_{\text{out}}$, k_B being the Boltzmann constant. We adopt the standard α -viscosity (not a form of diffusion-type stress tensor). Hence, no inner-boundary condition is required, except for the regularity condition at the critical radius. The mass of a central hole is $M = 10M_\odot$ and the ratio of the specific heats is $\gamma = 5/3$. The remaining parameters are then α , \dot{m} , and β . The results are summarized in figures 9.8 and 9.9.

Figure 9.8 shows the radial distributions of the physical quantities in three cases of $(\alpha, \dot{m}) = (10^{-1}, 10^{-1})$, $(10^{-2}, 10^{-3})$, $(10^{-3}, 10^{-5})$ with $\beta = 0.5$. In the inner region of the disks, the electron temperature is much lower than the ion temperature, and is saturated around a few times 10^9 K , which is the temperature corresponding to the rest-mass

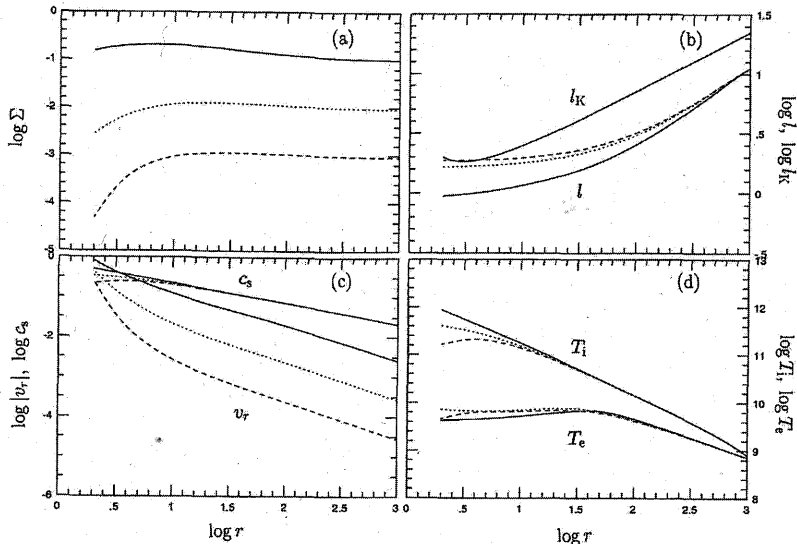


Figure 9.8

Radial dependence of various physical quantities for three cases of $(\alpha, \dot{m}) = (10^{-1}, 10^{-1})$ (solid curves), $(10^{-2}, 10^{-3})$ (dotted curves), $(10^{-3}, 10^{-5})$ (dashed curves) with $\beta = 0.5$. Panel (a) is for the surface density (in units of g cm^{-2}), (b) is for the specific angular momentum (in units of cr_g), (c) is for the radial flow velocity and sound velocity (in units of c). Panel (d) is for the ion and electron temperatures (in units of Kelvin). (After Nakamura et al. 1997)

energy of the electron. This is due to strong synchrotron cooling, as is well known (Narayan and Yi 1995b; Esin et al. 1996).

Figure 9.9 shows the radial distributions of the heating and cooling rates in units of Q_{vis}^+ . In the inner region, we have $Q_{\text{adv},i}^-/Q_{\text{vis}}^+ \sim 1$. That is, the approximation of advection-dominated flows holds well in the ion gas, and only a small fraction of energy is transported from the ion gas to the electron gas at the rate of the Coulomb coupling by rate Λ_{ie} . This energy transported to the electrons, Λ_{ie} , is a small fraction, even to the energy balance in the electron gas, as can be understood from $|Q_{\text{adv},e}^-| \sim Q_{\text{rad}}^- \gg \Lambda_{ie}$, where $Q_{\text{adv},e}^-$ is the cooling rate of the electron gas due to advection. In other words, what is balanced by radiative cooling in the electron gas is not the heating by the Coulomb coupling with ions but advective heating (advection acts as heating rather than cooling in the present case). The specific entropy of the electron gas actually *decreases* as it falls, since it is cooled by radiative processes,

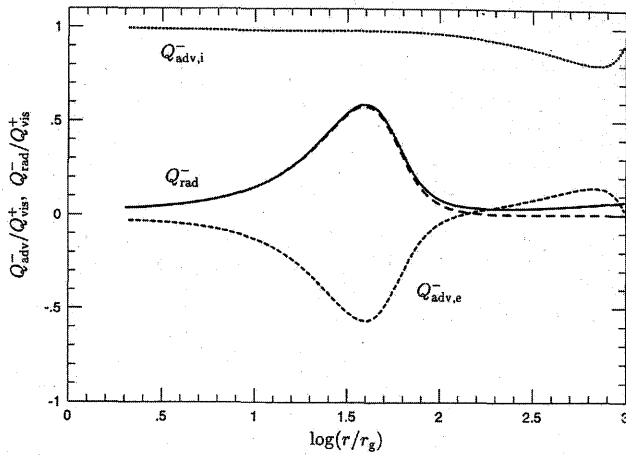


Figure 9.9

Radial dependences of the advective coolings of ions, $Q_{\text{adv},i}^-$ (dotted curve), and electrons, $Q_{\text{adv},e}^-$ (dashed curve), and radiative cooling of electrons, Q_{rad}^- (solid curve) and its fraction by synchrotron-Compton cooling, Q_{syn}^- (long-dashed curve), in units of the viscous heating rate Q_{vis}^+ . The other parameters are $\alpha = 0.1$, $\dot{m} = 0.1$, and $\beta = 0.5$. (After Nakamura et al. 1997)

while it has no efficient heating source. The electron temperature is kept roughly constant, however, because of adiabatic compression involved with the infall motion. This is in contrast with the case of ions, for which the specific entropy *increases* as it falls,¹³ since it obtains thermal energy by viscous heating, but loses little by Coulomb coupling to the electrons.

The above results justify the following approximate procedures to construct advection-dominated two-temperature disks. First, all physical quantities related to the ion gas and the gas flows are derived by using $Q_{\text{vis}}^+ \sim Q_{\text{adv},i}^-$; i.e., $f = 1$ for the ion gas. After the distributions of the ion temperature and flow structures are determined by the above approximation, the electron temperature can be obtained by solving the heat balance, $Q_{\text{adv},e}^- + Q_{\text{rad}}^- = 0$ (not $\Lambda_{ie}^+ - Q_{\text{rad}}^- = 0$), using the quantities calculated above.

¹³The storage of generated energy as internal energy increases entropy inwards, which has a tendency to make the disk convectively unstable (Narayan and Yi 1994).

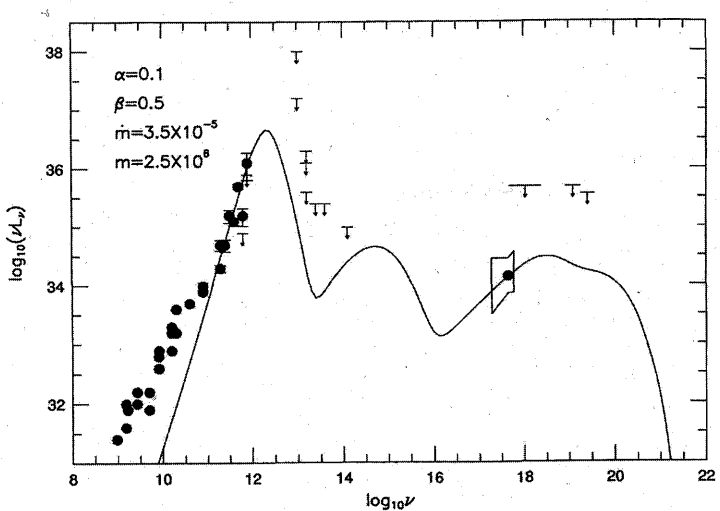


Figure 9.10

A typical ADAF spectrum. The parameters are $\alpha = 0.1$, $\beta \equiv 1 - \Pi_{\text{mag}}/\Pi = 0.5$, $\dot{M}/\dot{M}_{\text{crit}} = 3.5 \times 10^{-5}$, and a black-hole mass is $M = 2.5 \times 10^6 M_\odot$. (After Manmoto et al. 1997b)

9.3.2 Radiation Spectra

An excellent success of advection-dominated two-temperature disk models is that they can well reproduce the observed spectra of low luminous galactic nuclei as well as those of the hard state of galactic black-hole candidates. This was first shown for Sgr A* by Narayan et al. (1995) and then for NGC 4258 by Lasota et al. (1996) and for soft X-ray transients, A0620-00 and V404 Cyg, respectively, by Narayan et al. (1996) and by Narayan et al. (1997b). They showed that the models fit well the observed spectrum from radio to hard X-ray wavelength, and reconcile the low observed luminosity with a high mass-accretion rate. Following this pioneering work, two-temperature ADAF models have been widely applied to a variety of black-hole systems with great success. At the same time, the techniques used to construct two-temperature disk models have been refined.

Here, we present, as an example, the spectrum fitting of Sgr A* by Manmoto et al. (1997b).¹⁴ They calculated the spectra emitted from

¹⁴Spectrum calculations and a comparison with more recent observation data have been made by Yuan et al. (2003); see section 9.5.

two-temperature disk models by simultaneously solving the energy equations for ions and electrons. Figure 9.10 compares the observed and some theoretical spectra. The figure shows that there are three peaks in the model spectrum. The peak of the lowest frequency is due to synchrotron emission by the thermal electrons in the magnetic field of the plasma. The middle peak is due to inverse Compton scattering of the synchrotron radiation by hot electrons. The peak of the highest frequency is due to bremsstrahlung emission augmented by inverse Compton scattering of the photons in the middle peak. The agreement between the predicted spectrum and the observational data is indeed excellent.

A critical element of transonic, two-temperature optically-thin models is the presence of an event horizon at the center. Figure 9.10 demonstrates that the model with $\dot{M}/\dot{M}_{\text{crit}} \sim 3.5 \times 10^{-5}$ and $M = 2.5 \times 10^6 M_{\odot}$ gives the best fit to the observations. If there is no event horizon, but there is a solid surface of some object, the energy corresponding to the potential energy difference between the surface and infinity should be liberated; in other words, the disk luminosity should be on the order of $L = \eta \dot{M} c^2 \sim 3 \times 10^{-6} L_E \approx 10^{39} \text{ erg s}^{-1}$ for an energy-conversion factor of $\eta \sim 1/16$ and $M \sim 2.5 \times 10^6 M_{\odot}$. However, the observed luminosity, $L \sim \nu F_{\nu}$, is below $10^{37} \text{ erg s}^{-1}$ at every band. The success of the models may thus be viewed as a confirmation that there are black holes at the center of galactic nuclei and some galactic X-ray objects. This argument concerning the event horizon was first made by Narayan et al. (1996, 1997b).

9.4 Stability of Advection-Dominated Flow

Advection-dominated accretion flow (ADAF) is simply believed to be stable without any strict proof. This is the main reason why the ADAF model has been attracting researchers as a model of high-temperature disks. However, the stability properties of advection-dominated disks are rather distinct from those of the standard disks. Much more complexity, in fact, arises due to the pressure-gradient term introduced in formulating the advection-dominated disks. A rough coincidence of the thermal and viscous timescales, $t_{\text{vis}} \sim t_{\text{th}}$, also affects the thermal behaviors. Here, we examine the thermal instability of one-temperature, advection-dominated disks against local small-amplitude perturbations so as to understand the dynamical behavior of ADAF.

9.4.1 Thermal Stability against Global Perturbations

The basic approximation involved in analyses of the thermal instability of geometrically thin disks was that the surface density, Σ , is unchanged during the time evolution of thermal perturbations (see section 4.2). The validity of this approximation stems from the fact that in geometrically thin disks, the pressure-gradient force is negligible in the force balance in the radial direction, since strong centrifugal and gravitational forces are nearly balanced in the radial direction. In advection-dominated disks, however, the pressure-gradient force is not completely negligible, since the disk is hot. The significance of the pressure-gradient force is more enhanced, when we consider the force balance in imposed perturbations, since the magnitude of the pressure-gradient force ($\propto \nabla p$) depends on the size (wavelength) of the perturbations. The smaller is the size of the perturbations, the more pronounced is the importance of the pressure-gradient force in the stability criterion. Then, the assumption of a constant Σ would break down for the evolution of small-scale perturbations. This issue is discussed in the subsequent subsections.

If we are concerned with global (large-scale) perturbations in disks, conversely, the pressure force will not crucially affect the behavior of the thermal perturbations. In this sense, the assumption of a constant surface density is not very bad when we consider the relatively large-scale perturbations in the radial direction. Once we admit this point, we can judge, as a first approximation, the thermal stability of the disks from the slope of the equilibrium sequence in the T - Σ plane, as we did in chapters 3 and 4. As we already know from section 9.1, the sequences of the advection-dominated disks, both of optically thin and thick disks,¹⁵ have positive slopes in the T - Σ plane. Above these branches, advective cooling dominates over radiative cooling, and below the curve the situation is opposite. That is,

$$\left(\frac{\partial Q_{\text{vis}}^+}{\partial T} \right)_\Sigma - \left(\frac{\partial Q_{\text{adv}}^-}{\partial T} \right)_\Sigma < 0 \quad (9.41)$$

in advection-dominated disks, implying thermal stability.

- ~ In addition to the above consideration concerning the thermal behaviors, we should consider the fact that the viscous timescale becomes comparable to the thermal timescale in advection-dominated disks.¹⁶ This

¹⁵The optically thick ADAF (slim disk) will be introduced in chapter 10.

¹⁶In the arguments for geometrically thin disks (chapter 3), we estimated that the viscous timescale is $\sim (\alpha \Omega_K)^{-1} (r/H)^2$ and that the thermal timescale is $\sim (\alpha \Omega_K)^{-1}$ [see equation (3.71)]. These timescales are similar for $H \sim r$.

means that perturbations are transported inward by advection before growing much, which also acts as a stabilization effect.

Hence, we conclude that *advection-dominated disks (both optically thin and optically thick ones) are thermally stable against global perturbations.* This global stability is one of the important reasons why we pay great attention to ADAF in this book. In contrast, a disk of the sort without advection, proposed by Shapiro et al. (1976), is globally unstable.

9.4.2 Thermal Instability against Local Perturbations

The advection-dominated disks have such a high temperature that the pressure-gradient force is non-negligible compared with the centrifugal and gravitational forces. Because of this, the disk becomes moderately thick in the vertical direction; i.e., $H \lesssim r$. Thus, unlike the case of standard disks, it is not appropriate to assume that local perturbations in the radial direction (wavenumber k) have a longer wavelength than the disk thickness. In other words, the assumption that $H \ll 1/k \ll r$ does not hold.¹⁷

Furthermore, if we consider relatively short-wavelength perturbations in advection-dominated disks, the variation of the pressure-gradient force is the major part of the force variations. Since we can assume a steady force balance even in the perturbed state,¹⁸ this implies that

$$\left(\frac{1}{\rho} \nabla p \right)_1 \sim 0 \quad (9.42)$$

holds in the r - and z - directions when short-scale perturbations are considered.¹⁹ Here, subscript 1 denotes the perturbed part. This contrasts with the case of geometrically thin, standard disks, in which we have adopted $\Sigma = \text{constant}$, i.e., $\Sigma_1 = 0$, instead of equation (9.42).²⁰

¹⁷This assumption is implicitly adopted in local analyses in geometrically thin disks (see chapter 4).

¹⁸We can adopt this, since the dynamical timescale, $\sim \Omega^{-1}$, is shorter than the thermal timescale, $(\alpha\Omega)^{-1}$, for $\alpha < 1$.

¹⁹The variation of centrifugal force has been neglected in deriving approximation (9.42). This validity can be shown by using the final results obtained by approximation (9.42).

²⁰Even in geometrically thin disks, the variation of the pressure-gradient force is non-negligible, if we consider perturbations whose radial wavelength is as short as the vertical thickness of the disk; $\lambda \sim H \ll r$. Then, the approximation of $\Sigma_1 = 0$ is invalid. Such short-scale perturbations, however, are not interesting from observational viewpoints.

To describe the perturbations, cylindrical coordinates (r, φ, z) are introduced, where the origin of the coordinates is at the central object, and the z -axis is the rotation axis of the disk. Two important consequences are derived from equation (9.42).

- (i) The first is that the relative amplitude of the density perturbation should be much larger than the relative amplitude of the pressure perturbation; i.e., $\rho_1/\rho_0 \gg p_1/p_0$. This can be shown as follows. The radial component of equation (9.42) is written as²¹

$$\frac{\partial p_1}{\partial r} = \frac{\rho_1}{\rho_0} \frac{\partial p_0}{\partial r}. \quad (9.43)$$

Hence, for local perturbations we have

$$\frac{\rho_1}{\rho_0} \simeq \left(\frac{\partial \ln p_0}{\partial \ln r} \right)^{-1} r \frac{\partial}{\partial r} \left(\frac{p_1}{p_0} \right). \quad (9.44)$$

That is, if we write the radial wavenumber as k , we have

$$\frac{\rho_1}{\rho_0} \sim (kr) \frac{p_1}{p_0} \gg \frac{p_1}{p_0}, \quad (9.45)$$

since $\partial \ln p_0 / \partial \ln r \sim 1$ and $kr \gg 1$. This result can be understood as follows. When a thermal instability occurs, temperature varies. Since the wavelength of the perturbations is short, a large density change can occur due to a relatively weak expansion or contraction. In contrast, the pressure change by local expansion or contraction is relatively small, since the magnitude of the pressure is determined by the global structure of the disks, and the local variation of the density does not bring about much pressure variation (recall the thermal instability of shell burning in stars).²²

- (ii) The second consequence of equation (9.42) is that if we consider local perturbations in the radial direction, the perturbations should also

²¹Note that equation (9.42) is written as

$$-\frac{\rho_1}{\rho_0^2} \nabla p_0 + \frac{1}{\rho_0} \nabla p_1 \sim 0.$$

²²In the shell burning of stars the pressure in the shell is determined by the amount of matter lying above so that any perturbations added locally in the shell will produce little pressure variation, although they may give rise to a large density change. This is the cause of flickers (thermal instability) in the shell burning zone of stars (Schwarzschild and Härm 1967).

be local in the vertical direction. This implies that the procedure for treating the vertically integrated quantities is no longer valid in analyses of local perturbations in advection-dominated disks.

Taking into account these differences from the case of standard disks, we examine below the stability of advection-dominated disks against small-amplitude local thermal perturbations (Kato et al. 1996, 1997; Wu and Li 1996; Wu 1997a, b).

9.4.3 Equations Describing Local Perturbations

The unperturbed disks are assumed to be rotating cylindrically, $\Omega = \Omega(r)$, and the radial velocity of the flow, $u_{r,0}$, also depends only on the radius; i.e., $u_{r,0} \equiv u_0(r)$. The density, ρ_0 , and the pressure, p_0 , in the unperturbed state depends on r , as well as z . Axially-symmetric, Eulerian perturbations superimposed over the unperturbed quantities, ρ_0 , $u_{r,0}(= u_0)$, $u_{\varphi,0}(= r\Omega)$, and p_0 are denoted by ρ_1 , $u_{r,1}$, $u_{\varphi,1}$, and p_1 , respectively. All perturbed quantities are taken to be proportional to t and r , as $\exp(n\Omega t - ikr)$, where n is a dimensionless growth rate and will generally be complex. Hereafter, we adopt dimensionless variables defined by

$$\sigma = \frac{\rho_1}{\rho_0}, \quad v_r = \frac{u_{r,1}}{u_0}, \quad v_{\varphi} = \frac{u_{\varphi,1}}{r\Omega}, \quad \varpi = \frac{p_1}{p_0}. \quad (9.46)$$

(a) Hydrostatic balance

By using dimensionless variables, the ρ_1-p_1 relation given by equation (9.44) is expressed as

$$\sigma = \left(-\frac{\partial \ln p_0}{\partial \ln r} \right)^{-1} ikr\varpi. \quad (9.47)$$

(b) Angular-momentum balance

The φ -component of the equation of motion is (see appendix B)

$$\rho \left(\frac{du_{\varphi}}{dt} + \frac{u_r u_{\varphi}}{r} \right) = \frac{1}{r^2} \frac{\partial}{\partial r} (r^2 t_{r\varphi}), \quad (9.48)$$

where

$$\frac{d}{dt} = \frac{\partial}{\partial t} + u_r \frac{\partial}{\partial r} + u_z \frac{\partial}{\partial z}, \quad (9.49)$$

and $t_{r\varphi}$ is the $r\varphi$ -component of the turbulent stress tensor. The term coming from the φz -component of the stress tensor has been neglected

on the right-hand side of equation (9.48), since it is smaller than the term $t_{r\varphi}$.

For small-amplitude perturbations localized around the equator, we have, from equation (9.48),

$$n_* \Omega v_\varphi + \frac{\kappa^2}{2\Omega} \frac{u_0}{r\Omega} (\sigma + v_r) = - \frac{ik}{r\Omega\rho_0} t_{r\varphi,1}, \quad (9.50)$$

where n_* is the Doppler-shifted dimensionless growth rate, which is defined by

$$n_* = n - ikr \frac{u_0}{r\Omega}. \quad (9.51)$$

Here, we consider the case of $t_{r\varphi} = -\alpha p$. Furthermore, v_r is neglected compared with σ in equation (9.50), since a detailed examination using the equation of continuity and the final result concerning the growth rate shows that the order of v_r is smaller than that of σ .²³ Then, equation (9.50) gives

$$n_* v_\varphi + \frac{\kappa^2}{2\Omega^2} \frac{u_0}{r\Omega} \sigma - i\alpha kr \left(\frac{c_T}{r\Omega} \right)^2 \varpi = 0, \quad (9.52)$$

where c_T is the isothermal sound speed, defined by $c_T^2 = p_0/\rho_0$.

(c) Energy equation

The thermal-energy conservation is written as

$$\frac{dp}{dt} - \Gamma_1 \frac{p}{\rho} \frac{d\rho}{dt} = (\Gamma_3 - 1)(q_{\text{vis}}^+ - q_{\text{rad}}^-), \quad (9.53)$$

where Γ_1 and Γ_3 are the usual generalized ratios of the specific heat under the presence of radiation (see appendix B). As the heating, we have adopted the viscous one, which is

$$q_{\text{vis}}^+ = rt_{r\varphi} \frac{d}{dr} \left(\frac{u_\varphi}{r} \right), \quad (9.54)$$

with $t_{r\varphi} = -\alpha p$. The radiative cooling, q_{rad}^- , is neglected hereafter, since it is negligible in ADAF, compared with advective cooling [the left-hand

²³The dimensionless growth rate, n_* , obtained under this approximation is given by equation (9.57). If this result is adopted, the continuity equation,

$$n_* \sigma - ikr \left(\frac{u_0}{r\Omega} \right) v_r \sim 0,$$

shows that σ is larger than v_r by a factor of $(kr)^{1/2}(H/r)$. Here, $H/r \sim 1$ in ADAFs. In the above estimate we have used $u_0 \sim \alpha r\Omega(c_s/r\Omega)^2$ [see equation (3.72)].

side of equation (9.53)]. It might be necessary to add in equation (9.53) a term due to turbulent heat diffusion. Its effects on the stability are discussed in subsection 9.4.5.

Since p_1/p_0 can be neglected compared with ρ_1/ρ_0 [see equation (9.45)] and since q_{rad}^- can be neglected in advection-dominated disks, we have from equation (9.53)

$$n_* \Omega \left(-\frac{\Gamma_1}{\Gamma_3 - 1} \right) \sigma = i\alpha \Omega k r v_\varphi. \quad (9.55)$$

9.4.4 Growth Rate of Thermal Instability

In the above subsection we derived three relations [equations (9.47), (9.52), and (9.55)] among three quantities (σ , ϖ , and v_φ). From the condition that these equations have a non-trivial solution, we obtain a dispersion relation,

$$n_*^2 = i\alpha^2 kr \frac{\Gamma_3 - 1}{\Gamma_1} \left(\frac{c_T}{r\Omega} \right)^2 \left[\frac{\partial \ln p_0}{\partial \ln r} + \frac{\kappa^2}{2\Omega^2} \frac{u_0}{\alpha r \Omega} \left(\frac{c_T}{r\Omega} \right)^{-2} \right]. \quad (9.56)$$

Since the advective speed in the unperturbed state is

$$u_0 \sim \alpha r \Omega \left(\frac{c_T}{r\Omega} \right)^2 \sim \alpha r \Omega \left(\frac{H}{r} \right)^2, \quad (9.57)$$

[see equations (3.72)], the quantity in the brackets of equation (9.56) is on the order of unity. Hence, the dispersion relation (9.56) shows the presence of an unstable mode whose growth rate is on the order of

$$n_* \Omega \sim \alpha \Omega (kr)^{1/2} \frac{H}{r}. \quad (9.58)$$

These growing perturbations propagate inward with advective flow.

The cause of this thermal instability originates from the following situations. A local temperature increase brings about a local density decrease, since the pressure variation is generally weak [see inequality (9.45)]. This density decrease leads to a variation of u_φ , since the angular momentum per unit volume is roughly conserved during development of perturbations [see equation (9.52)]. We also note that the first and second terms of equation (9.52) are roughly balanced. This variation of v_φ gives rise to an increase in the viscous heating [equation (9.55)]. This heating increment, in turn, gives a positive feedback to the original temperature variation.

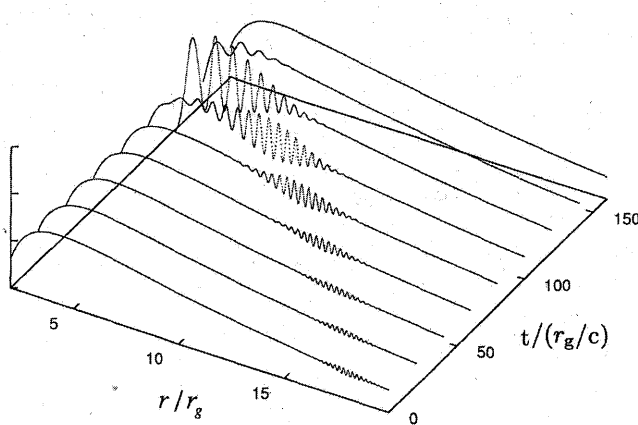


Figure 9.11

Growth of local perturbations in optically thin advection-dominated disks, showing a time development of small-amplitude density perturbations imposed around $r = 20r_g$ at $t = 0$. The $r\varphi$ -component of the stress tensor, $t_{r\varphi}$, has been taken to be $t_{r\varphi} = -\alpha p$. The parameters adopted are $kr = 30$, $\alpha = 0.3$, $M = 10M_\odot$, and $\dot{M} = 6.0 \times 10^{-7} \dot{M}_{\text{crit}}$. (After Manmoto et al. 1996a)

Numerical simulations examining non-linear time-development behavior of thermally unstable modes have been made by Manmoto et al. (1996a). An example of short-wavelength perturbations is shown in figure 9.11.²⁴ These results seem to confirm the results of linear analyses.

So far, we have adopted $t_{r\varphi} = -\alpha p$. The case where $t_{r\varphi}$ has a diffusion form,

$$t_{r\varphi} = \eta r \frac{\partial}{\partial r} \left(\frac{u_\varphi}{r} \right), \quad (9.59)$$

(η being turbulent viscosity), which can be examined in the same way with similar results (Kato et al. 1997). In this case the growth rate, $n_*\Omega$, is on the order of $\alpha\Omega$, smaller than that given by equation (9.58).

9.4.5 Effects of Turbulent Thermal Conduction

Let us consider the effects of turbulent heat diffusion on the time development of thermal perturbations. As mentioned in section 9.1, energy transport by turbulence is non-negligible in ADAFs. This suggests that

²⁴Rigorously speaking, they use the vertically integrated quantities in these simulations, while we are treating here local variations of physical quantities. However, the equations treated in their simulations and those in the present analysis are the same if appropriate replacements, say, ρ_1/ρ_0 by Σ_1/Σ_0 , are made.

the turbulent heat conduction will also have substantial effects on the thermal stability of advection-dominated disks.

Let us assume that the heating or cooling due to turbulent heat transport is a diffusion process. It is thus reasonable to suppose that diffusion occurs in the direction of the entropy gradient. Hence, as was done in section 7.1, we write the heating by turbulence, q_{turb}^+ , as

$$q_{\text{turb}}^+ = \frac{\partial}{\partial r} \left(r K \rho T \frac{\partial s}{\partial r} \right), \quad (9.60)$$

where s is the specific entropy, and K is the thermometric conductivity due to turbulence, which is usually on the order of the turbulent kinematic viscosity. This turbulent heating can be written as

$$q_{\text{turb}}^+ = \frac{\partial}{\partial r} \left[r \frac{K}{\Gamma_3 - 1} \left(\frac{\partial p}{\partial r} - \Gamma_1 \frac{p}{\rho} \frac{\partial \rho}{\partial r} \right) \right]. \quad (9.61)$$

If we assume that this expression is still applicable even when we consider local perturbations, we have

$$q_{\text{turb},1}^+ = - \frac{K}{\Gamma_3 - 1} k^2 (p_1 - c_s^2 \rho_1) \quad (9.62)$$

or

$$\frac{q_{\text{turb},1}^+}{p_0} = \frac{\Gamma_1}{\Gamma_3 - 1} K k^2 \sigma, \quad (9.63)$$

where k is the wavenumber of the perturbations. In deriving equation (9.63), we neglected p_1/p_0 compared with $\rho_1/\rho_0 (\equiv \sigma)$.

If we consider short-scale perturbations, $q_{\text{turb},1}$ is the major quantity among three perturbed ones, ($q_{\text{vis},1}^+$, $q_{\text{turb},1}^+$, and $q_{\text{rad},1}^-$), since $q_{\text{turb},1}^+ \propto k^2$, while $q_{\text{vis},1}^+ \propto k$. Hence, instead of equation (9.55), we have

$$n_* \Omega \left(- \frac{\Gamma_1}{\Gamma_3 - 1} \right) \sigma = \frac{\Gamma_1}{\Gamma_3 - 1} K k^2 \sigma \quad (9.64)$$

or simply

$$n_* \Omega = -k^2 K. \quad (9.65)$$

This shows that short-scale thermal perturbations are damped by turbulent heat diffusion (Kato et al. 1997; Wu 1997), as is generally expected.

For the turbulent thermometric conductivity, K , we adopt here $K = \alpha_{\text{turb}} c_s^2 / \Omega$, where α_{turb} ($0 < \alpha_{\text{turb}} < 1$) is a constant, since K is on the order of the velocity times the mean-free path of turbulent eddies contributing to the turbulent diffusion. Then, equation (9.65) shows that

the damping rate is on the order of $\alpha_{\text{turb}}\Omega(kH)^2$, which is larger than the growth rate given by equation (9.58) by $(\alpha_{\text{turb}}/\alpha)(kH)^{3/2}(r/H)^{1/2}$.²⁵

9.4.6 Shot Formation in Advection-Dominated Disks

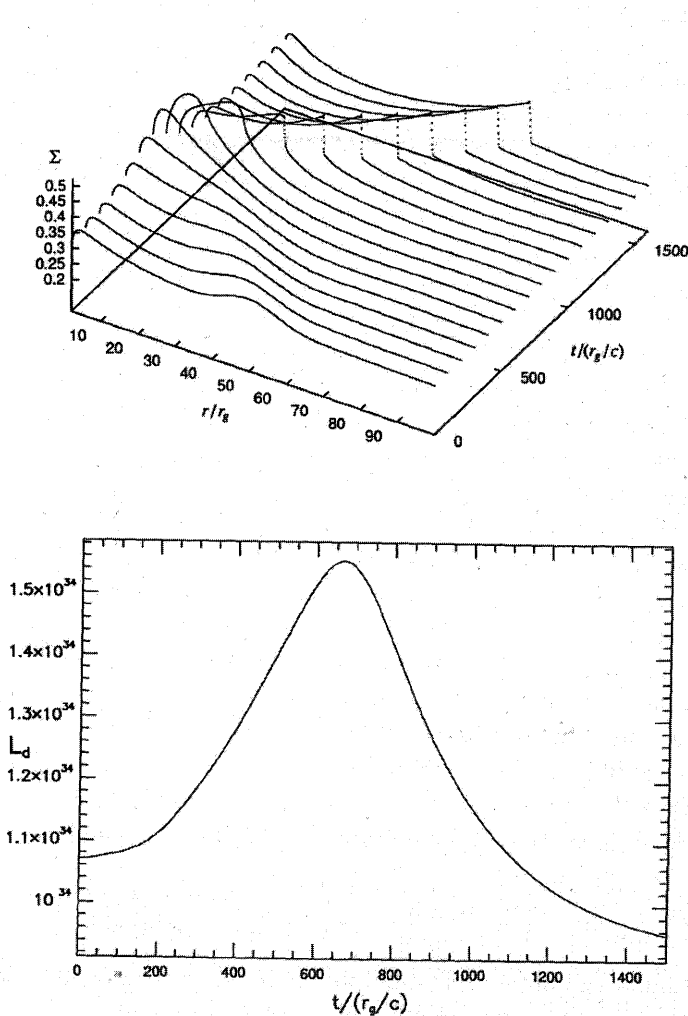
The local instability of ADAF against short-wavelength perturbations has a significant meaning; it can create variability in luminosity (see figure 1.23). The observational fact of enhanced variability during the low (hard) state indicates that the place where fluctuations are generated is not likely to be a standard-type disk, since it cannot produce hard, power-law X-rays, which are observed during those periods. Further, the disk cannot be of the type proposed by Shapiro et al. (1976), since their disk is thermally unstable and is difficult to produce variations for a long time. What is left and is the most promising disk model is an optically thin ADAF. Let us discuss its time-dependent processes, following Manmoto et al. (1996b).

To trigger a fluctuation, we assume spatial inhomogeneities of the disk-mass distribution; namely, we *a priori* give a density perturbation in a steady state disk and calculate how the perturbation evolves and how the disk luminosity varies with time by solving the time-dependent version of the basic equations (see section 7.4). Here, we simply assume a density perturbation (or disturbance) of the form $\Sigma_1/\Sigma_0 = \delta_0 \exp[-(r - r_0)^2/\lambda^2]$ on the steady-disk structure, where δ_0 , r_0 and λ are numerical constants.

The resultant blob propagation is illustrated in the upper panel of figure 9.12. Here, we have assigned a mass-input rate of $\dot{M}_0 = 1.6 \times 10^{-4} L_E/c^2$, the mass of a black hole, $M = 10M_\odot$, viscosity parameter, $\alpha = 0.3$, $\bar{\mu} = 0.62$ (cosmic abundance), $\gamma = 5/3$, the perturbation amplitude, $\delta_0 = 0.2$, the initial position of the perturbation, $r_0 = 50.0r_g$, and the initial perturbation wavelength, $\lambda = 5.0r_g$. In these calculations, the outer boundary is set at $r = 90r_g$, where we require that the viscous heating is balanced by radiative cooling, and $\Omega = \Omega_K$. The inner boundary is located at $2r_g$ (in the supersonic region). Hence, we assume free boundary conditions there. In the entire calculated region between the two boundaries, advection dominates over radiative cooling.

The lowest curve of the upper panel of figure 9.12 represents the initial state; i.e., a steady state with a disturbance. Although the disturbance

²⁵It is uncertain whether thermal energy generation by dissipation of turbulence can be described by such a diffusion form as equation (9.60). It is particularly so when the size of perturbations is shorter than the typical turbulent eddy size, i.e., $kH > 1$.

**Figure 9.12**

Time evolution of optically thin, advection-dominated disks under a density disturbance given at the outer parts. The upper panel shows the time changes of the surface-density distribution in the (r, t, Σ) plane. The lower panel depicts the light variations caused by the density disturbance shown above. A rather symmetric time profile is due to wave reflection. The unit of time is $r_g/c \sim 10^{-4}(M/10M_\odot)s$ (Adapted from Manmoto et al. 1996b)

slowly damps as it accretes, the damping timescale is comparable to the accretion timescale. Once a disturbance occurs at the outer portions of the disk, that disturbance will possibly persist as a blob, flowing inward with the same velocity as the accreting matter. The accretion velocity is comparable to the free-fall velocity. When the perturbation reaches the innermost region, it is reflected as an outgoing acoustic wave if the perturbation wavelength is relatively long. The reflection occurs outside the sonic point. As a result, the total disk luminosity ($L_d = 2 \int 2\pi r Q_{\text{rad}}^- dr$) depicted in the lower panel of figure 9.12 has a sharply peaked, (time) symmetric profile that is observed as an X-ray shot. Here, although we consider only optically thin bremsstrahlung for simplicity, the light variation does not sensitively depend on the emission mechanisms.

When the wavelength of the initial perturbations was short, $\lambda \lesssim r_g$, in contrast, the disturbance was just conveyed by the accreting flow and was directly swallowed by the hole without reflection (see figure 9.11). In other words, wave reflection occurred only when $\lambda > r_g$.

Using *Ginga* data, Negoro et al. (1994) directly obtained a mean time profile of flares (or shots) by superposing the number of flares aligning their peaks; it is sharply peaked and rather (time) symmetric. We here demonstrate that such a symmetric light variation can be reproduced by the advection-dominated disk model. Although the initial perturbation amplitude, δ_0 , was only $\sim 20\%$, the disk luminosity changed by a factor of $\sim 60\%$. Perturbations with amplitudes of 20–30% are sufficient to reproduce the observed light variations.

Note that in order to produce long shot durations, \sim seconds at maximum, we need to put the perturbation at sufficiently large radius ($r_0 \gg r_g$). Since the accretion timescale of ADAF is roughly,

$$t_{\text{acc}} \sim \frac{1}{\alpha} \left(\frac{r^3}{GM} \right)^{1/2} \simeq 1.5 \left(\frac{\alpha}{0.1} \right)^{-1} \left(\frac{r}{100r_g} \right)^{3/2} \left(\frac{M}{10M_\odot} \right) \text{ s}, \quad (9.66)$$

the initial radius of perturbations should be at least $r_0 \sim 10^2 r_g$ in order to achieve long durations of seconds for a black-hole mass of a few M_\odot . This number is in good agreement with the radius separating the outer standard-type and inner advection-dominated portions of the disk. It is encouraging to note that even at such a large radius the electron temperatures can be as high as $\sim 10^9 \text{ K}$ (see figure 9.8), thus being capable of producing hard X-ray photons. Thus, the structural changes involved with accretion of the blob will cause a variability of the X-ray emissivity on timescales of seconds.²⁶

²⁶As discussed in subsection 9.2.3, there is a possibility that the transition region

9.4.7 Physics of Wave Reflection

We have seen that only long-wavelength perturbations can produce a time-symmetric light variation. Why is this the situation?

Inward-propagating thermal perturbations are reflected as outward-propagating acoustic waves near to the sonic radius when the wavelengths of the initial perturbation are relatively long, compared with the characteristic length scale, over which the physical quantities in disks appreciably change near to the sonic radius. This reflection of long-wavelength perturbations is quite conceivable and is a general feature inherent in the region around the sonic radius.

In general, if the structure of a medium changes over a scale-length shorter than the wavelength of an incident perturbation of some mode, the perturbation can generate other modes through linear coupling.²⁷ In the present problem, there are four modes of perturbations involved: one viscous mode and one thermal mode, both propagating inward, and two acoustic modes; one propagating outward and the other inward. The characteristic speeds of the viscous and thermal modes are both v_r , while those of two acoustic perturbations are $v_r \pm c_s$, where v_r (< 0) is the advection (accretion) speed and c_s is the sound speed (see Kato et al. 1988).

Hence, an inward-propagating thermal mode with a relatively long wavelength generates three other modes of perturbations near to the sonic radius, where the disk structure changes sharply. Among these generated three modes, the inward-propagating acoustic mode and the viscous mode are swallowed into the hole, since they have negative characteristic speeds. The outward-propagating acoustic wave, on the other hand, can be a standing wave at the sonic radius, since the characteristic speed of the outward-propagating acoustic wave ($v_r + c_s$) vanishes there. Just outside the sonic radius, this wave have a small (positive) propagation velocity. Because of the very nature of their small (positive) propagation velocities, the amplitude of the generated acoustic waves can grow before the waves start to propagate outward. This is a reflection of the thermal perturbations into acoustic waves.

How can the initial perturbation basically retain its original shape?

between the outer SSD and the inner ADAF is time-dependent, which may produce blobs required here.

²⁷Mode coupling never occurs for linear perturbations in a homogeneous medium, unless they grow into nonlinear regimes, since the perturbations of different modes are linearly independent. It can take place, however, even for linear waves, if the medium is inhomogeneous.

Table 9.2 Representative Flow Structure of RIAFs.

Accretion mode	$\rho(r)$	$T(r)$	$v_r(r)$
ADAF	$\propto r^{-1.5}$	$\propto r^{-1}$	$\propto r^{-0.5}$
ADIOS*	$\propto r^{-1.5+s}$	$\propto r^{-1}$	$\propto r^{-0.5}$
CDAF	$\propto r^{-0.5}$	$\propto r^{-1}$	$\propto r^{-1.5}$

* Mass accretion rate is $\dot{M} \propto r^s$ with $0 \leq s < 1$.

This is related to a thermal instability in the optically thin ADAF. As already stated in the previous subsection, a thermal perturbation tends to grow weakly, unless turbulent heat diffusion is strong. The growth timescale is roughly on the same order as that of the accretion timescale. Thus, a perturbation propagates till the inner edge of the disk without significantly altering the global disk structure. We thus expect persistent X-ray radiation, although it could be constantly fluctuating. This is exactly what we observe in X-ray binaries during the hard (low) state and in active galactic nuclei.

9.5 Multi-Dimensional Effects

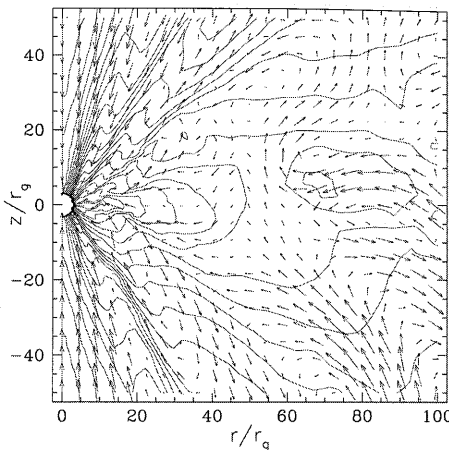
Since the ADAF can reproduce hard, power-law spectra in the X-ray range, as are observed, this model was thought to be a good representation of disks in low-luminosity AGNs (LLAGNs) and in the BHs during their low/hard state. However, we should be aware that there are a number of serious problems associated with the ADAF formulation (see comprehensive discussion in Narayan 2002).

9.5.1 CDAF and ADIOS

The original optically thin ADAF model is basically a radially one-dimensional model. Recently made 2D/3D hydrodynamical simulations, however, revealed distinct forms of accretion flows in the radiatively inefficient regimes. Igumenshchev and Abramowicz (2000), for example, claimed that a nearly one-dimensional ADAF appears only when the viscosity parameter, α , is moderate, $0.01 < \alpha \leq 0.1$.

If α is very small, convection occurs and largely modifies the flow structure (see figure 9.13) first discussed by Ryu & Goodman (1992). Such flow is called *convection-dominated accretion flow* (CDAF; Narayan et al. 2000; Quataert and Gruzinov 2000).

If α is large ($\alpha \sim 1$), on the other hand, strong outflows result. Blandford and Begelman (1999) constructed a model of ADIOS (*advection-dominated inflow-outflow solutions*) based on this idea. Due to mass

**Figure 9.13**

Typical patterns of convective motions in accretion flow revealed by hydrodynamic simulations with $\alpha = 0.01$. The solid curves represent density contours and the arrows indicate velocity vectors. (After Igumenshchev and Abramowicz 2000)

loss, they assumed that the mass-accretion rate varies as $\dot{M} \propto r^s$ with $0 \leq s < 1$. The restriction on s allows the accreting mass to decrease with decreasing radius, while the energy released can still increase. They exhibit somewhat different flow properties (see table 9.2), which can be naively understood in terms of the self-similar solutions.

9.5.2 Self-Similar Model of CDAF

Following Narayan et al. (2000), let us consider self-similar solutions of CDAF. The solutions are basically similar to that of ADAF (see section 9.2), since radiative cooling is dropped in both cases, but they need some modifications in the velocity (and, hence, density) profiles to allow for convective motion in the radial direction.

Here, we seek solutions of the forms similar to equation (9.31), except for $v_r(r)$ and ρ :

$$v_r \propto r^{a-2}, \quad v_\varphi \propto r^{-1/2}, \quad T \propto c_s^2 \propto r^{-1}, \quad \rho \propto r^{-a}, \quad (9.67)$$

with a being a numerical constant. Note that by setting $a = 3/2$ we can recover the self-similar solutions of the ADAF (see subsection 9.2.1).

The basic equations are the same as equations (9.28), except for the angular-momentum equation, which is

$$\dot{J}_{\text{adv}} + \dot{J}_{\text{vis}} + \dot{J}_{\text{conv}} = 0, \quad (9.68)$$

where $4\pi\dot{J}$ is the angular-momentum flow through the cylinder surface at radius r , and

$$\dot{J}_{\text{adv}} = (\rho r H v_r)(r^2 \Omega), \quad (9.69)$$

$$\dot{J}_{\text{vis}} = -\nu \rho H r^3 \frac{d\Omega}{dr}, \quad (9.70)$$

with $\nu (= \alpha c_s H)$ being the turbulent viscosity. Here, we adopt the torque-free condition at the inner boundary to have self-similar solutions.

So as to describe the convective transport of angular momentum, we have two options. The first one is the case that the convection behaves like normal viscosity; that is, the angular momentum transport is outward and is prescribed as

$$\dot{J}_{\text{conv}} = -\alpha_{\text{conv}} \frac{c_s^2}{\Omega_K} \rho H r^3 \frac{d\Omega}{dr}. \quad (9.71)$$

This gives the same r -dependence as that of \dot{J}_{vis} . Therefore, the basic properties of the self-similar solution are the same as those of the ADAF: $a = 3/2$ and, hence, $\rho \propto r^{-3/2}$. From angular-momentum conservation (9.68) we have

$$v_r = -\frac{3}{2}(\alpha + \alpha_{\text{conv}}) \frac{c_s^2}{r \Omega_K}, \quad (9.72)$$

approximating Ω by Ω_K . The value of α_{conv} can be determined by the requirement that self-similar solutions are realized.

The second option is that the convective flux is in the direction of the angular-momentum gradient, and is scaled as

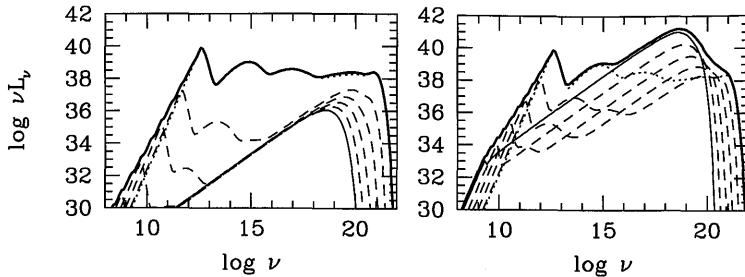
$$\dot{J}_{\text{conv}} = -\alpha_{\text{conv}} \frac{c_s^2}{\Omega_K} \rho H r \frac{d(\Omega r^2)}{dr}, \quad (9.73)$$

which gives *inward* angular-momentum transport in the Keplerian disk. This prescription allows two solutions: one with $a = 3/2$, as before, which gives

$$v_r = -\frac{1}{2}(3\alpha - \alpha_{\text{conv}}) \frac{c_s^2}{r \Omega_K}. \quad (9.74)$$

Obviously, an accretion solution exists when $v_r < 0$; i.e., $\alpha > \alpha_{\text{conv}}/3$. In other words, only when convective energy transport is weaker than that by viscosity does the solution describe an accretion motion of gas.

Another, but completely distinct solution is found when $a = 1/2$; i.e., $\rho \propto r^{-1/2}$. This is a very special solution, since from the continuity equation we find $v_r = 0$. That is, no accretion!! This solution is referred to as the CDAF (convection-dominated accretion flow).

**Figure 9.14**

Typical ADAF (left) and CDAF (right) spectra. The thick solid line in each panel represents the total spectrum, while the thin solid, dashed, and dotted lines represent the contributions from the outermost, middle, and innermost rings, respectively. (After Mineshige et al. 2002)

9.5.3 Spectral Properties of CDAF

We have seen the basic characteristics of CDAF, but its physical relevance is in question. To justify its reality, the most critical test of these flows is to examine their spectral properties.

Figure 9.14 displays the typical ADAF (left) and CDAF (right) spectra calculated based on the self-similar solutions in a way similar to that of Ball et al. (2001). A big distinction lies in their density profiles (see table 9.2): $\rho = \rho_0(r/r_g)^{-a}$ with $a = 3/2$ in ADAF and $a = 1/2$ in typical CDAF, respectively. The proportionality constant, ρ_0 , was chosen to reproduce the mass-accretion rate of $\log \dot{m} = -3.29$. We took the same ρ_0 in CDAF, as well, to make the comparison easier. Hence, figure 9.14 can be used only for demonstration purpose. The other adopted parameters are the same for both models: the inner-edge radius is $1.0r_g$, the outer-edge radius is $10^{2.5}r_g$, the mass of black hole is $M_{\text{BH}} = 10^8 M_\odot$, the ion temperature profile is $10^{12}(r/r_g)^{-1.0}\text{K}$, the electron temperature profile is $10^{10}(r/r_g)^{-0.6}\text{K}$, and magnetic field strengths are taken to be the equipartition values; i.e., $B^2 \propto (r/r_g)^{-(1+a)}$.

In the case of ADAF, emission from the innermost ring dominates over the contribution from the outer parts at all wavelengths because of its steep density profiles. Note that the density profile of $\rho \propto r^{-3/2}$ leads to bremsstrahlung emissivity of $dE \propto \rho^2 T^{1/2} r^2 dr \propto r^{-3/2} dr$. In the case of CDAF, in contrast, X-ray emission comes from the outer parts due to a less-steep density profile ($\rho \propto r^{-1/2}$ yields $dE \propto r^{1/2} dr$), while radio-to-optical emissions are from the innermost part. The different natures of ADAF and CDAF are well demonstrated in figure 9.14. We

also understand that bremsstrahlung is a dominant process in CDAF in X-rays, while Compton up-scattering of synchrotron emission is more important in ADAF.

In conclusion, the CDAF models have two problems: (1) CDAF predicts a rather flat ($f_\nu \propto \nu^0$) spectrum, unless we assume significant electron heating as well as ion heating (Ball et al. 2001), but the observations clearly show a power-law decline (e.g. $f_\nu \propto \nu^{-0.7}$) in the X-ray ranges. (2) Rapid variability seems to arise via time-dependent processes, probably associated with magnetic flares in the innermost region; however, in CDAF, X-ray emission from the inner part is negligible (see figure 9.14). In view of these arguments, ADAF appears to be more preferable to fit observations.

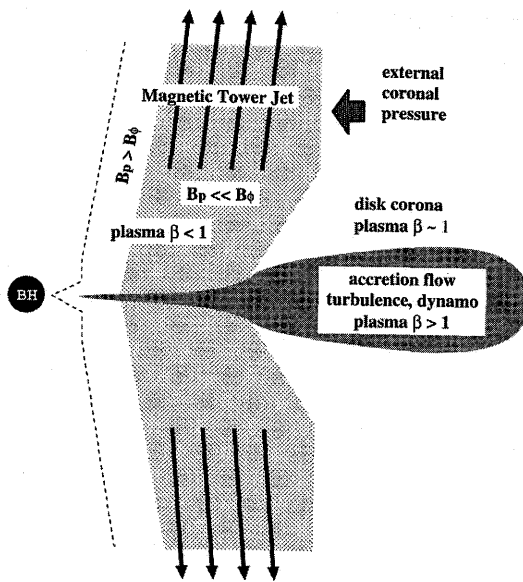
9.5.4 MHD Accretion Flow

In hydrodynamical models of accretion the magnitude of the viscosity is treated as a free parameter, although it should, in principle, be determined in accordance with magnetic field amplifications within the disk. In other words, we need to perform global MHD simulations.

There is a variety of important roles that magnetic fields play in accretion disks: (1) source of viscosity, (2) disk corona (and RIAF) heating, (3) cause of flares, producing variability, (4) source of radiation via synchrotron, and (5) jet and outflow formation. These processes have been most successfully simulated through global MHD simulations of the inner accretion disk by several groups.²⁸

The global 3D MHD simulations of RIAFs were first made by Matsumoto (1999), and have been extensively performed recently by several groups (see Mineshige and Makishima 2004 for a compilation of recent works). It has been revealed by the 3D MHD simulations that the flow pattern is considerably complicated and differs significantly from that of the ADAF model (Hawley 2000; Machida et al. 2000; Hawley and Krolik 2001; Machida et al. 2001; Hawley and Balbus 2002; Machida and Matsumoto 2003; Igumenshchev et al. 2003). Stone and Pringle (2001) established that the complex flow pattern is produced due to the magneto-rotational instability (MRI, see section 2.4, see also Hawley et al. 2001; Hawley 2001; Balbus 2003 for a review). Since the dynamics of the magnetic fields is fully solved, the 3D MHD models seem to be

²⁸What is not easily incorporated is thermal conduction, which is anisotropic in the presence of magnetic fields, although it seems to be an essential ingredient in disk-corona systems (see section 3.4).

**Figure 9.15**

Schematics of the MHD accretion flow and jet connection. (After Kato et al. 2004)

better for describing the RIAF than other models with no appropriate treatment of the magnetic fields.

They have found that magnetic fields can be amplified and maintained sufficiently enough to explain the observations; the estimated viscosity parameters are in a range of $0.01 < \alpha < 1.0$.²⁹ Large corona can be constructed by MHD processes. Also, it is possible to produce aperiodic variability with a power-law decline in power-spectral densities (Kawaguchi et al. 2000; Hawley and Krolik 2001).³⁰

9.5.5 MHD Disk-Jet Connection

It would be extremely important to examine a possible disk-jet connection by means of global MHD simulations. Here, we would like to remind readers that similar MHD simulations had already been performed in the 1980's by many groups in the context of astrophysical jets, pioneered by Uchida & Shibata (1985; see also Shibata & Uchida 1986). They calcu-

²⁹Rigorously speaking, however, we should distinguish α for angular-momentum transport and that for heat generation (e.g., Kato and Horiuchi 1986), although these are regarded as being the same in the standard α prescription.

³⁰This corresponds to the so-called $1/f^\beta$ (with $\beta \sim 1$) fluctuations (see chapter 12 of the first edition of this book (Kato et al. 1998).

lated the evolution of a disk being threaded with vertical fields extending to infinity and found the emergence of a strong magnetic jet. But, can such strong jets emerge even in the cases without initial vertical fields?

Kato et al. (2004) started calculations with a rotating torus threaded by localized, relatively weak poloidal magnetic fields to see if a magnetic jet is produced. The evolution of the magnetized torus that they simulated is as follows: When a disk material reaches the innermost region close to the central black hole, up-ward motion of gas appears, which is driven by increased magnetic pressure exerted by accumulated toroidal fields. Matter is blown away upward by inflating toroidal fields (a so-called magnetic tower; Lynden-Bell 1986, see figure G.10) with a large speed, about several tenths of c . A substantial amount of the matter then goes upward. Finally, a nearly quasi-steady state would be realized, when accretion occurs through a geometrically thick disk.

Figure 9.15 illustrates the close disk-jet connection through magnetic fields. Magnetic fields are amplified by a disk dynamo within the disk, and the amplified toroidal fields are accumulated and create a magnetic-tower jet. Within the jet region, marginally low- β (~ 1) plasmas threaded with poloidal (vertical) fields are surrounded by low- β (< 1) plasmas with toroidal fields (B_φ). The magnetic-tower jet is confined by the external pressure (Lynden-Bell and Boily 1994) by the corona with $\beta \sim 1$.

There exist some problems involved with this scenario, however. For example, it cannot produce a relativistic jet, since the jet speed is on the order of the Keplerian velocity at the footpoint of the jet. It is also unclear how initial magnetic field configurations affect evolution. Further studies are necessary.

9.5.6 Spectral Paradox of MHD Accretion Flow

Ohsuga et al. (2005) calculated the emergent spectra of MHD flow based on the simulation data by Kato et al. (2004), which is displayed in figure 9.16 (see the thick solid curves) together with the observed SED (spectral energy distribution) of Sgr A*. Apparently, the resultant spectra look similar to those of the ADAF model in the low-energy part. The lower energy peak in the radio band is a synchrotron peak created because of significant self-absorption of synchrotron emission. The IR emission at around $\log \nu = 14$ is due to inverse Compton scattering of the synchrotron photons.

Note that we can choose any value of ρ_0 , density normalization, since

every term in basic equations of MHD accretion flow with no radiation has the same dependence on density, as long as B^2 is scaled as gas pressure, p_{gas} . Even if we change ρ_0 , however, the electron temperatures do not vary much, and, hence, the radio parts (which depends primarily on the electron temperature) are roughly identical among different models with different ρ_0 . In contrast, the flux at $\log \nu > 12$ and the frequency of the lower-energy peak (in the radio band) are both sensitive to ρ_0 .

Remarkably, the density profile of MHD accretion flow is flatter than that of ADAF; typically $\rho \propto r^{-1}$. We thus again encounter the issue of the spectral paradox. It is found that the 3D MHD flow generally over-produces X-rays by means of bremsstrahlung radiation from the regions at large radii. A flatter density profile, $\rho \propto r^{-a}$, with $a < 1$, than that of the ADAF, $\rho \propto r^{-3/2}$, is a main reason for this. If we restrict the size of the emission region to be as small as $\sim 10r_g$, the MHD model can reproduce the basic features of the observed spectra of Sgr A* during its flaring state (see the upper dashed line). Yet, the spectrum in the quiescent state remains to be understood.

The results strongly indicate that some of fundamental assumptions made in MHD simulations need to be re-considered. What is a loophole? The key to resolving this issue might be whether the dissipated magnetic energy by reconnection goes directly to plasma or radiation. So far, most of the global MHD simulations postulate no radiative cooling,³¹ but if dissipated magnetic energy can be radiated away as a consequence of magnetic reconnection, the MHD flow structure should be more like that of ADAF, instead of CDAF, since the entropy increase towards the black hole is suppressed to some degree. This may explain both the spectral shape and the presence of X-ray variability.

9.5.7 Towards Successful Spectral Reproduction

Alternative possibilities are the effects of jet outflows and nonthermal electrons. If we start the MHD simulations with poloidal magnetic fields, strong outflow (or jet) results (Hawley et al. 2001; Kudoh et al. 2002; Kato et al. 2004). If MHD jets emerge (subsection 9.5.5), matter, angular momentum, and energy can be carried away to the infinity by jet material. We then expect emission from the jets.

Yuan et al. (2003, 2004) investigated the spectral properties of RIAF

³¹Recently three dimensional MHD simulations with radiative cooling have been performed under the shearing-box approximations (e.g., Turner 2004; Hirose et al. 2006), in which long-wavelength coupling of magnetic fields is neglected.

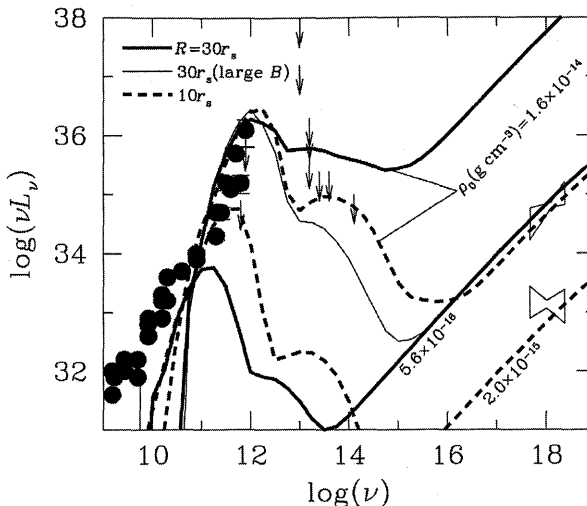


Figure 9.16

The emergent spectra of the MHD accretion flow and the observed data of Sgr A*. The thick solid curves are the resultant spectra for the entire zone, while the dashed curves are contributions only from the innermost part within $10r_s$. (Note that r_s represents the Schwarzschild radius in this figure.) The filled circles and the lines with arrows indicate the data and upper limits by the radio and IR observations. X-ray observations of flaring- and quiescent state are shown by the two ‘bowties’ (Baganoff et al. 2001, 2003). (After Ohsuga et al. 2005)

in general situations to try to fit the SED of Sgr A*. Recent linear polarization measurements in the sub-millimeter emission argues for accretion rates that are much less than the canonical Bondi rate, implying that the mass-accretion rate should decrease inward. Figure 9.17 shows one of their attempts. They adopted the ADIOS type solution: $\dot{M} \propto r^{0.27}$ (i.e., $s = 0.27$, see subsection 9.5.1). The fraction of energy which goes to electrons is assumed to be 0.55. The accretion rate close to the black hole is $\dot{M} \approx 4 \times 10^{-8} M_\odot \text{ yr}^{-1}$. To fit the entire spectra in the flaring state, both of the thermal and nonthermal electron populations are needed. The dot-dashed line is the synchrotron and inverse-Compton emission by thermal electrons, whereas the dashed line is the nonthermal electrons. The nonthermal electrons have $\approx 1.5\%$ of the thermal energy with $n(\gamma) \propto \gamma^{3.5}$ (with γ being the Lorentz factor). Nonthermal electrons are probably generated in turbulence and/or magnetic reconnection events in the innermost event. The dotted line is the total of the synchrotron and inverse-Compton emission, while the solid line is the

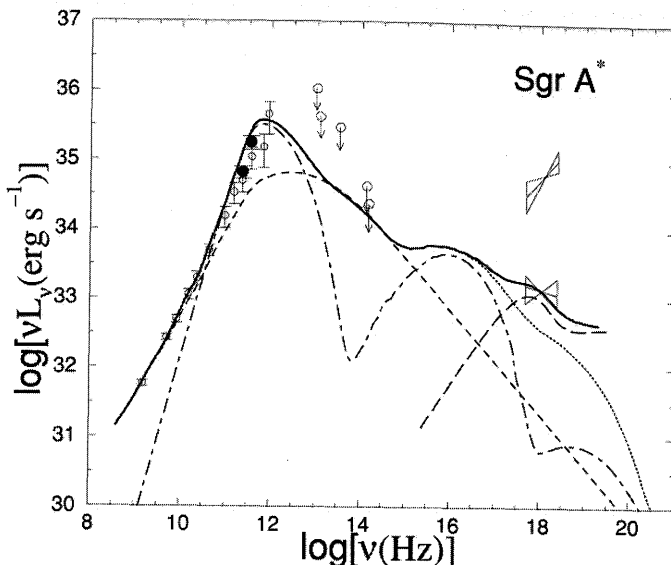


Figure 9.17

Model for the quiescent emission from Sgr A* based on the hybrid RIAF model together with observations of Sgr A*. See text for a detailed explanation. (After Yuan et al. 2003)

bremsstrahlung emission from the outer parts of the RIAF. Rather flat spectra are obtained due to a rather steep density profile, $\rho \propto r^{-1.2}$ (see table 9.2).

Their model is very attractive, but it is not yet clear how such flow structure is reproduced in the framework of MHD accretion flow models. Further numerical studies are necessary.

References

- Abramowicz M.A., Chen X., Kato S., Lasota J.P., Regev O. 1995, ApJ 438, L37
- Abramowicz M.A., Igumenshchev I.V., Lasota J.-P. 1998, MNRAS, 293, 443
- Abramowicz M.A., Kato S., Matsumoto R. 1989, PASJ 41, 1215
- Akizuki C., Fukue J. 2006, PASJ 58, 469
- Baganoff F.K. et al. 2001, Nature 413, 45
- Baganoff F.K. et al. 2003, ApJ 591, 891
- Balbus S.A. 2003, ARA&A 41, 555
- Beloborodov, A.M. 1998, MNRAS 297, 739

- Bisnovatyi-Kogan G.S., Lovelace R.V.E. 1997, ApJ 486, L43
Blandford R.D., Begelman M.C. 1999, MNRAS 303, L1
Chen X. 1995, MNRAS 275, 641
Chen X., Abramowicz M.A., Lasota J.P. 1997, ApJ 476, 61
Esin A.A., Narayan R., Ostriker E., Yi I. 1996, ApJ 465, 312
Gammie C., Popham R. 1998, ApJ 498, 318
Gracia J., Peitz J., Keller J., Camenzid M. 2003, MNRAS 344, 468
Gu W.M., Lu J.F. 2000, ApJ 540, L33
Hawley J.F., Balbus S.A. 2002, ApJ 573, 738
Hawley J.F., Krolik J.H. 2001, ApJ 548, 348
Hawley J.F., Balbus S.A., Stone J.M. 2001, ApJ 554, L49
Hawley J.F. 2001, ApJ 554, 534
Hawley J.F. 2000, ApJ 528, 462
Hayashi M.R., Matsumoto R. 2004, ApJ 600, 338
Hirose S., Krolik J.H., Stone J.M. 2006, ApJ 640, 901
Honma F. 1996, PASJ 48, 77
Ichimaru S. 1977, ApJ 214, 840
Igumenshchev I.V., Abramowicz M.A. 2000, ApJS 130, 463
Igumenshchev I.V., Narayan R., Abramowicz M.A. 2003, ApJ 592, 1042
Kato S., Abramowicz M.A., Chen X. 1996, PASJ 48, 67
Kato S., Horiuchi T. 1986, PASJ 38, 313
Kato S., Nakamura K.E. 1998, PASJ 50, 559
Kato S., Yamasaki T., Abramowicz M.A., Chen X. 1997, PASJ 49, 221
Kato Y., Mineshige S., Shibata K. 2005, ApJ 605, 307
Kato Y., Mineshige S., Shibata K. 2004, PTPS 155, 353
Kawaguchi T., Mineshige S., Machida M., Matsumoto R., Shibata K. 2000, PASJ 52, L1
Kudoh T. Matsumoto R., Shibata K. 2002, PASJ 54, 267
Lasota J.P., Abramowicz M., Chen X., Krolik J.H., Narayan R., Yi I. 1996, ApJ 462, 142
Lu J.F., Lin Y.Q., Gu W.M. 2004, ApJ 602, 37L
Lynden-Bell D. 1986, MNRAS 279, 389
Lynden-Bell D., Boily C. 1994, MNRAS 267, 146
Machida M., Nakamura K., Matsumoto R. 2004, PASJ 56, 671
Machida M., Matsumoto R. 2003, ApJ 585, 429
Machida M., Matsumoto R., Mineshige S. 2001, PASJ 53, L1
Machida M., Hayashi M.R., Matsumoto R. 2000, ApJ 532, L67
Mahadevan R. 1997, ApJ 477, 585
Manmoto T., Kato S. 2000, ApJ 538, 295
Manmoto T., Kato S., Nakamura K.E., Narayan R. 2000, ApJ 529, 127

- Manmoto T., Takeuchi M., Mineshige S., Kato S., Matsumoto R. 1996a, in *Physics of Accretion Disks*, eds. S. Kato, S. Inagaki, S. Mineshige, J. Fukue (Gordon and Breach, Amsterdam), p.57
- Manmoto T., Takeuchi M., Mineshige S., Matsumoto R., Negoro H. 1996b, ApJ 464, L135
- Manmoto T., Mineshige S., Kusunose M. 1997a, ApJ 489, 791
- Manmoto T., Mineshige S., Kusunose M. 1997b, in *Proc. IAU Symp. 184, Hot Universe*, ed. K. Koyama, p.417
- Matsumoto R., Kato S., Fukue J. 1985, in *Theoretical Aspects on Structure, Activity, and Evolution of Galaxies III*, eds S. Aoki, M. Iye, Y. Yoshii (Tokyo Astr. Obs. Publ., Tokyo), p102
- Matsumoto R., Kato S., Fukue J., Okazaki A.T. 1984, PASJ 36,71
- Matsumoto R. 1999, in *Numerical Astrophysics*, ed. S. M. Miyama et al. (Kluwer, Dordrecht), p.195
- Meier D.L. 2005, ApSS, 300, 55
- Mineshige S., Makishima K. 2004, *Proc. of Stellar-Mass, Intermediate-Mass, and Supermassive Black Holes*, PTPS 155
- Mineshige S., Umemura M. 1996, ApJ, 469, L49
- Mineshige S., Negoro H., Matsumoto R., Machida M., Manmoto T. 2002, in *Current High-Energy Emission around Black Holes*, ed. C.-H. Lee, H.-Y. Chang (World Scientific, Singapore), p.119
- Nakamura K.E. 1998, PASJ 50, L11
- Nakamura K.E., Kusunose M., Matsumoto R., Kato S. 1997, PASJ 49, 503
- Nakamura K.E., Matsumoto R., Kusunose M., Kato S. 1996, PASJ 48, 761
- Narayan R., Barret D, McClintock J.E. 1997b, ApJ 482, 448
- Narayan R., Igumenshchev I.V., Abramowicz M.A. 2000, ApJ 539, 798
- Narayan R., Kato S., Honma F. 1997a, ApJ 476, 49
- Narayan R., Mahadevan R., Grindlay J.E., Popham R.G., Gammie C. 1998, ApJ, 492, 554
- Narayan R., McClintock J.E., Yi I. 1996, ApJ 457, 821
- Narayan R., Yi I. 1994, ApJ 428, L13
- Narayan R., Yi I. 1995a, ApJ 444, 231
- Narayan R., Yi I. 1995b, ApJ 452, 710
- Narayan R., Yi I., Mahadevan R. 1995, Nature 374, 623
- Narayan R. 2002, in *Lighthouses of Universe*, ed. M. Gilfanov, R. Sunyaev, E. Churazov, (Springer, Berlin), p.405
- Negoro H., Miyamoto S., Kitamoto S. 1994, ApJ 423, L127
- Ohsuga K., Kato Y., Mineshige S. 2005, ApJ 627, 782

- Oka K., Manmoto T. 2003, MNRAS 340, 543
Papaloizou J.C.B., Stanley G.Q.G. 1986, MNRAS 220, 593
Popham R., Gammie C. F. 1998, ApJ 504, 419
Peitz J., Appl S. 1997, MNRAS 286, 681
Piran T. 1978, ApJ 221, 652
Pringle J.E. 1976, MNRAS 177, 65
Quataert E., Gruzinov A., 2000, ApJ 539, 809
Rees M.J., Begelman M.C., Blandford R.D., Phinney E.S. 1982, Nature 295, 17
Ryu D., Goodman J., 1992, ApJ 388, 438
Schwarzschild M., Härm R. 1967, ApJ 150, 961
Shadmehri M., Khajenabi F. 2005, MNRAS 361, 719
Shakura N.I., Sunyaev R.A. 1973, A&A 24, 337
Shapiro S.J., Lightman A.P., Eardley D.M. 1976, ApJ 204, 187
Shibata K., Uchida Y. 1986, PASJ 38, 631
Stone J.M., Pringle J.E. 2001, MNRAS 322, 461
Takeuchi M., Mineshige S. 1998, ApJ 505, L19
Turner N. 2004, ApJ 605, 45
Uchida Y., Shibata K. 1985, PASJ 37, 515
Yuan F., Quataert E., Narayan R. 2003, ApJ 598, 301
Yuan F., Quataert E., Narayan R. 2004, ApJ 606, 894
Wu X.B. 1997a, ApJ 489, 222
Wu X.B. 1997b, MNRAS 292, 113
Wu X.B., Li Q.B. 1996, ApJ 469, 776

CHAPTER 10

Slim Accretion Disks and Supercritical Flows

The standard-disk picture breaks down not only in low-luminosity regimes (see chapter 9), but also in high-luminosity regimes, in which the mass-accretion rates, \dot{M} , exceed the critical mass-accretion rate, $\dot{M}_{\text{crit}} \equiv L_{\text{E}}/c^2$. Recently, high-luminosity objects that seem to undergo such high- \dot{M} accretion flow have been successively discovered; good examples are microquasars, ultra-luminous X-ray sources (ULXs), and narrow-line Seyfert 1 galaxies (NLS1s). Gamma-ray bursts (GRBs) may also fall onto this category, if black holes are formed at their center and mass accretion onto new-born black holes is a central engine driving energetic explosion. In this chapter, we review the theory of high- \dot{M} accretion flows, sometimes called *supercritical* (or *super-Eddington*) accretion flow, in comparison with the observations. We first overview the basics in section 10.1, and then discuss the structure (section 10.2), spectra (section 10.3), time-dependent properties (section 10.4), and multi-dimensional effects (section 10.5). Finally, an even more extreme case of neutrino-emitting disks is outlined in section 10.6.

10.1 Photon Trapping and Slim Disk Model

The most important and unique feature of supercritical accretion flows is the presence of *photon trapping*, which has been extensively investigated in the context of spherical accretion (Katz 1977; Begelman 1978; Begelman and Meier 1982; Flammang 1984; Blondin 1986; Colpi 1988). In this section we overview the slim-disk model (see figure G.11), which treats photon trapping as the advection of radiation entropy.

10.1.1 What is Photon Trapping?

In optically thick accretion flow, frequent interactions between matter and photons delay the liberation of radiation energy arising from deeper

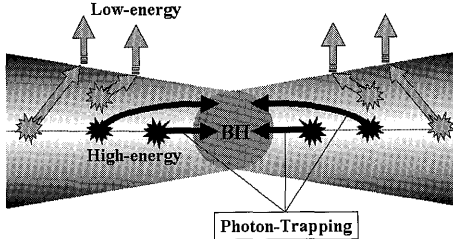


Figure 10.1

Schematic view explaining photon trapping in black-hole accretion. The fraction of trapped photons among entire emitted photons increase inward. (Courtesy of K. Ohsuga)

inside the disk. Thus, the radiation energy is trapped in the luminous flow and advected inward (see figure 10.1). Since the trapped photons fall onto the black hole with the accreting gas without being radiated away, the energy conversion efficiency is reduced in the luminous accretion flow to a black hole. In contrast, the advected energy should be finally radiated on the stellar surface in the case of a neutron star (Houck and Chevalier 1992).

Photon trapping occurs when the photon diffusion time (in the vertical direction), the time for photons to travel from the equatorial plane to the surface, exceeds the accretion time (in the radial direction). The radiation energy generated near the equatorial plane diffuses toward the disk surface at a speed of $\sim c/3\tau$ (Mihalas and Mihalas 1984), where τ is the vertical optical depth of the disk, so that the timescale of radiative diffusion is $t_{\text{diff}} = H/(c/3\tau)$, where H is the half thickness of the disk. Since the accretion timescale, t_{acc} , is given by $r/|v_r|$, the condition that the radiation energy is trapped in the flow is

$$t_{\text{diff}} \equiv \frac{3H\tau}{c} > t_{\text{acc}} \equiv \frac{r}{-v_r} = \frac{2\pi r^2 \Sigma}{\dot{M}}. \quad (10.1)$$

Here, r is the radius, and we use the continuity equation, $\dot{M} = -2\pi r v_r \Sigma$.

Using the relation $\tau = \kappa_{\text{es}} \Sigma / 2$, with κ_{es} being the opacity of the electron scattering, we obtain the photon-trapping radius, inside which

photon trapping is significant:

$$r_{\text{trap}} = \frac{3}{2} \dot{m} \left(\frac{H}{r} \right) r_g, \quad (10.2)$$

where $\dot{m} \equiv \dot{M}c^2/L_E$ and $r_g = 2GM/c^2$. Hence, the photon-trapping effects perform a significant role in the supercritical accretion flow ($\dot{m} \gg 1$ or $\dot{M} \gg L_E/c^2$) at $r < r_{\text{trap}} \sim \dot{m}r_g$, since H/r is on the order of unity at high luminosities. It is important to note that the photon-trapping effects do not depend on the accretion velocity nor viscosity for a fixed \dot{m} . This is because, as α increases, the accretion velocity increases, but the radiative diffusion velocity also increases in accordance with a decrease in the surface density of the disk (note that $\dot{M} \propto v_r \Sigma$ is kept constant).

10.1.2 Basics of the Slim-Disk Model

To a crude approximation, photon trapping can be treated as advection of the photon entropy in radially one-dimensional models. A global model for optically thick, near-critical accretion flow, which incorporates advective transport of the photon entropy, was constructed by Abramowicz et al. (1988), and confirmed by Abramowicz et al. (1989) using independent numerical codes. These disk models are continued in the standard Shakura-Sunyaev models in parameter space. In other words, these models exist for a high mass-accretion rate ($\dot{m} \gtrsim 1$). Since these disks are only moderately thick in the vertical direction, they are called *slim disks*.¹

In order to understand the significance of advective cooling in disks with a high mass-accretion rate, we compare here various heating and cooling rates by expressing them in terms of \dot{M} , Σ , and r . For simplicity, we approximate the angular-momentum balance, $(\ell - \ell_{\text{in}})\dot{M} = 2\pi r^2 \alpha \Pi$ [see equation (7.28)], leading to $\Pi \sim \Omega_K \dot{M}/(2\pi\alpha)$ [equation (9.1)]. Then, from equations (7.42) and (7.46) we obtain

$$Q_{\text{vis}}^+ = r T_{r\varphi} \frac{d\Omega}{dr} = -\alpha r \frac{d\Omega}{dr} \Pi \sim \frac{3}{4\pi} \Omega_K^2 \dot{M}. \quad (10.3)$$

The disk is assumed to be radiation-pressure dominated, and the opacity comes from electron scattering. The cooling rate by radiation is

¹The slim disks are sometimes referred to as being optically thick, advection-dominated disks. However, we should mention that although advective energy transport is important, its rate does not always exceed the radiative cooling rate in slim disks, especially when \dot{M} is barely above the critical rate (Abramowicz et al. 1988). We thus avoid using the terminology “optically thick ADAF” in this book.

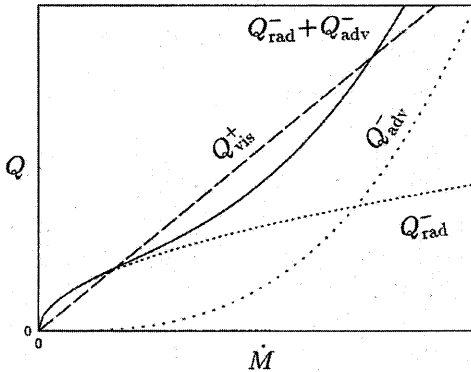


Figure 10.2

Schematic picture showing the \dot{M} -dependence of Q_{vis}^+ , Q_{adv}^- , and Q_{rad}^- for fixed r and Σ .

then approximated as, from equations (7.58),

$$Q_{\text{rad}}^- = \frac{8acT_c^4}{3\bar{\kappa}\rho_0 H} = \frac{8c\Pi}{\kappa_{\text{es}}\Sigma H} \sim \frac{8c}{(2\pi)^{1/2}\kappa_{\text{es}}} \Omega_K^{3/2} \left(\frac{\dot{M}}{\alpha\Sigma} \right)^{1/2}. \quad (10.4)$$

On the other hand, the advective cooling can be estimated from equation (7.40) as

$$Q_{\text{adv}}^- = \frac{\dot{M}}{2\pi r^2} \frac{\Pi}{\Sigma} \xi \sim \frac{\xi}{4\pi^2} \frac{\Omega_K}{r^2} \frac{\dot{M}^2}{\alpha\Sigma}, \quad (10.5)$$

where ξ is a dimensionless quantity of the order of unity [see equation (7.41)]. These equations [(10.3)–(10.5)] describe how the heating and cooling rates depend on r , Σ , and \dot{M} .²

10.1.3 Model Sequence on the \dot{M} - Σ Plane

To understand how distinct branches of solutions appear, we fix r and Σ and illustrate the \dot{M} -dependence of Q_{vis}^+ , Q_{adv}^- , and Q_{rad}^- in figure 10.2. As shown schematically, the energy balance, $Q_{\text{vis}}^+ = Q_{\text{adv}}^- + Q_{\text{rad}}^-$, is realized at two values³ of \dot{M} . We find that $Q_{\text{vis}}^+ \sim Q_{\text{rad}}^-$ for a solution

²In chapter 3, the heating and cooling rates are expressed in terms of r , Σ , and T (temperature). Discussions on the equilibrium models using r , Σ , and T as independent variables are briefly presented at the end of this section.

³We had only two values, since our attention was restricted to a radiation-pressure-dominated regime. If we consider a gas-pressure-dominated regime, an additional solution appears for a lower \dot{M} , corresponding to the usual Shakura-Sunyaev-type gas-pressure-dominated disks (see figure 10.3).

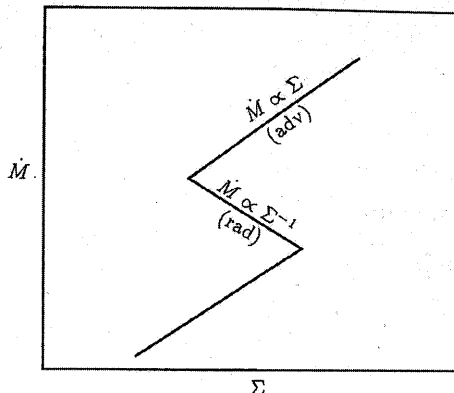


Figure 10.3

Schematic picture showing the middle and upper branches of the S-shaped equilibrium sequence. The lines indicated by "rad" and "adv" are the middle and upper branches given by equations (10.6) and (10.7), respectively. The lower branch (gas-pressure-dominated Shakura-Sunyaev disk) is also shown for a comparison (see figure 3.5).

with a smaller \dot{M} , while $Q_{\text{vis}}^+ \sim Q_{\text{adv}}^-$ for a solution with a larger \dot{M} . This result can be understood as follows.

For a fixed r and Σ , the advective cooling rate, Q_{adv}^- , is proportional to \dot{M}^2 , whereas Q_{rad}^- is proportional to $\dot{M}^{1/2}$. When the accretion rate is low, therefore, the heating is balanced by the radiative cooling, $Q_{\text{vis}}^+ = Q_{\text{rad}}^-$, which gives

$$\Sigma \propto \dot{M}^{-1}. \quad (10.6)$$

Namely, the surface density decreases as the mass-accretion rate increases. This equilibrium sequence of disk models on the \dot{M} - Σ plane is sketched schematically in figure 10.3 by the line labeled "rad". It corresponds to the middle branch of the S-shaped equilibrium sequence on the \dot{M} - Σ plane. The lower branch is also shown in figure 10.3.

As the accretion rate \dot{M} increases along the above-mentioned equilibrium sequence (middle branch), the advective cooling eventually becomes non-negligible, since $Q_{\text{rad}}^- \propto \dot{M}$ along the branch [see equations (10.4) and (10.6)], but $Q_{\text{adv}}^- \propto \dot{M}^3$ [see equations (10.5) and (10.6)]. When the advective cooling overcomes the radiative cooling, heat balance is realized by $Q_{\text{vis}}^+ = Q_{\text{adv}}^-$, and we have

$$\Sigma \propto \dot{M}. \quad (10.7)$$

That is, the equilibrium sequence on the \dot{M} - Σ plane turns to the right as \dot{M} increases, as shown in figure 10.3 by the line labeled “adv”. This is the upper branch of the S-shaped equilibrium sequences.

If the proportional coefficient in relation (10.7) is explicitly written, we have

$$\dot{M} \sim \frac{3\pi\alpha\Omega r^2}{\xi} \Sigma. \quad (10.8)$$

Further, the \dot{m} - Σ relation of the upper (slim disk) branch can be expressed approximately as

$$\dot{m} \equiv \frac{\dot{M}}{\dot{M}_{\text{crit}}} \sim \frac{3\sqrt{2}\kappa_{\text{es}}}{4\xi} \left(\frac{r}{r_g}\right)^{1/2} \alpha \Sigma \sim 0.42 \left(\frac{r}{r_g}\right)^{1/2} \alpha \left(\frac{\Sigma}{\text{g cm}^{-2}}\right). \quad (10.9)$$

The numerical coefficient in the final relation has been obtained for $\kappa_{\text{es}} = 0.4$ and $\xi = 1$. Expressions (10.7)–(10.9) are useful for order-of-magnitude arguments. At the same time, however, we should keep in mind that it is not sufficiently accurate in the innermost region of the disks, since we have used an approximation (9.1).

Next, we estimate \dot{M} at the turning point between the middle and upper branches of the equilibrium sequence. Naively, it can be obtained from $Q_{\text{rad}}^- = Q_{\text{adv}}^-$. This condition gives $\dot{M}_{\text{turn}} \sim 16\pi c r^2 / (\kappa_{\text{es}} \xi H)$. Normalizing it by the critical mass-accretion rate, we obtain

$$\dot{m}_{\text{turn}} \equiv \frac{\dot{M}_{\text{turn}}}{\dot{M}_{\text{crit}}} \sim \frac{8}{\xi} \left(\frac{H}{r}\right)^{-1} \left(\frac{r}{r_g}\right). \quad (10.10)$$

Cooling-dominated disks are geometrically thin; i.e., $H/r < 1$. As the mass accretion-rate increases and the disk approaches the slim-disk branch, the disk thickness, H/r , increases because of increasing disk temperature. Since

$$\frac{H}{r} \sim \frac{c_s}{\Omega r} \sim \frac{1}{\Omega r} \left(\frac{\Pi}{\Sigma}\right)^{1/2} \sim \frac{1}{\Omega r} \left(\frac{\Omega \dot{M}}{2\pi\alpha\Sigma}\right)^{1/2}, \quad (10.11)$$

and from $\dot{M} \sim (3\pi\alpha\Omega r^2/\xi)\Sigma$ [equation (10.8)], we have

$$\frac{H}{r} \sim 1 \quad (10.12)$$

for $\xi \sim 1$. That is, the flow is roughly conical⁴ with $H/r \sim 1$, independent of \dot{M} [cf. equation (9.17) in ADAF]. It then follows from equation (10.10)

⁴In flows with a small ξ (i.e., a small α), H/r exceeds unity. This suggests that the flows are quasi-spherical rather than disk-like. Similarity solutions by Narayan and Yi (1995a) actually show that the flows are quasi-spherical in many cases, rather than disk-like (see also section 10.5 for simulation results).

that near to the inner edge of the disk the mass-accretion rate at the turning point is on the order of the critical mass accretion rate.⁵

The importance of advective cooling in luminous accretion disks can also be demonstrated from a comparison of relevant timescales. The heating timescale, t_{heat} , defined by Π/Q_{vis}^+ , is $\sim 1/(\alpha\Omega)$ [see equation (3.71)]. This timescale does not depend on \dot{M} and Σ ; i.e.,

$$t_{\text{heat}} \sim \dot{M}^0 \Sigma^0. \quad (10.13)$$

The cooling timescale by radiation, t_{cool} , is Π/Q_{rad}^- and is

$$t_{\text{cool}} \propto \dot{M}^{1/2} \Sigma^{1/2}, \quad (10.14)$$

as can be understood from equation (10.4). The accretion timescale, t_{acc} , is $\sim r/|v_r|$. Mass conservation then leads to

$$t_{\text{acc}} \propto \dot{M}^{-1} \Sigma. \quad (10.15)$$

When the mass-accretion rate is low, t_{heat} is equal to t_{cool} and we have $\Sigma \propto \dot{M}^{-1}$ (the middle branch of the S-shaped equilibrium sequence). Thus, $t_{\text{acc}} \propto \dot{M}^{-2}$. Since $t_{\text{cool}} \sim t_{\text{heat}} \sim \dot{M}^0$ and $t_{\text{acc}} \propto \dot{M}^{-2}$, the accretion timescale decreases as the accretion rate increases, and eventually t_{acc} becomes shorter than t_{cool} , when the accretion rate exceeds a certain critical value. At this stage, the heat generated is balanced by the advective cooling and we have $t_{\text{heat}} \sim t_{\text{acc}}$. This means that $\Sigma \propto \dot{M}$ (the upper branch of the S-curve) and $t_{\text{cool}} \propto \dot{M}$. Since t_{cool} is certainly longer than t_{acc} , the radiative cooling is negligible compared with the advective cooling.

10.1.4 Model Sequence on the T - Σ Plane

How does the equilibrium sequence look on the T - Σ plane? Although the shape is qualitatively unchanged, the slopes are modified. Since in radiation-pressure-dominated disks we have $\Pi \propto T^4 H \propto T^4 (\Pi/\Sigma)^{1/2}$, $\Pi \propto T^8/\Sigma$. Hence, the angular-momentum balance [equation(9.1)] gives

$$\dot{M} \propto \frac{T^8}{\Sigma}. \quad (10.16)$$

The S-shaped curve on the \dot{M} - Σ plane runs as $\dot{M} \propto 1/\Sigma$ [cf. equation (10.6)] in the middle branch. If equation (10.16) is substituted into this relation, we obtain

$$T \propto \Sigma^0. \quad (10.17)$$

⁵Note that the radius where $\dot{M} = \dot{M}_{\text{turn}}$ holds is roughly equal to the trapping radius [see equation (10.2)].

That is, on the T - Σ plane the middle branch of the equilibrium curve is roughly horizontal. On the other hand, the upper branch of the S-curve behaves as $\dot{M} \propto \Sigma$ [equation (10.7)]. If this is combined with equation (10.16), we obtain

$$T \propto \Sigma^{1/4}. \quad (10.18)$$

This is the T - Σ relation on the upper branch of the S-curve.

10.1.5 Disk Luminosity

An important characteristics of slim disks is low efficiency of the energy conversion rate. That is, the accreted matter is swallowed into the central hole without losing the bulk of its internal energy as radiation. The cooling rate due to radiation from a unit surface is proportional to $(\dot{M}/\Sigma)^{1/2}$, as is shown in equation (10.4). This means that Q_{rad}^- is independent of \dot{M} in the slim disks, since $\Sigma \propto \dot{M}$ there [see equation (10.7)]. Although an increase in the accretion rate brings about an increase in luminosity in the standard disk, the amount of radiation is saturated if the accretion rate increases beyond a certain limit, which is $\sim \dot{M}_{\text{crit}}$ in the inner region. This comes from the fact that the temperature of the equatorial region increases with \dot{M} [$T \propto \Sigma^{1/4} \propto \dot{M}^{1/4}$; see equations (10.18) and (10.7)], while the radiative loss from the surface is limited due to an increase of Σ with an increase of \dot{M} [see equations (10.4) and (10.7)].

Then, how much is the maximally attainable luminosity, L_{\max} ? If the above argument about Q_{rad}^- is extended so that a full expression for Q_{rad}^- is obtained, we have

$$Q_{\text{rad}}^- \sim \left(\frac{24}{\xi} \right)^{1/2} \frac{L_E}{2\pi r^2}, \quad (10.19)$$

where $r\Omega_K^2 = GM/r^2$ and $L_E = 4\pi GMc/\kappa_{\text{es}}$ have been used. This result means

$$L_{\max} \sim \int_{r_{\text{in}}}^{r_{\text{out}}} Q_{\text{rad}} 2\pi r dr \sim \left(\frac{24}{\xi} \right)^{1/2} \ln \left(\frac{r_{\text{out}}}{r_{\text{in}}} \right) \cdot L_E, \quad (10.20)$$

where r_{in} and r_{out} are, respectively, the inner and outer radii of the slim-disk region.⁶ It should be noted that L_{\max} is free from the value of α as

⁶In quasi-spherical flows, the logarithmic term in equation (10.20) may not appear, since in disk-like flows radiation can escape from each radius, but in quasi-spherical flows it does only from quasi-spherical photospheres.

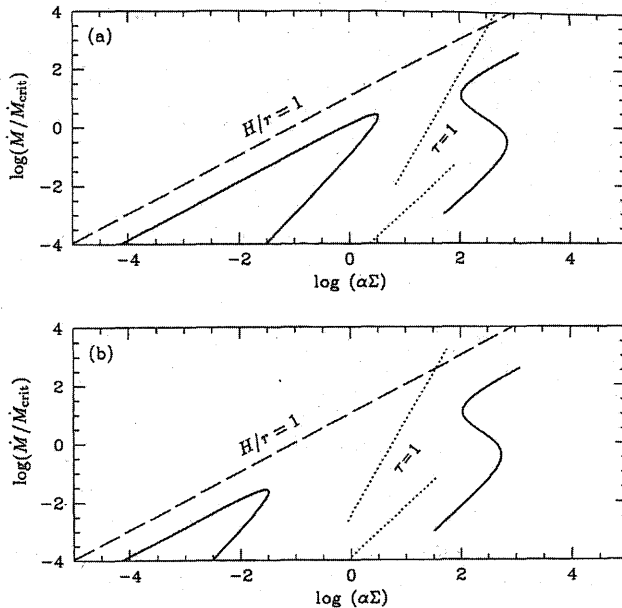


Figure 10.4

Thermal equilibria for optically thick (the right solid S-shaped curve) and optically thin (the left solid curve) accretion disks. The upper branch of the right sequence corresponds to the slim-disk solutions, whereas that of the left sequence corresponds to the optically thin ADAF. The configurations on the left side of the dotted lines ($\tau = 1$) are optically thin, where τ is the effective optical depth calculated by assuming that the pressure is dominated either by radiation (the upper one) or by gas (the lower one). The parameters are (a) $M/M_{\odot} = 10$, $r/r_g = 5$, $\xi = 1$, and $\alpha = 0.1$. (b) The same as those in (a) except for $\alpha = 0.01$. (After Abramowicz et al. 1995)

well as \dot{M} . Furthermore, L_{\max} can overcome the Eddington luminosity⁷ L_E by a factor of $\ln(r_{\text{out}}/r_{\text{in}})$. See figure 9.4 for the L - \dot{M} relation.⁸

Before discussing the S-shaped equilibrium sequence on the \dot{M} - Σ plane in more detail, we display in figure 10.4 a global view of all equilibrium sequences on the plane, which include not only optically thick branches, but also optically thin ones, taken from Abramowicz et al.

⁷These arguments postulate that the disk is nearly face-on to the observer. If the disk is nearly edge-on, conversely, the total disk luminosity could be much less than L_E , since the column density integrated over the line of sight would be much greater than $\Sigma = \int \rho dz$, and thus, photon diffusion time from the disk center to the observer could be much longer than the accretion timescale.

⁸For more careful derivation, see section 10.2. Since $r_{\text{out}} \simeq r_{\text{trap}} \propto \dot{M}$, we obtain $L_{\max} \propto \ln \dot{M}$.

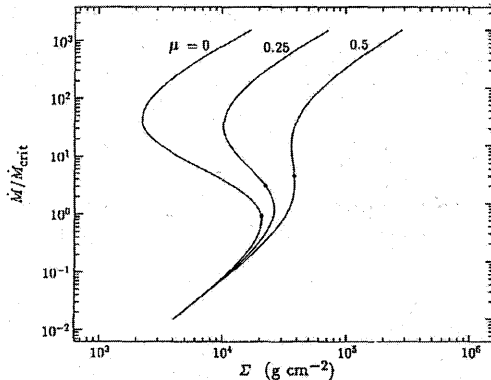


Figure 10.5

S-curves on the \dot{M} - Σ plane at $r = 7r_g$ for models with $\alpha = 0.1$ and $\mu = 0, 0.25$, and 0.5 . The locations of steady disks with $\dot{M}/\dot{M}_{\text{crit}} = 0.96, 3.2$, and 4.8 are indicated by dots on the curves for $\mu = 0, 0.25$, and 0.5 , respectively. (After Honma et al. 1991)

(1995). The S-shaped curve on the right-hand side on this \dot{M} - Σ plane is the sequence of optically thick disks (slim disks) that we are considering here. The left curve of this figure, the optically thin disk sequence, is discussed in section 9.1.

10.1.6 Numerical Models and S-Shaped Sequence

In the previous section, we presented rough models of slim disks based on the assumptions that $\xi = 1$ and $\Omega = \Omega_K$, without performing radial integrations of the momentum and energy equations. To obtain global models accurately, however, we need to numerically integrate the basic equations given in chapter 7. This has been done by many researchers. If the accretion rate is normalized by the critical accretion rate, \dot{M}_{crit} , and the linear scale of disks by the Schwarzschild radius, r_g , the dimensionless forms of the basic equations show that all physical quantities of the disks are described as functions of r/r_g with three⁹ dimensionless parameters: M/M_\odot , \dot{m} ($\equiv \dot{M}/\dot{M}_{\text{crit}}$), and α .

These dimensionless equations are solved under relevant boundary conditions. Usually, the outer boundary conditions are taken so that the disks tend to the Shakura-Sunyaev type α -disks far outside. The inner boundary condition is the regularity condition at the critical radius.¹⁰

⁹If $T_{r\varphi} = -\alpha\Pi_{\text{gas}}^\mu\Pi^{1-\mu}$ is adopted, one more parameter, μ , needs to be specified.

¹⁰Unlike the case of the SSD-ADAF transition (subsection 9.2.3), the SSD-slim disk

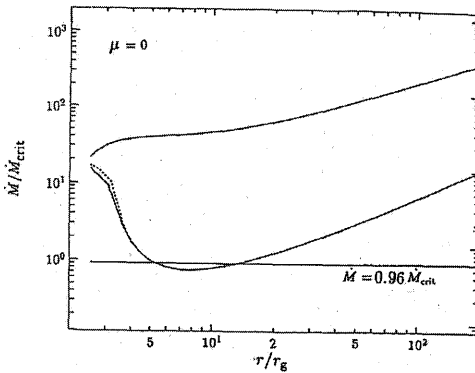


Figure 10.6

Radial distribution of the accretion rates corresponding to the turning points of the S-curves for models with $\mu = 0$. The value of α is 0.1 for all models. A horizontal line is drawn at $\dot{M} = 0.96\dot{M}_{\text{crit}}$. (The dotted curves have no relation to the present problem and should be disregarded here.) (After Honma et al. 1991)

In the case where $T_{r\varphi} = -\alpha\Pi$, or a similar stress form is adopted, no other inner boundary condition is necessary, if the calculations are made inside the critical radius. This is because no information can be transported upstream from inside the critical point. If a diffusion-type stress tensor [$T_{r\varphi} \propto d\Omega/dr$, see equation (7.47)] is adopted, however, one more boundary condition is necessary, since the order of the differential equation increases. This additional boundary condition is taken inside the critical radius. It is usually a no-torque condition at the surface of the black hole or at a certain radius inside of the critical radius.

The basic equations are radially integrated from the outer boundary inward by the semi-implicit method for an *a priori* given ℓ_{in} . When ℓ_{in} is larger (or smaller) than the correct value, the radial velocity vanishes (diverges) before r_g . We then iterate ℓ_{in} to find an appropriate value, for which a transonic solution is obtained.

Let us present the numerical results obtained by Honma et al. (1991) in the following. They adopted $T_{r\varphi} = -\alpha\Pi_{\text{gas}}^\mu\Pi^{1-\mu}$. Figure 10.5 is the $\dot{m}-\Sigma$ relation at $r = 7r_g$ with $M/M_\odot = 10$ and $\alpha = 0.1$. Three cases of $\mu = 0, 0.25$, and 0.5 have been considered. When the accretion rate is low, the disk is on the lower branch of the curve, where the gas pressure dominates over the radiation pressure. As the accretion rate,

transition is smooth, since there is no abrupt changes in the radiative cooling rate at a transition zone.

\dot{m} , increases, the disk enters into the middle branch of the curve, where the radiation pressure dominates over the gas pressure (see section 3.2). These two branches are nothing but a locus representing the balance between the viscous heating and the radiative cooling; i.e., $Q_{\text{vis}}^+ = Q_{\text{rad}}^-$. The heating dominates ($Q_{\text{vis}}^+ > Q_{\text{rad}}^-$) on the right-hand side of the curve, while the cooling dominates on the left-hand side ($Q_{\text{vis}}^+ < Q_{\text{rad}}^-$). If the accretion rate increases further, the disk enters into the upper branch, where advective energy transport is efficient.

Figure 10.6 shows the radial dependences of \dot{m} at the two (upper and lower) turning points of the S-shaped curve for models with $\mu = 0$. We fixed $\alpha = 0.1$. Figure 10.6 shows that the disk with $\dot{m} = 0.96$ is on the middle branch of the S-curve at $5r_g \lesssim r \lesssim 15r_g$. The disk is on the lower branch otherwise. When $\dot{m} = 1.6 \times 10^2$, on the other hand, the disk is on the upper branch at $r \lesssim 60r_g$ and is on the middle branch otherwise.

10.2 Radial Structure of Slim Disks

In this section, we examine a more detailed structure of the slim disk based on the numerical and semi-analytic models. For numerical integration, it is important to solve the equations even inside the marginally stable circular orbit at $3r_g$, since matter still exists inside and, as we will see later, there is significant amount of emission originating from the region inside $3r_g$, when $\dot{M} > 10\dot{M}_{\text{crit}}$ ($\dot{m} > 10$). Also, we need to consider that the flow is transonic (chapter 8).

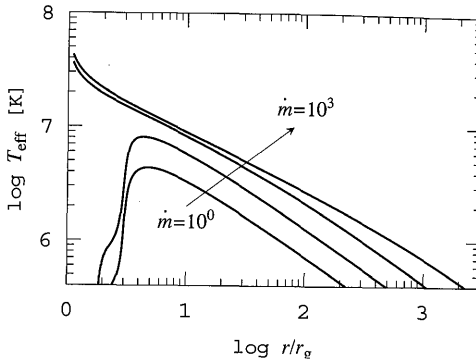
10.2.1 Effective Temperature Profiles

Let us first show the radial effective-temperature profiles in figure 10.7.¹¹ The adopted mass-input rate is $\dot{m} = 1, 10, 100$, and 10^3 . When \dot{m} is small, the disk is not affected by advection. When \dot{m} is large, on the other hand, the disk should inevitably be influenced by photon advection, at least in the innermost part.

As stated in section 3.2, a standard-type disk has an effective temperature profile of $T_{\text{eff}} \propto r^{-3/4}$. This no longer holds when advective energy transport is effective. Watarai and Fukue (1999) found $T_{\text{eff}} \propto r^{-1/2}$ in a slim disk based on a self-similar solution (see also Wang and Zhou 1999; Fukue 2000, 2004).¹² This can be simply understood as follows.

¹¹This calculation is based on the pseudo-Newtonian potential. A full relativistic treatment was made by Beloborodov (1998).

¹²In the case where the wind mass loss from the surface of disks is substantial, the effective temperature profile depends on the radial dependence of the wind mass-loss

**Figure 10.7**

Temperature profiles of the calculated disks. The parameters are $M = 10M_\odot$, $\alpha = 0.1$, and $\dot{m} = 1, 10, 10^2$, and 10^3 . (After Watarai et al. 2000)

In the case of standard-type disks, a (constant) fraction of gravitational energy released via accretion goes to radiation; that is,

$$2\pi r^2 \cdot \sigma T_{\text{eff}}^4 \propto \frac{GM\dot{M}}{r} \propto r^{-1}, \quad (10.21)$$

leading to $T_{\text{eff}} \propto r^{-3/4}$. In slim disks, in contrast, the fraction of energy that goes to radiation that can leave the disk surface is proportional to $t_{\text{acc}}/t_{\text{diff}} \propto r$ [see equation (10.1)¹³]. We thus find

$$2\pi r^2 \cdot \sigma T_{\text{eff}}^4 \sim \frac{GM\dot{M}}{r} \frac{t_{\text{acc}}}{t_{\text{diff}}} \propto r^0, \quad (10.22)$$

and obtain $T_{\text{eff}} \propto r^{-1/2}$.

10.2.2 Remark on the Inner Edge of the Disk

There is another important feature: an inward shift of the inner edge of the disk. Figure 10.7 clearly demonstrates that the inner edge of the disk practically moves inward from $\sim 3r_g$ to $\sim r_g$ as \dot{m} increases. How can we understand this shift?

When \dot{m} is small, we may set the inner boundary at $3r_g$, since the density abruptly decreases inside $\sim 3r_g$ (or more exactly, inside the critical radius at $< 3r_g$; recall that an abrupt increase of v_r leads to a rapid

rate (Kitabatake et al. 2002; Fukue 2004).

¹³This equation leads to $t_{\text{acc}}/t_{\text{diff}} = (2/3)(r/H)\dot{m}^{-1}(r/r_g) \propto r$ for a fixed r/H and \dot{m} .

decrease in the density because $\dot{m} \propto 2\pi r v_r \Sigma$ is kept constant in space). This is related to the well-known fact that there is no stable circular orbit of a test particle at radii inside the marginally stable circular orbit, $r < r_{\text{ms}}$ ($= 3r_g$ for cases of disks around non-rotating black holes). For this reason, this radius has been regarded as being the inner boundary of the disk (e.g., Shakura and Sunyaev 1973). In fact, it has been shown by X-ray observations of black-hole binaries that the radius of the inner boundary, estimated through a spectral fitting to the X-ray data, is constant in time despite large-amplitude variations in the luminosity, and it coincides with $3r_g$ within the error bars (see subsection 3.2.6).

Caution should be taken regarding this argument, however, since all of the accreting material should eventually pass through the regions of $r < r_{\text{ms}}$ before finally falling across the event horizon. That is, a certain amount of materials should at any time exist in the region inside r_{ms} . However, the matter density inside r_{ms} is extremely small in the case of $\dot{m} \ll 1$, so that the inner region should be optically thin, thus emitting fewer photons. Hence, it has no observational significance.

Contrary to this well-known fact, figure 10.7 clearly demonstrates that as \dot{m} increases the effective temperature drastically increases inside $\sim 3r_g$ when $\dot{m} \gtrsim 30$. This reflects the fact that the surface density inside this radius is so large that the innermost part can be optically thick. Why does this occur? A simple answer is because of very high accretion rates. For high \dot{M} , the density should also be high. (Although velocity is also high, it cannot exceed the free-fall velocity). Note also that in supercritical flow the accretion velocity is already close to the sound speed, even at $r > 3r_g$, and thus v_r does not significantly increase across the transonic (critical) point at $r_c \lesssim 3r_g$. Therefore, a considerable amount of matter exists even inside $3r_g$. We can expect significant emission from inside this radius, which should be observable (Watarai et al. 2000).

Further, and more importantly, matter in the slim disk is no longer in force balance between the gravity force due to the central black hole and the centrifugal force. Therefore, the classical argument regarding the inner edge of the disk (subsection 2.5.1) cannot apply to slim disks (Watarai and Mineshige 2003b). The same is true for optically thin ADAFs (see section 9.2).

To summarize, the inner edge of an accretion disk around a black hole depends on the definition; i.e., the turbulence edge, stress edge, reflection edge and radiation edge are defined by each physical process (Krolik and Hawley 2002). That is, the often-used expression “inner edge” does not always correspond to r_{ms} , and we need to properly calculate the radiation

edge, when comparing with observations.

10.2.3 Semi-Analytical Expression for L

To see how the luminosity increase is suppressed in the slim-disk regimes, let us consider a semi-analytical expression for the disk luminosity. Let r_0 be the radius¹⁴ separating the inner slim-disk part (where $T_{\text{eff}} \propto r^{-1/2}$) and the outer standard-disk part (where $T_{\text{eff}} \propto r^{-3/4}$). Then, when the inner part is in the slim-disk regime (i.e., $r_0 > r_g$), the emergent flux ($\propto T_{\text{eff}}^4$) is

$$F(r) = \begin{cases} C_1 \frac{GM}{r_0^3} \frac{L_E}{c^2} \dot{m} \left(\frac{r}{r_0} \right)^{-2} & \text{for } r < r_0 \\ C_1 \frac{GM}{r_0^3} \frac{L_E}{c^2} \dot{m} \left(\frac{r}{r_0} \right)^{-3} & \text{for } r \geq r_0, \end{cases} \quad (10.23)$$

where C_1 is a constant on the order of unity (to be determined later).

It is of great importance to note that r_0 and \dot{m} are mutually dependent via the relation $r_0 \propto \dot{m}$ [see equation (10.2)]. We thus set

$$\frac{r_0}{r_g} = \frac{\dot{m}}{C_2}, \quad (10.24)$$

with C_2 being a constant, about $C_2 \sim 10$ numerically. The total disk luminosity then becomes

$$\begin{aligned} L(r_0) &= 2 \int_{r_g}^{r_{\text{out}}} 2\pi r F(r) dr \\ &= 2\pi C_1 C_2 L_E \left[\ln \left(\frac{r_0}{r_g} \right) + 1 \right] \end{aligned} \quad (10.25)$$

for the case with $r_0 > 3r_g$ ($\dot{m} > 3C_2$) and

$$L = 2\pi C_1 C_2 L_E \left(\frac{r_0}{r_g} \right) \quad (10.26)$$

for the case with $r_0 < 3r_g$ ($\dot{m} < 3C_2$), where we have assumed $r_{\text{out}} \gg r_0$. By using equation (10.24), we finally have

$$\frac{L(\dot{m})}{L_E} \simeq \begin{cases} 1 + \ln \left(\frac{\dot{m}}{30} \right) & \text{for } \dot{m} \geq 30 \\ \frac{\dot{m}}{30} & \text{for } \dot{m} < 30, \end{cases} \quad (10.27)$$

¹⁴Roughly speaking, $r_0 \sim r_{\text{trap}}$.

where a numerical factor, C_1 , was chosen to assure that the formula [equation (10.27)] is continuous and smooth (its derivative is also continuous). For $\dot{m} \gg 1$, we recover equation (10.20).

We wish to stress that even if $\dot{M} \gg \dot{M}_{\text{crit}}$ (i.e., $\dot{m} \gg 1$), L cannot greatly exceed Eddington. Even for $\dot{m} = 10^3$, we find $L/L_E \sim 4.5$.

10.2.4 Semi-Analytic Solutions

Since the basic equations are differential equations with nonlinear terms, we need to rely on the numerical technique to solve the slim-disk structure. Fortunately, however, simple, semi-analytic solutions exist, as in the case of the RIAF (see subsection 9.2.1). Here, we derive the semi-analytic solutions, following Watarai (2006).

If we ignore the energy loss or mass loss via an outflow, the basic equations are:

$$\dot{M} = -2\pi r v_r \Sigma, \quad (10.28)$$

$$v_r \frac{dv_r}{dr} + \frac{1}{\Sigma} \frac{d\Pi}{dr} = r(\Omega^2 - \Omega_K^2) - \frac{\Pi}{\Sigma} \frac{d \ln \Omega_K}{dr}, \quad (10.29)$$

$$\dot{M}(\ell - \ell_{\text{in}}) = 2\pi r^2 \cdot \alpha \Pi, \quad (10.30)$$

$$(2N+3) \frac{\Pi}{\Sigma} = H^2 \Omega_K^2, \quad (10.31)$$

$$Q_{\text{adv}}^- = Q_{\text{vis}}^+ - Q_{\text{rad}}^- = f Q_{\text{vis}}^+, \quad (10.32)$$

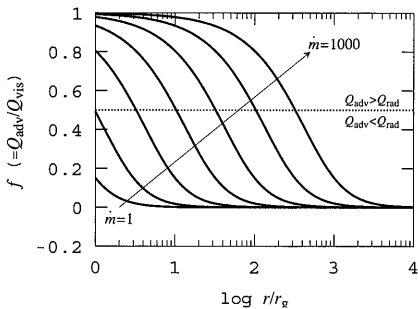
where Σ , ℓ , ℓ_{in} , Π , and H are the surface density, specific angular momentum ($\ell = r^2\Omega$), angular momentum at inner edge of the disk, the height-integrated total pressure as defined by $\Pi \equiv \int p dz$, and the scale height. We assumed a polytropic relationship, $p_0 = K\rho_0^{1+1/N}$, in the vertical direction, where N is the polytropic index (see subsection 7.2.1). Unlike the case of the RIAF self-similar solutions, the fraction of energy dissipated, f , is not assumed here to be constant in space.

We included the effect of radiative cooling on f using the following form:

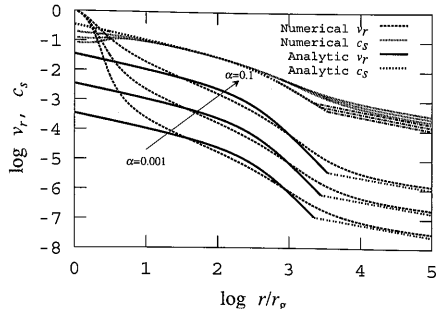
$$f = \frac{Q_{\text{adv}}^-}{Q_{\text{vis}}^+} = \frac{Q_{\text{adv}}^-}{Q_{\text{adv}}^- + Q_{\text{rad}}^-} = \frac{1}{1+g}, \quad (10.33)$$

where g is the ratio of radiative cooling to advective cooling. Assuming that f is constant, we can solve the basic equations to derive the expressions for physical quantities, such as Σ and H . For example, the explicit form of g is

$$g \equiv \frac{Q_{\text{rad}}^-}{Q_{\text{adv}}^-} = \frac{16\pi c r^2}{\kappa_{\text{es}} H \dot{M} \xi} = D x f^{-1/2}, \quad (10.34)$$

**Figure 10.8**

Ratio of the advective cooling rate to the viscous heating rate. The input mass-accretion rates are $\dot{m} = 10^0, 10^{0.5}, \dots, 10^3$ from the bottom to the top. The viscosity parameter is $\alpha = 0.1$ (After Watarai 2006)

**Figure 10.9**

Radial profiles of the radial velocity and the sound speed. The viscosity parameters are $\alpha = 0.001, 0.01$, and 0.1 from the bottom to the top. The input mass-accretion rate is $\dot{m} = 1000$. (After Watarai 2006)

where D is a constant of order unity ($D \approx 2.18$ for $N = 3$ and Keplerian rotation, for example) and $x \equiv \dot{m}^{-1}(r/r_g)$. Substituting equation (10.34) into equation (10.33), we obtained a quadratic equation in f ,

$$f^2 - (D^2 x^2 + 2)f + 1 = 0. \quad (10.35)$$

Thus, f depends on the radius and the accretion rate through x . (In this sense this solution is not an exact solution.)

It is clear from the discriminant of equation (10.35) that although two real roots exist for equation (10.35), the range of f is physically constrained to $0 \leq f \leq 1$. We can finally obtain an analytical solution for f :

$$f(\dot{m}, r) = f(x) = \frac{1}{2} \left(D^2 x^2 + 2 - D x \sqrt{D^2 x^2 + 4} \right). \quad (10.36)$$

In the limit $x \rightarrow 0$, $f(x)$ tends toward unity, which corresponds to a high \dot{M} disk.

Figure 10.8 represents the functional forms of $f(r)$, whereas figure 10.9 shows those of the radial velocity and the sound velocity for several values of α . Except at the inner boundaries, the semi-analytic model nicely reproduces the numerical model.

To conclude this section, we summarize the comparison of the standard disks and slim disks in table 10.1.

Table 10.1 Standard and Slim Disks.

Model	Standard disk	Slim disks
Energy balance	$Q_{\text{vis}}^+ = Q_{\text{rad}}^-$	$Q_{\text{vis}}^+ = Q_{\text{adv}}^-(\text{rad})^\dagger$
Temperature profile	$\propto r^{-0.75}$	$\propto r^{-0.5}$
Luminosity	$L \propto \dot{M}$	$L \propto \log \dot{M}$
Accretion timescale	$t_{\text{acc}} \gg t_{\text{ff}}$	$t_{\text{acc}} \gtrsim t_{\text{ff}}$
Scale-height	$H \ll r$	$H \lesssim r$
Flow shape	disk shape	(nearly) spherical shape

[†] Advection of radiation entropy.

10.3 Radiation Spectra of Slim Disks

To prove the presence of supercritical accretion flow, as well as to test the slim-disk theory, we need to calculate the expected observational spectra to be compared with the observations. In this section, we calculate the spectra of slim disks to clarify any differences from those of standard-type disks.

10.3.1 Basic Spectral Features of Slim Disks

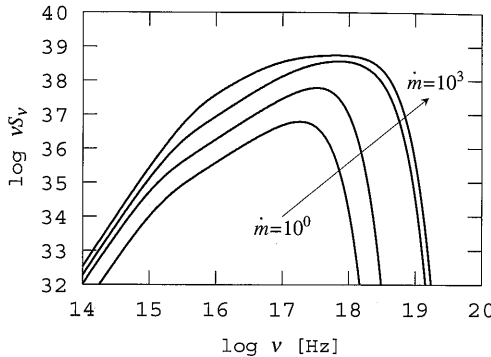
We can calculate the emergent spectra by summing up the blackbody radiation emitted from each radius,

$$S_\nu = \frac{\cos i}{D^2} \int_{r_{\text{in}}}^{r_{\text{out}}} B_\nu[T_{\text{eff}}(r)] \cdot 2\pi r dr, \quad (10.37)$$

where i is the disk inclination angle. The difference in the temperature profile causes a different slope in the spectra in the mid-frequency ranges, since in general $\nu S_\nu \propto \nu^{4-(2/p)}$ for the temperature profile of $T \propto r^{-p}$ (see section 3.2.5); $\nu S_\nu \propto \nu^{4/3}$ in the standard disk (with $p = 3/4$) and $\nu S_\nu \propto \nu^0$ in the slim disk (with $p = 1/2$). Thus, although both emergent spectra of the two models exhibit similar exponential cutoffs in soft X-ray bands, it is, in principle, possible to discriminate the two models by inspection of the p value (see subsection 10.3.3).

Figure 10.10 displays the spectra of the simulated disks for various values of \dot{m} . Again, we fix the black-hole mass to be $M = 10M_\odot$, and we simply assume $i = 0$ (face-on disk). When \dot{m} is low, the entire disk resides in the standard-disk regime, thus exhibiting $T_{\text{eff}} \propto r^{-3/4}$ and $\nu S_\nu \propto \nu^{4/3}$, while as \dot{m} increases, the parts with a flatter temperature profile ($\propto r^{-1/2}$) expand from the innermost zone, and accordingly, the spectra, νS_ν , becomes flatter and flatter from higher energy parts.

It should be stressed that self-occultation becomes important for high inclination systems (Fukue 2000; Watarai et al. 2005). Since the super-

**Figure 10.10**

Emergent spectra of the calculated disks. The parameters are $M = 10M_\odot$ and $\dot{m} = 1, 10, 10^2$, and 10^3 . (After Watarai et al. 2000)

critical disk is *geometrically thick* in the inner region, in the case of high inclination angles ($i \gtrsim 70^\circ$) the innermost region would be occulted by the outer limb of the disk (see figure G.12), and the observed spectra could be remarkably modified.

10.3.2 Luminosity-Temperature Diagram

To compare with the observations, it is informative to make a plot of the luminosity-temperature (L - T) diagram.

The standard MCD (multi-color disk) relation gives the L - T relation; $L \propto T_{\text{in}}^4$ for a fixed M (see subsection 3.2.6). If we set $r_{\text{in}} = \beta r_g$ with β (≤ 3) being constant, equation (3.89) leads

$$L_{\text{bol}} = 7.2 \times 10^{38} \left(\frac{\xi_1}{0.41} \right)^{-2} \left(\frac{\xi_2}{1.7} \right)^{-4} \beta^2 \left(\frac{M}{10 M_\odot} \right)^2 \left(\frac{T_{\text{in}}}{\text{keV}} \right)^4 \text{ erg s}^{-1}. \quad (10.38)$$

Here, ξ_1 and ξ_2 are correction factors associated with the disk blackbody model (see subsection 3.2.6). If we set $L_{\text{bol}} = \lambda L_E$, furthermore, we have another L - T relation for a given λ :

$$L_{\text{bol}} = 3.1 \times 10^{39} \left(\frac{\xi_1}{0.41} \right)^2 \left(\frac{\xi_2}{1.7} \right)^4 \beta^{-2} \lambda^2 \left(\frac{T_{\text{in}}}{\text{keV}} \right)^{-4} \text{ erg s}^{-1}. \quad (10.39)$$

The standard L - T relation does no longer hold when $\lambda > 1$ ($L > L_E$), since the apparent radius of the inner edge of the disk should shift inward as \dot{m} increases (see subsection 10.2.1). To see this effect more

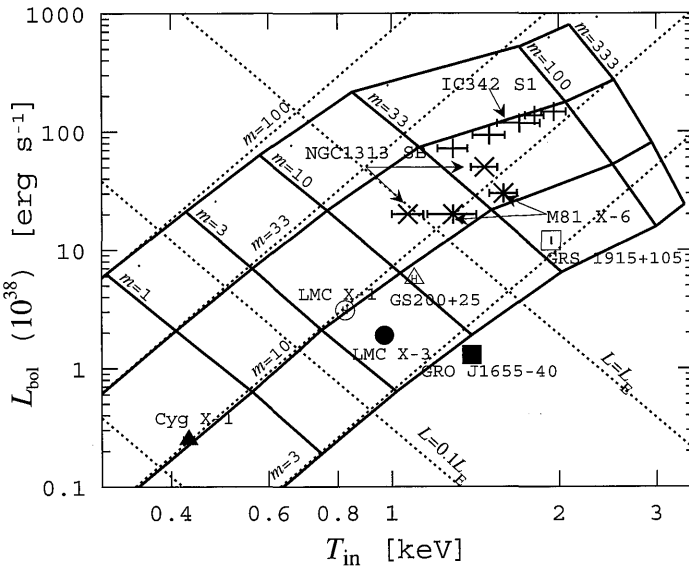


Figure 10.11

Theoretical luminosity-temperature diagram (solid lines) plotted with several observational data. The thin dotted lines indicate the same, but are based on the standard thin-disk models [see equations (10.38) and (10.39)]. ULXs tend to lie along the solid lines. (Adapted from Watarai et al. 2001)

explicitly, we display the relationship between the luminosity, L , and the temperature, T_{in} , in figure 10.11. The calculated ones (the thick lines) certainly deviate downward from those expected by the standard disk model (the thin dashed lines) at high-luminosity regimes. This downward shift could be the observational signatures of the system entering in the slim-disk regime. Interestingly, some ULXs basically follow the trend of the thick lines. This supports the view of the slim-disk model.¹⁵

10.3.3 Spectral Fitting

We next investigate how to obtain more direct identification of the slim disk from the X-ray spectral fitting. For this purpose, we need to recall the disk blackbody (DBB) model [see subsection 3.2.6] and its variant.

¹⁵To be more precise it is possible that color correction, ξ_2 , may increase as \dot{m} increases, thus producing similar trends (Shimura and Takahara 1995; Kawaguchi 2003, Davis et al. 2005). Further studies are necessary.

The extended disk blackbody model (extended DBB model, Mineshige et al. 1994) is the same as the DBB model, except for the temperature profile. In the DBB model, the effective temperature profile is fixed, $T_{\text{eff}} \propto r^{-3/4}$, while in the extended DBB model it is given by

$$T_{\text{eff}}(r) = T_{\text{in}} \left(\frac{r}{r_{\text{in}}} \right)^{-p}, \quad (10.40)$$

with r_{in} , T_{in} , and p being fitting parameters. We can simply calculate the entire disk spectra according to equation (10.37), but with $T_{\text{eff}}(r)$ given by equation (10.40). Making a transformation of the independent variable from r to $T(r)$ in equation (10.37), we have

$$S_{\nu} = \frac{2\pi r_{\text{in}}^2 \cos i}{p D^2} \int_{T_{\text{out}}}^{T_{\text{in}}} \left(\frac{T}{T_{\text{in}}} \right)^{-\frac{2}{p}} B_{\nu}(T) d \ln T. \quad (10.41)$$

To have a good fitting result, especially in p , wider spectral ranges are certainly preferable. In this fitting model, T_{in} and r_{in} are basically determined by the energy and the intensity at exponential roll-over, while p depends on the slope in the lower energy bands (i.e., soft X-rays). Soft X-ray observations are crucial for discriminating the slim disk from the standard disk. Since the soft X-ray slope does not explicitly depend on T_{in} nor r_{in} , the performance of the fitting is usually improved in cases with p deviating from a canonical value of 3/4.

Kubota and Makishima (2004) made spectral fitting of the RXTE PCA data of the black hole binary, XTE J1550–564, with the extended DBB model, finding that the p -value significantly deviates from 0.75 in high luminosity state. Vierdayanti et al. (2006) tried to fit the XMM-Newton EPIC spectra of four ULXs by the extended DBB model and obtained good fits with $p \sim 0.5$, just around the value predicted by the slim-disk theory (see also Okajima et al. 2006). The estimated black-hole masses are $M \lesssim 40M_{\odot}$, and the Eddington ratios are $L/L_E \gtrsim 0.4$. These give good evidence for the existence of supercritical accretion. Further, it is indicated that intermediate-mass black holes are not necessary to explain the observations of (at least some of) high-luminosity ULXs.

10.4 Relaxation Oscillations in Hot Accretion Disks

As discussed in section 10.1, optically thick disk models at a given radius produce an S-shaped equilibrium sequence on the T - Σ plane around $\dot{M} \sim \dot{M}_{\text{crit}}$. The presence of the S-shaped model sequence is quite reminiscent of that found in low-temperature disks with neutral hydrogens

(see chapter 5). However, the underlying physics is totally different; in the present case of radiation-pressure-dominated disks, the appearance of the middle and upper branches is due, respectively, to radiation pressure and advective heat transport (see table 10.2). Nevertheless, a similar disk behavior (i.e., relaxation oscillations) is expected, since in both cases the intermediate branch of the S-shaped curves is thermally unstable, while the other branches are stable (see chapters 4 and 5).

We are now ready to demonstrate how an optically thick disk behaves for a high mass-input rate (comparable to the critical rate). As we have shown in this section, although numerical simulations certainly produce relaxation oscillations, at the same time some difference between the two cases will become clear.

10.4.1 Historical Remarks

To begin with, we first make a few historical remarks. This is because, although plenty of numerical calculations have been made since the discovery of instabilities associated with optically thick, radiation-dominated disks (Lightman and Eardley 1974; Shibasaki and Hōshi 1975; Shakura and Sunyaev 1976), all of the necessary physics (e.g., advective energy transport, relativistic potential well, the nature of transonic flow, etc.) had not always been properly treated.

In 1988, Abramowicz et al. (1988) found that in optically thick disks a large mass-accretion rate leads to advection-dominated disks, where the viscous heating is balanced by advective cooling. This forms the upper branch of the S-shaped equilibrium sequence on the $\dot{M}-\Sigma$ (or $T-\Sigma$) plane (see section 10.1). It is thus natural to expect quasi-periodic bursts of unstable disks from an analogy with the case of dwarf novae (see chapter 5). Even before the discovery of this S-shaped sequence, Abramowicz et al. (1986) suggested that the thermal instability in radiation-pressure-dominated disks would lead to limit-cycle oscillations [see Kato (1983) for another independent suggestion].

After these studies concerning thermal-equilibrium sequences, time-dependent calculations of the thermal perturbations in optically thick, radiation-pressure-dominated disks were started (Matsumoto et al. 1989; Honma et al. 1991; Lasota and Pelat 1991; Chen and Taam 1994). In the following we discuss the behavior of optically thick disks, while presenting the simulation results, and mainly referring to Honma et al. (1991). For simplicity, we assume the disks to be optically thick throughout their

Table 10.2 Two S-Shaped Curves in Accretion Disks

Model (section)	Low-temperature Disk (sections 5.1 and 5.2)	High-temperature Disk (section 10.4)
Typical temperatures	$\sim 10^4$ K	$\sim 10^7$ K
Cause of instability	ionization of H and He	radiation pressure
Upper branch	standard disk (with HII)	slim disk
Middle branch	standard disk (with HI*)	standard disk (p_{rad} -dominated)
Lower branch	standard disk (with HI)	standard disk (p_{gas} -dominated)
Typical timescale	day – years	several seconds
Phenomena	DN and XN eruptions	bursts of GRS1915+105

evolution.¹⁶

We adopt the form of $T_{r\varphi}$ given by equation (7.48). As will be shown in the subsequent sections simulation results depend strongly on the form of $T_{r\varphi}$. This is easy to understand, since, as we have seen in section 10.1, the shape of the equilibrium model sequence on the $\dot{M}-\Sigma$ plane (or the $T-\Sigma$ plane) differs considerably, depending on the prescriptions of $T_{r\varphi}$ (see figure 10.5).

10.4.2 Time-Dependent Simulations

Let us first present the simulation results for $\mu = 0$ [see equation (7.14)] obtained by Honma et al. (1991).¹⁷ The mass-input rate to the disk is $\dot{M}_{\text{in}} = 0.96\dot{M}_{\text{crit}}$, and the mass of the central object and the viscosity parameter are $M = 10M_\odot$ and $\alpha = 0.1$, respectively. For these parameters, the initial location of the equilibrium disk is slightly above the lower turning point of the S-shaped equilibrium sequence at $r = 7r_g$ (see figures 10.5). This means that only in a narrow region around $r = 7r_g$ the initial equilibrium disk is locally unstable against thermal perturbations. Figure 10.6 shows this explicitly; the locally unstable region extends between $5.2r_g$ and $13.1r_g$.

¹⁶Lasota and Pelat (1991) emphasized that when $T_{r\varphi}$ is proportional to the total pressure (the sum of gas and radiation pressures), the inner region of the disks becomes effectively optically thin ($\tau_{\text{eff}} < 1$) and that the disk structure and its time evolution depend critically on the treatment of the transitions between optically thick and optically thin configurations. In the following, however, the disks are taken to be always optically thick, for simplicity.

¹⁷In Honma et al. (1991), the inner boundary is set to be at $2.7r_g$, so as to include the sonic radius within the calculated region. The physical quantities at this boundary are determined at each time step by extrapolating those at two mesh points just outside the boundary. This treatment is appropriate, since in the supersonic region the condition of a given point does not influence the condition of points on the windward side. A fixed outer boundary is set at $2 \times 10^3 r_g$. They employ $\gamma = 5/3$.

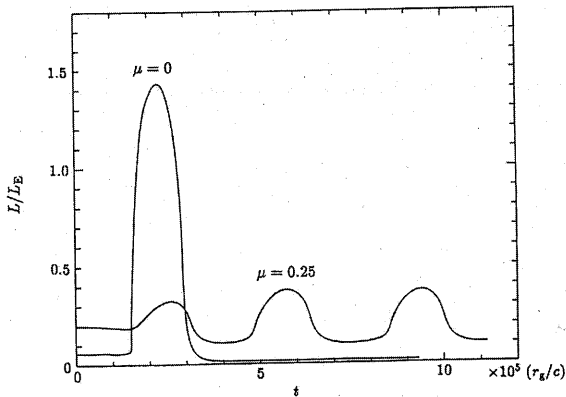


Figure 10.12

Time evolution of the disk luminosity for the cases with $(\mu, \alpha, \dot{M}_{\text{in}}/M_{\text{crit}}) = (0.0, 0.1, 0.96)$ and $(0.25, 0.1, 3.2)$, respectively. (After Honma et al. 1991)

The simulation results are illustrated in figure 10.12 (see the curve labeled $\mu = 0$).¹⁸ The disk exhibits a burst-like time variation. The burst durations are roughly

$$t_{\text{burst}} \sim 43 \left(\frac{\alpha}{0.1} \right)^{-0.64} \left(\frac{M}{10M_{\odot}} \right)^{1.36} \text{ s.} \quad (10.42)$$

Figure 10.13 shows the time evolution of the disk at various fixed radii. The left-hand panels show the paths of the disk evolution on the T - Σ plane, and the right-hand panels show the time variations of the temperature on the equatorial plane. Panels a, b, and c in figure 10.13 are drawn for $r = 5r_g$, $10r_g$, and $50r_g$, respectively.

The disk behavior is quite reminiscent of that of low temperature disks (see chapter 5). Both show a quasi-periodic outburst behavior. Note a difference in the timescales: the variation timescales are much shorter in the present case, on the order of sec to minutes, while it is days to years in the dwarf-nova type instability. Another difference is that the evolutionary paths never reach the upper branch of the S-shaped equilibrium sequence on the T - Σ plane in the present case. That is, the disk does not move straight upwards towards the upper branch of the S-curves after leaving the lower branch. Rather, it moves towards the left to reach a point near to the upper turning point.

¹⁸Also shown in figure 10.12 is the case of $\mu = 0.25$, which is discussed later.

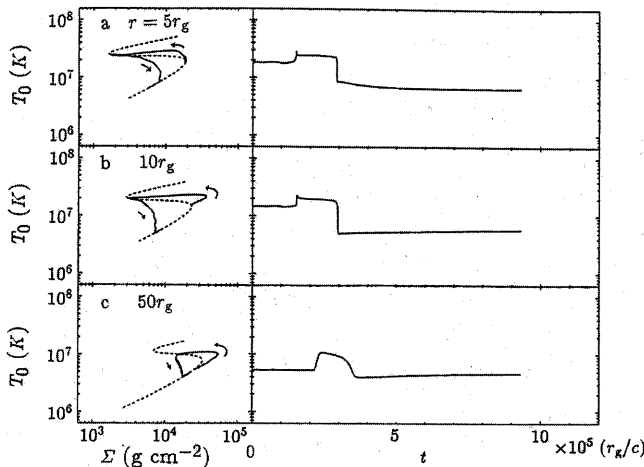


Figure 10.13

T - Σ plane (left panels) and time variations of T (right panels) in the simulation with $(\mu, \alpha, \dot{M}_{\text{in}}/\dot{M}_{\text{crit}}) = (0.0, 0.1, 0.96)$. The S-curves of the steady state are also shown in the left-hand panels by dotted curves. Panels a, b, and c are drawn for $r = 5r_g$, $10r_g$, and $50r_g$, respectively. (Adapted from Honma et al. 1991)

To demonstrate the global behavior of the disk evolution, we show in figure 10.14 the time changes in the radial Σ distribution. This figure shows that the peaks in the Σ distribution are propagating both inwards and outwards from $\sim 5r_g$. Together with figure 10.13, we can understand that the peaks found in figure 10.14 are nothing but transition wave fronts transforming a region in a low-temperature state into a high-temperature one. An inwardly propagating wave can reach the inner boundary (see the time sequence 1), whereas an outwardly propagating one stops at $r \sim 70-80r_g$ at times of $t \sim 3 \times 10^5(r_g/c)$, corresponding to the time sequence 8. After that, the temperature of the hot region suddenly drops, and the entire region settles down on the lower branch.

In the case of a dwarf-nova type instability, transitions from the upper to the lower branch are triggered as soon as the disk reaches the upper turning point. In the present case, however, the hot region of the disk stays for a while near to the upper turning point of the S-curve until the propagation of the outward transition wave stops. This fact implies that the hot region can behave as a global quasi-steady state with $M \gtrsim \dot{M}_{\text{crit}}$.

This difference reflects the fact that the upper branch of radiation-pressure-dominated optically thick disks is realized by a different energy

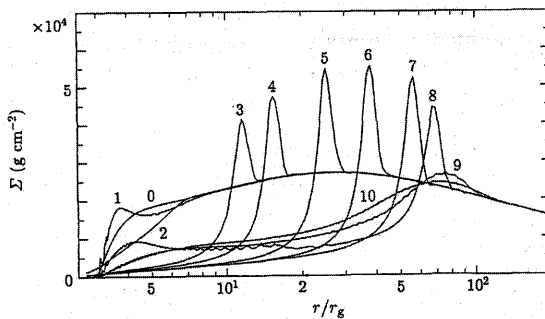


Figure 10.14

Time evolution of the radial distributions of the surface density, Σ , in a simulation with $(\mu, \alpha, \dot{M}_{\text{in}}/\dot{M}_{\text{crit}}) = (0.0, 0.1, 0.96)$. The curves indicated by 0 to 10 represent the Σ distribution at $t = 0, 1.49, 1.5, 1.55, 1.6, 1.75, 2.0, 2.5, 3.0, 5.0$, and 9.3 in units of $10^5(r_g/c)$. (After Honma et al. 1991.)

balance from that of the low-temperature disks (with $T \lesssim 10^4$ K). In the former case, the upper branch of the S-curve is realized by the viscous heating being balanced by advective cooling; in other words, the radial drift time scale is as short as the viscous heating time scale. Hence, the growth of instability is suppressed at a certain stage of evolution, making the hot region quasi-steady. This behavior of the hot region is the most significant feature of the present case of slim disks, in contrast with the case of the dwarf-nova-type instability.

The mass necessary to maintain such a high mass-accretion rate is supplied from the transition wave front continuing to propagate outwards. This is possible because the surface density for the steady state decreases as a point transits to the hot state from the cool state. A part of the excess mass accretes inwards, and the rest accumulates just behind the transition waves, thereby forming the surface density peaks seen in figure 10.14. This situation is exactly the same as that of a dwarf-nova-type instability (see peaks in Σ distribution in figure 5.6).

This continuous mass supply stops when the outward transition wave enters the gas-pressure-dominated region. In this region the surface density decreases outwards, while that of the steady flow with $\dot{M} \gtrsim \dot{M}_{\text{crit}}$ steeply increases outwards. When a region beyond a certain radius transits to the hot state, therefore, some amount of mass must be added to the point to maintain the hot state. The mass accumulated behind the transition wave is spent for this transition and for the mass supply to the inner hot region. When it is consumed, the propagation of the transition

wave as well as the inward mass supply ceases, and the inner hot region falls to the lower branch cooled by radiation.

We next examine the case of $\mu = 0.25$; i.e., $T_{r\varphi} = -\alpha(\Pi_{\text{gas}}\Pi^3)^{1/4}$. Other parameters are $\alpha = 0.1$ and $\dot{M}_{\text{in}} = 3.2\dot{M}_{\text{crit}}$. The location (at $r = 7r_g$) of the initial equilibrium disk on the S-shaped equilibrium sequence is indicated by the dot on the curve labeled with $\mu=0.25$ in figure 10.5; the dot is located in the middle of the middle branch of the S-curve; that is, the locally unstable region is widely distributed around $r = 7r_g$: from $r = 3.8r_g$ to $30.8r_g$. In this case the disk exhibits more regular oscillation patterns with smaller amplitude compared with the case $\mu = 0$. A light curve is shown in figure 10.12 by the curve labeled by $\mu = 0.25$.

Simulations were also performed for the case $\mu = 0.5$; i.e., $T_{r\varphi} = -\alpha(\Pi_{\text{gas}}\Pi)^{1/2}$. The results, however, show no oscillations at all. The disk is globally stable, although the locally unstable region extends over a certain range, say, between $4.0r_g$ and $11.9r_g$ for the case of $\alpha = 0.1$ and $\dot{M}_{\text{in}} = 4.8\dot{M}_{\text{crit}}$.

What is the most important quantity for determining the shape of the light curves? We find that it is \dot{M}_{hot} , the mass-accretion rate into the inner hot regions during a burst. As shown in figure 10.14, at the evolutionary stage when a burst has occurred, a transition wave propagates outwards and an inner hot region is formed and expands. In simulations this hot region is roughly in a steady state with a constant accretion rate, which we denote as $\dot{M}_{\text{hot}}(> \dot{M}_{\text{in}})$. The dependences of the burst duration, t_{burst} , and of the recurrence time of bursts, t_{recur} , on \dot{M}_{hot} are illustrated in figure 10.15 for several values of M . The viscosity parameter and input mass-flow rate are fixed at $\alpha = 0.1$ and $\dot{M}_{\text{in}} = 1.6\dot{M}_{\text{crit}}$, respectively. Note that t_{burst} is rather independent of \dot{M}_{hot} , whereas t_{recur} increases with increasing \dot{M}_{hot} . As a result, the light curve of disk oscillations varies from a burst-like profile to a sinusoidal, regular pattern, as \dot{M}_{hot} increases.

What parameters then determine \dot{M}_{hot} ? Roughly speaking, \dot{M}_{hot} corresponds to the mass-flow rate at $r_{\text{outer}}^{\text{U}}$, the outer edge of the locally unstable zone, and $r_{\text{outer}}^{\text{U}}$ depends on \dot{M}_{in} and μ . As \dot{M}_{in} increases, or as μ decreases, the unstable region tends to expand, thus increasing \dot{M}_{hot} . As shown in figure 10.12, burst-like light variations were obtained for $\mu = 0$ ($r_{\text{outer}}^{\text{U}} = 13.1r_g$), whereas the model with $\mu = 0.25$ ($r_{\text{outer}}^{\text{U}} = 30.8r_g$) produced rather smooth light variations.

Finally, we represent the more recent results by Watarai and Mineshige (2003a). Recently, rapid bursting behavior of a microquasar,

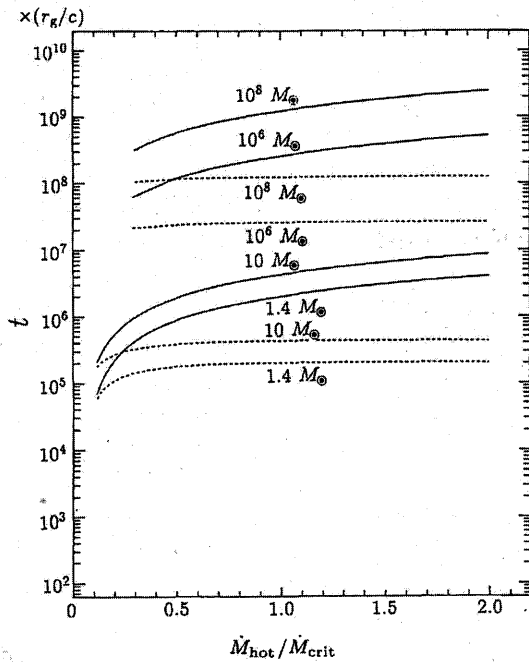


Figure 10.15

Burst duration, t_{burst} , and the recurrence time, t_{recur} , as functions of the accretion rate in the hot inner disk, \dot{M}_{hot} . The values of parameters α and M_{in} are 0.1 and $1.6 M_{\text{crit}}$, respectively. The solid curves are t_{recur} , while the dotted curves t_{burst} . Four cases with $M = 1.4 M_{\odot}$, $10 M_{\odot}$, $10^6 M_{\odot}$, and $10^8 M_{\odot}$ are shown. The value of M is attached for each curve. (After Honma et al. 1991)

GRS 1915+105 (see chapter 1) was discovered, and it has been nearly established that this can be explained by the disk instability model of the sort discussed in this section. Prompted by this discovery, Watarai and Mineshige (2003a) made similar calculations, but, more carefully solved the innermost part of the flow and succeeded in reproducing the basic features of the light variations of GRS 1915+105. Further, they calculated the spectra and fit them with the DBB model, deriving the innermost temperature and the disk inner edge. Figure 10.16 shows the numerical results displayed with the observations of GRS 1915+105. Interestingly, the disk inner edge decreases during the high state, since it is in a slim-disk state, as already explained. The theory nicely reproduces the basic observational trends, although there still exist some discrepancies in the numbers due probably to uncertainties in the spectral hardening factor.

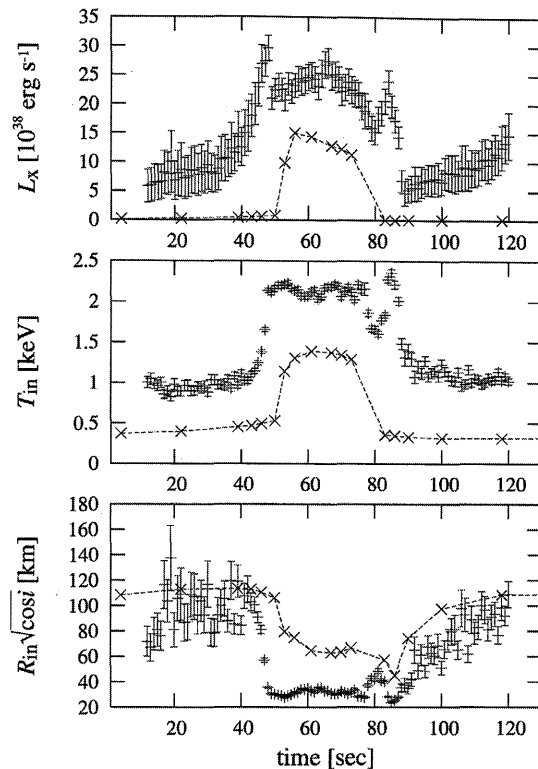


Figure 10.16

Time variations of the disk luminosity (upper), the disk temperature (middle), and the radius of the inner edge of the disk (bottom), respectively. The adopted values are $M = 10M_\odot$, $\dot{M}_{in} = 3.0\dot{M}_{crit}$, $\alpha = 0.1$, and $\mu = 0.1$. (After Watarai and Mineshige 2003a)

This firmly confirms the justification of the disk instability model.

Finally, we wish to note that such oscillations have also been obtained by two-dimensional radiation-hydrodynamical simulations (Ohsuga 2006).

10.5 Multi-Dimensional Effects of Supercritical Flow

As we have seen, the photon trapping effects are treated as radial advection of the photon entropy within the framework of the slim-disk model. However, the slim disk model does not fully consider the photon-trapping effects, since they are multi-dimensional effects. In fact, the photon-trapping is grossly underestimated in the slim-disk model, as we demonstrate in this section.

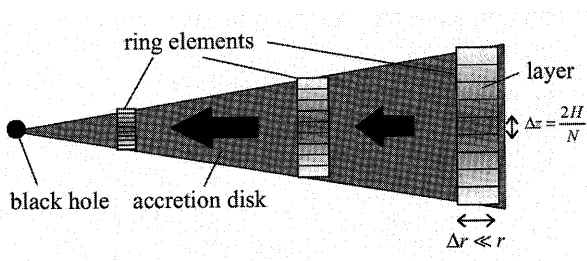


Figure 10.17

Schematic view of the black hole accretion system. We calculate the evolution of the energy fields in a moving ring element until the element reaches the inner edge of the disk. (After Ohsuga et al. 2003)

10.5.1 Issues with the Slim Disk Model

Let us recall what lacks in the slim-disk model more explicitly. The equation of energy balance, $Q_{\text{adv}}^- = Q_{\text{vis}}^+ - Q_{\text{rad}}^-$, is solved in the slim-disk model. The problem resides in that the radiative cooling is evaluated under the usual diffusion approximation (in the vertical direction); i.e., $Q_{\text{rad}}^- \sim \sigma T^4 / \tau$. This approximation may be justified, if the radial inflow of gas is totally negligible, so that photons can mainly diffuse in the vertical direction. This is not always the case, however, within the trapping radius [equation (10.2)], since all of the photons tend to be advected inward (see figure 10.1). A simple treatment for Q_{rad}^- leads to an over-estimation of Q_{rad}^- and, hence, an under-estimation of Q_{adv}^- , compared with the correct value.¹⁹ More importantly, photon trapping modifies the spectral energy distribution (SED), as well. We have found that large photon trapping yields spectral softening, because hard photons that are created deep inside the disk are more effectively trapped than soft photons (Ohsuga et al. 2003).

10.5.2 A Simple Model

To see the two-dimensional (2D) photon trapping effects, we here construct a simple model. In this model, we consider a part of the disk (ring element) that is accreting with time (see figure 10.17). For the given dynamics, we solve the radiation transfer in the vertical direction and the energy equations of gas and radiation within the ring element (Ohsuga et al. 2002, 2003).

¹⁹The viscous heating rate, Q_{vis}^+ , itself is determined solely by the mass-accretion rate, and is independent of the photon-trapping effects.

We consider that the accretion disk is axisymmetric and steady in the Eulerian description; $\partial/\partial\varphi = \partial/\partial t = 0$. The radial component of the velocity is expressed in terms of the free-fall velocity as

$$v_r = -\xi \left(\frac{GM}{r} \right)^{1/2}, \quad (10.43)$$

where ξ is a constant parameter, and its vertical component is prescribed as

$$v_z = \frac{z}{r} v_r, \quad (10.44)$$

i.e., we assume convergence (conical) flow. Note that v_r is related to the viscosity parameter, α , through $v_r \sim \alpha(H/r)c_s$ [equation (3.72)]. We focus on the accreting ring element, whose geometrical width and thickness are Δr and $2H$, respectively, where $\Delta r \ll r$ (see figure 10.17). We suppose the structure of the accretion disk to be locally plane parallel and assume the ratio of the disk-half thickness to the radius, H/r , to be a constant in radius, depending on \dot{m} . The vertical density profile is assumed to be Gaussian, $\rho(z) \propto \exp[-(z/H)^2]$.

We consider the time variations of gas and radiation energy densities in the ring element during the course of accretion motion until the element reaches the inner edge of the disk. Since the flow is steady ($\partial/\partial t = 0$), the time coordinate can be transformed to the spatial coordinates; i.e., $D/Dt = v_r \partial/\partial r + v_z \partial/\partial z$ with v_r and v_z being given by equations (10.43) and (10.44). We solve the energy equations of radiation and gas (see appendix D). To close the set of equations, we apply the multi-frequency flux-limited diffusion approximation (FLD, see appendix D.2).

We first plot the luminosity against the mass-accretion rate in figure 10.18, where the luminosity and mass-accretion rate are normalized by the Eddington luminosity and the critical mass-accretion rate, respectively. The aspect ratio is fixed to be $(H/r) = 1/100$ at $\dot{m}=100$. The luminosity should increase along the thin solid line, if the energy-conversion efficiency, $\eta \equiv Mc^2/L$, is constant. However, it is found that the energy-conversion efficiency decreases with an increase in the mass-accretion rate at $L \gtrsim 2L_E$ due to photon trapping. With figure 10.18 we confirm that photon trapping effects are underestimated in the slim-disk model.

We find an even more striking effect in the calculated spectra; as \dot{m} increases, the peak frequency first increases along with an increase in \dot{m} because of an increase in the disk temperature. When \dot{m} is larger than

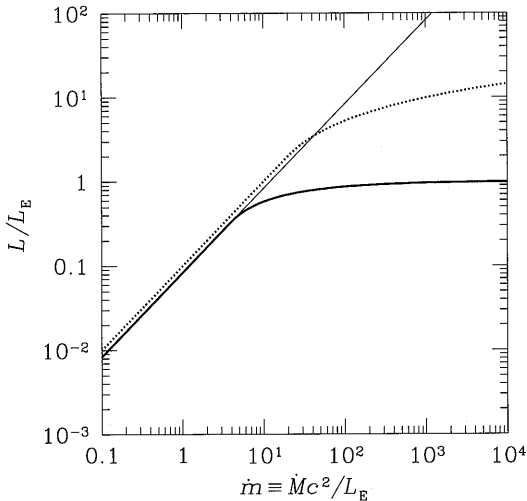
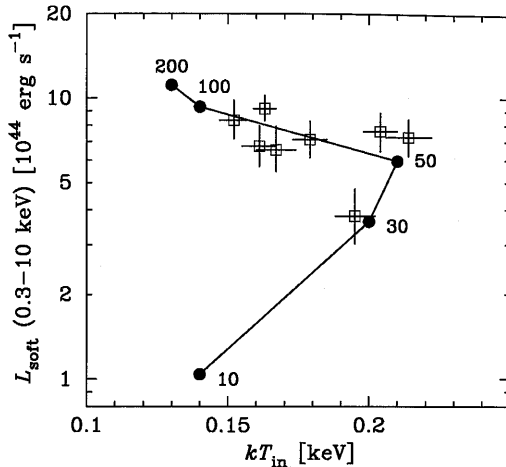


Figure 10.18

Luminosity, L , as a function of accretion rate, \dot{M} , in the units of L_E and L_E/c^2 , respectively. We adopt the parameter $\alpha = 0.1$ ($H/r = 1/100$ at $\dot{m} = 100$). We assume that viscous heat dissipation is available only in the vicinity of the equatorial plane (within $< 0.01H$ with H being the scale-height). For a comparison, we also plot the same but with a constant conversion efficiency (i.e. $L \propto \dot{M}$) by the thin solid line and that of the slim-disk model by the thin dotted line. (Adapted from Ohsuga et al. 2003)

30, in contrast, the peak frequency no longer increases, but decreases. This is because harder photons, which are created preferentially at lower z (near the equatorial plane) and at smaller r (near the black hole) than softer photons, tend to suffer more significant photon-trapping effects.

This, in turn, produces an interesting behavior on the luminosity-temperature diagram (see figure 10.19). We fit the theoretical spectra calculated based on the simple model described above with the DBB model (see subsection 3.2.6) and plot the innermost (maximum) blackbody temperature, T_{in} , as a function of the X-ray luminosity, L_x . The solid lines in figure 10.19 represent the theoretical predictions of the supercritical flow. The most conspicuous nature of supercritical accretion flow is a decrease of the blackbody temperature with an increase of the luminosity. This is actually observed in a narrow-line Seyfert 1 galaxy (NLS1s, see figure 10.19).

**Figure 10.19**

Luminosity-temperature diagram: model predictions and observations of a narrow-line Seyfert 1 galaxy (NLS1). The numbers in the figure indicate the value of \dot{m} . (After Haba et al. 2005)

10.5.3 Radiation-Hydrodynamical Simulations

When considering photon-trapping effects, we should also pay attention to the fact that the supercritical accretion flow becomes geometrically thick. Multi-dimensional gas motion, such as convective or large-scale circulation, might occur. Further, strong outflow might also be generated at the disk surface via the radiation-pressure force. Such complex flow motion will influence the radiation energy distribution through advective energy transport, which in turn affects the flow motion via the radiation-pressure force. We need to carefully solve such strong coupling between radiation and matter. For this purpose, two-dimensional radiation-hydrodynamical (2D-RHD) simulations are indispensable.

Such simulations were pioneered by Eggum et al. (1988) and were improved by Okuda (2002). Ohsuga et al. (2005) were the first to follow the evolution of the supercritical accretion flow until a quasi-steady state under the flux-limited diffusion (FLD) approximation.²⁰ In this subsection, we introduce their simulation results to explain the basic features of the supercritical accretion flow. In their simulations, the mass is continuously injected through the outer-disk boundary, and creates continuous

²⁰See Yin and Miller (1995) for a comparison between the calculations with and without the FLD approximation.

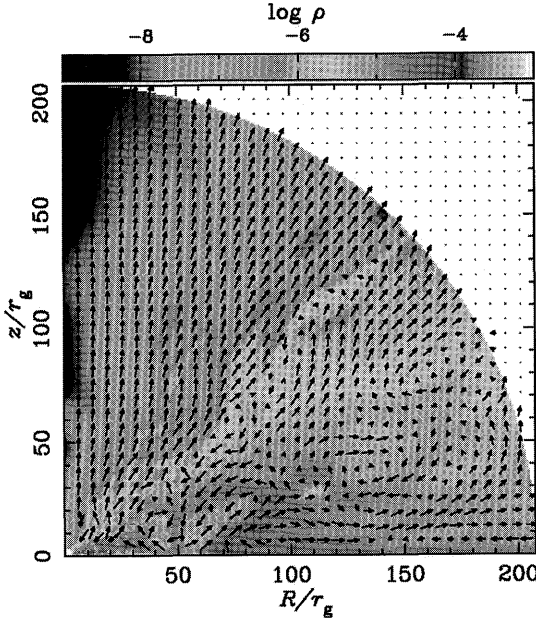


Figure 10.20

Matter distribution of the supercritical accretion flow, overlaid with the velocity vectors (with arrows), onto a black hole with mass of $10M_\odot$ based on the 2-D RHD simulation (see figure G.13 for the color figure). (After Ohsuga et al. 2005)

gas inflow because of the gravity force by the central black hole. Eventually, the viscosity starts to work so that the angular momentum of the gas can be transported outward, which drives inflow gas motion in a quasi-steady fashion. This is the quasi-steady phase.

Let us examine the quasi-steady structure in some detail. Figure 10.20 displays a cross-sectional view of the density distributions (with gray scales), overlaid with the velocity vectors (with arrows) in a quasi-steady state. (Note that starting from an empty disk, the system settles down in the quasi-steady state within several seconds.) We can understand by this figure that the flow structure is roughly divided into two regions: the disk region around the equatorial plane ($z < 0.8r$) and the outflow region above the inflow region ($z > 0.8r$). That is, the disk is geometrically and optically thick, as was predicted by the slim-disk model. However, the density distribution definitely deviates from that of the slim-disk model, since it is neither smooth nor plane parallel

in the vertical direction. We can even see a number of cavities in this figure.²¹ The flow pattern is also complex, though the slim-disk model predicts simple convergence flow. We found prominent circular motion within the disk and strong outflow that is generated at the disk surface.

The radiation energy distribution roughly coincides with the gas-density distribution. That is, the radiation energy tends to be larger around the equatorial plane than that around the rotation axis. Since the radiation energy distribution is smoothed due to radiative diffusion within the disk, there is no cavity found in the radiation energy distribution, which makes a marked difference from the density distribution.

Note that most of the regions are radiation-pressure dominated. Especially, the radiation energy greatly exceeds the gas energy in the entire region, including the outflow region. This confirms that strong radiation pressure supports the geometrically thick disk and drives the outflow. Why is then accretion possible? There are two main reasons: asymmetric matter distribution and photon trapping. Because of high concentration of gas in the disk region radiation flux within the disk region is grossly attenuated (recall radiation energy flux is $F \propto (\kappa\rho)^{-1}\nabla E_{\text{rad}}$ with κ and E_{rad} being the opacity and radiation energy, respectively). Photon trapping also works to reduce the outward radiation flux. Due to the combination of these effects radiation force is largely reduced, which makes accretion possible.

It is found that the gas is accelerated through radiation pressure and is blown away to a large distance. Such a flow component will be identified as a strong disk wind. The outflow will also produce large absorption in the emergent spectra. Therefore, there exists a strong velocity shear at the boundary between the disk region and the outflow region.

10.5.4 Mild Beaming

The most conspicuous signature of the supercritical flow will be a highly anisotropic radiation field. Since the supercritical accretion flows are geometrically and optically thick, the observed images and luminosity should strongly depend on the viewing (inclination) angle. Since the matter density is minimum in the directions along the rotation axis, photons preferentially go along that axis. In addition, the effect of an occultation of the innermost part of the flow by the outer parts should be

²¹Rigorously speaking, we should keep in mind that the FLD approximation may affect such small-scale features.

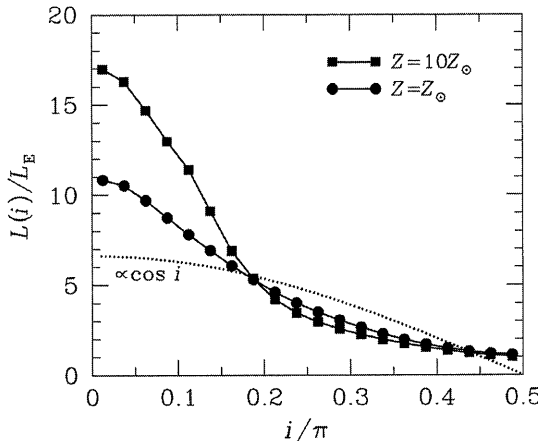


Figure 10.21

Dependence of the observed flux on the viewing angles. We find, at most, a factor of more than 10 variation in the flux. (After Ohsuga et al. 2005)

significant (see Fukue 2000; Watarai et al. 2005). Hence, the innermost region cannot be seen for large inclination angles, i .

The emission from the supercritical accretion flows is mildly collimated for the same reason. Figure 10.21 represents the viewing angle-dependence of the isotropic luminosity²² (normalized by bolometric luminosity) for metallicity values of $Z = Z_\odot$ (circles) and $Z = 10Z_\odot$ (squares), respectively. The other parameters are $\dot{m}_{\text{input}} = 1000$ and $M = 10M_\odot$. Here, the isotropic luminosity is calculated by assuming isotropic radiation field. As expected, the isotropic luminosity is quite sensitive to the viewing angle, indicating that the emission from the flow is mildly collimated. If the flow shape would be flat and (geometrically) thin, and if no collimation would occur, the observed luminosity should vary along the cosine curve, as is indicated by the dotted curve.

Then, why does such a mild beaming occur? There are several reasons for this (Heinzeller et al. 2006). (1) Lower densities and therefore less effective absorption and scattering in the photosphere allow a deeper look into the hotter regions for the face-on case, compared with the edge-on case. (2) The frequency of the escaping photons is shifted by the Doppler effect, increasing the average photon energy for the face-on case. (3) Photons can escape more easily through the diluted medium along the polar axis, while they get stuck in the dense disk-like structure

²²This is the luminosity calculated from the observed flux for a viewing angle i based on the assumption of isotropic radiation field.

concentrated in the mild-plane. To summarize, both of average photon energy and the photon number increase as the viewing angle decreases, causing mild beaming.

We also find that the angle dependence of the isotropic luminosity is more enhanced in the large-metallicity case of $Z = 10Z_{\odot}$ than that of $Z = Z_{\odot}$. This is because of a different density distribution. The mass-outflow rate is smaller in the high-metallicity case than in the low-metallicity case. As a result, the density contrast between the disk region and the outflow region above the disk becomes larger with an increase of the metallicity. Accordingly, the hot innermost region of the high metal flows is easier to be observed, owing to a smaller optical depth in the outflow region for small viewing angles.

Supercritical accretion flows can be identified as very high L/L_E objects in the face-on case, since the emission is mildly collimated in the polar direction, and the bolometric luminosity, itself, exceeds the Eddington luminosity. The former effect is enhanced in the case of high metallicity (large absorption opacity). It is also true that supercritical flow may be identified as a fairly sub-critical source, if the viewing angle is large (Watarai et al. 2005).

10.6 Neutrino-Cooled Disks

Finally, we outline the theory of a hyper-critical accretion disk (or hyperaccreting disk) with huge accretion rates of $\dot{M} \sim M_{\odot} \text{ s}^{-1}$. Since such disks can cool efficiently via neutrino emission, the disk structure is similar to that of standard disks, and not of slim disks.

10.6.1 Accretion Model of Gamma-Ray Bursts

Gamma-ray bursts (GRBs) are the most energetic explosions that ever occur in the Universe (see reviews by, e.g., Piran 2005; Mészáros 2002, 2006). They release an enormous amount of energy of $\sim 10^{51} - 10^{53}$ erg in only a few seconds to a few tens of seconds. It is also widely argued that GRBs result from converting the kinetic energy of ultra-relativistic particles created within fireballs. However, the central engines of GRBs creating the initial hot plasma or extremely energetic particles are not well understood yet, mainly due to the fact that they are hidden from our view.

It is usually argued that relativistic phenomena should be somehow involved, since otherwise it is difficult to explain the huge fluence and

rapid burst profiles (Narayan et al. 1992). Along this line, many interesting possibilities have been proposed so far, such as (1) mergers of double neutron-star binaries, or those of a neutron star and a black hole, (2) a black hole-white dwarf merger, (3) a black hole-helium star merger, (4) a failed supernova (or collapsars), and (5) a magnetar, rapidly spinning neutron star with extremely large magnetic fields. It is of great importance to note that almost all of the models (except for the magnetar hypothesis) predict a similar configuration for the end products; namely, the formation of a few solar-mass black hole surrounded by a debris disk with a mass of $0.01 - 1.0 M_{\odot}$, whose accretion can provide a sudden release of gravitational energy (Mészáros et al. 1999). This gives rise to a huge accretion rate, as

$$\dot{M} \sim \frac{M_{\text{disk}}}{t_{\text{ff}}} \simeq 2 \times 10^{31} \left(\frac{M_{\text{disk}}}{M_{\odot}} \right) \left(\frac{t_{\text{ff}}}{100 \text{s}} \right)^{-1} \text{ g s}^{-1} \quad (10.45)$$

(with M_{disk} being the disk mass and t_{ff} being the free-fall timescale of gas onto the disk), which is more than 10 orders of magnitude larger than the critical rate, $\dot{M}_{\text{crit}} \sim 10^{18} \text{ g s}^{-1}$, for a few solar-mass object. Then, the key issue will be to understand the properties of such a compact and massive disk associated with a huge mass-accretion rate.

Accretion models of GRBs were first considered by Narayan et al (1992), and recently discussed in more detail by Popham et al. (1999) and Narayan et al. (2001). According to them, neutrino cooling, instead of advective cooling or radiation cooling, dominates over radiative loss at very huge accretion rates. Then, the disk can cool and become geometrically thin so that a standard-disk like picture can apply. Therefore, such disks (or flows) are called *neutrino-dominated accretion flow* (NDAF), or neutrino-cooled disks. In the following section, we consider some basics of NDAF, following mostly Kohri and Mineshige (2002).

10.6.2 Basic Physics of Neutrino-Cooled Disks

Since the structure is like that of an optically thick standard disk, the basic equations are rather similar. Hence, we here describe only the basic equations which differ from those of the standard disks (see chapter 3).

First of all, electrons (and nucleon) can be degenerate under such high density ($\rho > 10^8 \text{ g cm}^{-3}$) and temperature ($T > 10^{10} \text{ K}$) regimes. Accordingly, the equation of state needs to be modified. The pressure is composed of three terms:

$$p = p_{\text{rad}} + p_{\text{gas}} + p_{\text{deg}}, \quad (10.46)$$

where p_{rad} is the radiation pressure, p_{gas} is the gas pressure of the nonrelativistic and non-degenerate particles, and p_{deg} is the pressure of the degenerate particles. Note that contributions by a relativistic e^+e^- plasma should be included in the expression of radiation pressure.

Next, we need to make substantial modifications to the cooling rate, which is the summation of three major contributions:

$$Q^- = Q_{\text{rad}}^- + Q_{\text{adv}}^- + Q_{\nu}^-, \quad (10.47)$$

where Q_{rad}^- is the radiative cooling rate, Q_{adv}^- is the advective energy transport (chapter 9), and Q_{ν}^- is the cooling rate due to neutrino loss. The former two are the same as those in the standard disk, but we need to consider electron-positron pairs and neutrino trapping, when the optical depth of neutrino radiation exceeds unity (Di Matteo et al. 2002; Kohri et al. 2005; Gu et al. 2006). The neutrino cooling rate is composed of four terms:

$$Q_{\nu}^- = 2(\dot{q}_{\text{Ne}} + \dot{q}_{e^+e^-} + \dot{q}_{\text{brems}} + \dot{q}_{\text{plasmon}})H, \quad (10.48)$$

where \dot{q}_{Ne} is the electron-positron capture rate by a nucleon, “N”, $\dot{q}_{e^+e^-}$ is the electron-positron pair annihilation rate, \dot{q}_{brems} is the nucleon-nucleon bremsstrahlung rate, and \dot{q}_{plasmon} is the rate of plasmon decay.

Figure 10.22, plotted on the (Σ, T) plane, discriminates between the regions where each pressure component is dominant and also the regions where electrons and/or nucleons are degenerate. We understand that the degeneracy pressure is important at high-density and low-temperature regimes. Such regimes inevitably appear in very massive disks, and one can never neglect the contributions by degeneracy pressure in GRBs, unlike the cases of binary systems or galactic centers. It is interesting to note that the region where advective energy transport dominates covers a rather wide, large- Σ and high- T part of the $\Sigma - T$ diagram. This is because Q_{adv} ($\propto T^{16}$) has a stronger T dependence than Q_{rad} ($\propto T^4$). Also notice that neutrino cooling is essential only at very high temperatures ($T \gtrsim 10^{11}$ K) and very high matter density, $\rho \gtrsim 10^{10}-10^{13}$ g cm $^{-3}$. Here, we adopt the case of the electron fraction, $Y_e \simeq 0.1$, which the numerical simulations of coalescing neutron stars predict (see, e.g., Ruffert et al. 1997).

10.6.3 Equilibrium Curves of Neutrino-Cooled Disks

Since the heating and cooling rates are calculated, we can equate them to obtain the thermal-equilibrium solutions as functions of Σ (or \dot{M}).

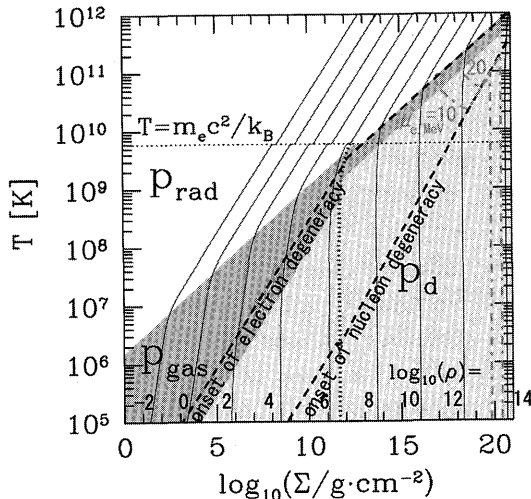


Figure 10.22

Plot of the density contours and the most dominant component in the pressure on the (Σ, T) plane. The adopted parameters are the viscosity parameter, $\alpha = 0.1$, the black-hole mass, $M = 3M_\odot$, and $r = 4r_g$. (After Kohri & Mineshige 2002)

Table 10.3 Various Branches in Optically Thick Disks

branch name	pressure	cooling (entropy)
standard disk I	p_{gas}	Q_{rad}^-
standard disk II	p_{rad}	Q_{rad}^-
slim disk	p_{rad}	$Q_{\text{adv}}^-(s_{\text{rad}})$
degenerate disk	p_{deg}	$Q_{\text{adv}}^-(s_{\text{rad}})$
ν -cooled disk	p_{gas}	Q_ν^-
ν -trapped disk	p_{gas}	$Q_{\text{adv}}^-(s_\nu)$

Figure 10.23 plots the thermal-equilibrium solutions on the (Σ, T) plane for $r = 4r_g$ (left panel) and for $r = 40r_g$ (right panel), respectively. In the parameter region where neutrino cooling is effective, the most dominant cooling process is electron capture ($N + e \rightarrow N' + \nu$). The striped region represents the place where heavy elements are produced, which are expected from the point of view in the equation of state of nuclear matter (Shen et al, 1998; Ishizuka et al. 2002). We can also express the mass-accretion rate, \dot{M} , as a function of Σ .

There are basically 6 distinct branches in the optically thick regimes

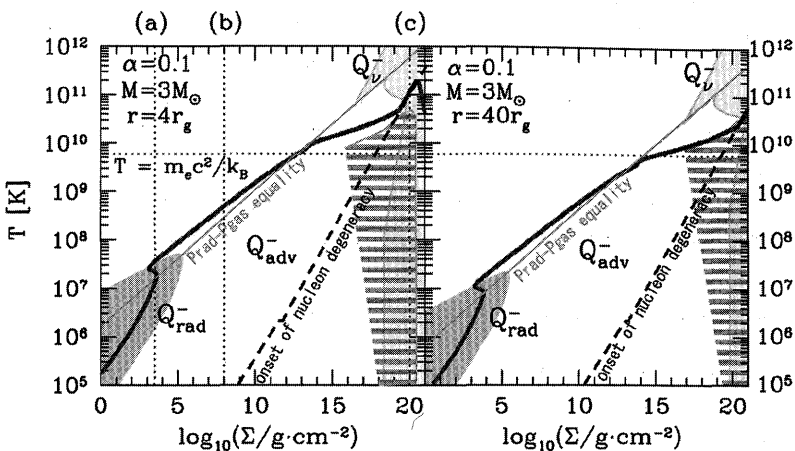


Figure 10.23

Thermal-equilibrium curves of the near- and supercritical the accretion flow. The dominant cooling sources are also indicated. The adopted parameters are the viscosity parameter, $\alpha = 0.1$, the black-hole mass, $M = 3M_{\odot}$, and $r = 4r_g$ (left) and $40r_g$ (right), respectively. The striped region represents place where heavy elements are produced, and there exist just a small amount of free nucleons. (After Kohri and Mineshige 2002)

(table 10.3; see also figure 10.23). In the lower-left parts of both panels, the equilibrium sequence has an S shape (see section 10.1), which arises because of changes in the sources of pressure (gas and radiation pressure) and in the sources of cooling (radiation and advection). In the upper branch of the S shape, advective energy transport takes over radiative cooling. Then, because generated photons inside the disk take a long time to go out from the disk surface, photons are advected inward and are finally swallowed by the central black hole with accreting matter. Such trapping effects should occur for an even higher \dot{M} . Neutrino cooling is dominant only in the high-temperature, high-density regimes, in which neutrinos, instead of radiation, can carry away the generated energy inside the disk. For even higher \dot{M} , neutrino trapping takes place. In the degenerate disk branch (4-th line of table 10.3) although advective cooling is still dominant, the entropy, which is transported by advection, is contributed by non-degenerate nucleons, since the entropy of degenerate particles is small.

It is interesting to examine the stability of each branch. The criteria for the thermal and secular (viscous) instabilities are given in section 4.3. We can understand immediately from figure 10.23 that only radiation pressure-dominant standard disks are unstable for both of thermal and secular (viscous) modes, and that all other branches, including the NDAF branch, are stable for any modes, as already noted by Narayan et al. (2001).

Finally, we should note that massive disks are in general unstable for gravitational instability. This may occur in high- \dot{M} branches.

10.6.4 Properties of Neutrino-Cooled Disks

From the equilibrium solutions of neutrino-cooled disks we derive the following expressions for the temperature and density on the equatorial plane and for the corresponding mass-accretion rates as functions of the radius for a given value of $\Sigma_{20} \equiv \Sigma/10^{20} \text{ g cm}^{-2}$:

$$T = 1.1 \times 10^{11} \Sigma_{20}^{\frac{4}{7}} \left(\frac{r}{4r_g} \right)^{-\frac{6}{7}} \left(\frac{M}{3M_\odot} \right)^{\frac{2}{7}} \text{ K}, \quad (10.49)$$

$$\rho = 2.3 \times 10^{13} \Sigma_{20}^{\frac{6}{7}} \left(\frac{r}{4r_g} \right)^{-\frac{9}{7}} \left(\frac{M}{3M_\odot} \right)^{\frac{3}{7}} \text{ g cm}^{-3}, \quad (10.50)$$

$$\dot{M} = 1.1 \times 10^{17} \dot{M}_{\text{crit}} \left(\frac{\alpha}{0.1} \right) \Sigma_{20}^{\frac{9}{7}} \left(\frac{r}{4r_g} \right)^{\frac{15}{14}} \left(\frac{M}{3M_\odot} \right)^{-\frac{5}{14}}. \quad (10.51)$$

Note that the disk mass, M_{disk} , and its size, r_{out} , are roughly related to the surface density as

$$\Sigma \approx \frac{2M_{\text{disk}}}{\pi b r_{\text{out}}^2} \sim \frac{10^{20}}{b} \left(\frac{M_{\text{disk}}}{1M_\odot} \right) \left(\frac{r_{\text{out}}}{5 \times 10^6 \text{ cm}} \right)^{-2} \text{ g cm}^{-2}, \quad (10.52)$$

where b is a constant on the order of unity, which varies depending on the geometry of the initial torus; we assumed a uniform surface density distribution. Since neutrino emission is substantial at large surface density of $\Sigma \gtrsim 10^{19} \text{ g cm}^{-2}$ (see figure 10.23), we can understand that neutrino cooling dominates only if a solar-mass material is contained within a disk with a size of $\sim 10^7 \text{ cm}$. In other words, if the disk mass is less, or if the disk size is larger, neutrino cooling never becomes dominant.

By comparing the left and right panels in figure 10.23, we can notice that even at such a high surface density as $\Sigma \sim 10^{20} \text{ g cm}^{-2}$, the neutrino cooling does not become dominant at a somewhat larger radius (i.e.,

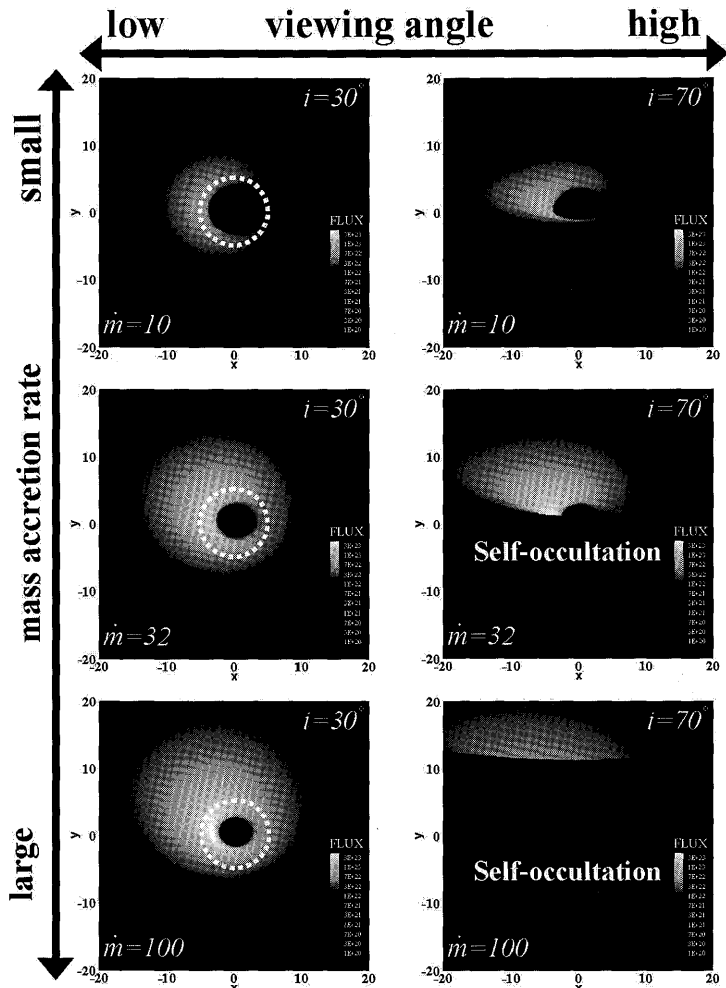
$r \gtrsim 40r_g$). This also supports the claim by Narayan et al. (2001) that the NDAF solution only appears in a rather compact region around the center.

References

- Abramowicz M.A., Chen X., Granath M., Lasota J.-P. 1996, ApJ 471, 762
- Abramowicz M.A., Chen X., Kato S., Lasota J.-P., Regev O. 1995, ApJ 438, L37
- Abramowicz M.A., Kato S., Matsumoto R. 1989, PASJ 41, 1215
- Abramowicz M.A., Czerny B., Lasota J.P., Szuszkiewicz E. 1988, ApJ 332, 646
- Begelman M.C. 1978, MNRAS 184, 53
- Begelman M.C., Meier D.L. 1982, ApJ 253, 873
- Beloborodov A.M. 1998, MNRAS 297, 739
- Boller T. 2000, NewA 44, 387
- Blondin J.M. 1986, ApJ 308, 755
- Chen X., Taam R.E. 1993, ApJ 412, 254
- Chen X., Taam R.E. 1994, ApJ 431, 732
- Colbert E.J.M., Mushotzky R.F. 1999, ApJ 519, 89
- Colpi M. 1988, ApJ 326, 223
- Dotani T., Inoue H., Mitsuda K., Nagase F., Negoro H., Ueda Y., Makishima K., Kubota A., Ebisawa K., Tanaka Y. 1997, ApJ 485, L87
- Czerny B., Elvis M. 1987, ApJ 321, 305
- Davis S.W., Blaes O.M., Hubeny I., Turner N.J. 2005, ApJ 621, 372
- Di Matteo, T., Perna R., Narayan R. 2002, ApJ 579, 706
- Eggum G.E., Coroniti F.V., Katz J.I. 1987, ApJ 323, 634
- Eggum G.E., Coroniti F.V., Katz J.I. 1988, ApJ 330, 142
- Flammang R.A. 1984, MNRAS 206, 589
- Fujita M., Okuda T. 1998, PASJ 50, 639
- Fukue J. 2000, PASJ 52, 829
- Fukue J. 2004, PASJ 56, 569
- Gu W.-M., Liu T., Lu J.-F. 2006, ApJ 643, L87
- Haba Y., Terashima Y., Kunieda H., Ohsuga K. 2004, in *Proc. 35th COSPAR Scientific Assembly*, p.1791
- Heinzeller, D., Mineshige, S., Ohsuga, K. 2006, hMHRAS 372, 1208
- Honma F., Matsumoto R., Kato S. 1991, PASJ 43, 147
- Houck J.C., Chevalier R.A. 1992, ApJ 395, 592

- Kato, S. 1983, in *Theoretical Aspects on Structure, Activity, and Evolution of Galaxies*, eds S. Aoki, M. Iye, Y. Yoshii (Tokyo Astr.Obs. Publ., Tokyo), p.43
- Katz J.E. 1977, ApJ 215, 265
- Kawaguchi T. 2003, ApJ 593, 69
- King A.R., Frank J., Kolb U., Ritter H. 1997, ApJ 482, 919
- Kitabatake E., Fukue J., Matsumoto K. 2002, PASJ 54, 235
- Kohri K., Mineshige S. 2002, ApJ 577, 311
- Kohri K., Narayan R., Piran T. 2005, ApJ 629, 341
- Krolik J.H., Hawley J.F. 2002, ApJ 573, 754
- Kubota A., Makishima K. 2004, ApJ 601, 428
- Ishizuka C., Ohnishi A., Sumiyoshi K. 2002, PTPS 146, 373
- Laor A., Netzer, H. 1989, MNRAS 238, 897
- Lasota J. P., Pelat D. 1991, A&A 249, 574
- Leighly K.M. 1999, ApJS 125, 317
- Lightman A.P., Eardley D.M. 1974, ApJ 187, L1
- Makishima K. et al. 2000, ApJ 535, 632
- Matsumoto H. et al. 2001, ApJ 547, L25
- Matsumoto R., Kato S., Honma, F. 1989, in *Theory of Accretion Disks* ed. F. Meyer, W. J. Duschl, J. Frank, E. Meyer-Hofmeister (Kluwer Academic Publishers, London), p.167
- Mészáros P. 2002, ARA&A 40, 137
- Mészáros P. 2006, Rep. Prog. Phys. 69, 2259
- Mészáros P., Rees M.J., Wijers R.A.M.J. 1999, NewA 4, 303
- Mihalas D., Mihalas B.W. 1984, *Foundations of Radiation Hydrodynamics* (Oxford Univ. Press,Oxford)
- Mineshige S., Kawaguchi T., Takeuchi M., Hayashida K. 2000, PASJ 52, 499
- Mineshige S., Hirano A., Kitamoto S., Yamada T.T., Fukue J. 1994, ApJ 426, 308
- Mitsuda K. et al. 1984, PASJ 36, 741
- Miwa T., Fukue J., Watanabe Y., Katayama M. 1998, PASJ 50, 325
- Narayan R., Yi I. 1995a, ApJ 444, 231
- Narayan R., Paczyński B., Piran, T. 1992, ApJ 395, L83
- Narayan R., Piran T., Kumar P. 2001, ApJ 557, 949
- Ohsuga, K. 2006, ApJ 640, 923
- Ohsuga K., Mineshige S., Mori M., Umemura M. 2002, ApJ 574, 315
- Ohsuga K., Mineshige S., Watarai K. 2003, ApJ 596, 429
- Ohsuga K., Mori M., Nakamoto T., Mineshige S. 2005, ApJ 628, 368
- Okajima T., Ebisawa K., Kawaguchi T. 2006, ApJ 652, L105

- Okuda T., Fujita M. 2000, PASJ 52, L5
Okuda T. 2002, PASJ 54, 253
Piran T. 2005, Rev. Mod. Phys. 76, 1143
Popham R.G., Narayan R. 1992, ApJ 394, 255
Popham R., Woosley S.E., Fryer C. 1999, ApJ 518, 356
Pozdnyakov L.A., Sobol' I.M., Sunyaev R.A. 1977, Soviet Astron. 21, 708
Ross R.R., Fabian A.C., Mineshige S. 1992, MNRAS 258, 189
Ruffert M., Janka H.-T., Takahashi K., Schaefer G. 1997, A&A 319, 122
Shakura N.I., Sunyaev R.A. 1973, A&A 24, 337
Shakura N.I., Sunyaev R.A. 1976, MNRAS 175, 613
Shen H., Toki H., Oyamatsu K., Sumiyoshi K. 1998, PTP 100, 1013
Shibasaki N., Hoshi R. 1975, PTP 54, 706
Shimura T., Takahara F. 1993, ApJ 419, 78
Shimura, T., Takahara, F. 1995, ApJ 445, 780
Stone J.M., Mihalas D., Norman M.L. 1992, ApJS 80, 819
Turner N.J., Stone J.M. 2001, ApJS 135, 95
Vierdayanti K., Mineshige S., Ebisawa K., Kawaguchi T. 2006, PASJ 58, 915
Wang J.-M., Zhou Y.-Y. 1999, ApJ 516, 420
Watarai K., Fukue J. 1999, PASJ 51, 725
Watarai K., Fukue J., Takeuchi M., Mineshige S. 2000, PASJ 52, 133
Watarai K., Mineshige S. 2003a, ApJ 596, 421
Watarai K., Mineshige S. 2003b, PASJ 55, 959
Watarai K., Mizuno T., Mineshige S. 2001, ApJ 549, L77
Watarai K., Ohsuga K., Takahashi R., Fukue J. 2005, PASJ 57, 513
Watarai K. 2006, ApJ 648, 523
Yin, W.-W., Miller, G.S. 1995, ApJ 449, 826



The appearance of black holes with luminous disks at the low inclination angle of $i = 30^\circ$ (left panels) and the high inclination angle of $i = 70^\circ$ (right panels). The normalized mass-accretion rates are $\dot{m} = 10, 32$ and 100 from top to bottom. The dashed curves represent the apparent circles of $5 r_g$. (Courtesy of K. Watarai)

Part IV Oscillations and Waves

CHAPTER 11

Fundamentals of Disk Oscillations

One of the most prominent observational features of stellar-mass black-hole candidates and AGNs is strong and chaotic time variations in X-rays. Power-spectral analyses have revealed that these variations extend in their frequencies over the range of several orders [see chapter 12 of the first edition (Kato et al. 1998)]. In addition, quasi-periodic oscillations (QPOs) are occasionally observed, especially when the sources are X-ray bright. The origins of such a variability still remain to be investigated. Some of them are supposed to be caused by an ensemble of oscillations and waves in the innermost region of accretion disks. Thus, examinations of oscillations and waves in relativistic disks will provide fruitful information regarding the innermost structure of black-hole accretion disks. In fact, solar and stellar interior structures can now be investigated through observations of non-radial oscillations; this method is called helio- and stellar seismology. The field of studying the disk structures by means of disk oscillations is called *discoseismology*. In this chapter we discuss the basic properties of oscillations and waves in disks, emphasizing the unique characteristics of general-relativistic effects.

11.1 Classification of Disk Oscillations

Oscillations and waves¹ are ubiquitous phenomena in physical systems. In accretion disks, as in other systems, we can expect various types of oscillatory motions. They are, in general, the results of restoring forces acting on perturbations. Thus, the characteristics of oscillations can be understood by considering the nature of the restoring forces. In this section we classify oscillations in disks according to the restoring forces acting on them.

¹In this chapter we make no particular distinction between oscillations and waves.

When we consider oscillations and waves in disks, we soon notice that general-relativistic effects are essential. Although one of our main goals here is to clarify the unique characteristics of general-relativistic effects on disk oscillations, we adopt Newtonian dynamics, using a pseudo-Newtonian potential given by Paczyński and Wiita (1980). The reasons are that Newtonian dynamics is a perspective for non-experts of general relativity, and also that the pseudo-Newtonian approximation is sufficient to qualitatively understand some general-relativistic effects. Readers who are interested in general-relativistic formulations of disk oscillations are recommended to consult Ipser and Lindblom (1991a, b, 1992), Ipser (1994, 1996), Perez et al. (1997), and papers referred therein.

11.1.1 Restoring Force and Disk Oscillations

The restoring forces in non-rotating, extended hydrodynamical systems are those due to pressure as well as entropy stratification. The former gives rise to *acoustic oscillations*, while the latter causes *internal gravity oscillations*, or *convection*. If there are magnetic fields, additional restoring forces resulting from magnetic pressure and tension appear.

In accretion disks, in addition to the above-mentioned restoring forces, strong restoring forces act on perturbations. One is a force resulting from rotation, and the other from a vertical gravitational field. The former gives rise to *radial (horizontal) epicyclic oscillations*, while the latter causes *vertical epicyclic oscillations*.

(a) Horizontal oscillations (Inertial oscillations)

Unless the specific angular momentum decreases outwards in disks, a fluid element, which is displaced in the radial direction, will return to its original radius due to a restoring force resulting from rotation.² The oscillations resulting from this restoring force are called *inertial oscillations (epicyclic oscillations)*. The frequency of these inertial oscillations is the radial epicyclic frequency, κ (hereafter, we simply call it *epicyclic frequency*, unless there is confusion with the vertical epicyclic frequency), which is given by

$$\kappa^2 = \frac{2\Omega}{r} \frac{d}{dr} (r^2 \Omega) = 2\Omega \left(2\Omega + r \frac{d\Omega}{dr} \right), \quad (11.1)$$

²When a fluid element moves inside (or outside) the equilibrium radius, where the centrifugal force is balanced by the gravitational force due to the central object, the former (latter) acting on the displaced element dominates over the latter (former) on the element so that the element is pushed outward (inward) to return to the equilibrium position.

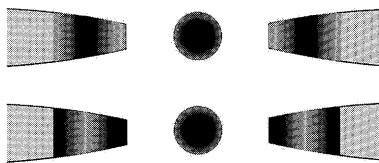


Figure 11.1

Schematic picture showing an inertial-acoustic oscillation in the innermost region of disks. Two phases (just anti-phases) of oscillation are shown. Light and shade show density variation. The central circle represents a black hole.

in a Newtonian case, where $\Omega(r)$ is the angular velocity of disk rotation. Moreover, in a Keplerian disk, $\Omega = \Omega_K$ and $\kappa = \Omega_K$.

In geometrically thin disks, the epicyclic frequency, κ , is much higher than the frequency of the pressure restoring force. That is, the former is on the order of Ω , while the latter is $c_s k$, where k is the radial wavenumber of the perturbations and c_s is the speed of sound. Unless k is larger than $1/H$, we have $c_s k < c_s/H \sim \Omega \sim \kappa$, implying that $\kappa > c_s k$. This means that in the radial oscillations of disks the acoustic oscillations are masked by the inertial oscillations, unless we consider extremely short-wavelength perturbations in the radial direction. In this sense, the acoustic waves in the horizontal direction are called *inertial-acoustic waves*. Hereafter, we use this term when we emphasize the effects of the inertial force. Otherwise, the waves are simply called acoustic waves or p -modes. Figure 11.1 schematically shows an example of inertial-acoustic oscillations in the innermost region of disks.

In figure 11.2, characteristic flow patterns of various oscillation modes are schematically summarized. The uppermost panel of figure 11.2 is the inertial-acoustic oscillations. A classification of various oscillation modes is shown in table 11.1. The inertial-acoustic oscillations are shown in the second line in the table. As described later in detail in section 11.3, n in figure 11.2 and table 11.1 represents the number of node(s) that the horizontal motions have in the vertical direction. The inertial acoustic oscillations have no node ($n = 0$). In this sense, the inertial-acoustic oscillations are the fundamental mode of disk oscillations.

The frequency of the inertial-acoustic waves is on the order of the epicyclic frequency, as mentioned above. Hence, it is very important to know how the epicyclic frequency changes with the radius in order to understand the global behavior of the inertial-acoustic waves in accretion

disks. In Newtonian (and Keplerian) disks, we have $\kappa = \Omega_K \propto r^{-3/2}$. That is, the epicyclic frequency increases monotonically along with a decrease in the radius. In relativistic (and Keplerian) disks, however, the radial distribution of the epicyclic frequency is quite different from that in Newtonian ones; i.e., its distribution in the radial direction is not monotonic (see section 2.5 and figures 2.14 and 2.15). Related to this fact, wave trapping occurs in a relativistic disk, whereas it does not usually occur in the Newtonian case. (This problem is discussed in section 11.3.)

(b) Vertical oscillations

We next consider vertical oscillations of disks. Then, another characteristic of disks appears. This is related to the geometry of the disks, themselves. If a part of the disk plane is perturbed in the vertical direction, a restoring force (i.e., the vertical component of the gravitational force due to the central object) acts so as to restore the perturbed part toward the equatorial plane. This brings about disk oscillations in the vertical direction. The restoring force towards the equatorial plane is roughly $(GM/r^2)(z/r)$, which is $\Omega_K^2 z$ in the Newtonian approximation. This means that the disks make harmonic oscillations around the equatorial plane, *vertical epicyclic oscillations*, and the frequency of the oscillations is called the *vertical epicyclic frequency*, Ω_\perp , which is Ω_K when the central object has no rotation, i.e.,

$$\Omega_\perp = \Omega_K. \quad (11.2)$$

In the case where the central object is rotating, however, Ω_\perp differs from Ω_K , and its general-relativistic expression is given in section 2.5 (see figure 2.15).

The wave resulting from Ω_\perp is similar to the surface waves that occur at the interface between two distinct fluids. In this sense, the waves might be called surface gravity waves. This term, however, could be confused with the naming of gravity waves, which is introduced below. Hence, following a terminology sometimes used in galactic dynamics, we, hereafter, call these waves *corrugation waves* (*c-modes*) (see figure 11.2 and table 11.1). In these vertical waves the vertical displacement associated with the oscillations has no node in the vertical direction (see figure 11.2), i.e., the flows make up-down motions around the equatorial plane. Except for an idealized case, however, horizontal motions are associated with the oscillations [see (c) below], and the horizontal motions have

one node in the vertical direction just on the equator as shown in figure 11.2. In this sense these oscillations belong to the modes of $n = 1$.

Let us proceed to the higher overtones of the vertical oscillations. The corrugation waves discussed in the above paragraph are the fundamental mode in the sense that the vertical displacement of a fluid element has no node in the vertical direction (horizontal motions associated with the waves, however, have one node in the vertical direction as mentioned in the previous paragraph). In the overtones, on the other hand, the vertical displacement has node(s) in the vertical direction. The restoring force acting on such overtones can be regarded as being pressure when there are many nodes in the vertical direction. In this sense, such oscillations are called *vertical-acoustic waves* or *vertical p-modes* (see figure 11.2 and table 11.1).

It is noted that the number of node(s) in the vertical direction, n , in table 11.1 is that for *radial displacement*, but not for vertical displacement. The former is generally larger than the latter by one (see section 11.3 for details).

(c) Coupled oscillations

In the above discussions we have considered horizontal and vertical oscillations in idealized situations. In real disks, however, vertical motions are generally coupled with horizontal motions when their horizontal wavelength is finite. This is because the disks are highly inhomogeneous and finite systems in the vertical direction, and thus vertical motions inevitably induce horizontal motions. Therefore, linear coupling between the horizontal and vertical oscillations inevitably occurs. This generally brings about two kinds of coupled modes (see section 11.3), except for the case where the oscillations are composed of nearly horizontal motions (i.e., inertial-acoustic oscillations). These coupled modes are *higher-frequency modes* and *lower-frequency modes*.³

The vertical epicyclic frequency, Ω_{\perp} , is always higher than the horizontal epicyclic frequency, κ , i.e.,

$$\Omega_{\perp} > \kappa \quad (11.3)$$

(see figure 2.15 in section 2.5). Related to this, the frequencies (in the corotating frame) of the higher-frequency modes are higher than Ω_{\perp} and those of the lower-frequency ones are lower than κ .

³In this subsection, the terms of the “higher frequency” and “lower frequency” refer to the frequency observed in the frame corotating with the disk rotation. That is, they are classified by $\tilde{\omega}$, not by ω [see equation (11.6)].

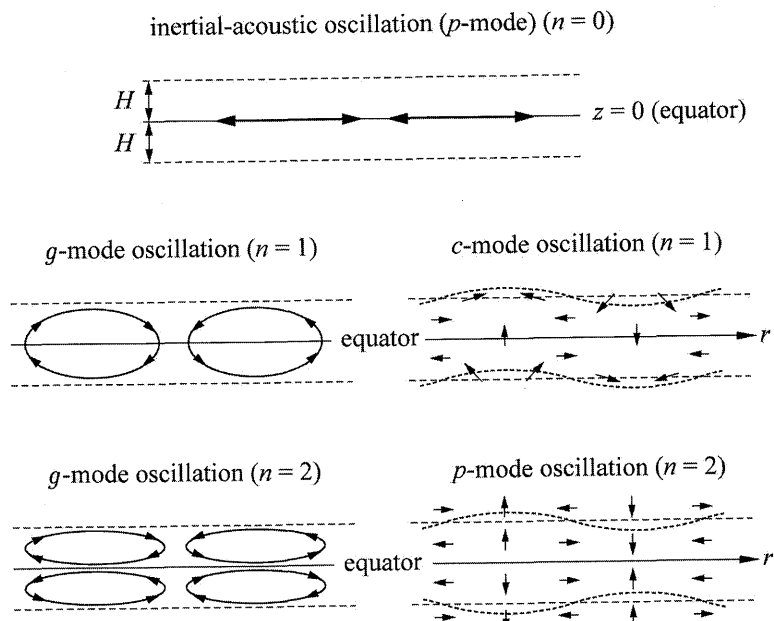


Figure 11.2

Sketches showing flow patterns of basic oscillation modes (with $m = 0$) in the $(r-z)$ plane. The uppermost panel is for inertial-acoustic ($n = 0$) oscillations. The middle two panels are for modes of $n = 1$; g -mode (gravity waves) with $n = 1$ and c -mode (corrugation waves) with $n = 1$. The lower-most panel is for modes of $n = 2$; the g -mode with $n = 2$ and the vertical p -mode with $n = 2$. In each panel, two parallel dashed lines show the typical positions of disk surfaces in the unperturbed state and the solid horizontal line represents the equator. Corrugation waves are mainly up-down motions of the disk gas with a finite radial wavelength, the corresponding deformation of the disk plane being shown by the dashed curve. The arrows in each panel show the direction of flows at a phase, which changes with time.

The wave modes mentioned in (b), i.e., corrugation and vertical p -modes, belong to higher-frequency modes and their characteristics are less changed by the couplings between horizontal and vertical motions. However, the lower-frequency modes of oscillations are new modes of oscillations which are introduced by the coupling. They are called g -mode oscillations (see figure 11.2 and table 11.1).

(d) Buoyancy

So far, we have implicitly assumed that disks are isentropic. If this is not the case, one more important restoring force appears on disk oscillations. This is *buoyancy*. In the case of a star, if the buoyancy is positive,

convection occurs. If it is negative, a fluid element perturbed from the equilibrium position is returned to the original position to make an oscillation around the position. This is the *internal-gravity wave* and the characteristic frequency specifying this oscillation is the *Brunt-Väisälä frequency*.⁴

In the case of disks, however, the situation is somewhat different because of a strong restoring force in the radial direction coming from rotation (inertial force). The effects of buoyancy on oscillations in disks are mainly on the lower-frequency modes classified above [see section 13.3 of the first edition (Kato et al. 1998)]. Even on such modes, however, the effects of buoyancy are rather restrictive for the following reasons.

Table 11.1 Classification of Oscillation Modes.

number of node	frequency	mode	value of $\tilde{\omega}^2$
$n = 0$	low	none	$\tilde{\omega}^2 = 0$
	high	p -modes (inertial-acoustic waves)	$\tilde{\omega}^2 > \kappa^2$
$n = 1$	low	g -modes	$\tilde{\omega}^2 < \kappa^2$
	high	c -modes (corrugation waves)	$\tilde{\omega}^2 \sim \Omega_\perp^2$
$n \geq 2$	low	g -modes	$\tilde{\omega}^2 < \kappa^2$
	high	p -modes (vertical p -modes)	$\tilde{\omega}^2 > n\Omega_\perp^2$

Let us write the square of the *Brunt-Väisälä frequency* in the radial and vertical directions as N_r^2 and N_z^2 , respectively (see the next section for their detailed expressions). If $N_r^2 < 0$, for example, the buoyancy force in the radial direction is positive and acts so that a radially displaced fluid element is further displaced from the equilibrium position (i.e., convection occurs). However, flows in which radial motions dominate over vertical ones (i.e., radially elongated flows) cannot become convective motions, even if N_r^2 is moderately negative. This is because the strong restoring force by rotation overcomes the effects of N_r^2 and suppresses the onset of convection, unless $|N_r^2|$ is rather large.

In the case of vertically elongated flows, unlike the case of radially elongated flows, they can become convective motions if N_z^2 is moderately negative. This is because the restoring force by rotation does not work in the vertical direction.

It is emphasized here that buoyancy does not increase the number of modes of oscillations. The main effects of buoyancy are to change the

⁴In the case of spherically symmetric stars, *Brunt-Väisälä frequency*, N , is given by

$$N^2 = g \left(\frac{1}{\Gamma_1} \frac{d \ln p}{dr} - \frac{d \ln \rho}{dr} \right),$$

where $g (> 0)$ is the gravitational acceleration, p and ρ are pressure and density, respectively, and Γ_1 is a generalized ratio of specific heats (see appendix B).

lower-frequency modes classified above to convective motions or Brunt-Väisälä-type oscillations in an extreme limit. That is, the lower-frequency modes change continuously from those classified above to Brunt-Väisälä oscillations or convections, by a change of the relative importance of the inertial force and (positive or negative) buoyancy force.

Mathematically speaking, the evidence that buoyancy does not increase the number of modes, but changes only the characteristics of the existing modes, is related to the fact that buoyancy does not introduce any additional term with the time derivative in the set of basic equations describing the disk motions (see section 11.2).

(e) Magnetic forces

If global magnetic fields are present in disks, additional restoring forces resulting from magnetic pressure and magnetic tension appear. Unlike the case of buoyancy, they introduce additional new modes of oscillations or instabilities. For example, the mode of (torsional) Alfvén waves gives rise to a magneto-rotational instability (MRI) (section 2.4). Since the MRI comes from a different mode from those classified in (a)–(c), the oscillation modes considered in (a)–(c) are still present on the disks without much modification, as long as the plasma β ($= c_s/c_A$) is larger than unity, even if the disks are turbulent due to the magneto-rotational instability.

11.1.2 Summary on Classification

Summing the above considerations, we introduce the following terms for disk oscillations (see, for details, table 11.1):

1. *Inertial-acoustic modes*: Their frequencies in the corotating frame are slightly higher than κ . They are classified as p -modes in the sense that pressure force is one of the major restoring forces.
2. *Corrugation modes*: They are the high-frequency modes in the corotating frame. The restoring force acting on them is not an inertial force, nor a pressure force. It is a gravitational force and the flow is nearly incompressible. One-armed corrugation waves can have low frequencies in the inertial frame (see section 11.4).
3. *Vertical p -modes*: They are the high-frequency modes, which can be regarded as overtones of the corrugation waves in the sense that the vertical components of the oscillations have nodes in the vertical direction. The pressure force is one of the major restoring

forces of the oscillations. In this sense they can be classified as *p*-modes.

4. *Gravity modes*: They are the lower-frequency ones in the corotating frame, and called *g*-modes.⁵

The classification of oscillation modes is schematically shown in table 11.1, and the characteristics of the flow patterns of the basic oscillation modes are sketched in figure 11.2. In the table and figure, *n* represents the number of node(s) of ξ_r in the *vertical* direction, ξ_r being the radial displacement associated with the oscillations. The number is larger than that of ξ_z by one, where ξ_z is the vertical displacement associated with the oscillations.

Another useful classification of waves is whether the oscillations are axisymmetric or non-axisymmetric. Non-axisymmetric oscillations are important in the sense that they can transport angular momentum in the radial direction. In addition to this, one-armed oscillations have a particular important position in the sense that they can propagate over a wide region of disks and are, under certain conditions, extremely low-frequency modes with a global pattern. This point is discussed in section 11.4.

The oscillations of accretion disks have been extensively investigated by many researchers. Recent reviews concerning disk oscillations are given by Wagoner (1999) and Kato (2001).

11.2 Basic Equations

The behaviors of oscillatory motions in accretion disks are complicated because of the presence of viscous and non-adiabatic processes. Their main effects on oscillations are damping or amplification of the waves. In addition, radial accretion flow introduces further complications. Its effects are mainly frequency shift and transport of the waves with flows. Hence, the main characteristics of the wave modes in accretion disks can be studied by considering the limit of inviscid and adiabatic perturbations, while neglecting the effects of radial accretion flows.

⁵Rigorously speaking, this terminology is confusing and misleading, since the name of the gravity mode might be used only for oscillation modes resulting from entropy stratification in the sense that $N_z^2 > 0$. In the terminology introduced here, however, the gravity modes are present, even when $N_z^2 = 0$ and $N_r^2 = 0$. The reason why we adopt this terminology is twofold: the first is that this classification seems to have been used widely; the second is that the behaviors of the modes are affected by the presence of a non-zero N_z .

An unperturbed disk is assumed to be geometrically thin, steady, axisymmetric, non-self-gravitating, and rotating around a non-rotating compact object. We employ cylindrical coordinates (r, φ, z) , the origin of which is at the central object and the z -axis is the rotation axis of the disk. To mimic the relativistic effects, the gravitational potential due to the central object is taken to be a pseudo-Newtonian one,

$$\psi(r, z) = -\frac{GM}{(r^2 + z^2)^{1/2} - r_g} \quad (11.4)$$

(Paczyński and Wiita 1980), where r_g is the Schwarzschild radius specified by the mass M of the central object. Except for this point, Newtonian dynamics is adopted. The pressure, p_0 , and density, ρ_0 , in the unperturbed disk are assumed to be barotropic; i.e., $p_0 = p_0(\rho_0)$. Hence, the disk rotation is cylindrical in the sense that the angular velocity of rotation, Ω , is a function of r alone; i.e., $\Omega = \Omega(r)$.

Let us consider small-amplitude, non-axisymmetric, inviscid, and adiabatic perturbations on the disk mentioned above. Hereafter, we consider particular modes of perturbations that vary as $\exp[i(\omega t - m\varphi)]$, where ω is the frequency of the perturbations, and m ($= 0, 1, 2, \dots$) denotes the number of arms in the azimuthal direction.

(a) Equation of continuity

The equation of continuity expressed by using cylindrical coordinates is equation (B.27) in appendix B. The velocity (v_r, v_φ, v_z) is decomposed into an unperturbed part, $(0, r\Omega, 0)$, and a perturbed one, (u_r, u_φ, u_z) . The density perturbation over the unperturbed one, ρ_0 , is denoted by ρ_1 . Then, the equation of continuity describing small amplitude perturbations is

$$i\tilde{\omega}\rho_1 + \frac{\partial}{\partial r}(r\rho_0 u_r) - i\frac{m}{r}\rho_0 u_\varphi + \frac{\partial}{\partial z}(\rho_0 u_z) = 0, \quad (11.5)$$

where

$$\tilde{\omega} \equiv \omega - m\Omega. \quad (11.6)$$

(b) Equations of motion

The equation of motion expressed by cylindrical coordinates comprises equations (B.28)–(B.30) in appendix B. Subtracting the terms de-

scribing unperturbed steady flows⁶ from those equations, and retaining only the linear parts with respect to perturbations, we have the r - and φ - , and z -components of the equations of motion as (notice that ψ has no variation and $N = 0$)

$$i\tilde{\omega}u_r - 2\Omega u_\varphi = -\frac{1}{\rho_0}\frac{\partial p_1}{\partial r} + \frac{\rho_1}{\rho_0^2}\frac{\partial p_0}{\partial r}, \quad (11.7)$$

$$i\tilde{\omega}u_\varphi + \frac{\kappa^2}{2\Omega}u_r = i\frac{m}{r\rho_0}p_1, \quad (11.8)$$

$$i\tilde{\omega}u_z = -\frac{1}{\rho_0}\frac{\partial p_1}{\partial z} + \frac{\rho_1}{\rho_0^2}\frac{\partial p_0}{\partial z}, \quad (11.9)$$

where p_1 is the Eulerian perturbation of pressure over p_0 and $\kappa(r)$ is the epicyclic frequency, defined by equation (11.1).

(c) Energy equation

The linearized energy equation for adiabatic and inviscid perturbations is written as [see equation (B.43)]

$$i\tilde{\omega}(p_1 - c_s^2\rho_1) + (\mathbf{u} \cdot \nabla)p_0 - c_s^2(\mathbf{u} \cdot \nabla)\rho_0 = 0, \quad (11.10)$$

where c_s is the speed of sound, defined by $c_s^2 \equiv \Gamma_1 p_0 / \rho_0$, Γ_1 being a generalized ratio of specific heats (see appendix B). Using the *Schwarzschild discriminant vector* \mathbf{A} defined by

$$\mathbf{A} \equiv \nabla \ln \rho_0 - \frac{1}{\Gamma_1} \nabla \ln p_0 = -\frac{1}{\Gamma_1} \nabla \left(\ln \frac{p_0}{\rho_0^{\Gamma_1}} \right), \quad (11.11)$$

the above energy equation is expressed as

$$i\tilde{\omega}(p_1 - c_s^2\rho_1) = \Gamma_1 p_0(\mathbf{u} \cdot \mathbf{A}). \quad (11.12)$$

The Schwarzschild discriminant vector, \mathbf{A} , denotes the degree of the convective instability. If $A_z > 0$, for example, the temperature distribution in the vertical direction is super-adiabatic, and convection can occur in the vertical direction.

⁶The equations of motion describing the unperturbed steady disk are

$$\begin{aligned} -\Omega^2 r &= -\frac{1}{\rho_0}\frac{\partial p_0}{\partial r} - \frac{\partial \psi}{\partial r}, \\ 0 &= -\frac{1}{\rho_0}\frac{\partial p_0}{\partial z} - \frac{\partial \psi}{\partial z}, \end{aligned}$$

for r - and z -components, respectively.

Let us introduce the effective gravitational acceleration, \mathbf{g}_{eff} , defined by

$$\mathbf{g}_{\text{eff}} \equiv r\Omega^2 \mathbf{i}_r - \nabla\psi = \frac{1}{\rho_0} \nabla p_0, \quad (11.13)$$

where \mathbf{i}_r is the unit vector in the radial direction. This is the difference between the gravitational force and the centrifugal force in the unperturbed state. Let us now define N_r and N_z by

$$N_r^2 = -g_{r,\text{eff}} A_r = \left(-\frac{\partial\psi}{\partial r} + \Omega^2 r \right) \frac{1}{\Gamma_1} \frac{\partial}{\partial r} \left(\ln \frac{p_0}{\rho_0^{\Gamma_1}} \right), \quad (11.14)$$

$$N_z^2 = -g_z A_z = -\frac{\partial\psi}{\partial z} \frac{1}{\Gamma_1} \frac{\partial}{\partial z} \left(\ln \frac{p_0}{\rho_0^{\Gamma_1}} \right). \quad (11.15)$$

When $N_z^2 > 0$, the entropy is stratified in the vertical direction so that the medium is convectively stable. The quantity N_z is then a measure of the frequency of oscillations due to entropy stratification, and is called the *Brunt-Väisälä frequency* in vertical oscillations. If $N_z^2 < 0$, the medium is convectively unstable in the vertical direction. A similar argument can be made concerning the radial direction⁷ by using N_r^2 .

It is convenient to introduce in place of p_1 a new variable, h_1 , defined by

$$h_1 \equiv \frac{p_1}{\rho_0}. \quad (11.16)$$

By using h_1 as well as the energy equation, the right-hand side of the equation of motion, equations (11.7) – (11.9), can be written as

$$-\frac{1}{\rho_0} \nabla p_1 + \frac{\rho_1}{\rho_0^2} \nabla p_0 = -(\mathbf{A} + \nabla) h_1 + \frac{i}{\tilde{\omega}} \mathbf{g}_{\text{eff}} (\mathbf{u} \cdot \mathbf{A}). \quad (11.17)$$

In convectively neutral disks, i.e., $\mathbf{A} = 0$, the right-hand side of the equation of motion is reduced simply to $-\nabla h_1$.

In summary, the set of basic equations comprises equations (11.5), (11.7)–(11.9), and (11.12). In some cases, especially in the case of convectively neutral disks (i.e., $\mathbf{A} = 0$), the right-hand sides of equations (11.7)–(11.9) are written in simple forms by using h_1 , as mentioned above.

⁷Unlike the case of the vertical convection, even when $N_r^2 < 0$, we cannot simply conclude that the medium is convectively unstable in the radial direction. This is because there is a strong restoring force exerted in the radial direction due to rotation.

(d) Epicyclic frequency

As the wave classification in the previous section suggests, the epicyclic frequency, $\kappa(r)$, plays an important role in the oscillations of the disk. Furthermore, its radial distribution in relativistic disks is distinct from that of Newtonian disks (see section 2.5), which makes the properties of oscillations in black-hole accretion disks distinct from those in Newtonian disks. Before discussing the details of wave phenomena, therefore, it will be instructive to summarize here the radial profile of $\kappa(r)$ in relativistic disks. We show only the results here (for details, see section 2.5).

In the case of the Schwarzschild metric, we have

$$\kappa_{\text{GR}} = \left[\left(1 - \frac{3r_g}{r} \right) \frac{GM}{r^3} \right]^{1/2} \quad (11.18)$$

for Keplerian rotation, where the subscript GR is attached to κ in order to emphasize that it is the result of general-relativistic calculations (the central source has no rotation). The effects of general relativity appear as the factor $1 - 3r_g/r$. An important result shown in equation (11.18) is that κ has its maximum $(1/16)(GM/r_g^3)^{1/2} = 0.0625(GM/r_g^3)^{1/2}$ at $r = 4r_g$, and becomes zero at $r = 3r_g$. The latter observation corresponds to the well-known fact that a circular orbit at $r = 3r_g$ is marginally stable (see figures 2.14 and 2.15 in chapter 2).

In this chapter a full general-relativistic treatment is not given, and a pseudo-Newtonian potential is adopted, since it is much simpler and suffices for our purpose of basic understanding. In this case the epicyclic frequency becomes

$$\kappa_{\text{PN}} = \left[\left(1 - \frac{3r_g}{r} \right) \frac{GM}{(r - r_g)^3} \right]^{1/2}, \quad (11.19)$$

where subscript PN attached to κ indicates that the frequency is due to the “pseudo-Newtonian” potential. It is zero at $r = 3r_g$, as required, and has the maximum $[(\sqrt{3} - 1)(2 + \sqrt{3})^{-1}(1 + \sqrt{3})^{-3}]^{1/2}(GM/r_g^3)^{1/2} \sim 0.098(GM/r_g^3)^{1/2}$ at $r = (2 + \sqrt{3})r_g \sim 3.73r_g$ (see also figure 2.14). The epicyclic frequency calculated by the pseudo-Newtonian potential, κ_{PN} , satisfies the requirement that it must have a maximum at around $r = 4r_g$, and vanishes at $r = 3r_g$, just the same as in the general-relativistic treatment.

11.3 Dispersion Relation and Basic Properties

In this section our attention is restricted to the case of $\mathbf{A} = 0$ (i.e., $N_r^2 = N_z^2 = 0$, and thus $N^2 \equiv N_r^2 + N_z^2 = 0$), in order to avoid any

complication resulting from the buoyancy force. For brief discussions of the effects of $N_r^2 \neq 0$ and $N_z^2 \neq 0$ on oscillations, see subsection 11.3.6. Also see section 13.3 of the first edition (Kato et al. 1998).

11.3.1 Basic Equations in the Case of $N^2 = 0$

In the case of $\mathbf{A} = 0$, energy equation (11.12) becomes

$$h_1 = c_s^2 \frac{\rho_1}{\rho_0}, \quad (11.20)$$

where we used equation (11.16). Since $\mathbf{A} = 0$, the equations of motion, equations (11.7)–(11.9), are also simplified as [see equation (11.17)]

$$i\tilde{\omega}u_r - 2\Omega u_\varphi = -\frac{\partial h_1}{\partial r}, \quad (11.21)$$

$$i\tilde{\omega}u_\varphi + \frac{\kappa^2}{2\Omega}u_r = i\frac{m}{r}h_1, \quad (11.22)$$

$$i\tilde{\omega}u_z = -\frac{\partial h_1}{\partial z}. \quad (11.23)$$

The remaining equation is the equation of continuity, which is

$$i\tilde{\omega}\rho_1 + \frac{\partial}{r\partial r}(r\rho_0u_r) - i\frac{m}{r}\rho_0u_\varphi + \frac{\partial}{\partial z}(\rho_0u_z) = 0. \quad (11.24)$$

The above five equations comprise the set of basic equations that we study in this section.

The elimination of u_φ from equations (11.21) and (11.22) gives

$$\frac{\partial h_1}{\partial r} - \frac{2m\Omega/\tilde{\omega}}{r}h_1 = \frac{\tilde{\omega}^2 - \kappa^2}{i\tilde{\omega}}u_r. \quad (11.25)$$

Another relation between h_1 and u_r is obtained by eliminating ρ_1 , u_φ , and u_z from equations (11.20) and (11.22)–(11.24):

$$\frac{1}{\rho_0} \frac{\partial}{\partial z} \left(\rho_0 \frac{\partial h_1}{\partial z} \right) + \left(-\frac{m^2}{r^2} + \frac{\tilde{\omega}^2}{c_s^2} \right) h_1 = i\tilde{\omega} \frac{\partial u_r}{\partial r} + i\tilde{\omega} \left(\frac{\partial \ln r \rho_0}{\partial r} + \frac{m\kappa^2/\tilde{\omega}}{2\Omega r} \right) u_r. \quad (11.26)$$

Equations (11.25) and (11.26) are a set of partial differential equations of u_r and h_1 . They should be solved under suitable boundary conditions as eigen-value problems.⁸

⁸If u_r is eliminated from equations (11.25) and (11.26), we have a partial differential equation with respect to h_1 . The corresponding equation in more general situations, i.e., $N^2 \neq 0$, has been derived by Ipser and Lindblom (1992) in the framework of general relativity.

11.3.2 Derivation of Ordinary Differential Equations

Generally, solving the set of partial differential equations (11.25) and (11.26) is complicated. Now, a simple approximate method is introduced to reduce the above set of partial differential equations to a set of ordinary differential equations with respect to z and r . This is made by assuming that the radial wavelength of disk perturbations is less than r (the scale of the radial variation of the equilibrium properties of the disk) (local approximation). The use of this approximation allows us to write the solution of the set of equations (11.25) and (11.26) in separable forms:

$$u_r(r, z) = g(\zeta) \hat{u}_r(r), \quad (11.27)$$

$$h_1(r, z) = g(\zeta) \hat{h}_1(r), \quad (11.28)$$

where ζ is defined by $\zeta = z/H$, $H(r)$ being the disk half-thickness.

Studies of disk oscillations in geometrically thin disks by this approximation have been extensively adopted in the field of discoseismology (e.g., Okazaki and Kato 1985; Okazaki et al. 1987; Nowak and Waggoner 1991, 1992; Perez et al. 1997; Silbergleit et al. 2001). Here, we present the simplest and fundamental case. That is, the disk is assumed to be isothermal in the vertical direction with a nearly constant vertical thickness.⁹ In isothermal disks, the disk thickness, H , is given by $H(r) = c_s/\Omega_K$ and the density is stratified in the vertical direction as (see section 7.2)

$$\rho_0(r, z) = \rho_{00}(r) \exp\left(-\frac{z^2}{2H^2}\right), \quad (11.29)$$

where ρ_{00} is the density on the equator ($z = 0$). This density distribution is obtained by integrating the equation of vertical hydrostatic balance.

Then, an inspection of equations (11.25) and (11.26) shows that they can be separated as follows (Okazaki et al. 1987):

$$\frac{d\hat{h}_1}{dr} - \frac{2m\Omega/\tilde{\omega}}{r} \hat{h}_1 = \frac{\tilde{\omega}^2 - \kappa^2}{i\tilde{\omega}} \hat{u}_r, \quad (11.30)$$

$$\frac{d\hat{u}_r}{dr} + \left(\frac{d \ln r \rho_{00}}{dr} + \frac{m\kappa^2/\tilde{\omega}}{2\Omega r} \right) \hat{u}_r = \frac{1}{i\tilde{\omega}} \left(-\frac{m^2}{r^2} + \frac{\tilde{\omega}^2}{c_s^2} - K \right) \hat{h}_1, \quad (11.31)$$

$$\frac{d^2 g}{d\zeta^2} - \zeta \frac{dg}{d\zeta} + KH^2 g = 0, \quad (11.32)$$

⁹Exactly speaking, the set of the above two approximations (vertical isothermality and $H = \text{const.}$) is inconsistent with the assumptions that the unperturbed disk consists of barotropic gas and is convectively neutral.

where K is a constant resulting from the separation of variables, and should be determined by boundary conditions on the disk surface.

Equation (11.32) is nothing but the Hermite equation. A relevant boundary condition on the surface imposes that KH^2 must be zero or a positive integer (Okazaki et al. 1987). We thus write $KH^2 = n(\geq 0)$. Then, $g(\zeta)$ is the following Hermite polynomial:

$$g(\zeta) = H_n(\zeta) \quad (n = 0, 1, 2, 3, \dots). \quad (11.33)$$

The mode of $n = 0$ is the fundamental one in the vertical direction and h_1 has no node in the vertical direction, while $n = 1$ is the first overtone; h_1 has one node in the vertical direction, just on the equator (odd mode). Higher overtones are represented by n larger than unity.

Since $KH^2 = n$, the set of ordinary differential equations of \hat{u}_r and \hat{h}_1 , i.e., equations (11.30) and (11.31), are written as (hereafter, the hats over u_r and h_1 are omitted without confusion)

$$\frac{dh_1}{dr} - \frac{2m\Omega/\tilde{\omega}}{r} h_1 = \frac{\tilde{\omega}^2 - \kappa^2}{i\tilde{\omega}} u_r, \quad (11.34)$$

$$\frac{du_r}{dr} + \left(\frac{d\ln r \rho_{00}}{dr} + \frac{m\kappa^2/\tilde{\omega}}{2\Omega r} \right) u_r = \frac{1}{i\tilde{\omega}} \left(-\frac{m^2}{r^2} - n \frac{\Omega_K^2}{c_s^2} + \frac{\tilde{\omega}^2}{c_s^2} \right) h_1. \quad (11.35)$$

Hereafter, the term of $-m^2/r^2$ in the parentheses on the right-hand side of equation (11.35) is neglected, since the term is small unless we consider extremely large number of m .

11.3.3 Dispersion Relations

The set of equations (11.34) and (11.35) are now transformed into *canonical forms*. To do so, new variables, Y and F , are introduced, respectively, by

$$F = h_1 \exp \left(- \int \frac{2m\Omega/\tilde{\omega}}{r} dr \right), \quad (11.36)$$

$$Y = r u_r \rho_{00} \exp \left(\int \frac{m\kappa^2/\tilde{\omega}}{2\Omega r} dr \right). \quad (11.37)$$

The set of equations (11.34) and (11.35) are then reduced to their canonical forms:

$$\frac{dF}{dr} = \frac{\tilde{\omega}^2 - \kappa^2}{i\tilde{\omega}} A^{-1} Y, \quad (11.38)$$

$$\frac{dY}{dr} = \frac{1}{i\tilde{\omega}} \left(-n \frac{\Omega_K^2}{c_s^2} + \frac{\tilde{\omega}^2}{c_s^2} \right) A F, \quad (11.39)$$

where

$$A = r\rho_{00} \exp\left[\int \frac{m}{r\tilde{\omega}} \left(2\Omega + \frac{\kappa^2}{2\Omega}\right) dr\right]. \quad (11.40)$$

Equations (11.38) and (11.39) are the starting equations for studying the behaviors of the perturbations. Except for one-armed waves, the radial wavelength of perturbations is usually not long (see subsequent sections). Hence, in many cases a *local approximation* in the radial direction is sufficient for studying the behaviors of perturbations. Taking F and Y as being proportional to $\exp(-ik_r r)$, we have from equations (11.38) and (11.39) a dispersion relation (Okazaki et al. 1987; Kato 1989; Nowak and Wagoner 1991, 1992):¹⁰

$$(\tilde{\omega}^2 - \kappa^2)(\tilde{\omega}^2 - n\Omega_K^2) = \tilde{\omega}^2 k_r^2 c_s^2. \quad (11.41)$$

Here, we briefly discuss special cases of this dispersion relation. If we consider the fundamental mode ($n = 0$) in the vertical direction, the dispersion relation reduces to

$$\omega^2 = \kappa^2 + k_r^2 c_s^2. \quad (11.42)$$

This dispersion relation is well known in density-wave theory in disk galaxies. This is a typical form of dispersion relation for inertial-acoustic waves.

Next, let us consider a limiting case. If the right-hand side of equation (11.41) is neglected, the dispersion relation shows that the waves are decomposed as

$$\tilde{\omega}^2 = \kappa^2 \quad \text{and} \quad \tilde{\omega}^2 = n\Omega_K^2. \quad (11.43)$$

The former represents inertial oscillations in the horizontal plane, and the latter is the vertical oscillations of the disks under the gravitational and pressure-restoring forces. Equation (11.41) shows, however, that if we consider oscillations with finite wavelengths in the radial direction, the oscillations cannot be purely radial, nor purely vertical. Both oscillations are inevitably coupled.

¹⁰This dispersion relation has been obtained by using the pseudo-Newtonian potential. It is not clear enough how this dispersion relation can be generalized to the case of the Kerr metric. A physical consideration, however, suggests that a simple replacement of $n\Omega_K^2$ on the right-hand side to $n\Omega_\perp^2$ may be allowed as the lowest order of approximation. That is, we have (e.g., Kato 1990)

$$(\tilde{\omega}^2 - \kappa^2)(\tilde{\omega}^2 - n\Omega_\perp^2) = \tilde{\omega}^2 k_r^2 c_s^2,$$

where κ and Ω_\perp are the radial and vertical epicyclic frequencies in the Kerr metric, respectively.

As mentioned before, in deriving the dispersion relation (11.41) the disk is assumed to be vertically isothermal. The derivation of a more general form of dispersion relation has been considered, for example, by Nowak and Wagoner (1991) using the pseudo-Newtonian potential and by Perez et al. (1997) and Silbergleit et al. (2001) for relativistic cases.

11.3.4 Classification of Waves by Dispersion Relation

Equation (11.41) has two solutions with respect to the square of the corotation frequency, $\tilde{\omega}^2$, say $\tilde{\omega}_+^2$ (fast modes) and $\tilde{\omega}_-^2$ (slow modes) with $\tilde{\omega}_+^2 > \tilde{\omega}_-^2$ [see (c) in subsection 11.1.1]. We call the higher-frequency mode with respect to $\tilde{\omega}$ (i.e., the mode with $\tilde{\omega}_+$) the *acoustic waves* (*p*-mode) and the lower-frequency mode the *gravity waves* (*g*-mode). In the case of $n = 0$ and $n = 1$, however, we introduce some exception, as discussed below.

In the case of $n = 0$, we have

$$\tilde{\omega}_+^2 > \kappa^2 \quad \text{and} \quad \tilde{\omega}_-^2 = 0, \quad (11.44)$$

and the *g*-mode disappears within the framework of the present local approximation, although this may not always be true. In the present case of $n = 0$, the oscillations are purely radial and the restoring forces acting on the oscillations come from rotation and pressure. The main restoring force, however, comes from rotation, and the restoring force by pressure is subsidiary, except when the radial wavelength is extremely short. In this sense the mode is called an inertial-acoustic oscillation.

In the case of $n \geq 1$, on the other hand, we have

$$\tilde{\omega}_+^2 > n\Omega_K^2 \quad \text{and} \quad 0 < \tilde{\omega}_-^2 < \kappa^2, \quad (11.45)$$

since $\Omega_K^2 > \kappa^2$ generally.

Here, some comment is given on the mode of $\tilde{\omega}_+$, which is necessary when $n = 1$. In the case of $n = 1$, the disk plane flutters up and down in the vertical direction with a certain radial wavelength and with a fluttering frequency nearly equal to the vertical epicyclic frequency Ω_\perp .¹¹ In this oscillation mode, the Lagrangian time derivative of density, which is close to $i\tilde{\omega}\rho_1 + u_z\partial\rho_0/\partial z$, nearly vanishes.¹² This means that

¹¹In pseudo-Newtonian disks that mimic the Schwarzschild metric, the vertical epicyclic frequency, Ω_\perp , is equal to the Keplerian frequency, Ω_K .

¹²In the mode, h_1 is proportional to z , since $n = 1$, i.e., $h_1 \propto z$. The z -component of equation of motion, equation (11.23), then gives $i\tilde{\omega}u_z = -h_1/z$. Hence, we have $i\tilde{\omega}\rho_1 = i\tilde{\omega}\rho_0 h_1/c_s^2$ and $u_z\partial\rho_0/\partial z = -i\rho_0 h_1/(\tilde{\omega}H^2)$ in vertically isothermal disks. The sum of them is nearly canceled out, since $\tilde{\omega}^2 \sim \Omega_K^2$.

the oscillations are nearly incompressible and the restoring force on the oscillations is the gravitational force acting so as to return a fluid element to the original equatorial plane. In this sense, it is not suitable to classify the mode as a p -mode. The mode is called a c -mode (*corrugation waves*), following the terminology used in the field of galactic dynamics [see also (b) in subsection 11.1.1].

If disks with $N_r^2 \neq 0$ or $N_z^2 \neq 0$ are considered, the characteristics of the oscillations with lower frequency $\tilde{\omega}_-$ are modified [see, e.g., section 13.3 of the first edition (Kato et al. 1998)]. In this sense, it is relevant to call the oscillations of $\tilde{\omega}_-$ the g -mode. Based on these considerations, oscillations on thin disks are classified as shown in table 11.1¹³

11.3.5 Propagation Region and Wave Trapping

Here, for simplicity, we restrict our attention to axisymmetric oscillations, in which $m = 0$, and hence $\tilde{\omega} = \omega$. Generalization to the case of non-axisymmetric oscillations ($m \neq 0$) is easy, although arguments become somewhat complicated (see section 11.4 for examination of some special modes of non-axisymmetric oscillations).

(a) Inertial-acoustic mode ($n = 0$)

We first consider the fundamental mode ($n = 0$) in the vertical direction. The dispersion relation for the mode is $\omega^2 = \kappa^2 + k_r^2 c_s^2$. Generally, for waves to propagate in the radial direction, k_r^2 must be positive. Hence, in the present case, the region where the waves can propagate is specified by $\omega^2 > \kappa^2$. Figure 11.3 schematically shows the region where this condition is satisfied. An important result is that the wave propagation region is separated into two regions (inner region of $r < r_1$ and outer region of $r > r_2$) when $\omega < \kappa_{\max}$, although waves with $\omega > \kappa_{\max}$ can propagate throughout the entire region of the disks. The presence of κ_{\max} is due to general-relativistic effects.

Let us consider a wave propagating inward from a far outer region with frequency ω ($< \kappa_{\max}$). As the wave approaches radius r_2 , where $\omega = \kappa$, the wavelength of the wave increases and finally becomes infinite at $r = r_2$. This means that the waves are reflected back outward. If $\omega > \kappa_{\max}$, however, the waves can propagate inward until the inner edge of the disk. This is in contrast with the case of non-relativistic disks, in

¹³It should be noted that this classification of oscillation modes is based on the local dispersion relation. In global oscillations, the above separation of oscillations becomes less clear.

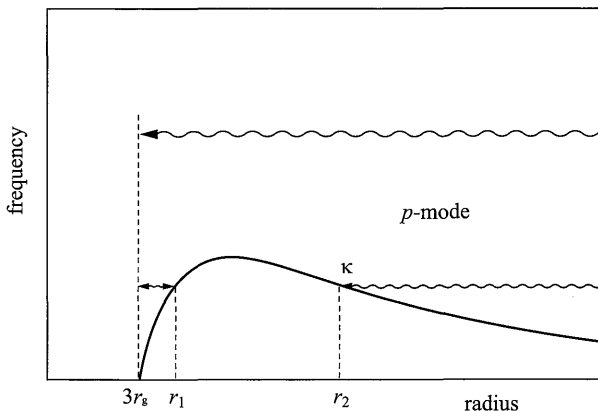


Figure 11.3

Propagation diagram showing the radial region where the inertial-acoustic ($n = 0$) waves can propagate. For waves with $\omega < \kappa_{\max}$, the propagation region is separated into two portions: $3r_g < r < r_1$ and $r > r_2$.

which the epicyclic frequency increases inward without limit so that all waves should be reflected back outward at a certain radius.

More importantly, there is a wave-propagation region in the innermost region of disks when $\omega < \kappa_{\max}$ and waves can be trapped there (Kato and Fukue 1980; Ortega-Rodríguez et al. 2002). Let us consider an inertial-acoustic wave propagating outward in the region just outside the inner edge ($\sim 3r_g$) of the disks. If $\omega < \kappa_{\max}$, the wave is reflected back inward by the wall of the epicyclic frequency. A wave propagating inward toward the inner edge, on the other hand, would be partially reflected back outward at the inner edge. The inner edge of disks is a sharp boundary where the density decreases sharply inward. Because of this, perturbations transported there with accretion flow are partially reflected back as outgoing acoustic waves. It is noted that inside the sonic radius no wave can propagate outward, since the accretion flow is supersonic there. Just outside the sonic radius, however, inward-going waves can be reflected back as outward-going waves. This is true even in the case where the disk has accretion flows, and has been confirmed by numerical simulations (see figure 9.11 in section 9.4).

Because of this reflection of waves at the inner edge of disks, waves whose frequency ω is smaller than κ_{\max} can be trapped in the innermost region of relativistic disks. This *wave trapping* in the innermost disks plays an important role in creating quasi-periodic time variations in black-hole accretion disks, as discussed in chapter 12.

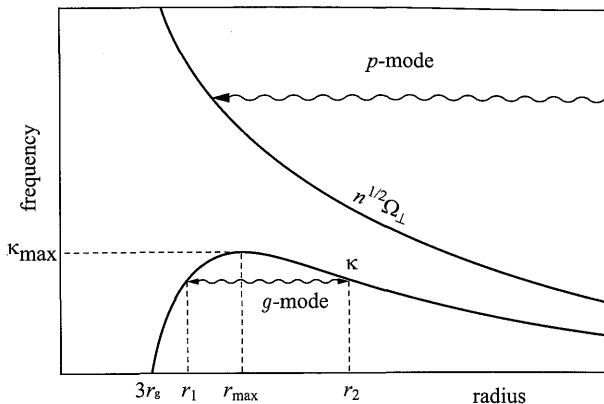


Figure 11.4

Propagation diagram showing trapping of a gravity mode with $n = 1$ in the region between r_1 and r_2 . Waves whose frequencies are slightly smaller than κ_{\max} are trapped around r_{\max} . The upper curve, labeled by $(n\Omega_K^2)^{1/2}$, is the lower boundary of the propagation region of acoustic waves. These waves can exist only in the right-upper region of the curve.

(b) Gravity modes ($n \geq 1$) and corrugation modes ($n = 1$)

Let us next consider the cases of $n \neq 0$. Waves are still taken to be axially symmetric ($m = 0$). As shown in equation (11.41), there are two wave modes, i.e., the modes with ω_+ and ω_- (see also table 11.1).

First, we consider the latter modes, i.e., gravity waves ($n \geq 1$). Since κ has a maximum at a certain radius (r_{\max}) and decreases both inward and outward, the propagation region of the waves with frequencies $\omega < \kappa_{\max}$ is restricted in a finite region ($r_1 < r < r_2$) around r_{\max} , as is shown in figure 11.4. In other words, we can expect trapped oscillations of gravity waves in the region around r_{\max} with frequencies of $\sim \kappa_{\max}$ (Okazaki et al. 1987; Nowak and Wagoner 1992; Perez et al. 1997).

A characteristic nature of these trapped oscillations is that their frequencies are insensitive to changes of the disk structure as long as the disks are moderately geometrically thin. This is because κ_{\max} depends only on the mass of the central black hole in the Keplerian disks (see section 2.5). As an inspection of equation (11.18) shows, $\kappa_{\max} \propto 1/M$, since $r_{\max} = 4r_g \propto M$. Detailed calculations of the eigen-frequency of the trapped oscillations have been made by Perez et al. (1997) with Kerr geometry. The resultant oscillation frequency f is

$$f = 700 \left(\frac{M}{M_\odot} \right)^{-1} F(a_*) (1 - \epsilon) \text{ Hz}, \quad (11.46)$$

where ϵ is a small correction factor involving the disk thickness, and radial and vertical mode numbers. The effects of rotation of the central black hole appear in the factor $F(a_*)$, where a_* is the dimensionless spin parameter ($0 \leq a_* < 1$; see appendix A) and $F(a_*)$ monotonically increases with an increase of a_* from $F(0) = 1$ to $F(0.998) = 3.443$. Nowak et al. (1997) suggested that these trapped oscillations might be the origin of the 67 Hz oscillations observed in the black-hole candidate GRS 1915+105. The derived black hole mass is $10.6M_\odot - 36.3M_\odot$ for the cases of a non-rotating and a maximally rotating black hole, respectively.

So far, we have examined the basic characteristics of relativistic disk-oscillations, based on the local dispersion relation. To obtain more reliable information on disk oscillations, global analyses of them are required, which are mathematically complicated. Studies in such a direction, however, have been made carefully and extensively by Wagoner and his group for more than a decade. Their results are summarized by Wagoner et al. (2001), and further developments in recent years are given by Ortega-Rodrígues et al. (2006). It is shown that c -mode ($n = 1$) oscillations are also trapped, in addition to the inertial-acoustic mode ($n = 0$) and g -mode ($n = 1$) oscillations. One of their results concerning the frequencies of normal-mode oscillations are duplicated in figure 11.5. The dependences of the frequencies on the spin parameter of the central source, a_* , are shown there.

(c) Other types of trapping

So far, we have considered wave trappings due to general-relativistic effects. In addition to this kind of wave trapping, purely geometrical effects can also trap waves in some particular regions of disks. It is conceivable that the inner region of disks could be much hotter and geometrically thicker than the outer portions. For example, in radiation-pressure-dominated disks, thermal instability sets in in the inner region of disks and a transition wave propagates outwards (section 10.4). Another example is that in advection-dominated disks a transition from an optically thin inner region to outer optically thick standard disks occurs at a certain transition radius (see subsection 9.2.3). A similar situation arises in disks undergoing a dwarf-nova type instability (section 5.2). In these cases, due to a sharp change in the disk thickness, waves propagating outward in the radial direction in the inner hot region are reflected back inward at the transition region. This kind of trapped oscillation has been considered by Yamasaki et al. (1995).

So far, we have concentrated on cases of axisymmetric waves ($m =$

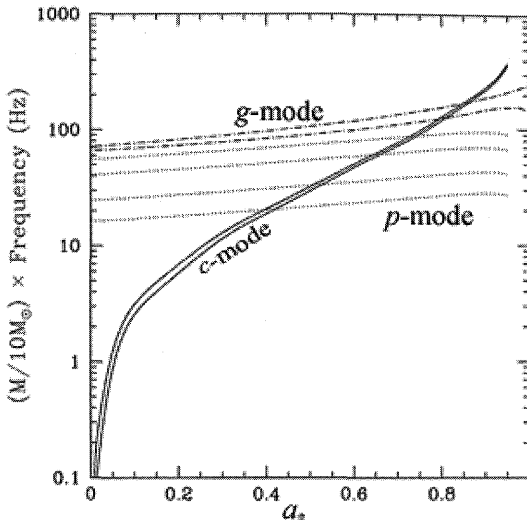


Figure 11.5

Dependence of the frequencies of trapped inertial-acoustic ($m = n = 0$), g -mode ($m = 0, n = 1$), and c -mode ($m = 0, n = 1$) oscillations on the angular momentum of the black hole. The spread of each corresponds to the range $0.01 \leq L/L_{\text{Edd}} \leq 1.0$ and is relatively insensitive to the choices of M/M_{\odot} and α . The upper and lower bands for the p -mode correspond to differences of disk models [see Wagoner et al. (2001) for details]. Also see Ortega-Rodrígues et al. (2006) for an extension of this figure to the region of negative a_* , including the low frequency inertial-acoustic oscillations in the outer region of disks. (After Wagoner et al. 2001)

0). If non-axisymmetric waves ($m \neq 0$) are considered, the propagation diagram is changed, since ω should be changed to $\omega - m\Omega(r)$. However, the method for examining the propagation region of waves is the same as in the case of $m = 0$, and is straightforward. General discussions and results concerning the case of $m \neq 0$ are thus omitted here. Some important cases, however, are discussed in section 11.4.

11.3.6 Comments on Effects of Buoyancy

So far, we have considered oscillations in disks where $N_r^2 = N_z^2 = 0$. This is, however, not generally the case; i.e., $N_r^2 \neq 0$ and $N_z^2 \neq 0$. Here, we are satisfied only in making qualitative discussions concerning the change of the g -mode oscillations to the convection modes when $N_r^2 < 0$ and $N_z^2 < 0$.

In moderately thin disks, the quantity $|N_r^2|$ is smaller than $|N_z^2|$ by the

factor $(H/r)^2$ [see equations (11.14)–(11.15)]. Furthermore, the effects of a non-zero N_r^2 on oscillations are apt to be masked by the effects of the strong restoring force due to rotation. Because of this, the effects of $N_z^2 \neq 0$ on the characteristics of the g-mode oscillations are stronger, compared with those of $N_r^2 \neq 0$. In the case of $N_z^2 < 0$, the g-mode oscillations with vertically elongated flow pattern (i.e., $|k_z/k_r| < 1$) have a tendency to be changed from oscillations (*g*-mode) to convective (convection mode). This is because in such flows, they receive much energy from buoyancy by moving in the same direction as the direction of the buoyancy force.

The vertically elongated convection can transport energy in the vertical direction, but have little effects on energy and angular momentum transports in the radial direction. For global convections in the radial direction to occur, the buoyancy force must exceed the restoring force due to rotation. Roughly speaking, the condition is

$$N_r^2 + \kappa^2 < 0. \quad (11.47)$$

Such a situation is known to really occur in radiatively inefficient accretion flow (RIAF). Such a flow is called convection-dominated accretion flow, or CDAF (see section 9.5 and Ryu and Goodman 1992).

11.4 One-Armed Low-Frequency Global Oscillations

In geometrically thin disks the strongest restoring force is that due to rotation. The characteristic frequency representing this restoring force is the epicyclic frequency, κ . In disks, κ changes strongly in the radial direction. For example, in Newtonian Keplerian disks we have $\kappa \sim \Omega_K \propto r^{-3/2}$. This implies that if we consider an acoustic wave whose frequency ω is close to κ at a particular radius, the frequency difference between ω and $\kappa(r)$ increases as the wave propagates outward. To keep ω constant, this difference must be supplemented by a pressure-restoring force. To increase the pressure-restoring force, the wavelength of the wave becomes shorter and shorter as the wave propagates (remember a typical dispersion relation, $\omega^2 = \kappa^2 + c_s^2 k_r^2$).

Such short-wavelength oscillations are, however, generally uninteresting from both theoretical and observational points of view. That is, they will be damped by phase-mixing. Furthermore, short-wavelength oscillations will not be observed with large amplitude because their wavelength will be shorter than the spatial resolution of observations. This consideration suggests that for wave phenomena in disks to be interesting: (i) they must be trapped in a particular region of the disks, or (ii) they have

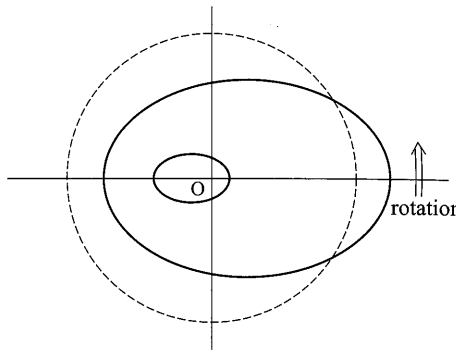


Figure 11.6

Schematic picture of one-armed oscillations observed from the pole-on direction. In an isolated system, the center of the system must be fixed. Because of this, the direction of deformation of disks will be different in the outer and inner regions. The broken circle shows, for a comparison, a constant distance from the center.

global patterns by some particular reasons. The former is discussed in the previous section. Here, we discuss the latter possibility.

There are two kinds of wave modes with a global pattern: (i) one-armed ($m = 1$), inertial-acoustic waves ($n = 0$) (Kato 1983), and (ii) one-armed ($m = 1$), corrugation waves ($n = 1$) (Kato 1989). Both of them are low-frequency oscillations. A pattern for the one-armed global deformation of disks is illustrated in figure 11.6, emphasizing that the center of the disks must be fixed in spite of any deformation.

11.4.1 One-Armed Inertial-Acoustic Waves ($m = 1$ and $n = 0$)

Let us first consider the fundamental mode ($n = 0$) in the vertical direction. The values of N_r and N_z are taken to be zero in order to show a typical case. The dispersion relation is then

$$(\omega - m\Omega)^2 - \kappa^2 = k_r^2 c_s^2. \quad (11.48)$$

The purpose here is to demonstrate that the one-armed ($m = 1$) waves are low-frequency modes with global patterns in cases of $\Omega \sim \kappa$. If $m = 1$ and ω^2 is neglected, $(\omega - m\Omega)^2 - \kappa^2$ can be approximated as $-2\omega\Omega + (\Omega^2 - \kappa^2)$. We then have

$$\omega \sim -\frac{1}{2}\Omega \left(\frac{k_r c_s}{\Omega} \right)^2 + \frac{1}{2}\Omega \frac{\Omega^2 - \kappa^2}{\Omega^2}. \quad (11.49)$$

The validity of having neglected ω^2 in deriving equation (11.49) is examined later.

(a) Case of Newtonian disks

In Newtonian disks, $\Omega^2 - \kappa^2$ is on the order of $c_s^2/(lr)$,¹⁴ where $l(\sim r)$ is the characteristic radial scale by which the pressure changes appreciably. Hence, the second term on the right-hand side of equation (11.49) can be neglected compared with the first term as long as $(k_r r)(k_r l) > 1$. We then have

$$\omega \sim -\frac{1}{2}\Omega\left(\frac{k_r c_s}{\Omega}\right)^2. \quad (11.50)$$

This relation shows that the wave is retrograde and the frequency is $|\omega| \sim \Omega_K(k_r c_s / \Omega_K)^2 \sim \Omega_K(k_r H)^2 \ll \Omega_K$ in geometrically thin disks, showing the validity of neglecting ω^2 in deriving equation (11.49).

The reason why one-armed ($m = 1$) inertial-acoustic oscillations have a low-frequency global pattern is simple (Kato 1983). Let us consider a cold non-relativistic Keplerian disk, and superpose on the disk a weak large-scale density pattern of $m = 1$. The superposition of such a pattern is possible by introducing particles having eccentric orbits. In collisionless Keplerian disks the eccentric orbits are closed after one revolution. The period of the revolution is the same as that of a circular orbit as long as the mean radii of the orbits are the same. Hence, a pattern of $m = 1$ is maintained stationary on the disk. Actual gaseous disks, however, have pressure. The pressure force changes the rotation period from a pure Keplerian one, which distorts the one-armed pattern. The pressure, however, has another effect. It makes individual oscillations at various radii coherent as a whole. That is, by the effects of pressure a one-armed pattern becomes a coherent oscillation. The rotation of the coherent pattern is, however, very slow, since the coherence of the oscillations is the result of pressure, and the pressure-restoring force is much weaker than the restoring force due to rotation in geometrically thin disks. In this way, the one-armed pattern is a global-oscillation mode whose pattern frequency (i.e., precession frequency) is extremely low compared with the Keplerian frequency. This type of slow precession of Newtonian disks is considered to be the cause of the V/R spectral variation of Be stars (Kato 1983; Okazaki 1991, 1996).

(b) Case of tidally deformed disks

In disks where rotation is moderately deformed from the Keplerian one, the second term on the right-hand side of equation (11.49) becomes

¹⁴If there is no pressure, we have $\Omega = \Omega_K = \kappa$. In other words, the difference between $\Omega^2 r$ and $\kappa^2 r$ comes from the pressure force [$\sim (1/\rho)\partial p/\partial r$], which is on the order of c_s^2/l .

larger than the first term, and determines the frequency of one-armed oscillations. In the case in which the Newtonian Keplerian disks are perturbed by the tidal effect of a secondary star, we have

$$\frac{\Omega^2 - \kappa^2}{\Omega^2} \sim \left(\frac{r}{a} \right)^3 \frac{M_2}{M_x}, \quad (11.51)$$

where a is the separation of the binary components, M_x is the mass of the central star (primary) surrounded by the disk and M_2 is the mass of the secondary star. Then, ω becomes (Osaki 1985)

$$\omega \sim \frac{1}{2} \Omega \left(\frac{r}{a} \right)^3 \frac{M_2}{M_x}, \quad (11.52)$$

and the one-armed pattern is prograde. This slow precession of the eccentric pattern is the cause of slight period deviations of the superhump period in dwarf novae (Osaki 1985) and in some X-ray novae (Mineshige et al. 1992) from the orbital periods of the corresponding binary systems [see chapter 6 of the first edition (Kato et al. 1998) for more details].

(c) Case of weakly relativistic disks

In relativistic disks, the Keplerian angular velocity of rotation and the radial epicyclic frequency are no longer equal. In weakly relativistic disks, we have

$$\frac{\Omega^2 - \kappa^2}{\Omega^2} \sim \frac{3r_g}{r}, \quad (11.53)$$

and thus, from equation (11.49),

$$\omega \sim \frac{3}{2} \Omega \left(\frac{r_g}{r} \right). \quad (11.54)$$

In strongly relativistic disks, however, this mode of oscillations ceases to be a low-frequency, global pattern. This is because $\kappa \sim \Omega$ no longer holds there. However, there are still low-frequency, global-oscillation modes in strongly relativistic disks, when the spin of the central source is small. This is the one-armed corrugation waves, and is discussed below.

11.4.2 One-Armed Corrugation Waves ($m = 1$ and $n = 1$)

One-armed ($m = 1$) corrugation waves ($n = 1$) are of interest in the sense that even in relativistic disks they have low frequency and long wavelength in the radial direction, as long as the rotation of the central black hole is slow. In addition, they can propagate over a wide region

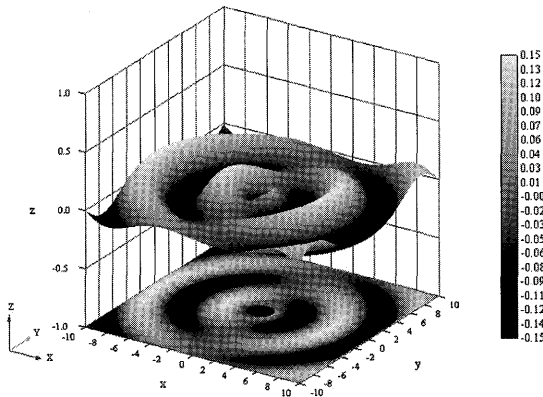


Figure 11.7

Schematic picture of one-armed corrugation waves. The disk plane flutters in the vertical direction with anti-phase when the azimuthal angle is separated by π (radian). The lower panel shows the projection on the equatorial plane.

in the disks. A schematic picture of one-armed corrugation waves is illustrated in figure 11.7.

The values of N_r^2 and N_z^2 are again taken to be zero, for simplicity. The dispersion relation (11.41) is then written as

$$[(\omega - \Omega)^2 - \kappa^2][(\omega - \Omega)^2 - \Omega_{\perp}^2] = (\omega - \Omega)^2 k_r^2 c_s^2, \quad (11.55)$$

where Ω_{\perp} has been used instead of Ω_K [see the footnote attached to equation (11.41)].

(a) Case of Newtonian disks

Although the main purpose here is to show that corrugation waves can have low frequencies in relativistic disks, we first discuss the characteristics of corrugation waves in Newtonian Keplerian disks, since they are also low-frequency modes. In such disks, $\Omega \sim \Omega_K \sim \kappa$. Hence, we have

$$(\omega - \Omega)^2 - \kappa^2 \sim -2\Omega\omega \quad \text{and} \quad (\omega - \Omega)^2 - \Omega_{\perp}^2 \sim -2\Omega\omega \quad (11.56)$$

when ω is sufficiently low.¹⁵ If these approximations are adopted, equation (11.55) gives

$$\omega \sim \pm \frac{1}{2} k_r c_s. \quad (11.57)$$

¹⁵The final result (11.57) shows that the approximations (11.56) are really valid.

This shows that the waves tilting (warping) the disk plane propagate on the disk with acoustic speed.

(b) Case of relativistic disks

In relativistic disks, the first approximation of equations (11.56) no longer holds. The closeness of the frequency of vertical oscillations, Ω_{\perp} , and the frequency of disk rotation, Ω , however, still hold even in relativistic disks, unless the spin of the central object is fast. This closeness gives us low-frequency oscillations, when the spin is slow. That is, assuming the presence of low frequency oscillations, we approximate $(\omega - \Omega)^2 - \Omega_{\perp}^2$ as $-2\omega\Omega + (\Omega^2 - \Omega_{\perp}^2)$. On the other hand, since κ is no longer close to Ω in the relativistic disks, we can approximate $(\omega - \Omega)^2 - \kappa^2$ as $\Omega^2 - \kappa^2$. Then, from dispersion relation (11.55) we have

$$\omega \sim -\frac{1}{2}\Omega \frac{\Omega^2}{\Omega^2 - \kappa^2} \frac{k_r^2 c_s^2}{\Omega^2} + \frac{1}{2}\Omega \frac{\Omega^2 - \Omega_{\perp}^2}{\Omega^2}. \quad (11.58)$$

In the limit of no spin of the central source, i.e., $a_* = 0$, we have $\Omega_{\perp} = \Omega_K$. Then, the second term in equation (11.58) can be neglected compared with the first term, unless $(k_r r)(k_r \ell) < 1$, where ℓ is the characteristic radial scale by which the pressure changes appreciably in the radial direction. In this limit, the frequency of corrugation waves is given by the first term of equation (11.58), i.e.,

$$\omega \sim -\frac{1}{2}\Omega \frac{\Omega^2}{\Omega^2 - \kappa^2} \frac{k_r^2 c_s^2}{\Omega^2}. \quad (11.59)$$

The waves have low frequency and are retrograde.

The reason why the one-armed corrugation waves have low frequency can be understood as follows. Let us consider a displacement of a particle from the equatorial plane in the vertical direction. The particle feels the gravitational restoring force toward the equator. The force is proportional to the vertical displacement when the displacement is small. Hence, the particle undertakes harmonic oscillations around the equatorial plane with the vertical epicyclic frequency. This frequency is equal to the Keplerian frequency of disk rotation when the metric is the Schwarzschild one. In other words, the vertical oscillation period of the particle coincides with the Keplerian rotation period by which the particle rotates around the central object. This means that in the limit of no temperature a one-armed corrugation pattern is maintained without any time change. Hence, if a pressure-restoring force is present, the corrugation pattern is no longer stationary, but slowly changes with time.

Since $\kappa < \Omega_\perp \sim \Omega$, dispersion relation (11.55) shows that the propagation regions of waves are those where $(\omega - \Omega)^2 < \kappa^2$ or $(\omega - \Omega)^2 > \Omega_\perp^2$ is satisfied. The condition $(\omega - \Omega)^2 > \Omega_\perp^2$ is satisfied over a wide range of radius, when $\omega < 0$ and $\Omega \sim \Omega_\perp$. This means that the corrugation waves described by equation (11.59), which has $\omega < 0$, can propagate throughout the disk from the outer region to the inner region, or vice versa. This is important, since they can transport angular momentum far away, as emphasized by Vishniac and Diamond (1989).

In the case where the central source has a high spin, the second term of equation (11.58) is no longer negligible. Then, the frequency of corrugation waves may not be slow, but could be rather high.

One of the purposes of studying low-frequency oscillations in disks is that they are possible origins of the low-frequency quasi-periodic oscillations (LF QPOs) observed in X-ray binaries. Corrugation waves (including warps) are mainly a deformation of the disk plane, and show no large change of the surface brightness of the disks themselves. They can, however, bring about the observed luminosity variations by hiding the central source, or the luminous parts of the disk, from observers.

11.4.3 Summary of Low-Frequency Oscillations

In this section we have shown that one-armed ($m = 1$) oscillations have a particular position among disk oscillations in the sense that they can become low-frequency global patterns on differentially rotating disks. Here, we summarize in table 12.2 in what cases they become low-frequency patterns. In table 12.2, p -mode oscillations mean the inertial-acoustic oscillations.

Table 11.2 Low-Frequency, One-Armed Global Oscillations.

mode	disks	applications
$n = 0$		
p -mode	non-relativistic, Keplerian	V/R variations in Be stars
p -mode	non-relativistic, non-Keplerian	superhumps in CVs
p -mode	weakly relativistic	
$n = 1$		
g - and c -modes	non-relativistic	warp with slow precession
c -mode	relativistic	warp with slow precession

In this section as well as in previous sections in this chapter, we have discussed the basic characteristics of wave modes, based on the local dispersion relations of waves in vertically isothermal disks. When disks to be discussed are not vertically isothermal, the decomposition of the partial differential equations, say equations (11.25) and (11.26) or more

general relativistic ones, into ordinary differential equations by using separability of variables are complicated. Such studies, however, have been made when vertical distributions of the density and pressure are polytropic in order to examine the trapping nature of oscillations. They are for one-armed low-frequency oscillations by Okazaki and Kato (1985), for the inertial-acoustic oscillations by Nowak and Wagoner (1991, 1992) and Ortega-Rodríguez et al. (2002), and for the g-mode oscillations by Perez et al. (1997), and for the c-mode oscillations by Silbergleit et al. (2001). See Ortega-Rodríguez et al. (2006) for recent extensive studies.

11.5 Amplification of Disk Oscillations by Viscosity

In the previous sections, we have considered various types of disk oscillations. Without good excitation mechanisms, however, such oscillations will eventually be damped by dissipations. The next subject to be examined is thus whether these oscillations can be excited on disks, and what are the excitation processes. We emphasize that in the case of disk oscillations, there are excitation processes related to turbulent viscosity, which are practically absent in the case of stellar oscillations. They are related to the facts that the turbulent viscosity is the major momentum and energy transport processes in disks (Kato 1978), whereas this is not so in stars.

11.5.1 Role of Turbulent Viscosity

Accretion disks are rapidly rotating systems with turbulence. The turbulence thus becomes one of the main dissipative processes in disks, in addition to radiative processes. This point is quite different from the case of stars, where dissipative processes are practically radiative processes alone.

It is well known in stellar-pulsation theory that thermal energy transport and thermal energy generation in stars can amplify stellar oscillations, if these processes are in some favorable phase relation with that of the oscillations. The main amplification processes related to these non-adiabatic processes are the so-called ϵ and κ processes (e.g., Unno et al. 1989). In rotating disks, these thermal processes are still effective as excitation processes of disk oscillations. However, in addition to them, viscous processes due to turbulence can also amplify oscillations, if a favorable phase relation between the oscillations and time variations of the viscous force and viscous dissipation is realized. This is really realized

when a conventional description of the viscous stress tensor is adopted (Kato 1978).

However, we should always have the following situations in mind, when we adopt the conventional description of turbulent viscosity in time-dependent disks. Interactions between turbulence and oscillations are very complicated, especially when the time scales both of turbulence and oscillations are close. Adoption of the conventional description of turbulent viscosity implies that the turbulence responds immediately to a change in the environment.¹⁶ If the above simplification is adopted, we find that the turbulent viscosity increases in the compressed phase of oscillations. This comes from the following situations. The coefficient of turbulent viscosity, η , is usually written as $\eta = \rho v_{\text{turb}} l$, where v_{turb} is the turbulent velocity and l is the mean free path of turbulent eddies. If v_{turb} is a constant fraction of sound speed c_s and the mean free path l is of the order of the disk half-thickness, H ($\sim c_s/\Omega$), we have $\eta \propto \rho c_s^2 \propto \rho T$. That is, the viscosity increases in the compressed phase of oscillations.

11.5.2 Amplification Mechanisms by Turbulent Viscosity

Turbulent viscosity contributes to the amplification of oscillations in rotating disks by two processes. One is thermal and the other is dynamical. The essences of both processes are discussed separately below.

The thermal process is discussed first, since it is simple and can be easily understood as a counterpart of the ϵ -mechanism in stellar pulsation. The essence of the thermal amplification process is as follows: In the compressed phase of oscillations, the density, temperature and pressure increase. This usually brings about an increase of viscous heat generation, leading to an increase of the pressure-restoring force. In other words, the increase of the pressure-restoring force during the compressed phase is more than that due solely to adiabatic compression. Thus, the oscillations are pushed back towards the next expansion phase with a stronger force, and the amplitude of the oscillations during this expansion phase becomes larger than that of the previous expansion phase.

¹⁶In general, turbulence cannot respond immediately to a change in the environment. A finite time lag occurs to the response. This time lag is generally non-negligible, since the characteristic time of turbulence is not much shorter than that of oscillations. Examinations of the effects of the time lag on oscillations are, however, complicated. Some detailed examinations of the effects of the time lag have been made (Kato 1994; Yamasaki and Kato 1996). The effects of time lag are usually to decrease growth or damping rate of oscillations, and may change the stability criterion. These effects are not discussed in this section.

In the expansion phase a similar situation occurs. The amplitude of oscillations thus increases with time (*overstability*).

Another effect of viscosity on the amplification of disk oscillations is dynamical. This is related to a change of the viscous force in the azimuthal direction during oscillations. This dynamical process can be understood by examining the sign of work done on a given fluid element by the viscous stress force during one cycle of oscillations. Let us consider, for simplicity, axisymmetric oscillations. A given fluid element inevitably undergoes a time-periodic displacement, ξ_φ , in the azimuthal direction, in addition to the radial direction during the oscillations, since in the limit of no dissipation, the angular momentum of a given fluid element must be conserved during the oscillations. On the other hand, the viscous force acting on the fluid element in the azimuthal direction, say N_φ , also changes time-periodically during the oscillations. If the Lagrangian velocity variation in the azimuthal direction due to viscous processes, δu_φ , and the Lagrangian change of N_φ , say, δN_φ , are in phase, positive work is done on the oscillations, and they grow when their energy is positive. This phase matching really occurs if the viscosity increases during the compression phase of oscillation. Whether this has a sufficient magnitude to amplify the oscillations against other normal viscous damping processes depends on the characteristics of the oscillations and the forms of the viscosity.

An instability criterion in a simple case is presented here. Oscillations are assumed to be axially symmetric. Then, the growth rate of the oscillations, $-\Im\omega$, is given by (Kato 1978, 2001)

$$\begin{aligned} & 2(-\Im\omega) \int \rho_0(u_r u_r^* + u_z u_z^*) d^3 r \\ &= \Re \int \rho_0 \left(u_r^* N_{r,1} + \frac{4\Omega^2}{\kappa^2} u_\varphi^* N_{\varphi,1} + u_z^* N_{z,1} \right) d^3 r \\ &+ \Re \int \frac{\delta T}{T_0} (-\operatorname{div} \mathbf{F} + \Phi)_1 d^3 r, \end{aligned} \quad (11.60)$$

where the asterisk * denotes the complex conjugate; subscripts 0 and 1 represent unperturbed quantities and the Eulerian perturbations. The integration is performed throughout the disk. The integral on the left-hand side represents the wave energy.

The first integral with three integrands on the right-hand side of equation (11.60) represents the work done on oscillations by the dynamical process mentioned above. Among three terms, the term contributing to instability (overstability) is $u_\varphi^* N_{\varphi,1}$.

The second integral on the right-hand side of equation (11.60) represents the thermal processes. The quantity Φ is the rate of viscous heat generation and the integration of $(\delta T/T_0)\Phi_1$ over the disk represents the thermal excitation process of viscosity. Here, we call this a viscous ϵ -process, since this is an extension of the conventional ϵ -mechanism in stars to a case of viscous heat generation in disks.¹⁷ The quantity \mathbf{F} is the heat flux in disks, and the integration of $(\delta T/T_0)(-\operatorname{div}\mathbf{F})_1$ over the disk thus represents the term of conventional pulsational instability of stars, which has been known since Eddington (e.g., Unno et al. 1989). Here, $(-\operatorname{div}\mathbf{F} + \Phi)_0 = 0$ is assumed.

To summarize the case of accretion disks compared with that of stars, two processes contribute to the stability criterion in addition to those that appear in stellar oscillations. One is a dynamical process of viscosity, which is shown by the first integral on the right-hand side of equation (11.60). The other one is a thermal process of viscosity, which is shown by the second term of the second integral on the right-hand side of equation (11.60). The first term of the second integral is the conventional term representing the criterion of stellar pulsational instability, including the κ -mechanism. Table 11.3 summarizes the processes (mechanisms) involved in stability criterion, demonstrating the differences between stars and disks.

Table 11.3 Processes Contributing to Stability (Overstability) Criterion.

	processes	stars	disks
thermal	κ -mechanism	yes	yes
	ϵ -mechanism	yes	yes
	viscous ϵ -mechanism	no	yes
dynamical	work done by viscous force	no	yes

A rigorous mathematical derivation of the stability criterion is usually done by a perturbation method. That is, the effects of dissipative processes on oscillations are taken to be small perturbations on the oscillations, and are obtained by successively solving the wave equations. To do so, we first write down wave equations, including the effects of dissipative processes (non-adiabatic and viscous processes). Then, the wave equations are solved in the limit of no dissipative processes, giving the zeroth-order eigen-frequency, which is real, and the zeroth-order eigen-functions. Next, the first-order wave equations are derived, which

¹⁷If nuclear energy generation is present in the disk with energy generation rate, ϵ_N , its effects on the stability criterion can be examined by adding the time variation of the rate of nuclear energy generation, $(\epsilon_N)_1$, in Φ_1 . This is the conventional ϵ -mechanism known in the stellar pulsation theory.

are inhomogeneous wave equations describing small perturbations on the zeroth-order eigen-functions and eigen-frequencies. To solve these inhomogeneous wave equations with relevant boundary conditions, we use the fact that the zeroth-order differential operators describing the zeroth-order wave equations are Hermitians. By using this Hermitian nature of the operators, we can explicitly write down the first-order perturbations of the eigen-value by using only the zeroth order quantities and dissipative processes.

In order to derive the zeroth-order wave equations in the form where the operator describing wave equations is Hermitian, there are two ways. One is to derive the wave equations in the required forms by using the Lagrangian variables (Lynden-Bell and Ostriker 1967), while the other is to use the Eulerian variables (Ipser and Lindblom 1991a, b, 1992). Formulations by the former approach are given in section 14.3 of the first edition (Kato et al. 1998, see also Kato 2001). Those of the latter approach are made by Ortega-Rordíguez and Wagoner (2000). The results by Ortega-Rordíguez and Wagoner show that viscosity causes the inertial-acoustic and *g*-mode oscillations to grow, while the *c*-mode could have either sign of the damping rate.

References

- Ipser J.R. 1994, ApJ 435, 767
Ipser J.R. 1996, ApJ 458, 508
Ipser J.R., Lindblom L. 1991a, ApJ 373, 213
Ipser J.R., Lindblom L. 1991b, ApJ 379, 285
Ipser J.R., Lindblom L. 1992, ApJ 389, 392
Kato S. 1978, MNRAS 185, 629
Kato S. 1983, PASJ 35, 249
Kato S. 1989, PASJ 41, 745
Kato S. 1990, PASJ 42, 99
Kato S. 2001, PASJ 53, 1
Kato S., Fukue J. 1980, PASJ 32, 377
Lynden-Bell D., Ostriker J.P. 1967, MNRAS 136, 293
Mineshige S., Hirose M., Osaki Y. 1992, PASJ 44, L15
Nowak M.A., Wagoner R.V. 1991, ApJ 378, 656
Nowak M.A., Wagoner R.V. 1992, ApJ 393, 697
Nowak M.A., Wagoner R.V., Begelman M.C., Lehr D.E. 1997, ApJ 277, L91
Okazaki A.T. 1991, PASJ 37, 683
Okazaki A.T. 1996, PASJ 48, 305

- Okazaki A.T., Kato S. 1985, PASJ 37, 683
- Okazaki A.T., Kato S., Fukue, J. 1987, PASJ 39, 457
- Ortega-Rodríguez M., Wagoner R.V. 2000, ApJ 537, 922
- Ortega-Rodríguez M., Silbergbeit A. S., Wagoner R. V. 2002, ApJ 567, 1043
- Ortega-Rodríguez M., Silbergbeit A. S., Wagoner R. V. 2006, astro-ph/0611101
- Osaki Y. 1985, A&A 144, 369
- Paczyński B., Wiita, P.J. 1980, A&A 88, 23
- Perez C.A., Silbertgleit A.S., Wagoner R.V., Lehr, D.E. 1997, ApJ 476, 589
- Ryu D., Goodman J. 1992, ApL 388, 438
- Silbergbeit A. S., Wagoner R. V., Ortega-Rodríguez M. 2001, ApJ 548, 335
- Unno W., Osaki Y., Ando H., Saio H., Shibahashi H. 1989, *Nonradial Oscillation of Stars* (University of Tokyo Press, Tokyo)
- Vishniac E.T., Diamond P. 1989, ApJ 347, 435
- Wagoner R.V. 1999, Phys. Rep. 311, 259
- Wagoner R.V., Silbergbeit A.S., Ortega-Rodríguez M. 2001, ApJ 559, L25
- Yamasaki T., Kato S., Mineshige S. 1995, PASJ 47, 59

Quasi-Periodic Oscillations

The launch of Rossi X-ray Timing Explorer (*RXTE*) led to the discovery of high-frequency quasi-periodic oscillations (≥ 100 Hz) in X-ray binaries in 1996. They are kHz QPOs in neutron-star low-mass X-ray binaries, and high-frequency QPOs (HF QPOs) in black-hole X-ray binaries. Both of them are supposed to be related phenomena, originating in a strong gravitational field. The origins of kHz QPOs and HF QPOs are still being debated, but similarities among kHz QPOs and HF QPOs suggest that they are all phenomena in relativistic disks. In this chapter, after a brief review of various kinds of quasi-periodic oscillations in compact objects, we present quasi-periodic phenomena which are expected to occur in the innermost region of relativistic disks due to the transonic nature of accretion flows (section 12.2), or by the effects of strong gravity (sections 12.3 – 12.5).

12.1 Observations of Quasi-Periodic Oscillations

First, we briefly review various kinds of quasi-periodic oscillations observed in compact sources, and then focus our attention on high-frequency QPOs in X-ray binaries, i.e., kHz QPOs and HF QPOs.

12.1.1 Brief Summary of Quasi-Periodic Oscillations

(a) Cataclysmic variables

The presence of quasi-periodic light variations in binary systems was first noticed in cataclysmic variables (CVs). During their eruption phase there are short-period coherent oscillations with a period of 20 s and an amplitude of 0.002 mag, so-called dwarf nova oscillations (DNOs), as well as quasi-periodic oscillations (QPOs) with timescales of 32–165 s and an

amplitude of 0.005–0.01 mag (Robinson and Nather 1979). Dynamical timescale of white dwarfs is $\sqrt{R_{\text{WD}}^3/GM_{\text{WD}}} \sim$ a few seconds for $R_{\text{WD}} \sim 8 \times 10^8$ cm and $M_{\text{WD}} \sim 1M_{\odot}$. Since the timescales of DNOs and QPOs are longer than the dynamical one, some of them will be attributed to oscillations in accretion disks around white dwarfs.

Recent observational evidences concerning time variability in CVs are reviewed by Warner et al. (2003). One of the characteristic points to be emphasized here is the presence of a period correlation between DNOs and QPOs, i.e., $P_{\text{QPO}} \sim 15 P_{\text{DNO}}$.

(b) Low-mass X-ray binaries

Recent observations of QPOs in low-mass X-ray binaries (LMXBs) have been reviewed (van der Klis 2000, 2004; Remillard et al. 2002; McClintock and Remillard 2004, 2006). Variabilities in LMXBs are classified by van der Klis (2004) into four groups: (1) high-frequency phenomena (≥ 100 Hz), (2) a low-frequency complex (a group of correlated $10^{-2} - 10^2$ Hz phenomena), (3) power-law components, and (4) other phenomena. The high-frequency phenomena (QPOs) are further classified into three subclasses (van der Klis 2004); i) neutron-star kilohertz QPOs (kHz QPOs), ii) black-hole high-frequency QPOs (HF QPOs), and iii) neutron-star hectohertz QPOs (hHz QPOs) (see figure 12.1). It is noted that the frequencies of the high-frequency QPOs are on the order of the Keplerian one in the innermost region of relativistic disks.

Our main subject of this chapter is to present current disk-oscillation models of high-frequency QPOs in X-ray binaries. Hence, a more detailed review of observational evidence concerning high-frequency QPOs is given in a separate subsection.

The low-frequency ($10^{-2} \sim 10^2$ Hz) quasi-periodic oscillations (LF QPOs) in X-ray binaries have much variability [for reviews see, e.g., van der Klis (2000, 2004)]. The timescale of these QPOs is several hundred- or thousand-times longer than the dynamical timescale of neutron stars, $\sqrt{R_{\text{NS}}^3/GM_{\text{NS}}} \sim 10^{-4}$ s, for the mass and radius of a neutron star of $M_{\text{NS}} = 1M_{\odot}$ and $R_{\text{NS}} = 10$ km, respectively. Although much discussion has been made so far, there seems to be no widely accepted mechanism.

One interesting observational evidence to be noted here is that some of low-frequency and high-frequency QPOs in neutron-star X-ray binaries are correlated in their frequency changes (Psaltis et. al. 1999; Belloni et al. 2002), and this correlation can be phenomenologically extended to the correlation, $P_{\text{QPO}} \sim 15 P_{\text{DNO}}$, in CVs (Mauche 2002; Warner and Woudt 2005). This is shown in figure 12.2. Another interesting issue

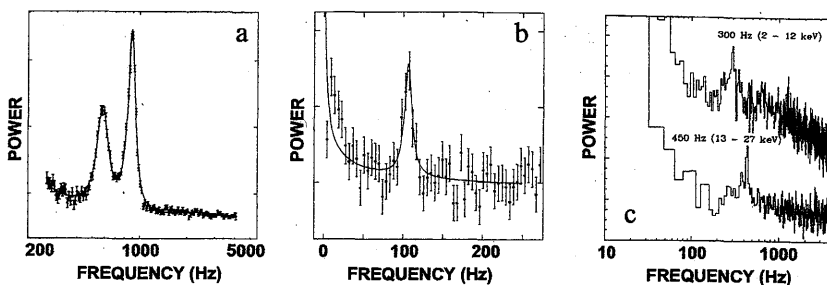


Figure 12.1

Various high-frequency QPOs in X-ray binaries. (a) Twin kHz QPOs in Sco X-1 (van der Klis et al. 1997), (b) hectohertz QPO in 4U 0614+09, (c) HF QPOs in GRO J1655-40 (Strohmayer 2001). In panel (c), the lower curve is the power in the energy range of 13–27 keV and a QPO can be seen at 450 Hz, while the upper curve is the power in the range of 2–12 keV and a QPO is seen at 300 Hz. (After van der Klis 2004)

to be noted here is that in the black-hole candidate GRS 1915+105, in addition to transient low-frequency 10–20 Hz QPOs and high-frequency pair QPOs (113 Hz and 168 Hz), stationary 67 Hz oscillations have been observed (Morgan et al. 1996, 1997), their frequencies having remained constant, despite factors of ~ 2 luminosity variations in the source.

(c) Galactic nuclei

Regarding active galactic nuclei, Ozernoy and Usov (1977) have argued long-timescale quasi-periodic variations from several hundred days to a few years. In X-ray wavelengths, AGNs were usually thought to have no periodic time variations; however, recent observations suggest the presence of a periodic one in AGN (IRAS 18325–5926, Iwasawa et al. 1998), whose frequency is close to that which is scaled up the 67 Hz oscillations to a massive object of $\sim 10^7 M_\odot$.

Recently, the time variations of Sgr A*, the most convincing supermassive black hole in the Universe, have attracted much attention. In its flaring phase, quasi-periodic oscillations of $P = 16.8$ min were detected at IR (Genzel et al. 2003). The results are duplicated in figure 12.3. Variabilities of similar timescale have also been found in the phases of X-ray flares (Achenbach et al. 2004). Furthermore, Miyoshi et al. (2005) have detected spatially resolved quasi-periodic oscillations close to 16.8 min from the data of VLBA observations at 43 GHz, including other quasi-

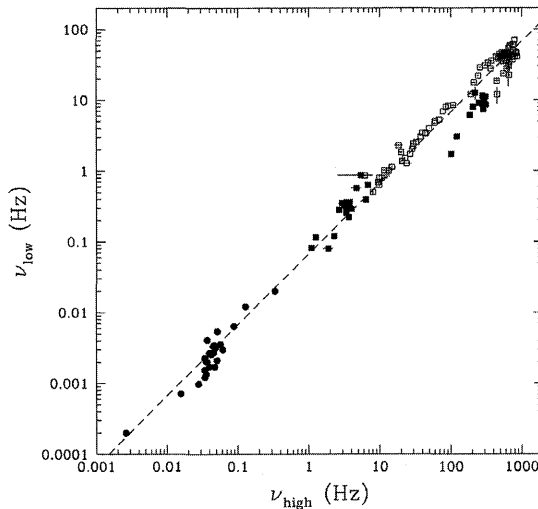


Figure 12.2

Diagram showing that the frequency correlation between the high and low QPOs is extended from CVs to X-ray binaries. The filled circles are for CVs, the open squares are for neutron-star binaries, and the filled squares are for black-hole binaries. (After Warner et al. 2003)

period oscillations. They were observed 1.5 days after a millimeter-wave short-time flare. The detection of oscillations by VLBA is important, since the places where oscillations exist are resolved.

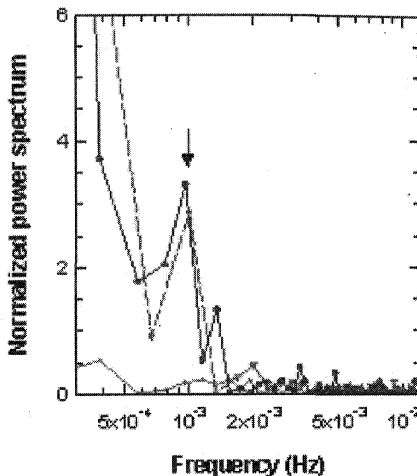
Although possible observational evidence for quasi-periodic oscillations is being accumulated for various kinds of compact sources surrounded by accretion disks, their existence and characteristics still remain an open issue, or must be confirmed.

12.1.2 Observational Review on High-Frequency QPOs

As mentioned before, high-frequency QPOs are classified into three subclasses (see also figure 12.1). Their basic characteristic features are summarized below by separating them into those of neutron-star sources and of black-hole sources.

(a) KHz and hectohertz QPOs in neutron-star sources

KHz QPOs in neutron-star sources usually appear in pairs, although occasionally only one peak is observed. There are similarities between the kHz QPOs in neutron-star X-ray binaries and the HF QPOs in black-hole

**Figure 12.3**

Normalized power spectrum of flares of Sgr A* on 15 June (broken curve) and on 16 June (solid curve), 2003. There is a significant peak with a time period of 16.8 ± 2 min (shown by arrow). The third curve with low power is for a comparison star, which does not show such a quasi-periodic structure. (After Genzel et al. 2002. Reproduced by permission from Nature Vol. 425 No. 6961 pp. 934–937 30 Oct. 2003 @Macmillian Magazines Ltd.)

X-ray binaries. Since black holes have no rigid surface, these similarities suggest that any variability in both X-ray binaries must have originated in accretion disks with strong gravitational fields. Unlike HF QPOs in black-hole X-ray binaries, however, the frequencies of kHz QPOs in neutron-star X-ray binaries change with time over hundreds of hertz in correlation with the source state, so that an increase of the mass accretion rate increases the frequencies (van der Klis et al. 1997). The peak separation usually decreases by a few tens of Hz when both peaks move up by hundreds of Hz. Recent analyses of observational data confirm that the frequency ratio is not compatible with the idea that it is a constant (Belloni et al. 2005). In cases in which the neutron-star spin frequency is observed, the separation frequency of the twin peaks is typically within 20% of the spin frequency, or half of that, depending on the source.

Neutron-star hectohertz QPOs (hHz QPOs) have a frequency range of 100–200 Hz. They are seen in atoll sources (less luminous neutron-star LMXBs) in most states, but their presence in Z sources (luminous neutron-star LMXBs) is uncertain (van der Klis 2004). Different from

kHz QPOs, the frequencies of hHz QPOs are approximately constant, which is similar across sources.

Finally, figure 2.9 of van der Klis (2004) concerning frequency correlations among various QPOs in neutron-star LMXBs (including the low-frequency QPOs) is duplicated as figure 12.4.

(b) HF QPOs in black-hole sources

The high-frequency QPOs in black-hole LMXBs are in the range of 100 to 450 Hz. So far, they have been detected in seven sources. Remarkably, three sources [GRO J1665-40 (300, 450 Hz), XTE J1550-564 (92, 184, 276 Hz), and GRS 1915+105 (41, 67, 113, 168 Hz)] exhibit pairs of QPOs that have commensurate frequencies in a 3:2 ratio (e.g., see the review by McClintock and Remillard 2004, 2006). In four other sources, only single-component HF QPOs have been observed: 4U1630-47 (184Hz), XTE J1859+226 (190 Hz), XTE J1650-500 (250 Hz), and H1743-322 (240 Hz) (see the review by McClintock and Remillard 2004, and also table 12.1). Different from neutron-star kHz QPOs, HF QPOs in black holes occur at fixed frequencies. In pair QPOs, the higher frequency QPO is sharper in width than that of the lower one, and observed at higher energy (Remillard 2005).

Table 12.1 Frequencies of HF QPOs in black-hole binaries.

source name	frequencies (Hz)
GRO J1665-40	300, 450
XTE J1550-564	92, 184, 276
GRS 1915+105	41, 67, 113, 168
H1743-322	240
4U 1630-47	184
XTE J1859+226	190
XTE J1650-500	250

The appearance of HF QPOs is correlated to the state of the sources. They do not occur in the high/soft state [the thermal disk state (TD state)], where the power-law component is absent, nor in the low/hard state, where there is radio emission and the power-law is flatter. They occur mainly in the very high state [the steep power-law state (SPL)], where the disk consists of a power-law component and a thermal disk, except for the 67 Hz QPOs in GRS 1915+105, which appear in the high/soft state, especially when $L_x > 10^{38}$ erg s⁻¹ (McClintock and Remillard 2004). To sum up, these QPOs appear only in high-luminosity states where $L > 0.1L_E$.

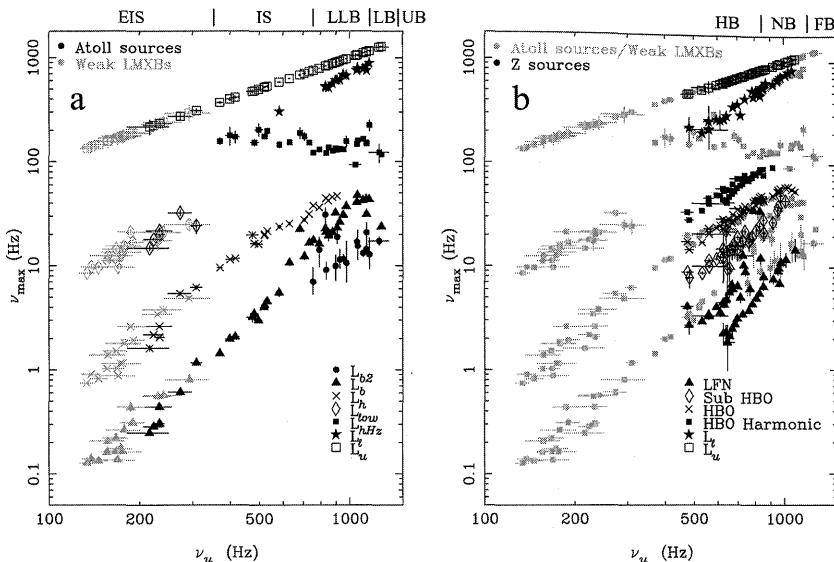


Figure 12.4

Frequency correlations. (a) Atoll sources and weak LMXBs, (b) Z sources compared with these objects. The characteristic frequencies of the components are plotted as indicated; approximate source state ranges are indicated at the top. The abscissa is the upper frequency of the pair kHz QPOs. (After van der Klis 2004)

12.2 Sonic-Point Instability and Trapped Oscillations

In this section we show that the innermost region of relativistic accretion disks is a particular place where the disks have a tendency to become time-variable with the time scale on the order of the Keplerian time. This is shown by demonstrating a relation between topology and instability and also by performing numerical simulations.

12.2.1 Relation between Topology and Instability

In relation to high-frequency QPOs, we should remember that the innermost region of steady transonic accretion flows are unstable against perturbations, depending on the type of transonic point (Kato et al. 1988a,b). That is, a nodal-type critical point is unstable against small-amplitude local perturbations around the point, although a saddle-type critical point is stable.

The sonic radius is a critical point in the sense that in the differential equation describing the radial flow, v_r (i.e., $dv_r/dr = N/D$), the denom-

inator D vanishes at that point. To pass the radius, the accretion flow must satisfy the regularity condition $N = 0$ there, as discussed in section 8.2. Since the sonic radius is a critical point in the above sense, the topology around the point on the v_r - r plane has a particular structure. As mentioned in section 8.3, if the Shakura-Sunyaev type α -viscosity is adopted, steady accretion flows, which tend to the Shakura-Sunyaev type standard solution in the outer region, should pass either a nodal-type or a saddle-type critical point, depending on the magnitude of the viscosity parameter, α . That is, the sonic radius is a saddle for α smaller than a critical value, α_{crit} , while it is nodal for $\alpha > \alpha_{\text{crit}}$. Here, the critical value, α_{crit} , is slightly smaller than 0.1 in standard disks (see section 8.4).

Let us first consider an isothermal disk, since in this case stability analyses are simple. We treat the vertically integrated, or averaged, quantities. Then, we have three characteristic speeds¹ in the radial direction, describing the flow. Corresponding to them, there are three modes of flow. Two of them are acoustic modes whose fronts propagate in the radial direction with characteristic speeds, $v_r \pm c_T$, and the other is a viscous mode that propagates in the radial direction with a characteristic speed, v_r , where $v_r (< 0)$ and c_T are the accretion speed and the isothermal sound speed, respectively.

We now consider small-amplitude perturbations superposed over the steady accretion flow. Then, we have three fronts of perturbations that propagate in the radial direction with $v_0 + c_T$, $v_0 - c_T$, and v_0 , respectively, where $v_0 (< 0)$ is the radial accretion speed in the unperturbed disks. For the perturbation that propagates with $v_0 + c_T$ (this is nothing but the outgoing acoustic perturbation), the sonic radius, $v_0 + c_T = 0$, is a singular point (critical point). This means that at the sonic radius, this outgoing acoustic perturbation becomes just *standing*. In other words, the relative amplitude of this perturbation to those of the other modes (i.e., ingoing acoustic perturbation with $v_0 - c_T$ and viscous modes with v_0) becomes infinite there, since other modes can freely pass with finite speeds the sonic radius, while the first one does not.

Detailed analyses of how outgoing acoustic perturbations behave at and near to this singular point have been made by Kato et al. (1988a) [also see chapter 15 of the first edition (Kato et al. 1998)]. The results show that the perturbations are unstable and grow at, and near to, the

¹See, for example, Shu (1992) for general discussion on the characteristics.

sonic point, when

$$\alpha\Omega_c > \left. \frac{dv_0}{dr} \right|_c \quad (12.1)$$

is satisfied, where Ω_c and $(dv_0/dr)_c$ are the angular velocity of disk rotation and the radial derivative of the unperturbed accretion velocity at the sonic point, respectively. It is noted that $(dv_0/dr)_c$ is positive.

An interesting point is that the above condition of instability is just equal to the condition of the nodal-type critical point. That is, *the criterion for the appearance of a nodal-type sonic radius coincides with that for instability of the sonic point against inertial-acoustic perturbations* (Kato et al. 1988a).

12.2.2 Comments on General Relation between Topology and Instability

We have noticed above that in the case of isothermal disks a nodal-type critical point is unstable against small-amplitude, isothermal perturbations localized around the point. This relation between the topological type of critical point and its stability is, however, free from the assumption of isothermality. In the case of non-isothermal disks, at least one more differential equation (i.e., energy equation) is added to describe disks. Nevertheless, we can generally show that there is still a one-to-one correspondence between the topological type of critical point and the stability (Kato et al. 1988b). That is, the saddle-type critical point is stable, while the nodal-type one is unstable against local perturbations around the point.

It is, however, noted here that the above results are for the case of the Shakura-Sunyaev-type α -model, i.e., for the case in which the $r\varphi$ -component of the stress tensor, $T_{r\varphi}$, is taken as

$$T_{r\varphi} = -\alpha\Pi. \quad (12.2)$$

It seems to be not yet examined whether the above one-to-one correspondence between the topological type and the stability still holds in the case when a diffusion form of the $r\varphi$ -component of $T_{r\varphi}$,

$$T_{r\varphi} = -2\eta H r \frac{d}{dr} \left(\frac{v_\varphi}{r} \right), \quad (12.3)$$

is adopted, where H is the half-thickness of the disks, and η is the viscosity.

If a diffusion-type stress tensor [i.e., equation (12.3)] is adopted, the critical point is always a saddle (Abramowicz and Kato 1989) and stable (Kato et al. 1993) when the disks are isothermal. In the case when non-isothermal disks are considered, with the diffusion form of $T_{r\varphi}$, a nodal-type critical point appears (Chen and Taam 1993; Chen et al. 1997). The stability of the critical points in this case, however, has not yet been examined.²

We should always be reminded that there is a possibility that the appearance of a nodal-type critical point in disks is a result of some unphysicalness of the adopted equations. For example, an unphysicalness might arise in the procedure of vertical integration of the basic equations. Furthermore, we should remember that both the algebraic form of $T_{r\varphi}$, i.e., equation (12.2), and the diffusion-type form of $T_{r\varphi}$, i.e., equation (12.3), are unrealistic. For example, a diffusion-type stress tensor violates the causality in the sense that information can propagate with infinite speed. This means that acoustic perturbations can pass through the sonic point from inside to outside. There have been some attempts to overcome this causal inconsistency by introducing a velocity-dependent viscosity coefficient (Narayan 1992), or by introducing additional differential equations to describe $T_{r\varphi}$ (Kato and Inagaki 1994; Narayan et al. 1994; Papaloizou and Szuszkiewicz 1994; Kato 1994). Even in the case of the above non-local description of the stress tensor by Kato (1994), however, nodal-type critical points still appear, although the parameter range where a nodal-type critical point appears is narrow (Nakamura 1995).

12.2.3 Numerical Simulations Examining Stability of Innermost Region

Numerical simulations examining the stability of the innermost region of black-hole accretion disks against small-amplitude perturbations have been made. Since the growing perturbations are the inertial-acoustic oscillations, before describing the results of numerical simulations, we present here several situations in favour of growth of the inertial-acoustic oscillations in the innermost region of disks.

²The appearance of the nodal-type critical point is not restricted to rotating systems. For example, in the case of line-driven stellar winds in early-type stars, linear momentum is transported by radiation pressure in non-diffusion forms. In this case the sonic point of the wind can become nodal (e.g., Poe et al. 1990), and the nodal-type critical point is unstable against localized perturbations (Kato et al. 1993).

(a) **Situations in favor of growth of inertial-acoustic oscillations**

(1) *Viscous oscillatory instability*

The innermost region of relativistic disks is a place where inertial-acoustic oscillations (see section 11.1) are easy to be excited due to effects of viscosity. The reason is partially related to the fact that the rotation is high there and highly differential, while the frequency of oscillations, which is about the radial epicyclic frequency, is relatively low compared with the frequency of rotation [see section 14.2 of the first edition (Kato et al. 1998)].

(2) *Instability of the nodal-type critical point*

The sonic point becomes unstable when a nodal-type critical point appears (see section 8.3). In the case of nodal-type critical point, inertial-acoustic perturbations localized around the radius grow there with time, as discussed in the previous subsection.

(3) *Wave reflection and trapping*

In the innermost region of geometrically thin relativistic disks, the radial distribution of the epicyclic frequency, κ , has a maximum κ_{\max} at a certain radius, say r_{\max} , and κ decreases inward to become zero at the radius of the marginally stable circular orbit, r_{ms} (see sections 2.5 and 11.2). In addition, the inner edge of geometrically thin disks, whose radius is nearly equal to r_{ms} , is a sharp boundary where the density sharply decreases inward. Because of the presences of κ_{\max} and of the sharp inner edge, axially-symmetric inertial-acoustic oscillations with $\omega < \kappa_{\max}$ are partially trapped in an inner region (between r_{ms} and r_{\max}) of disks (see section 11.3).

It is noted that the reflection of perturbations at the inner edge of disks is not only acoustic perturbations. The reflection of the thermal mode to the outgoing acoustic mode at the sonic radius by mode change also occurs, which is demonstrated by figure 9.12 in section 9.4.

(4) *Smallness of group velocity at $\omega \simeq \kappa_{\max}$*

Waves whose frequencies are higher than κ_{\max} will propagate away, outward through a radius of κ_{\max} . In accretion disks with no outer boundary, such waves propagate to infinity, and are finally phase-mixed with each other.

For waves with $\omega \simeq \kappa_{\max}$, however, the situations is different. These

waves have a low group velocity and long wavelength around a radius of κ_{\max} , say r_{\max} . That is, if we simply take the dispersion relation as

$$\omega^2 = \kappa^2 + c_s^2 k^2, \quad (12.4)$$

the group velocity, v_g , is

$$v_g = \frac{\partial \omega}{\partial k} = \pm c_s \frac{(\omega^2 - \kappa^2)^{1/2}}{\omega}. \quad (12.5)$$

For waves with $\omega = \kappa_{\max}$, the group velocity, v_g , vanishes at $r = r_{\max}$. When $\omega \simeq \kappa_{\max}$, the waves have a low group velocity and a long wavelength over a moderately wide region around $r = r_{\max}$, since κ changes little around $\kappa \sim \kappa_{\max}$.

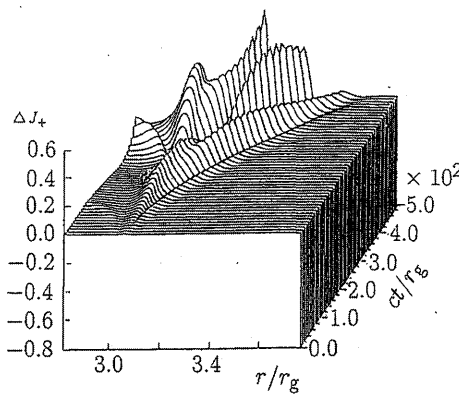
This suggests that oscillations of $\omega \sim \kappa_{\max}$ stay for a long time around $r \sim r_{\max}$ as a moderately long-scale feature without being transported away, if once excited.

(b) Simulations in isothermal disks

Hydrodynamical simulations to examine stability of the innermost region of relativistic disks were started by Matsumoto et al. (1988, 1989) by using time-dependent hydrodynamical equations given in section 7.4. Matsumoto et al. (1988) considered isothermal perturbations in isothermal disks with the standard Shakura-Sunyaev-type α -viscosity; i.e., $T_{r\varphi} = -\alpha\Pi$. We present here their results first, since the essential behaviors of oscillations and instabilities are shown there.

They first examined whether small-amplitude perturbations localized around the sonic point grow or are damped with time. They confirmed that no perturbation really grows when $\alpha < 0.1$, but perturbations grow when $\alpha \geq 0.1$. This is consistent with the fact that the saddle-type critical point is stable, but the nodal-type one is unstable.

As a typical example of unstable cases, simulation results in the case in which $\alpha = 0.3$ and $c_T/c = 10^{-3}$ are presented in figure 12.5. A small-amplitude perturbation imposed near to the sonic point r_c ($\sim 3.06r_g$) propagates both inward and outward as acoustic waves, while being amplified. In addition, there is another perturbation, which is just standing around the critical point. At the early stage when the amplitude is small, this perturbation grows monotonically, but later becomes oscillatory. Figure 12.6 shows that the outward propagation of perturbations is blocked around a radius of $4r_g$ by a barrier of the epicyclic frequency. In this case of large viscosity ($\alpha = 0.3$), the amplitude of the oscillations grows until shock waves are formed in both the outward and inward

**Figure 12.5**

Time variation of $\tilde{J}_+ \equiv (v_r/c_s + \ln \Sigma)/2$ in isothermal disks with $\alpha = 0.3$, $c_T/c = 10^{-3}$, and $\dot{M}/\dot{M}_{\text{crit}} = 1.6$, where \dot{M}_{crit} is the critical accretion rate defined by $\dot{M}_{\text{crit}} = L_E/c^2$. (After Matsumoto et al. 1988)

propagating perturbations (see also figure 12.5). In the later stage of evolution, quasi-periodic global oscillation is established, which is also clear in figure 12.6. The kinetic energy of the oscillations is trapped around the radius $3.2 < r/r_g < 3.8$.

The period of the quasi-periodic oscillations, P , is given roughly by

$$P \sim 100 \frac{r_g}{c} \sim 10^{-3} \left(\frac{M}{M_\odot} \right) \text{ s}, \quad (12.6)$$

which is comparable to the period corresponding to κ_{\max} . The appearance of oscillations whose frequencies are $\sim \kappa_{\max}$ seems to be a common feature, even in more general cases, as will be shown later.

Figure 12.7 shows the time variation of the accretion rate onto the central object when $\alpha = 0.15$ and $c_T/c = 10^{-3}$. In this case the amplitude of oscillations modulates. The time scale of the modulation is 2000–4000 r_g/c , about the time by which an acoustic wave travels across the trapped region of oscillations.

(c) Simulations in non-isothermal disks

Matsumoto et al. (1989) extended their simulations to non-isothermal cases. More elaborated simulations of non-isothermal cases, however, have been made (Honma et al. 1992; Chen and Taam 1995), and they are extended to cases of two-dimensional disks (Milsom and Taam 1997).

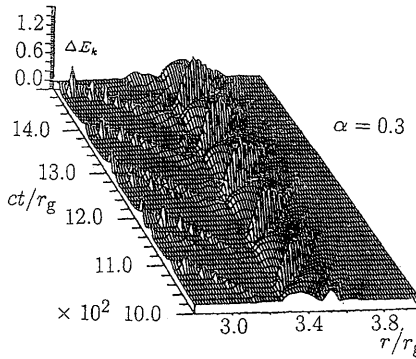


Figure 12.6

Time variation of the kinetic energy, $E_K \equiv \Sigma v_r^2/2$, of the radial motion (in units of $\Sigma_c c_T^2$, Σ_c being the surface density at r_c) in the same case as figure 12.5. (After Matsumoto et al. 1988)

These studies seem to qualitatively confirm the results by Matsumoto et al. (1988).

In the case of simulations by Chen and Taam (1995), the disk is assumed to be optically thick, and the mass of the central object is $10M_\odot$. They considered the case in which the stress tensor has a diffusion form. Furthermore, they took into account the effects of the viscous force in the radial force balance as well as in the azimuthal force balance. They performed simulations for a long time span, and derived the power spectrum of the disk-luminosity variations. They found that an oscillatory non-steady behavior exists in the inner region of disks ($r < 10r_g$) for a sufficiently large α (≥ 0.2) and for mass-accretion rates of less than about 4.8-times \dot{M}_{crit} . The variations of the integrated bolometric luminosity are less than 3%.

Prior to Chen and Taam (1995), similar simulations of time variations had been made by Honma et al. (1992), who investigated the case of supermassive central objects with a mass of $M = 10^4 M_\odot$.³ The values

³The computations for the case of massive central objects are really time-consuming, since with an increase of the black-hole mass the sound speed in the innermost region of accretion disks falls off and the wavelength of oscillations measured in units of r_g decreases (notice the dispersion relation to the inertial-acoustic oscillations), provided that the frequency of oscillations is fixed in units of c/r_g . Hence,

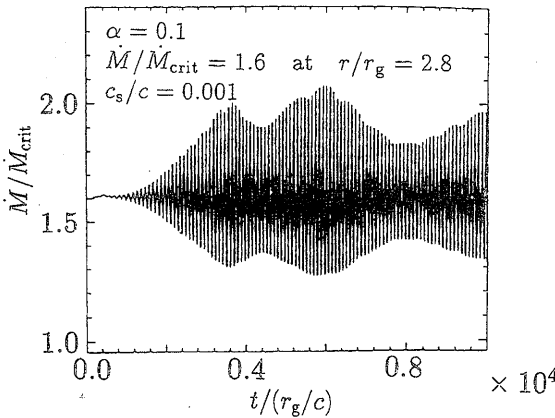


Figure 12.7

Time variation of the accretion rate at $r/r_g = 2.8$ (inside the sonic point). The parameters adopted are $\alpha = 0.15$, $c_T/c = 10^{-3}$ and the mass accretion rate, \dot{M} , from the outside is $1.6\dot{M}_{\text{crit}}$. (After Matsumoto et al. 1988)

of the other parameters adopted in their calculations were $\alpha = 0.1$ and $\dot{M} = 0.8\dot{M}_{\text{crit}}$. In their simulations, different from those by Chen and Taam (1995), the Shakura-Sunyaev-type α -model was adopted, and no term of viscous stress was taken into account in the r -component of the momentum equation.

The overall features of the disk behavior are essentially the same as those obtained by others (Matsumoto et al. 1988; Chen and Taam 1995) to $1-10 M_\odot$, except that in the present case the wavelength of oscillation in units of r_g is shorter than the latter ones. That is, the innermost region of the disk with a radius of $\sim 3-3.5 r_g$ is highly disturbed, and waves are generated there and propagate both inwards and outwards, as shown in figure 12.8. Both waves propagating inwards and outwards immediately grow to shock waves (cf., figures 12.5 and 12.6).

In their simulations, quasi-periodic oscillations, whose frequency is $\simeq 100(r_g/c)$, again exist. It is notable that this period roughly corresponds to the frequency of κ_{max} , similar to the case of a stellar-mass central object (Matsumoto et al. 1988, 1989; Chen and Taam 1995). From this fact, we expect that the presence of an oscillation whose frequency is

more calculation mesh points, and thus longer computation times, are needed. To avoid this difficulty Honma et al. (1992) adopted a relatively small black-hole mass, but nevertheless the results of the simulations were sufficiently useful to demonstrate the overall behavior of the unstable phenomena.

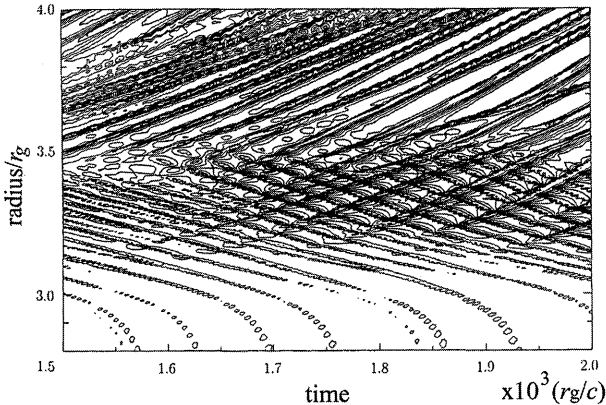


Figure 12.8

Equi-contour curves of the time-dependent local accretion rate on the r - t plane in a simulation with $M_{\text{BH}} = 10^4 M_{\odot}$, $\alpha = 0.1$, and $\dot{M}_{\text{init}} = 0.8 \dot{M}_{\text{crit}}$. The curves for $\dot{M} = -160, -96.0, -32.0, -16.0, -9.6, -3.2, 3.2, 9.6, 16.0, 32.0, 96.0$, and $160 \dot{M}_{\text{crit}}$ are shown. (After Honma et al. 1992)

around κ_{\max} is a rather general feature of oscillations of the innermost regions of geometrically thin relativistic disks,⁴ independent of α , M , and \dot{M} . This might be related to the fact that a wave of $\omega \sim \kappa_{\max}$ has a long wavelength and a low group velocity over a relatively wide region around r_{\max} , as mentioned before.

Two-dimensional (r - z) numerical simulations by Milsom and Taam (1997) also show the presence of oscillations with κ_{\max} . This might be understandable if we consider that waves whose frequency is close to κ_{\max} are nearly horizontal oscillations (i.e., inertial-acoustic oscillations).

So far, we have summarized simulation results based on the Shakura-Sunyaev-type α -viscosity, or diffusion-type viscosity, the coefficient of viscosity being taken to be a parameter. After the magneto-rotational instability (Balbus and Hawley 1991) became widely recognized as the origin of the turbulence required in magnetized accretion disks, full magnetohydrodynamical 2D or 3D simulations have been made without introducing α parameter.

Some recent full MHD numerical simulations (Kato 2004; Matsumoto and Machida 2006; Machida and Matsumoto 2006) really show the presence of quasi-periodic oscillations in the innermost region of transonic

⁴There is another type of oscillations of $\omega \sim \kappa_{\max}$, as discussed in section 11.3; that is, gravity waves (g-modes) trapped around the radius of $\kappa = \kappa_{\max}$.

accretion flows. Their origins, however, seem not to be directly related to the unstable oscillations presented here. These simulations seem to rather suggest the presences of oscillatory phenomena of purely hydro-magnetic origins, or of phenomena related to oscillations which will be discussed in section 12.3 or section 12.5. Further simulations are of importance to clarify whether, and in what cases, the innermost region of accretion disks is time-dependent, and whether it is related to the observed quasi-periodic oscillations.

12.3 Resonant Oscillations in Warped Disks

The frequencies of quasi-periodic oscillations discussed in the previous section qualitatively agree with those of high-frequency QPOs observed in LMXBs. They, however, cannot describe why in many cases they appear in a pair and the frequency ratio of the pair is close to 3:2.

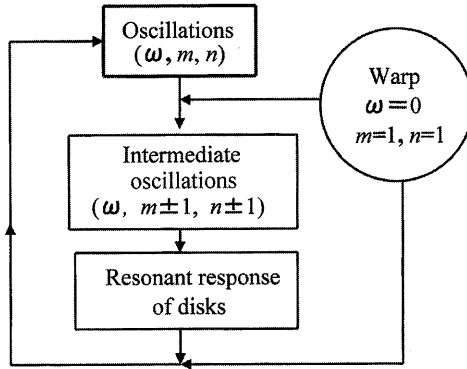
The closeness of the frequency ratio to commensurability suggests that some resonance processes play important roles in the origins of high-frequency QPOs. A group led by Abramowicz and Klużniak was the first to have directed one's attention to the importance of resonant oscillation processes (Abramowicz and Klużniak 2001; Klużniak and Abramowicz 2001). Their parametric resonant models are briefly reviewed later in section 12.5.

12.3.1 Resonance in Deformed Disks

Here, we should remember that in externally deformed disks, the excitation of disk oscillations by a resonance process is generally expected. A well-known example of this excitation of oscillations in deformed disks is superhumps known in dwarf nova (Whitehurst 1988; Hirose and Osaiki 1990; Lubow 1991). This is a resonant excitation of slowly rotating one-armed oscillations on a tidally deformed disk by a 3:1 parametric resonance, which is called the tidal instability (see section 6.1 of the first edition of this book). Another example of excitation of disk oscillations on deformed disks is the formation of a spiral pattern on galactic disks deformed by ram-pressure (Tosa 1994; Kato and Tosa 1994).

As a global and external disk-deformation of black-hole binaries, a warp would be most conceivable.⁵ In the following we show that the ba-

⁵A warp is a disk deformation of $m = n = 1$ (see chapter 11). A deformation of $m = 1$ and $n = 0$ (i.e., a kind of one-armed inertial-acoustic oscillations) is also conceivable as one of possible candidates of disk oscillations. Even in the latter case, the main conclusions concerning frequencies of resonant oscillations in this chapter

**Figure 12.9**

Feedback processes of nonlinear resonant interaction acting on disk oscillations. The original oscillations are characterized by ω , m , and n . Since the warp corresponds to a wave mode of $(\omega, m, n) = (0, 1, 1)$, the nonlinear interaction between them brings about intermediate modes of oscillations of $\omega, m \pm 1$, and $n \pm 1$. To these intermediate oscillations, the disk resonantly responds at the radius where the dispersion relation of the intermediate oscillations is satisfied. The intermediate oscillations feedback to the original oscillations after the resonance. This feedback process amplifies or dampens the original oscillations, since resonance is involved in the interaction processes. (After Kato 2004b)

sic characteristics of observed high-frequency QPOs can be described as disk oscillations resonantly excited on warped disks (Kato 2003, 2004a,b; Klužniak et al. 2004; Kato 2005a,b; Kato and Fukue 2006). It is important to note that the resonance in warped disks is a result of strong relativistic gravity, as shown below. In other words, in nonself-gravitating Newtonian Keplerian disks, where $\Omega \sim \kappa$, the resonant conditions discussed below are never realized.

As mentioned before, HF QPOs in black-hole sources appear only in a very high state [steep power-law state (SPL state)] (McClintock and Remillard 2006). In a transition from a high/soft state (thermal disk state) to a very high state (SPL state), disks may be warped, since triggers that make the phase transition will not always occur axisymmetrically nor plane-symmetrically.

12.3.2 Overview of Resonance Processes on Warped Disks

An overview of the non-linear resonant processes between disk oscillations and a warped disk is sketched in figure 12.9.

are little changed. It is also noted that excitation of disk oscillations by asymmetric gravitational potential is proposed by Pétri (2006).

(a) Warp

A warp is a global deformation of disks, belonging to perturbations of $m = 1$ and $n = 1$, where m and n are the numbers of nodes of oscillations in the azimuthal and vertical directions, respectively (for details, see section 11.3). Let us denote the displacement associated with the warp by $(\xi_r^W, \xi_\varphi^W, \xi_z^W)$. Then, in the lowest order of approximations, $\xi_r^W = \xi_\varphi^W = 0$ and ξ_z^W is

$$\xi_z^W \propto \exp[i(\omega_p t - \varphi)], \quad (12.7)$$

where ω_p is the angular frequency of precession of the warp, which is taken, for a while, to be zero. The effects of ω_p are discussed later. It is noted that in the lowest order of approximations, ξ_z^W is independent of z .⁶

(b) Oscillations in disks

On the warped disks described above, a disk oscillation is superposed. For simplicity, we consider a vertically isothermal disk.⁷ Then, the radial component of displacement, ξ_r , associated with an oscillation mode of (ω, m, n) is approximately expressed, in local approximations, as (see section 11.3)

$$\xi_r = \exp[i(\omega t - m\varphi)] f(r) H_n\left(\frac{z}{H}\right), \quad (12.8)$$

where ω is the frequency of the oscillation. The quantity $H_n(z/H)$ is a Hermite polynomial of order n with argument z/H , representing the eigen-function of the oscillations in the vertical direction. Here, H is the half thickness of the disk, which is defined by $H(r) = c_T(r)/\Omega_K(r)$ (section 7.2), $c_T(r)$ being the isothermal sound speed. The radial dependence of the oscillations is denoted by $f(r)$.

The azimuthal component of the displacement, ξ_φ , and the pressure perturbation (normalized by unperturbed density), i.e., p_1/ρ_0 , have the same φ - and z -dependences as ξ_r . However, the vertical component of the displacement, ξ_z , has a different z -dependence. That is, they are proportional to dH_n/dz [i.e., proportional to $H_{n-1}(z/H)$] and the number of nodes in the vertical direction is smaller than that of ξ_r by one [see equation (11.23)]. In the fundamental mode ($n = 0$) of oscillations in the vertical direction (i.e., inertial-acoustic oscillations), for example, ξ_r has no z -dependence, and $\xi_z \sim 0$. In the first overtone ($n = 1$), ξ_r

⁶See the second paragraph of the next item (b) with notice that $n = 1$ in the warp.

⁷The case of a vertically polytropic disk is qualitatively described later [(d) in subsection 12.3.2].

has one node (on the equator) in the vertical direction, while ξ_z has no node in the vertical direction, and the flow crosses the equator upward and downward (see figure 11.2).

If we adopt local approximations and some other subtle approximations to describe the oscillations of (ω, m, n) , the local dispersion relation of the oscillations is (see section 11.3)

$$[(\omega - m\Omega)^2 - \kappa^2][(\omega - m\Omega)^2 - n\Omega_{\perp}^2] = c_s^2 k^2 (\omega - m\Omega)^2, \quad (12.9)$$

where k is the wavenumber in the radial direction and c_s is the acoustic speed. The quantity Ω_{\perp} on the left-hand side of equation (12.9) is the frequency of the vertical oscillation of a fluid element around the equator (i.e., the vertical epicyclic frequency, see section 2.5), and is nothing but the Keplerian frequency, Ω_K , in the limit of the Schwarzschild metric. If we want to extend our present analyses to cases of the Kerr metric, a simple approximate way is to still use equation (12.9) with κ and Ω_{\perp} for the Kerr metric. In order to be able to trace back the origin of some terms in the final results, we hereafter keep the notation Ω_{\perp} , without using Ω_K , even when the Schwarzschild metric is considered.

As discussed in section 11.3, the dispersion relation (12.9) shows that there are two types of oscillation modes, except for the case of $n = 0$. In the case of $n = 0$ we have inertial-acoustic oscillations alone, while in the case of $n = 1$ we have c -mode and g -mode oscillations. Furthermore, two types of oscillations in $n \geq 2$ are g - and vertical p -mode oscillations (see table 11.1 in section 11.1).

(c) Non-linear coupling and resonance

A nonlinear coupling between an oscillation specified by (ω, m, n) and a warp specified by $(0, 1, 1)$ is now considered (see figure 12.9). Our interest here is to examine non-linear couplings that can feedback into the original oscillation (ω, m, n) after passing a resonance. The nonlinear couplings of this type consist of two steps. The first step is a direct coupling between the oscillation of (ω, m, n) and the warp of $(0, 1, 1)$. This brings about oscillations specified by $(\omega, \tilde{m}, \tilde{n})$ (see figure 12.9), where

$$\tilde{m} = m + 1 \quad \text{or} \quad m - 1 \quad (12.10)$$

and

$$\tilde{n} = n + 1 \quad \text{or} \quad n - 1. \quad (12.11)$$

Any combination of \tilde{m} and \tilde{n} is possible. That is, there are four types of combinations. We call these oscillations *intermediate oscillations* (see figure 12.9).

An important point to be emphasized here is that if the amplitude of the initial oscillations of (ω, m, n) is fixed, the disk experiences a forced oscillation resulting from intermediate oscillations with $(\omega, \tilde{m}, \tilde{n})$. This forced oscillation has resonance at particular radii with the disk, and there a secular energy exchange between the intermediate oscillations and the disk is realized. The radii are the places where the dispersion relation of the intermediate oscillations is satisfied. If local approximations are adopted, the dispersion relation is given by $D = 0$, where

$$D \equiv [(\omega - \tilde{m}\Omega)^2 - \kappa^2][(\omega - \tilde{m}\Omega)^2 - \tilde{n}\Omega_{\perp}^2] - c_s^2 k^2 (\omega - \tilde{m}\Omega)^2. \quad (12.12)$$

Here, k is practically the same as the radial wavenumber of the original oscillation of (ω, m, n) , since the radial wavenumber of the warp is assumed to be sufficiently small compared with that of the oscillations.

For a resonance to really occur at radii of $D = 0$, the radii must be the poles of $1/D(r) = 0$ in the complex r -plane, in addition to $D = 0$ there. In this sense, the case of $\tilde{n} = 0$ is special. In this case D given by equation (12.12) is

$$D = [\omega - (m \pm 1)\Omega]^2 \{[\omega - (m \pm 1)\Omega]^2 - \kappa^2 - c_s^2 k^2\}, \quad (12.13)$$

and the places of $\omega = (m \pm 1)\Omega$ are not resonant points, although $D = 0$ there, since D is proportional to the square of $\omega - (m \pm 1)\Omega$. That is, in the case of $\tilde{n} = 0$, resonances do not occur at the radius of $\omega = (m \pm 1)\Omega$, but occur only at radii where $[\omega - (m \pm 1)\Omega]^2 - \kappa^2 - c_s^2 k^2 = 0$.

Except for the above case of $\tilde{n} = 0$, the resonances occur at two radii. One is near to the radii of

$$[\omega - (m \pm 1)\Omega]^2 - \kappa^2 = 0 \quad (\text{horizontal resonance}) \quad (12.14)$$

and the other is near to

$$[\omega - (m \pm 1)\Omega]^2 - \tilde{n}\Omega_{\perp}^2 = 0 \quad (\text{vertical resonance}). \quad (12.15)$$

[The last term of equation (12.12), i.e., the term with $c_s^2 k^2$ is assumed to be small compared with the other terms, since we are considering geometrically thin disks.] The former is a resonance through horizontal motions. Hence, hereafter, we call the resonance a *horizontal resonance*. The latter one is a resonance through vertical motions. Hence, we hereafter call it a *vertical resonance*.

The second step of coupling is a non-linear interaction between the above intermediate oscillations and the warp. This is necessary because

by this process the resonant interaction can feedback to the original oscillation of (ω, m, n) (see figure 12.9). This interaction leads to amplification or dampening of the original oscillation. Whether resonant processes excite or dampen the oscillations is a complicated problem. Kato (2004b) examines this problem and shows that in the case of vertically isothermal disks, the horizontal resonances of inertial-acoustic oscillations ($n = 0$) and of g -mode oscillations ($n \neq 0$) lead to amplification of these oscillations, while other types of resonance lead to a damping of oscillations. Hence, in the following, the detailed discussion is confined only to the case of a horizontal resonance of the inertial-acoustic ($n = 0$) or that of g -mode oscillations. Before doing this, however, the resonant conditions for various cases are briefly summarized, including other cases.

12.3.3 Resonant Conditions

Three cases are considered separately: (a) a horizontal resonance of inertial-acoustic oscillations or g -mode oscillations, (b) a vertical resonance of inertial-acoustic oscillations or g -mode oscillations, and (c) a horizontal resonance of other modes of oscillations (i.e., c -mode oscillations and vertical p -mode oscillations with $n \geq 1$). It is noted that cases of vertical resonance of c -mode oscillations and vertical p -mode oscillations with $n \geq 1$ are absent, since the resonant condition in this case is not satisfied anywhere.

As long as the vertically isothermal disks are considered, no parameter characterizing the vertical disk structure is involved in the expression for the resonant condition, as shown below. In order to demonstrate cases in which the resonant condition (and thus the resonant radius) depends on the vertical disk structure, the vertical resonance in vertically polytropic disks is briefly presented in the final part of this subsection.

(a) Horizontal resonance of inertial-acoustic or g -mode oscillations

If the local dispersion relation [equation (12.9)] is adopted, the group velocity of waves in the radial direction, $\partial\omega/\partial k$, is given by

$$\frac{\partial\omega}{\partial k} = \pm c_s \frac{(\omega - m\Omega)^2[(\omega - m\Omega)^2 - \kappa^2]^{1/2}[(\omega - m\Omega)^2 - n\Omega_\perp^2]^{1/2}}{(\omega - m\Omega)^4 - n\kappa^2\Omega_\perp^2}. \quad (12.16)$$

Hence, in the case of inertial-acoustic ($n = 0$) or g -mode oscillations, the

group velocity vanishes at the radius where⁸

$$(\omega - m\Omega)^2 - \kappa^2 = 0. \quad (12.17)$$

This means that these waves predominantly exist around the radius of $(\omega - m\Omega)^2 - \kappa^2 = 0$.⁹ The radius is nothing but the boundary between the propagation region and the evanescent region of the waves, and here the wavenumber tends to zero. In the case of inertial-acoustic oscillations, the radial region of $(\omega - m\Omega)^2 < \kappa^2$ is an evanescent region of the oscillations (see section 11.3), while in the case of *g*-mode oscillations, $(\omega - m\Omega)^2 > \kappa^2$ is an evanescent region.

The resonance occurs at the radius of $D = 0$, as discussed in the previous subsection. In the case of horizontal resonance in geometrically thin disks, the radius is specified by equation (12.14).

For resonance efficiently to occur, the places where the oscillations stay for a long time and the place where the resonance occurs must be the same. This means that equations (12.17) and (12.14) must be simultaneously satisfied. Combining equations (12.17) and (12.14), we find that the horizontal resonance of inertial-acoustic or *g*-mode oscillations occurs at

$$\kappa = \frac{\Omega}{2} \quad (\text{horizontal resonance}). \quad (12.18)$$

In deriving this relation we have used the fact that κ is always smaller than $\Omega (\sim \Omega_K)$ in relativistic Keplerian disks. The radial distributions of κ and $\Omega_K/2$ in the case of the Schwarzschild metric are shown in figure 12.10. The resonance occurs around the radius where two curves of $\kappa(r)$ and $\Omega_K(r)/2$ cross. The radius is $4r_g$ (the radius of κ_{\max}) in the case of the Schwarzschild metric. It is noted that the resonant condition, equation (12.18), is never realized in nonself-gravitating Newtonian Keplerian disks, where $\kappa = \Omega$.

(b) Vertical resonance of inertial-acoustic or *g*-mode oscillations

In the case of vertical resonance, resonance occurs at the radius where equation (12.15) is satisfied. Combining equations (12.17) and (12.15), we find that the vertical resonance of inertial-acoustic or *g*-mode oscillations occurs at

$$\kappa = \tilde{n}^{1/2}\Omega_{\perp} - \Omega \quad (\text{vertical resonance}). \quad (12.19)$$

⁸In gravity waves $(\omega - m\Omega)^2 - n\Omega_{\perp}^2$ is always negative.

⁹This is really shown numerically in the case of axisymmetric ($m = 0$) oscillations (see section 12.2).

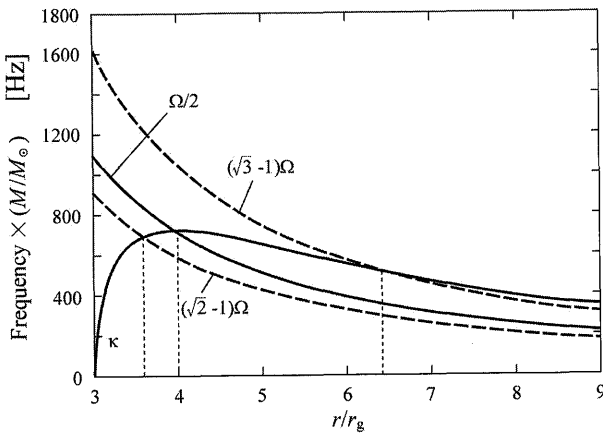


Figure 12.10

Radial distributions of κ , $\Omega_K/2$, $(\sqrt{2}-1)\Omega_K$, and $(\sqrt{3}-1)\Omega_K$ in the case of the Schwarzschild metric. The radii where the curves of $\Omega_K/2$, $(\sqrt{2}-1)\Omega_K$, and $(\sqrt{3}-1)\Omega_K$ cross that of κ give resonant radii as discussed in the text. In the case of the Schwarzschild metric, the above three radii are $4.0r_g$, $3.62r_g$, and $6.46r_g$.

In deriving this relation, we have again used the fact that κ is always smaller than $\Omega(\sim \Omega_K)$ in relativistic disks. The radial distributions of $(\sqrt{2}-1)\Omega_K$ and $(\sqrt{3}-1)\Omega_K$ are also shown in figure 12.10. The radii of $\kappa = (\sqrt{2}-1)\Omega_K$ and $\kappa = (\sqrt{3}-1)\Omega_K$ are, respectively, $3.62r_g$ and $6.46r_g$ in the Schwarzschild metric. There is no resonance for $\tilde{n} \geq 4$.

(c) Horizontal resonance of *c*-mode or vertical *p*-mode (with $n \geq 2$) oscillations

Next, we consider *c*-mode or vertical *p*-mode (with $n \geq 2$) oscillations. Discussion concerning the group velocity at the beginning of (a) shows that in the present case the oscillations predominantly exist near to the radius where

$$(\omega - m\Omega)^2 - n\Omega_{\perp}^2 = 0 \quad (12.20)$$

is satisfied.

In the case of horizontal resonance, the resonance occurs around the radius where equation (12.14) is satisfied. Hence, combining equations (12.14) and (12.20), we find that the horizontal resonance of *c*-mode or vertical *p*-mode (with $n \geq 2$) oscillations occurs around the radius where

$$\kappa = n^{1/2}\Omega_{\perp} - \Omega \quad (\text{horizontal resonance}) \quad (12.21)$$

is satisfied. This is formally the same expression as equation (12.19), except for the difference of \tilde{n} and n .

(d) Resonant conditions in vertically polytropic disks

So far, we have considered vertically isothermal disks. Here, a case of vertically polytropic disks is briefly considered, since in this case the resonant condition of a vertical resonance depends on the vertical disk structure. This leads to the possibility that the resonant radius, and thus the resonant frequency, change with time by a change of mass accretion rate, since a change of mass accretion rate may change the vertical disk structure.

The temperature, density, and pressure distributions in the vertical direction in vertically polytropic disks are given in section 7.2. In this case of polytropic disks, the derivation of wave equation and solving it are complicated. However, a rough estimate of the resonant condition of vertical resonance is possible.

We now write the square of the frequencies of vertical p -mode oscillations ($n \neq 0$) by $\Psi_n \Omega_\perp^2$, where n represents the number of node(s) in the vertical direction. If we neglect the horizontal motions associated with the oscillations, we can easily calculate Ψ_n as (Kato 2005b)

$$\Psi_0 = 0, \quad \Psi_1 = 1, \quad (12.22)$$

$$\Psi_2 = 2 + \frac{1}{N}, \quad \Psi_3 = 3 + \frac{3}{N}, \quad (12.23)$$

where N is the polytropic index describing the vertical distributions of the temperature, density, and pressure (i.e., $p \propto \rho^{(1+1/N)}$; see section 7.2). Vertically isothermal disks are the limit of $N = \infty$, and in this limit we have $\Psi_n = n$. This result tells us that the resonance conditions obtained for isothermal disks are now generalized to the case of polytropic disks by changing \tilde{n} in equation (12.19) to $\Psi_{\tilde{n}}$, and n in equations (12.20) and (12.21) to Ψ_n , respectively.

12.3.4 Frequencies of Horizontal Resonance of Inertial-Acoustic or G-mode Oscillations

Among four resonant cases, (a)–(d), discussed in the above subsection, we restrict, hereafter, our attention only to the first one, i.e., the horizontal resonance of inertial-acoustic ($n = 0$) or g-mode oscillations ($n \geq 1$). This is because the resonance in case (a) can excite the oscillations (Kato 2004b).

In case (a) the frequencies of resonant oscillations are $m\Omega \pm \kappa$ [see equation (12.17)] at the resonant radius. They are a set of frequencies, since there are various m . Among them, the most observable ones will

be those with a small number of m . The axially symmetric oscillations, $m = 0$, however, will be less observable, as far as long-wavelength perturbations in the radial direction are considered. Hence, the oscillations that are most interesting are those with $m = \pm 1$ or $m = \pm 2$ (cases of $m = -1$ and $m = -2$ are practically the same as those of $m = 1$ and $m = 2$, respectively). Considering this situation, we introduce frequencies defined by¹⁰

$$\omega_{\text{LL}} = (\Omega - \kappa)_r, \quad \omega_L = (2\Omega - \kappa)_r, \quad \omega_H = (\Omega + \kappa)_r, \quad (12.24)$$

where subscript r represents the values at the resonant radius, which is the radius of $\kappa = \Omega/2$ [see equation (12.18)].

Since the resonance occurs at the radius where $\kappa = \Omega/2$, we have

$$\omega_{\text{LL}} = \frac{1}{2}\kappa_r, \quad \omega_L = \omega_H = \frac{3}{2}\kappa_r, \quad (12.25)$$

where κ_r is the epicyclic frequency at the resonant radius, and

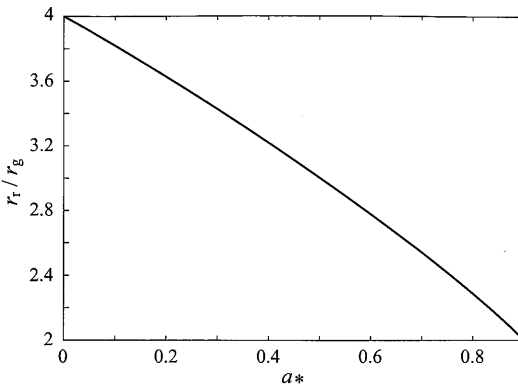
$$\omega_{\text{LL}} : \omega_L (= \omega_H) = 1 : 3 \quad (12.26)$$

So far, we have adopted the pseudo-Newtonian approximation introduced by Paczyński and Wiita (1980) in deriving the resonant conditions and the frequencies of resonant oscillations. The derived expressions, however, can be applied to the case of the Schwarzschild metric. A careful inspection of the procedures of the derivations further shows that they can be extended to the case of the Kerr metric. That is, both expressions for resonant conditions [i.e., equations (12.18), (12.19), and (12.21)] and for the frequencies of resonant oscillations [i.e., equations (12.24)] are still valid, if Ω (which is practically Ω_K), κ , and Ω_\perp are regarded as those in the Kerr metric.

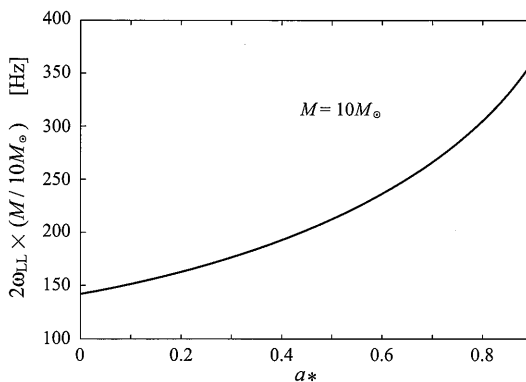
The horizontal resonance occurs at the radius where $\kappa = \Omega/2$, and the radius is $4r_g$ in the case of the Schwarzschild metric, as mentioned before. In the case where the central source has a spin, i.e., $a_* > 0$, the resonance occurs at a radius smaller than $4r_g$. From the relation $\kappa = \Omega/2$, we can calculate how the resonant radius, r_r , depends on a_* . The results are shown in figure 12.11. Using $r_r(a_*)$, we can calculate the a_* -dependence of $2\omega_{\text{LL}}$, which is shown in figure 12.12.¹¹

¹⁰The oscillation mode with $2\Omega + \kappa$ (i.e., $m = 2$) is not considered here, since the frequency is rather high compared with the Keplerian one at the radius of the marginally stable circular orbit, and such high frequency QPOs are not yet well examined observationally.

¹¹The lower frequency of the pair QPOs is regarded as $2\omega_{\text{LL}}$ (not ω_{LL}), as mentioned in the next section 12.4.

**Figure 12.11**

Dependence of the resonant radius, r_r , on the spin parameter, a_* , in the case of (a) in subsection 12.3.2. The metric is the Kerr.

**Figure 12.12**

Dependence of $2\omega_{LL}$ on the spin parameter, a_* , in the case of (a) in subsection 12.3.2. The mass is taken to be $10M_\odot$.

Application of the present results concerning resonant oscillations to observed QPOs is considered in the next section.

12.3.5 Effects of the Precession of Warps

So far, we have assumed that warps have no precession. In real situations, especially in neutron-star X-ray binaries, they will have precession more or less according to magnetic or radiative couplings of the disks with the surface of the central star. For example, the radiative force from the cen-

tral star produces torques on warped disks, so that precession is induced (Pringle 1992, 1996; Maloney et al. 1996). Furthermore, the results of section 11.4 show that one-armed low-frequency global oscillations generally have precession.¹² If precession is present, the resonant radius, and thus the resonant frequencies, are modified (Kato 2005a) from those discussed above.

(a) Resonant condition

Let us consider the coupling between a wave described by (ω, m, n) and a warp described by $(\omega_p, 1, 1)$, where ω_p is the angular frequency of precession. The essence of the coupling and resonant processes is the same as that described above in the case of $\omega_p = 0$. We thus present only an outline for deriving the resonance radii and frequencies of resonant oscillations.

By the presence of precession, the resonant condition for horizontal resonance is changed from equation (12.14) to

$$[\omega - m\Omega \pm (\omega_p - \Omega)]^2 - \kappa^2 = 0. \quad (12.27)$$

The sign \pm appears here, since there are two types of nonlinear coupling. In the case of vertical resonance, the resonance condition is

$$[\omega - m\Omega \pm (\omega_p - \Omega)]^2 - \Psi_{\tilde{n}}\Omega_{\perp}^2 = 0, \quad (12.28)$$

where $\tilde{n} = n \pm 1$. This is a generalization of equation (12.15).

(b) Horizontal resonance of inertial-acoustic or *g*-mode oscillations

In the present case,

$$(\omega - m\Omega)^2 - \kappa^2 = 0 \quad (12.29)$$

must be satisfied at the resonant radii. Hence, by combining equations (12.27) and (12.29), we have, as the resonant condition for horizontal resonance,

$$\kappa = \frac{1}{2}(\Omega - \omega_p) \quad (\text{horizontal resonances}). \quad (12.30)$$

Equation (12.30) is a generalization of the resonant condition (12.18).

The r_r - ω_p relation, obtained by solving equation (12.30), is shown in figure 12.13 for two cases of $a_* = 0$ and $a_* = 0.3$. An interesting

¹²Warps belong to one-armed oscillations ($m = 1$) with $n = 1$.

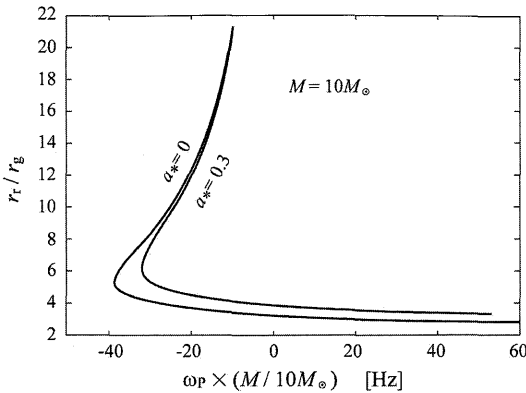


Figure 12.13

Dependence of the resonant radius, r_r , on the frequency of precession, ω_p , in the case of horizontal resonance of inertial-acoustic and/or g -mode oscillations. Two cases of $a_* = 0$ and $a_* = 0.3$ are shown. The mass is taken to be $10M_\odot$. $\omega_p > 0$ means that the precession is prograde, and $\omega_p < 0$ retrograde. It is noted that in the case where the precession is retrograde, resonance occurs at two radii.

result shown in figure 12.13 is that when the precession is retrograde (i.e., $\omega_p < 0$), we have two resonant radii for a given ω_p . That is, when the precession is retrograde and slow, one resonant radius is close to $4.0r_g$, and the other is far outside. When the precession is fast, the inner resonant radius shifts outward, while the outer one shifts inward. At a certain value of precession, both resonant radii coincide, and no resonance occurs for a larger precession. In the case where the precession is prograde, however, we have only one resonance at a radius smaller than $4r_g$.

(c) Other types of resonance

Other types of resonance are less interesting, compared with the horizontal resonance of the inertial-acoustic or g -mode oscillations, since results by Kato (2004b) suggest that the resonances in these cases dampen oscillations. Hence, we summarize here only the final results concerning the resonant conditions.

In the case of the vertical resonance of inertial-acoustic or g -mode oscillations, from equations (12.28) and (12.29) we obtain, as the equation describing the resonance radii,

$$\kappa = \Psi_{\tilde{n}}^{1/2} \Omega_\perp - \Omega + \omega_p \quad (\text{vertical resonance}). \quad (12.31)$$

We have two resonant radii for a given value of precession, when the

precession is prograde (i.e., $\omega_p > 0$).¹³

Next, the condition of horizontal resonance of c -mode and vertical p -mode (with $n \geq 2$) oscillations is considered. Combining equation (12.27) with the condition of c -mode or vertical p -mode (with $n \geq 2$) oscillation [a generalization of equation (12.20) to cases of polytropic disks] we have, as the equation describing the resonance radii,

$$\kappa = \Psi_n^{1/2} \Omega_{\perp} - \Omega + \omega_p \quad (\text{horizontal resonance}). \quad (12.32)$$

Equation (12.32) is formally the same as equation (12.31), except for the difference that \tilde{n} in equation (12.31) is now changed to n .

12.4 Comparison of Warp Models with Observations

In this section we discuss whether the present warp models can account for the observed characteristics of high-frequency QPOs in LMXBs. Among four types of resonant oscillations discussed in subsection 12.3.3, (a) inertial-acoustic or g -mode oscillations with horizontal resonance are of interest, since, as mentioned before, these oscillations are excited (Kato 2004b). Hence, we focus here our attention mainly on that case. It is noted that the vertical resonance of inertial-acoustic or g -mode oscillations [i.e, case (b) in subsection 12.3.3] has been discussed by Kato (2005b).

12.4.1 HF QPOs in Black-Hole Binaries

First, we should emphasize that the frequencies of resonant oscillations obtained in the previous section, ω_{LL} , $\omega_L (= \omega_H)$, and ω_H , are not always directly related to the observed HF QPOs. This is because in the case of one-armed oscillations, the first harmonics will dominate over the fundamental one for the following reasons (Kato and Fukue 2006):

(a) Double periodicity of one-armed oscillations

Observations show (Remillard 2005) that all high-frequency QPOs are associated with the very high state (steep power-law state) of sources. They are not observed in the thermal state (i.e., the high/soft state with no corona), nor in the hard state (i.e., low/hard state with no thermal disk component). The steep power-law state consists of a thermal disk

¹³This is different from the case of horizontal resonance. In the latter case, we have two resonant radii when the precession is retrograde.

and a compact hot torus (corona) surrounding the disk. Observations further show that the QPOs are observed in the high-energy photons of the power-law component, not in the soft photons of the thermal-disk component.

This observational evidence suggests that a thermal disk is a place where oscillations are generated, but the observed QPO photons are those Comptonized in the hot compact corona (a hot torus). Here, we consider one-armed disk oscillations propagating in the azimuthal direction with angular frequency ω . The hot disk region associated with the oscillations is assumed to be inside a torus. We now consider the paths of observed photons that are originally emitted from the hot region of the disk as soft photons, and are observed as high-energy photons by Comptonization in the torus. The path length of the photons in the torus depends on the phase relation between the hot region and the observer, as shown in figures 12.14 and 12.15. In the phase shown in figure 12.14, the path length of photons in the torus is short. (This phase is hereafter called phase 0.) In the phase shown in figure 12.15, however, the path length within the torus is long. The latter occurs when the phase is close to 0.75 as well as 0.25. In the phase 0.5, the path in the torus is shorter than that in the phase of figure 12.15, but longer than that in the phase of figure 12.14 (phase 0). Hence, the observed Comptonized photon numbers vary as shown in figure 12.16. That is, we have two peaks during one cycle of the one-armed oscillations.

Here, a brief comment is made concerning the depths of the primary minimum (phase 0) and the secondary minimum (phase 0.5) in figure 12.16. In the phase of the primary minimum, the path length of photons in the torus is short, but they pass through an inner hotter and denser region of the torus (see figure 12.14). This increases the Comptonized photon flux, compared with that in the case in which photons pass an outer cooler and less-dense region. The phase of the secondary minimum (phase 0.5) corresponds to the latter case. This consideration suggests that the difference between the Comptonized photon fluxes in phases 0 and 0.5 is smaller than that simply estimated from the difference in the geometrical path lengths. Figure 12.16 should be regarded as being results in which the above effects are already taken into account.

In summary, one-armed oscillations with frequency ω bring about two time-varying components of ω and 2ω with a larger amplitude of the latter.

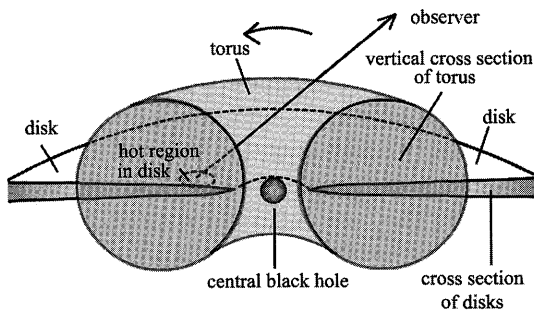


Figure 12.14

Schematic picture showing the light path from a hot region in disks to an observer in the phase in which the hot region is just at the opposite side of the central source to the observer. The path within the torus is shown by a dashed line. It is noticed that the path length in the torus is short, and the observed high-energy QPO photons are not many. This phase is referred to phase 0, and the phase in which the hot region of the disk is between the central source and the observer is referred to phase 0.5. (After Kato and Fukue 2006)

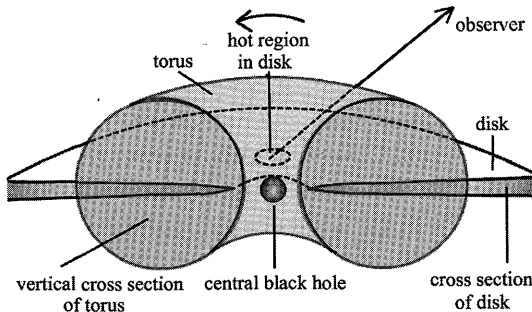


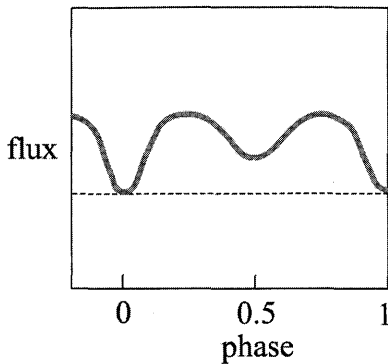
Figure 12.15

Schematic picture showing a straight light path from the hot region in disks to an observer in a phase close to 0.75. The part of the pass within the torus is shown by the dashed line. The pass within the torus is the longest in this phase as well as in a phase close to 0.25, compared with in other phases. (After Kato and Fukue 2006)

(b) Comparison with observations

The above consideration suggests that the main QPO frequencies to be observed in case (a) in subsection 12.3.3 are ω_L and $2\omega_{LL}$ (not ω_{LL}), since the oscillations with ω_{LL} are one-armed.¹⁴ The frequency ratio of

¹⁴The resonant oscillations with ω_H will be observed mainly as QPOs with frequency $2\omega_H$, since they are one-armed oscillations. We think, however, that there is still no

**Figure 12.16**

Schematic light curve during one revolution of an one-armed oscillation around a central source. We have two peaks during one cycle of oscillations around phases of 0.25 and 0.75. (After Kato and Fukue 2006)

these two oscillations is just 3:2, i.e.,

$$\omega_L : 2\omega_{LL} = 3 : 2. \quad (12.33)$$

This frequency ratio is consistent with that of the observed pair of QPOs. In this picture, there is no reason why QPOs with ω_{LL} are not observed, although they may be weak. We think that they are really observed in some sources. In a source (XTE J1550-564), three QPOs (272 Hz, 184 Hz, 92 Hz) have been observed with a ratio of 3:2:1. Furthermore, in a black-hole X-ray transient, XTE J1650-500, QPO frequencies consistent with 3:2:1 have been observed, although their frequencies vary with time (Homan et al. 2003).

There are three sources with pair QPOs where the masses have been derived from other observations. They are GRO J1665-40 (300, 450 Hz), XTE J1550-564 (92, 184, 276 Hz), and GRS 1915+105(113, 168 Hz). Using the data of these objects, McClintock and Remillard (2006) derived an interpolation formula giving a relation between the observed upper frequency of the pair HF QPOs, $3\nu_0$, and M , which is

$$3\nu_0 = 2.79 \times 10^3 \left(\frac{M}{M_\odot} \right)^{-1} \text{Hz}, \quad (12.34)$$

where ν_0 is the fundamental frequency of the observed 1:2:3 frequencies, which corresponds to ω_{LL} in our model. In the case where the central

serious attempt to detect such high frequency QPOs, since the frequency is higher than the Keplerian frequency in the innermost region of disks.

source has no spin, i.e., $a_* = 0$, our model gives

$$\omega_L (= \omega_H) = 2.14 \times \left(\frac{M}{M_\odot} \right)^{-1} \text{ Hz}, \quad (a_* = 0) \quad (12.35)$$

which is smaller than $3\nu_0$. This suggests that the central sources must have spins. The a_* -dependence of $2\omega_{LL} [= (2/3)\omega_L]$ in our warp model is shown in figure 12.12 in section 12.3. The frequency $2\omega_{LL}$ (and thus ω_L) increases with an increase of a_* . Using the curve in figure 12.12 and the mass obtained from other observations, we can estimate the spins of the above three sources, so that the $2\omega_{LL}$ for these sources become equal to the observed $2\nu_0$ (not $3\nu_0$) of these sources. The results are given in table 12.2. In this table, the observed mass range of each source is taken from table 4.2 of McClintock and Remillard (2004).

Table 12.2 Estimated spin parameter, a_* .

Sources	$2\nu_0$ (Hz)	M/M_\odot	a_*
GRS 1915+105	112	10.0 – 18.0	negative – 0.44
XTE 1550-564	184	8.4 – 10.8	0.11 – 0.42
GRO 1655-40	300	6.0 – 6.6	0.31 – 0.42

Table 12.2 shows that in the case of GRS 1915+105, the spin parameter a_* becomes negative if a mass of around $10 M_\odot$ is adopted. This suggests that the mass of GRS 1915+105 will be much larger than $10 M_\odot$, close to $18 M_\odot$. It is noted that the value of a_* of GRO 1655-40 is around 0.4 in the present model. Shafee et al. (2006), on the other hand, estimated the value of a_* of this object to be around 0.8 by comparing a model spectrum of this object with the observed one.

12.4.2 Why Do the Frequencies of kHz QPOs in Neutron-Star Binaries Change?

One of important observational characteristics of kHz QPOs in NS binaries, which is different from those of HF QPOs in BHs, is that the frequency ratio of the pair is close to 3:2, but changes with time, so that the ratio decreases with an increase of the frequencies. If we try to explain this time variation of kHz QPOs by the *horizontal* resonance of inertial-acoustic or g-mode oscillations, one possibility is to assume that the resonant radius changes with time by the presence of a time-dependent precession of the warp.¹⁵

¹⁵The possibility of explaining the time variability of kHz QPOs in NS binaries by *vertical* resonance of inertial-acoustic ($n = 0$) or g-mode oscillations has been discussed by Kato (2005b).

An important question that arises here is why warps in neutron-star X-ray binaries have time-dependent precession, although those in the black-hole ones should have little precession. We suppose that this is related to the difference in the surface of the central sources. If the central source has a surface, the couplings between the surface of the central source and the surrounding disk by radiation and magnetic fields will give rise to precession on the disk. For example, Pringle (1992) indicated that the forces due to radiation pressure induce torque on disks to produce the precession of warps. A question is whether interactions between the surface of the central source and the disk can give rise to such high-frequency precession as required in the present model, which is a subject to be examined further.

Here, we should emphasize that the mutual relations among ω_H , ω_L , and ω_{LL} are universal,¹⁶ free from detailed processes of the time change of the resonant radius. That is, the $2\omega_{LL} - \omega_L$ relation depends only on a_* . This relation is shown in figure 12.17 for two cases of $a_* = 0$ and $a_* = 0.5$. For a comparison, the $\omega_H - \omega_L$ relation is also drawn. (It is noted that ω_H and ω_L are no longer equal when the resonant condition is changed from $\kappa = \Omega/2$ by the presence of precession.) The $2\omega_{LL} - \omega_L$ relation in this figure is similar to the observed $\nu_\ell - \nu_u$ relation drawn by van der Klis [figure 2.9 of van der Klis (2004), see figure 12.4 of this chapter], where ν_u and ν_ℓ are, respectively, the upper and lower frequencies of the observed pair QPOs. This similar trend suggests that the observed pair kHz QPOs are really related to $2\omega_{LL}$ and ω_L .

A closer examination of how the observed frequencies of the pair QPOs change with the correlation was made by Bursa for a few typical sources (Bursa 2002, see also Abramowicz 2005, Kluźniak 2005). He plotted the observed data on a diagram of the upper QPO frequency versus the lower QPO frequency. The plots are duplicated in figure 12.18. (The curves of ω_H and ω_L are not in the original figure by Bursa. They are superposed here for a comparison by regarding ν_ℓ as $2\omega_{LL}$. See the next paragraph.) His data show that the frequencies and their ratio change with time, but their changes are along a nearly straight line with a gradient slower than 3:2. The line crosses the line of frequency ratio 3:2, roughly at a point of (600 Hz, 900 Hz).

¹⁶The radius where resonance occurs depends on the frequency of precession, ω_p , and the spin parameter a_* (see the resonant conditions given in subsection 12.3.4). However, frequencies, ω_H , ω_L , and ω_{LL} , are unique functions of the resonant radius r_r alone (for a given mass and spin) [see equation (12.24)]. Hence, elimination of the resonant radius from these frequencies give unique relations among ω_H , ω_L , and ω_{LL} , independent of the resonant processes determining the resonant radius.

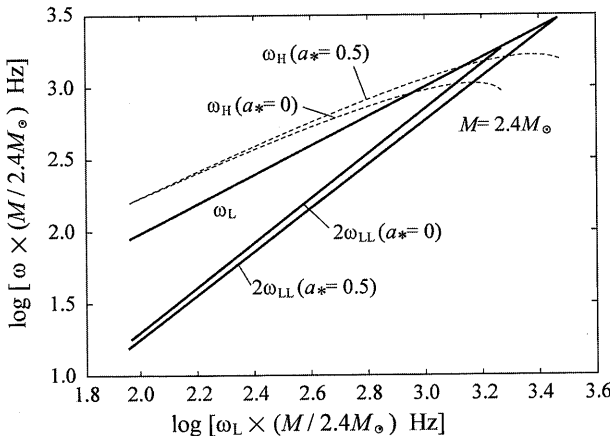


Figure 12.17

Frequency–frequency relation between $2\omega_{\text{LL}}$ and ω_{L} for two cases of $a_* = 0$ and $a_* = 0.5$. The $\omega_{\text{H}} - \omega_{\text{L}}$ relation is also drawn by thin dashed curves for comparison. The case in which $\omega_{\text{H}} = \omega_{\text{L}}$ represents the case of no precession, and there $\omega_{\text{L}} : 2\omega_{\text{LL}} = 3 : 2$. The mass of the central source is taken as $2.4M_{\odot}$ so that the set of ω_{L} and $2\omega_{\text{LL}}$ in the limit of no precession and $a_* = 0$ become 900 Hz and 600 Hz.

In our present warp model, the frequency ratio of $\omega_{\text{L}} : 2\omega_{\text{LL}}$ is 3:2 when the warp has no precession, but the magnitude of the frequencies depends on a_* and M (see figure 12.12). That is, in the case of no disk precession, the points of $(\omega_{\text{L}}, 2\omega_{\text{LL}})$ of different sources should distribute along the line of gradient 3/2 in figure 12.18. The observational data plotted by Bursa, however, are on the line of 3:2 only around a point of (600 Hz, 900 Hz). This suggests that the sources adopted by Bursa have such mass and spin parameters as their pair frequencies become 600 Hz and 900 Hz, respectively, in the limit of no precession. Considering this, we restrict here our attention only to cases in which ω_{L} and $2\omega_{\text{LL}}$ become 900 Hz and 600 Hz, respectively, in the limit of no precession. Furthermore, for simplicity, we consider here the case of $a_* = 0$.¹⁷ For such sources, the $\omega_{\text{H}} - 2\omega_{\text{LL}}$ and $\omega_{\text{L}} - 2\omega_{\text{LL}}$ relations are superposed in figure 12.18.

Figure 12.18 shows that the warp model can qualitatively account for

¹⁷In the case of $a_* = 0$, we have $2\omega_{\text{LL}} = 1.41 \times 10^3 (M/M_{\odot})^{-1}$ Hz [see that ω_{L} is given by equation (12.35)]. Hence, adoption of $a_* = 0$ and $2\omega_{\text{LL}} = 600$ Hz imply that the mass M is taken as $M = (1.41 \times 10^3 / 6 \times 10^2) M_{\odot} = 2.35 M_{\odot}$.

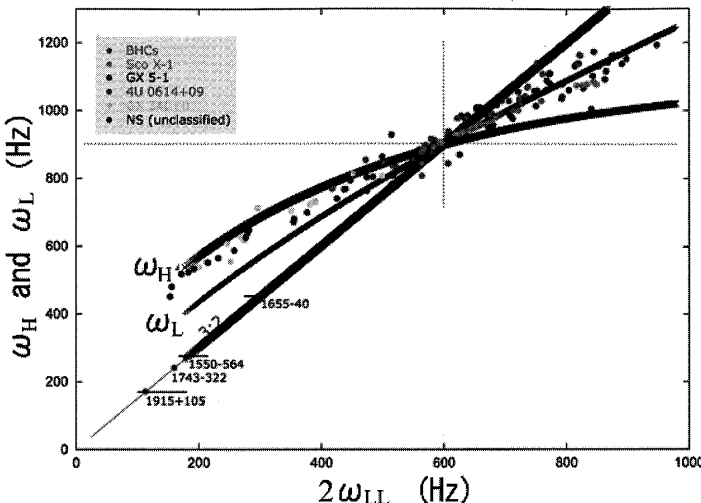


Figure 12.18

Frequency-frequency diagram of the observed upper and lower QPOs frequencies in some typical neutron star sources (Bursa's diagram) (Bursa 2002). The frequency ratio becomes 3:2 in adopted sources when the lower QPO frequency is about 600 Hz. The dependences of ω_H and ω_L on $2\omega_{LL}$ are superposed on the Bursa diagram by taking ω_H or ω_L as the ordinate and $2\omega_{LL}$ as the abscissa. The case of $a_* = 0$ is shown. The frequency $2\omega_{LL}$ in the case of no precession (in this case the frequency ratio of $\omega_L : \omega_{LL}$ is 3:2) is normalized so that it becomes 600 Hz by adjusting the mass, M , of the central source. This means that we have adopted $M = 2.4M_\odot$. The straight line of gradient 3/2 is shown in order to see how much the observed frequency ratio, and also the ratio of ω_L (and ω_H) to $2\omega_{LL}$, deviate from 3:2, as the frequency $2\omega_{LL}$ is apart from 600 Hz. (Bursa's plots on the frequency-frequency diagram is adapted from Abramowicz 2005, see also Kluźniak 2005.)

the observations, but there seems to be a systematic deviation between the distribution of the observed data points and the $\omega_L - 2\omega_{LL}$ curve in the low-frequency region.¹⁸ This discrepancy between the observed data points and the $\omega_L - 2\omega_{LL}$ curve cannot be solved by considering a weak deviation of the disk rotation from the Keplerian one. Examination of the cause of this discrepancy is a subject to be examined in the future.

Next, let us consider how much precession is required to explain the frequency deviation of $2\omega_{LL}$ from 600 Hz. To do so, the $2\omega_{LL} - \omega_p$ relation is shown in figure 12.19 for $a_* = 0$. The frequency $2\omega_{LL}$ in the

¹⁸In the low-frequency region, the $\omega_H - 2\omega_{LL}$ curve seems to better represent the observed data than does the $\omega_L - 2\omega_{LL}$ curve.

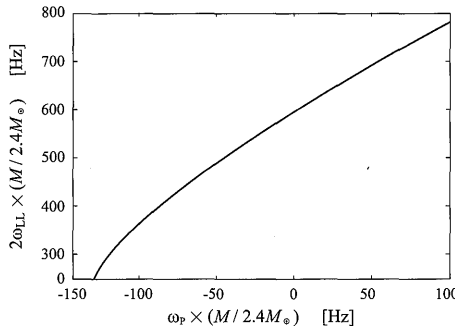


Figure 12.19

Dependence of $2\omega_{LL}$ on the precession frequency, ω_p , in the case of the horizontal resonance of inertial-acoustic g -mode oscillations. As in figure 12.18, $2\omega_{LL}$ in the case of no precession is normalized to 600 Hz. The central source is taken to have no spin.

case of no precession is again normalized to 600 Hz by adjusting the mass, i.e., $M = 2.4M_\odot$ has been adopted. The observed data in figure 12.18 show that variation of $2\omega_{LL}$ in a given source is, at maximum, about 300 Hz. Figure 12.19 shows that such a variation of $2\omega_{LL}$ is realized if the precession frequency, ω_p , changes from zero to about 100~150 Hz. It is noted here that such frequencies are on the order of those of hectohertz QPOs. This suggests that the observed hectohertz QPOs may be a manifestation of disk precession.

12.5 Other Disk-Oscillation Models of QPOs

In this section we first briefly review the epicyclic resonance model proposed by Abramowicz, Klużniak and their group. Next, oscillations of tori are briefly discussed in relation to QPOs.

12.5.1 Epicyclic Resonance Model

The frequency ratio of 3:2 in black-hole QPOs was first noticed, and its importance was stressed by Abramowicz and Klużniak (2001) as well as Klużniak and Abramowicz (2001). They tried to explain the pair QPOs of 3:2 ratio or of other commensurable frequency ratios by a parametric resonance between the radial and vertical epicyclic oscillations (see, for example, Klużniak et al. 2004). Figure 12.20 shows the radial distributions of the (radial) epicyclic frequency, κ , and the (vertical) epicyclic frequency, Ω_\perp , in the case of $a_* = 0$. We can see that at some particular radii their ratio becomes commensurable with small integers.

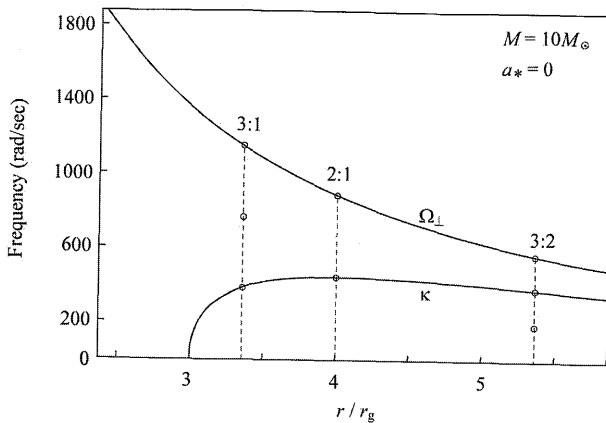


Figure 12.20

Radial distributions of the vertical epicyclic frequency, Ω_{\perp} , and the radial epicyclic frequency, κ , in the Schwarzschild metric. The radii where the ratio of these two frequencies becomes 3:1, 2:1, and 3:2 are shown. (After Abramowicz 2005)

Let us first consider an idealized situation where disks have no pressure. A disk consists of particles that circularly rotate around a central source. Then, at each radius we can expect two kinds of harmonic oscillations of particles over the pure rotational motions, when the particles are weakly disturbed from the circular motion. One is horizontal and the other is vertical. That is, a horizontal displacement, ξ_r , of a disk particle causes an oscillation in the horizontal direction with a (radial) epicyclic frequency, κ , which are described by

$$\frac{d^2\xi_r}{dt^2} + \kappa^2 \xi_r = 0. \quad (12.36)$$

A vertical displacement, ξ_z , on the other hand, causes an oscillation in the vertical direction with a (vertical) epicyclic frequency, Ω_{\perp} , of

$$\frac{d^2\xi_z}{dt^2} + \Omega_{\perp}^2 \xi_z = 0. \quad (12.37)$$

In gaseous systems, however, these two oscillations are coupled by the presence of a pressure force (see chapter 11), and also by non-linear coupling processes.

These interactions can be partially described by introducing time periodic parts in κ^2 and Ω_{\perp}^2 . That is, the term κ^2 in equation (12.36) is modified as $\kappa^2(1 + \chi_1 \cos \Omega_{\perp} t)$. Similarly, the Ω_{\perp}^2 term in equation (12.37) is modified as $\Omega_{\perp}^2(1 + \chi_2 \cos \kappa t)$. Here, χ_1 and χ_2 are constant.

The resulting equations are Mathieu's equations, and thus we might expect parametric excitation of epicyclic oscillations at particular radii where κ and Ω_\perp are commensurable (Abramowicz et al. 2003).

The above argument, however, is not enough to demonstrate that at the radii where κ and Ω_\perp become commensurable the epicyclic oscillations are really excited. This is because the above modifications of κ^2 and Ω_\perp^2 by introducing terms with χ_1 and χ_2 take only partially into account the effects of the interactions. Energy exchange between the radial and vertical epicyclic oscillations really occur at the resonant radii. However, the energy exchange will not lead to an instability, since what occurs is a time-dependent energy exchange between two oscillations, but the total oscillation energy is conserved in conservative systems.

Considering the above situations, Abramowicz and his collaborators extended their original idea, and suggest the importance of external periodic forces and external stochastic turbulent forces on the excitation of resonant oscillations.¹⁹ That is, they add, on the left-hand sides of equations (12.36) and (12.37), forcing terms of external periodic forces and stochastic turbulent forces, in addition to the terms of non-linear interaction terms between horizontal and vertical oscillations:

$$\frac{d^2\xi_r}{dt^2} + \kappa^2 \xi_r = F(\xi_r, \xi_z, \dot{\xi}_r, \dot{\xi}_z) + A\cos(\omega_0 t) + N_1(t), \quad (12.38)$$

and

$$\frac{d^2\xi_z}{dt^2} + \Omega_\perp^2 \xi_z = G(\xi_r, \xi_z, \dot{\xi}_r, \dot{\xi}_z) + B\cos(\omega_0 t) + N_2(t). \quad (12.39)$$

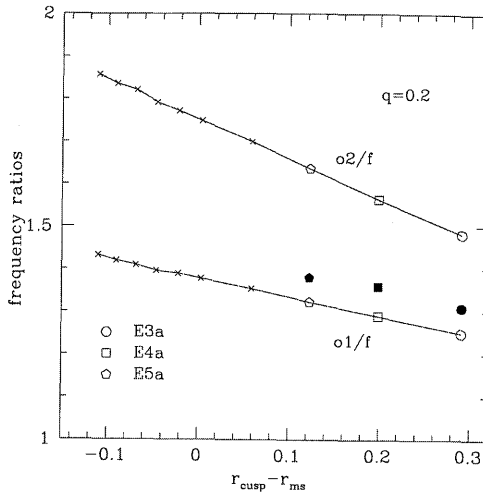
Here, the terms F and G account for the non-linear couplings, the $\cos(\omega_0 t)$ terms describe an external forcing,²⁰ and N 's describe the influences of turbulence on disk oscillations. They have examined these equations to know what happens when the resonance conditions are satisfied, by the method of multiple scaling. Work in this direction is now in progress (e.g., Horák and Karas 2006; Vio et al. 2006).

12.5.2 Oscillations of Inner Tori

The accretion flow in the innermost region is pressure-driven when the viscosity is small (see table 8.3). That is, a gas with large angular momentum is pushed inward by the pressure force so that it can pass a

¹⁹It is known in solar physics that the solar oscillations are excited by stochastic turbulent forces resulting from convective motions.

²⁰In the case of NS, the frequencies of the pair QPOs are sometimes correlated with the spin of the central sources.

**Figure 12.21**

Frequency ratios of the first two overtones (in the radial direction) to the fundamental inertial-acoustic ($n = 0$) mode for some model tori. The spin parameter, a_* , of the central source is 0.9, and the power-law index, q , characterizing the angular momentum distribution in tori, is $q = 0.2$. The abscissa is $r_{\text{cusp}} - r_{\text{ms}}$ in units of GM/c^2 , i.e., half of the Schwarzschild radius. Here, r_{cusp} is the radius of the cusp of the torus and r_{ms} is the radius of the marginally stable circular orbit. As the cusp of the torus penetrates deeper into the potential well, the ratios approach 1.5 and 2.0. (After Zanotti et al. 2005)

disk-like critical point to fall to a central object. In this case, the pressure has a maximum at a certain radius of the innermost region, since it must finally decrease outward in a far outer region. In other words, the disk has a small torus in the innermost region. Furthermore, observations show that high-frequency QPOs are not observed when the disk is at the high/soft state, and observed only at the very high state (Remillard 2005). In the very high state, a compact corona (a torus) exists in the innermost region. This may suggest that the presence of a hot torus is of importance for the appearance of QPOs.

Oscillations in a torus have discrete eigen-frequencies, since they are trapped in a finite region. Such oscillations may be one of the possible origins of high-frequency QPOs and of their appearance in pairs.

Oscillations of isolated thick tori around black holes have recently been investigated in relation to QPOs (e.g., Rezzolla et al. 2003a; Rezzolla et al. 2003b; Zanotti et al. 2005). They numerically solved the

oscillations of tori, or analytically solved hight-integrated equations describing the oscillations of tori. The results suggest that the axisymmetric inertial-acoustic oscillations ($m = 0$ and $n = 0$) account for the high-frequency QPOs. That is, their results show that the frequency ratio of the fundamental model to the first harmonics in the radial direction is close to 2:3. The ratio is, however, slightly sensitive to the radial distribution of the angular momentum in the torus, and may differ from 2:3 up to 15% (Zanotti et al. 2005). One of the results by Zanotti et al. (2005) is shown in figure 12.21.

Further examinations on the oscillations of tori have been made, including studies on the excitation of oscillations, by many researchers (e.g., Lee et al. 2004; Rubio-Herrela and Lee 2005a, b; Blaes et al. 2006).

Table 12.3 Various Models of High Frequency QPOs.

Models	excitation	3:2 frequency ratio	frequency variation	section
Oscillation	yes	no	marginal	12.2
Warp	yes	yes	probably	12.4
Epicycle	probably	yes	marginal	12.5.1
Tori	probably	marginal	marginal	12.5.2

12.5.3 Epilogues

To conclude chapter 12, we summarize how much each model discussed in this chapter can account for important observational characteristics of QPOs. Our personal view is given in table 12.3. In table 12.3, for simplicity, we call the models discussed in section 12.2 ‘oscillation’, those in sections 12.3–12.4 ‘warp’, those in subsection 12.5.1 ‘epicycle’, and those in subsection 12.5.2 ‘tori’.

In the case of the warp model, one of the important subjects remaining to be clarified is whether the disks of X-ray binaries are really warped,²¹ and why the warps have precession in neutron-star X-ray binaries, although they should have little precession in black-hole binaries. In models of epicyclic resonance, one of the important subjects to be examined is whether the observed *large* deviation of the frequency-frequency correlation from commensurable relations can be described. In the model

²¹Our preliminary investigation shows that the presence of a warp is not always necessary. One-armed disk-deformations which are symmetric with respect to the equator [i.e., one-armed inertial-acoustic-type deformation of disks with $m = 1$ and $n = 0$ (not $n = 1$)] can also excite inertial-acoustic or g-mode oscillations with horizontal resonance. Even in this type of disk deformation and resonance, the radii where resonance occurs and the frequencies of excited oscillations are unchanged from those in horizontal resonance in warped disks.

of tori, any commensurability of the frequency ratio is considered to be only by chance.

Reference

- Abramowicz M.A. 2005, Astron. Nachr. 326, No 9
Abramowicz M.A., Kato S. 1989, ApJ 336, 304
Abramowicz M. A., Klužniak W. 2001, A&A, 374, L19
Abramowicz M.A., Karas V., Klužniak, W., Lee W., Rebusco P., 2003,
PASJ 65, 467
Achenbach B., Gross N., Porquet D., Predehl P. 2004, A&A 417, 71
Balbus S.A., Hawley J.F. 1991, ApJ 376, 214
Belloni T., Méndez M., Homan, J. 2005, A&A 437, 209
Belloni T., Psaltis D., van der Klis M. 2002, ApJ, 572, 392
Blaes O.M., Arras P., Fragile P.C. 2006, MNRAS 369, 1225
Bursa M. 2002, unpublished (private communication)
Chen X., Abramowicz M.A., Lasota J.P. 1997, ApJ 476, 61
Chen X., Taam R.E. 1993, ApJ 412, 254
Chen X., Taam R.E. 1995, ApJ 441, 351
Genzel R., Schödel R., Ott T., Eckart A., Alexander T., Lacombe F.,
Rouan D., Aschenbach B. 2003, Nature 425, 934
Hirose M., Osaki Y. 1990, PASJ 42, 135
Homan J., Klein-Wolt M., Rossi S., Miller J.M., Wijnands R., Belloni,
T., van der Klis M., Lewin W.H.G. 2003, ApJ 586, 1262
Honma F., Matsumoto R., Kato S. 1992, PASJ 44, 529
Horák J., Karas V. 2006, A&A 451, 377
Iwasawa K., Fabian A.C., Brandt W.N., Kunieda H., Misaki, K., Reynolds
C.S., Terashima Y. 1998, MNRAS 295, 20
Kato S. 1994, PASJ 46, 589
Kato S. 2003, PASJ 55, 801
Kato S. 2004a, PASJ 56, 559
Kato S. 2004b, PASJ 56, 905
Kato S. 2005a, PASJ 57, L17
Kato S. 2005b, PASJ 57, 699
Kato S., Fukue J. 2006, PASJ 58, 909
Kato S., Honma F., Matsumoto R. 1988a, MNRAS 231, 37
Kato S., Honma F., Matsumoto R. 1988b, PASJ 40, 709
Kato S., Inagaki S., 1994, PASJ 46, 289
Kato S., Tosa, M. 1994, PASJ 46, 559
Kato S., Wu X.B., Yang L.T., Yang Z.L. 1993, MNRAS 260, 317
Kato Y. 2004, PASJ 56, 931

- Kluźniak W. 2005, Astron. Nachr. 326, 820
- Kluźniak W., Abramowicz M.A. 2001, Acta Phys. Pol. B32, 3605
- Kluźniak W., Abramowicz M. A., Kato S., Lee W. H., Stergioulas, N. 2004, ApJ 603, L89
- Lee W.H., Abramowicz M.A., Kluźniak W. 2004, ApJ 603, L93
- Lubow S. H. 1991, ApJ 381, 259
- Machida M., Matsumoto R. 2006, IAU Symp. 238, 131
- Maloney P.R., Begelman M.C., Pringle J.E. 1996, ApJ 472, 582
- Matsumoto R., Kato S., Honma F. 1988, in *Physics of Neutron Stars and Black Holes*, ed Y. Tanaka (Universal Academy Press, Tokyo), p155
- Matsumoto R., Kato S., Honma F. 1989, in *Theory of Accretion Disks*, ed F. Meyer, W.J. Duschl, J. Frank, E. Meyer-Hofmeister (Kluwer Academic Publisher, Dordrecht), p167
- Matsumoto R., Machida M. 2006, IAU Symp. 238, 38
- Mauche C. W. 2002, ApJ 580, 423
- McClintock J., Remillard R. 2004, in *Compact Stellar X-ray Sources*, eds. W.H.G. Lewin and M. van der Klis (Cambridge University Press, Cambridge), 157
- McClintock J., Remillard R. 2006, ARA&A 44, 49
- Milsom J.A., Taam R.E. 1997, MNRAS 286, 358
- Miyoshi et al. 2005, private communication
- Morgan E., Remillard R., Greiner J. 1996, IAUC 6392
- Morgan E., Remillard R.A. Greiner J. 1997, ApJ 482, 993
- Nakamura K. 1995, Master Thesis (Kyoto Univ.)
- Narayan R. 1992, ApJ 394, 261
- Narayan R., Loeb A., Kumar P. 1994, ApJ 431, 359
- Ozernoy L.M., Usov V.V. 1977, A&A 56, 163
- Papaloizou J., Szuszkiewicz E. 1994, MNRAS 268, 29
- Pétri J. 2006, Astrophys. Space Sci. 362, 117
- Poe C.H., Owocki S.P., Castor J.I. 1990, ApJ 358, 199
- Pringle J.E. 1992, MNRAS 258, 811
- Pringle J.E. 1996, MNRAS 281, 357
- Psaltis D., Belloni T., van der Klis M. 1999, ApJ 520, 262
- Remillard R. 2005, Astron. Nachr. 326, 804
- Remillard R., Munoz M., McClintock J., Orosz J. 2002, ApJ 580, 1030
- Rezzolla L., Yoshida S., Maccarone T.J., Zanotti O. 2003a, MNRAS 344, L37
- Rezzolla L., Yoshida S., Zanotti O. 2003b, MNRAS 344, 978
- Robinson E.L., Nather R.E. 1979, ApJS 39, 461

- Rubio-Herrera E., Lee W.H. 2005a, MNRAS 357, L31
Rubio-Herrera E., Lee W.H. 2005b, MNRAS 362, 989
Shafee R., McClintock J.E., Narayan R., Davis S.W., Li L.-X. Remillard
R.A. 2006, ApJ 636, L113
Shu F.H. 1992, *The Physics of Astrophysics* Vol. 2: *Gas Dynamics*
(University Science Books, California)
Strohmayer T.E. 2001, ApJ 552, L49
Tosa M. 1994, ApJ 426, L81
van der Klis M. 2000, ARA&A 38, 717
van der Klis M. 2004, in *Compact Stellar X-ray Sources*, eds. W.H.G.
Lewin and M. van der Klis (Cambridge University Press, Cambridge),
39
van der Klis M., Wijnands R.A.D., Horne K., Chen W. 1997, ApJ 481,
L97
Vio R., Rebusco P., Andreani P. Madsen H., Overgaard R.V. 2006, A&A
452, 383
Warner B., Woudt P.A., Pretorius M.L. 2003, MNRAS 344, 1193
Whitehurst R. 1988, MNRAS 232, 35
Zanotti O., Font J.A., Rezzolla L., Montero P.J. 2005, MNRAS 356, 1371

Appendix

Kerr Metric and its Basic Properties

John A. Wheeler, who coined a *black hole* in a December 29, 1967 lecture, also remarked “A black hole has no hair.” According to this “no-hair theorem”, the stationary black hole has only three physical quantities; mass M , angular momentum J , and charge Q . By means of these “three” hairs, black holes are classified into four types; the *Schwarzschild* black hole, which is a spherically symmetric one without charge ($J = 0$ and $Q = 0$), the *Kerr* black hole, which is an axisymmetric spinning one without charge ($Q = 0$), the *Reissner-Nordstrøm* black hole, which is a spherically symmetric charged one ($J = 0$), and the *Kerr-Newman* black hole, which is an axisymmetric charged one.¹ In the real world astronomical objects are more or less spinning, and therefore, black holes reasonably have angular momenta. Charge, on the other hand, is easily neutralized by counter charge, if black holes are immersed in a plasma. Hence, we believe that black holes formed after the collapse of realistic astronomical objects are usually spinning Kerr holes.

In this book we have usually considered non-rotating black holes, and further used a pseudo-Newtonian potential for simplicity, except for in several chapters. For the convenience of readers, however, we summarize here several basic properties of Kerr black holes.

A.1 Basic Properties

Roy Kerr discovered the space-time metric describing rotating black holes in 1963. Sometime later, the nature of Kerr space-time was clarified by Boyer and Lindquist (1967). Some basic properties of the Kerr metric,

¹From a different viewpoint, black holes are classified by their mass; the *mini/micro* black hole, whose mass is typically on the order of 10^{15} g, the *stellar-size* black hole, whose mass is typically $10M_{\odot}$, the *intermediate-mass* black hole, whose mass is $\sim 10^{3-4} M_{\odot}$, and the *supermassive* black hole, whose mass is typically $10^8 M_{\odot}$.

which are closely related to accretion-disk problems, have been summarized (Bardeen et al. 1972). Regarding general relativity, there are many excellent textbooks, including those by Landau and Lifshitz (1971) and Misner et al. (1973).

(a) Kerr metric

Let us consider a spinning black hole with mass M and angular momentum J (figure A.1). The specific angular momentum a of a black hole is defined by

$$a \equiv \frac{J}{Mc} \quad (\text{A.1})$$

in geometrized units (this a has the dimension of length). In order to express the magnitude of the spin by a dimensionless parameter, we introduce the *spin parameter* a_* :

$$a_* \equiv \frac{c^2}{GM} a = \frac{c}{GM^2} J. \quad (\text{A.2})$$

This spin parameter has a value of between 0 (Schwarzschild hole) and 1 (extreme Kerr hole), as shown below.

The Kerr metric in Boyer-Lindquist coordinates is expressed as²

$$\begin{aligned} ds^2 = & \left(1 - \frac{r_g r}{\varrho^2}\right) c^2 dt^2 + \frac{2r_g r}{\varrho^2} a \sin^2 \theta d\varphi c dt \\ & - \frac{\varrho^2}{\Delta} dr^2 - \varrho^2 d\theta^2 - \left(r^2 + a^2 + \frac{r_g r}{\varrho^2} a^2 \sin^2 \theta\right) \sin^2 \theta d\varphi^2, \end{aligned} \quad (\text{A.3})$$

where

$$\Delta \equiv r^2 - r_g r + a^2, \quad (\text{A.4})$$

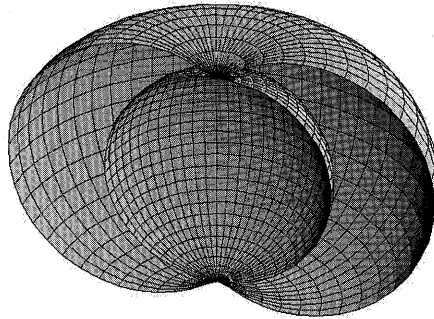
$$\varrho^2 \equiv r^2 + a^2 \cos^2 \theta, \quad (\text{A.5})$$

and $r_g = 2GM/c^2$ is the Schwarzschild radius. This metric is stationary and axisymmetric about the polar axis of $\theta = 0$. The square root of the determinant of $g_{\mu\nu}$ is $\sqrt{-g} = c\varrho^2 \sin \theta$. The Kerr metric above is reduced to the Schwarzschild one if we set $a = 0$.³

²It should be noted that in the literature the *geometrized unit* is often used, where $c = G = 1$. In this book, however, we generally use a physical unit for the convenience of the readers.

³In the spherical coordinates (r, θ, φ) the Schwarzschild metric becomes

$$ds^2 = \left(1 - \frac{r_g}{r}\right) c^2 dt^2 - \left(1 - \frac{r_g}{r}\right)^{-1} dr^2 - r^2 d\theta^2 - r^2 \sin^2 \theta d\varphi^2.$$

**Figure A.1**

Schematic picture of a Kerr black hole. The black hole has the event horizon, which is expressed by a spherical surface. Outside the horizon, there is a surface of the static limit, which is expressed by an ellipsoidal-like surface. The space between the horizon and the static limit is the ergosphere. The spin parameter $a_* = 0.998$.

(b) Horizon

The event horizon of the Kerr hole locates the place where the function Δ vanishes. From the larger root of the quadratic equation $\Delta = 0$, we have the radius r_H of the (outer) horizon:

$$r_+ = r_H = \frac{r_g}{2} + \sqrt{\left(\frac{r_g}{2}\right)^2 - a^2} = \frac{r_g}{2} \left(1 + \sqrt{1 - a_*^2}\right). \quad (\text{A.6})$$

In order for a black hole to exist, the signature inside the square-root of the above equation must be non-negative; i.e., $a_*^2 \leq 1$. The specific angular momentum a must be thus less than GM/c^2 , or the maximum value of the angular momentum of the Kerr hole is given as

$$a_{\max} = \frac{GM}{c^2} \quad \text{and} \quad J_{\max} = \frac{GM^2}{c}. \quad (\text{A.7})$$

A black hole with this maximum value is called a *maximally rotating* black hole.⁴ The spin parameter is just expressed as

$$a_* \equiv \frac{a}{a_{\max}} = \frac{J}{J_{\max}}. \quad (\text{A.8})$$

⁴Of course, the “maximal rotation” may be never realized, like the absolute-temperature zero. The maximum value of a_* is usually set to be 0.9998, through a consideration of the different cross sections for capturing photons with positive and negative angular momentum (Thorne 1974). If the Blandford-Znajek process operates effectively, the maximum value may become lower (Lu et al. 1996; Moderski and Sikora 1996).

(c) Stationary observer

If an observer is located at fixed r and θ , but rotates with a constant angular velocity, he would see an unchanging world. He is called a *stationary* observer.

The angular velocity with respect to the stationary observer, measured at infinity, is

$$\Omega \equiv \frac{d\varphi}{dt} = \frac{u^\varphi}{u^t}, \quad (\text{A.9})$$

where u^μ is the four-velocity. From the condition that an observer follows a timelike worldline,

$$u_\mu u^\mu = 1 = (u^t)^2 [g_{tt} + 2\Omega g_{r\varphi} + \Omega^2 g_{\varphi\varphi}] > 0. \quad (\text{A.10})$$

Since $(u^t)^2$ is positive, the quantities within the brackets $[g_{tt} + 2\Omega g_{r\varphi} + \Omega^2 g_{\varphi\varphi}]$ must be positive. Furthermore, since $g_{\varphi\varphi}$ is negative in the present signature system, the above condition is satisfied only if Ω lies at

$$\Omega_{\min} < \Omega < \Omega_{\max}, \quad (\text{A.11})$$

where

$$\Omega_{\max/\min} = \frac{-g_{t\varphi} \pm \sqrt{g_{t\varphi}^2 - g_{tt}g_{\varphi\varphi}}}{g_{\varphi\varphi}}. \quad (\text{A.12})$$

(d) Static limit and ergosphere

An observer with $\Omega = 0$ is said to be *static* (relative to the “fixed stars”). In flat space-time, static observers can always exist. Near to black holes, however, this is not true.

When $g_{tt} = 0$ (i.e., $\varrho^2 = r_g r$), $\Omega_{\min} = 0$. From the root of $\varrho^2 = r_g r$, this condition is realized at

$$r_E = \frac{r_g}{2} + \sqrt{\left(\frac{r_g}{2}\right)^2 - a^2 \cos^2 \theta} = \frac{r_g}{2} \left(1 + \sqrt{1 - a_*^2 \cos^2 \theta}\right). \quad (\text{A.13})$$

Hence, for observers between r_H and r_E , $g_{tt} < 0$ and we have $\Omega_{\min} > 0$; Ω must be positive and no static observers can exist within $r_H < r < r_E$.

In this sense the surface of $r = r_E$ is called the *static limit* (static observers can exist only outside the static limit). Moreover, the region between the horizon r_H and the static limit r_E is called an *ergosphere*.

(e) Locally non-rotating frame

An observer, who is non-rotating with respect to locally free-falling test particles with zero angular momentum, is called a *locally inertial*

observer or a Bardeen observer (Bardeen et al. 1972). His reference frame is a *locally non-rotating frame* (LNRF).

The angular velocity of the LNRF, ω , is

$$\omega \equiv -\frac{g_{t\varphi}}{g_{\varphi\varphi}} = \frac{acr_g r}{(r^2 + a^2)^2 - \Delta a^2 \sin^2 \theta}. \quad (\text{A.14})$$

This ω is just interpreted as being the angular velocity of *dragging of the inertial frame*.

From the angular velocity Ω of a general observer and that ω of the LNRF, $\tilde{\Omega}$ with respect to the LNRF is given as

$$\tilde{\Omega} = \Omega - \omega. \quad (\text{A.15})$$

(f) Hole spin

From equations (A.12) and (A.14), when $g_{t\varphi}^2 = g_{tt}g_{\varphi\varphi}$, it is easily shown that

$$\Omega_{\min} = \Omega_{\max} = -\frac{g_{t\varphi}}{g_{\varphi\varphi}} = \omega. \quad (\text{A.16})$$

The above condition ($g_{t\varphi}^2 = g_{tt}g_{\varphi\varphi}$) is equivalent to the condition of the horizon ($\Delta = r^2 - r_g r + a^2 = 0$).

The angular velocity Ω_H of a hole is defined to be the angular velocity of dragging of the inertial frame at the horizon. Hence, from equation (A.14),

$$\Omega_H \equiv \omega|_{\Delta=0} = \frac{J}{2M} \frac{1}{\left(\frac{r_g}{2}\right)^2 \left(1 + \sqrt{1 - a_*^2}\right)} = \frac{ac}{r_g} \frac{1}{r_H}. \quad (\text{A.17})$$

Since this Ω_H does not depend on θ , the hole rotation is just like in the case of a rigid body.

The dimensionless angular velocity of the hole is also defined as

$$\hat{\Omega}_H \equiv \frac{GM}{c^3} \Omega_H = \frac{a_*}{2 \left(1 + \sqrt{1 - a_*^2}\right)} = \frac{a_*}{4\hat{r}_H}, \quad (\text{A.18})$$

where $\hat{r}_H = r_H/r_g$ is the dimensionless radius of the horizon.

A.2 Circular Motion in Kerr Space-Time

Since an accretion disk may lie in the equatorial plane of a Kerr hole, we restrict ourselves to considering circular motions in the equatorial

plane. We review the dynamical properties of circular motions, following Novikov and Thorne (1973) and Page and Thorne (1974).

(a) Metric and relativistic correction factors

In and near the equatorial plane ($\theta \sim \pi/2$, $\varrho \sim r$, $z = r \cos \theta$), an appropriate form of the Kerr metric becomes (Novikov and Thorne 1973)

$$\begin{aligned} ds^2 &= \left(1 - \frac{r_g}{r}\right) c^2 dt^2 + \frac{2r_g}{r} ad\varphi cdt \\ &\quad - \frac{r^2}{\Delta} dr^2 - \left(r^2 + a^2 + \frac{r_g}{r} a^2\right) d\varphi^2 - dz^2 \\ &= \frac{r^2 \Delta}{A} c^2 dt^2 - \frac{A}{r^2} (d\varphi - \omega dt)^2 - \frac{r^2}{\Delta} dr^2 - dz^2, \end{aligned} \quad (\text{A.19})$$

where

$$\Delta = r^2 - r_g r + a^2 = r^2 \mathcal{D}, \quad (\text{A.20})$$

$$A \equiv r^4 + r^2 a^2 + r_g r a^2 = r^4 \mathcal{A}, \quad (\text{A.21})$$

$$\omega = \frac{acr_g r}{A} = \frac{acr_g}{r^3} \frac{1}{\mathcal{A}}. \quad (\text{A.22})$$

Note that $\sqrt{-g} = cr$. Here and hereafter, relativistic correction factors are introduced as follows (Novikov and Thorne 1973):

$$\mathcal{A} \equiv 1 + \frac{a^2}{r^2} + \frac{a^2 r_g}{r^3} = 1 + \frac{a_*^2}{4\hat{r}^2} + \frac{a_*^2}{4\hat{r}^3}, \quad (\text{A.23})$$

$$\mathcal{B} \equiv 1 + a \sqrt{\frac{r_g}{2r^3}} = 1 + a_* \sqrt{\frac{1}{8\hat{r}^3}}, \quad (\text{A.24})$$

$$\mathcal{C} \equiv 1 - \frac{3r_g}{2r} + 2a \sqrt{\frac{r_g}{2r^3}} = 1 - \frac{3}{2\hat{r}} + 2a_* \sqrt{\frac{1}{8\hat{r}^3}}, \quad (\text{A.25})$$

$$\mathcal{D} \equiv 1 - \frac{r_g}{r} + \frac{a^2}{r^2} = 1 - \frac{1}{\hat{r}} + \frac{a_*^2}{4\hat{r}^2}, \quad (\text{A.26})$$

$$\mathcal{E} \equiv 1 + \frac{4a^2}{r^2} - \frac{2a^2 r_g}{r^3} + \frac{3a^4}{r^4} = 1 + \frac{a_*^2}{\hat{r}^2} - \frac{a_*^2}{2\hat{r}^3} + \frac{3a_*^4}{16\hat{r}^4}, \quad (\text{A.27})$$

$$\mathcal{F} \equiv 1 - 2a \sqrt{\frac{r_g}{2r^3}} + \frac{a^2}{r^2} = 1 - 2a_* \sqrt{\frac{1}{8\hat{r}^3}} + \frac{a_*^2}{4\hat{r}^2}, \quad (\text{A.28})$$

$$\mathcal{G} \equiv 1 - \frac{r_g}{r} + a \sqrt{\frac{r_g}{2r^3}} = 1 - \frac{1}{\hat{r}} + a_* \sqrt{\frac{1}{8\hat{r}^3}}, \quad (\text{A.29})$$

$$\mathcal{J} \equiv \exp \left[+\frac{3}{4} \int_{\hat{r}}^{\infty} \frac{\mathcal{F}}{\mathcal{B}\mathcal{C}} \frac{d\hat{r}}{\hat{r}^2} \right], \quad (\text{A.30})$$

$$\mathcal{L} \equiv \frac{\ell - \ell_{\text{ms}}}{(GMr)^{1/2}} = \frac{\mathcal{F}}{\mathcal{C}^{1/2}} - \frac{\ell_{\text{ms}}}{(GMr)^{1/2}}, \quad (\text{A.31})$$

$$\mathcal{Q} \equiv \mathcal{L} - \frac{3}{4\hat{r}_{\text{ms}}^{1/2}} \mathcal{J} \int_{\hat{r}_{\text{ms}}}^{\hat{r}} \frac{\mathcal{F}^2}{\mathcal{B}\mathcal{C}^{3/2}\mathcal{J}} \frac{d\hat{r}}{\hat{r}^{3/2}}, \quad (\text{A.32})$$

where

$$\hat{r} \equiv \frac{r}{r_g} \quad (\text{A.33})$$

is the dimensionless radius, \hat{r}_{ms} ($\equiv r_{\text{ms}}/r_g$) the dimensionless radius of the marginally stable orbit, which will be given below, and $a_* = a/(r_g/2)$ the spin parameter already defined. The specific angular momenta ℓ and ℓ_{ms} at r_{ms} are defined below. These correction factors tend to unity far from the center.⁵

In addition, the correction factor \mathcal{Q} is analytically integrated to yield the explicit expression (Page and Thorne 1974) as

$$\begin{aligned} \mathcal{Q} = & \frac{\mathcal{B}}{\mathcal{C}^{1/2}} \frac{1}{\sqrt{\hat{r}}} \left[\sqrt{\hat{r}} - \sqrt{\hat{r}_{\text{ms}}} - \frac{3}{2\sqrt{2}} a_* \ln \frac{\sqrt{\hat{r}}}{\sqrt{\hat{r}_{\text{ms}}}} \right. \\ & - \frac{3}{2\sqrt{\hat{r}_1}(\sqrt{\hat{r}_1} - \sqrt{\hat{r}_2})(\sqrt{\hat{r}_1} - \sqrt{\hat{r}_3})} \ln \frac{\sqrt{\hat{r}} - \sqrt{\hat{r}_1}}{\sqrt{\hat{r}_{\text{ms}}} - \sqrt{\hat{r}_1}} \\ & - \frac{3}{2\sqrt{\hat{r}_2}(\sqrt{\hat{r}_2} - \sqrt{\hat{r}_1})(\sqrt{\hat{r}_2} - \sqrt{\hat{r}_3})} \ln \frac{\sqrt{\hat{r}} - \sqrt{\hat{r}_2}}{\sqrt{\hat{r}_{\text{ms}}} - \sqrt{\hat{r}_2}} \\ & \left. - \frac{3}{2\sqrt{\hat{r}_3}(\sqrt{\hat{r}_3} - \sqrt{\hat{r}_1})(\sqrt{\hat{r}_3} - \sqrt{\hat{r}_2})} \ln \frac{\sqrt{\hat{r}} - \sqrt{\hat{r}_3}}{\sqrt{\hat{r}_{\text{ms}}} - \sqrt{\hat{r}_3}} \right], \end{aligned} \quad (\text{A.34})$$

where

$$\sqrt{\hat{r}_1} = \sqrt{2} \cos \left(\frac{1}{3} \cos^{-1} a_* - \frac{\pi}{3} \right), \quad (\text{A.35})$$

$$\sqrt{\hat{r}_2} = \sqrt{2} \cos \left(\frac{1}{3} \cos^{-1} a_* + \frac{\pi}{3} \right), \quad (\text{A.36})$$

$$\sqrt{\hat{r}_3} = -\sqrt{2} \cos \left(\frac{1}{3} \cos^{-1} a_* \right). \quad (\text{A.37})$$

⁵It should be noted that in the non-relativistic limit these correction factors become unity, except for \mathcal{L} and \mathcal{Q} , which become

$$\mathcal{L} \rightarrow 1 - \frac{\ell_{\text{ms}}}{\ell} \quad \text{and} \quad \mathcal{Q} \rightarrow 1 - \frac{\ell_{\text{ms}}}{\ell}.$$

(b) Keplerian motion

For circular motion in the equatorial plane, the angular velocity Ω_K of the corotating (+) and counterrotating (-) Keplerian orbits becomes

$$\Omega_K^\pm = \pm \frac{\sqrt{GM}}{r^{3/2} \pm a\sqrt{GM/c^2}} = \sqrt{\frac{GM}{r^3}} \frac{1}{\mathcal{B}}, \quad (\text{A.38})$$

where the last equality holds for a corotating case. The linear velocity $V_{(\varphi)}$ of the orbit relative to a “locally non-rotating observer” is

$$V_{(\varphi)} = \frac{A}{r^2 \Delta^{1/2}} (\Omega - \omega) = \sqrt{\frac{GM}{r}} \frac{\mathcal{F}}{\mathcal{D}^{1/2} \mathcal{B}}. \quad (\text{A.39})$$

The corresponding Lorentz factor γ is

$$\gamma_{(\varphi)} = \frac{1}{\sqrt{1 - V_{(\varphi)}^2/c^2}} = \frac{\mathcal{BD}^{1/2}}{\mathcal{A}^{1/2} \mathcal{C}^{1/2}}. \quad (\text{A.40})$$

The $r\varphi$ -component of the shear stress tensor is

$$t_{r\varphi} = \eta \frac{A}{r^3} \gamma^2 \frac{d\Omega}{dr} = -\eta \frac{3}{2} \sqrt{\frac{GM}{r^3}} \frac{\mathcal{D}}{\mathcal{C}}, \quad (\text{A.41})$$

and all other t_{ij} vanish.

The specific energy e_K for a circular orbit is

$$e_K^\pm = |u_t| = c^2 \frac{r^2 - r_g r \pm a\sqrt{r_g r/2}}{r\sqrt{r^2 - 3r_g r/2 \pm 2a\sqrt{r_g r/2}}} = c^2 \frac{\mathcal{G}}{\mathcal{C}^{1/2}}, \quad (\text{A.42})$$

where the last equality holds for a corotating case. The specific angular momentum ℓ_K for a circular motion is

$$\ell_K = u_\varphi = \pm \frac{\sqrt{GM}(r^2 \mp 2a\sqrt{r_g r/2} + a^2)}{r^{1/2}\sqrt{r^2 - 3r_g r/2 \pm 2a\sqrt{r_g r/2}}} = \sqrt{GM}r \frac{\mathcal{F}}{\mathcal{C}^{1/2}}, \quad (\text{A.43})$$

where the last equality is for a corotating case.

Note that for the specific energy and angular momentum of a circular geodesic orbit the following relations hold:

$$\frac{de}{dr} - \Omega \frac{d\ell}{dr} = 0, \quad (\text{A.44})$$

$$e - \Omega\ell = c^2 \frac{\mathcal{C}^{1/2}}{\mathcal{B}}. \quad (\text{A.45})$$

The epicyclic frequency κ_K is (Okazaki et al. 1987; see also Fukue 1980; Aliev and Galtsov 1981)

$$\kappa_K^2 = \frac{GM}{r^3} \left[1 - \frac{3r_g}{r} \pm 8a_* \left(\frac{r_g}{2r} \right)^{3/2} - 3a_*^2 \left(\frac{r_g}{2r} \right)^2 \right] \left[1 \pm a_* \left(\frac{r_g}{2r} \right)^{3/2} \right]^{-2}. \quad (\text{A.46})$$

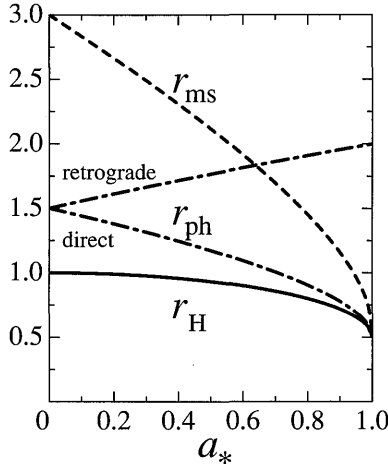


Figure A.2

Radii of the event horizon (solid curve), of the marginally stable orbit (dashed one), and of the direct/retrograde photon orbits (chain-dotted one) as a function of the spin parameter a_* . The radii r_H , r_{ms} , and r_{ph} are in units of r_g .

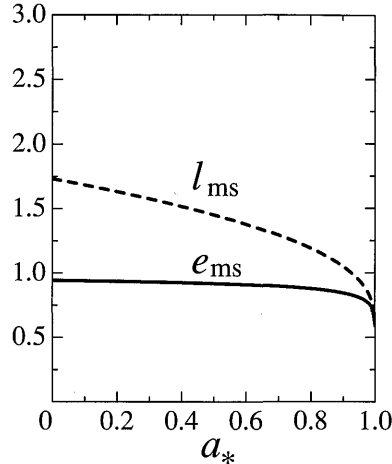


Figure A.3

Specific energy (solid curve) and specific angular momentum (dashed one) of a test particle at the marginally stable orbit as a function of the spin parameter a_* . The specific energy e_{ms} and angular momentum l_{ms} are in units of c^2 and $r_g c$, respectively.

(c) Marginally stable circular orbit

Besides the horizon and static limit, in the vicinity of a black hole there exist several characteristic radii (for a circular motion).

One is a *marginally stable circular orbit*, which is the innermost stable circular geodesic orbit. The radius of the marginally stable orbit, r_{ms} , is determined by

$$r_{ms}^2 - 3r_g r_{ms} \pm 4a\sqrt{2r_g r_{ms}} - 3a^2 = 0. \quad (\text{A.47})$$

The analytical solution of this equation is (Bardeen et al. 1972)

$$r_{ms}^\pm = \frac{r_g}{2} \left[3 + Z_2 \mp \sqrt{(3 - Z_1)(3 + Z_1 + 2Z_2)} \right], \quad (\text{A.48})$$

where

$$Z_1 \equiv 1 + (1 - a_*^2)^{1/3} \left[(1 + a_*)^{1/3} + (1 - a_*)^{1/3} \right], \quad (\text{A.49})$$

$$Z_2 \equiv \sqrt{3a_*^2 + Z_1^2}. \quad (\text{A.50})$$

For a Schwarzschild hole ($a_* = 0$), $r_{\text{ms}} = 3r_g$, while for an extreme Kerr hole ($a_* = 1$), $r_{\text{ms}} = r_g/2$ (direct orbit) or $r_{\text{ms}} = 4.5r_g$ (retrograde orbit) (see figure A.2).

In the standard picture of geometrically thin accretion disks, the radius of the inner edge of the disk is supposed to be the radius of the marginally stable orbit; $r_{\text{in}} = r_{\text{ms}}$.

Another is a *marginally bound circular orbit*, which is the innermost (unstable) circular orbit. The radius of a marginally bound orbit, r_{mb} , is determined by the condition of $e = c^2$ and given by

$$r_{\text{mb}}^\pm = r_g \left(1 \mp \frac{a_*}{2} + \sqrt{1 \mp a_*} \right). \quad (\text{A.51})$$

For a Schwarzschild hole ($a_* = 0$), $r_{\text{mb}} = 2r_g$, while for an extreme Kerr hole ($a_* = 1$), $r_{\text{mb}} = r_g/2$ (direct) or $r_{\text{mb}} = 2.91r_g$ (retrograde).

The third is a *photon circular orbit*. The radius of the photon circular orbit, r_{ph} , is

$$r_{\text{ph}}^\pm = r_g \left\{ 1 + \cos \left[\frac{2}{3} \cos^{-1}(\mp a_*) \right] \right\}. \quad (\text{A.52})$$

For a Schwarzschild hole ($a_* = 0$), $r_{\text{ph}} = 1.5r_g$, while for an extreme Kerr hole ($a_* = 1$), $r_{\text{ph}} = r_g/2$ (direct) or $r_{\text{ph}} = 2r_g$ (retrograde).

(d) Efficiency

The specific energy e_{ms} of a test particle rotating in a marginally stable circular orbit is expressed, after some manipulations, as

$$e_{\text{ms}} = c^2 \sqrt{1 - \frac{r_g}{3r_{\text{ms}}}}. \quad (\text{A.53})$$

In addition, the specific angular momentum ℓ_{ms} is expressed as

$$\ell_{\text{ms}} = \pm \frac{GM}{c} 2\sqrt{3} \left(1 \mp \frac{2ac}{3\sqrt{GMr_{\text{ms}}}} \right) = \pm \sqrt{3}r_g c \left(1 \mp \frac{\sqrt{2}a_*}{3\sqrt{r_{\text{ms}}/r_g}} \right). \quad (\text{A.54})$$

For a direct orbit, e_{ms}/c^2 varies from $\sqrt{8/9}$ (Schwarzschild hole) to $\sqrt{1/3}$ (extreme Kerr hole), while for a retrograde one it varies from $\sqrt{8/9}$

(Schwarzschild) to $\sqrt{25/27}$ (extreme Kerr) (see figure A.3).⁶

The ratio of the specific binding energy of the last stable circular orbit, $c^2 - e_{\text{ms}}$, to the specific rest-mass energy, c^2 , is just the *efficiency* for converting the rest-mass energy into radiation (the total amount of gravitational energy which can be released between r_{ms} and infinity). Thus, the efficiency within the framework of general relativity is given as

$$1 - e_{\text{ms}}/c^2 = \begin{cases} 1 - \sqrt{\frac{8}{9}} = 0.0572 & \text{Schwarzschild} \\ 1 - \sqrt{\frac{1}{3}} = 0.420 & \text{extreme Kerr.} \end{cases} \quad (\text{A.55})$$

References

- Aliev A.N., Galtsov D.V. 1981, General Relativity and Gravitation 13, 899
 Bardeen J.M., Press W.H., Teukolsky S.A. 1972, ApJ 178, 347
 Blandford R.D., Znajek R.I. 1977, MNRAS 179, 433
 Boyer R.H., Lindquist R.W. 1967, JMathPhys 8, 265
 Fukue J. 1980, Master Thesis of Kyoto University (in Japanese)
 Kerr R.P. 1963, PhysRevLett 11, 237
 Kozłowski M., Jaroszyński M., and Abramowicz M. 1978, A&A 63, 209
 Landau L.D., Lifshitz E.M. 1971, *The Classical Theory of Fields* (Pergamon Press, Oxford)
 Lu Y.J., Zhou Y.Y., Yu K.N., Young E.C.M. 1996, ApJ 472, 564
 Misner C.W., Thorne K.S., Wheeler J.A. 1973, *Gravitation* (W.H. Freeman and Co., San Francisco)
 Moderski R., Sikora M. 1996, MNRAS 283, 854
 Novikov I.D. and Thorne K.S. 1973, in *Black Holes*, eds. C. DeWitt and B. DeWitt (Gordon and Breach, New York)
 Okazaki A.T., Kato S., Fukue J. 1987, PASJ 39, 473
 Page D.N., Thorne K.S. 1974, ApJ 191, 499
 Thorne K.S. 1974, ApJ 191, 507

⁶Here, we derived the quantities under a particle picture. These values change if the gas pressure is taken into account; e.g., $\ell_{\text{ms}} = \sqrt{27/8r_g c}$ (for details see Kozłowski et al. 1978).

APPENDIX B

Navier-Stokes Equations

In this appendix we summarize the basic equations for a viscous fluid, the *Navier-Stokes equations*, in the non-relativistic regime. The basic equations include the continuity equation, the equation of motion, and the energy equation, supplemented by the equation of state. We first show these basic equations in a vector form, and then we give them in cylindrical coordinates.

B.1 General Form

We first write the basic equations in a vector form.

(a) Continuity equation

The conservation of mass (continuity equation) is written as

$$\frac{\partial \rho}{\partial t} + \operatorname{div}(\rho \mathbf{v}) = 0, \quad (\text{B.1})$$

where ρ is the density and \mathbf{v} the velocity vector. In terms of the *Lagrange derivative*:

$$\frac{d}{dt} = \frac{\partial}{\partial t} + (\mathbf{v} \cdot \nabla), \quad (\text{B.2})$$

the continuity equation (B.1) is expressed as

$$\frac{d\rho}{dt} + \rho \operatorname{div} \mathbf{v} = 0. \quad (\text{B.3})$$

(b) Equation of motion

The equation of motion is described as

$$\rho \frac{d\mathbf{v}}{dt} = \rho \left[\frac{\partial \mathbf{v}}{\partial t} + (\mathbf{v} \cdot \nabla) \mathbf{v} \right] = -\rho \nabla \psi - \nabla p + \rho \mathbf{N}, \quad (\text{B.4})$$

where ψ is the gravitational potential and p is the pressure. In addition, $\rho \mathbf{N}$ is the viscous force per unit volume, given by

$$\rho N_i = \frac{\partial t_{ik}}{\partial x_k}, \quad (\text{B.5})$$

where t_{ik} is the viscous stress tensor:

$$t_{ik} \equiv \eta \left(\frac{\partial v_i}{\partial x_k} + \frac{\partial v_k}{\partial x_i} - \frac{2}{3} \delta_{ik} \frac{\partial v_j}{\partial x_j} \right) + \zeta \delta_{ik} \frac{\partial v_j}{\partial x_j}, \quad (\text{B.6})$$

η being the dynamical viscosity (first viscosity) and ζ the bulk viscosity (second viscosity) (the latter is usually ignored). Here and hereafter, the summation abbreviation is used.

The equation of motion is also written in a conservative form as

$$\frac{\partial}{\partial t} (\rho v_i) + \frac{\partial}{\partial x_j} (\rho v_i v_j + p \delta_{ij} - t_{ij}) = -\rho \frac{\partial \psi}{\partial x_i}, \quad (\text{B.7})$$

where δ_{ij} is the Kronecker delta.

The Navier-Stokes equation is explicitly written in the form:

$$\begin{aligned} \rho \frac{dv_i}{dt} &= -\rho \frac{\partial \psi}{\partial x_i} - \frac{\partial p}{\partial x_i} \\ &\quad + \frac{\partial}{\partial x_k} \left[\eta \left(\frac{\partial v_i}{\partial x_k} + \frac{\partial v_k}{\partial x_i} - \frac{2}{3} \delta_{ik} \frac{\partial v_j}{\partial x_j} \right) + \zeta \delta_{ik} \frac{\partial v_j}{\partial x_j} \right]. \end{aligned} \quad (\text{B.8})$$

(c) Energy equation

We consider three kinds of energy, i.e., total, kinetic, and thermal energies.

(i) Total energy

The conservation of total energy is written as

$$\frac{\partial}{\partial t} \left[\rho \left(e + \psi + \frac{1}{2} v^2 \right) \right] + \operatorname{div} \left[\rho \left(H + \psi + \frac{1}{2} v^2 \right) \mathbf{v} - \mathbf{v} : \mathbf{t} + \mathbf{F} \right] = \rho \epsilon, \quad (\text{B.9})$$

where $\rho \epsilon$ is the thermal energy density per unit volume, ψ the non-selfgravitating steady potential, H the enthalpy defined by $H = e + p/\rho$.

Furthermore, $-\mathbf{v} \cdot \mathbf{t}$ represents the vector of viscous heat flux: the product of $-\mathbf{v}$ and the stress tensor \mathbf{t} , defined by equation (B.6). That is, its i -component is $-v_k t^{ik}$. Moreover, \mathbf{F} is the other thermal energy flux (which includes, e.g., the radiative flux \mathbf{F}_{rad} , the convective one \mathbf{F}_{conv} , and the conductive one \mathbf{F}_{cond}). Finally, ϵ is the other net heating rate (such as nuclear energy generation and optically thin radiative cooling) per unit mass (i.e., $\rho\epsilon$ per unit volume).

In the disk with gas and radiation, ρe is described as

$$\rho e = \frac{1}{\gamma - 1} p_{\text{gas}} + 3p_{\text{rad}} = \left[\frac{\beta}{\gamma - 1} + 3(1 - \beta) \right] p, \quad (\text{B.10})$$

where γ is the ratio of specific heats, and p_{gas} and p_{rad} are the gas and radiation pressures, respectively. Here,

$$\beta \equiv \frac{p_{\text{gas}}}{p} = \frac{p_{\text{gas}}}{p_{\text{gas}} + p_{\text{rad}}} \quad (\text{B.11})$$

is the ratio of the gas pressure to the total pressure.

(ii) Kinetic energy

The kinetic energy conservation is written as

$$\frac{d}{dt} \left(\frac{1}{2} v^2 \right) = \mathbf{v} \cdot \left(-\text{grad}\psi - \frac{1}{\rho} \text{grad}p + \mathbf{N} \right), \quad (\text{B.12})$$

which results from equation of motion.

(iii) Thermal energy

By eliminating the part of kinetic energy from equation (B.9) by using equation (B.12), we have the conservation of thermal energy, which is

$$\rho \frac{de}{dt} - \frac{p}{\rho} \frac{dp}{dt} = \Phi + \rho\epsilon - \text{div}\mathbf{F}, \quad (\text{B.13})$$

where Φ is the viscous heat dissipation per unit volume and given by

$$\Phi = t_{ik} \frac{\partial v_i}{\partial x_k}. \quad (\text{B.14})$$

If we use the first law of thermodynamics: $Tds = de + pd(1/\rho)$, the thermal energy conservation is also written as

$$\rho T \frac{ds}{dt} = \rho T \left[\frac{\partial s}{\partial t} + (\mathbf{v} \cdot \nabla)s \right] = \rho \frac{de}{dt} - \frac{p}{\rho} \frac{dp}{dt} = \Phi + \rho\epsilon - \text{div}\mathbf{F}, \quad (\text{B.15})$$

where s is the entropy.

(iv) Adiabatic exponents

The gas pressure, $p_{\text{gas}} (= \beta p)$, is a function of ρ and T ; $p_{\text{gas}} = \beta p \propto \rho T$. This means that βp is a function of ρ and $(1 - \beta)p$ ($= p_{\text{rad}} = aT^4/3$); $\beta p \propto \rho(1 - \beta)^{1/4}p^{1/4}$. Taking the time derivative of this relation, we have

$$\frac{4 - 3\beta}{3(1 - \beta)} \frac{d\ln\beta}{dt} = -\frac{d\ln p}{dt} + \frac{4}{3} \frac{d\ln\rho}{dt}. \quad (\text{B.16})$$

Using this relation (B.16) and equation (B.10), we can express the left-hand side of the energy equation (B.13) as

$$\rho \frac{de}{dt} - \frac{p}{\rho} \frac{d\rho}{dt} = \frac{1}{\Gamma_3 - 1} \left[\frac{dp}{dt} - \Gamma_1 \frac{p}{\rho} \frac{d\rho}{dt} \right], \quad (\text{B.17})$$

where

$$\Gamma_1 = \beta + \frac{(\gamma - 1)(4 - 3\beta)^2}{\beta + 12(\gamma - 1)(1 - \beta)}. \quad (\text{B.18})$$

An expression for Γ_3 is given later [see equation (B.22)].

If motions are adiabatic, i.e., $\rho T ds/dt = 0$, the changes of p and ρ are related through $dp/dt - (\Gamma_1 p/\rho)d\rho/dt = 0$ and Γ_1 is an adiabatic exponent describing the relation between p and ρ .

If adiabatic changes are described by a relation between p and T as

$$\frac{1}{p} \frac{dp}{dt} + \frac{\Gamma_2}{1 - \Gamma_2} \frac{1}{T} \frac{dT}{dt} = 0, \quad (\text{B.19})$$

we have

$$\Gamma_2 = 1 + \frac{(4 - 3\beta)(\gamma - 1)}{\beta^2 + 3(\gamma - 1)(1 - \beta)(4 + \beta)}. \quad (\text{B.20})$$

Similarly, if adiabatic changes are described as a relation between T and ρ as

$$\frac{1}{T} \frac{dT}{dt} - (\Gamma_3 - 1) \frac{1}{\rho} \frac{d\rho}{dt} = 0, \quad (\text{B.21})$$

then Γ_3 is given by

$$\Gamma_3 = 1 + \frac{(4 - 3\beta)(\gamma - 1)}{\beta + 12(\gamma - 1)(1 - \beta)}. \quad (\text{B.22})$$

These Γ_i 's are generalized adiabatic exponents (Chandrasekhar 1967), and shown in figure B.1 as function of β .

In the limit of $\beta = 1$ (gas-pressure-dominated case) we have $\Gamma_1 = \Gamma_2 = \Gamma_3 = \gamma$, while in the limit of $\beta = 0$ (radiation-pressure-dominated case), we have $\Gamma_1 = \Gamma_2 = \Gamma_3 = 4/3$. See Chandrasekhar (1967) for details of adiabatic exponents.

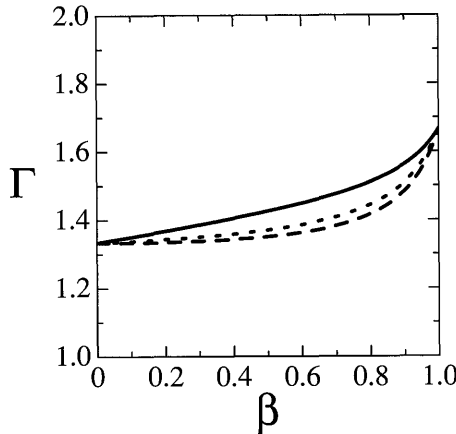


Figure B.1

Generalized adiabatic exponents as a function of β . A solid curve denotes Γ_1 , a dashed one Γ_2 , and a dotted one Γ_3 . The ratio of specific heats is fixed as $\gamma = 5/3$.

(v) Dissipation terms

The viscous dissipation function Φ , which expresses the viscous heating rate per unit volume, is expressed as

$$\Phi = t_{ik} \frac{\partial v_i}{\partial x_k} = \frac{1}{2} \eta \left(\frac{\partial v_i}{\partial x_k} + \frac{\partial v_k}{\partial x_i} \right)^2 + \left(\zeta - \frac{2}{3} \eta \right) \left(\frac{\partial v_j}{\partial x_j} \right)^2. \quad (\text{B.23})$$

The energy flux \mathbf{F} is generally written in the form

$$\mathbf{F} = -K \nabla T, \quad (\text{B.24})$$

where K is the ‘conductivity’. For example, in the optically thick regime, the radiative flux \mathbf{F}_{rad} is

$$\mathbf{F}_{\text{rad}} = -\frac{4acT^3}{3\bar{\kappa}\rho} \nabla T, \quad (\text{B.25})$$

where a the radiation constant and $\bar{\kappa}$ the (Rosseland-mean) total opacity (see appendix D).

(d) Equation of state

Finally, the equation of state is

$$\begin{aligned} p &= p_{\text{gas}} + p_{\text{rad}} = \beta p + (1 - \beta)p, \\ &= \frac{\mathcal{R}}{\bar{\mu}} \rho T + \frac{1}{3} a T^4, \end{aligned} \quad (\text{B.26})$$

where \mathcal{R} ($= 8.3145 \times 10^7 \text{ erg mol}^{-1} \text{ K}^{-1}$) is the gas constant and $\bar{\mu}$ is the mean molecular weight.

B.2 Cylindrical Coordinate Expression

In this book we focus our attention on accretion disks having an axisymmetric configuration. Hence, for the convenience of the readers, we explicitly write down the basic equations for a viscous fluid in cylindrical coordinates (r, φ, z) , where the z -axis is coincident with the axis of symmetry.

(a) Continuity equation

$$\frac{\partial \rho}{\partial t} + \frac{\partial}{r \partial r} (r \rho v_r) + \frac{\partial}{r \partial \varphi} (\rho v_\varphi) + \frac{\partial}{\partial z} (\rho v_z) = 0, \quad (\text{B.27})$$

where (v_r, v_φ, v_z) are the components of velocity in the cylindrical coordinates.

(b) Equation of motion

$$\frac{\partial v_r}{\partial t} + v_r \frac{\partial v_r}{\partial r} + v_\varphi \frac{\partial v_r}{r \partial \varphi} + v_z \frac{\partial v_r}{\partial z} - \frac{v_\varphi^2}{r} = -\frac{\partial \psi}{\partial r} - \frac{1}{\rho} \frac{\partial p}{\partial r} + N_r, \quad (\text{B.28})$$

$$\frac{\partial v_\varphi}{\partial t} + v_r \frac{\partial v_\varphi}{\partial r} + v_\varphi \frac{\partial v_\varphi}{r \partial \varphi} + v_z \frac{\partial v_\varphi}{\partial z} + \frac{v_r v_\varphi}{r} = -\frac{\partial \psi}{r \partial \varphi} - \frac{1}{\rho r} \frac{\partial p}{\partial \varphi} + N_\varphi, \quad (\text{B.29})$$

$$\frac{\partial v_z}{\partial t} + v_r \frac{\partial v_z}{\partial r} + v_\varphi \frac{\partial v_z}{r \partial \varphi} + v_z \frac{\partial v_z}{\partial z} = -\frac{\partial \psi}{\partial z} - \frac{1}{\rho} \frac{\partial p}{\partial z} + N_z, \quad (\text{B.30})$$

where (N_r, N_φ, N_z) are the components of the viscous force \mathbf{N} .

In cylindrical coordinates the components of the viscous force are expressed as

$$\rho N_r = \frac{1}{r} \frac{\partial}{\partial r} (r t_{rr}) + \frac{1}{r} \frac{\partial t_{r\varphi}}{\partial \varphi} - \frac{t_{\varphi\varphi}}{r} + \frac{\partial t_{rz}}{\partial z}, \quad (\text{B.31})$$

$$\rho N_\varphi = \frac{1}{r^2} \frac{\partial}{\partial r} (r^2 t_{\varphi r}) + \frac{1}{r} \frac{\partial t_{\varphi\varphi}}{\partial \varphi} + \frac{\partial t_{\varphi z}}{\partial z}, \quad (\text{B.32})$$

$$\rho N_z = \frac{1}{r} \frac{\partial}{\partial r} (r t_{zr}) + \frac{1}{r} \frac{\partial t_{z\varphi}}{\partial \varphi} + \frac{\partial t_{zz}}{\partial z}, \quad (\text{B.33})$$

where the viscous stress tensor t_{ik} are given by

$$t_{rr} = 2\eta \frac{\partial v_r}{\partial r} + \left(\zeta - \frac{2}{3}\eta \right) \operatorname{div} \mathbf{v}, \quad (\text{B.34})$$

$$t_{r\varphi} = t_{\varphi r} = \eta \left[r \frac{\partial}{\partial r} \left(\frac{v_\varphi}{r} \right) + \frac{1}{r} \frac{\partial v_r}{\partial \varphi} \right], \quad (\text{B.35})$$

$$t_{rz} = t_{zr} = \eta \left(\frac{\partial v_z}{\partial r} + \frac{\partial v_r}{\partial z} \right), \quad (\text{B.36})$$

$$t_{\varphi\varphi} = 2\eta \left(\frac{1}{r} \frac{\partial v_\varphi}{\partial \varphi} + \frac{v_r}{r} \right) + \left(\zeta - \frac{2}{3}\eta \right) \operatorname{div} \mathbf{v}, \quad (\text{B.37})$$

$$t_{\varphi z} = t_{z\varphi} = \eta \left(\frac{\partial v_\varphi}{\partial z} + \frac{1}{r} \frac{\partial v_z}{\partial \varphi} \right), \quad (\text{B.38})$$

$$t_{zz} = 2\eta \frac{\partial v_z}{\partial z} + \left(\zeta - \frac{2}{3}\eta \right) \operatorname{div} \mathbf{v}, \quad (\text{B.39})$$

$$\operatorname{div} \mathbf{v} = \frac{1}{r} \frac{\partial}{\partial r} (rv_r) + \frac{1}{r} \frac{\partial v_\varphi}{\partial \varphi} + \frac{\partial v_z}{\partial z}. \quad (\text{B.40})$$

For the accretion disk, only the $r\varphi$ -component of the viscous stress tensor, $t_{r\varphi}$, is dominant; therefore,

$$\rho N_\varphi = \frac{1}{r^2} \frac{\partial}{\partial r} (r^2 t_{r\varphi}) \quad \text{and} \quad t_{r\varphi} = \eta r \frac{\partial}{\partial r} \left(\frac{v_\varphi}{r} \right) = \eta r \frac{\partial \Omega}{\partial r}; \quad (\text{B.41})$$

and therefore,

$$\rho N_\varphi = \frac{1}{r^2} \frac{\partial}{\partial r} \left(\eta r^3 \frac{d\Omega}{dr} \right), \quad (\text{B.42})$$

where we introduce the angular speed $\Omega = v_\varphi/r$.

It should be noted that the alpha prescription means that $t_{r\varphi} = \eta r d\Omega/dr = -\alpha p$. In this case $\rho N_\varphi = -(1/r^2) \partial(r^2 \alpha p)/\partial r$.

(c) Energy equation

$$\begin{aligned} & \frac{1}{\Gamma_3 - 1} \left[\left(\frac{\partial}{\partial t} + v_r \frac{\partial}{\partial r} + v_\varphi \frac{\partial}{r \partial \varphi} + v_z \frac{\partial}{\partial z} \right) p \right. \\ & \quad \left. - \Gamma_1 \frac{p}{\rho} \left(\frac{\partial}{\partial t} + v_r \frac{\partial}{\partial r} + v_\varphi \frac{\partial}{r \partial \varphi} + v_z \frac{\partial}{\partial z} \right) \rho \right] \\ &= \Phi + \rho \varepsilon + \frac{\partial}{r \partial r} \left(r K \frac{\partial T}{\partial r} \right) \\ & \quad + \frac{\partial}{r \partial \varphi} \left(K \frac{\partial T}{r \partial \varphi} \right) + \frac{\partial}{\partial z} \left(K \frac{\partial T}{\partial z} \right). \end{aligned} \quad (\text{B.43})$$

In cylindrical coordinates the viscous dissipation function Φ is expressed as

$$\begin{aligned}\Phi = & \eta \left[2 \left(\frac{\partial v_r}{\partial r} \right)^2 + 2 \left(\frac{\partial v_\varphi}{\partial r} + \frac{\partial v_r}{\partial \varphi} \right)^2 + 2 \left(\frac{\partial v_z}{\partial z} \right)^2 \right. \\ & + \left(\frac{\partial v_\varphi}{r \partial \varphi} + \frac{\partial v_\varphi}{\partial r} - \frac{v_\varphi}{r} \right)^2 + \left(\frac{\partial v_\varphi}{\partial z} + \frac{\partial v_z}{r \partial \varphi} \right)^2 + \left(\frac{\partial v_z}{\partial r} + \frac{\partial v_r}{\partial z} \right)^2 \left. \right] \\ & + \left(\zeta - \frac{2}{3} \eta \right) \left[\frac{\partial(rv_r)}{r \partial r} + \frac{\partial v_\varphi}{r \partial \varphi} + \frac{\partial v_z}{\partial z} \right]^2.\end{aligned}\quad (\text{B.44})$$

In the case of accretion disks, where the shear due to the rotational motion is important, we retain the dominant term and have

$$\Phi = t_{r\varphi} \left(\frac{\partial v_\varphi}{\partial r} - \frac{v_\varphi}{r} \right) = \eta \left(\frac{\partial v_\varphi}{\partial r} - \frac{v_\varphi}{r} \right)^2 = \eta r^2 \left(\frac{d\Omega}{dr} \right)^2. \quad (\text{B.45})$$

Under the alpha prescription, $\Phi = -\alpha p r (d\Omega/dr)$, since $t_{r\varphi}$ is written as $t_{r\varphi} = -\alpha p$.

References

Chandrasekhar S. 1967, *Stellar Structure* (The University of Chicago Press, Chicago)

APPENDIX C

Equations for Relativistic Viscous Fluid

In this appendix we summarize the basic equations for a viscous fluid within the framework of general relativity. The basic equations include the continuity equation, the equation of motion, and the energy equation, supplemented by the equation of state. We first give the metric and energy-momentum tensor, and then show the basic equations in a tensor form.

C.1 Metric and Energy-Momentum Tensor

Of many textbooks concerning general relativity, we would like to refer to Landau and Lifshitz (1971) and Misner et al. (1973) as a standard. In this book the $(+, -, -, -)$ space-time signature is adopted, and the Greek suffixes $\alpha, \beta, \gamma, \dots$ take values of 0, 1, 2, and 3, while the Latin suffixes i, j, k, \dots take values of 1, 2, and 3. The semicolon denotes covariant differentiation.

(a) Metric

The square of the invariant line element ds^2 is written in a form

$$ds^2 = c^2 d\tau^2 = g_{\mu\nu} dx^\mu dx^\nu, \quad (\text{C.1})$$

where c is the speed of light, τ the proper time, x^μ the space-time coordinates ($x^0 = ct$ in this appendix), and $g_{\mu\nu}$ the space-time metric. The three-dimensional part of the metric, γ_{ij} , is defined by

$$\gamma_{ij} \equiv -g_{ij} + \frac{g_{0i}g_{0j}}{g_{00}}. \quad (\text{C.2})$$

If space-time is described by the spherically symmetric static one, the Schwarzschild metric, the components of the space-time metric in

the cylindrical coordinates (r, φ, z) are explicitly written as

$$\begin{aligned} g_{00} &= \left(1 - \frac{r_g}{R}\right), & g^{00} &= \left(1 - \frac{r_g}{R}\right)^{-1}, \\ g_{11} &= -\left(1 - \frac{r_g}{R}\right)^{-1} \left(1 - \frac{r_g z^2}{R^3}\right), & g^{11} &= -\left(1 - \frac{r_g z^2}{R^3}\right), \\ g_{22} &= -r^2, & g^{22} &= -\frac{1}{r^2}, \\ g_{33} &= -\left(1 - \frac{r_g}{R}\right)^{-1} \left(1 - \frac{r_g r^2}{R^3}\right), & g^{33} &= -\left(1 - \frac{r_g z^2}{R^3}\right), \\ g_{13} &= g_{31} = -\left(1 - \frac{r_g}{R}\right)^{-1} \frac{r_g r z}{R^3}, & g^{13} &= g^{31} = \frac{r_g r z}{R^3}, \\ \sqrt{-g} &= r, \end{aligned} \tag{C.3}$$

where $R = \sqrt{r^2 + z^2}$ and r_g ($= 2GM/c^2$) is the Schwarzschild radius.¹

(b) Four-velocity of matter

The four-velocity u^μ of matter is defined by

$$u^\mu \equiv \frac{dx^\mu}{ds} = \left(\frac{\gamma}{\sqrt{g_{00}}} - \gamma \frac{g_{0k}}{g_{00}} \frac{v^k}{c}, \gamma \frac{v^i}{c} \right), \tag{C.4}$$

where

$$\gamma = \left(1 - \frac{v^2}{c^2}\right)^{-1/2}, \tag{C.5}$$

$$v^2 = v_i v^i = \gamma_{ik} v^i v^k = \left(-g_{ik} + \frac{g_{0i} g_{0k}}{g_{00}}\right) v^i v^k. \tag{C.6}$$

The covariant components are $u_\mu = g_{\mu\nu} u^\nu$, and $u_\mu u^\mu = g_{\mu\nu} u^\mu u^\nu = 1$.

When $g_{0i} = 0$ and $g_{ij} = 0$ ($i \neq j$),

$$u^\mu = \left(\frac{\gamma}{\sqrt{g_{00}}}, \gamma \frac{v^i}{c} \right) \quad \text{and} \quad u_\mu = \left(\gamma \sqrt{g_{00}}, -\gamma \frac{v_i}{c} \right), \tag{C.7}$$

where

$$v^2 = v_i v^i \quad \text{and} \quad v_i = -g_{ik} v^k. \tag{C.8}$$

¹In the spherical coordinates (R, θ, φ) the space-time metric becomes

$$\begin{aligned} g_{00} &= 1/g^{00} = (1 - r_g/R), & g_{11} &= 1/g^{11} = -(1 - r_g/R)^{-1}, \\ g_{22} &= 1/g^{22} = -R^2, & g_{33} &= 1/g^{33} = -R^2 \sin^2 \theta, \\ \sqrt{-g} &= R^2 \sin \theta. \end{aligned}$$

The straightforward transformation from the spherical coordinates (R, θ, φ) to the cylindrical ones (r, φ, z) gives the components (C.3).

(c) Energy-momentum tensor

The energy-momentum tensor for a viscous fluid, $T^{\mu\nu}$, is

$$\begin{aligned} T^{\mu\nu} &= \varepsilon u^\mu u^\nu + p^{\mu\nu} + u^\mu q^\nu + u^\nu q^\mu, \\ &= (\varepsilon + p) u^\mu u^\nu - pg^{\mu\nu} + t^{\mu\nu} + u^\mu q^\nu + u^\nu q^\mu, \end{aligned} \quad (\text{C.9})$$

where

$$p^{\mu\nu} = -p(g^{\mu\nu} - u^\mu u^\nu) + t^{\mu\nu} \quad (\text{C.10})$$

is the pressure stress tensor, ε the internal energy per unit proper volume, p the pressure measured in the comoving frame ($\varepsilon + p$ is the enthalpy per unit proper volume), $t^{\mu\nu}$ the viscous stress tensor, and q^μ the energy-flow vector.

The pressure stress tensor $p^{\mu\nu}$ is a symmetric tensor and is orthogonal to u^μ ; $u_\mu p^{\mu\nu} = 0$. The energy-flow vector q^μ is also orthogonal to u^μ ; $u_\mu q^\mu = 0$. The viscous stress tensor $t^{\mu\nu}$ is defined by

$$\begin{aligned} t^{\mu\nu} &\equiv c\eta(u^{\mu;\nu} + u^{\nu;\mu} - u_{;\sigma}^\mu u^\sigma u^\nu - u^\mu u_{;\sigma}^\nu u^\sigma) \\ &\quad + c\lambda u_{;\sigma}^\sigma (g^{\mu\nu} - u^\mu u^\nu), \end{aligned} \quad (\text{C.11})$$

where $\lambda = \zeta - 2\eta/3$, $u_{;\sigma}^\sigma$ the expansion, and $g^{\mu\nu} - u^\mu u^\nu$ the projection tensor, η being the dynamical viscosity and ζ the bulk viscosity. Finally, the heat flux q^μ is expressed as

$$q^\mu \equiv -\frac{K}{c}(g^{\mu\nu} - u^\mu u^\nu)(T_{,\nu} - Tu_{\nu;\sigma} u^\sigma), \quad (\text{C.12})$$

where K is the thermal conductivity, T the temperature, and $u_{\nu;\sigma} u^\sigma$ the four-acceleration.

C.2 General Form

We can now give the basic equations for viscous fluid within the framework of general relativity (Landau and Lifshitz 1971; Misner et al. 1973).

(a) Mass conservation

The particle number conservation, $(nu^\mu)_{;\mu}$, is

$$\frac{1}{\sqrt{-g}} \frac{\partial}{\partial x^\mu} (\sqrt{-g} n u^\mu) = 0, \quad (\text{C.13})$$

where x^μ is the space-time coordinates, u^μ the four-velocity, and n the proper number density.

(b) Momentum conservation

The relativistic equations of motion, $T_i{}^\mu_{;\mu} = 0$, are written as

$$\begin{aligned} & (\varepsilon + p) \left(u^\mu \frac{\partial u^i}{\partial x^\mu} + \Gamma_{\mu\nu}^i u^\mu u^\nu \right) - (g^{i\mu} - u^i u^\mu) \frac{\partial p}{\partial x^\mu} \\ &= -(g^{i\mu} - u^i u^\mu) t_\mu{}^\nu_{;\nu} - (g^{i\mu} - u^i u^\mu) (u_\mu q^\nu + u^\nu q_\mu)_{;\nu}. \end{aligned} \quad (\text{C.14})$$

(c) Energy conservation

The energy conservation, $u^\mu T_\mu{}^\nu_{;\nu} = 0$, is written as

$$\frac{1}{\sqrt{-g}} \frac{\partial}{\partial x^\mu} (\sqrt{-g} \varepsilon u^\mu) + \frac{p}{\sqrt{-g}} \frac{\partial}{\partial x^\mu} (\sqrt{-g} u^\mu) = -u^\mu t_\mu{}^\nu_{;\nu} - (q^\nu_{;\nu} + u^\nu u^\mu q_{\mu;\nu}). \quad (\text{C.15})$$

The internal energy per unit proper volume is expressed as

$$\varepsilon = nmc^2 + \frac{1}{\gamma - 1} p = \rho c^2 + \frac{1}{\gamma - 1} p \quad (\text{C.16})$$

for an ideal gas, where γ is the ratio of the specific heats. From the relation $t_{\mu\nu} u^\mu = 0$, we have $-u^\mu t_\mu{}^\nu_{;\nu} = t_\mu{}^\nu u^\mu_{;\nu}$. Thus, the energy-conservation equation (C.15) becomes

$$\begin{aligned} & \frac{1}{\gamma - 1} \left[u^\mu \frac{\partial p}{\partial x^\mu} + \gamma p \frac{1}{\sqrt{-g}} \frac{\partial}{\partial x^\mu} (\sqrt{-g} u^\mu) \right] \\ &= \frac{1}{\gamma - 1} \left(u^\mu \frac{\partial p}{\partial x^\mu} - \frac{\gamma p}{\rho} u^\mu \frac{\partial \rho}{\partial x^\mu} \right) = t_\mu{}^\nu u^\mu_{;\nu} - (q^\nu_{;\nu} + u^\nu u^\mu q_{\mu;\nu}). \end{aligned} \quad (\text{C.17})$$

References

- Landau L.D., Lifshitz E.M. 1971, *The Classical Theory of Fields* (Pergamon Press, Oxford)
 Misner C.W., Thorne K.S., Wheeler J.A. 1973, *Gravitation* (W.H. Freeman and Co., San Francisco)

APPENDIX D

Radiative Transfer Equations

In highly energetic astronomical systems, such as accretion disks, matter and radiation are often coupled to each other. Matter emits or absorbs radiation, while radiation gives (or removes) energy and momentum to (or from) matter. The behavior of radiation interacting with matter is known as *radiative transfer*. In this appendix we summarize the basic equations of radiative transfer in the Newtonian regime.

D.1 Radiation Fields

In astrophysics the theory of radiative transfer has been developed in the fields involving the stellar atmosphere. In this appendix we only consider a minimum of the concepts of radiative transfer. More general and detailed treatments can be found in many textbooks (e.g., Chandrasekhar 1960; Mihalas 1970; Rybicki and Lightman 1979; Mihalas and Mihalas 1984; Shu 1991; Peraiah 2002; Castor 2004).

(a) Specific intensity and other quantities

The *specific intensity*, $I_\nu(\mathbf{r}, \mathbf{l}, t)$ [$\text{erg s}^{-1} \text{ cm}^{-2} \text{ sr}^{-1} \text{ Hz}^{-1}$], is the radiation energy carried off by the rays per unit time, unit area, unit solid angle, and unit frequency. By integrating the specific intensity over the frequency $d\nu$, we obtain the total intensity $I(\mathbf{r}, \mathbf{l}, t)$ as

$$I = \int_0^\infty I_\nu d\nu. \quad (\text{D.1})$$

Integrating the specific intensity I_ν , multiplied by the direction cosine vector \mathbf{l} , over a solid angle $d\Omega$ (and frequency), we obtain quantities describing the radiation fields and their frequency-integrated forms, as

follows:

$$\begin{aligned} E_\nu &\equiv \frac{1}{c} \int I_\nu d\Omega, & E &\equiv \int E_\nu d\nu, \\ \mathbf{F}_\nu &\equiv \int I_\nu \mathbf{l} d\Omega, & \mathbf{F} &\equiv \int \mathbf{F}_\nu d\nu, \\ P_\nu^{ij} &\equiv \frac{1}{c} \int I_\nu l^i l^j d\Omega, & P^{ij} &\equiv \int P_\nu^{ij} d\nu, \end{aligned} \quad (\text{D.2})$$

where E_ν (E) is the radiation energy density, \mathbf{F}_ν (\mathbf{F}) the radiative flux, and P_ν^{ij} (P^{ij}) the radiation stress.¹

(b) Blackbody radiation

Under thermodynamic equilibrium, the specific intensity becomes a Planck distribution (blackbody):

$$I_\nu(\mathbf{r}, \mathbf{l}, t) = B_\nu(T) = \frac{2h}{c^2} \frac{\nu^3}{\exp(h\nu/k_B T) - 1}, \quad (\text{D.3})$$

where T is the blackbody temperature, c ($= 2.9979 \times 10^{10} \text{ cm s}^{-1}$) the speed of light, h ($= 6.6261 \times 10^{-27} \text{ erg s}$) the Planck constant, and k_B ($= 1.3807 \times 10^{-16} \text{ erg K}^{-1}$) the Boltzmann constant.

In this case, for example, the frequency-integrated intensity I and the radiation energy density E become, respectively,

$$I(\mathbf{r}, \mathbf{l}, t) = B(T) = \frac{1}{\pi} \sigma T^4, \quad (\text{D.4})$$

$$E(\mathbf{r}, t) = \frac{4\pi}{c} B(T) = aT^4, \quad (\text{D.5})$$

where σ ($= 5.6705 \times 10^{-5} \text{ erg s}^{-1} \text{ cm}^{-2} \text{ K}^{-4}$) is the Stefan-Boltzmann constant and a ($= 7.5660 \times 10^{-15} \text{ erg cm}^{-3} \text{ K}^{-4}$) is the radiation constant; $\sigma = ac/4$. Furthermore, at the surface of a blackbody radiator, such as a star or an accretion disk, the outward radiative flux F becomes

$$F(\mathbf{r}, t) = \pi B(T) = \sigma T^4. \quad (\text{D.6})$$

D.2 Equations of Radiative Transfer

We first derive the basic equations describing the behavior of the radiation fields interacting with matter.

¹Often used are the mean intensity J_ν , the Eddington flux H_ν , and the mean pressure stress K_ν . They are related to the one-dimensional components of E_ν , F_ν^i , and P_ν^{ij} by

$$J_\nu = \frac{c}{4\pi} E_\nu, \quad H_\nu = \frac{1}{4\pi} F_\nu, \quad K_\nu = \frac{c}{4\pi} P_\nu.$$

D.2.1 Transfer Equation

A change in the specific intensity is expressed by the *transfer equation*, which is equivalent to the Boltzmann equation for matter.

By means of the mass emissivity (i.e., emissivity per unit mass) j_ν [erg s⁻¹ g⁻¹ sr⁻¹ Hz⁻¹], the mass absorption coefficient (i.e., absorption cross-section per unit mass) κ_ν [cm² g⁻¹] ($= \kappa_\nu^{\text{abs}} + \kappa_\nu^{\text{sca}}$, where κ_ν^{abs} is for the true absorption and κ_ν^{sca} for scattering), the *transfer equation* is expressed as

$$\frac{1}{c} \frac{\partial I_\nu(\mathbf{l})}{\partial t} + (\mathbf{l} \cdot \nabla) I_\nu(\mathbf{l}) = \frac{1}{4\pi} \rho j_\nu - \rho \kappa_\nu^{\text{abs}} I_\nu(\mathbf{l}) - \rho \kappa_\nu^{\text{sca}} \int \phi_\nu(\mathbf{l}, \mathbf{l}') I_\nu(\mathbf{l}') d\Omega' + \rho \kappa_\nu^{\text{sca}} \int \phi_\nu(\mathbf{l}, \mathbf{l}') I_\nu(\mathbf{l}') d\Omega', \quad (\text{D.7})$$

where $\phi_\nu(\mathbf{l}, \mathbf{l}')$ is the scattering probability function ($\int \phi_\nu d\Omega = 1$).

If the scattering is isotropic, $\phi_\nu = 1/4\pi$ and the transfer equation (D.7) becomes

$$\frac{1}{c} \frac{\partial I_\nu}{\partial t} + (\mathbf{l} \cdot \nabla) I_\nu = \frac{1}{4\pi} \rho j_\nu - \rho (\kappa_\nu^{\text{abs}} + \kappa_\nu^{\text{sca}}) I_\nu + \rho \kappa_\nu^{\text{sca}} \frac{c}{4\pi} E_\nu. \quad (\text{D.8})$$

This equation is an integro-differential equation on I_ν , and generally too difficult to obtain precise solutions.

D.2.2 Moment Equations

We often take *moments* of the transfer equation, since it has too much information to directly solve.² Integrating the transfer equation (D.8) over a solid angle, we obtain the zeroth moment. Integrating it over a solid angle, after being multiplied by the direction cosine, we obtain the first moment. The zeroth and first moments of equation (D.8) are, respectively,

$$\frac{\partial E_\nu}{\partial t} + \frac{\partial F_\nu^k}{\partial x^k} = \rho (j_\nu - c \kappa_\nu^{\text{abs}} E_\nu), \quad (\text{D.9})$$

$$\frac{1}{c^2} \frac{\partial F_\nu^i}{\partial t} + \frac{\partial P_\nu^{ik}}{\partial x^k} = - \frac{\rho (\kappa_\nu^{\text{abs}} + \kappa_\nu^{\text{sca}})}{c} F_\nu^i. \quad (\text{D.10})$$

The former corresponds to the energy conservation of radiation with the energy exchange with matter, whereas the latter corresponds to the momentum conservation of radiation with the momentum loss to matter.

²For matter we usually use the hydrodynamical equations instead of the Boltzmann equation.

Moreover, integrating equations (D.8), (D.9), and (D.10) over the frequency, we obtain a frequency-integrated transfer equation and its moment equations:

$$\frac{1}{c} \frac{\partial I}{\partial t} + (\mathbf{l} \cdot \boldsymbol{\nabla}) I = \rho \left(\frac{j}{4\pi} - \bar{\kappa}_I I + \bar{\kappa}_E^{\text{sca}} \frac{c}{4\pi} E \right), \quad (\text{D.11})$$

$$\frac{\partial E}{\partial t} + \frac{\partial F^k}{\partial x^k} = \rho (j - c \bar{\kappa}_E^{\text{abs}} E), \quad (\text{D.12})$$

$$\frac{1}{c^2} \frac{\partial F^i}{\partial t} + \frac{\partial P^{ik}}{\partial x^k} = -\frac{1}{c} \rho \bar{\kappa}_F F^i, \quad (\text{D.13})$$

where

$$j \equiv \int j_\nu d\nu, \quad (\text{D.14})$$

$$\bar{\kappa}_I \equiv \frac{1}{I} \int (\kappa_\nu^{\text{abs}} + \kappa_\nu^{\text{sca}}) I_\nu d\nu, \quad (\text{D.15})$$

$$\bar{\kappa}_E^{\text{abs}} \equiv \frac{1}{E} \int \kappa_\nu^{\text{abs}} E_\nu d\nu, \quad (\text{D.16})$$

$$\kappa_E^{\text{sca}} \equiv \frac{1}{E} \int \kappa_\nu^{\text{sca}} E_\nu d\nu, \quad (\text{D.17})$$

$$\bar{\kappa}_F \equiv \frac{1}{F^i} \int (\kappa_\nu^{\text{abs}} + \kappa_\nu^{\text{sca}}) F_\nu^i d\nu. \quad (\text{D.18})$$

It should be noted that

$$f_{\text{rad}}^i = \frac{\rho}{c} \int (\kappa_\nu^{\text{abs}} + \kappa_\nu^{\text{sca}}) F_\nu^i d\nu = \frac{1}{c} \rho \bar{\kappa}_F F^i \quad (\text{D.19})$$

is the radiative force per unit volume, acting on matter.

D.2.3 Closure Relation (Eddington Approximation)

The zeroth-moment equation (D.9) contains the radiative flux, which is determined by the first-moment equation (D.10). Furthermore, the first-moment equation (D.10) contains the radiation stress, which is determined by the second-moment equation. This means that in order to solve the moment equations we need some relation to close the sequence. As a closure relation, we often adopt the *Eddington approximation*:

$$P_\nu^{ij} = \frac{\delta^{ij}}{3} E_\nu. \quad (\text{D.20})$$

This approximation is valid when the radiation fields are almost *isotropic*.

In the case of a flat-disk configuration, this relation holds with good accuracy in an optically thin regime as well as in an optically thick one.³ In general cases of a two-dimensional configuration, such as geometrically thick disks, however, this relation would not be adequate in an optically thin regime, and alternative closure relation is necessary (see section D.3).

D.2.4 Rosseland Approximation

When the medium is sufficiently *optically thick*, as well as the radiation isotropy, we may use the *diffusion approximation* (Rosseland approximation).

In an optically thick regime local thermodynamic equilibrium (LTE),

$$j_\nu = 4\pi\kappa_\nu^{\text{abs}} B_\nu(T), \quad (\text{D.21})$$

holds, while equation (D.9) can be approximated as $j_\nu = c\kappa_\nu^{\text{abs}} E_\nu$ as long as the radiation intensity is a slowly varying function of space and time. Hence,

$$E_\nu = \frac{4\pi}{c} B_\nu \quad \text{and} \quad P_\nu^{ij} = \frac{\delta^{ij}}{3} \frac{4\pi}{c} B_\nu. \quad (\text{D.22})$$

In the steady state, from equation (D.10), we thus obtain

$$\begin{aligned} F_\nu^i &= -\frac{c}{\rho(\kappa_\nu^{\text{abs}} + \kappa_\nu^{\text{sca}})} \frac{\partial P^{ik}}{\partial x^k} \\ &= -\frac{4\pi}{3\rho(\kappa_\nu^{\text{abs}} + \kappa_\nu^{\text{sca}})} \frac{\partial B_\nu}{\partial T} \frac{\partial T}{\partial x^i}. \end{aligned} \quad (\text{D.23})$$

This means that the radiation energy is transported by an isotropic diffusion of photons.

Integrating equation (D.23) over the frequency, we obtain

$$\mathbf{F} = \int \mathbf{F}_\nu d\nu = -\frac{4\pi}{3\rho} \nabla T \frac{\int \frac{1}{\kappa_\nu^{\text{abs}} + \kappa_\nu^{\text{sca}}} \frac{\partial B_\nu}{\partial T} d\nu}{\int \frac{\partial B_\nu}{\partial T} d\nu} \int \frac{\partial B_\nu}{\partial T} d\nu. \quad (\text{D.24})$$

Since

$$\int \frac{\partial B_\nu}{\partial T} d\nu = \frac{d}{dT} \int B_\nu d\nu = \frac{d}{dT} \left(\frac{1}{\pi} \sigma T^4 \right) = \frac{4}{\pi} \sigma T^3, \quad (\text{D.25})$$

³In the spherical case $P_\nu^{rr} = E_\nu$, while all other components vanish in an optically thin regime.

we finally obtain a frequency-integrated radiative flux,

$$\mathbf{F} = -\frac{4acT^3}{3\bar{\kappa}_R\rho} \nabla T, \quad (\text{D.26})$$

where $\bar{\kappa}_R$ is the Rosseland mean opacity:

$$\frac{1}{\bar{\kappa}_R} = \frac{\int_0^\infty \frac{1}{\kappa_\nu^{\text{abs}} + \kappa_\nu^{\text{sca}}} \frac{\partial B_\nu}{\partial T} d\nu}{\int_0^\infty \frac{\partial B_\nu}{\partial T} d\nu}. \quad (\text{D.27})$$

Equation (D.26) is often called a radiative conduction equation, where the effective ‘conductivity’ is $4acT^3/3\bar{\kappa}_R\rho$, which is inversely proportional to the opacity.

The Rosseland mean opacities for free-free and bound-free absorptions, κ_{ff} and κ_{bf} , are approximately expressed by Kramers’ law:

$$\begin{aligned} \kappa_{\text{ff}} &= 3.68 \times 10^{22} g_{\text{ff}}(X+Y)(1+X)\rho T^{-7/2} \text{ cm}^2 \text{ g}^{-1} \\ &\sim 6.24 \times 10^{22} \rho T^{-7/2} \text{ cm}^2 \text{ g}^{-1}, \end{aligned} \quad (\text{D.28})$$

$$\begin{aligned} \kappa_{\text{bf}} &= 4.34 \times 10^{25} (g_{\text{bf}}/t)Z(1+X)\rho T^{-7/2} \text{ cm}^2 \text{ g}^{-1} \\ &\sim 1.50 \times 10^{24} \rho T^{-7/2} \text{ cm}^2 \text{ g}^{-1}, \end{aligned} \quad (\text{D.29})$$

where g_{ff} and g_{bf} are the mean Gaunt factors, of order unity, for the free-free and bound-free transitions, respectively, t is the guillotine factor of order unity, and X , Y , and Z are the abundances of hydrogen, helium, and metal, respectively (Morse 1940; Schwarzschild 1958). In the low metalicity case the free-free absorption dominates the bound-free one, while the bound-free absorption will dominate the free-free one in the high metalicity case (Schwarzschild 1958).

In addition, the electron scattering opacity is given by

$$\kappa_{\text{es}} = 0.20(1+X) \text{ cm}^2 \text{ g}^{-1} \sim 0.4 \text{ cm}^2 \text{ g}^{-1}. \quad (\text{D.30})$$

D.2.5 Source Function

When the transfer equation (D.8) is expressed as

$$\frac{1}{c} \frac{\partial I_\nu}{\partial t} + (\mathbf{l} \cdot \nabla) I_\nu = \rho (\kappa_\nu^{\text{abs}} + \kappa_\nu^{\text{sca}}) (S_\nu - I_\nu), \quad (\text{D.31})$$

the *source function* S_ν is introduced as

$$S_\nu \equiv \frac{1}{\kappa_\nu^{\text{abs}} + \kappa_\nu^{\text{sca}}} \left(\frac{j_\nu}{4\pi} + \frac{c\kappa_\nu^{\text{sca}}}{4\pi} E_\nu \right). \quad (\text{D.32})$$

In the case of the local thermodynamic equilibrium (LTE), the source function (D.32) becomes

$$\begin{aligned} S_\nu &= \frac{1}{\kappa_\nu^{\text{abs}} + \kappa_\nu^{\text{sca}}} \left(\kappa_\nu^{\text{abs}} B_\nu + \frac{c \kappa_\nu^{\text{sca}}}{4\pi} E_\nu \right) \\ &= (1 - A_\nu) B_\nu + A_\nu \frac{c}{4\pi} E_\nu, \end{aligned} \quad (\text{D.33})$$

where

$$A_\nu = \frac{\kappa_\nu^{\text{sca}}}{\kappa_\nu^{\text{abs}} + \kappa_\nu^{\text{sca}}} \quad (\text{D.34})$$

is the *single scattering albedo*.

In terms of this source function, for example, equation (D.8) and (D.9), and (D.10) with the Eddington approximation (D.20) are, respectively, reexpressed as

$$\frac{1}{c} \frac{\partial I_\nu}{\partial t} + (\mathbf{l} \cdot \nabla) I_\nu = \rho (\kappa_\nu^{\text{abs}} + \kappa_\nu^{\text{sca}}) (S_\nu - I_\nu), \quad (\text{D.35})$$

$$\frac{\partial E_\nu}{\partial t} + \frac{\partial F_\nu^k}{\partial x^k} = \rho (\kappa_\nu^{\text{abs}} + \kappa_\nu^{\text{sca}}) (4\pi S_\nu - c E_\nu), \quad (\text{D.36})$$

$$\frac{1}{c^2} \frac{\partial F_\nu^i}{\partial t} + \frac{1}{3} \frac{\partial E_\nu}{\partial x^i} = -\frac{\rho (\kappa_\nu^{\text{abs}} + \kappa_\nu^{\text{sca}})}{c} F_\nu^i. \quad (\text{D.37})$$

D.3 Optically Thick to Thin Regimes

The Eddington approximation (D.20) as a closure relation holds when the radiation field is *nearly isotropic*.⁴ In the optically thin regime, or in the case where the anisotropy of radiation becomes important, we should carefully treat the Eddington approximation.⁵ Indeed, in the particular configuration of plane-parallel flat disks, the Eddington approximation (D.20) holds, but it would be violated in general configurations. In this part, we briefly show the treatment in such general cases.

D.3.1 Variable Eddington Factor

Generalization of the Eddington approximation (D.20) is useful in semi-analytical cases,

$$P^{ij} = f^{ij} E, \quad (\text{D.38})$$

⁴The Rosseland approximation holds when the medium is sufficiently optically thick and the photon mean-free path is sufficiently smaller than the typical scale, and when the velocity gradient is sufficiently small and the local diffusion is isotropic.

⁵In the relativistic regime, where the flow speed is on the order of the speed of light, we also carefully treat the closure relation. See appendix E.

where f^{ij} is the Eddington tensor, and is generally a function of the optical depth τ . This relation (D.38) is reduced to equation (D.20), if we assume the radiation field is isotropic: $f^{ij} = \delta^{ij}/3$.

Suitable forms of the Eddington tensor are adopted in each problem and configuration. For example, in the spherically symmetric case, the diagonal part of the Eddington tensor is often set as

$$\left(f(\tau), \frac{1}{2} - \frac{1}{2}f(\tau), \frac{1}{2} - \frac{1}{2}f(\tau) \right), \quad (\text{D.39})$$

where

$$f(\tau) = \frac{1 + \tau}{1 + 3\tau} \quad (\text{D.40})$$

is a *variable Eddington factor* (Tamazawa et al. 1975; see figure D.1). In the plane-parallel case, on the other hand, we can use $f = 1/3$, even in the optically thin regime for a static atmosphere.

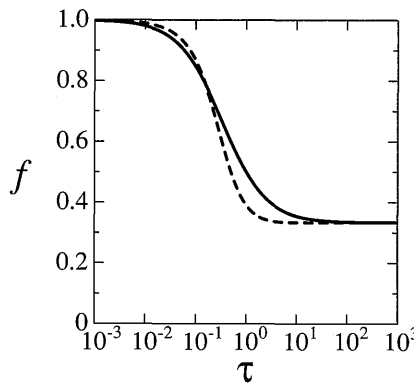


Figure D.1

Variable Eddington factors as a function of the optical depth τ . A thick solid curve denotes a variable Eddington factor (D.40), while a thick dashed one means a variable Eddington factor (D.46), where R_ν is read as τ^{-1} .

D.3.2 Flux-Limited Diffusion

The diffusion (Rosseland) approximation implies that in a steady state the radiation energy is transported by an isotropic diffusion of photons:

$$\mathbf{F} = -\frac{c}{3\bar{\kappa}_R\rho} \nabla E \quad (\text{D.41})$$

[see equation (D.26)]. This gives the correct flux in an optically thick regime, where the photon mean-free path of $\sim 1/(\bar{\kappa}_R \rho)$ is sufficiently smaller than the typical scale for the change of E . In an optically thin regime, where the mean-free path diverges, on the other hand, this flux tends to infinity. Such a situation, however, is unphysical, since the rate at which radiation transports energy is finite, even in an optically thin regime. That is, the magnitude of the flux can be no greater than the radiation energy density times the maximum transport speed.⁶ Namely, the radiative flux \mathbf{F} should be *limited* in the optically thin regime in some way, which is the *flux-limited diffusion theory* (Levermore and Pomraning 1981; Pomraning 1983 for a relativistic correction; Melia and Zylstra 1991 for a scattering medium; Anile and Romano 1992 for a covariant form; Turner and Stone 2001 for a numerical calculation).

(a) General forms

In the flux-limited diffusion (FLD) theory, we also assume Fick's law of diffusion for radiation:

$$\mathbf{F}_\nu = -\frac{c\lambda_\nu}{\kappa_\nu\rho} \nabla E_\nu, \quad (\text{D.42})$$

where $\kappa_\nu = \kappa_\nu^{\text{abs}} + \kappa_\nu^{\text{sca}}$. Here, we introduce the *flux limiter* $\lambda_\nu(E_\nu)$, which is restricted in the range of 0 (thin) $\leq \lambda_\nu \leq 1/3$ (thick). The appropriate form of this flux limiter is given later.

Using the flux limiter λ_ν , we obtain (Levermore and Pomraning 1981)

$$P_\nu^{ij} = f_\nu^{ij} E_\nu, \quad (\text{D.43})$$

where the Eddington tensor f_ν^{ij} is expressed as

$$f_\nu^{ij} = \frac{1}{2} (1 - f_\nu) \delta^{ij} + \frac{1}{2} (3f_\nu - 1) n^i n^j. \quad (\text{D.44})$$

In this equation (D.44),

$$n^i \equiv \frac{\nabla E_\nu}{|\nabla E_\nu|} \quad (\text{D.45})$$

is the unit vector in the direction of the radiation energy density gradient, i.e., the radiative flux, which is determined by the local radiation field. Furthermore, the Eddington factor $f_\nu(E_\nu)$ is expressed as

$$f_\nu = \lambda_\nu + \lambda_\nu^2 R_\nu^2, \quad (\text{D.46})$$

⁶In a spherical case the flux is limited as $|\mathbf{F}| \leq cE$, while it is limited as $|\mathbf{F}| \leq cE/2$ in a plane-parallel case.

where

$$R_\nu \equiv \frac{|\nabla E_\nu|}{\kappa_\nu \rho E_\nu} \quad (\text{D.47})$$

is the optical depth parameter, since $R_\nu \sim 1/\tau$, and is also determined by the local quantities.

Thus, if we give some appropriate form of λ_ν , all relations are fixed by the local quantities. As a choice of λ_ν , Levermore and Pomraning (1981) proposed a relation,

$$\lambda_\nu = \frac{2 + R_\nu}{6 + 3R_\nu + R_\nu^2}, \quad (\text{D.48})$$

although many other choices are possible, which preserve causality and are consistent with the assumption of smoothness in the radiation field.⁷

In the optically thick limit ($R_\nu \rightarrow 0$), we find $\lambda_\nu \rightarrow 1/3$ and $f_\nu \rightarrow 1/3$. In the optically thin limit ($R_\nu \rightarrow \infty$), on the other hand, we have $\lambda_\nu \rightarrow 1/R_\nu$ and $f_\nu \rightarrow 1 - 1/R_\nu$.

(b) Vertical case

For the problem of an accretion disk concentrating to the vertical direction, the flux-limited diffusion approximation is expressed as

$$F_\nu^z = -\frac{c\lambda_\nu}{\kappa_\nu \rho} \frac{\partial E_\nu}{\partial z}, \quad (\text{D.49})$$

$$P_\nu^{rr} = P_\nu^{\varphi\varphi} = \frac{1}{2}(1 - f_\nu)E_\nu \quad \text{and} \quad P_\nu^{zz} = f_\nu E_\nu. \quad (\text{D.50})$$

In the optically thick diffusion limit we have $F_\nu^z = -(c/3\kappa_\nu\rho)\partial E_\nu/\partial z$ and $P_\nu^{rr} = P_\nu^{\varphi\varphi} = P_\nu^{zz} = E_\nu/3$, while in the optically thin streaming limit we have $|F_\nu^z| = cE_\nu$, $P_\nu^{rr} = P_\nu^{\varphi\varphi} = 0$, and $P_\nu^{zz} = E_\nu$. These give correct relations in the optically thick and thin limits, respectively.

D.4 Matter Coupling

The radiative force exerting on matter per unit mass is, from equation (D.13),

$$-\frac{1}{\rho} \left(\frac{1}{c^2} \frac{\partial F^i}{\partial t} + \frac{\partial P^{ik}}{\partial x^k} \right) = \frac{\bar{\kappa}_F}{c} F^i, \quad (\text{D.51})$$

⁷For example, we quote two of them (Castor 2004):

$$\lambda_\nu = \frac{3}{3 + R_\nu}, \quad \lambda_\nu = \frac{1}{R_\nu} \left(\coth R_\nu - \frac{1}{R_\nu} \right).$$

while the net energy transfer rate to matter per unit mass is, from equation (D.12),

$$-\frac{1}{\rho} \left(\frac{\partial E}{\partial t} + \frac{\partial F^k}{\partial x^k} \right) = -j + c\bar{\kappa}_E^{\text{abs}} E. \quad (\text{D.52})$$

Thus, under the present approximation, the equation of motion and the energy equation for matter are written as, respectively,

$$\frac{\partial \mathbf{v}}{\partial t} + (\mathbf{v} \cdot \nabla) \mathbf{v} = -\nabla \psi - \frac{1}{\rho} \nabla p + \frac{\bar{\kappa}_F}{c} \mathbf{F}, \quad (\text{D.53})$$

$$\left(\frac{\partial}{\partial t} + \mathbf{v} \cdot \nabla \right) e + \frac{p}{\rho} \nabla \cdot \mathbf{v} = \frac{1}{\rho} q^+ - j + c\bar{\kappa}_E^{\text{abs}} E, \quad (\text{D.54})$$

where \mathbf{v} is the velocity, ψ the gravitational potential, p the pressure, e the internal energy per unit mass, and q^+ the (viscous) heating rate per unit volume. For an ideal gas, the internal energy is expressed as $e = [1/(\gamma - 1)](p/\rho)$, and the energy equation (D.54) is rewritten as

$$\frac{1}{\gamma - 1} \left(\frac{dp}{dt} - \gamma \frac{p}{\rho} \frac{d\rho}{dt} \right) = q^+ - \rho(j - c\bar{\kappa}_E^{\text{abs}} E). \quad (\text{D.55})$$

D.5 Plane-Parallel Expression

For a static atmosphere in the plane-parallel geometry (z), the hydrodynamic equations and transfer equations become as follows.

For matter, the vertical momentum balance and energy equation are, respectively,

$$0 = -\rho \frac{d\psi}{dz} - \frac{dp}{dz} + \frac{\bar{\kappa}_F}{c} \rho F, \quad (\text{D.56})$$

$$0 = q_{\text{vis}}^+ - \rho(j - c\bar{\kappa}_E^{\text{abs}} E), \quad (\text{D.57})$$

where ψ is the gravitational potential, p the gas pressure, and q_{vis}^+ the viscous-heating rate per unit volume. The opacities are assumed to be independent of the frequency (gray approximation). Under the α prescription, the viscous-heating rate is proportional to the pressure, and therefore may depend on z .

For radiation, the frequency-integrated transfer equation (D.11), the zeroth moment equation (D.9), and the first moment equation (D.10)

become, respectively,

$$\cos \theta \frac{dI}{dz} = \rho \left(\frac{j}{4\pi} - \bar{\kappa}_I I + \bar{\kappa}_E^{\text{sca}} \frac{c}{4\pi} E \right), \quad (\text{D.58})$$

$$\frac{dF}{dz} = \rho (j - c \bar{\kappa}_E^{\text{abs}} E), \quad (\text{D.59})$$

$$\frac{dP}{dz} = -\frac{1}{c} \rho \bar{\kappa}_F, \quad (\text{D.60})$$

where I is the frequency-integrated specific intensity, E the radiation energy density, F the vertical component of the radiative flux, P the zz -component of the radiation stress tensor, and θ the polar angle. The mass emissivity j and opacities are assumed to be independent of the frequency (gray approximation).

Application to standard disks are discussed in subsection 3.2.9.

References

- Anile A.M., Romano V. 1992, ApJ 386, 325
 Castor J.I. 2004, *Radiation Hydrodynamics* (Cambridge University Press, Cambridge)
 Chandrasekhar S. 1960, *Radiative Transfer* (Dover Publishing, Inc., New York)
 Levermore C.D., Pomraning G.C. 1981, ApJ 248, 321
 Melia F., Zylstra G.J. 1991, ApJ 374, 731
 Mihalas D. 1970, *Stellar Atmospheres* (W.H. Freeman and Co., San Francisco)
 Mihalas D., Mihalas B.W. 1984, *Foundations of Radiation Hydrodynamics* (Oxford University Press, Oxford)
 Morse P.M. 1940, ApJ 92, 27
 Peraiah A. 2002, *An Introduction to Radiative Transfer: Methods and applications in astrophysics* (Cambridge University Press, Cambridge)
 Pomraning G.C. 1983, ApJ 266, 841
 Rybicki G.B., Lightman A.P. 1979, *Radiative Processes in Astrophysics* (John Wiley & Sons, New York)
 Schwarzschild M. 1958, *Structure and Evolution of the Stars* (Dover Publications, Inc., New York)
 Shu F.H. 1991, *The Physics of Astrophysics Vol.1: Radiation* (University Science Books, California)
 Tamazawa S., Toyama K., Kaneko N., Ôno Y. 1975, ApSpSci 32, 403
 Turner N.J., Stone J.M. 2001, ApJS 135, 95

APPENDIX E

Equations for Relativistic Radiation Hydrodynamics

In this appendix we derive the basic equations for radiation hydrodynamics (photohydrodynamics) within the framework of special relativity. We first give the metric and quantities of the radiation fields, and then show the basic equations, including matter coupling.

E.1 Metric and Energy-Momentum Tensor

The full set of basic equations for photohydrodynamics can be found in several literature (e.g., Lindquist 1966; Anderson and Spiegel 1972; Hsieh and Spiegel 1976; Thorne 1981; Fukue et al. 1985; Park 2006; Takahashi 2007). It is usually expressed in a general form. In this appendix we derive and write explicitly the basic equations for relativistic radiation hydrodynamics, which are correct within the framework of special relativity. The derivation is based on Hsieh and Spiegel (1976), while correcting minor errors in their paper. In this book the $(+, -, -, -)$ signature is adopted, and the Greek suffixes $\alpha, \beta, \gamma, \dots$ take values of 0, 1, 2, and 3, while the Latin suffixes i, j, k, \dots take values of 1, 2, and 3. The semicolon denotes not covariant differentiation but partial differentiation, since we do not consider the space-time curvature here.

(a) Metric

The square of the invariant line element, ds^2 , is written as

$$ds^2 = c^2 d\tau^2 = g_{\mu\nu} dx^\mu dx^\nu, \quad (\text{E.1})$$

where c is the speed of light, τ the proper time, x^μ the space-time coordinates ($x^0 = ct$ in this appendix), and $g_{\mu\nu}$ the space-time metric. The three-dimensional part of the metric, γ_{ij} , is defined by $\gamma_{ij} = -g_{ij}$.

In the case of cylindrical coordinates (r, φ, z) , the line element (E.1) becomes, in a flat space-time,

$$ds^2 = c^2 dt^2 - dr^2 - r^2 d\varphi^2 - dz^2. \quad (\text{E.2})$$

(b) Four-velocity of matter

The four-velocity u^μ of matter is defined by

$$u^\mu \equiv \frac{dx^\mu}{ds} = \left(\gamma, \gamma \frac{v^i}{c} \right) = \gamma \left(1, \frac{\mathbf{v}}{c} \right), \quad (\text{E.3})$$

where

$$\gamma = \left(1 - \frac{v^2}{c^2} \right)^{-1/2}, \quad (\text{E.4})$$

$$v^2 = v_i v^i = \gamma_{ik} v^i v^k = -g_{ik} v^i v^k. \quad (\text{E.5})$$

The covariant components become

$$u_\mu = g_{\mu\nu} u^\nu = \left(\gamma, -\gamma \frac{v_i}{c} \right). \quad (\text{E.6})$$

It should be noted that $u_\mu u^\mu = g_{\mu\nu} u^\mu u^\nu = 1$.

(c) Four-momentum of photon

The four-momentum k^μ of a photon is defined by

$$k^\mu = (\nu, \nu l^k) = \nu (1, \mathbf{l}), \quad (\text{E.7})$$

where ν is the photon frequency and \mathbf{l} is the direction cosine vector of a photon. The covariant components become

$$k_\mu = \nu (1, -\mathbf{l}). \quad (\text{E.8})$$

Since $\mathbf{l}^2 = 1$, the contraction of the four-momentum is null:

$$k_\mu k^\mu = \nu^2 (1 - \mathbf{l}^2) = 0. \quad (\text{E.9})$$

(d) Doppler and aberration effects

The four-velocity u_μ and the four-momentum k^μ expressed in comoving frames are, respectively,

$$u_\mu = (1, 0), \quad (\text{E.10})$$

$$k^\mu = \nu_0 (1, \mathbf{l}_0), \quad (\text{E.11})$$

where the subscript 0 means the values measured in the comoving (fluid) frame. Using equations (E.6) and (E.7), we have

$$u_\mu k^\mu = \gamma\nu - \gamma\nu \frac{\mathbf{v} \cdot \mathbf{l}}{c} = \nu_0. \quad (\text{E.12})$$

Thus, the transformation of the photon frequency between the inertial and comoving frames (relativistic Doppler effect) becomes

$$\nu_0 = \nu\gamma \left(1 - \frac{\mathbf{v} \cdot \mathbf{l}}{c}\right), \quad (\text{E.13})$$

$$\nu = \nu_0\gamma \left(1 + \frac{\mathbf{v} \cdot \mathbf{l}_0}{c}\right). \quad (\text{E.14})$$

Similarly, the transformation of the direction cosine (relativistic aberration effect) becomes

$$\mathbf{l}_0 = \frac{\nu}{\nu_0} \left[\mathbf{l} + \left(\frac{\gamma - 1}{v^2/c^2} \frac{\mathbf{v} \cdot \mathbf{l}}{c} - \gamma \right) \frac{\mathbf{v}}{c} \right], \quad (\text{E.15})$$

$$\mathbf{l} = \frac{\nu_0}{\nu} \left[\mathbf{l}_0 + \left(\frac{\gamma - 1}{v^2/c^2} \frac{\mathbf{v} \cdot \mathbf{l}_0}{c} + \gamma \right) \frac{\mathbf{v}}{c} \right]. \quad (\text{E.16})$$

The transformation of the solid angle is

$$d\Omega_0 = \frac{\nu}{\nu_0} \frac{d\nu}{d\nu_0} d\Omega = \left[\gamma \left(1 - \frac{\mathbf{v} \cdot \mathbf{l}}{c}\right) \right]^{-2} d\Omega, \quad (\text{E.17})$$

$$d\Omega = \left[\gamma \left(1 + \frac{\mathbf{v} \cdot \mathbf{l}_0}{c}\right) \right]^{-2} d\Omega_0. \quad (\text{E.18})$$

(e) Quantities of radiation fields

The specific intensity I_ν is related to the photon occupation number n_ν by $I_\nu = (2h\nu^3/c^2)n_\nu$. The relativistic invariant is not I_ν , but I_ν/ν^3 :

$$\frac{I_\nu}{\nu^3} = \frac{I_{\nu 0}}{\nu_0^3} \equiv f. \quad (\text{E.19})$$

Using these quantities, the energy-momentum tensor of the radiation field is defined as

$$R^{\mu\nu} \equiv \frac{2h}{c^3} \int n_\nu l^\mu l^\nu \nu^3 d\nu d\Omega = \frac{1}{c} \int I_\nu l^\mu l^\nu d\nu d\Omega, \quad (\text{E.20})$$

where $l^\mu = (1, l^k)$. Hence, the components of $R^{\mu\nu}$ become

$$R^{00} = \frac{1}{c} \int I_\nu d\nu d\Omega \equiv E, \quad (\text{E.21})$$

$$R^{0i} = \frac{1}{c} \int I_\nu l^i d\nu d\Omega \equiv \frac{1}{c} F^i, \quad (\text{E.22})$$

$$R^{ij} = \frac{1}{c} \int I_\nu l^i l^j d\nu d\Omega \equiv P^{ij}, \quad (\text{E.23})$$

where E is the radiation energy density, F^i the radiative flux, and P^{ij} the radiation stress tensor.

Integrating over the frequency, we obtain the following frequency-integrated quantities:

$$I \equiv \int I_\nu d\nu, \quad E \equiv \int E_\nu d\nu, \quad F^i \equiv \int F_\nu^i d\nu, \quad P^{ij} \equiv \int P_\nu^{ij} d\nu. \quad (\text{E.24})$$

(f) Transformation rules

The transformation of the frequency-integrated intensity I between the inertial and comoving frames is

$$I_0 = \left(\frac{\nu_0}{\nu} \right)^4 I = \left[\gamma \left(1 - \frac{\mathbf{v} \cdot \mathbf{l}}{c} \right) \right]^4 I. \quad (\text{E.25})$$

Integrating equation (E.25) over a solid angle, we obtain the transformation rule of E :

$$E_0 = \gamma^2 \left(E - 2 \frac{\mathbf{v} \cdot \mathbf{F}}{c^2} + \frac{v_i v_k}{c^2} P^{ik} \right). \quad (\text{E.26})$$

Multiplying equation (E.25) by l_0^i and integrating the resultant equation over a solid angle, we have the transformation rule of F^i :

$$F_0^i = \gamma \left\{ F^i + \left[\left(\gamma + \frac{\gamma - 1}{v^2/c^2} \right) \frac{\mathbf{v} \cdot \mathbf{F}}{c^2} - \gamma E - \frac{\gamma - 1}{v^2/c^2} \frac{v_j v_k}{c^2} P^{jk} \right] v^i - v_k P^{ik} \right\}. \quad (\text{E.27})$$

Multiplying equation (E.25) by $l_0^i l_0^j$ and integrating the resultant equation over a solid angle, we have the transformation rule of P^{ij} :

$$\begin{aligned} P_0^{ij} &= P^{ij} + \frac{\gamma - 1}{v^2/c^2} \left(\frac{v^i v_k}{c^2} P^{jk} + \frac{v^j v_k}{c^2} P^{ik} \right) \\ &\quad + \left(\frac{\gamma - 1}{v^2/c^2} \right)^2 \frac{v^i v^j}{c^2} \frac{v_k v_m P^{km}}{c^2} + \gamma^2 \frac{v^i v^j}{c^2} E \\ &\quad - \gamma \left(\frac{v^i F^j}{c^2} + \frac{v^j F^i}{c^2} \right) - 2\gamma \frac{\gamma - 1}{v^2/c^2} \frac{v^i v^j}{c^2} \frac{\mathbf{v} \cdot \mathbf{F}}{c^2}. \end{aligned} \quad (\text{E.28})$$

(g) **Energy-momentum tensor**

The energy-momentum tensor for an ideal gas, $T^{\mu\nu}$, is

$$T^{\mu\nu} = (\varepsilon + p) u^\mu u^\nu - p g^{\mu\nu}, \quad (\text{E.29})$$

where ε is the internal energy per unit proper volume and p is the pressure measured in the comoving frame ($\varepsilon + p$ is the enthalpy per unit proper volume).

The energy-momentum tensor for radiation, $R^{\mu\nu}$, is

$$R^{\mu\nu} = \begin{pmatrix} E & \frac{1}{c} F^i \\ \frac{1}{c} F^i & P^{ij} \end{pmatrix}, \quad (\text{E.30})$$

where E is the radiation energy density, F^i the radiative flux, and P^{ij} the radiation stress tensor.

The momentum and energy conservations are expressed, respectively, as

$$(T_\mu^\nu + R_\mu^\nu)_{;\nu} = 0, \quad (\text{E.31})$$

$$u^\mu (T_\mu^\nu + R_\mu^\nu)_{;\nu} = 0, \quad (\text{E.32})$$

where the semicolon means the partial differentiation in the present case.

E.2 Equations of Radiative Transfer

We first derive the basic equations describing the behavior of radiation interacting with matter within the framework of special relativity.

E.2.1 Transfer Equation

As in the case of a non-relativistic regime (appendix D), a change in the specific intensity is expressed by the *transfer equation*, although it should be written down in a Lorentz-invariant form.

By means of the Lorentz invariant f ($= I_\nu/\nu^3 = I_{\nu 0}/\nu_0^3$), we can write the transfer equation of the form (Hsieh and Spiegel 1976):

$$\begin{aligned} k^\mu \frac{\partial f}{\partial x^\mu} &= \rho(\alpha - \beta f) - \rho \kappa_{\nu 0}^{\text{sca}} \int \phi_\nu(\mathbf{l}', \mathbf{l}) f(\mathbf{l}) \nu' d\nu' d\Omega' \\ &\quad + \rho \kappa_{\nu 0}^{\text{sca}} \int \phi_\nu(\mathbf{l}, \mathbf{l}') f(\mathbf{l}') \nu' d\nu' d\Omega', \end{aligned} \quad (\text{E.33})$$

where ρ is the proper mass density, α the invariant form of the emission coefficient, β the invariant form of the absorption coefficient, $\kappa_{\nu 0}^{\text{sca}}$ the

scattering opacity in the comoving frame, and ϕ_ν the scattering redistribution function. It is noted that $\nu d\nu d\Omega (= \nu' d\nu' d\Omega')$ is also a relativistic invariant.

Of these, α and β are related, respectively, to the mass emissivity $j_{\nu 0}$ and the mass absorption coefficient $\kappa_{\nu 0}^{\text{abs}}$ in the comoving frame by

$$j_{\nu 0} = 4\pi\nu_0^2\alpha \quad \text{and} \quad \kappa_{\nu 0}^{\text{abs}} = \frac{\beta}{\nu_0}. \quad (\text{E.34})$$

For Thomson scattering, the scattering redistribution function in the comoving frame is

$$\phi_\nu = \frac{3}{4} \left[1 + (\mathbf{l}_0 \cdot \mathbf{l}'_0)^2 \right] \delta(\nu_0 - \nu'_0) \frac{1}{4\pi}. \quad (\text{E.35})$$

It should be noted that $\int \phi_\nu \nu_0 d\nu_0 d\Omega_0 = \nu'_0$ and $\int \phi_\nu \nu'_0 d\nu'_0 d\Omega'_0 = \nu_0$.

Substituting these quantities into equation (E.33), the transfer equation is rewritten as

$$\begin{aligned} \nu \left[\frac{\partial f}{c\partial t} + (\mathbf{l} \cdot \boldsymbol{\nabla}) f \right] &= \rho \frac{j_{\nu 0}}{4\pi\nu_0^2} - \rho\nu_0\kappa_{\nu 0}^{\text{abs}} f - \rho\nu_0\kappa_{\nu 0}^{\text{sca}} f \\ &\quad + \frac{3}{4}\rho\kappa_{\nu 0}^{\text{sca}}\nu_0 \int \left[1 + (\mathbf{l}_0 \cdot \mathbf{l}'_0)^2 \right] f(\mathbf{l}') \frac{d\Omega'_0}{4\pi}. \end{aligned} \quad (\text{E.36})$$

Furthermore, replacing f by I_ν (or $I_{\nu 0}$), we finally obtain the (angle-dependent) *radiative transfer equation* in the mixed frame:

$$\begin{aligned} \frac{1}{c} \frac{\partial I_\nu}{\partial t} + (\mathbf{l} \cdot \boldsymbol{\nabla}) I_\nu &= \left(\frac{\nu}{\nu_0} \right)^2 \rho \\ &\times \left[\frac{j_{\nu 0}}{4\pi} - (\kappa_{\nu 0}^{\text{abs}} + \kappa_{\nu 0}^{\text{sca}}) I_{\nu 0} + \frac{3}{4}\kappa_{\nu 0}^{\text{sca}} \frac{c}{4\pi} (E_{\nu 0} + l_{0i}l_{0j}P_{\nu 0}^{ij}) \right], \end{aligned} \quad (\text{E.37})$$

where we use the definitions of E and P^{ij} . This transfer equation (E.37) seems to be similar to the non-relativistic one (D.7), except for the ν/ν_0 -term. It should be noted, however, that the left-hand side is written by the quantities evaluated in the inertial (fixed) frame, while the right-hand side by the quantities in the comoving (fluid) frame.

E.2.2 Moment Equations

Next, we derive the (frequency-integrated) moment equations. After a long time since Eddington, who first introduced a moment expansion to radiation transfer in the early 20th century, moment equations for relativistic radiation transfer have been derived by several studies for

a special relativistic case (Thomas 1930; Hazlehurst and Sargent 1959; Castor 1972; Mihalas and Mihalas 1984) and in a curved space-time (Lindquist 1966; Anderson and Spiegel 1972; Thorne 1981; Udey and Israel 1982; Nobili et al. 1993; Park 2003, 2006; Takahashi 2007). A complete set of moment equations for a relativistic flow is given by the projected symmetric trace-free (PSTF) formalism (Thorne 1981).

Integrating the transfer equation (E.37) over the frequency, with the help of the Lorentz transformation (E.14) [$d\nu = (d\nu/d\nu_0)d\nu_0 = \gamma(1 + \mathbf{v} \cdot \mathbf{l}_0/c)d\nu_0$], we obtain a frequency-integrated angle-dependent transfer equation:

$$\frac{1}{c} \frac{\partial I}{\partial t} + (\mathbf{l} \cdot \nabla) I = \rho\gamma^3 \left(1 + \frac{\mathbf{v} \cdot \mathbf{l}_0}{c} \right)^3 \times \left[\frac{j_0}{4\pi} - (\kappa_0^{\text{abs}} + \kappa_0^{\text{sca}}) I_0 + \frac{3}{4}\kappa_0^{\text{sca}} \frac{c}{4\pi} (E_0 + l_{0i}l_{0j}P_0^{ij}) \right], \quad (\text{E.38})$$

where

$$I \equiv \int I_\nu d\nu, \quad I_0 \equiv \int I_{\nu 0} d\nu_0, \quad (\text{E.39})$$

$$E_0 \equiv \int E_{\nu 0} d\nu_0, \quad P_0^{ij} \equiv \int P_{\nu 0}^{ij} d\nu_0, \quad (\text{E.40})$$

$$j_0 \equiv \int j_{\nu 0} d\nu_0, \quad \kappa_0^{\text{abs}} + \kappa_0^{\text{sca}} \equiv \frac{1}{I_0} \int (\kappa_{\nu 0}^{\text{abs}} + \kappa_{\nu 0}^{\text{sca}}) I_{\nu 0} d\nu_0. \quad (\text{E.41})$$

Integrating the transfer equation (E.38) over a solid angle, with the help of a transformation of the solid angle (E.18), we obtain the zeroth-moment of equation (E.38):

$$\frac{\partial E}{\partial t} + \frac{\partial F^k}{\partial x^k} = \rho\gamma (j_0 - c\kappa_0^{\text{abs}} E_0) - \rho\gamma (\kappa_0^{\text{abs}} + \kappa_0^{\text{sca}}) \frac{\mathbf{v} \cdot \mathbf{F}_0}{c}. \quad (\text{E.42})$$

Integrating the transfer equation (E.38) over a solid angle, after being multiplied by the direction cosine, with the help of transformations (E.18) and (E.16), we obtain the first-moment of equation (E.38):

$$\begin{aligned} \frac{1}{c^2} \frac{\partial F^i}{\partial t} + \frac{\partial P^{ik}}{\partial x^k} &= \rho\gamma \frac{v^i}{c^2} (j_0 - c\kappa_0^{\text{abs}} E_0) \\ &\quad - \rho (\kappa_0^{\text{abs}} + \kappa_0^{\text{sca}}) \frac{\gamma - 1}{v^2} \frac{v^i}{c} (\mathbf{v} \cdot \mathbf{F}_0) \\ &\quad - \frac{1}{c} \rho (\kappa_0^{\text{abs}} + \kappa_0^{\text{sca}}) F_0^i. \end{aligned} \quad (\text{E.43})$$

In general, such a moment expansion gives an infinite set of equations. In order to make the transfer problem tractable, one must truncate the

expansion at the finite order by adopting a suitable closure assumption. For example, we here truncate the equations at the second order, and we introduce some additional closure relation among E , F^i , and P^{ik} , as given in the next subsection.

As already noted, the left-hand sides of these moment equations (E.42) and (E.43) are described by the quantities in the inertial (fixed) frame, while the right-hand sides by those in the comoving (fluid) frame. Thus, using the transformation rules (E.26)–(E.28), let us rewrite the right-hands side of these moment equations. After several manipulations, we finally obtain the moment equations expressed by the quantities in the inertial (fixed) frame:

$$\begin{aligned} \frac{1}{c} \frac{\partial I}{\partial t} + (\mathbf{l} \cdot \nabla) I &= \rho \gamma^{-3} \left(1 - \frac{\mathbf{v} \cdot \mathbf{l}}{c}\right)^{-3} \\ &\times \left[\frac{j_0}{4\pi} - (\kappa_0^{\text{abs}} + \kappa_0^{\text{sca}}) \gamma^4 \left(1 - \frac{\mathbf{v} \cdot \mathbf{l}}{c}\right)^4 I + \frac{\kappa_0^{\text{sca}}}{4\pi} \frac{3}{4} \gamma^{-2} \left(1 - \frac{\mathbf{v} \cdot \mathbf{l}}{c}\right)^{-2} \right. \\ &\times \left\{ \gamma^4 \left[\left(1 - \frac{\mathbf{v} \cdot \mathbf{l}}{c}\right)^2 + \left(\frac{v^2}{c^2} - \frac{\mathbf{v} \cdot \mathbf{l}}{c}\right)^2 \right] cE + 2\gamma^2 \left(\frac{v^2}{c^2} - \frac{\mathbf{v} \cdot \mathbf{l}}{c}\right) \mathbf{F} \cdot \mathbf{l} \right. \\ &- 2\gamma^4 \left[\left(1 - \frac{\mathbf{v} \cdot \mathbf{l}}{c}\right)^2 + \left(1 - \frac{\mathbf{v} \cdot \mathbf{l}}{c}\right) \left(\frac{v^2}{c^2} - \frac{\mathbf{v} \cdot \mathbf{l}}{c}\right) \right] \frac{\mathbf{v} \cdot \mathbf{F}}{c} \\ &\left. + l_i l_j c P^{ij} - 2\gamma^2 \left(1 - \frac{\mathbf{v} \cdot \mathbf{l}}{c}\right) v_i l_j P^{ij} + 2\gamma^4 \left(1 - \frac{\mathbf{v} \cdot \mathbf{l}}{c}\right)^2 \frac{v_i v_j P^{ij}}{c} \right\}, \end{aligned} \quad (\text{E.44})$$

$$\begin{aligned} \frac{\partial E}{\partial t} + \frac{\partial F^k}{\partial x^k} &= \rho \gamma \left(j_0 - c \kappa_0^{\text{abs}} E + \kappa_0^{\text{abs}} \frac{\mathbf{v} \cdot \mathbf{F}}{c} \right) \\ &+ \rho \gamma^3 \kappa_0^{\text{sca}} \left[\frac{v^2}{c} E + \frac{v_i v_j}{c} P^{ij} - \left(1 + \frac{v^2}{c^2}\right) \frac{\mathbf{v} \cdot \mathbf{F}}{c} \right], \end{aligned} \quad (\text{E.45})$$

$$\begin{aligned} \frac{1}{c^2} \frac{\partial F^i}{\partial t} + \frac{\partial P^{ik}}{\partial x^k} &= \frac{\rho \gamma}{c} \left(\frac{v^i}{c} j_0 - \kappa_0^{\text{abs}} F^i + \kappa_0^{\text{abs}} v_k P^{ik} \right) \\ &- \frac{\rho \gamma}{c} \kappa_0^{\text{sca}} \left[F^i - \gamma^2 E v^i - v_k P^{ik} + \gamma^2 v^i \left(\frac{2\mathbf{v} \cdot \mathbf{F}}{c^2} - \frac{v_j v_k}{c^2} P^{jk} \right) \right]. \end{aligned} \quad (\text{E.46})$$

E.2.3 Closure Relation

As a closure relation, we usually adopt the Eddington approximation *in the comoving frame*:

$$P_0^{ij} = \frac{\delta^{ij}}{3} E_0. \quad (\text{E.47})$$

It should be noted that we here do not consider the radiative viscosity. In a relativistic regime, this closure relation should be modified, as discussed in the next subsection.

Substituting the transformation rules (E.26)–(E.28) into this relation (E.47), we obtain the closure relation in the inertial frame:

$$\begin{aligned} P^{ij} - \frac{\delta^{ij}}{3} \gamma^2 \frac{v_k v_m}{c^2} P^{km} + \frac{\gamma^2}{\gamma + 1} \left(\frac{v^i v_k}{c^2} P^{jk} + \frac{v^j v_k}{c^2} P^{ik} \right) \\ + \left(\frac{\gamma^2}{\gamma + 1} \right)^2 \frac{v^i v^j}{c^2} \frac{v_k v_m}{c^2} P^{km} = \frac{\delta^{ij}}{3} \gamma^2 \left(E - 2 \frac{\mathbf{v} \cdot \mathbf{F}}{c^2} \right) - \gamma^2 \frac{v^i v^j}{c^2} E \\ + \gamma \left(\frac{v^i F^j}{c^2} + \frac{v^j F^i}{c^2} \right) + 2\gamma \frac{\gamma^2}{\gamma + 1} \frac{v^i v^j}{c^2} \frac{\mathbf{v} \cdot \mathbf{F}}{c^2}. \end{aligned} \quad (\text{E.48})$$

To the first order in \mathbf{v}/c , the closure relation becomes (Hsieh and Spiegel 1976)

$$P^{ij} = \frac{\delta^{ij}}{3} E + \frac{v^i F^j}{c^2} + \frac{v^j F^i}{c^2} - \frac{2}{3} \delta^{ij} \frac{\mathbf{v} \cdot \mathbf{F}}{c^2}. \quad (\text{E.49})$$

E.3 Relativistic Regimes

The radiation moment formalism is quite convenient and essential, especially in a relativistic regime, and it is a powerful tool for tackling problems of relativistic radiation hydrodynamics (e.g., Thorne et al. 1981; Flammang 1982, 1984; Nobili et al. 1991, 1993; Park 2001, 2006 for spherically symmetric problems; Takahashi 2007 for the Kerr metric). However, its validity is never known unless a fully angle-dependent radiation transfer equation is solved. Thus, the relativistic moment equations with a closure relation must be carefully treated, and applied to black-hole accretion flows, relativistic jets and winds, and relativistic explosions, such as gamma-ray bursts.

Actually, the pathological behavior in relativistic radiation moment equations has been pointed out and examined (Turolla and Nobili 1988; Nobili et al. 1991; Turolla et al. 1995; Dullemond 1999). Namely, the moment equations for radiation transfer in relativistically moving media

can generally have singular (critical) points. As a result, solutions behave pathologically in a relativistic regime. The appearance of singularities is supposed to be related to the approximation of the full transfer equations with a finite number of moments (Dullemond 1999).

For example, in one-dimensional relativistic flows using the closure relation (E.47), where the moment equations are truncated at the second order, the singularity appears when the flow velocity v becomes $\pm c/\sqrt{3}$, which corresponds to the relativistic sound speed (Turolla and Nobili 1988; Turolla et al. 1995). Hence, we cannot obtain solutions accelerated beyond $c/\sqrt{3}$, although there exists a decelerating solution (Fukue 2005).

The invalidity of the Eddington approximation in such a relativistic flow can be understood as follows. In adopting the Eddington approximation (E.47), we assume that within the photon mean-free path the radiation field is *isotropic* in the comoving frame. However, in the relativistic regime, where the velocity gradient becomes large and there exist the Doppler and aberration effects of photons, the isotropy of the radiation field may break down even in the comoving frame.

For example, the photon mean-free path ℓ in the comoving frame is $\ell \sim 1/(\kappa\rho)$, where κ is the opacity measured in the comoving frame and ρ is the proper density. When there exists a (strong) velocity gradient, say dv/ds , the velocity increase at the distance of ℓ is estimated as

$$\Delta v = \ell \frac{dv}{ds} = \frac{dv}{\kappa\rho ds} = \frac{dv}{d\tau}, \quad (\text{E.50})$$

where $\tau (= \kappa\rho s)$ is the optical depth. In order for the radiation fields to be isotropic in the comoving frame, this velocity increase should be sufficiently smaller than the speed of light. In such a case, we should modify the closure relation in the case of subrelativistic to relativistic regimes, as in the case of optically thick to thin regimes.

E.3.1 Velocity-Dependent Variable Eddington Factor

In order to improve the situation we are confronted with, instead of the usual Eddington approximation, we can adopt a *variable Eddington factor*, which depends on the flow velocity $\beta (= v/c)$ and the velocity gradient $d\beta/d\tau$ as well as the optical depth τ (Fukue 2006; Akizuki and Fukue 2007; Fukue 2007b; Koizumi and Umemura 2007). In one-dimensional flows the variable Eddington factor $f(\tau, \beta)$ is generally defined as

$$P_0 = f(\tau, \beta) E_0, \quad (\text{E.51})$$

where E_0 and P_0 are the radiation energy density and the radiation stress tensor in the comoving frame, respectively. The closure relation in the inertial frame for one-dimensional flows then becomes

$$cP(1 - f\beta^2) = cE(f - \beta^2) + 2F\beta(1 - f), \quad (\text{E.52})$$

where E , F , and P are the radiation energy density, the radiative flux, and the radiation pressure in the inertial frame, respectively.

The function $f(\tau, \beta)$ must reduce to 1/3 or appropriate values in the non-relativistic limit of $\beta = 0$, whereas it would approach unity in the extremely relativistic limit of $\beta = 1$. Furthermore, in the sufficiently optically thick regime this function approaches 1/3 except for $\beta = 1$, while in the optically thin limit it reduces to an appropriate form determined by the geometry under the considerations.¹ The appropriate form is now under construction.

E.4 Matter Coupling

We can now write the basic equations for matter (Hsieh and Spiegel 1976; Fukue et al. 1985; Park 2006 for the Schwarzschild metric; Takahashi 2007 for the Kerr metric).

(a) Mass conservation

The particle number conservation is

$$(nu^\mu)_{;\mu} = \frac{1}{\sqrt{-g}} \frac{\partial}{\partial x^\mu} (\sqrt{-g}nu^\mu) = 0, \quad (\text{E.53})$$

where x^μ is the space-time coordinates, u^μ the four-velocity, and n the proper number density.

In the three-dimensional form, the mass conservation becomes

$$\frac{\partial}{\partial t}(\rho\gamma) + \text{div}(\rho\gamma\mathbf{v}) = 0, \quad (\text{E.54})$$

where ρ ($= nmc^2$) is the proper density.

¹In the plane-parallel case, for instance, the variable Eddington factor in the optically thin limit is analytically derived as

$$f = \frac{1 - 3\beta + 3\beta^2}{3 - 3\beta + \beta^2}.$$

(b) **Momentum conservation**

The relativistic equations of motion, $(T_i^{\mu} + R_i^{\mu})_{;\mu} = 0$, are written as

$$(\varepsilon + p) \left(u^{\mu} \frac{\partial u^i}{\partial x^{\mu}} + \Gamma_{\mu\nu}^i u^{\mu} u^{\nu} \right) - (g^{i\mu} - u^i u^{\mu}) \frac{\partial p}{\partial x^{\mu}} = -(g^{i\mu} - u^i u^{\mu}) R_{\mu}^{\nu}_{;\nu}, \quad (\text{E.55})$$

where ε is the internal energy per unit proper volume, p the pressure measured in the comoving frame, $T^{\mu\nu}$ the energy-momentum tensor of matter, and $R^{\mu\nu}$ the stress-energy tensor of radiation.

The right-hand side of equation (E.55) are, from (E.30), (E.42), (E.43), (E.45) and (E.46),

$$\begin{aligned} & - (g^{i\mu} - u^i u^{\mu}) R_{\mu}^{\nu}_{;\nu} \\ &= - \left(\frac{1}{c^2} \frac{\partial F^i}{\partial t} + \frac{\partial P^{ik}}{\partial x^k} \right) \\ & \quad - \frac{\gamma^2}{c^2} v^i \left[- \left(\frac{\partial E}{\partial t} + \frac{\partial F^k}{\partial x^k} \right) + v_j \left(\frac{1}{c^2} \frac{\partial F^j}{\partial t} + \frac{\partial P^{jk}}{\partial x^k} \right) \right] \\ &= \frac{\rho}{c} (\kappa_0^{\text{abs}} + \kappa_0^{\text{sca}}) \left[F_0^i + \frac{\gamma - 1}{v^2} v^i (\mathbf{v} \cdot \mathbf{F}_0) \right] \\ &= \frac{\rho \gamma}{c} (\kappa_0^{\text{abs}} + \kappa_0^{\text{sca}}) \\ & \quad \times \left[F^i - \gamma^2 E v^i - v_k P^{ik} + \gamma^2 v^i \left(\frac{2\mathbf{v} \cdot \mathbf{F}}{c^2} - \frac{v_j v_k}{c^2} P^{jk} \right) \right]. \end{aligned} \quad (\text{E.56})$$

Thus, the relativistic equations of motion are

$$\begin{aligned} & c^2 \left(u^{\mu} \frac{\partial u^i}{\partial x^{\mu}} + \Gamma_{\mu\nu}^i u^{\mu} u^{\nu} \right) \\ &= \frac{c^2}{\varepsilon + p} (g^{i\mu} - u^i u^{\mu}) \frac{\partial p}{\partial x^{\mu}} + \frac{\rho c^2}{\varepsilon + p} \frac{1}{c} (\kappa_0^{\text{abs}} + \kappa_0^{\text{sca}}) \\ & \quad \times \left[F_0^i + \frac{\gamma - 1}{v^2} v^i (\mathbf{v} \cdot \mathbf{F}_0) \right] \\ &= \frac{c^2}{\varepsilon + p} (g^{i\mu} - u^i u^{\mu}) \frac{\partial p}{\partial x^{\mu}} + \frac{\rho c^2}{\varepsilon + p} \frac{\gamma}{c} (\kappa_0^{\text{abs}} + \kappa_0^{\text{sca}}) \\ & \quad \times \left[F^i - \gamma^2 E v^i - v_k P^{ik} + \gamma^2 v^i \left(\frac{2\mathbf{v} \cdot \mathbf{F}}{c^2} - \frac{v_j v_k}{c^2} P^{jk} \right) \right]. \end{aligned} \quad (\text{E.57})$$

(c) Energy conservation

The energy conservation, $u^\mu(T_\mu^\nu + R_\mu^\nu)_{;\nu} = 0$, is written as

$$\frac{1}{\sqrt{-g}} \frac{\partial}{\partial x^\mu} (\sqrt{-g} \varepsilon u^\mu) + \frac{p}{\sqrt{-g}} \frac{\partial}{\partial x^\mu} (\sqrt{-g} u^\mu) = -u^\mu R_{\mu;\nu}^\nu. \quad (\text{E.58})$$

The right-hand side of equation (E.58) is, from (E.30), (E.42), (E.43), (E.45) and (E.46),

$$\begin{aligned} -u^\mu R_{\mu;\nu}^\nu &= -\frac{\gamma}{c} \left(\frac{\partial E}{\partial t} + \frac{\partial F^k}{\partial x^k} \right) + \frac{\gamma v_i}{c} \left(\frac{1}{c^2} \frac{\partial F^i}{\partial t} + \frac{\partial P^{ik}}{\partial x^k} \right) \\ &= -\frac{\rho}{c} (j_0 - c\kappa_0^{\text{abs}} E_0) \\ &= \frac{\gamma^2 \rho}{c} \left(-\frac{j_0}{\gamma^2} + c\kappa_0^{\text{abs}} E - \kappa_0^{\text{abs}} \frac{2\mathbf{v} \cdot \mathbf{F}}{c} + \kappa_0^{\text{abs}} \frac{v_i v_k}{c} P^{ik} \right). \end{aligned} \quad (\text{E.59})$$

Thus, the energy equation is

$$\begin{aligned} \frac{c}{\sqrt{-g}} \frac{\partial}{\partial x^\mu} [\sqrt{-g} (\varepsilon - \rho c^2) u^\mu] + c \frac{p}{\sqrt{-g}} \frac{\partial}{\partial x^\mu} (\sqrt{-g} u^\mu) \\ &= -\rho (j_0 - c\kappa_0^{\text{abs}} E_0) \\ &= \gamma^2 \rho \left(-\frac{j_0}{\gamma^2} + c\kappa_0^{\text{abs}} E - \kappa_0^{\text{abs}} \frac{2\mathbf{v} \cdot \mathbf{F}}{c} + \kappa_0^{\text{abs}} \frac{v_i v_k}{c} P^{ik} \right). \end{aligned} \quad (\text{E.60})$$

(d) Sub-relativistic Regime

To the first order of (\mathbf{v}/c) , the equations of motion and energy equation for matter are written as, respectively,

$$\begin{aligned} \frac{\partial \mathbf{v}}{\partial t} + (\mathbf{v} \cdot \nabla) \mathbf{v} &= -\nabla \psi - \frac{1}{\rho} \nabla p \\ &\quad + \frac{\kappa_0^{\text{abs}} + \kappa_0^{\text{sca}}}{c} (\mathbf{F} - E\mathbf{v} - v_k P^{ik}), \end{aligned} \quad (\text{E.61})$$

$$\left(\frac{\partial}{\partial t} + \mathbf{v} \cdot \nabla \right) e + \frac{p}{\rho} \nabla \cdot \mathbf{v} = \frac{1}{\rho} q^+ - j_0 + c\kappa_0^{\text{abs}} E - \kappa_0^{\text{abs}} \frac{2\mathbf{v} \cdot \mathbf{F}}{c}, \quad (\text{E.62})$$

where \mathbf{v} is the velocity, ψ the gravitational potential, p the pressure, e the internal energy per unit mass, and q^+ the (viscous) heating rate per unit volume (Hsieh and Spiegel 1976; Fukue et al. 1985).

The equations for radiation are, on the other hand,

$$\frac{\partial E}{\partial t} + \nabla \cdot \mathbf{F} = \rho \left[j_0 - c\kappa_0^{\text{abs}} E + (\kappa_0^{\text{abs}} - \kappa_0^{\text{sca}}) \frac{\mathbf{v} \cdot \mathbf{F}}{c} \right], \quad (\text{E.63})$$

$$\frac{1}{c^2} \frac{\partial F^i}{\partial t} + \frac{\partial P^{ik}}{\partial x^k} = \frac{\rho}{c} \left(\frac{v^i}{c} j_0 - \kappa_0^{\text{abs}} F^i + \kappa_0^{\text{abs}} v_k P^{ik} \right) - \frac{\rho}{c} \kappa_0^{\text{sca}} \left(F^i - E v^i - v_k P^{ik} \right), \quad (\text{E.64})$$

$$P^{ij} = \frac{\delta^{ij}}{3} E + \frac{v^i F^j}{c^2} + \frac{v^j F^i}{c^2} - \frac{2}{3} \frac{\mathbf{v} \cdot \mathbf{F}}{c^2} \delta^{ij}. \quad (\text{E.65})$$

E.5 Plane-Parallel Expression

For a relativistically moving atmosphere in the plane-parallel geometry (z), the hydrodynamic equations and transfer equations become as follows (Fukue 2006, 2007a, b).

For matter, the continuity equation is

$$\rho c u = \rho \gamma \beta c = J \text{ (= const.)}, \quad (\text{E.66})$$

where ρ is the proper gas density, u the vertical four velocity, J the mass-loss rate per unit area, and c the speed of light. The four velocity u is related to the proper three velocity v by $u = \gamma \beta = \gamma v/c$, where γ is the Lorentz factor, $\gamma = \sqrt{1 + u^2} = 1/\sqrt{1 - (v/c)^2}$.

The equation of motion is

$$\begin{aligned} c^2 u \frac{du}{dz} &= c^2 \gamma^4 \beta \frac{d\beta}{dz} \\ &= -\frac{d\psi}{dz} - \gamma^2 \frac{c^2}{\varepsilon + p} \frac{dp}{dz} \\ &\quad + \frac{\rho c^2}{\varepsilon + p} \frac{\kappa_0^{\text{abs}} + \kappa_0^{\text{sca}}}{c} \gamma^3 \left[F(1 + \beta^2) - (cE + cP)\beta \right], \end{aligned} \quad (\text{E.67})$$

where ψ is the gravitational potential, p the gas pressure, κ_0^{abs} and κ_0^{sca} are the absorption and scattering opacities (gray), defined in the comoving frame, E the radiation energy density, F the radiative flux, and P the radiation pressure observed in the inertial frame. The first term in the square brackets on the right-hand side of equation (E.67) means the radiatively-driven force, which is modified to the order of u^2 , whereas the second term is the radiation drag force, which is also modified, but roughly proportional to the velocity.

When the gas pressure is ignored, the advection terms of the energy equation are dropped, and heating is balanced with the radiative terms,

$$0 = \frac{q^+}{\rho} - \left(j_0 - \kappa_0^{\text{abs}} c E \gamma^2 - \kappa_0^{\text{abs}} c P u^2 + 2 \kappa_0^{\text{abs}} F \gamma u \right), \quad (\text{E.68})$$

where q^+ is the internal heating and j_0 is the emissivity defined in the comoving frame. In this equation (E.68), the third and fourth terms on the right-hand side appear in the relativistic regime. Under the α prescription, the viscous-heating rate is proportional to the pressure, and therefore, may depend on z .

For radiation, the frequency-integrated transfer equation (E.44), the zeroth moment equation (E.45), and the first moment equation (E.46) become, respectively:

$$\begin{aligned} \mu \frac{dI}{dz} = & \rho \frac{1}{\gamma^3(1-\beta\mu)^3} \left[\frac{j_0}{4\pi} - (\kappa_0^{\text{abs}} + \kappa_0^{\text{sca}}) \gamma^4 (1-\beta\mu)^4 I \right. \\ & + \frac{\kappa_0^{\text{sca}}}{4\pi} \frac{3}{4} \gamma^2 \left\{ \left[1 + \frac{(\mu-\beta)^2}{(1-\beta\mu)^2} \beta^2 + \frac{(1-\beta^2)^2}{(1-\beta\mu)^2} \frac{1-\mu^2}{2} \right] cE \right. \\ & - \left[1 + \frac{(\mu-\beta)^2}{(1-\beta\mu)^2} \right] 2F\beta \\ & \left. \left. + \left[\beta^2 + \frac{(\mu-\beta)^2}{(1-\beta\mu)^2} - \frac{(1-\beta^2)^2}{(1-\beta\mu)^2} \frac{1-\mu^2}{2} \right] cP \right\} \right], \end{aligned} \quad (\text{E.69})$$

$$\begin{aligned} \frac{dF}{dz} = & \rho\gamma \left[j_0 - \kappa_0^{\text{abs}} cE + \kappa_0^{\text{sca}} (cE + cP) \gamma^2 \beta^2 \right. \\ & \left. + \kappa_0^{\text{abs}} F\beta - \kappa_0^{\text{sca}} F(1+\beta^2)\gamma^2\beta \right]. \end{aligned} \quad (\text{E.70})$$

$$\begin{aligned} \frac{dP}{dz} = & \frac{\rho\gamma}{c} \left[j_0\beta - \kappa_0^{\text{abs}} F + \kappa_0^{\text{abs}} cP\beta \right. \\ & \left. - \kappa_0^{\text{sca}} F\gamma^2(1+\beta^2) + \kappa_0^{\text{sca}} (cE + cP) \gamma^2 \beta \right], \end{aligned} \quad (\text{E.71})$$

where $\mu = \cos\theta$.

Finally, a closure relation is

$$cP(1-f\beta^2) = cE(f-\beta^2) + 2F\beta(1-f), \quad (\text{E.72})$$

where $f(\tau, \beta)$ is the variable Eddington factor depending on the velocity as well as the optical depth.

References

- Akizuki C., Fukue J. 2007, submitted to PASJ
- Anderson J.L., Spiegel E.A. 1972, ApJ 171, 127
- Castor J.I. 1972, ApJ 178, 779
- Dullemond C.P. 1999, A&A 343, 1030
- Flammang R.A. 1982, MNRAS 199, 833
- Flammang R.A. 1984, MNRAS 206, 589
- Fukue J. 2005, PASJ 57, 1023

- Fukue J. 2006, PASJ 58, 461
Fukue J. 2007a, PASJ 59, 687
Fukue J. 2007b, submitted to PASJ
Fukue J., Kato S., Matsumoto R. 1985, PASJ 37, 383
Hazlehurst T., Sargent W.L.W. 1959, ApJ 130, 276
Hsieh S.-H., Spiegel E. A. 1976, ApJ 207, 244
Koizumi T., Umemura M. 2007, submitted to MNRAS
Lindquist R. W. 1966, Ann. Phys. 37, 487
Mihalas D., Mihalas B.W. 1984, *Foundations of Radiation Hydrodynamics* (Oxford University Press, Oxford)
Nobili L., Turolla R., Zampieri L. 1991, ApJ 383, 250
Nobili L., Turolla R., Zampieri L. 1993, ApJ 404, 686
Park M.-G. 2001, JKAS 34, 305
Park M.-G. 2003, A&A 274, 642
Park M.-G. 2006, MNRAS 367, 1739
Takahashi R. 2007, MNRAS in press
Thomas L.H. 1930, QuartJ.Math 1, 239
Thorne K.S. 1981, MNRAS 194, 439
Thorne K.S., Flammang R.A., Źytkow A.N. 1981, MNRAS 194, 475
Turolla R., Nobili L. 1988, MNRAS 235, 1273
Turolla R., Zampieri L., Nobili L. 1995, MNRAS 272, 625
Udey N., Israel W. 1982, MNRAS 199, 1137

APPENDIX F

Magnetohydrodynamical Equations

In this appendix we summarize the basic equations for an ionized fluid being subject to the magnetic fields under magnetohydrodynamical approximations, the *magnetohydrodynamical equations*, in the non-relativistic regime. The basic equations include the continuity equation, the equation of motion, the energy equation, and the induction equation, supplemented by the equation of state. We first show these basic equations in a vector form, and then we give them in cylindrical coordinates.

F.1 Maxwell Equations and MHD Approximations

Magnetohydrodynamical (MHD) approximations are introduced to describe low-frequency global phenomena (hydrodynamical phenomena) in highly conductive ionized plasmas. Since long-timescale phenomena in highly conductive media are considered, we safely assume charge neutrality at each time and place. We use the cgs-Gauss units in this appendix.

(a) Maxwell equations

The Maxwell equations, which are used to MHD approximations, are

$$\operatorname{div} \mathbf{B} = 0, \quad (\text{F.1})$$

$$\operatorname{rot} \mathbf{E} = -\frac{1}{c} \frac{\partial \mathbf{B}}{\partial t}, \quad (\text{F.2})$$

$$\operatorname{rot} \mathbf{B} = \frac{4\pi}{c} \mathbf{J}, \quad (\text{F.3})$$

where \mathbf{B} is the magnetic flux density, \mathbf{E} the electric vector, and \mathbf{J} the electric current vector.¹ Here, in equation (F.3) the term of the displace-

¹One of the Maxwell equations, $\operatorname{div} \mathbf{E} = 4\pi\rho_e$ (ρ_e being the electric charge density), is unnecessary here, since the charge neutrality is assumed. This equation should be used to determine the weak charge, after solutions are obtained under the assumption of the charge neutrality, independent of other equations.

ment current has been neglected, since long-timescale phenomena are treated in MHD approximations. Due to this neglect, we can filter out electromagnetic waves, which are generally high-frequency phenomena. Since the permeability is not always a very useful concept for a plasma, we use $\text{rot } \mathbf{B}$ (instead of $\text{rot } \mathbf{H}$) in equation (F.3) and consider all of the plasma current explicitly in \mathbf{J} .

The electric current is approximated by the generalized Ohm's law:

$$\mathbf{J} = \sigma_e \left(\mathbf{E} + \frac{1}{c} \mathbf{v} \times \mathbf{B} \right), \quad (\text{F.4})$$

where σ_e is the electric conductivity and \mathbf{v} is the velocity of the plasma gas. In equation (F.4), instead of \mathbf{v}_e (the velocity of the electron gas), we use \mathbf{v} , neglecting the Hall current.

(b) Induction equation

Eliminating \mathbf{E} and \mathbf{J} from equations (F.2)–(F.4), we obtain

$$\frac{\partial \mathbf{B}}{\partial t} = \text{rot}(\mathbf{v} \times \mathbf{B}) + \eta \Delta \mathbf{B}, \quad (\text{F.5})$$

where η [$\equiv c^2/(4\pi\sigma_e)$] is called the magnetic diffusivity, and has been taken to be constant for simplicity. This equation (F.5) is called an *induction equation*.

F.2 MHD Equations

We can now write the basic equations for matter in the MHD approximation.

(a) Continuity equation

The conservation of mass (continuity equation) is written as

$$\frac{\partial \rho}{\partial t} + \text{div}(\rho \mathbf{v}) = 0, \quad (\text{F.6})$$

where ρ is the density and \mathbf{v} the velocity vector.

(b) Equation of motion

The equation of motion is described as

$$\rho \frac{d\mathbf{v}}{dt} = \rho \left[\frac{\partial \mathbf{v}}{\partial t} + (\mathbf{v} \cdot \nabla) \mathbf{v} \right] = -\rho \nabla \psi - \nabla p + \frac{1}{c} \mathbf{J} \times \mathbf{B}, \quad (\text{F.7})$$

where ψ is the gravitational potential, p the pressure, and $\mathbf{J} \times \mathbf{B}/c$ the electromagnetic force (Lorentz force).

With the help of equation (F.3), we finally have the equation of motion under an MHD approximation:

$$\rho \frac{d\mathbf{v}}{dt} = \rho \left[\frac{\partial \mathbf{v}}{\partial t} + (\mathbf{v} \cdot \nabla) \mathbf{v} \right] = -\rho \nabla \psi - \nabla p + \frac{1}{4\pi} \text{rot} \mathbf{B} \times \mathbf{B}, \quad (\text{F.8})$$

which is also written as

$$\rho \left[\frac{\partial \mathbf{v}}{\partial t} + (\mathbf{v} \cdot \nabla) \mathbf{v} \right] = -\rho \nabla \psi - \nabla \left(p + \frac{B^2}{8\pi} \right) + \frac{1}{4\pi} (\mathbf{B} \cdot \nabla) \mathbf{B}, \quad (\text{F.9})$$

where $B^2/8\pi$ is the magnetic pressure.

(c) Energy equation

The conservation of energy is described as

$$\rho T \frac{ds}{dt} = \rho T \left[\frac{\partial s}{\partial t} + (\mathbf{v} \cdot \nabla) s \right] = \Phi - \text{div} \mathbf{F} + \frac{\mathbf{J}^2}{\sigma_e}, \quad (\text{F.10})$$

where T is the temperature, s the specific entropy, Φ the viscous dissipative function, and \mathbf{F} the energy flux. The last term on the right-hand side is the *Joule heating*.

(d) Equation of state

Finally, the equation of state is

$$p = \frac{\mathcal{R}}{\bar{\mu}} \rho T + \frac{1}{3} a T^4, \quad (\text{F.11})$$

where \mathcal{R} is the gas constant and $\bar{\mu}$ is the mean molecular weight.

Equations (F.6), (F.8), (F.10), (F.11), and (F.5) constitute the basic equations of magnetohydrodynamics.

F.3 Cylindrical Coordinate Expression

In this book we focus our attention on accretion disks having an axisymmetric configuration. Hence, for the convenience of the readers, we explicitly write the electromagnetic force and the induction equations in cylindrical coordinates (r, φ, z) , where the z -axis is coincident with the axis of symmetry (for other parts see appendix B).

(a) $\mathbf{J} \times \mathbf{B}/c$ -term

The electromagnetic force is explicitly written in cylindrical coordinates as

$$\begin{aligned} \frac{1}{c} [\mathbf{J} \times \mathbf{B}]_r &= \frac{1}{4\pi} [\text{rot } \mathbf{B} \times \mathbf{B}]_r \\ &= \frac{1}{4\pi} \left[\left(\frac{\partial B_r}{\partial z} - \frac{\partial B_z}{\partial r} \right) B_z - \left(\frac{\partial}{r\partial r} r B_\varphi - \frac{\partial B_r}{r\partial\varphi} \right) B_\varphi \right], \quad (\text{F.12}) \end{aligned}$$

$$\begin{aligned} \frac{1}{c} [\mathbf{J} \times \mathbf{B}]_\varphi &= \frac{1}{4\pi} [\text{rot } \mathbf{B} \times \mathbf{B}]_\varphi \\ &= \frac{1}{4\pi} \left[\left(\frac{\partial}{r\partial r} r B_\varphi - \frac{\partial B_r}{r\partial\varphi} \right) B_r - \left(\frac{\partial B_z}{r\partial\varphi} - \frac{\partial B_\varphi}{\partial z} \right) B_z \right], \quad (\text{F.13}) \end{aligned}$$

$$\begin{aligned} \frac{1}{c} [\mathbf{J} \times \mathbf{B}]_z &= \frac{1}{4\pi} [\text{rot } \mathbf{B} \times \mathbf{B}]_z \\ &= \frac{1}{4\pi} \left[\left(\frac{\partial B_z}{r\partial\varphi} - \frac{\partial B_\varphi}{\partial z} \right) B_\varphi - \left(\frac{\partial B_r}{\partial z} - \frac{\partial B_z}{\partial r} \right) B_r \right]. \quad (\text{F.14}) \end{aligned}$$

(b) Induction equation

In the limit of the frozen-in approximation ($\eta = 0$), we have

$$\frac{\partial B_r}{\partial t} = \frac{\partial}{r\partial\varphi} (v_r B_\varphi - v_\varphi B_r) - \frac{\partial}{\partial z} (v_z B_r - v_r B_z), \quad (\text{F.15})$$

$$\frac{\partial B_\varphi}{\partial t} = \frac{\partial}{\partial z} (v_\varphi B_z - v_z B_\varphi) - \frac{\partial}{\partial r} (v_r B_\varphi - v_\varphi B_r), \quad (\text{F.16})$$

$$\frac{\partial B_z}{\partial t} = \frac{\partial}{r\partial r} [r(v_z B_r - v_r B_z)] - \frac{\partial}{r\partial\varphi} (v_\varphi B_z - v_z B_\varphi). \quad (\text{F.17})$$

APPENDIX G

Equations for Relativistic Magnetohydrodynamics

In this appendix we summarize the basic equations for an ionized fluid being subject to the magnetic fields under magnetohydrodynamical approximations, the *relativistic MHD equations*, within the framework of general relativity. The basic equations include the continuity equation, the equation of motion, the energy equation, the relativistic Maxwell equations, and the induction equation, supplemented by the equation of state. We first give the metric and energy-momentum tensor, and then show the basic equations in a tensor form.

G.1 Metric and Energy-Momentum Tensor

Of many textbooks concerning general relativity, we would like to refer to Landau and Lifshitz (1971) here as a standard. In this book the $(+, -, -, -)$ space-time signature is adopted, and the Greek suffixes $\alpha, \beta, \gamma, \dots$ take values of 0, 1, 2, and 3, while the Latin suffixes i, j, k, \dots take values of 1, 2, and 3. The semicolon denotes covariant differentiation.

The space-time metric and four-velocity are given in appendix C.

(a) Energy-momentum tensor

The energy-momentum tensor for an ideal gas, $T^{\mu\nu}$, is

$$T^{\mu\nu} = (\varepsilon + p) u^\mu u^\nu - p g^{\mu\nu}, \quad (\text{G.1})$$

where ε is the internal energy per unit proper volume and p is the pressure measured in the comoving frame ($\varepsilon + p$ is the enthalpy per unit proper volume).

The energy-momentum tensor for the magnetic fields, $M^{\mu\nu}$, is

$$M^{\mu\nu} = \frac{1}{4\pi} \left(\frac{1}{4} g^{\mu\nu} F_{\sigma\tau} F^{\sigma\tau} - F^{\mu\lambda} F^\nu{}_\lambda \right). \quad (\text{G.2})$$

Here, $F^{\mu\nu}$ is the *electromagnetic field tensor*, an anti-symmetric tensor, whose components are related to four vectors; the electric vector \mathbf{E} , the electric displacement field \mathbf{D} , the magnetic flux density \mathbf{B} , and the magnetic field strength \mathbf{H} by (see Landau and Lifshitz 1971)

$$E_i = F_{0i} \quad \text{and} \quad E^i = \gamma^{ij} F_{0j}, \quad (\text{G.3})$$

$$D^i = -\sqrt{g_{00}} F^{0i} \quad \text{and} \quad D_i = -\sqrt{g_{00}} \gamma_{ij} F^{0j} \quad (\text{G.4})$$

$$B^i = -\frac{1}{2} \frac{\sqrt{g_{00}}}{\sqrt{-g}} \varepsilon^{ijk} F_{jk} \quad \text{and} \quad F_{ij} = -\frac{\sqrt{-g}}{\sqrt{g_{00}}} \varepsilon^{ijk} B^k \quad (\text{G.5})$$

$$H_i = -\frac{1}{2} \sqrt{-g} \varepsilon_{ijk} F^{jk} \quad \text{and} \quad F^{ij} = -\frac{1}{\sqrt{-g}} \varepsilon^{ijk} H_k \quad (\text{G.6})$$

where the metric is given in appendix C and $\varepsilon^{123} = \varepsilon_{123} = 1$.

G.2 Relativistic Maxwell Equations

Magnetohydrodynamical (MHD) approximations are introduced. We use the cgs-Gauss units in this appendix.

(a) Maxwell equations in curved spacetime

The Maxwell equations in curved spacetime are expressed as

$$F_{\mu\nu;\lambda} + F_{\lambda\mu;\nu} + F_{\nu\lambda;\mu} = 0, \quad (\text{G.7})$$

$$F^{\mu\nu}{}_{;\nu} = -\frac{4\pi}{c} J^\mu, \quad (\text{G.8})$$

where J^μ is the electric current four vector.

The four vector J^μ is given by

$$J^\mu = \rho_e c u^\mu + \sigma_e u_\nu F^{\mu\nu}, \quad (\text{G.9})$$

where ρ_e is the proper density of electric charge and σ_e the electric conductivity. In equation (G.9), the first term on the right-hand side means the convective current, while the second term is the conduction current.

The first set (G.7) is more explicitly written as

$$\frac{\partial F_{ij}}{\partial x^0} + \frac{\partial F_{0i}}{\partial x^j} - \frac{\partial F_{0j}}{\partial x^i} = 0, \quad (\text{G.10})$$

which is a generalized form of $\text{rot } \mathbf{E} = -\partial \mathbf{B}/(c\partial t)$, and

$$\frac{\partial F_{ij}}{\partial x^k} + \frac{\partial F_{ki}}{\partial x^j} + \frac{\partial F_{jk}}{\partial x^i} = 0, \quad (\text{G.11})$$

which is a generalized form of $\text{div } \mathbf{B} = 0$.

With the help of the anti-symmetry of $F^{\mu\nu}$, the second set (G.8) is also written as

$$\frac{1}{\sqrt{-g}} \frac{\partial}{\partial x^k} (\sqrt{-g} F^{0k}) = -\frac{4\pi}{c} J^0, \quad (\text{G.12})$$

which is a generalized form of $\text{div } \mathbf{E} = 4\pi\rho_e$ (that is not used in the MHD approximation), and

$$\frac{1}{\sqrt{-g}} \frac{\partial}{\partial x^k} (\sqrt{-g} F^{ik}) + \frac{1}{\sqrt{-g}} \frac{\partial}{\partial x^0} (\sqrt{-g} F^{i0}) = -\frac{4\pi}{c} J^i, \quad (\text{G.13})$$

which is a generalized form of $\text{rot } \mathbf{B} = 4\pi \mathbf{J}/c$. The second term on the left-hand side of equation (G.13) is dropped in the MHD approximation.

(b) Induction equation

In the MHD approximation, where charge neutrality is assumed, equation (G.9) becomes

$$F^{\mu\nu} u_\nu = \frac{1}{\sigma_e} J^\mu \quad \text{or} \quad F_{\mu\nu} u^\nu = \frac{1}{\sigma_e} J_\mu. \quad (\text{G.14})$$

Hence, F_{0i} can be written as

$$F_{0i} = \frac{1}{u^0} \left(F_{ik} u^k - \frac{1}{\sigma_e} J_i \right). \quad (\text{G.15})$$

Eliminating F_{0i} from equations (G.10) and (G.15), we obtain

$$\begin{aligned} \frac{\partial F_{ij}}{\partial x^0} &= -\frac{\partial}{\partial x^j} \left(F_{ik} \frac{u^k}{u^0} \right) + \frac{\partial}{\partial x^i} \left(F_{jk} \frac{u^k}{u^0} \right) \\ &\quad + \frac{\partial}{\partial x^j} \left(\frac{1}{\sigma_e} \frac{J_i}{u^0} \right) - \frac{\partial}{\partial x^i} \left(\frac{1}{\sigma_e} \frac{J_j}{u^0} \right), \end{aligned} \quad (\text{G.16})$$

where J_i is, from equation (G.13),

$$J^i = -\frac{c}{4\pi} \frac{1}{\sqrt{-g}} \frac{\partial}{\partial x^k} (\sqrt{-g} F^{ik}). \quad (\text{G.17})$$

These equations (G.16) and (G.17) consist of the *relativistic induction equation*.

G.3 Relativistic MHD Equations

We here write the basic equations for matter in the MHD approximation.

(a) Mass conservation

The particle number conservation, $(nu^\mu)_{;\mu}$, is

$$\frac{1}{\sqrt{-g}} \frac{\partial}{\partial x^\mu} (\sqrt{-g} n u^\mu) = 0, \quad (\text{G.18})$$

where x^μ is the space-time coordinates, u^μ the four-velocity, and n the proper number density.

(b) Momentum conservation

The relativistic equations of motion, $(T_i{}^\mu + M_i{}^\mu)_{;\mu} = 0$, are

$$(\varepsilon + p) \left(u^\mu \frac{\partial u^i}{\partial x^\mu} + \Gamma_{\mu\nu}^i u^\mu u^\nu \right) - (g^{i\mu} - u^i u^\mu) \frac{\partial p}{\partial x^\mu} = -(g^{i\mu} - u^i u^\mu) M_{\mu;\nu}. \quad (\text{G.19})$$

The term, $-M_{\mu;\nu}$, is the Lorentz force, and is expressed as, after several manipulations,

$$-M_{\mu;\nu} = \frac{1}{4\pi} F_\mu{}^\lambda F_{\lambda;\nu} = \frac{1}{c} F_\mu{}^\nu J_\nu = \frac{1}{c} F_{\mu\nu} J^\nu. \quad (\text{G.20})$$

Or, using equations (G.13) and (G.17), the Lorentz force is expressed as

$$-M^{\mu\nu}{}_{;\nu} = -\frac{1}{4\pi} \frac{g^{\mu\lambda} F_{\lambda\nu}}{\sqrt{-g}} \frac{\partial}{\partial x^\sigma} (\sqrt{-g} F^{\nu\sigma}). \quad (\text{G.21})$$

(c) Energy conservation

The energy conservation, $u^\mu (T_\mu{}^\nu + M_\mu{}^\nu)_{;\nu} = 0$, is written as

$$\frac{1}{\sqrt{-g}} \frac{\partial}{\partial x^\mu} (\sqrt{-g} \varepsilon u^\mu) + \frac{p}{\sqrt{-g}} \frac{\partial}{\partial x^\mu} (\sqrt{-g} u^\mu) = -u^\mu M_{\mu;\nu}. \quad (\text{G.22})$$

Here, the term on the right-hand side is the *Joule heating*, and, using equations (G.20) and (G.14), this term can be expressed as

$$-u^\mu M_{\mu;\nu} = \frac{1}{c} u^\mu F_\mu{}^\nu J_\nu = \frac{1}{c} u^\mu F_{\mu\nu} J^\nu = -\frac{1}{c\sigma_e} J_\nu J^\nu. \quad (\text{G.23})$$

References

Landau L.D., Lifshitz E.M. 1971, *The Classical Theory of Fields* (Pergamon Press, Oxford)

APPENDIX H

Relativistic Equation of State

In accretion onto a relativistic object, such as a black hole, the relevant temperature range is very wide from the non-relativistic regime to the relativistic one. Hence, in some cases we should use the rigorous equations of state derived from the relativistic Maxwell-Boltzmann distribution of gas, instead of the polytropic relation. We here summarize several relations: the equations of state, the adiabatic sound speed, and the effective adiabatic index.

H.1 Equation of State

For the a -th species (rest mass m_a), the pressure p_a and the internal energy ε_a (per unit volume) are expressed, respectively, in terms of the number density n_a and the temperature T_a as

$$p_a = n_a k_B T_a, \quad (\text{H.1})$$

$$\varepsilon_a = n_a f_a(T_a), \quad (\text{H.2})$$

where k_B is the Boltzmann constant (Chandrasekhar 1967; Cox and Giuli 1968).¹

In equation (H.2) the function $f_a(T_a)$ and its derivative df_a/dT_a are, respectively,

$$f_a(T_a) = m_a c^2 \left[\frac{3k_B T_a}{m_a c^2} + \frac{K_1(m_a c^2/k_B T_a)}{K_2(m_a c^2/k_B T_a)} \right], \quad (\text{H.3})$$

$$\frac{df_a}{k_B dT_a} = 3 + 3 \frac{f_a}{k_B T_a} - \left(\frac{f_a}{k_B T_a} \right)^2 + \left(\frac{m_a c^2}{k_B T_a} \right)^2, \quad (\text{H.4})$$

¹For an electron-proton gas with the same temperature T , the pressure and internal energy become, respectively, $p = (n_p + n_e)k_B T = 2n_p k_B T$ and $\varepsilon = n_p f_p(T) + n_e f_e(T) = n_p[f_p(T) + f_e(T)]$.

where K_n 's are the modified Bessel functions of the second kind of order n .²

The function $f_a(T_a)$ and its derivative df_a/dT_a are depicted in figure (H.1) as a function of T_a .

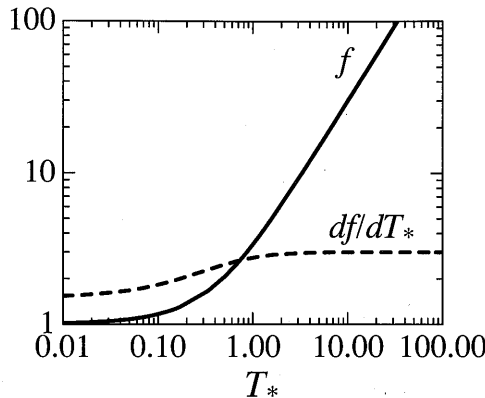


Figure H.1

Function f_a and its derivative df_a/dT_a as a function of T_a . The abscissa is the dimensionless temperature $k_B T_a / (m_a c^2)$, whereas the ordinates are $f_a / (m_a c^2)$ (thick solid curve) and $df_a / (k_B dT_a)$ (thick dashed curve).

In the non-relativistic limit of $k_B T_a / m_a c^2 \ll 1$, K_1/K_2 is approximated by $1 - (3/2)(k_B T_a / m_a c^2)$. We then have

$$f_a(T_a) \sim m_a c^2 + \frac{3}{2} k_B T_a. \quad (\text{H.5})$$

In the extreme relativistic limit of $k_B T_a / m_a c^2 \gg 1$, on the other hand, K_1/K_2 becomes 1. We then have

$$f_a(T_a) \sim m_a c^2 + 3k_B T_a. \quad (\text{H.6})$$

The transition temperature (defined by $kT_a/m_a c^2 = 1$) between the non-relativistic regime and extremely relativistic one is

$$\begin{aligned} T_1 &= 5.93 \times 10^9 \text{ K} && \text{for electron,} \\ T_2 &= 1.08 \times 10^{12} \text{ K} && \text{for proton.} \end{aligned} \quad (\text{H.7})$$

²In terms of the dimensionless temperature Θ_a defined by $\Theta_a \equiv k_B T_a / m_a c^2$, the function $\Phi_a \equiv f_a / (m_a c^2)$ and its derivative are expressed as

$$\Phi_a(\Theta_a) = 3\Theta_a + \frac{K_1(1/\Theta_a)}{K_2(1/\Theta_a)} \quad \text{and} \quad \frac{d\Phi_a}{d\Theta_a} = 3 + \frac{3\Phi_a}{\Theta_a} - \frac{\Phi_a^2 - 1}{\Theta_a^2}.$$

H.2 Adiabatic Sound Speed and Effective Adiabatic Index

In the relativistic regime the adiabatic sound speed c_s and effective adiabatic index Γ are defined, respectively, by

$$\frac{c_s^2}{c^2} \equiv \left(\frac{\partial p}{\partial \varepsilon} \right)_s = \Gamma \frac{p}{\varepsilon + p}, \quad (\text{H.8})$$

$$\Gamma = 1 + \frac{p}{\sum T_a n_a f'_a(T_a)}, \quad (\text{H.9})$$

where the prime denotes the differentiation with respect to T [see Fukue (1986, 1987, 2004) for more general expressions].

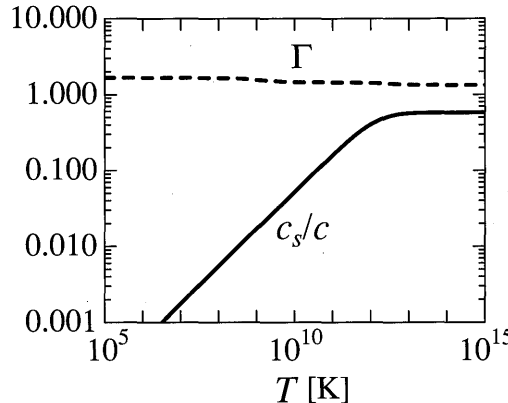


Figure H.2

Adiabatic sound speed c_s in units of c and the effective adiabatic index Γ as a function of T .

For an electron-proton gas with the same temperature, equations (H.8) and (H.9) are reduced, respectively, to

$$\frac{c_s^2}{c^2} = \Gamma \frac{2k_B T}{f_p(T) + f_e(T) + 2k_B T}, \quad (\text{H.10})$$

$$\Gamma = 1 + \frac{2k_B}{f'_p(T) + f'_e(T)}. \quad (\text{H.11})$$

The adiabatic sound speed and effective adiabatic index are shown in figure H.2 as a function of T .

It is worth noting that the value of Γ is nearly constant in three regions; that is, $5/3$ at $kT < m_e c^2$ where both electrons and protons are non-relativistic, ~ 1.44 at $m_e c^2 < kT < m_p c^2$ where electrons become relativistic while protons remain non-relativistic, and $4/3$ at $kT > m_p c^2$ where both are relativistic.

References

- Chandrasekhar S. 1967, *Stellar Structure* (The University of Chicago Press, Chicago)
- Cox J.P., Giuli R.T. 1968, *Principles of Stellar Structure*, Vol. 2 (Gordon and Breach, New York), chap 24
- Fukue J. 1986, PASJ 38, 167
- Fukue J. 1987, PASJ 39, 309
- Fukue J. 2004, PASJ 56, 959

APPENDIX I

Cooling of Relativistic Gas

In optically-thin, high-temperature disks, the electron temperature becomes much lower than the ion temperature, since the electron gas cools efficiently by bremsstrahlung and synchrotron processes, while interactions between ion and electron gases are generally weak. In this appendix we summarize here the rates of these cooling processes, since they are important for determining the spectra emitted from the disks as well as the electron temperature.

I.1 Bremsstrahlung Cooling

Bremsstrahlung loss per unit volume from an electron gas with temperature T_e and number density n_e is (Svensson 1984)

$$\dot{E}_{\text{brems}}(\Theta_e, n_i) = \alpha_f r_e^2 m_e c^3 n_i^2 F_{\text{brems}}(\Theta_e), \quad (\text{I.1})$$

where α_f ($= e^2/2\pi\hbar c \sim 1/137$) is the fine-structure constant, r_e ($= e^2/m_e c$) the classical electron radius, and Θ_e ($= k_B T_e / m_e c^2$) the dimensionless electron temperature.

In equation (I.1), $F_{\text{brems}}(\Theta_e)$ is the dimensionless radiation rate due to relativistic bremsstrahlung, which can be decomposed into a part due to proton-electron collisions, F_{ep} , and that due to electron-electron collisions, F_{ee} , as

$$F_{\text{brems}}(\Theta_e) = F_{ep}(\Theta_e) + F_{ee}(\Theta_e), \quad (\text{I.2})$$

where $F_{ep}(\Theta_e)$ and $F_{ee}(\Theta_e)$ are approximated according to the following forms (Svensson 1984):

$$F_{ep} = \begin{cases} \frac{32}{3} \left(\frac{2}{\pi} \right)^{1/2} \Theta_e^{1/2} (1 + 1.78\Theta_e^{1.34}) & (\Theta_e \leq 1), \\ 12\Theta_e \left[\ln(2\eta_E \Theta_e + 0.42) + \frac{3}{2} \right] & (\Theta_e \geq 1), \end{cases} \quad (\text{I.3})$$

$$F_{ee} = \begin{cases} \frac{20}{9\pi^{1/2}} (44 - 3\pi^2) \Theta_e^{3/2} (1 + 1.1\Theta_e + \Theta_e^2 - 1.25\Theta_e^{2.5}) & (\Theta_e \leq 1), \\ 24\Theta_e \left[\ln(2\eta_E\Theta_e) + \frac{5}{4} \right] & (\Theta_e \geq 1). \end{cases} \quad (I.4)$$

Here, $\eta_E = \exp(-\gamma_E)$ and γ_E (≈ 0.5772) is Euler's number.

The cooling rate per unit surface area of disks by bremsstrahlung, Q_{brems}^- , is thus given by

$$Q_{\text{brems}}^- = \sqrt{\pi} (\dot{E}_{\text{brems}})_0 A_{\text{brems}}^C H, \quad (I.5)$$

where A_{brems}^C is the amplification factor by Compton processes, which is discussed in subsection H.3, and H the half thickness.

I.2 Synchrotron Cooling

The spectrum of synchrotron emission by relativistic Maxwellian electrons with density n_e , $\epsilon_{\text{syn}}(\nu)d\nu$, was calculated by Pacholczyk (1970) under an optically thin condition. Mahadevan et al. (1996) fitted it by a simple functional form:

$$\epsilon_{\text{syn}}d\nu = 4.43 \times 10^{-30} \frac{4\pi\nu n_e}{K_2(1/\Theta_e)} \frac{4.0505}{x_M^{1/6}} \left(1 + \frac{0.40}{x_M^{1/4}} + \frac{0.5316}{x_M^{1/2}} \right) \times \exp(-1.8899x_M^{1/3})d\nu \quad (I.6)$$

in units of erg cm⁻³ s⁻¹ Hz⁻¹, where

$$x_M = \frac{2\nu}{3\nu_0\Theta_e^2} \quad \text{and} \quad \nu_0 = \frac{eB}{2\pi m_e c}. \quad (I.7)$$

Here, B is the magnetic-field strength.

Below some critical frequency, ν_c , however, the emission becomes self-absorbed and the formula (I.6) is no longer valid there. Following Esin et al. (1996), we estimate ν_c by considering a cylindrical geometry and assume that for frequencies below ν_c the emission is completely self-absorbed, and the volume emissivity can be approximated by the blackbody emission from the disk surface divided by the disk volume.

The cooling rate per unit volume by synchrotron emission integrated over the frequency, q_{syn}^- , is then given by (Esin et al. 1996)

$$q_{\text{syn}}^- = \frac{2\pi k T_e \nu_c^3}{3 H c^2} + 6.76 \times 10^{-28} \frac{n_e}{K_2(1/\Theta_e) a_1^{1/6}} \left[\frac{1}{a_4^{11/2}} \Gamma \left(\frac{11}{2}, a_4 \nu_c^{1/3} \right) \right]$$

$$+ \frac{a_2}{a_4}^{19/4} \Gamma \left(\frac{19}{4}, a_4 \nu_c^{1/3} \right) + \frac{a_3}{a_4^4} \left(a_4^3 \nu_c + 3a_r^2 \nu_c^{2/3} + 6a_4 \nu_c^{1/3} + 6 \right) e^{-a_4 \nu_c^{1/3}} \Big], \quad (\text{I.8})$$

where the parameters a_1 , a_2 , a_3 , and a_4 are defined as

$$a_1 = \frac{2}{3\nu_0 \Theta_e^2}, \quad a_2 = \frac{0.4}{a_1^{1/4}}, \quad a_3 = \frac{0.5316}{a_1^{1/2}}, \quad a_4 = 1.8899 a_1^{1/3}, \quad (\text{I.9})$$

and the incomplete gamma function $\Gamma(a, x)$ is defined by

$$\Gamma(a, x) = \int_x^\infty t^{a-1} e^{-t} dt. \quad (\text{I.10})$$

The cooling rate by synchrotron emission, Q_{syn}^- , is thus given by

$$Q_{\text{syn}}^- = \sqrt{\pi} (q_{\text{syn}}^-)_0 A_{\text{syn}}^C (\nu_c) H, \quad (\text{I.11})$$

where $A_{\text{syn}}^C(\nu_c)$ is the amplification factor by Compton processes, which is discussed in the next subsection.

I.3 Comptonization

For spectra by bremsstrahlung, the Compton amplification factor A_{brems}^C is written as (Svensson 1984)

$$A_{\text{brems}}^C = 1 + f_{\text{brems}} \frac{3}{4} \ln^2 \left(\frac{\Theta_e}{x_m} \right). \quad (\text{I.12})$$

Here, f_{brems} is the fraction of bremsstrahlung photons which are scattered into the Wien peak:

$$f_{\text{brems}} = 2 [y_1^2 - y_1(1+y_1) \exp(-1/y_1)], \quad (\text{I.13})$$

$$y_1 = \frac{\tau_{\text{es}}^2 \ln(1+4\Theta_e + 16\Theta_e^2)}{\ln(\Theta_e/x_m)}. \quad (\text{I.14})$$

The quantity x_m ($\equiv h\nu_m/m_e c^2$) is the dimensionless photon frequency, above which photons can be scattered into the Wien peak, and is given by

$$a_T = a_{\text{abs}}(x_m) \frac{\tau_{\text{es}}(1+\tau_{\text{es}})}{1 + \tau_{\text{es}}^2 \min(1, 8\Theta_e)}, \quad (\text{I.15})$$

where a_T ($= \sigma_T \rho = \kappa_T \rho$) is the Thomson-scattering coefficient and a_{abs} ($= \kappa_{\text{abs}} \rho$) is the standard frequency-dependent free-free absorption coefficient. For $x \equiv h\nu/m_e c^2 \ll \Theta_e$, a_{abs} becomes

$$a_{\text{abs}} = \left(\frac{r_e}{\alpha_f} \right)^3 \frac{\pi^2}{c} \frac{1}{x \Theta_e} [\dot{n}_{\text{ep}}(x) + \dot{n}_{\text{ee}}(x)], \quad (\text{I.16})$$

where \dot{n}_{ep} and \dot{n}_{ee} are the spectral emissivities for ep-bremsstrahlung and ee-bremsstrahlung, respectively.

For the synchrotron spectrum, which has a strong peak at the critical frequency ν_c , the Comptonization enhancement factor A_{syn}^C , which is defined as the average ratio of the energy of a photon while escaping to its initial energy, is derived by Esin et al.(1996):

$$A_{\text{syn}}^C(\nu_c) = e^{s(A-1)}[1 - P(j_m + 1, As)] + \eta_{\max}P(j_m + 1, s), \quad (\text{I.17})$$

where

$$P(a, x) = \frac{1}{\Gamma(a)} \int_0^x t^{a-1} e^{-t} dt \quad (\text{I.18})$$

and

$$A = 1 + 4\Theta_e + 16\Theta_e^2, \quad s = \tau_{\text{es}} + \tau_{\text{es}}^2, \quad j_m = \frac{\ln(\eta_{\max})}{\ln(A)}, \quad \eta_{\max} = \frac{3k_B T}{h\nu_c}. \quad (\text{I.19})$$

The parameter A is the average increase in energy of a soft photon in each scattering by a Maxwellian distribution of electrons at temperature Θ_e , τ_{es} is the Thomson optical depth, and j_m is the number of scattering required for the maximum possible energy enhancement η_{\max} .

References

- Esin A.A., Narayan R., Ostriker E., Yi I., 1996, ApJ 465, 312
- Mahadevan R., Narayan R., Ostriker E., Yi I. 1996, ApJ 465, 312
- Pacholczyk A.G. 1970, *Radio Astrophysics* (Freeman, San Francisco), §3
- Svensson R. 1984, MNRAS 209, 175

List of Symbols

Symbols	meanings
$(+, -, -, -)$	space-time signature
Greek suffix $\alpha, \beta, \gamma, \dots$	0, 1, 2, 3
Latin suffix i, j, k, \dots	1, 2, 3
(x, y, z)	Cartesian coordinates
(r, φ, z)	cylindrical coordinates
(R, θ, φ)	spherical coordinates
(ϱ, χ)	polar coordinates
A	relativistic correction factor (§3.5)
A, A_i	Schwarzschild discriminant vector [eq. (11.11)]
A, A_ν	albedo
A^C	Compton amplification factor
B	relativistic correction factor (§3.5)
$\mathbf{B} = (B_r, B_\varphi, B_z)$	magnetic flux density
$B = \sigma T^4 / \pi, B_\nu$	(frequency-integrated) blackbody intensity
C	relativistic correction factor (§3.5)
D	denominator (§2.2)
D	relativistic correction factor (§3.5)
D	distance
$D = (1 - \mathbf{n} \cdot \mathbf{v}/c)$	Doppler factor (§6.1)
E	relativistic correction factor (§3.5)
\mathbf{E}, E^i	electric field
E	energy
E, E_ν	(frequency-integrated) radiation energy density
E_{tot}	total energy per unit surface
$E_{\text{mb}}, E_{\text{ms}}$	energy at $r_{\text{mb}}, r_{\text{ms}}$
\dot{E}_{ie}	Coulomb energy-exchange-rate per unit volume
\mathcal{F}	relativistic correction factor (§3.5)
$F^{\mu\nu}$	electromagnetic field tensor
\mathbf{F}, F^i	radiative flux vector
F, F_ν	(frequency-integrated) radiative flux
F_s	surface (emergent) flux
\mathcal{G}	growth rate
G	relativistic correction factor (§3.5)
G	gravitational constant
$G(r)$	torque at radius r (§2.3)
\mathcal{H}	relativistic correction factor (§3.5)
H	disk half-thickness
H	scaleheight
H_0, H_1, H_2, \dots	Hermite polynomials
\Im	imaginary part
I, I_ν	(frequency-integrated) specific intensity
\mathcal{J}	relativistic correction factor (§3.5)
\mathbf{J}	electric current vector
J	total angular momentum (§2.3)
J_d	total disk angular momentum
\mathbf{K}, K_i	external force

Symbols	meanings
K	kinetic energy
K	thermometric conductivity
K_0, K_1, \dots	modified Bessel functions
\mathcal{L}	relativistic correction factor (§3.5)
$L = \sqrt{1 - r_g/r}$	lapse function (§6.1)
L	luminosity
L_\odot	solar luminosity
L_{bol}	bolometric luminosity
L_d	disk luminosity
$L_E = 4\pi cGM/\kappa_{\text{es}}$	Eddington luminosity
L_{\max}	maximum luminosity (of a slim disk) (§10.1)
L_x	X-ray luminosity
M	Mach number
$M^{\mu\nu}$	energy-momentum tensor for magnetic field
M	mass
M_\odot	solar mass
M_\bullet	black-hole mass
M_2	mass of companion star
M_d	disk mass
M_{NS}	mass of neutron star
M_{WD}	mass of white dwarf
M_x	mass of compact object
\dot{M}	mass-flow rate (as function of r)
\dot{M}_{acc}	mass-accretion rate (onto compact object)
$\dot{M}_{\text{crit}} = L_E/c^2$	critical accretion rate
\dot{M}_{in}	mass input rate (into disk)
\dot{M}_{out}	mass output rate (from disk)
\mathcal{N}	numerator (§2.2)
\mathbf{N}, N^i	viscous force
N	polytropic index
N	Brunt-Väisälä frequency (§11.1)
N_r, N_z	Brunt-Väisälä frequency (radial/vertical) (§11.2)
P	period
P^{ij}, P_ν^{ij}	(frequency-integrated) radiation stress tensor
P_{orb}	binary orbital period
\mathcal{Q}	relativistic correction factor (§3.5)
$Q^- = \int q^- dz$	vertically integrated cooling rate
$Q_{\text{adv}}^- = \int q_{\text{adv}}^- dz$	vertically integrated advective cooling rate
$Q_{\text{brems}}^- = \int q_{\text{rad}}^- dz$	vertically integrated bremsstrahlung cooling rate
$Q_{\text{rad}}^- = \int q_{\text{rad}}^- dz$	vertically integrated radiative cooling rate
$Q_{\text{syn}}^+ = \int q_{\text{vis}}^+ dz$	vertically integrated synchrotron cooling rate
$Q^+ = \int q^+ dz$	vertically integrated heating rate
$Q_{\text{vis}}^+ = \int q_{\text{vis}}^+ dz$	vertically integrated viscous heating rate
Q_ν^-	vertically integrated neutrino cooling rate (§10.6)
\mathcal{R}	gas constant
\Re	real part
$R^{\mu\nu}$	energy-momentum tensor for radiation
$R = \sqrt{r^2 + z^2}$	radial distance
R_\odot	solar radius

Symbols	meanings
R_ν	optical depth parameter
R_2	radius of companion star
S	rate-of-strain (§2.1)
S, S_ν	source function
S_ν	observed flux
$T^{\mu\nu}$	energy-momentum tensor of matter
$T_{ij} = \int t_{ij} dz$	vertically integrated viscous stress tensor
T	temperature
T_0, T_c	disk temperature at $z = 0$
T_e	electron temperature
T_{eff}	effective temperature
T_i	ion temperature
T_{in}	temperature at inner radius r_{in}
T_{vir}	virial temperature
$\mathbf{U} = (U_r, U_\varphi, U_z)$	unperturbed velocity vector
U	potential energy
W	total energy flux (§9.2.3)
X	hydrogen abundance
Y	helium abundance
Z	metal abundance
a	binary separation
$a = J/Mc$	black-hole spin parameter
$a_* = a(c^2/GM)$	normalized spin parameter
$a = 4\sigma/c$	radiation constant
$\mathbf{b} = (b_r, b_\varphi, b_z)$	perturbed magnetic field
b	impact parameter
c	speed of light
c_A	Alfvén speed
c_s	adiabatic sound speed
c_T	isothermal sound speed
d	distance
e	specific energy
f, f^i	radiation flux (vector)
$f = 1 - \sqrt{3r_g/r}$	boundary factor
f	(Fourier) frequency
f	fraction of energy dissipated rate in corona (§3.4)
$f = Q_{\text{adv}}/Q_{\text{vis}}^+$	fraction of Q_{adv} to Q_{vis}^+ (§9.2, §10.2)
$f(M)$	mass function
$f = I_\nu/\nu^3$	relativistic invariant
f	variable Eddington factor
$g_{\mu\nu}$	space-time metric
\mathbf{g}, g, g_r, g_z	gravitational acceleration
g_{eff}	effective gravitational acceleration
h	Planck constant
$h = H_1/H_0$	perturbed scaleheight (§4.4)
$h_1 = p_1/\rho_0$	perturbed pressure (§11.2, §11.3)
i	inclination angle
j, j_ν	(frequency-mean) mass emissivity
k, k_i	wavenumber (vector)

Symbols	meanings
k_r	radial wavenumber
k_B	Boltzmann constant
k^μ	four-momentum of photon
l, l^i	direction cosine
ℓ	characteristic length
$\ell = rv_\varphi$	specific angular momentum
ℓ_c	specific angular momentum at r_c
ℓ_{in}	specific angular momentum swallowed
ℓ_K	Keplerian specific angular momentum
ℓ_{mb}	specific angular momentum at r_{mb}
ℓ_{ms}	specific angular momentum at r_{ms}
$\ln \Lambda$	Coulomb logarithm
m	particle mass
m	number of nodes in the φ -direction
$m = M/M_\odot$	normalized mass
m_H	mass of hydrogen atom
m_e	electron mass
m_i	ion mass
m_p	proton mass
$\dot{m} = \dot{M}/\dot{M}_{\text{crit}}$	normalized accretion rate
\mathbf{n}	normal vector
n	number density
$n \propto I_\nu/\nu^3$	photon occupation number
n	dimensionless growth rate
n_e	electron number density
n_i	ion number density
n_p	proton number density
n_+	positron number density
p	pressure
p_0	unperturbed pressure
p_1	Eulerian perturbation of pressure
p_d, p_{deg}	degenerate pressure (§10.6)
p_{gas}	gas pressure
p_{mag}	magnetic pressure
p_{rad}	radiation pressure
p_{tot}	total pressure
δp	Lagrangian variation of pressure
q^μ	heat flux vector
$q = M_2/M_x$	mass ratio
q^-	cooling rate per unit volume
q_{adv}^-	advective cooling rate
q_{rad}^-	radiative cooling rate
q^+	heating rate per unit volume
q_{cond}^+	conductive heating rate
q_{turb}^+	turbulent heating rate
q_{vis}^+	viscous heating rate
r	radius
r_c	critical radius
r_d	disk size

Symbols	meanings
r_E	Einstein-ring radius (§6.5)
$r_g = 2GM/c^2$	Schwarzschild radius
r_H	radius of event horizon
r_{in}, r_{inner}	radius of inner edge
r_{out}, r_{outer}	radius of outer edge
r_{max}	radius where $\kappa = \kappa_{max}$ (§11.3)
r_{mb}	radius of marginally bound circular orbit
r_{ms}	radius of marginally stable circular orbit
r_{ph}	radius of photon orbit
r_{trap}	trapping radius (§10.1)
r_{tr}	transition radius
$\hat{r} = r/r_g$	normalized radius
s	specific entropy
$t^{\mu\nu}$	viscous stress tensor
t_{ij}	viscous stress tensor
$t_{r\varphi}$	$r\varphi$ -component of t_{ij}
t	time
t_{acc}	accretion timescale (§9.4, §10.1)
t_{cool}	cooling timescale (§10.1)
t_{diff}	photon diffusion time in vertical direction (§10.1)
t_{dyn}	dynamical timescale
t_{ff}	free-fall timescale
t_{heat}	heating timescale (§10.1)
$t_{hyd} = H/c_s$	hydrodynamical (hydrostatic) timescale
t_{th}	thermal timescale
t_{vis}	viscous timescale
u^μ	four velocity of matter
$\mathbf{u} = (u_r, u_\varphi, u_z)$	perturbed velocity vector
$u = v_{r1}/(r\Omega)$	perturbed rotational velocity (§4.4)
$\mathbf{v} = (v_r, v_\varphi, v_z)$	velocity vector
v_K	Keplerian velocity
v_c	velocity at r_c
v_{ff}	free-fall velocity
v_g	group velocity
v_{orb}	binary orbital velocity (§6.4)
y	Compton y -parameter
z	(disk) height
z	redshift
Γ	effective adiabatic index
$\Gamma_1, \Gamma_2, \Gamma_3$	generalized specific heat ratios
Δ	variation
$\Theta_e = k_B T_e / m_e c^2$	normalized electron temperature
$\Theta_i = k_B T_i / m_i c^2$	normalized ion temperature
Λ_{ie}	vertically integrated Coulomb coupling rate
$\Pi = \int p dz$	vertically integrated pressure
Π_e	vertically integrated electron pressure
$\Pi_{gas} = \int p_{gas} dz$	vertically integrated gas pressure
Π_i	vertically integrated ion pressure
$\Pi_{mag} = \int p_{mag} dz$	vertically integrated magnetic pressure

Symbols	meanings
$\Pi_{\text{rad}} = \int p_{\text{rad}} dz$	vertically integrated radiation pressure
Π_{ij}	vertically integrated viscous stress tensor
Π_+	vertically integrated positron pressure
$\Sigma = \int \rho dz$	surface density
Σ_e	electron surface density
Σ_i	ion surface density
Φ	viscous dissipation function
Ω	angular speed of rotation
Ω	solid angle
Ω_\perp	vertical epicyclic frequency (§2.5, §11.1)
Ω_c	angular speed at r_c
Ω_K	Keplerian angular speed
Ω_{orb}	(binary) orbital angular speed
α	viscosity parameter
$\alpha_B = c_A^2/c_s^2$	ratio of two wave speeds (§2.4)
$\beta = v/c$	normalized velocity
$\beta = p_{\text{gas}}/(p_{\text{rad}} + p_{\text{gas}})$	ratio of gas to total pressure
$\beta_{\text{mag}} = p_{\text{gas}}/p_{\text{mag}}$	plasma beta
$\gamma = (1 - v^2/c^2)^{-1/2}$	Lorentz factor
γ	specific heat ratio, adiabatic index
$\gamma_{ij} = -g_{ij}$	three-dimensional part of space-time metric
δ_{ij}	Kronecker's delta
δ	Lagrangian variation
$\epsilon = \varepsilon/\rho - c^2$	internal energy per unit mass
ϵ	energy-dissipation rate
ϵ_e	internal energy of electron per unit mass (§7.3)
ϵ_i	internal energy of ion per unit mass (§7.3)
$\epsilon = \rho c^2 + \rho \epsilon$	internal energy per unit proper volume
η	dynamical viscosity
η	energy-conversion efficiency (§1.1)
η	magnetic diffusivity
$\eta_\nu = j_\nu \rho$	volume emissivity
ζ	bulk viscosity
θ	polar angle
θ_E	apparent Einstein-ring radius (§6.5)
κ	epicyclic frequency
$\bar{\kappa}$	(frequency-mean) total opacity
κ_{es}	electron scattering opacity
$\kappa_{\text{ff}} = \kappa_0 \rho T^{-3.5}$	free-free opacity
κ_{max}	maximum epicyclic frequency
κ_ν	total opacity, (mass) absorption coefficient
κ_ν^{abs}	absorption opacity
κ_ν^{sca}	scattering opacity
$\kappa_0 = \kappa_0^{\text{abs}} + \kappa_0^{\text{sca}}$	(frequency-mean) total opacity [†]
$\kappa_0^{\text{abs}}, \kappa_{\nu 0}^{\text{abs}}$	(frequency-mean) absorption opacity [†]
$\kappa_0^{\text{sca}}, \kappa_{\nu 0}^{\text{sca}}$	(frequency-mean) scattering opacity [†]
λ	eigenvalue
λ	wavelength

[†] measured in the comoving frame

Symbols	meanings
λ_e	emitted wavelength (§3.2)
λ_ν	flux limiter
μ	direction cosine
μ	parameter ($t_{r\varphi} = -\alpha p_{\text{gas}}^\mu p^{1-\mu}$)
$\bar{\mu}$	mean molecular weight
$\nu = \eta/\rho$	kinematic viscosity
ν	(photon) frequency
ν_e	emitted (photon) frequency (§6.3)
ν_{turb}	turbulent viscosity
$\xi = (\xi_r, \xi_\varphi, \xi_z)$	Lagrangian displacement
ξ	dimensionless entropy gradient [eq. (7.40)]
ξ_1	correction factor for r_{in} (§3.2.6)
ξ_2	correction factor for T_{in} (§3.2.6)
$\varpi = \Pi_1/\Pi_0$	perturbed pressure (§4.4)
$\varpi = p_1/p_0$	perturbed pressure (§9.4)
$\rho = mn$	density
ρ_0	unperturbed density
ρ_1	Eulerian perturbation of density
$\sigma = ac/4$	Stefan-Boltzmann constant
$\sigma = \rho_1/\rho_0$	perturbed density (§4.4, §9.4)
σ_e	electric conductivity
σ_T	Thomson scattering cross section
τ, τ_ν	optical depth
$\tau_* = \sqrt{(\tau_{\text{es}} + \tau_{\text{ff}})\tau_{\text{ff}}}$	effective optical depth
φ	azimuthal angle
ϕ_ν	scattering redistribution function
χ	ionization degree
$\chi_\nu = \kappa_\nu \rho$	volume absorption coefficient
$\psi < 0$	gravitational potential
ψ_{eff}	effective potential
ω	angular frequency of waves
ω	vorticity (§2.1)
ω_p	precession frequency (§12.3)
$\tilde{\omega} = \omega - m\Omega$	angular frequency of waves (§11.1)

INDEX

- 1/f fluctuation 325
 3C catalogue 6
- A**
- accretion-disk corona (see also disk corona) 138-139
 accretion flow
 advection-dominated [ADAF] 12, 44, 49, 242, 274, 283-284, 288, 291, 293, 295-296, 298-302, 306-309, 312, 314, 316, 318-324, 326-327, 335, 338, 341-342, 346
 convection-dominated [CDAF] 320-324, 327, 404
 MHD 324-325, 327-329
 neutrino-dominated [NDAF] 370, 374-375
 radiatively inefficient [RIAF] 12, 49, 283, 288, 298, 320, 324-325, 327, 329, 348, 404
 supercritical 333, 335, 346, 350, 364-368
 super-Eddington 333
 accretion torus 138
 acoustic oscillation 161, 382-383, 385, 398, 403, 406, 410-411, 426-427, 430, 432-433, 435-436, 438-439, 458
 acoustic wave 271, 318-319, 383, 385, 387, 397-398, 400-401, 404-405, 428-429
 active galactic nuclei [AGN] 17-19, 39, 41-44, 46-47, 49, 59, 72-73, 119, 125, 133, 137-139, 141, 143, 161, 221, 229, 298, 320, 381, 419
 active galaxy 13, 39, 41, 43, 125
 ADAF (see advection-dominated accretion flow)
 ADIOS 320, 328
 advection
 -dominated accretion flow [ADAF] 12, 44, 49, 242, 274, 283-284, 288, 291, 293, 296, 298-302, 306-309, 312, 314, 316, 318-324, 326-327, 335, 338, 341-342, 346
 -dominated disk 133, 240, 249, 253, 284, 289-292, 294, 298, 302, 307-309, 311, 313-315, 317-318, 354, 402
 advective
 cooling 177-178, 246-247, 256, 272, 283-286, 291, 293, 305, 308, 312, 335-337, 339, 348-349, 354, 358, 370, 373, 533, 535
 energy transport [.... heat transport] 12, 178, 237, 242, 335, 344, 354, 365, 371, 373
 heating 242, 304
 motion 226, 237
 Alfvén speed 76, 78, 81, 140, 534
 alpha disk [α disk, α model] 12, 97, 103, 115, 117, 163, 177, 180, 206, 263, 272, 292, 342, 425, 431
 angular-momentum barrier 260
- B**
- Balmer lines 7, 45, 221
 Bernoulli
 constant 62, 296
 equation 62-63
 parameter 296
 theorem 296
 big blue bump [BBB] 44, 298
 BL Lac object 39-40
 black hole binary [BHB] 17-19, 30-33, 119, 122, 138, 141, 161, 196, 284, 301, 320, 346, 353, 420, 422, 433, 450, 458
 black hole shadow 217, 258
 black hole silhouette 215
 blackbody radiation 106, 117-118, 218, 350, 489
 blazar 40, 43
 Bondi accretion [Bondi-type accretion] 61, 260, 262, 264
 Boussinesq approximation 77
 Boyer-Lindquist coordinates 466
 bremsstrahlung 240, 250-251, 253-254, 285, 288, 302-303, 307, 318, 323-324, 327, 329, 371, 528-531, 533
 Brunt-Väisälä frequency 77, 387-388, 392, 533
 buoyancy 77, 79-80, 139, 386-388, 394, 404
- C**
- canonical form 396

cataclysmic variable [CV] 18-19, 21-28, 125, 127, 129, 196, 200, 206, 410, 417-418, 420
 causality 426, 497
 CDAF (see convection-dominated accretion flow)
 classical T-Tauri star [CTTS] 19-20
 closure relation 130, 491-492, 494, 507-510, 514
 coherent scattering 122, 124
 comoving frame 146, 152, 230, 284, 486, 501-505, 508-511, 513-514, 520, 537
 Compton
 bump 298
 cooling 285, 288, 303, 305
 process 42, 123, 135, 250, 253-255, 302-303, 529-530
 y parameter 124, 137, 141, 536
 unsaturated 134, 137
 Comptonization 122, 124-125, 137, 141, 447, 530-531
 conductivity 197, 240, 291, 315, 480, 486, 493, 517, 521, 533, 538
 convection [convective]
 -dominated accretion flow [CDAF] 320-324, 327, 404
 instability 186, 391
 motion 186, 321, 387-388, 456
 corona
 accretion disk 138-139
 solar 139, 141
 corotation 398
 corrugation wave (mode) [c-mode] 384-388, 399, 401-403, 405, 407-411, 415, 436, 438, 440, 446
 Coulomb coupling 242, 251, 303-305, 536
 critical
 accretion rate 50, 114, 342, 429, 533
 point 62-66, 172, 259-262, 264-265, 267-279, 343, 346, 423-428, 457
 point, center-type 265
 point, nodal-type 265, 268-270, 274-275, 423, 425-427
 point, saddle-type 265, 268-269, 273, 275, 423-425, 428
 point, spiral-type 267, 269
 radius 63, 84, 242, 259-260, 262-266, 269-271, 275, 288, 297, 303, 342-343, 345, 535

D

diffusion approximation 129, 362-363, 492, 497
 discoseismology 381, 395
 disk blackbody [DBB] (model) 15, 30, 33, 119, 121, 206, 218, 351-353, 360, 364
 disk corona 133, 138, 143, 228, 324
 disk-like accretion flow [disk-type accretion] 262, 264
 Doppler
 effect 125, 128, 211, 213, 215-216, 218, 221, 225, 368, 502
 effect, longitudinal 213-214
 effect, transverse 213
 double-peaked line 25-26, 221
 dwarf nova [DN] 22-23, 28, 174, 183-186, 190-191, 193, 198, 200, 202, 205-206, 354-358, 402, 407, 417-418, 433
 dwarf-nova-type instability 185, 356-358, 402

E

Eddington
 approximation 130-131, 231, 491, 494, 508-509
 factor 230-231, 495-496, 509, 514, 534
 luminosity 44, 49, 57-61, 111, 115, 341, 363, 369, 533
 timescale 60
 super-.... accretion flow 333
 super-.... luminosity 61
 effective adiabatic index 277, 524, 526, 536
 effective potential 83, 213, 538
 efficiency 4-5, 9, 11, 15, 17, 23, 59, 82, 85, 108, 186, 290, 334, 340, 363-364, 474-475, 537
 energy-conversion 4, 15, 23, 59, 290, 334, 363, 537
 electric conductivity 517, 521, 538
 electron-positron annihilation line 125
 electron-positron pair 230, 251, 371
 energy-dissipation rate 537
 energy-momentum tensor 152, 484, 486, 502, 504, 511, 520-521, 533-534
 epicyclic frequency 85-86, 91-92, 178, 382-385, 391, 393, 398, 400, 404, 407, 409, 427-428, 436, 442, 454-455, 473, 537

- vertical 91-92, 382, 384-385, 398, 409, 436, 454-455, 537
 equipotential surface 154-156
 evaporation 140-142, 299
 excitation 411, 414, 433-434, 456, 458
 exponential decay 30, 35, 200-203
 extended disk blackbody model 121, 353
 extreme Kerr hole 466, 474
- F**
- Fe fluorescence line 125
 Ferraro's isorotation law 75
 flickering 24
 flux-limited diffusion [FLD] 363, 365, 367, 496-497
 four-momentum of photon 501, 535
 four-velocity 145, 152, 277, 468, 485-486, 501, 510, 513, 520, 523, 536
 frequency
 Brunt-Väisälä 77, 387, 392, 533
 epicyclic 85-86, 91-92, 178, 382-385, 391, 393, 398, 400, 404, 407, 409, 427-428, 436, 442, 454-455, 473, 537
 vertical epicyclic 91-92, 382, 384-385, 398, 409, 436, 454-455, 537
 fundamental mode 81, 383, 385, 397, 399, 405, 435
 funnel 61, 156
- G**
- galaxy
 active 13, 39, 41, 43, 125
 broad-line radio 40
 narrow-line radio 40
 narrow-line Seyfert 1 galaxy [NLS1] 333, 364-365
 radio 8, 39-40, 222
 Seyfert [Seyfert 1, Seyfert 2] 39-41, 45, 143, 222, 333, 364-365
 starburst 39, 41
 gamma-ray burst [GRB] 3, 229, 231, 333, 369-371, 508
 geometrical effect 24, 402
 gravitational
 energy 3-5, 9-12, 16-17, 23, 67, 108, 133, 139, 345, 370, 475
 focusing 215, 217, 225-226
 microlensing 226
 redshift 7, 82, 211, 213, 215, 218-219
 gravity wave (mode) [g-mode] 384, 386-387, 389, 398-399, 401-404, 411, 415, 432, 436, 438-439, 441, 444-446, 450, 454, 458
 gray approximation 130, 498-499
 group velocity 427-428, 432, 438-440, 536
- H**
- hard state (see also low state) 33, 35-36, 49, 301, 306, 316, 320, 422, 446
 high state (see also soft state) 33, 35-36, 138, 360, 422, 434, 446, 457
 high-mass X-ray binary [HMXB] 27-28, 31, 34
 highly polarized quasar [HPQ] 40
 hot spot 24, 224-226
 hydrogen line 125
- I**
- induction equation 516-520, 522
 inertial-acoustic wave (mode) 383, 387-388, 397, 399-400, 402, 405
 inner edge 13-14, 82, 84, 104, 110, 118-120, 122, 151, 154, 156, 189, 206, 211-212, 215, 217, 242, 297-298, 320, 339, 345-346, 348, 351, 360-363, 399-400, 427, 474, 536
 instability
 convective 186, 391
 dwarf-nova-type 185, 356-358, 402
 magnetic 57, 74, 78
 magnetic Rayleigh-Taylor 80
 magneto-rotational [MRI] 73-78, 80, 324, 388, 432
 mass-overflow 184
 nonlinear 73
 Parker 74, 78-81
 pulsational 414
 secular 161-163, 165-167, 169, 171-175, 194
 thermal 136, 161, 168-174, 190, 195-196, 206-207, 280, 301, 307-310, 313, 320, 354, 402
 thermal-ionization 183-185
 tidal 433
 viscous 162
 viscous oscillatory 427
 intermediate-mass black hole [IMBH] 18-19, 39, 353, 465
 irradiated disk 118-119

irradiation 144, 184, 196, 201, 204, 206-
208
iso-redshift contour 126, 220
isovelocity contour 126-127, 220

J

Joule heating 518, 523

K

Keplerian
.... angular momentum (velocity) 84, 154, 244-245, 273, 407, 537
.... disk 66, 72-73, 76, 81, 224-226, 272, 322, 383-384, 401, 404, 406-408, 434, 439
.... velocity 97, 134, 326, 536
Kerr metric 84-86, 88, 298, 397, 436, 442, 465-466, 470, 508, 510
Kompaneets equation 136

L

Lagrange point 22
lapse function 213, 533
l'Hospital theorem 272
limit cycle (behavior) 185-186, 190, 194-197, 207, 354
line
.... Balmer 7, 45, 221
.... double-peaked 25-26, 221
.... electron-positron annihilation 125
.... Fe fluorescence 125
.... hydrogen 125
local approximation 178, 395, 397-398, 435-437
local thermodynamic equilibrium [LTE] 492, 494
locally inertial observer 468-469
locally non-rotating frame 469
longitudinal Doppler effect 213
Lorentz factor 36, 213-214, 277, 328, 472, 513, 537
low-ionization nuclear emission-line re-gion [LINER] 41
low-luminosity AGN [LLAGN] 39, 41, 44, 49, 320
low-mass X-ray binary [LMXB] 27-31, 183, 206, 417-418, 421-423, 433, 446
low state (see also hard state) 33, 73, 320
luminosity-temperature diagram [L-T diagram] 351-352, 365

M

$\dot{M}-\Sigma$ diagram [$\dot{M}-\Sigma$ plane] 114-116, 136, 172-174, 183, 194, 284, 286, 289, 337-339, 341-342, 355
Mach number 64, 260, 262, 277-278, 533
magnetic
.... diffusivity 517, 537
.... flux density 516, 521, 532
.... tower [jet] 326
magnetohydrodynamics [MHD] 73, 140, 280, 324-329, 432, 516-518, 520-523
marginally bound orbit 298, 474
marginally stable orbit 87, 471, 473-474
marginally stable radius 84, 145, 147, 211
mass emissivity 130, 490, 499, 505, 534
mass function 31, 34, 38, 534
maximally rotating black hole 402, 467
Maxwell stress tensor 75
mean molecular weight 148, 166, 240, 481, 518, 538
MHD (see magnetohydrodynamics)
.... accretion flow 324-325, 327-329
.... approximations 73, 516-518, 522-523
microquasar 30, 35, 38-39, 229, 333, 359
minimum energy configuration 69
minimum energy state 67, 97
mode (see also oscillation, wave)
.... corrugation [c-....] 384, 386-388, 399, 401-403, 410-411, 415, 436, 438, 440, 446
.... gravity [g-....] 386-387, 389, 398-399, 401-404, 411, 415, 432, 436, 438-439, 441, 444-446, 450, 454, 458
.... inertial-acoustic [p-....] 383, 385-389, 399-403, 410, 436, 438, 440-441, 446
.... vertical acoustic [vertical p-....] 385-388, 436, 438, 440-441, 446
modified blackbody 123-124
moment equation 130-131, 230, 490-491, 498, 505-509, 514
multi-color [disk, spectrum] 15, 110, 118-119, 218, 351
multiple sonic point 279

N

- narrow-line Seyfert 1 galaxy [NLS1] 333, 364-365
 NDAF (see neutrino-dominated accretion flow)
 negative diffusion 163
 neutrino-cooled disk 370, 374
 neutrino-dominated accretion flow [NDAF] 370, 374-375
 neutrino trapping 371, 373
 neutron star [NS] 5, 11, 13, 18-19, 27-33, 36, 208, 211, 215, 217-218, 229, 261, 276-278, 334, 370-371, 417-418, 420-422, 443, 450-451, 453, 456, 458, 532-533
 node 66, 268, 273-274, 383-385, 387-389, 396, 435-436, 441, 535
 nova 13, 22-23, 28, 30-31, 35, 174, 183-186, 190, 198, 200-201, 205-206, 294, 354, 356-358, 370, 402, 407, 417, 433

O

- one-zone approximation 98, 104-106, 185-186
 opacity
 bound-free 107, 122, 148, 240
 electron scattering 59, 122-123, 148, 493, 537
 free-free 107, 122, 148, 240, 537
 Rosseland-mean 106, 185, 207, 480, 493
 optically-thin two-temperature disk 302
 optically violent variable [OVV] 40
 oscillation (see also wave)
 of torus 454, 458
 acoustic 161, 382-383, 385, 398, 403, 406, 410-411, 426-427, 430, 432-433, 435-436, 438-439, 458
 axisymmetric 389, 399, 413
 inertial 382-383, 397
 inertial-acoustic 383, 385, 398, 403, 406, 410-411, 426-427, 430, 432-433, 435-436, 438-439, 458
 limit-cycle(see also limit cycle) 185-186, 194-197, 207, 354
 non-axisymmetric 389-390, 399
 one-armed 389, 405, 407, 433, 444, 446-449
 relaxation 183, 195, 354
 trapped 401-402
 overstability 413
 overtone 385, 388, 396, 435, 457

P

- p-mode 383, 385-389, 399-401, 403, 410, 436, 438, 440-441, 446
 vertical 385-387, 436, 438, 440-441, 446
 Paczyński-Wiita potential 87-89, 91
 phase-mixing 404
 photohydrodynamics 500
 photon orbit 473, 536
 photon trapping 49, 333-335, 361-365, 367
 Planck distribution 489
 plane-parallel 129-130, 132, 187, 363, 366, 494-496, 498, 510, 513
 polar 22-23, 27-28, 87, 130, 211, 213-214, 228, 368-369, 466, 499, 532, 537
 Polish doughnut 12, 152
 polytropic relation 62, 244, 348, 524
 power spectrum 39, 421, 430
 precession 36-38, 222, 406-407, 410, 435, 443-446, 450-454, 458, 538
 pressure
 -driven 156, 274, 298, 456
 -gradient force 145, 154, 241, 298, 308-309
 stress tensor 229, 486
 propagation diagram 403
 pseudo-Newtonian potential 82, 86-87, 91, 152, 243, 272, 344, 382, 393, 397-398, 465

Q

- Q-T* plane 116
 quasar [QSO] 4, 6-11, 13-14, 16-17, 30, 35, 38-40, 42-44, 222, 227, 229, 333, 359
 broad absorption line [BAL] 40
 highly polarized [HPQ] 40
 radio-loud 40, 44, 222
 radio-quiet 40
 quasi-periodic oscillation [QPO] 39, 381, 410, 417-423, 427, 429, 431-434, 442-443, 446-451, 453-454, 456-458
 hectohertz [hHz QPO] 418-421, 454
 high-frequency [HF QPO] 417-423, 433-434, 446, 449-450, 457-458
 kHz [kHz QPO] 417-423, 450-451
 low-frequency [LF QPO] 410, 418, 422
 quasi-stellar radio source [QSS] 40

R

radiation

- drag 229-230, 513
- hydrodynamics [RHD] 365-366, 500, 508
- pressure 57-58, 61, 102, 106, 108, 115-116, 163-164, 166, 168, 170, 231, 240-242, 244, 247-249, 335-336, 339, 343-344, 354-355, 365, 367, 371, 373-374, 426, 451, 478-479, 510, 513, 535, 537
- stress tensor 130, 499, 503-504, 510, 533

radiative diffusivity 250

radiative flow 230-231

radiative transfer equation 130-131, 505

radiatively inefficient accretion flow [RIAF] 12, 49, 283, 288, 298, 320, 324-325, 327, 329, 348, 404

radio galaxy [RG] 8, 39-40, 43-44, 222

ray-tracing method 211-213, 215, 220

Rayleigh criterion 74

regularity condition 63, 242, 259, 263-264, 271-272, 297, 303, 342, 424

relativistic

- Maxwell equation 520
 - Maxwell-Boltzmann distribution 524
 - Rankine-Hugoniot relation 276
- relaxation oscillation 183, 195, 353-354
- resonance 433-434, 436-442, 444-446, 450-451, 454, 456, 458
- epicyclic 454, 458
- horizontal 437-442, 444-446, 450, 454, 458
- parametric 433, 454
- vertical 437-439, 441, 444-446, 450

restoring force 75, 80, 91, 381-388, 392, 397-399, 404, 406, 409, 412

returning radiation 144

RIAF (see radiatively inefficient accretion flow) 12, 49, 283, 288, 298, 320, 324-325, 327, 329, 348, 404

Roche overflow 22, 24

Rosseland approximation 492, 494-495

S

S-curve [S-shaped] 183, 186, 190, 195, 208, 337-344, 353-359

scattering albedo 494

scattering probability function 490

Schwarzschild

- black hole 16, 86, 151, 211-212, 214-216, 465
- discriminant vector 391, 532
- metric 82, 85-87, 89, 153, 393, 398, 436, 439-440, 442, 455, 466, 484, 510
- radius 14, 57, 82, 84, 87, 111, 113, 141, 212, 217, 227, 243, 277, 290, 328, 342, 390, 457, 466, 485, 536

self-similar model 293, 295, 321

Seyfert galaxy [Sy 1, Sy 2] 40-41, 44, 143, 222

Shakura-Sunyaev disk [SSD, Shakura-Sunyaev model] 12, 103-104, 108, 120, 164, 237, 298-301, 319, 335, 337, 342

shear stress 98, 102, 107, 146, 188, 472

shock 36, 41, 262, 265, 276-280, 428, 431

multiple 279

stability of 279

slim disk 12, 49, 118, 216, 224, 274, 291, 308, 333, 335, 338, 340-342, 344-350, 352-353, 355, 358, 361-364, 366-367, 369, 372, 533

soft state (see also high state) 33, 36, 49, 119-120, 422, 434, 446, 457

soft X-ray excess 125

soft X-ray transient [SXT] 28, 30, 34-36, 119, 125, 174, 306

soft-hard transition 34

solar wind 61, 65, 274

sonic point [radius] 63, 66, 241-242, 259-260, 264, 269, 272, 274-275, 279, 296-298, 318-319, 355, 400, 423-428, 431

source function 133, 493-494, 534

space-time metric 465, 484-485, 500, 520, 534, 537

spectral energy distribution [SED] 19, 42, 44, 138, 143, 326, 328, 362

spectrum

blackbody 15, 30, 33, 106, 110, 119, 122-124, 206, 218-220

disk blackbody 119, 206, 218

modified blackbody 123-124

power 39, 421, 430

- spin parameter 15, 87, 92, 145, 152, 402, 443, 450-452, 457, 466-467, 471, 473, 534
 starburst [SB] 39, 41
 static limit 467-468, 473
 stationary observer 468
 super-Eddington accretion flow 333
 supercritical accretion flow 333, 335, 346, 350, 364-368
 superhump 407, 410, 433
 supermassive black hole [SMBH] 8, 11, 18-19, 43-44, 46, 49, 59, 114, 217, 226-227, 419, 465
 supersoft X-ray source [SSXS] 19, 22-24, 26-27, 125
 synchrotron 42, 141, 240, 253, 285, 288, 303, 305, 307, 324, 326, 328, 528-531, 533
 cooling 250, 254, 302, 304, 529, 533
 emission 254-255, 307, 324, 326, 529-530

T
T- Σ plane 172-174, 274, 288-289, 308, 339-340, 353-357
 terminal speed 229-230
 thermal
 conductivity 486
 -equilibrium curve 114-115, 190, 192-193, 207-208, 373
 instability 136, 161, 168-174, 190, 195-196, 206-207, 280, 301, 307-308, 310, 313, 320, 354, 402
 Thomson scattering 122, 505, 530, 538
 tidal instability 433
 timescale [time]
 accretion 190, 298, 318, 320, 334, 339, 341, 350, 536
 diffusion 106, 200, 203,
 dynamical 98, 169, 238, 309, 418, 536
 Eddington 60
 hydrostatic 98, 536
 photon diffusion 334, 341
 thermal 98, 106, 161, 168, 190, 194, 308-309, 536
 viscous 72-73, 98, 101-102, 136, 161-162, 165, 194, 201, 203, 238, 307-308, 536
 topology 241, 259-260, 264-265, 267-268, 272-274, 423-425
 torque 71, 100-101, 104, 297, 322, 343, 444, 451, 532
 torus 12, 41, 43, 61, 138, 152, 154-156, 326, 374, 447-448, 454, 457-458,
 inner 138
 relativistic 152
 total-energy flux 299-300
 transfer equation 130-131, 489-491, 493, 495, 497-499, 504-506, 508-509, 513-514
 transonic
 [accretion] flow 61, 242, 260-265, 267, 271, 274, 276, 278, 354, 423
 nature 147, 237, 241, 296, 417
 point 63, 66, 269, 423
 transverse Doppler effect 213
 trapping
 radius 334, 339, 362, 536
 neutrino 371, 373
 photon 49, 333-335, 361-365, 367
 wave 384, 399-400, 402
 turbulence
 hydromagnetic 73, 241
 magnetic 302
 turbulent
 conduction 240, 291-292
 kinematic viscosity 197, 240, 315
 viscosity 72, 107, 314, 322, 411-412, 538
 two-temperature disk 251, 271, 302-303, 305-307

U
 ultra-luminous X-ray source [ULX] 18-19, 27, 38-39, 333, 352-353
 UV bump 42, 44

V
 vertical p-mode 385-387, 436, 438, 440-441, 446
 very high state 35-36, 138, 422, 434, 446, 457
 virial 133, 135, 242, 284, 289, 296, 303, 534
 virial temperature 242, 284, 289, 303, 534
 viscosity
 bulk 477, 486, 537
 diffusion-type 263, 432

dynamical 70, 477, 486, 537
 kinematic 70, 99, 101, 197, 201,
 240, 315, 538
 turbulent 72, 107, 314, 322,
 411-412, 538
 turbulent kinematic 197, 240,
 315
-driven 156, 274, 298
 parameter 107, 148, 198, 349,
 355, 359, 537

viscous
 accretion flow 263
 diffusion 67, 100-102, 134, 200-
 201, 203
 dissipation function 480, 483,
 537
 -heating rate 105, 108, 114, 130,
 190, 239, 253, 305, 349, 362, 480,
 498, 512, 514
 stress 99, 103, 147, 163, 175,
 238, 248, 412-413, 431, 477, 482,
 486, 534, 536-537
 vorticity 61, 538

W

warp 409-410, 433-437, 443-444, 446,
 450-452, 458
 warped disk 434-435, 444, 458
 water maser 44, 47
 wave (see also oscillation)
 acoustic 271, 318-319, 383- 385,
 387, 397-398, 400-401, 404-405, 428-
 429
 corrugation 384-388, 399, 405,
 407-410
 gravity 384, 386-387, 398, 401,
 432, 439
 inertial-acoustic 383, 387, 397,
 400, 405
 one-armed 397
 surface gravity 384
 torsional 388
 transition 197, 200, 357-359,
 402
 vertical acoustic 385
 reflection 317-319, 427
 weak-line T-Tauri star [WTTS] 19-20
 wind equation 63-65

X

X-ray

.... binary, high-mass [HMXB] 27-
 28, 31, 34
 binary, low-mass [LMXB] 27-
 31, 183, 206, 417-418, 421-423, 433,
 446
 burster 27-28
 excess, soft 125
 nova [XN] 28, 30, 35, 183-184,
 196, 198, 200, 208, 355, 407
 pulsar 27-28
 transient, soft [SXT] 28, 30,
 34-36, 119, 125, 174, 306

Y

young stellar object [YSO] 18-19

Z

zero-age main sequence [ZAMS] 19-20

 α -viscosity 269, 273, 303, 424, 428, 432
 ϵ -mechanism 412, 414
 viscous 414
 κ -mechanism 414

Credits with Kind Permissions

Fig. G.2 courtesy of R. Takahashi Copyright ©; **Fig. G.10** courtesy of Y. Kato Copyright ©; **Fig. G.12** courtesy of K. Watarai Copyright ©; **Fig. G.13** courtesy of K. Ohsuga Copyright ©

Fig. 1.2 courtesy of T.T. Takeuchi and T.T. Ishii **Fig. 1.4** from figs. 2 and 4 of Türler M. et al. 1999, A&Ap Supl. 134, 89 Copyright ©; **Fig. 1.10** illustrated by M. Uezono and M. Toshiyoshi; **Fig. 1.11** from fig. 2 of Lada C.J. 1987, in *Star Forming Regions*, IAU Symp No.115, ed. M. Peimbert, J. Jugaku, p1 (with kind permission from Kluwer Academic Publishers) Copyright ©; from figs. 1, 2, and 3 of Shu F.H., Adams F.C. 1987, in *Circumstellar Matter*, IAU Symp No.122, ed. I. Appenzeller, C. Jordan, p7 (with kind permission from Kluwer Academic Publishers) Copyright ©; **Fig. 1.12** courtesy of N. Kaifu; **Fig. 1.14** illustrated by M. Uezono and M. Toshiyoshi; **Fig. 1.15** from fig. 2 of Warner B. 1976, in *Structure and Evolution of Close Binary Systems*, IAU Symp. No. 73, eds. P. Eggleton, S. Mitton, J. Whelan, p85 (with kind permission from Kluwer Academic Publishers) Copyright ©; **Fig. 1.16** from fig. 2 of Knigge C., Long K.S., Blair W.P., Wade R.A. 1997, ApJ 476, 291 (reproduced by permission of the AAS) Copyright ©; **Fig. 1.17** courtesy of M. Uemura; **Fig. 1.18** from fig. 1 of Alcock C. et al. 1997, MNRAS 287, 699 (reproduced by permission of Blackwell Publishing) Copyright ©; **Fig. 1.20** from fig. 11 of Parmer A.N., White N.E., Giommi P., Gottwald M. 1986, ApJ 308, 199 (reproduced by permission of the AAS) Copyright ©; **Fig. 1.21** from fig. 4 of Mitsuda K., Inoue H., Koyama K., Makishima K., Matsuoka M., Ogawara Y., Shibasaki N., Suzuki K., Tanaka Y., Hirano T. 1984, PASJ 36, 741 Copyright ©; **Fig. 1.22** illustrated by M. Uezono and M. Toshiyoshi; **Fig. 1.23** courtesy of S. Kitamoto Copyright ©; **Fig. 1.24** from fig. 1 of Gierliński M., Zdziarski A.A., Poutanen J., Coppi P.S., Ebisawa K., Johnson W.N. 1999, MNRAS 309, 496 (reproduced by permission of Blackwell Publishing) Copyright ©; **Fig. 1.27** from fig. 2 of Kaluzienski L.J., Holt S.S., Boldt E.A., Serlemitsos P.J. 1977, ApJ 212, 203 (reproduced by permission of the AAS); from fig. 20 of Tanaka, Y. 1992, Ginga Memorial Symp., ed. F. Makino, F. Nagase (ISAS, Sagamihara), p19 Copyright ©; **Fig. 1.28** from fig. 7 of Fender R.P., Belloni T.M., Gallo E. 2004, MNRAS 355, 1105 (reproduced by permission of Blackwell Publishing) Copyright ©; **Fig. 1.31** courtesy of A. Cherepaschuk Copyright ©; **Fig. 1.33** illustrated by M. Uezono and M. Toshiyoshi; **Fig. 1.34** from fig. 10 of Lichti G.G., Balonek T., Courvoisier T.J.-L., Johnson N., McConnel M. McNamara B., von Montigny C., Paciesas W., Robson E.I., Sadun A., Schalinski C., Smith A.G., Staubert R., Steppa H., Swanenburg B.N., Turner M.J.L., Ulrich M.-H., Williams O.R. 1995, A&A 298, 711 Copyright ©; **Fig. 1.35** from fig. 1 of Chen K., Halpern J.P. 1989, ApJ 344, 115 (reproduced by permission of the AAS) Copyright ©; **Fig. 1.36** from fig. 2 of Tanaka Y., Nandra K., Fabian A.C., Inoue H., Otani C., Dotani T., Hayashida K., Iwasawa K., Kii T., Kunieda H., Makino F., Matsuoka M. 1995, Nature 375, 659 (with kind permission from Macmillan Magazines Ltd.) Copyright ©; **Fig. 1.37** from fig. 1 of Ford H.C., Harms R.J., Tsvetanov Z.I., Harfig G.F., Dressel L.L., Kriss G.A., Bohlin R.C., Davidsen A.F., Margon B., Kochhar A.K. 1994, ApJ 435, L27 (reproduced by permission of the AAS) Copyright ©; **Fig. 1.38** from fig. 1 of Jaffe W., Ford H.C., Ferrarese L., van den Bosch F., O'Connel R.W. 1993, Nature 364, 213 (with kind permission from Macmillan Magazines Ltd.) Copyright ©; **Fig. 1.39** from fig. 3 of Miyoshi M., Moran J., Herrnstein J., Greenhill L., Nakai N., Diamond P., Inoue M. 1995, Nature 373, 127 (with kind permission from Macmillan Magazines Ltd.) Copyright ©; **Fig. 1.40** from fig. 2 of Schödel R., Ott T., Genzel R. et al. 2002, Nature 419, 694 (with kind permission from Macmillan Magazines Ltd.) Copyright ©

Fig. 2.3 illustrated by M. Uezono and M. Toshiyoshi **Fig. 2.7** from fig. 1 of Balbus S.A., Hawley J.F. 1991, ApJ 376, 214 (reproduced by permission of the AAS) Copyright ©; **Fig. 2.15** from fig. 1 of Perez C.A., Silbertgleit A.S., Waggoner R.V., Lehr D.E. 1997, ApJ 476, 589 (reproduced by permission of the AAS) Copyright ©

Figs. 3.5–3.6 illustrated by T. Kawaguchi; **Figs. 3.8** from fig. 1 of Mineshige S., Hirano A., Kitamoto S., Yamada T.T., Fukue J. 1994, ApJ 426, 308 (reproduced by permission of the AAS) Copyright ©; **Fig. 3.13** from fig. 2 of Fukue J., Akizuki C. 2006, PASJ 58, 1039 Copyright ©; **Fig. 3.17** from fig. 5 of Liu B.F., Mineshige S., Ohsuga K. 2003, ApJ 587, 571 (reproduced by permission of the AAS) Copyright ©; **Figs. 3.19–3.21** from figs. 1–3 of Abramowicz M., Jaroszyński M., Sikora M. 1978, A&A 63, 221 Copyright ©

Fig. 4.1 illustrated by Yamasaki T.; **Figs. 4.2, 4.3** illustrated by Ideta M.; **Fig. 4.4** illustrated by Yamasaki T.

Fig. 5.1 courtesy of E. Kawazoe; **Fig. 5.2** from fig. 1 of Cannizzo J.K., Wheeler J.C. 1984, ApJS 55, 367 (reproduced by permission of the AAS) Copyright ©; **Figs. 5.3, 5.4** from figs. 3 and 2 of Mineshige S., Osaki Y. 1983, PASJ 35, 377 Copyright ©; **Fig. 5.6** from figs. 1 and 2 of Mineshige S. 1987, ApSS 130, 331 (with kind permission from Kluwer Academic Publishers) Copyright ©; **Fig. 5.7** from fig. 10 of Mineshige S., Wheeler J.C. 1989, ApJ 343, 241 (reproduced by permission of the AAS) Copyright ©; **Fig. 5.8** from fig. 1 of Mineshige S. 1994, ApJ 431, L99 (reproduced by permission of the AAS) Copyright ©; **Fig. 5.9** from fig. 1 of Mineshige S., Kim S.-W., Wheeler J.C. 1990, ApJ 358, L5 (reproduced by permission of the AAS) Copyright ©; **Fig. 5.10** from figs. 1 and 2 of Tuchman Y., Mineshige S., Wheeler J.C. 1990, ApJ 359, 164 (reproduced by permission of the AAS) Copyright ©

Fig. 6.3 from fig. 3 of Fukue J., Yokoyama T. 1988, PASJ 40, 15 Copyright ©; **Fig. 6.5** from fig. 2 of Yamada T., Mineshige S., Ross R.R., Fukue J. 1994, PASJ 46, 553 Copyright ©; **Fig. 6.8** from fig. 3 Watarai K., Takahashi R., Fukue J. 2005, PASJ 57, 827 Copyright ©; **Fig. 6.9** from fig. 2 of Fukue J. 2003, PASJ 55, 1121 Copyright ©; **Fig. 6.10** from fig. 2 of Takahashi R., Yonehara A., Mineshige S. 2001, PASJ 53, 387 Copyright ©; **Fig. 6.11** from fig. 1 of Fukue J. 2006, PASJ 58, 461 Copyright ©

Fig. 8.7 from fig. 5 of Matsumoto, R., Kato S., Fukue J., Okazaki A.T. 1984, PASJ 36, 71 Copyright ©; **Fig. 8.8** from fig. 1 of Kato S., Honma F., Matsumoto R. 1988, PASJ 40, 709 Copyright ©; **Figs. 8.9, 8.10** from figs. 6 and 7 of Fukue J. 1987, PASJ 39, 309 Copyright ©

Figs. 9.1–9.4 illustrated by K. Yoshikawa; **Figs. 9.5, 9.6** from figs. 1 and 2 of Narayan R., Kato S., Honma, F. 1997, ApJ 476, 49 (reproduced by permission of the AAS) Copyright ©; **Fig. 9.7** from fig. 8 of Manmoto T., Kato S. 2000, ApJ 538, 295 (reproduced by permission of the AAS) Copyright ©; **Figs. 9.8, 9.9** from figs. 1 and 7 of Nakamura K.E., Kusunose M., Matsumoto R., Kato S. 1997, PASJ 49, 503 Copyright ©; **Fig. 9.10** from fig. 1 of Manmoto T., Mineshige S., Kusunose M. 1997, in *Proc. IAU Symp. 184, Hot Universe*, ed. K. Koyama, p.417 Copyright ©; **Fig. 9.11** from fig. 1 of Manmoto T., Takeuchi M., Mineshige S., Kato S., Matsumoto R. in *Physics of Accretion Disks*, eds S. Kato, S. Inagaki, S. Mineshige, J. Fukue, p60 (with kind permission from G+B Publishing Group) Copyright ©; **Fig. 9.12** from figs. 1 and 2 of Manmoto T., Takeuchi M., Mineshige S., Matsumoto R., Negoro H. 1996, ApJ 464, L135 (reproduced by permission of the AAS) Copyright ©; **Fig. 9.13** from fig. 15 of Igumenshchev I.V., Abramowicz M.A. 2000, ApJS 130, 463 (reproduced by permission of the AAS) Copyright ©; **Fig. 9.14** from fig. 3 of Mineshige S., Negoro H., Matsumoto R., Machida M., Manmoto T. 2002, in *Current High-Energy Emission around Black Holes*, ed. C.-H. Lee, H.-Y. Chang (World Scientific, Singapore), p.119 Copyright ©; **Fig. 9.15** from fig. 11 of Kato Y., Mineshige S., Shibata K. 2005, ApJ 605, 307 (reproduced by permission of the AAS) Copyright ©; **Fig. 9.16** from fig. 1 of Ohsuga K., Kato Y., Mineshige S. 2005, ApJ 627, 782 (reproduced by permission of the AAS) Copyright ©; **Fig. 9.17** from fig. 1 of Yuan F., Quataert E., Narayan R. 2003, ApJ 606, 894 (reproduced by permission of the AAS) Copyright ©

Fig. 10.1 illustrated by K. Ohsuga; **Figs. 10.2, 10.3** illustrated by K. Yoshikawa; **Fig. 10.4** from fig. 3 of Abramowicz M.A., Chen X., Kato S., Lasota J.P., Regev, O. 1995, ApJ 438, L37 (reproduced by permission of the AAS) Copyright ©; **Figs. 10.5, 10.6** from fig. 1 of Honma F., Matsumoto R., Kato S. 1991, PASJ 43, 147 Copyright ©; **Fig. 10.7** from fig. 2 of Watarai K., Fukue J., Takeuchi M., Mineshige S. 2000, PASJ 52, 133 Copyright ©; **Figs. 10.8, 10.9** from figs. 1 and 4 of Watarai K. 2006, ApJ 648, 523 (reproduced by permission of the AAS) Copyright ©; **Fig. 10.10** from fig. 2 of Watarai K., Fukue J., Takeuchi M., Mineshige S. 2000, PASJ 52, 133; Copyright ©; **Fig. 10.11** from fig. 1 of Watarai K., Mizuno T., Mineshige S. 2001, ApJ 549, L77 (reproduced by permission of the AAS) Copyright ©; **Figs. 10.12–10.15*** from figs. 1, 2a, 3, 4, 5, and 11 of Honma F., Matsumoto R., Kato S. 1991, PASJ 43, 147 (* axes being adapted by K. Nakagawa)

Fig. 10.16 from fig. 5 of Watarai K., Mineshige S. 2003, ApJ 596, 421 (reproduced by permission of the AAS) Copyright ©; **Fig. 10.17** from fig. 1 of Ohsuga K., Mineshige S., Watarai K. 2003, ApJ 596, 429 (reproduced by permission of the AAS) Copyright ©; **Fig. 10.18** from fig. 3 of Haba Y., Terashima Y., Kunieda H., Ohsuga K. 2004, in *Proc. 35th COSPAR Scientific Assembly*, p.1791 Copyright ©; **Figs. 10.19, 10.20** from figs. 3 and 10 of Ohsuga K., Mineshige S., Mori M., Umemura M. 2002, ApJ 574, 315 (reproduced by permission of the AAS) Copyright ©; **Figs. 10.21, 10.22** from figs. 1 and 4 of Kohri K., Mineshige S. 2002, ApJ 577, 311 (reproduced by permission of the AAS) Copyright ©

Figs. 11.3, 11.4 illustrated by Ideta M.; **Fig. 11.5** from fig. 1 of Wagoner R.V., Silbergleit A.S., Ortega-Rodriguez M. 2001, ApJ 559, L25 (reproduced by permission of the AAS) Copyright ©; **Fig. 11.7** illustrated by Watarai K.

Fig. 12.1 from fig. 2.6 of van der Klis 2002, in *Compact Stellar X-Ray Sources*, eds W.H.G. Lewin and M. van der Klis (Cambridge Univ. Press, Cambridge), 39 Copyright

©; **Fig. 12.2** from fig. 30 of Warner B., Woudt P.A., Pretorius M.L. 2003, MNRAS 344, 1193 (reproduced by permission of Blackwell Publishing) Copyright ©; **Fig. 12.3** from fig. 2 of Genzel R., Schödel R., Ott T., Eckart A., Alexander T., Lacombe F., Rouan D., Acschenbach B. 2003, Nature 425, 934 (with kind permission from Macmillan Magazines Ltd.) Copyright ©; **Fig. 12.4** from fig. 2.9 of van der Klis 2002, in *Compact Stellar X-Ray Sources*, eds W.H.G. Lewin and M. van der Klis (Cambridge Univ. Press, Cambridge), 39 Copyright ©; **Figs. 12.5 – 12.7** from figs. 1, 3, and 4 of Matsumoto R., Kato S., Honma F. 1988, in *Physics of Neutron Stars and Black Holes*, ed. Y. Tanaka (Universal Academy Press, Tokyo), 155 Copyright ©; **Fig. 12.8** from fig. 2 of Honma F., Matsumoto R., Kato S. 1992, PASJ 44, 529 Copyright ©; **Fig. 12.9** from fig. 1 of Kato S. 2004, PASJ 56, 905 Copyright ©; **Figs. 12.14 – 12.16** from figs. 2 – 4 of Kato S., Fukue J. 2006, PASJ 58, 909 Copyright ©; **Figs. 12.18** partially from fig. 1 of Abramowicz M.A. 2005, Astron. Nachr. 326, No.9; **Fig. 12.20** from fig. 2 of Abramowicz M.A. 2005, Astron. Nachr. 326, No.9 Copyright ©; **Fig. 12.21** from fig. 6 of Zanotti O. Font J.A., Rezzolla L., Montero P.J. 2005, MNRAS 356, 1371 (reproduced by permission of Blackwell Publishing) Copyright ©